PB267298

HYSTERETIC BEHAVIOR OF REINFORCED CONCRETE FRAMED WALLS

by

T. Y. Wang
Research Assistant

V. V. Bertero
Professor of Civil Engineering

E. P. Popov
Professor of Civil Engineering

A Report on Research Sponsored by
the National Science Foundation

Report No. EERC 75-23
Earthquake Engineering Research Center
College of Engineering
University of California
Berkeley, California

December 1975

ABSTRACT

Two identical three-story framed wall specimens, representing the lower portion of a ten-story framed wall building, were tested under monotonic and cyclic loading to study the behavior of the wall under seismic excitations. One-third-scale models of the specimen were used. The code-designed building consisted of ductile moment-resisting frames with two framed walls in the north-south direction and four framed walls in the east-west direction. Its floor system consisted of a flat reinforced concrete slab.

To simulate the boundary condition of the prototype wall as well as to transfer uniformly the applied shear force through the whole width of the wall, a portion of the flat slab was cast with the wall specimen. Shear force, axial force, and bending moment were applied to simulate the effects of gravity loads and earthquake excitations on the prototype.

After incipient failure, each specimen was repaired to study the effectiveness of the repairing technique.

Free vibration tests were carried out to determine the critical damping ratio and the frequency of vibration of each specimen before and after loading them to different levels of damage.

The test data permitted comparison of (1) the directly measured lateral displacements at different floor levels with the computed lateral displacement based on the measured flexural and shear deformation, (2) the external energy applied to the specimens with the internal energy dissipated by the specimens, and (3) the measured strength with the theoretical strength.

Based on the mechanical behavior of the wall element, nonlinear

dynamic analyses were carried out to study the response of the prototype building under different ground excitations. The main objectives of these analyses were to determine the distribution of shear and axial forces and bending moments in the different structural elements and to define the ductility demands at the critical regions of these elements.

Experimental and analytical results showed that walls of a wall-frame structural system could fail in shear when subjected to severe seismic ground motions. Depending on the plastic hinge rotation capacity of the critical regions of the frame elements, columns and beams, and on the dynamic characteristics of the ground excitations, wall failure could also lead to collapse of the entire building.

Present code design methods for wall and wall-frame systems are assessed. In addition, recommendations for designing the wall against shear failure and for improving present methods of designing dual bracing systems are offered.

ACKNOWLEDGEMENTS

The investigation reported herein is the initial phase of an ongoing series of studies conducted at the University of California, Berkeley, on the behavior of wall-frame systems under seismic excitations. Financial support for this investigation was provided by the National Science Foundation under Grant No. AEN7307734A02, subproject no. 0-21997 and Grant No. ENV76-04263, subproject no. 0-21198.

A large number of individuals contributed to this investigation. The authors are indebted to Professors R. W. Clough and C. S. Hsu for their helpful discussion and valuable suggestions. The authors would also like to express their gratitude to B. Lotz and D. Clyde for constructing the test specimens and to the staff of the Davis Hall Structural Laboratory. Graduate students S. Viwathanatepa and J. Vallenas assisted with the testing. The nonlinear dynamic analyses were carried out with the valuable technical assistance of Dr. S. Mahin, for whose help the authors are extremely grateful.

The authors would also like to acknowledge the editorial assistance of L. Tsai and the technical illustrations by L. Hashizume.

TABLE OF CONTENTS

Page

Page

Page

NOTATION

a	spiral spacing
A1, A2	linear potentiometers measuring total axial deformation of edge columns (Fig. 4.7)
A_c	area of core of spirally reinforced column
A_g	gross area of section
A_s	area of reinforcement
A_s''	area of spiral reinforcement
A_t	total floor area of first story
A_v	effective shear area of section
A_v'	area of shear reinforcement within a spacing, s
A_w	sectional area of first story walls along longitudinal direction of building
b	width of column
b_w	thickness of wall panel
C	numerical coefficient for base shear
$[C]$	damping matrix
C1, C2, ..., C7, C11, C22, ..., C77	clip gages measuring regional axial deformation of edge columns (Fig. 4.7)
CC 1, CC 2	concrete strain gages (Fig. 4.8)
CL 1, CL 2, ..., CL6	strain gages mounted on vertical reinforcement of edge columns (Fig. 4.10)
d	distance from extreme compression fiber to centroid of tensile reinforcement
$\{dr\}$, $\{d\dot{r}\}$, $\{d\ddot{r}\}$	incremental relative nodal displacement, velocity and acceleration, respectively.
$d\ddot{r}_{gH}$	scalar increment during time step in horizontal ground accelerations
D	dead load; or dimension of building in feet in a direction parallel to the applied forces

D_s	diameter of spirally reinforced concrete core
E	earthquake load
E_c	modulus of concrete
EI	flexural stiffness of section
$(EI)_i$	average flexural stiffness of i^{th} region
E_s	modulus of steel
f'_c	compressive strength of concrete
f_y	yield strength of steel
f'_y	yield strength of shear reinforcement
f''_y	yield strength of spiral reinforcement
g	standard gravity, 9.8 m-sec^{-2} (386 in-sec^{-2})
G	shear modulus
h	overall thickness of member
h_n	height in feet above base to level n
h_w	total height of wall from its base to its top
H	clear height of column
I	moment of inertia of section
K	numerical coefficient as set forth in Table No. 23-I of the UBC
[K]	stiffness matrix
K 1, K 11	clip gages measuring regional axial deformation of edge columns (Fig. 4.7)
$[K_T]$	tangential stiffness matrix
ℓ_i	length of i^{th} measured curvature region of wall specimen
ℓ'_i	length of i^{th} measured shear distortion region of wall specimen
ℓ_w	horizontal length of wall
L	live load

LP	load point
[M]	mass matrix
M_B	base moment of wall specimen
M_i	moment at center of i^{th} measured curvature region of wall specimen
M_I	moment at node I of column
M_J	moment at node J of column
M_t	torsional moment
M_T	applied top overturning moment
M_u	applied design load moment at a section
M_y	yield moment of section
N_G	net axial compressive force applied on wall specimen (195 kips)
N_u	design tensile force acting simultaneously with V_u
p	rate of strain hardening
P	force applied by lateral loading jack
P_T	total applied lateral force
P_u	axial design load in compression member
$\{r\}$, $\{\dot{r}\}$, $\{\ddot{r}\}$	displacement, velocity and acceleration, respectively, of nodal points relative to ground
$\ddot{r}_{gH}$	horizontal ground acceleration
R_i	drift index of i^{th} story
$(R_i)_{rot}$	R_i due to rotation of $(i-1)^{th}$ story
$(R_i)_{tan}$	R_i due to flexural and shear deformation occurring at i^{th} story
s	shear reinforcement spacing
SW 1, SW 2	original wall specimens
SW 1R, SW 2R	repaired wall specimens
T	fundamental period of vibration of building in direction under consideration

T_n	n^{th} period of vibration of building in direction under consideration
v_c	nominal permissible shear stress carried by concrete
v_u	total applied design shear stress
V	total lateral shear at base
V_{col}	design shear force taken by edge columns
V_{max}	shear capacity of wall
V_u	total applied design shear force at section
V_w	design shear force taken by wall panel
V_z	total applied design shear force at section of framed wall
W	total dead load of building
W 1, W 2, ..., W 6	clip gages (Fig. 4.6)
WD 1, WD 2, WD 3, WD 4	45° oriented clip gages (Fig. 4.7)
WL 1, WL 2, ..., WL 6	strain gages mounted on vertical wall panel reinforcement (Fig. 4.10)
WS 1, WS 2, ..., WS 7	strain gages mounted on horizontal wall panel reinforcement (Fig. 4.10)
Z	numerical coefficient depending upon earthquake zones (Chap. 23, UBC)
α	scalar quantity of mass proportional damping
β	scalar quantity of stiffness proportional damping
δ_1, δ_2, δ_3	total lateral displacement of wall specimen at level of first, second and third floors
δ_{1R}, δ_{2R}, δ_{3R}	displacement of wall specimen at level of first, second and third floors relative to footing of specimen
δ_{3y}	yield displacement of wall specimen at level of third floor
ΔP	lateral force correction
ε_1	abbreviation of ε_{11}, unit elongation in 1 direction

ε_{av}	average strain
ε_c	concrete strain
ε_{cu}	maximum usable strain of concrete
ε_s	steel strain
ϕ	capacity reduction factor
ϕ_i	average curvature of i^{th} measured region
γ_i	average shear distortion of i^{th} story wall panel
$\mu_{\delta 3}$	displacement ductility, equal to δ_{3R}/δ_{3y}
μ_ϕ	curvature ductility
σ_1	abbreviation of σ_{11}, normal component of stress parallel to 1 direction
σ_{12}	shear stress
σ_{av}	average stress
θ_{pl}	plastic hinge rotation capacity (fixed-end rotation excluded)
θ'_{pl}	plastic hinge rotation capacity (fixed-end rotation included)
θ_T	rotation at top of wall specimen
ξ_n	critical damping ratio corresponding to n^{th} period of vibration of building
ρ_h	ratio of horizontal shear reinforcement area to gross concrete area of horizontal section
ρ_n	ratio of vertical shear reinforcement area to gross concrete area of horizontal section
ρ_s	ratio of volume of spiral reinforcement to total volume of core
τ	equivalent to σ_{12}

1. INTRODUCTION

1.1 GENERAL

Because of the uncertainty of the magnitude and the characteristics of future earthquakes, it is not economically feasible to design structures to resist major earthquake shaking elastically [1,2,3]. According to the present design philosophy for the performance of earthquake-resistant structures, a building should be able to resist minor earthquake ground shaking without undergoing structural or nonstructural damage, to resist a sequence of moderate earthquake ground shaking with only minor repairs, and to resist major earthquake ground shaking without suffering collapse. More specifically, a structural system must provide the building with sufficient stiffness under service loading in addition to sufficient strength and energy absorption and energy dissipation capacities against severe seismic excitations.

Many structures of low and medium height consist of ductile moment-resisting frames. As the height of the structure increases, more than ten stories [4,5], for example, it is more efficient to provide the building with the required lateral strength and stiffness by means of a frame system interacting with structural walls. These structural walls, because they are usually designed to resist the total lateral shear forces, are referred to as "shear walls." However, if the length-to-depth ratio of these walls is large enough, greater than two for a cantilever wall loaded in the top [6], for example, it will be possible to design the wall such that its failure mechanism will be controlled by flexural behavior. These "flexural walls" may provide a considerable amount of energy absorption and dissipation capacity and thereby act as efficient earthquake-resisting elements.

According to the damage study of past earthquakes [7-11], some structures with structural wall elements performed very well. Other structures with similar wall elements collapsed or suffered heavy damage during severe earthquakes. Damage to the latter was primarily due to poor design or poor construction, not due to the inadequacy of the wall-frame system itself. For instance, damage to the Mt. McKinley Building and the 1200L Apartment Building during the 1964 Alaska earthquake was due to the inadequate flexural capacities of their wall piers (each containing vertical reinforcements of only two layers of #5 rebars spaced at 18-inch intervals) as well as the brittle failure of their coupling beams [7,8]. Now that the behavior of beams under high shear is better understood, the ductility of coupling beams may be improved by using the diagonal reinforcement suggested by Paulay [6] and by various methods suggested by Bertero and Popov [12,13].

Damage to the J. C. Penney Building during the Alaska earthquake was partially due to high torsional moments that developed but were perhaps mainly due to poor detailing and poor workmanship [7]. Had the main lateral force resisting elements of the building, the walls, been arranged symmetrically, most of the torsional moment generated by the earthquake excitations would no doubt have been eliminated and had the construction joint been designed according to code requirements and constructed accordingly, damage could have been minimized.

The collapse of the core towers of the Four Seasons Apartment house during the Alaska Earthquake [7] was due to the bond failure at the vertical reinforcing bar splice. Although some damage was found in the shear walls of the Indian Hills Medical Center during the 1971 San Fernando earthquake [2,10], the overall performance of the building was satisfactory. The major damage to these shear walls occurred at the location where the main vertical wall reinforcement was lapped and where the lightweight concrete floor joints the wall. This damage was repairable.

Shiga, Shibata, and Takahashi [14] have made a statistical study which shows that structures with the sectional area of the first story walls along the longitudinal direction, A_w, greater than 0.8 percent of the total floor area of that story, A_t, suffered no observable damage during past earthquakes. Some of the damaged buildings described above belong to this category (Table 1), however. Both the Mt. McKinley and 1200L Apartment Buildings have A_w/A_t ratios approximately equal to 2.8 percent; the A_w/A_t for the J.C. Penney Building is 0.8 percent. The Indian Hills Medical Center has an A_w/A_t ratio equal to only 0.5 percent. Although damage to these buildings could have been lessened with careful construction, most of the damage was due to poor design.

Building and design codes have been greatly improved based on past experiences with major earthquakes. It has been widely recognized [15,16], however, that present code design forces for relatively rigid structures can be at most one-third as great as those expected in a linear response to a severe earthquake record, even if high damping is assumed. Therefore, one must rely on the energy absorption and dissipation capacity of structural members in their inelastic range for the building to survive major ground motions. For structures designed using shear walls as their main lateral force resisting element, information on the hysteretic behavior of such walls is essential for studying the behavior of the entire structure under major earthquake excitations.

Although wall systems have been used extensively in actual buildings, information on their hysteretic behavior is sparse, especially for medium- and high-rise walls. In the past quarter-century, most of the experimental results were obtained from tests of one- or two-story reinforced concrete walls or infilled reinforced concrete frames which were subjected to simplified loading conditions. These walls had rectangular cross-sections [17], I-sections [18], or wall panels with boundary elements [19-22]. Results of tests on several rectangular high-rise walls have been reported by Cardenas and Magura [17]. They found that, depending on the percentage and distribution of the vertical reinforcement, the behavior of this type of wall is controlled by either shear or flexure.

To achieve large ductility, it is necessary to concentrate the vertical reinforcement near the outer, vertical edges of the wall cross section [17]. It is also necessary to provide good confinement for the concrete near the edges of the wall and to prevent buckling of the vertical reinforcement at the same location. It was therefore decided to investigate the behavior of the medium-rise wall with spirally reinforced edge columns because this type of framed wall has the potential for providing large strength, stiffness, and energy absorption and energy dissipation.

1.2 OBJECTIVES AND SCOPE

This report represents the first phase of an ongoing investigation at Berkeley on the mechanical behavior of walls subjected to seismic excitations. The ultimate objective of the investigation is to develop practical methods for the seismic design of combined wall-frame structural systems.

This report is concerned with studying the hysteretic behavior of medium-rise framed wall specimens when subjected to simulated earthquake loads. Special emphasis is placed on the stiffness, strength, ductility, plastic hinge rotation and energy dissipation capacity of the walls as well as their modes of failure when they are subjected to the largest predictable shear stresses. The variations of the critical damping ratio and of the frequency of the wall were studied by measuring these values after the specimens were subjected to different levels of loading and damage. The effectiveness of present methods of repairing structures was a secondary objective.

To reach the above objectives, a prototype wall-frame building was designed according to 1973 UBC [23] regulations. The nominal shear stress of the walls used in this building was selected as the maximum value allowed by the UBC, that is,

$$v_u = 10\sqrt{f'_c}$$

The dynamic response of the prototype building to the N-S component of the 1940 El Centro earthquake and to the S-16°-E component of the derived Pacoima base rock motion from the 1971 San Fernando earthquake, was analyzed by using the TABS computer program [24]. With the most critical shear to moment ratio obtained from these analyses with regard to induced shear, two identical specimens representing the three lower stories of a ten-story framed wall were tested under different loading programs to study the effect of loading reversals on their behavior. The boundary conditions of the specimens were kept as close to the realistic case as possible. The specimens were instrumented to obtain sufficient data to study the strength of the specimen, the lateral displacement at each floor level, the flexural deformation, the shear distortion, and the strain of the reinforcement and concrete at various locations.

After testing, the specimens were repaired to study the effectiveness of a commonly used repairing technique. Repairs were effected by first removing and recasting the crushed concrete and then injecting the cracks with epoxy. Free vibration tests were conducted, first, on the undamaged wall and then on the specimen at different stages of damage to determine its critical damping ratio and its frequency at each of these stages.

The experimental results were compared with the theoretical values predicted by the nonlinear finite element analysis. This nonlinear finite element analysis technique was also adopted to carry out the parametric studies of the shear capacity of the wall specimen.

The nonlinear response of the prototype building to the El Centro and derived Pacoima base rock motion was studied. Based on the results obtained from the tests and from the nonlinear dynamic analyses, present seismic design methods are evaluated and suggestions for their improvement are offered.

2. TEST SPECIMENS

2.1 PROTOTYPE BUILDING

A ten-story reinforced concrete building was designed consisting of two framed walls running along the N-S direction and four framed walls running along the E-W direction. The floor plan and elevation view of the building referred to as the prototype, are shown in Fig. 2.1. The building is symmetric with respect to both directions, thus minimizing the unfavorable torsional force that could develop during an earthquake.

The walls of the prototype selected for this study are those in the N-S direction. Because the main objective of this study is the investigation of the behavior of framed walls under the largest predictable shear stresses, it was decided to use the minimum number of two walls in the N-S direction. Although this study utilizes only two walls, it is usually desirable to have a larger number of structural walls. For example, the same prototype building designed according to AIJ Code specifications [26,27] requires a minimum number of four walls. Four framed walls running along the transverse direction were also used in the Indian Hills Medical Center which has a floor plan similar to the prototype used in this investigation (Fig. 2.2)[9].

The design of the prototype building results in panels of the walls in the N-S direction having a thickness of twelve inches and those in the E-W direction having a thickness of eight inches. The floor system diaphragms of the building consist of an eight-inch thick flat slab. The exterior columns of the prototype building, including the boundary columns of the E-W walls, are all 20 inches by 20 inches. All the interior columns are 24 inches by 24 inches. The exterior columns are further interconnected with twelve-inch wide and 16-inch deep spandrel beams.

The prototype building was designed according to the third category specified in Table 23-I of the 1973 UBC. That is, the horizontal force factor, K, of Eq. (14-1), Chap. 23 of the UBC, was selected to be 0.8. The building was assumed to be located in Seismic Zone Number 3. Therefore, the value of Z in this equation was 1.0.

2.2 DESIGN OF N-S FRAMED WALLS

According to item 2 of Table 23-I of the UBC, walls acting independently of the ductile moment-resisting portion of space frames should be capable of resisting the total required lateral forces. According to Eqs. (14-3), (14-2), and (14-1), Chap. 23 of the UBC:

$$T = \frac{0.05\ h_n}{\sqrt{D}} = \frac{0.05 \times 93}{\sqrt{61}} = 0.595 \tag{2.1}$$

$$C = \frac{0.05}{\sqrt[3]{T}} = 0.0594 \tag{2.2}$$

$$V = ZKCW = 1.0 \times 0.8 \times 0.0594 \times 19988 = 950 \text{ kips} \tag{2.3}$$

The estimation of the total weight of the building, W, is given in Appendix A.

Section 2314(g) of the UBC also requires that walls be capable of resisting a minimum torsional moment equal to the story shear acting with an eccentricity of five percent of the maximum building dimension at that level. This is computed to be:

$$M_t = 0.05 \times 180 \times 950 = 8550 \text{ k-ft.} \tag{2.4}$$

Thus total base shear per wall $= \frac{1}{2}\,950 + \frac{8550}{140} = 536$ kips

where 140 feet is the distance between the walls (assuming that all the torsional moments are resisted by the N-S walls alone, which is a conservative assumption).

The distribution of the total base shear along the height of the wall is in accord with Eqs.(14-4) and (14-5), Chap. 23 of the UBC. Fig. 2.3(a) shows the magnitude and distribution of the code specified lateral forces multipled by the load factor, 1.4 [Sect. 2627(a) of the UBC]. However, the base axial force, 1760 kips, is only equal to the unfactored axial force of 1.0 x (D + L) which was used in the tests. During severe earthquake ground shakings, the probability that either the dead or live load existing in the building has been increased by 1.4 times is very small. It is believed that a reasonable estimation of the loading condition on the wall originated by the gravitational force during a severe seismic shaking is that assuming a load factor of 1.0.

2.2.1 Edge Columns of Walls

According to Sect. 2627(c) of the UBC, edge columns should be designed to carry all the vertical stresses resulting from the wall loads in addition to tributary dead and live loads from the specified horizontal earthquake force. In this case the specified yield strength of the reinforcement was 60 ksi and the specified concrete compressive strength was 4 ksi.

(a) Tension column. - The ϕ factor for the axial tension column is 0.9 [UBC Sect. 2609(c)]; thus:

$$\frac{P_u}{\phi} = \frac{1.4(E + \text{torsion}) - 0.9\ D}{\phi}$$

$$= \frac{1.4 \times 1668 - 0.9 \times 782}{\phi} = 1812 \text{ kips} \qquad (2.5)$$

where

$$1668 \text{ k} = \frac{588{,}000 \text{ k-in.}}{1.4 \times 252 \text{ in.}} \qquad \text{(Fig. 2.3)}$$

and 782 kips is the distributed dead load transferred to the column.

Using eight #18 rebars,

$$\frac{P_u}{\phi} = 60 \times 8 \times 4 = 1920 \text{ kips} > 1812 \text{ kips}$$

(b) Compression column. - The ϕ factor for the axial compression column with spiral reinforcement is 0.75; thus:

$$\frac{P_u}{\phi} = \frac{1.4[E + \text{torsion} + (D+L)]}{\phi}$$

$$= \frac{1.4(1668 + 782 + 98)}{0.75} = 4756 \text{ kips} \qquad (2.6)$$

Using a 30-inch by 30-inch column with eight #18 rebars,

$$\frac{P_u}{\phi} = 0.85 \times 4 \times [(30\text{x}30) - 32] + 60 \times 32 = 4871 \text{ kips} > 4756 \text{ kips}$$

(c) Column spirals [UBC Eq. (10-3), Sect. 2610]

$$\rho_s = 0.45 \left(\frac{A_g}{A_c} - 1\right) \frac{f'_c}{f_y} = 0.45 \left(\frac{900}{573} - 1\right) \frac{4}{60} = 0.0172 \qquad (2.7)$$

Using #5 rebars at approximately 2-1/2-inch intervals,

$$\rho_s = \frac{\pi D_s A''_s}{\frac{\pi}{4} D_s^2 a} = \frac{4A''_s}{D_s a} = \frac{4 \times 0.31}{27 \times 2.5} = 0.0183 > 0.0172 \qquad (2.8)$$

2.2.2 Wall Panel

Section 2627(a) of the UBC specifies a load factor of 2.8 for calculating shear stresses in shear walls of buildings without a 100 percent moment-resisting space frame. This load factor is twice as large as that required to compute the flexural capacity of walls. The philosophy of using this larger load factor in designing the shear capacity of the wall is to prevent undesirable brittle shear failure. Even with this extra safety factor of two, however, there still remains the danger of the wall failing in shear. For shear, the ϕ factor is equal to 0.85; thus:

$$\frac{V_u}{\phi} = \frac{2.8(536)}{0.85} = 1765 \text{ kips} \tag{2.9}$$

Using a twelve-inch thick wall panel, the effective depth, d, of the wall is taken to be 0.8 l_w = 226 inches, wherein:

$$v_u = \frac{V_u}{\phi hd} = \frac{1765 \times 10^3}{12 \times 226} = 650 \text{ psi} \tag{2.10}$$

According to the UBC, v_u shall be less than $10\sqrt{f'_c}$ = 633 psi. However, the value of d taken as 0.8 l_w is conservative in this case since the framed wall is designed such that most of its vertical reinforcement is concentrated at its edge columns. For instance, if no vertical reinforcement is provided for the wall panel, the value of d, being the distance between the extreme compression fiber and the centroid of the tension column, becomes equal to 267 inches. In the case where a large amount of vertical reinforcement is used for the wall panel, the value of d will be less than 267 inches but still greater than 0.8 l_w (226 inches) for the following reason. According to the theoretical computation of the yield moment of the wall specimen (Sect. 5.4), the neutral axis is located 30 inches from the extreme compression fiber when the section yields. If the d value of the wall specimen is taken as the distance from the extreme compression fiber to the centroid of the area of the rebars in tension, it is equal to 78.3 inches for the specimen and 235 inches for the corresponding prototype. If this value is adopted, v_u = 626 psi < 633 psi. Therefore, the twelve-inch thick wall panel is acceptable.

(a) Horizontal wall panel reinforcement. - Using Eq. (11-33), UBC Sect. 2611:

$$v_c = 0.6\sqrt{f'_c} + \frac{l_w\left(1.25\sqrt{f'_c} + 0.2\,\frac{N_u}{l_w h}\right)}{\frac{M_u}{V_u} - \frac{l_w}{2}} > 2\sqrt{f'_c} = 127 \text{ psi} \qquad (2.11)$$

$$v_c = 0.6 \times 63.3 + \frac{282 \times (1.25 \times 63.3 + 0)}{788 - 141} = 72 \text{ psi} \qquad (2.12)$$

Therefore, v_c is taken as $2\sqrt{f'_c}$ = 127 psi when N_u is in compression. Using #6 rebars in a double layer:

$$S = \frac{A_v f_y}{(v_u - v_c)b_w} = \frac{0.88 \times 60{,}000}{(650 - 127) \times 12} = 8.42 \text{ inches} \qquad (2.13)$$

The spacing may be increased to nine inches if the more realistic value of d, 235 inches, is used in computing v_u (Eq. 2.10).

(b) Vertical wall panel reinforcement. - From Sect. 2.2.2(a):

$$\rho_h = \frac{0.88}{9 \times 12} = 0.00815 \qquad (2.14)$$

Thus according to Eq. (11-34), UBC Sect. 2611, vertical shear reinforcement shall not be less than:

$$\rho_n = 0.0025 + 0.5\left(2.5 - \frac{h_w}{l_w}\right)(\rho_h - 0.0025) = 0.0016$$

$$(\rho_n > 0.0025) \qquad (2.15)$$

According to the SEAOC recommendation [28], however, the value of ρ_n shall be the same as that for ρ_h.

The vertical wall panel reinforcement will not increase the shear capacity of a wall with a h_w/l_w value greater than 2.5 [29,30], although it will increase the flexural capacity. The use of a larger amount of vertical wall panel reinforcement is conservative from the flexural point of view, but not necessarily from the point of view of preventing shear failure. A more detailed discussion of this concept will be presented in Sects. 3.4.2 and 3.5.3.

2.3 SELECTION OF TEST SPECIMEN AND MECHANICAL CHARACTERISTICS OF MATERIALS

2.3.1 Test Specimen

For a rational selection of test specimens, it is necessary to determine first, the basic subassemblage whose test could supply the required information for the whole structure, and second, the model scale for reproducing this subassemblage. Determination of the basic subassemblage and model scale cannot be done independently since they are interrelated.

Scale. - There are many factors which can be influenced by the scale of a model. For example, the bond characteristics between presently available reinforcement and the concrete vary according to the bar sizes. Even the yielding characteristics of different bar sizes are different. While Gamble [31] has reported that the average yield strength of #18 rebars is 8.5 percent lower than that specified for Grade 60 steel (60 ksi), the yield strength of the #6 rebars used in this investigation to model the #18 rebars is 20 percent higher than the specified value of 60 ksi (Table 2). In addition, the maximum size of the aggregate used in the concrete may affect the aggregate interlocking properties in a cracked region of a reinforced concrete member. Furthermore, the influence of errors in the fabrication of specimens increases with the reduction in scale. For all these reasons, it is desirable to test specimens on the largest possible scale.

Basic Subassemblage.- Since the inelastic behavior of the wall is of the greatest interest, the whole critical (yield) zone of the prototype wall, when subjected to severe seismic excitations, must be reproduced in the test specimen. According to the moment diagram of the wall shown in Fig. 2.3(d), the base moment (588,000 k-in.) is 1.42 times the moment at the bottom of the third story (399,000 k-in.). It is unlikely that the wall can develop an ultimate moment capacity which is 1.42 times its yield moment. Therefore, it can be judged that when the base moment reaches the ultimate moment of the wall, the moment in the bottom section of the third story will be smaller than its yield moment. This, together with the fact that the total height of the first two stories (seven feet) is slightly larger than the effective depth of the wall (six feet), leads to the assumption that the yield zone or "critical region" of the wall will probably not extend into the third story. Thus, the wall specimen could be selected to represent only the two first stories. However, simulation of boundary conditions (force applications) demanded the selection of a three-story subassemblage. As will be described in Sect. 3.3, the gravity load and top overturning moment are applied at the tip of the edge columns of the wall specimen. In order to keep the local effect of these concentrated applied loads away from the critical region of the specimen and to provide a correct boundary condition for that region, it was decided to design the specimen with three stories.

According to the above consideration and the capacity of the available testing facilities, a three-story, one-third scale subassemblage model was finally selected for this study.

Except for the slab thickness, the dimensions of the specimen correspond to exactly one-third the dimensions of those in the prototype. The dimension of the specimen and the details of its reinforcement are shown in Fig. 2.4.

2.3.2 Mechanical Characteristics of Model Materials

As discussed in Sect. 2.2.1, the prototype wall structure was designed on the basis of a f'_c = 4 ksi and a f_y = 60 ksi. Thus, similar design strengths were adopted for the model materials.

2.3.2.1 Steel Reinforcing Bars

The stress-strain curves of the #6 rebars shown in Fig. 2.5 were obtained by averaging the curves of three similar test specimens. Although the specified yield strength of all the reinforcements was 60 ksi, the actual yield strength of the #6 rebars reached 73 ksi. The strain-hardening of the #6 rebars began when their strain reached 0.01. The initial strain-hardening modulus was 1000 ksi. The maximum nominal stress of the #6 rebars, 106 ksi, was reached at a strain of 0.09. Necking of the rebar could be observed when the rebar reached maximum stress. The stress-strain curve of the #2 rebars (not shown) is very close to that of the #6 rebars. Only small differences in the yield and ultimate strength of these two sizes of rebars can be found (Table 2).

The yield stress of the spiral reinforcement was 82 ksi. No clear plastic plateau could be seen on the stress-strain curve of the spirals (Fig. 2.5). Comparing the ultimate strain of the spirals, 0.024 with that of the #6 rebars, 0.200, it can be concluded that the wire used for the spiral was considerably less ductile than those for the deformed #2 and #6 bars.

2.3.2.2 Concrete

The specified 28-day compressive strength of the concrete was 4000 psi. The specimens were cast story by story. The footing concrete was purchased as ready-mixed and the rest of the concrete was mixed in the Davis Hall Structural Laboratory. Although all the concrete had the same mix design, the strength of the ready-mixed footing concrete never reached 4000 psi. The 28-day compressive strength of the concrete mixed in the laboratory was almost 4000 psi; on the day of testing, however, the strength of this mixture reached 5300 psi due to the age effect (Table 2). The typical stress-strain curve of concrete is shown in Fig. 2.6. The elastic modulus of the concrete, E_c, taken as the slope of the line connecting the origin and the point, having a stress value of 0.45 f'_c, is equal to 2800 ksi. This value is considerably lower than the UBC value of 57,000 $\sqrt{f'_c}$, which is equal to 4150 ksi for an f'_c equal to 5300 psi.

2.4 SECTIONAL STRENGTH OF FRAMED WALL MODEL

2.4.1 Flexural Strength

The flexural strength of the wall model computed in this section is based on the axial compressive force of 195 kips (195 = 1760/9, Sect. 2.2). The axial force-moment interaction diagram of the specimen is shown in Fig. 2.7 and will be discussed in Sect. 3.6.

As discussed in Sect. 2.2.1, the external moment for the design of the prototype wall is assumed to be carried by the edge columns of the framed wall. According to this assumption, the flexural strength of the framed wall model is equal to:

$$M_u = \phi(213 \times 84 + 195 \times 84/2) = 0.9 \times 26{,}100$$
$$= 23{,}500 \text{ k-in.} \tag{2.16}$$

where 213 kips is the tensile strength of the column, 195 kips is the unfactored gravitational force, and 84 inches is the distance between the centroid of the columns. The flexural capacity contributed from the wall panel of the framed wall was not included in the above calculation. If the entire framed wall is considered as a flexural member, its flexural strength computed according to the UBC will be equal to:

$$\frac{M_u}{\phi} = 34{,}000 \text{ k-in.}^{*} \tag{2.17}$$

$$M_u = 0.75 \times 34{,}000 = 25{,}500 \text{ k-in.} \tag{2.18}$$

This value is 8.5 percent higher than the value computed according to the criteria given by Eq. 2.16 . If the actual strength of the materials and the strain-hardening of the reinforcement had been considered during the computation and had a more realistic maximum usable concrete strain of 0.0038** been adopted, the flexural strength of the specimen would be equal to 42,000 k-in.*** (Table 3). This value is 179 percent of the value computed in Eq. 2.16 and is 124 percent of that computed in Eq. 2.17 . The significance of these percentages will be discussed in Sect. 3.4.2.

2.4.2 Shear Strength

According to the assumption made in Sect. 2.2.2, the shear strength of the prototype wall is equal to:

---

*This computation is based on: (1) the linear variation of strains along a section; (2) an equivalent bilinear concrete stress-strain curve; (3) a maximum usable strain of concrete, chosen as 0.003; and (4) the specified strength of the materials. Strain-hardening of the steel is not considered.

**According to the stress-strain curve of the concrete shown in Fig. 2.6, the strain corresponding to the maximum stress is 0.0031. Therefore, the maximum usable strain of the concrete could be 0.0038, rather than the value of 0.003 suggested by the UBC.

***This value is very close to the actual strength of the specimen (43,220 k-in., Table 3).

$$V_u = 0.85 \times [2\sqrt{f'_c} \times 12 \times 0.8 \times 94 + 0.8 \times \frac{94}{3} \times 0.10 \times 60]$$

$$= 158 \text{ kips} \tag{2.19}$$

If the actual strength of the materials is used and the ϕ factor is not included (f'_c = 5.3 ksi and f_y = 73 ksi), V_u/ϕ will be equal to 223 kips.* However, the value of V_u/ϕ does not consider the shear capacity of the web reinforcement of the wall edge columns. Neither the UBC nor the ACI Code [25] suggests any method for evaluating the shear capacity of the wall with edge columns; and although the AIJ Code [26] considers the shear capacity of the edge columns, it neglects the nominal permissible shear stress carried by the concrete wall panel [30]. The ultimate shear strength computed according to the AIJ Code becomes equal to that computed according to the UBC; wherein:

$$V_z = V_w + \Sigma V_{col}$$

$$= \rho_n f_y b\, l_w + 2 \times \frac{7}{8}\, bd[1.5\, v_c + 0.5\, f'_y\, (\rho'_n - 0.002)] \tag{2.20}$$

where

$f_y \leq$ 42.5 ksi, as required by the AIJ Code when $f_y >$ 42.5 ksi.

V_c = 108 psi + 0.015 f'_c = 108 + 0.05 x 4000 = 168 psi

V_z = 105 + 2 x 26.5 = 158 kips

(compared with V_u = 158 kips by the UBC) (2.21)

---

*This value is ten percent smaller than the actual strength of the specimen (248 kips, Table 3).

The test results discussed in Chapter 5 also show that the slabs offered considerable constraint to the opening of the diagonal cracks which passed through them. These results indicate that the presence of slabs also increased the shear strength of the wall specimen. However, this factor was not considered in computing the shear strength of the wall specimen.

It is clear from the above discussion that the actual shear strength of the wall specimen is difficult to estimate. Therefore, until more data on the shear capacity of a framed wall become available, it is advisable at present to estimate the ultimate shear strength of the wall according to UBC provisions, since it results in a conservative value.

2.5 FABRICATION OF SPECIMENS

In order to simulate the construction procedure in the field, the specimens were cast story by story in their vertical position. As illustrated in Fig. 2.8, the steel cage for the edge columns and the wall panel up to the second story was ready at the time that the footing was cast. Three days after each casting, the formwork for the next story was placed. The period between each casting ranged from eight to thirteen days. Figure 2.9 shows the arrangement of the slab reinforcement and Fig. 2.10 shows the formwork for casting the second story.

Following this procedure, the specimens had three construction joints. These construction joints did not influence the strength or failure mode of the specimen during testing. Unlike actual construction, however, these specimens had no vertical bar splices in their vertical reinforcement. This discrepancy was considered to be acceptable since the splices in actual structures are always located in the second story or above, which is away from the most critical region of the wall, the first story.

Specimens SW 1 and SW 2 were cast simultaneously to have a similar quality of concrete in order that their performance under different loading programs might be compared. Although the concrete strength of Specimen SW 2 was higher than that of SW 1 due to the age effect, this difference is very small and can be neglected (Table 2).

During casting, the concrete was compacted with a high frequency vibrator and cured by covering it with wet sacks under a plastic cover for one week. The forms of the lower stories were not removed until fabrication of the entire specimen was completed.

Ten days after the final casting the forms were stripped and the specimen was transferred from its cast position to its horizontal test position by a pick-up frame. Figure 2.11 shows the specimen with its pick-up frame during transfer. The specimen was then tied to reaction blocks by means of 20 1-3/8-inch diameter prestressing rods in the longitudinal direction and by four 1-3/8-inch diameter rods in the horizontal direction. Each of these rods was prestressed to 120 kips.

2.6 REPAIR OF SPECIMENS

2.6.1 Specimen SW 1

After testing of Specimen SW 1, most of the damage was concentrated in the first story. As shown in Fig. 2.12, buckling of the wall reinforcement and spalling of the entire concrete cover of the left edge column occurred. The concrete inside the confined core of the column remained in good condition. After removing all the loose concrete pieces, new concrete was cast conforming to the initial dimensions of the specimen. The compressive strength of the recast concrete at the time of testing was 3270 psi. Except for the narrow cracks in the columns of the third story, all flexural cracks in the columns and diagonal cracks in the wall panels were injected with epoxy. Figure 2.13 shows the specimen during epoxy repair. After repair, Specimen SW 1 was denoted as Specimen SW 1R.

During repair, little attention was paid to the buckled wall reinforcement. Because it was only partially straightened before recasting, premature buckling of the wall reinforcement occurred during the test of Specimen SW 1R.

2.6.2 Specimen SW 2

The condition of Specimen SW 2 before repair was similar to that of Specimen SW 1. Figure 2.14 shows the crushed zone of SW 2 after removal of the loose concrete pieces. From the experience with Specimen SW 1, it was attempted to straighten all of the buckled reinforcement. The buckled vertical and horizontal reinforcement bars that could not be straightened were cut and welded with new rebars. In addition, new horizontal reinforcement bars were placed across the crushed band between every two original horizontal reinforcement bars. In this way, the horizontal wall reinforcement in the crushed band was doubled. Further, the two layers of the wall reinforcement mesh were tied together every two intersections by a transverse hook, as shown in Fig. 2.15. This figure also shows the condition of the reinforcement in the crushed zone after repair. New concrete was cast in this zone and its compressive strength on the day of testing was 4800 psi.

The cracks in this specimen were not injected with epoxy. The presence of these cracks reduced the initial stiffness of the specimen but did not noticeably affect the energy dissipation capacity of the specimen. The behavior of the cracked reinforced concrete flexural member after the cracks on the compression side closed is similar to that of an initially uncracked member and most of the internal energy is dissipated through the plastic deformation of the longitudinal reinforcement. Therefore, sufficient information regarding the inelastic behavior of the repaired specimen can be obtained whether or not its cracks are injected with epoxy. In the case of the real structure, not only the safety but the serviceability must be considered. Thus, cracks should also be repaired to improve serviceability conditions.

2.6.3 Alternate Method of Repair

Since failure of the specimens was primarily due to the crushing of their first story wall panels, the performance of the specimens can be improved by repairing the crushed panels. One method would be to put two new layers of reinforcement on the outside of the original wall panel in the first story and then to increase the thickness of that panel. Ideally, all original concrete, crushed or uncrushed, should be removed and replaced by new concrete. If this is not done, the surface of the original concrete must be treated such that good bond can develop between the original and recast concrete. As will be discussed in Chapter 5, a nominal unit shear stress of $11.3\sqrt{f'_c}$ had been reached at the time of crushing of the wall panel. Increasing the thickness of the wall would greatly reduce the nominal unit shear stress, and, consequently, improve the overall performance of the specimen.

3. LOADING CONDITION OF WALL SPECIMENS

3.1 GENERAL REMARKS

As discussed in Sect. 2.2, the framed wall prototype was designed for the UBC specified critical load combination of gravity loads and lateral forces shown in Fig. 2.3. Unfortunately, this loading combination does not simulate the actual loading condition of the framed wall under seismic excitations. As specified by the UBC, the influence of frames and higher modes of vibration are not properly considered in the distribution of the required total base shear. An attempt to find a more realistic and more critical loading condition for the wall when the whole building is subjected to severe seismic excitations has been made and the results are reported herein. The possibility of simplifying the complicated loading condition for implementation in the available testing facility was also studied. All the elastic static analyses and the elastic response spectrum analyses made for the study described in this chapter were carried out by using the TABS computer program [24].

3.2 SEISMIC FORCES

The seismic inertial forces are generated by the vertical and horizontal ground movements and induced through the mass of the structure. The vertical ground movements will not be considered in this investigation. The reason for this is twofold. First, the axial forces generated by the vertical ground accelerations do not significantly affect the moment-axial force relationship of the wall. (This relationship will be discussed in more detail in Sect. 3.6.) Second, the peaks of the structural response to the vertical ground accelerations do not necessarily coincide with the peaks of the response to the horizontal ground accelerations. Consequently, the axial force applied on the wall specimen corresponds with the unfactored dead and live loads, and remains constant throughout the tests.

The lateral forces acting on the wall are due to the inertial forces induced in the mass of the building by the horizontal ground movements. These forces are transferred to the wall through the diaphragm (slab) of the building, and a small amount is distributed along the height of the wall according to its own mass. Because the mass of the wall is relatively small compared to the mass of the entire building, the distributed inertial forces were not considered during the tests.

3.3 SIMULATION OF SEISMIC FORCES

Figure 3.1(1)(a) shows the free-body diagram of the lower portion of the prototype wall loaded as shown in Fig. 2.3(a). The total axial force or gravity load (1760 k) at the base can be replaced by two axial loads placed at the top of the edge columns of the third story wall [Fig. 3.1(1)(b)] This type of axial force simulation differs from the actual one in that it introduces an axial force which remains constant throughout the height of the bottom three stories of the wall as well as induces some stress concentration in the upper part of the third story of the wall. Since the combination of applied forces - shear, axial and bending moment - in the third story of the wall is far from inducing critical stresses to this story, the stress concentration introduced by the simulated forces should not affect the overall performance of the wall.

The top overturning moment of the third story wall was simulated by a pair of axial forces, equal and opposite in sign, and applied at the edge columns of the wall as shown in Fig. 3.1(1)(b). As shown in Fig. 3.1(1)(a), much of the horizontal force acting on the top of the wall, 662 kips, is the shear force transferred directly from the wall in the fourth story.

The remaining force of 42 kips is the inertial force generated by the mass of the third floor and transferred to the wall through the slab of that floor. In the model these forces were all transferred to the top of the wall specimen by distributing them through a loading fixture along the length on both sides of the six-inch thick slab adjoining the wall. The details of this loading fixture will be discussed in Sect. 4.4.3.

3.4 SIMPLIFICATION OF LOADING CONDITION

3.4.1 Prototype

The loading condition shown in Fig. 3.1(1)(a) is too complicated to be reproduced in the test. To reduce the number of jacks and controllers, the two small inertial forces and the two small axial forces acting on the first two floors of the wall were applied on the top of the wall specimen. The two small overturning moments acting on the first two floors were neglected. The loading condition of the bottom three stories of the prototype wall after simplification is shown in Fig. 3.1(1)(b). This simplified loading attempts to simulate the state of internal forces on the bottom section of the prototype wall subjected to the loads shown in Fig. 3.1(1)(a). The bottom section is critical because of the manner in which the walls have been designed. Figure 3.1(1)(b) also represents the free-body diagram of the bottom three stories of the wall subjected to the equivalent lateral force shown in Fig. 2.3(b). The difference between the moment-shear diagrams in the bottom three stories of the prototype wall which resulted from the simplified loading compared with those resulting from the actual loading [Figs. 2.3(c) and 2.3(d)], is negligible.

3.4.2 Model

Since the model is one-third scale, the force to be imposed on it would be one-ninth of the corresponding force acting on the prototype.

If the inertial force generated by the earthquake excitations were to be reproduced, the mass of the model would have to be increased three times in order to simulate the corresponding inertial force acting on the prototype. However, it was not necessary to do so in this case because the type of loading selected was pseudo-static as previously discussed. The loading condition shown in Fig. 3.1(1)(c) is obtained by dividing the forces and moment shown in Fig. 3.1(1)(b) by 9 and 27, respectively. Since the specimens are to be loaded up to failure, it is necessary to know the maximum forces expected when failure occurs in order to design the testing facilities and to plan such tests. During the tests, the top overturning moment and the lateral shear were increased proportionally according to Fig. 3.1(1)(c). Because the flexural strength of the wall specimen could control the failure, the base moment of the specimen should be loaded until reaching its ultimate flexural capacity. The loading condition at this ultimate state is referred to as the ultimate loading condition and is shown in Fig. 3.1(1)(d).

The estimated ultimate moment capacity of the wall (42,000 k-in.) shown in Fig. 3.1(1)(d) was computed according to the actual strength of the materials as discussed in Sect. 2.4.1. Since this value is 179 percent of the moment capacity (23,500 k-in.) estimated according to the UBC provisions [Sect. 2.4.1, Eq.(2.16)], the maximum shear force that could develop in the wall [160 kips, Fig. 3.1(1)(d)] corresponding to this moment (42,000 k-in.) is 179 percent of the value (90 kips) corresponding to the UBC ultimate moment (23,500 k-in.). The unexpected 79 percent of extra shear force could result in the brittle shear failure of the wall.

The loading condition shown in this figure is not actually used in the tests because the ratio between the shear and overturning moment given by the UBC is not realistic. The story shears specified by the UBC are not equivalent to those that could occur during an actual earthquake. Thus, the ultimate loading condition to be selected is the one among all the realistically possible situations, which produces the most critical load combination with respect to the stresses controlling the inelastic behavior of the wall. The selection of this critical combination is discussed in the next section.

3.5 CRITICAL LOADING CONDITION OF WALL

3.5.1 Influence of Frames

The UBC requires the loading condition of the wall to be checked when the wall interacts with frames to resist the total lateral forces. This loading condition, shown in Fig. 3.1(2)(a), is not the controlling condition because the presence of the frames helps the wall to resist the total lateral forces. If the code specified lateral forces were the maximum probable forces that could be developed during an actual earthquake, the presence of the frames would be favorable to the walls. According to the loading condition shown in Fig. 3.1(2)(b), however, from the point of view of developing shear stresses for major earthquake excitations, the restraint provided by the frames is unfavorable to the wall. The shear span* of the wall is reduced to 2.5 under frame restraint. More specifically,

---

* The shear span of the wall under a particular loading condition is defined as the fraction obtained by dividing the elevation at which the equivalent lateral force corresponding to that loading condition is applied [which is equal to 784 inches as shown in Fig. 2.3(b)] by the effective depth of the wall; that is, $0.8\ l_w = 225.6$ inches. The shear span of the wall under the loading condition shown in Fig. 2.3(a) is 3.5.

to reach the same amount of ultimate base moment, the base shear of the wall specimen must increase by 39 percent as indicated by comparing the values in Figs. 3.1(1)(d) and 3.1(2)(d). This significant increase in shear could change the failure mode of the wall from ductile flexural failure to brittle shear failure.

3.5.2 Influence of Higher Modes of Vibration

The results of the dynamic response spectrum analysis of the prototype building is shown in Figs. 3.1(3) and 3.1(4). The spectrum used was the N-S component of the 1940 El Centro earthquake record, with five percent critical damping. Using the fundamental mode alone [Fig. 3.1(3)], the distribution of lateral forces specified by the UBC is equivalent to the dynamic response spectrum analysis of the structure [32]. Correspondingly, the ultimate loading conditions of the wall specimen shown in Figs. 3.1(2)(d) and 3.1(3)(d) have similar values. If the influence of the higher modes is included, there will be a tendency for the shear span of the wall to further decrease. The results shown in Fig. 3.1(4) were obtained by considering the square root of the sum of the square of the response from the first three modes of the prototype. In this case the shear span of the wall would be equal to 2.30. For the same ultimate moment, the shear force developed in Fig. 3.1(4)(d) is 52 percent higher than that shown in Fig. 3.1(1)(d). Similar analysis was done by using the spectrum of the S-16°-E component of the derived Pacoima base rock motion of the 1971 San Fernando earthquake. The results of this analysis are shown in Fig. 3.1(5). The ultimate loading condition shown in Fig. 3.1(5)(d) is very close to that shown in Fig. 3.1(4)(d).

3.5.3 Summary

According to the discussions in Sects. 3.4.2, 3.5.1, and 3.5.2, the actual shear force that can be developed in the wall could be considerably higher than the unfactored UBC specified shear force. This is because the amount of shear force that can be developed would be controlled by the actual flexural strength of the wall, and affected by the interaction between the walls and the frames and by the higher modes of vibration. The different loading conditions are shown in Figs. 3.1(1) to 3.1(5). The most critical loading condition is shown in Fig. 3.1(4); this was the condition selected for use in the tests. Using this loading condition, the shear force, 2187 kips (which is equal to 9 x 243 kips), that could have developed in the prototype wall during ground accelerations of the 1940 El Centro earthquake is 4.03 times the unfactored UBC force of 536 kips [1.0 x (E + torsion), Sect. 2.2]. Although the UBC also specifies a load factor of 2.8 in designing the shear strength of walls, this load factor together with this code strength reduction factor, ϕ, ($2.8/0.85 = 3.3 < 4.08$) is apparently not large enough to prevent the actual shear that could be induced in the wall from exceeding the code designed wall shear strength before it reaches its flexural strength and resulting in shear failure.

Except for some advanced methods such as the nonlinear finite element analysis technique, the shear strength of reinforced concrete members is still estimated using empirical formulas. As discussed in Sect. 2.4.2, these empirical formulas are not very accurate and usually result in conservative values. More specifically, the actual shear capacity of the wall may be larger than that estimated and as such, this larger value of shear capacity might prevent brittle shear failure from occurring. However, because at present there is a lack of reliable test data, there is no quarantee that walls designed according to UBC specifications, despite the higher specified load factor of 2.8 for shear design, will not undergo brittle shear failure. Therefore, a more rational design method is necessary

3.6 N-M INTERACTION DIAGRAM OF THE WALL

The axial force-moment interaction of the wall specimen is controlled by its shear strength and is determined according to the 1971 ACI Code [25].* The diagram of this interaction is indicated by solid lines in Fig. 2.7. The ϕ factor for the N-M curve above the N_G line (since N_G is approximately equal to 0.1 $f'_c A_g$ = 198 kips) is taken as 0.75, and that below the N_G line is increased linearly to 0.90 as the axial force decreases from N_G to zero [Sect. 2609(c).2.D of the UBC]. The M_u/V_u value used to determine the solid line of the shear strength versus axial force curve is taken to be 262.5 inches, which corresponds to the M_u and V_u value shown in Fig. 3.1(1)(d). The dashed line curves shown in Fig. 2.7 are computed without considering the ϕ factor and are determined according to (1) the actual stress-strain curve of the steel; (2) a more realistic maximum usable strain of concrete, 0.0038; and (3) the actual strength of concrete, f'_c = 5300 psi. The M_u/V_u value used in determining the dashed line of the shear strength versus axial force was 173 inches, which corresponds to the M_u/V_u value shown in Fig. 3.1(4)(d).

As shown in Fig. 2.7, the actual strength of the wall specimen is much higher than that computed using either the UBC or ACI Code. This figure also reveals the danger of shear failure because the dashed N-M

---

*In computing the shear strength, the only difference between the UBC and ACI Code is the value of N_u. According to Eq. (11-33) in Chap. 26 of the UBC, the value of N_u, when compressed, shall be taken as zero for buildings located in Seismic Zone 3. The ACI Code does not offer an equivalent recommendation.

curve is outside the dashed shear strength curve for an axial force level above 100 kips and below 1000 kips. The axial force at the balanced point of the dashed curve, 1040 kips, is 5.3 times the axial force corresponding to the unfactored gravity load of 195 kips [1.0 x (D + L)]. Therefore, even under a vertical ground acceleration as large as 0.5 g, the fact that the total probable maximum axial force (195 + 0.5 x 195 = 293 kips) is well below the balanced point, leads to the conclusion that the effect of this force (293 kips) on the ductility of the specimen will be small.

4. EXPERIMENTAL SETUP AND TESTING PROCEDURE

4.1 GENERAL SETUP

The experimental setup, including the wall specimen and the testing facility is shown in Fig. 4.1. As shown in this figure, the specimen is tested in a horizontal position. The testing facility consists of reaction blocks, loading devices, ancillary devices and instrumentation using a data aquisition system. These are briefly described below.

4.2 REACTION BLOCKS

As shown in Fig. 4.1(a), the reaction blocks include reinforced concrete blocks supporting the specimen and the axial jacks, as well as a steel anchor box supporting the lateral loading jack. Except for reinforced concrete blocks D and E, all the other reinforced concrete blocks and the steel box were anchored to the tied-down slab of the laboratory test floor by six two-inch diameter prestressing rods. Each rod provides 300 kips of prestressed force. Reinforced concrete blocks A1, D and A2 were laterally tied together by eight 1-3/8-inch diameter prestressing rods with each rod providing 120 kips of prestressed force. Reinforced concrete blocks B1, E and B2 were laterally tied in the same manner except that reinforced concrete block C, designed to take the total applied lateral force, was also attached to them by four 1-3/8-inch diameter rods.

The forces acting on the reaction blocks were transferred to the test floor through friction between these blocks and the floor. The frictional design coefficient between them was assumed to be one-third. During the test of Specimen SW 1, however, it was discovered that these blocks were unable to supply the necessary reaction for testing up to failure of that specimen. The main reason these reinforced concrete blocks failed to supply sufficient reaction was that a tar paper had been placed on the floor slab when these blocks were being cast. This tar paper consisted of two layers of paper with one layer of tar between them. The tar layer acted like a lubricated lamina during the test and reduced the frictional coefficient between the reaction blocks and the floor to 0.02 as proven by a series of friction tests carried out in the Structural Laboratory at the University of California at Berkeley [33].

After the movement of the reinforced concrete blocks was detected, Blocks A1, D and A2 were temporarily supported by a steel reaction frame which was tied to the test floor by eight two-inch diameter rods. Blocks B1, E and B2 were supported by one-inch thick steel plates partially surrounding them. These plates were tied to the test floor by eight two-inch diameter and twelve 1-3/8-inch diameter prestressing rods. After anchorage of the reinforced concrete blocks was improved, their movement became considerably restrained during the remainder of the test. In the future, it is planned to lift the blocks, remove the paper, and set the blocks over a thin layer of hydrostone.

The performance of the steel anchorage box was excellent during the tests because the base plate was set on a thin layer of hydrostone before being anchored with short prestressed bolts to the tie-down slab.

4.3 LOADING DEVICES

4.3.1 Hydraulic Jacks

All the hydraulic jacks were double-acting, with a 14-inch bore diameter and a seven-inch shaft diameter. The lateral loading jack is of a rear trunnion mounting type. Its maximum loading capacity, push or pull, is 346 kips when operating at the maximum 3000 psi oil pressure of the laboratory hydraulic system. This jack has a maximum stroke of 12 inches which was considered adequate for accommodating the maximum expected lateral deformation capacity of the specimen. The force applied by this jack is directly measured by a 350-kip capacity load cell connected to one end of the hydraulic cylinder's shaft (Fig. 4.1).

The two axial loading jacks are identical. They are clevis mounted and have a maximum stroke of ten inches. When operating at a hydraulic pressure of a 3000 psi, they have a loading capacity of 460 kips when acting in compression, and a 346-kip loading capacity when acting in tension. The capacity of the load cells mounted on them is 460 kips.

4.3.2 Servo-Hydraulic Controlling System

Each of the hydraulic jacks was operated by an electrically controlled 16-10 DYVAL servo-valve. The force generated by each jack was measured by a load cell attached to it as shown in Fig. 4.2. Each of the servo-valves was controlled by an MTS 406.11 controller. The basic systems using MTS 406.11 controllers are also shown in this figure.

The electrical output from the load cell measuring lateral force and from the linear potentiometer measuring lateral displacement of the specimen at the level of the third floor is used as input to the transducer conditioners of controller A, Fig. 4.2. The signal from these two conditioners is then transferred to the feedback selector. The feedback selector then determines whether signals from either one of the two conditioners or a signal from an external transducer conditioner will then be used as input to the servo-controller. In this manner, the lateral loading jack could be operated under load or displacement control. The signal of the transducer conditioner of controller A, which is connected to the load cell of the lateral loading jack, is also used as the program input to controllers B and C, (Fig. 4.2).

During the tests, two 97.5-kip forces simulating the gravity load are first applied to the specimen by manually operating controllers B and C of the two axial loading jacks. By adjusting the input amplitude in controllers B and C to set the ratio between the lateral force and the additional axial forces, the whole loading system is automatically controlled by an input function to controller A. At present, this controller is manually operated.

The output of linear potentiometer δ_3 (Fig. 4.2) is continuously plotted by the Y-channel of an X-Y recorder. The output of the load cell of the two axial loading jacks is plotted by the Y- and Y'-channels of an X-Y-Y' recorder. The output signal of the lateral loading jack load cell is used to drive the X-channel of all X-Y and X-Y-Y' recorders (Fig. 4.2).

4.4 ANCILLARY DEVICES

4.4.1 Actuator Supporting Device

According to the arrangement of the loading system selected (Fig. 4.1), as long as the shafts of the actuators are not connected to the specimen, they will remain hanging as cantilevers from their supports at the reaction blocks. Because of their large weight, it was necessary to support these shafts on auxiliary frames, Fig. 4.3. By sliding on teflon pads attached to these frames, the actuators can be rotated around their pin-connections at the reaction blocks. This enables the actuators to be displaced from their testing position, thereby facilitating installation and removal of the specimens.

4.4.2 Deformation Guidance Device

The flexural stiffness of the specimen is relatively small about its weak axis. If the specimen is not supported somewhere along its length, the bending moment due to its own weight and the weight of the transferring devices attached to it will produce flexural cracks at the face of the footing. It is therefore convenient to support the specimen along the edge of its slabs, as indicated in Fig. 4.4. To minimize friction, special steel plates are anchored to the edge of the slabs. These plates slide on teflon pads attached to the slabs.

Because high axial force is applied on the specimen, there is the danger that the specimen will become unstable and start to deform upward. Special holding-down devices were therefore added to prevent such upward movement of the specimen. These devices are shown in Fig. 4.4.

4.4.3 Transfer Loading Device

In order to have a uniform distribution of the applied lateral shear force on the top of the specimen, this shear force was transferred to the specimen through a loading fixture as shown in Fig. 4.5. This loading fixture consists of two pairs of 10 x 15.3 channels and a loading yoke. The lateral shear was transferred from each pair of channels through ten one-inch diameter bolts to the slab of the specimen. Because of the relative axial stiffness between the channels and the slab, the shear stress transferred to the slab near the loading yoke is initially higher than that at the opposite end. However, when the slab was subjected to high shear forces, the slabs cracked and this permitted more uniform distribution of the shear stress. The forces simulating the gravity load and top overturning moment were directly applied on the tip of the edge columns as shown in Fig. 4.1.

4.5 SPECIMEN INSTRUMENTATION AND DATA AQUISITION SYSTEM

4.5.1 External Instrumentation

The schematic plan of the external instrumentation is shown in Figs. 4.6 and 4.7. This instrumentatior was designed to obtain data on lateral displacement, curvature, shear distortion, and concrete strain, using electrical and mechanical transducers, as well as photogrammetric readings.

4.5.1.1 Measurement of Lateral Displacement

The lateral displacement of the specimen at the mid-depth of each floor was measured by three linear potentiometers marked as δ_3, δ_2 and δ_1 in Fig. 4.6. These measurements are based on the assumption that the slabs and the walls between the edge columns are laterally inextensible so that the lateral displacement measured at the left and the right sides of the specimen have the same value. Although several hair cracks were found in the slabs during the tests, it is believed that the amount of slab extension is very small compared with the lateral displacement. As shown in Fig. 4.8, another error introduced in the lateral displacement measurement was due to the axial deformation of the specimen. This error is also negligible. For instance, at LP 181 or Specimen SW 1, the total extension of the left column was 1.1 inches, which introduced an error of 0.013 inches in the measurement of δ_3. This error was only 0.3 percent of the δ_3 value at that load point.

Three dial gages were placed against the footing surface to measure the lateral translation and the rotation of the footing, Fig. 4.6. All gages have a total travel length of 0.5 inches. Although these three gages were sufficient for defining the rigid body movement of the footing, the value computed could be in error if this movement were large and the surfaces around the points, which the gages were in contact with, were not well-defined (flat and smooth). As will be discussed in Sect. 5.2.1, the movement of the reaction blocks was large at LP 90 of Specimen SW 1 due to the insufficient frictional force between the blocks and the tied down slab. It is believed that large errors were involved in computing the rigid body movement of the specimen at this load point.

4.5.1.2 Measurement of Curvature

The variation of the curvature throughout the height of the specimen was studied by dividing the height of the wall in seven consecutive regions and determining the average curvature in each region. The average curvature in each region was determined by measuring the relative rotation between the two sections bounding each region. This was accomplished by a pair of clip gages mounted near the centerline of the edge columns (Fig. 4.6). The small dots shown in this figure represent the steel pins embedded inside the concrete. The deformation measured between two adjacent pins divided by the original distance between these two pins gives the average concrete strain between them.

In order to install clip gages K 1 and K 11 (Fig. 4.6), the measurement of the first regional curvature was begun one inch away from the face of the footing. As shown in the lower corner of Fig. 4.6, the lower end of clip gage K 11 was mounted on the pin embedded inside the column, one inch away from the footing. The lower end of clip gage C 11 was attached to the surface of the footing. Therefore, the difference between the readings in gages K 11 and C 11 primarily represents the width of the crack along the footing, which is largely the result of the slippage of the reinforcement anchored inside the footing. This type of deformation is referred to as the fixed-end rotation of the specimen, θ_F.

According to the nonlinear finite element analysis of the bond study reported in Ref. 34, the concrete in the anchorage zone surrounding the deformed reinforcing bar tends to form inclined ring cracks and deforms together with the bar. In the tests, the reference surface of the fixed-end rotation measurement, the footing surface, was deformed in the same direction as the slippage of the reinforcing bar, introducing an error into the measurement of this slippage. As a result of this error, the measured fixed-end rotation was smaller than the actual value, but the difference is believed to be slight.

The axial deformation and the tip rotation of the specimen can be measured either by linear potentiometers A 1 and A 2, or by summing the clip gage readings from C 1, C 2 to C 7, and C 11; and C 22 to C 77. Since the lateral displacement of the specimen was larger than its axial deformation, however, an error was introduced, sometimes reaching 16 percent, in the A 1 and A 2 readings. Therefore, the computation of the tip rotation of the specimen, θ_T, is based on the clip gage readings.

4.5.1.3 Measurement of Shear Distortion

The average shear distortior of the wall panel in each story was measured by a pair of linear potentiometers placed diagonally across from each other. The principle of relating the measurement of the relative movement of two diagonally oriented points to the average shear distortion is discussed in Ref. 12. Data on the shear distortion of the wall panel in the third story was not available for Specimens SW 1 or SW 1R.

The 45-degree oriented clip gages WD 1 and WD 2 shown in Fig. 4.7 were installed in Specimen SW 2 to measure the diagonal strain in the lower corners of the first story wall panel. They were mounted on the pins embedded in the concrete wall panel. Two additional clip gages, WD 3 and WD 4, were installed in Specimen SW 2R with their mounting bases glued on the surface of the concrete.

4.5.1.4 Direct Measurement of Concrete Strain

Two rosette strain gages and three longitudinal strain gages were attached to the surface of the concrete as shown in Fig. 4.7. Except for gage CC 2, information could not be obtained from these gages because they were broken by the cracks passing through them during the very early stages of testing.

4.5.1.5 Photogrammetric Measurements

The upper surface of the specimen in its test position was marked with a rectangular grid as shown in Fig. 4.9. This grid was used to obtain the deformation pattern of this surface through a photogrammetric technique. Two stretched wires, running completely independent of the specimen, served as reference lines. Targets were attached at every intersection of the grid lines and at several points along the reference lines to assist with the subsequent data reduction. Supported by a rigid independent steel frame, two cameras were fixed eleven feet above the specimen for taking photographs (Fig. 4.1).

4.5.2 Internal Instrumentation

Several microdot strain gages were welded on the first story reinforcement and on the part of this reinforcement embedded in the footing. The exact location of these gages is shown in Fig. 4.10. These gages permit: (1) determination of the first yielding of the specimen; (2) recording of the strain history of the reinforcement at some important location so that the stress history of the reinforcement at that location can be estimated and compared with predicted values, and that the effectiveness of the respective reinforcement can be studied; and (3) studying the anchorage effectiveness of the vertical reinforcement.

4.5.3 Data Acquisition System

For the most complete information, it would be ideal to record continously the output from all transducers by X-Y or X-Y-Y' recorders. However, only eight to ten Y- or Y'-channels were available during the tests. These channels were used to record the histories of the two axial forces: lateral displacements, δ_3, δ_2 and δ_1; curvature, ϕ_1; shear distortion, γ_1 and γ_2; and strain readings, CL 1 and WS 4. Each X-channel of these recorders was connected in series to the lateral load transducer to have plots of each of these main parameters versus the lateral load. The output from the rest of the transducers was read at selected stages of the test directly through a low-speed data aquisition system, whose heart is a NOVA minicomputer.

4.6 DETERMINATION OF TOTAL LATERAL LOAD

Due to the lateral movement of the specimen, the net axial force of 195 kips has a horizontal component, ΔP, acting on the specimen, as shown in Fig. 4.11. The distance between the hinge of the clevis mounted jack and the hinge at the clevis attachment at the tip of the column is 83 inches when there is no axial deformation of the specimen. When the specimen undergoes axial deformation, this distance varies between -0.6 inches and +1.8 inches. Because this variation has a small influence on computing the corrected lateral loads so that the distance between those two hinges is taken as a constant, 83 inches, the load correction, ΔP, can be computed according to the following equation:

$$\Delta P = \left(\sum P\right) \times \frac{\delta_3}{83}$$

For specimens tested,

$$\sum P = P_1 + P_2 = 195 \text{ kips}$$

Hence,

$$\Delta P = 195 \times \frac{\delta_3}{83} \qquad (4.1)$$

where ΔP is in kips and δ_3, the total lateral displacement of the specimen at the level of the third floor, is in inches.

The corrected lateral force, P_T, is equivalent to the total lateral force or the total shear of the specimen, and can be computed as:

$$P_T = P + \Delta P \qquad (4.2)$$

where P is the force applied by the lateral loading jack.

The maximum value of ΔP at LP 158 of Specimen SW 1 is equal to 10.6 kips, or 4.5 percent of the P value at that load point.

The vertical component of the lateral force, P, due to the axial deformation of the specimen is always less than 2 percent of the net axial force. Since the response of the specimen is less sensitive to the small variation of the net axial force, the vertical component due to the application of force P was neglected.

4.7 TESTING PROCEDURE AND LOADING SEQUENCE

4.7.1 Testing Procedure

The first specimen, SW 1, was whitewashed before testing. For the subsequent three experiments, the specimens were painted with a white, water-soluble Latex paint. All cracks could be clearly observed on the concrete surface using these kinds of surface treatment. A number was assigned to each peak and zero lateral load of a loading cycle as well as at several intermediate load points. These load points were used to define the stage of loading so that the output from the transducers at the same stage of loading could be referred to while presenting the test results. Crack progress was monitored by marking them with colored pens and labeling them with the corresponding load point numbers.

In the case of cyclic loading, the loading cycle with the same peak lateral load or same peak lateral displacement was repeated three or four times. At the peak of each loading reversal the lateral displacement was kept constant for a short period of time to read the instruments, to mark the cracks, and to take the photogrammetric readings. The same procedure was followed at zero lateral load and at several intermediate load points. The application of the third loading cycle with the same peak load or the same peak displacement was usually done without interruption. For these loading cycles, only the output of the transducers recorded by the X-Y and X-Y-Y' recorders were available.

4.7.2 Loading Sequence

The gravity load, 97.5 kips of compressive force per column, was first gradually applied to the specimen. Since the controllers commanding the axial loading jacks had to be manually operated while applying this gravity axial force, it was difficult to apply simultaneously the forces on the two jacks. Ten kips were first applied on one jack, and then 20 kips were applied on the other jack. Then a 20-kip load increment was placed on the first and the second jack in sequence; this was repeated until the load in each jack finally reached 97.5 kips. In this manner, the difference between the load in these two jacks never exceeded 10 kips while the net axial force was being applied. The top overturning moment produced by this unequal force was always below 420 k-in. (10 kips x 42 inches), which is equal to five percent of the flexural cracking moment of the specimen.

After the net axial force of 195 kips had been applied, the specimen was loaded with the lateral force and the top overturning moment. The lateral force was applied according to the loading programs shown in Figs. 5.1 to 5.4, and the top overturning moment, M_T, was varied linearly with the lateral force, P. The ratio between M_T and P was:

$$M_T \text{ (in kips-in.)} = 0.644 \times P \text{ (in kips)} \times 84 \text{ in.} \qquad (4.3)$$

where 0.644 is obtained from 238/370 [Sect. 3.5.3, Fig. 3.1(4)(c)], and 84 inches is the distance between the two axial loading jacks.

5. EXPERIMENTAL RESULTS

5.1 LOADING STAGES

To plan effectively the loading program and the loading stages at which readings of the low-speed scanner would be taken, it was necessary to define the main limits of usefulness (cracking, serviceability, yielding, etc.) of the specimen when loaded from zero up to collapse. It was also necessary to compute the resistances (bending moment, shear and axial forces) of the specimen expected at these limits of usefulness. According to the above resistances, the values of the controlling loads (lateral shears) that would force the specimen to develop such resistances were then computed. The definitions and theoretical computations of these loading stages are discussed in the following sections. These computations are compared with the experimental values in Table 3. The theoretical values were computed according to the actual material properties, rather than the UBC specified material properties. In this case, the compressive strength of concrete, f'_c, is equal to 5.3 ksi; the yield stress of reinforcement, f_y, is equal to 73 ksi (Table 2); and the elastic modulus of concrete is equal to 2800 ksi (Fig. 2.4). (According to the UBC, $E_c = 57,000\sqrt{f'_c} = 57,000\sqrt{4000} = 3,600,000$ psi.)

The experimental values of the total lateral force, P_T, corresponding to these loading stages are also indicated in Figs. 5.1 to 5.4 . Since the net axial force was kept constant throughout testing, and the top overturning moment was linearly proportional to the lateral force, all the external loads can be defined in function of the lateral force alone.

5.1.1 Flexural Cracking Load

The flexural cracking load is defined as the load which produced the first flexural crack. Its theoretical value is computed by Eq. (9-5), Chap. 26 of the UBC. During testing, the appearance of the first crack was visually noted while the applied loads were gradually increased. As soon as the crack appeared, the loads were temporarily held constant to take the scanner readings and to mark the crack. The actual cracking load is always less than the value reported because the crack must become visible before it can be detected.

5.1.2 Flexure-Shear Cracking Load

The flexure-shear cracking load is defined as the load which produces the first inclined crack resulting from the combined moment and shear. Its theoretical values (76 kips) were computed using Eq.(11-11), Chap. 26 of the UBC. Although this equation has been derived for prestressed concrete members, it is also applicable to reinforced concrete members subjected to axial compression [29]. The same observation procedure reported in Sect. 5.1.1 was used here; hence, the reported values are somewhat higher than the actual values. The web shear cracking load of the specimen computed using Eq.(11-12), Chap. 26 of the UBC, is 272 kips. This value was never reached during the tests.

5.1.3 Working Load

According to Sect. 2608(j) of the UBC, under the working load the tensile stress in the reinforcement shall not exceed the specified allowable stress of 24 ksi and the extreme concrete compressive strength shall not exceed 0.45 f'_c. Although UBC Section 2303 permits the allowable stresses to be increased by one-third when considering wind and earthquake forces, the primary concern in this investigation is to restrict the damage of the specimen when the working load is applied. More specifically, the specimen shall not have noticeable permanent deformation or excessive cracks under service loads. By limiting the stress in the reinforcement below 24 ksi, the number and size of flexural cracks can be checked. By limiting the stress in the concrete below 0.45 f'_c, concrete will be restricted to the elastic range. For these reasons, the provision made in Sect. 2303 of the UBC was not considered.

In cases where the wall specimens were loaded as described in Sect. 3.5.3, the allowable tensile stress of the reinforcement, 24 ksi, was the controlling factor. More specifically, the stress of the reinforcement will reach 24 ksi before the extreme concrete compressive stress reaches 0.45 f'_c. The theoretical working loads, based on the allowable stress in the reinforcement and in the concrete, were 87 kips and 121 kips, respectively (Table 3).

The measured working load controlled by the allowable stress in the reinforcement was estimated using the average strain indicated by strain gages CL 1 and CL 2. The corresponding load controlled by the allowable stress in the concrete is indicated by concrete strain gage CC 2. The locations of these gages are shown in Figs. 4.7 and 4.10.

5.1.4 Yield Load

The yield load is significant in that it provides data for evaluating the inelastic behavior of the wall. This includes, among others, computations of its ductility and plastic hinge rotation. For reinforced concrete beams with one row of tensile reinforcement, the yield load can be clearly defined as the load that produces yielding of the reinforcement in that row. When considering reinforced concrete walls with distributed vertical reinforcement, however, this definition is not necessarily applicable. In this investigation, the wall specimen had eight vertical rebars in the column. In this case, it would be unreasonable to define the yield load as the first yielding since the latter applies to the yielding of only one of the eight rebars. Because most of the tensile reinforcement of the wall remains elastic when the first yield occurs at the most stressed column bar, the sectional flexural stiffness of the wall, EI, will not undergo much change. On the other hand, it is no more plausible to define the yield load as that which produces yielding of all vertical reinforcement in tension. In the closely distributed vertical reinforcement of the wall specimen there will always be some vertical tensile reinforcement near the neutral axis which will not yield even if the effective EI of the region were lowered considerably. To compromise between these two extreme definitions, the yield load of the specimen was defined as that which produces yielding of all vertical reinforcement in the tension column of the specimen. Since 74 percent of the vertical reinforcement is concentrated in its edge columns, this definition seems reasonable. However, values for first yielding of the steel are also offered in this report.

The experimental determination of this yield load was based on the reading of strain gage CL 2 (Fig. 4.10). When the strain measured by this gage exceeded the yield strain, 0.0025 (Fig. 2.5), the specimen was assumed to have yielded.

There were no abrupt changes in the slope of the P_T-δ_{3R} or M_1-ϕ_1 diagrams at the yield load. This yield load corresponded to LP 79 in Figs. 5.5 and 5.20 and to LP 35 in Figs. 5.7 and 5.29. These changes were observed when about 25 percent of the vertical reinforcement of the wall panel had yielded.

5.1.5 Crushing of Column Concrete Cover

When the strain of the extreme compressive concrete fiber exceeds the maximum usable strain of concrete, 0.0038 (Sect. 2.4.1), the corresponding load will be defined as the column concrete cover crushing load.

The experimental determination of this load was based on the reading of strain gage CC 2, attached to the concrete surface close to the extreme compressive corner. At LP 87 of Specimen SW 1, the strain reading of this gage was 0.00382. As the applied loads increased to LP 88, however, this reading dropped to 0.0036. It continued to drop as the loads were increased. Therefore, the column concrete cover must have crushed between LP 87 and LP 88. Although no such gage had been installed in Specimen SW 2R, crushing of its column concrete cover could be visually observed just before LP 31, and a sudden decline in strength could subsequently be detected in the P_T-δ_{3R} diagram (Fig. 5.8). The average strain of the column compression measured by clip gage C 22 at LP 30 of Specimen SW 2R was 0.0032. At LP 31, this value increased to 0.0061, thereby exceeding the maximum usable strain of the concrete.

5.1.6 Crushing of Wall Panel

There is no accurate theoretical value computed for this loading. Although the shear capacity of the wall specimen (223 kips) estimated in Sect. 2.4.2 did not agree with the measured crushing load of 248 kips, the difference is only about ten percent. The experimental value can always be determined by observing the sudden drop in strength which occurs immediately after the wall panel crushes. After examining the experimental data of Specimen SW 1, it was found that crushing of the wall panel was primarily due to the shear stress. To detect the stress flow, several 45-degree oriented clip gages were installed on Specimens SW 2 and SW 2R in the regions where crushing had been observed. The results of these findings will be discussed in Sects. 5.5 and 6.2.1.

5.2 GENERAL BEHAVIOR AND FAILURE MODE OF SPECIMENS

Most of the experimental results are presented as the hysteretic loops shown in Figs. 5.5-5.101. The significance of these loops will be discussed in Sects. 5.3 to 5.11. Only the general behavior and failure mode of the specimens observed during the tests as well as some important experimental results will be reported in this section.

5.2.1 Specimen SW 1

The testing program for this specimen was planned such that after several loading reversals under the working load level, it would be monotonically loaded up to incipient failure. Unfortunately, the program was interrupted three times during testing. At LP 52 (Fig. 5.1), the amplifier of the MTS 406.11 controller which commands the movement of the south axial loading jack broke down unexpectedly and the jack placed a compressive force of approximately 250 kips on the south column of the specimen. (The correct force should be 151 kips in compression.) In the meantime, the reaction blocks holding the axial loading jacks were found to have rotated and the maximum movement of the south corner of these blocks was 1/2 inch. The test had to be halted to repair the amplifier of the MTS controller and to restrain the reaction blocks from movement. Fortunately, this specimen was not significantly damaged by this accident. The maximum strain in the reinforcement recorded at LP 52 when the accident occurred was below two-thirds of the yield strain. At LP 54, after all external loads were released, only very small residual external displacements and internal strains could be detected.

At LP 80, just after yeilding, there were some difficulties in the automatic control system and the specimen was unloaded. The specimen was then monotonically reloaded up to LP 90, with a displacement ductility of four, at which time the rigid body translation and rotation of the reaction blocks supporting the specimen became significant. The tip lateral displacement of the specimen due to the rigid body movement of the support was 1.26 inches, about 32 percent of its 3.89-inch total lateral displacement. This rigid body movement increased even under constant applied external loads. It was therefore decided to unload the specimen and reload it in the opposite sense up to a displacement reversal great enough to ensure that after unloading, it reached a position close to that of the original, that is, zero lateral displacement. After improving the anchorage restraint of the reaction blocks, the specimen was subjected to a series of cycles of full displacement reversals in the working load range. Considerable initial stiffness deterioration was observed. It was then monotonically loaded up to LP 158 where a significant reduction in strength due to crushing of the concrete in the wall was observed, with a δ_{3R} = 4.25 inches (Fig. 5.5). At this point, the specimen was unloaded to avoid further serious damage. After unloading, a few cycles of full reversals at working load level were applied, resulting in very stable hysteretic loops. The specimen was then loaded in the opposite direction up to δ_{3R} = 1.9 inches, and then unloaded. This loading reversal further induced damage to the specimen, as can be seen from the unstable hysteretic behavior that resulted when the specimen was finally subjected to loading cycles in the working load range. The photos of Fig. 5.102 illustrate the damages induced at the first story of this specimen at different stages of the test. Regarding the overall behavior of this wall, the following observations can be made.

(1) The envelope from LP 0 to LP 158 of Fig. 5.5 may be considered to represent the behavior of the wall under a monotonically increasing load. This will be discussed in greater detail in Sect. 6.1.

(2) The overall behavior up to near crushing of the wall panel was essentially that expected from a ductile flexural member.

(3) At first yielding, flexural cracks in the tension column and diagonal cracks in the wall panel traversed the entire length of the specimen. All these cracks were uniformly and closely spaced at about three inches, and the diagonal cracks were inclined at approximately 45 degrees [Fig. 5.102(a)]. The spacing between the cracks was relatively small compared to the overall dimension of the specimen; consequently, much energy can be dissipated by the internal friction between numerous cracks. This can be demonstrated by the high damping ratio (nine percent) obtained from the free vibration test* of Specimen SW 2 (Sect. 5.11).

(4) Some of the diagonal cracks which formed in the wall panel of the second and third story of the specimen penetrated through the slabs and extended to the wall panel of the lower story. However, the slab offered tremendous restraint, preventing large cracks from developing.

(5) The first flexural crack appeared near the bottom of the tension column, while the first diagonal crack appeared in the first story near

---

* During the free vibration tests the amplitude of vibration was relatively small, and the axial force was not applied. The results obtained from such tests can therefore be used only as guidelines.

the upper right corner of the wall panel.

(6) The biggest flexural crack appeared at the bottom of the tension column and was 5/16-inches wide at LP 158.

(7) The column concrete cover was crushed in a progressive manner. No sudden drop in strength could be observed during this process.

(8) At LP 158, the first story wall panel crushed at the lower left corner. Immediately after crushing, the wall reinforcement in the crushed zone buckled in both directions. The direction in which the wall reinforcement first buckled was not observed. Buckling of the horizontal reinforcement tends to propagate along its length* after the load was applied in the opposite sense. At LP 181, the lower right corner of the wall panel also crushed. Finally, a crushed horizontal band across the whole width of the wall panel was formed at LP 186. The width of this crushed band ranged from eight inches near the center to 16 inches near the two ends [Fig. 2.12 and 5.102(e)]. The manner in which crushing of the wall panel occurred will be analyzed in Sect. 6.2.

Part of the important test data regarding the strength and ductility of the specimen are summarized below.

(1) The measured yield load (as defined in Sect. 5.1.4) was $P_T = 190$ kips and the corresponding yield displacement was $\delta_{3R} = 0.7$ inches. The latter is defined as being equivalent to a displacement ductility of one.

(2) The maximum load obtained in the test was $P_T = 248$ kips and the

---

* At LP 180, the crushed zone at the lower left corner was horizontally extended to the right corner, exactly at the location of the third horizontal wall reinforcement from the bottom section [Fig. 5.102(d)].

corresponding displacement was δ_{3R} = 4.25 inches, which is equivalent to a displacement ductility of 6.1 (Sect. 6.5 and Table 4). At this load, the nominal unit shear stress* was $11.3\sqrt{f'_c}$ (f'_c = 5300 psi, the actual concrete strength), that is, about 2.6 times the value ($5\sqrt{f'_c}$, f'_c = 4000 psi, the design concrete strength) expected according to the UBC design force, 1.4 E.

(3) The maximum plastic hinge rotation was 0.0207 radians (Sect. 6.5 and Table 4). This inelastic rotation was due to yielding of the tensile column steel. This steel yielded along a length of about 62 inches, that is, close to 83 percent of the effective depth of the specimen, 75.2 inches. When the plastic hinge rotation due to yielding of the steel that was embedded in the foundation was included, the total plastic hinge rotation reached a maximum value of 0.0226 radians.

5.2.2 Specimen SW 1R

The loading program of this specimen is shown in Fig. 5.2. As this was a repaired specimen, many strain gages damaged during the previous test of the original specimen could not be replaced. Therefore, information obtained from this test was less than that obtained during testing of Specimen SW 1. However, several general observations were made during testing and these are as follows.

(1) Because some cracks were too narrow to be injected with epoxy, the average initial stiffness of this specimen up to the working load (P_T = 90 kips) was about 60 percent of that of Specimen SW 1. However, no pinched shape hysteretic loops could be detected in the first few working load cycles

(2) Some of the original cracks repaired by epoxy re-opened; other

---

*The nominal shear stress is equal to $V/0.8(l_w)b_w$, where l_w is the horizontal length of the wall, and b_w is the thickness of the wall panel.

cracks newly developed between the old repaired cracks.

(3) Since most of the vertical reinforcement had been loaded into the strain-hardening region, no obvious yield point could be found either in the P_T-δ_{3R} or the M-ϕ diagrams.

(4) The initiation of wall panel crushing could be observed at LP 40 (Fig. 5.6). (As mentioned before, the buckled wall reinforcement was not straightened out during the repair of this specimen.) At LP 34, the vertical wall reinforcement near the tension column yielded and the newly cast concrete was seriously cracked in this region. Furthermore, the tensile force in the wall reinforcement where these rebars were bent inwards generated an outward force. This component forced the concrete cover to spall (Fig. 5.103). The cracked concrete cover of the newly cast wall panel near the tension column was severely damaged at LP 34 as a result of these outward forces. When the wall reinforcements in this region was subjected to high compression at LP 40, they buckled as a result of the reduction in restraining force provided by the concrete cover. This reduction was attributed to the damage incurred in the previous peak loading (LP 34). The crushed band across the whole cross-section of the wall panel (Fig. 5.104) was almost exactly the same as that of Specimen SW 1 (Fig. 2.12). This band was formed before LP 45.

(5) Splitting of the entire concrete cover of the edge columns adjacent to the crushed band was observed before LP 48, leaving only the confined core to resist the shear and axial forces.

(6) Loading reversals continued after formation of the crushed horizontal band. During these reversals, most of the lateral deformations were due to the concentrated relative deformations at this band. The part of the specimen

above the crushed region of the wall underwent a rigid body deformation.

(7) The spirals of the compression column ruptured following LP 72. The lateral resisting strength of the specimen suddenly dropped to one-half of its strength before rupture occurred. However, the specimen was still capable of resisting the axial load. Not until the spirals of the other column broke at LP 78, after the lateral load reversed, did the specimen become unstable under the axial load. Crushing of the confined cores could then be easily observed.

The steel of the spirals was more brittle than that of other reinforcements used in the specimen. As shown in Fig. 2.5, the stress-strain curve of the spiral did not have a yield plateau and its ultimate strain was smaller than that of the others. If more ductile spirals had been used, complete failure of the specimen might have been delayed.

(8) No buckling of the vertical column reinforcement was detected prior to the rupture of the spirals.

Some of the more significant test data include the following.

(1) The maximum load obtained in the test was P_T = 220.4 kips, and the corresponding displacement was δ_{3R} = 1.4 inches, which is equivalent to a displacement ductility of two. Generally speaking, the performance of this specimen was poor because of the relatively low value of ductility reached. The strength of the specimen, however, was able to reach 88.5 percent of the maximum load of Specimen SW 1.

(2) The maximum plastic hinge rotation was 0.0045, less than one-quarter the value of Specimen SW 1.

5.2.3 <u>Specimen SW 2</u>

As illustrated in Fig. 5.3, this specimen was tested under repeated reversals of lateral load and corresponding overturning moment, where the peak value of the load and/or displacement was gradually increased after three or four cycles at the same value. Under shear, this kind of excitation is critical because the stiffness and the strength of the specimen in resisting shear deteriorated under each loading reversal in the inelastic range, as shown in the V-γ_1 diagram of Fig. 5.43. Several general observations of the test and a comparison between the general behavior of this specimen and that of Specimen SW 1 are discussed in the following.

(1) The crack pattern, the spacing between the cracks, and the first appearance of flexural and diagonal cracks, is similar to that of Specimen SW 1 (Sect. 5.2.1).

(2) The largest flexural crack appeared at the bottom of the tension column and was 5/16-inches wide at LP 124. At this load point, the width of other large flexural cracks in the first story tension column ranged from 1/16-inch to 5/32 inch. The largest diagonal crack in the first story wall panel was 3/32-inches wide. The width of the cracks in the second and third stories of the specimen never exceeded 1/16 inch.

(3) Except for the flexural crack running along the face of the footing, no other horizontal crack opened up across the cross section of the specimen. This observation differed from that noted in tests on full-size reinforced concrete cantilever beams under a similar loading program [12,13]. In those tests, several cracks nearly perpendicular to the axis of the beam were observed across the whole beam cross-section.

(4) Each time the absolute value of the peak deformation of a hysteretic loop was increased, there was a degradation in the initial stiffness and energy dissipated during the following cycle, as compared with the

values in the previous cycle.

(5) Although the mechanism of failure was not significantly affected, crushing of the concrete at the wall corner and buckling of the wall reinforcement were accelerated by repeated cycles of reversed deformation. No crushing of column concrete cover was observed until the wall concrete crushed. The entire column cover split due to dowel action after the wall concrete crushed. (The column was subjected to dowel action in the band wherein the wall concrete had crushed and the wall reinforcing bars had buckled.) During the reversal after the lower left corner of the wall crushed (LP 129), the concrete in the lower right corner also started to crush (LP 133). During the next cycle of reversals, the concrete crushed and spalled along a band extending horizontally through the wall about ten inches from the footing [Fig. 5.105(c)]. At this stage, nearly all the shear was resisted by the dowel action offered by the confined core of the edge columns which began acting as short columns of a frame, Fig. 5.106.

(6) Although testing of Specimens SW 1 and SW 2 were stopped after a considerable decrease in lateral resistance, both specimens were capable of resisting the effect of gravity loads because their edge columns did not undergo failure.

Some important test data are summarized below and compared with those obtained for Specimen SW 1.

(1) The measured yield load was 202 kips. This value is 12 kips higher than that of SW 1, probably due to the higher concrete strength of this specimen (Table 2) and the fewer working load cycles it had undergone before yielding (Figs. 5.1 and 5.3). The corresponding yield displacement of this specimen was δ_{3R} = 0.7 inches, exactly the same as that of SW 1.

(2) The maximum load obtained in the test was P_T = 245 kips, slightly less than that of SW 1, 248 kips. Its maximum lateral displacement before a significant drop in strength occurred was δ_{3R} = 2.94 inches, corresponding to a displacement ductility of 4.2. This value is about 70 percent of that for SW 1.

(3) The maximum plastic hinge rotation was 0.0125 radians, about 60 percent of that for SW 1. If the plastic hinge rotation due to yielding of the reinforcement inside the anchorage zone were included, this value would increase to 0.0142 radians, about 63 percent of that obtained for SW 1.

5.2.4 Specimen SW 2R

This specimen was tested under a loading program similar to that used for Specimen SW 1 (Fig. 5.4). Instead of unloading and reloading in the opposite sense after incipient failure, however, this specimen was continuously loaded in the same direction until complete failure. Several general observations were made during the test. The most significant of these follow.

(1) As discussed in Sect. 2.6.2, this specimen was not repaired with epoxy. As expected, the initial stiffness of this specimen was about one-sixth of that observed in the uncracked specimen. A pronounced pinching shape of the hysteretic loops could be observed during the first few working load cycles.

(2) The column concrete cover crushed just prior to LP 31, when P_T = 200 kips and δ_{3R} = 1.6 inches. Nearly all the new concrete cover of the compression column spalled simultaneously and a noticeable drop in strength was observed in the P_T-δ_{3R} diagram (Fig. 5.8). Compared with SW 1, whose concrete cover gradually crushed at P_T = 235 kips and δ_{3R} = 2.1 inches, the concrete cover of this repaired specimen crushed relatively

early as well as suddenly.

(3) Unlike the other three specimens, the crushed band of this specimen did not widen at both ends (Fig. 5.107). The double curvature deformation shape of the edge columns was restricted to a small length of about ten inches. This length should be compared with the length for the other three specimens, which ranged from 16 inches to 22 inches. Since the diameter of the confined core of the edge column was nine inches, the shear span of the confined core was less than one when deformed in a double curvature shape. [The effective depth of the core, $d = 0.8\ D_W = 0.8 \times 9 = 7.2$ inches; hence, the shear span is $(10 \div 2) \div 7.2 = 0.69 < 1.0$.]. When the columns were deformed in this shape, no significant increase in the overall ductility of the specimen could be achieved.

(4) The rupture of the spirals near the base of the compression column was due to the combination of shear stress concentrated at that region and the radial expansion of the confined column core due to the axial compressive stress. At the time the spirals ruptured (LP 35, SW 2R), the estimated shear stress acting on the column core was very high (approximately 1100 psi). Affected by this high shear stress, the spirals ruptured along an inclined line with respect to the longitudinal axis (Fig. 5.108).

Several important test data are summarized below and compared with those of Specimens SW 1 and SW 2.

(1) The maximum load obtained in the test was $P_T = 231.7$ kips, which is equal to 93 percent of that for SW 1. The maximum lateral displacement before crushing of the wall panel was $\delta_{3R} = 3.3$ inches, which is equivalent to a displacement ductility of 4.7. This value is 78 percent of that for SW 1, and is 112 percent of that for SW 2.

(2) The maximum plastic hinge rotation was 0.0166, 80 percent of that for SW 1, and 133 percent of that for SW 2. If the inelastic fixed-end rotation were included, this value would increase to 0.0186, which is 82 percent of that for SW 1 and 131 percent of that for SW 2.

5.3 LATERAL LOAD-RELATIVE LATERAL DISPLACEMENT DIAGRAMS

The relative lateral displacements measured at each floor level are denoted as δ_{3R}, δ_{2R}, and δ_{1R}. These terms refer to the displacement with respect to the footing of the specimen. To be more specific, the lateral displacement caused by the rigid body translation and rotation of the footing has been excluded. As illustrated in Fig. 4.6, the rigid body translation and rotation of the footing were measured by three dial gages. After the reaction blocks were restrained by the addition of steel plates, the contribution of rigid body movements to the lateral displacement was lessened and was approximately proportional to the applied loads. The component of the third floor lateral displacement, which was the result of a maximum rigid body movement, was equal to 0.099 inches. This maximum rigid body movement occurred at LP 157 of Specimen SW 1; the value of 0.099 inches is about 2.5 percent of the total lateral displacement at that load point.

The P_T - δ_{3R} diagrams are shown in Figs. 5.5 through 5.8. The careful observation of these continuously recorded diagrams enabled selection of the appropriate loading stages at which the discrete low-speed scanner readings were to be taken and also permitted changes in the preselected loading programs of the specimens. The P_T - δ_{2R} and P_T - δ_{1R} diagrams are shown in Figs. 5.9 through 5.15. The displacement scale of the P_T - δ_{3R} and P_T - δ_{1R} diagrams of Specimen SW 1R is smaller than that of the others.

The displacement ductility factor, μ_δ, unless otherwise specified, is defined as δ_{3R}/δ_{3Y}, where δ_{3Y} is the value of δ_{3R} at the first yield load. In defining the total lateral displacement ductility, it is necessary to specify clearly the location at which the deformation is measured because lateral displacements measured at different locations will lead to different ductility factors. For example, Figs. 5.94 to 5.96 show that at the same load point, the value of δ_{iR}/δ_{iY} gradually decreased as the i was increased from 1 to 3. Because the specimens were modeled for the lower portion of a ten-story wall, it is believed that the value of $\delta_{10R}/\delta_{10Y}$, if it existed, would be smaller than the obtained value of δ_{3R}/δ_{3Y}. That is, if the test specimen consisted of ten stories rather than three, the ductility factor obtained in the test would be lower. Since the inelastic deformations were concentrated at the bottom two stories of the specimens, however, the energy dissipation, as well as the plastic hinge rotation, capacities of the specimens obtained in the tests would be the same whether the specimen consisted of ten or three stories.

The stiffness of the specimen against lateral movement is defined as the slope of the P_T-δ_{3R} diagram. The stiffness can also be estimated from the free vibration tests of the specimens (Sect. 5.11). For an uncracked specimen, the initial stiffness underwent little change after the appearance of the first flexural crack. This is because the first flexural crack did not penetrate into the wall panel of the specimen. Therefore, its influence on the sectional moment of inertia of the specimen was small. The obvious weakening of the stiffness occurred after the appearance of diagonal cracks. At this stage, the number of flexural cracks increased, and one of them penetrated into the wall panel due to the combined effect of the flexural and shear stress. The stiffness again became weaker when the load increased slightly above the working load level, P_T = 90 kips. At this stage, the number of diagonal cracks increased considerably in the first story wall panel and both the flexural and diagonal cracks appeared on the upper stories. The load-displacement curves were flattened when about 25 percent of the vertical reinforcement of the wall panel passed yield strain. The initial stiffness for repaired specimens was weaker than that for the uncracked ones because in the former, parts of the cracks were not filled with epoxy or new concrete.

5.3.1 <u>Effect of Friction and Relaxation of Specimens</u>

During the first few cycles of loading for each specimen, a frictional force of about 10 to 15 kips was observed during unloading. This force could be detected by the vertical lines shown in the P_T - δ_{3R} diagrams. The frictional force gradually disappeared or became negligible as the load cycles increased. There was no attempt to compensate the frictional force in the data reduction process. That the deformation did not recover when the specimen was initially unloaded [see the vertical line immediately after LP 158 of Specimen SW 1 (Fig. 5.5)] is not believed to have been caused by friction. It was mainly due to the relaxation of the specimen. After initiation of crushing at the first wall panel at LP 158, the resistance of the specimen decreased without a decrease in displacement. This was because part of the shear force which was originally resisted by the wall panel was gradually transferred to the edge columns as the panel crushed, and because the maximum resistance of two edge columns was smaller than the total applied force. As the tip displacement was held constant in order to inspect the damage, the load continued to drop until it reached a stable state. Although this type of relaxation occurred at almost every load point of high external loads, it was not significant until the wall panel crushed.

5.3.2 Effect of Crushing of Column Concrete Cover

When the crushing process was gradual and slow, it usually had little effect on the strength of the specimen, as in the case of Specimen SW 1. For Specimen SW 2R, however, crushing was sudden. This may be attributed to the poor bond between the new concrete cover and the old concrete core and the discontinuities that existed between them. Nearly all the recast concrete spalled at the same time. As illustrated in Fig. 5.109, several cracks existed in the column concrete core at the time of casting the new concrete cover. These cracks were caused by the residual tensile inelastic deformation of the vertical reinforcement during the previous test. Consequently, when the whole column section was subjected to compression, the stress was concentrated at the new concrete cover where old cracks in the concrete core were located. This, together with the ineffective bond between the original and recast concrete, caused the entire new concrete cover to undergo premature crushing and spalling. The strength drop due to crushing of the column concrete cover of SW 2R was small and it was overcome after a very small increase in displacement (Fig. 5.8).

The edge columns of the wall were designed such that even after its cover spalled, the remaining confined core was able to provide the same strength. Together with the experimental evidence described above, this leads to the conclusion that crushing of the concrete cover, whether it be sudden or gradual, has little effect on the strength of the specimen.

Since the crushed cover did not affect the ductility of the wall, the safety of the structure was not jeopardized. Sudden crushing of the concrete cover may, however, cause occupants to panic and large fragments of falling concrete may result in serious injuries. Therefore, it is suggested that the existing cracks in the confined core be injected with epoxy and that the surface of the confined core be treated to ensure better bond between the core concrete and the newly cast cover concrete. Another solution would be to use a light wire mesh close to the surface of the edge column to basket the concrete so as to prevent large concrete fragments from falling down after the concrete cover of the edge column crushes.

5.3.3 Behavior of Walls after Crushing of Wall Panel

For Specimens SW 1, SW 1R, and SW 2, after crushing of the wall panel and unloading, the load was immediately reversed. The tests of Specimens SW 1 and SW 2 were stopped one loading reversal after crushing to avoid the complete failure of the specimens and to facilitate their repair. Specimen SW 1R, however, continued to be cycled at the same peak displacement three times and then loaded to its maximum ductility, which was controlled by the rupture of the spirals of its compression column. The behavior of the walls after crushing of the wall panel is illustrated by the load-displacement diagrams of Specimens SW 1R and SW 2R (Figs. 5.6 and 5.8).

After crushing of the wall panel, the specimen can be modeled as a rigid body with two short columns as shown in Fig. 5.106. The length of the columns is approximately 16 inches for SW 1R, and only ten inches for SW 2R. Figure 5.110 shows the N-M interaction diagram of the confined core of the edge columns as controlled by shear. At LP 72 of SW 1R (Fig. 5.6), the axial forces in the two edge columns near the bottom section of the specimen were 373 kips in compression and 178 kips in tension, respectively.

The corresponding shear capacities of these edge columns were 84 kips and 48 kips, respectively. These values were calculated according to Eqs.(11-6), (11-8) and (11-13), Chap. 26 of the UBC, using the actual strength of the materials. The sum of the theoretical shear capacities of the two edge columns, 84 + 48 = 132 kips, is in good agreement with the total lateral force, 132.4 kips, obtained at the same load point of the test.

The deformation pattern shown in Fig. 5.106 was monitored by the pair of diagonally oriented linear potentiometers installed in the wall panel of the first story. Although this type of deformation can be regarded as the shear distortion of the overall wall specimen, the resistance at this stage resulted primarily from the shear resistance of the edge columns which was due to the bending deformation (plastic hinge rotations of the two short edge columns). Under this deformation pattern, the lateral displacement values measured at the three floor levels, δ_{3R}, δ_{2R} and δ_{1R}, were approximately the same, as shown in the P_T-δ_{3R} and P_T-δ_{1R} diagrams of SW 1R after LP 45 (Figs. 5.6 and 5.11).

When the lateral displacement was increased in the same direction after the wall panel crushed, the slope of the P_T-δ_{3R} diagram (after LP 34, SW 2R) became negative as shown in Fig. 5.8. Therefore, if the applied pseudo-static load could have been sustained, the specimen would have become unstable and precipitated complete collapse. However, because the loading of the specimen was under displacement control, it was possible to obtain the descendent branch of the P_T-δ_{3R} diagram (from LP 34 to LP 36, Fig. 5.8). Just before LP 35, (Fig. 5.8), the spirals of the compression edge column ruptured one after another. The load sharply dropped to one-half and thereafter remained stable. As the lateral displacement was continuously increased, more spirals broke and buckling of the column vertical reinforcement could be observed. In the region where the spirals ruptured, the concrete core was broken down into small pieces. The axial loading jack was controlled by a servo-valve which was under load command (as described in Sect. 4.3.2). Because a sudden failure of the compression column could drive the corresponding jack to its maximum displacement capacity and damage the jack, the specimen was unloaded.

Considerable energy was dissipated by Specimen SW 1R after its first story wall panel crushed (see Table 5, which will be discussed in Sect. 6.4). In the case of an actual earthquake excitation, the inertial force might force the wall to continue deforming in the same direction after the wall panel crushed [cf. loading program of SW 2R (Sect. 5.2.4)]. Since the wall became unstable in resisting the pseudo-static, applied lateral force, its additional energy dissipation capacity could not be depended upon for this kind of sustained loading, although it might be useful under actual inertial forces.

5.3.4 Working Load Cycles

The working load cycle was defined as the load cycle in which the peak values of the load varied between -90 kips to +90 kips.

After a severe earthquake, a wall may be subjected to a certain degree of structural damage even if it does not undergo failure. For this reason, it was necessary to investigate the behavior of the damaged wall when it is subjected to working loads under wind or minor earthquake conditions. To study this problem, several dynamic tests and working load cycles were run at different stages of testing. The dynamic tests were carried out under low amplitudes and with no axial force (Sect. 5.11). Some observations regarding the obtained response at these working load cycles follow.

(1) For an undamaged specimen, no pinching effect could be detected in the hysteretic loops with peak loads within the working load range, e.g., the loop from LP 60 to LP 65 of SW 1 shown in Fig. 5.5; the energy dissipated within these loops was very small.

(2) After the specimen had been cycled three times in a ductility range of one, a slight pinching effect could be noted in the hysteretic loops under working loads (LP 54 to LP 58 of SW 2, Fig. 5.7). At this time, some residual displacement and energy dissipation within these loops was observed. The initial stiffness of the specimen was reduced to one-quarter of that of the uncracked specimen.

(3) When the specimen had undergone considerable damage, such as that after the inelastic cycle (LP 74 to LP 100 of SW 1, Fig. 5.5), the working load loops became pinched (LP 136 to LP 140 of SW 1, Fig. 5.5). The energy dissipated in these loops was reduced to one-half of that dissipated in the loop described in item (2).

(4) After the wall panel crushed in one corner, the energy dissipated within the working load loops increased to approximately three times that described in item (3) (LP 163 to LP 168 of SW 1, Fig. 5.5); however, the deflection increased about 1.8 times. This energy increment was primarily due to the inelastic shear distortion shown in Fig. 5.41. Up to this stage, the working load loops were still stable; the shape of the loop in the previous loading cycle could be approximately reproduced in the following cycles, and no significant drop in strength could be observed in the successive repeated cycles.

(5) After the crushing band of the wall panel developed, the working load loops became unstable. A large amount of reduction in the strength could be observed in two successive loops (i.e., the loop from LP 186 to LP 191, and the loop from LP 191 to LP 195 of SW 1, Fig. 5.5). Even under working loads, in such a condition the wall could have been gradually cycled to failure. The wall was therefore considered incapable of fulfilling its function under this condition.

(6) For repaired specimens, the initial shape of the working load loops depends on the method of repair. Since most of the large cracks of Specimen SW 1R were epoxy-repaired, the initial shape of its working load loops was more or less similar to the undamaged specimens, except that its initial stiffness was reduced by 40 percent. Since most of the cracks remained open for Specimen SW 2R, the initial shape of its working load loops were pinched; these were similar to those described in item (3).

5.3.5 P_T - δ_{2R} and P_T - δ_{1R} Diagrams

Most of the characteristics found in the P_T - δ_{3R} diagrams can also be found in the P_T - δ_{2R} diagrams and P_T - δ_{1R} diagrams. However, the shear distortion of the specimen seems to have had a greater effect on the characteristics of the last two diagrams. This can be clearly observed in the curves of the diagrams between LP 158 and LP 159 of SW 1 (Figs. 5.5, 5.9 and 5.10). After LP 158, the value of δ_{3R} was held constant but δ_{2R} and δ_{1R} continued to increase. At this load point crushing of the wall panel occured. The internal stresses of the specimen were then redistributed, during which time the shear distortion of the specimen increased due to the considerable drop in shear resistance at the first story (Fig. 5.41). However, the flexural deformation decreased mainly because the externally applied load (and the corresponding external moments) decreased from 248 kips to 180 kips and the drop in flexural resistance at the critical region of the first story was very small (Figs. 5.20 through 5.24). The compensation for the increase in shear distortion and the decrease in flexural deformation allowed the displacement, δ_{3R}, to remain unchanged. Displacement values δ_{2R} and δ_{1R} increased, however, because they were more greatly affected by the shear distortion. Similar observations can be made on the other specimens.

5.4 M - ϕ DIAGRAMS

5.4.1 Experimental Results

Flexural deformation measurements were recorded in the seven consecutive regions for which the entire length of the specimen was divided (Sect. 4.2). The average curvature of the specimen section was computed according to the average concrete strain in the edge columns and to the hypothetical linear strain variation along a section. Since significant yielding took place only up to the top of the fourth region from the footing, only the M - ϕ diagrams up to the top of that region are reported (Figs. 5.20 through 5.36). The values of the regional moment shown in these diagrams include the component contributed from the P-Δ effect. This component, however, is always less than two percent of the total regional moment. Several general observations on these diagrams are discussed below.

(1) Because of the existence of diagonal cracks, the curvature readings for the first three regions had approximately the same value. This can be explained by Fig. 5.111. If the force taken by the vertical and horizontal wall panel reinforcement are neglected, then tensile forces T_B and T_C should be equal. Therefore, the strains of the reinforcement at points B and C (and the corresponding curvatures) have approximately

the same value.

(2) The average flexural strength of the i^{th} region of the specimen, $(EI)_i$, is defined by the slope of the $M_i - \phi_i$ diagram. Although the wall specimen has a constant cross-sectional area and the same vertical reinforcement throughout its height, the value of $(EI)_i$ becomes smaller as region i moves away from the base. This is because the curvature value remains the same as a consequence of item (1), while the value of the moment decreases (Figs. 5.20 through 5.36). Because the slabs offer some restraint against the opening of diagonal cracks, the flexural stiffness of the fourth region, $(EI)_4$, becomes larger than that of the third region, $(EI)_3$, and closer to that of the first region, $(EI)_1$. This phenomenon can be seen by comparing the initial slope of the $M_1 - \phi_1$, $M_2 - \phi_2$, $M_3 - \phi_3$, and $M_4 - \phi_4$ diagrams for each specimen (Figs. 5.20 through 5.36).

(3) When the specimen was deformed to a high displacement ductility ratio, wide cracks opened up due to the inelastic deformation of the vertical reinforcement. When the applied lateral force was reversed, the flexural stiffness of the first and fourth regions were very similar to, although sometimes less than, the sectional flexural stiffness computed considering only the vertical reinforcement, which was equal to 3.8×10^8 k-in.^{2} (The flexural stiffness of the cracked wall section was equal to 8.5×10^8 k-in.^{2})

(4) Although the loops of the $M - \phi$ diagrams revealed some pinching, there was less than that usually observed in other reinforced concrete flexural members. For a flexural reinforced concrete member subjected to loading reversals in the inelastic range, it is possible that a continuous crack (or several cracks) develops across the entire cross-section of the member just when the load is reversed. The flexural stiffness of the member at this section where the continuous crack

develops may be greatly reduced because no concrete is initially in contact in that section and therefore cannot participate in resisting the moment. This reduction leads to a significantly pinched shape on the hysteretic loops of the M - ϕ diagram. In the case of the wall specimens used in this investigation, however, the sectional flexural stiffness provided by the vertical reinforcement alone (3.8×10^8 k-in.^{2}) was very large and close to the total flexural stiffness of the partially cracked section, i.e. when the concrete is considered to contribute to resisting compressive forces. Hence, very little pinching effect could be detected in the M - ϕ loops of the specimens.

(5) After crushing of the wall panel, the specimen deformed in a pattern similar to that shown in Fig. 5.106. In this state, the overall curvature readings of the specimen in the first story were greatly disturbed. Because each column of the specimen deformed as an individual flexural member, the curvature readings were rendered useless for accurately describing the flexural behavior of the overall specimen section.

5.4.2 Comparison of Experimental M - ϕ Diagrams with Analytical Predictions

A computer program was written to predict the cyclic moment-curvature diagrams of the wall specimen. The following assumptions are used in the computation: (1) linear strain variations along a section, (2) no tensile concrete strength, and (3) idealized cyclic stress-strain curves of the materials. (These curves are shown in Figs. 5.112 through 5.114.)

Under monotonic loading, the stress-strain relationship of the steel follows the virgin curve shown in Fig. 5.112. This virgin curve tries to reproduce the experimental curve of the #6 rebars as shown in Fig. 2.5.

Under cyclic loading, the stress-strain relationship of the steel was first assumed to follow the virgin curve (Fig. 5.112). If the maximum absolute strain of the steel exceeds 0.003, the unloading curve of the steel will follow a Ramberg-Osgood function. For absolute strains less than 0.003, the unloading curve will follow the initial elastic stiffness of the steel.

As shown in Fig. 2.6, both the strength and the stiffness of the concrete will be reduced when it is cyclically loaded under a high stress level. The maximum usable strain, ε_{cu}, will, however, increase. As shown in this figure, the value of ε_{cu} increased to 0.0045 under cyclic loading, compared with the ε_{cu} value of 0.0038 under monotonic loading. The idealized cyclic stress-strain diagram of concrete (Fig. 5.113) tries to simulate these characteristics, although the data used in establishing this idealized diagram are limited to cyclic tests on a few concrete cylinders. The idealized diagram should be modified after more information is obtained.

The maximum stress of the confined concrete (Fig. 5.114) was computed according to the following equation [35]:

$$f_{c_{max}} = 0.85\, f'_c + \frac{8.2\, A''_s\, f''_y}{a\, D_s} \qquad (5.1)$$

where a is the spacing of the spirals, and D_s is the diameter of the confined core. The corresponding strain, 0.009, was selected according to the test data reported by Bresler and Bertero [36].

The cross-section of the wall specimen was divided into 20 segments of steel elements, 20 segments of concrete elements and six segments of confined concrete elements (Fig. 5.115). The computer program used an iterative procedure. This procedure was carried out first, by assuming an extreme strain value and a curvature for calculting the strain at the centroid of each segment. The corresponding stress was then obtained by using the idealized stress-strain relationships defined above. Finally, the equilibrium of the net sectional force was checked. If it were satisfied within the tolerance of 1 kip (about 0.5 percent of the net axial force, 195 kips), the moment was computed and the procedure repeated. If not, the curvature was revised for calculating the strain at the centroid of each segment and the procedure was continued.

The comparison between the experimental and the analytical $M - \phi$ diagrams is shown in Figs. 5.116 and 5.117. As shown in Fig. 5.115, the agreement between them for the first monotonic curve (LP 74 to LP 90) and for the first unloading is excellent. After the moment is reversed, however, a disagreement becomes obvious. The experimental curve is stiffer than the analytical curves. There are two primary reasons for this discrepancy. First, the cracked concrete contacts earlier in the actual case due to the previous shear movement of the specimen which dislocated the irregular cracked concrete surface as shown in Fig. 5.118 and discussed in Ref. 34. Secondly, the measured curvature represents the average value of the curvature at all sections in the first 15-inch length of the specimen. The concrete between cracks takes part in resisting the tensile force so that the average curvature over the 15-inch length is smaller than that measured at the cracked section as assumed in the theoretical computation.

After the concrete starts contacting again in the analytical curve (point A, Fig. 5.115), the agreement between these two curves improves.

5.5 $V - \gamma$ DIAGRAMS AND V - WD DIAGRAMS

5.5.1 $V - \gamma$ Diagrams

For Specimens SW 1 and SW 1R, only the shear distortion of the wall panels in the first two stories were measured. After observing that diagonal cracks spread across the entire wall panel in the third story for Specimens SW 1 and SW 1R, the third story shear distortion was also measured for Specimens SW 2 and SW 2R.

The average shear stiffness of the i^{th} story of a specimen, $(GA_\nu)_i$, is defined as the slope of the V - γ_i diagram of that specimen, where G is the shear modulus of concrete and A_ν is the effective shear area of the section. For the uncracked specimen, the theoretical prediction of the value of G will be $E_c/2(1+\nu)$, where Poisson's ratio of concrete is approximately equal to 0.15, and E_c equals 2800 ksi (Sect. 2.3.2.2). The value of A_v is approximately the area of the wall panel, 296 in.^{2}; hence, $GA_\nu = 3.6 \times 10^5$ kips.

From the experimental results, only the average value of $(GA_\nu)_i$ for each story can be determined. The values of GA_ν reported herein are based on the V - γ_1 diagram of Specimen SW 2, Fig. 5.43. These values indicate the deterioration of the GA_ν value at different stages of loading. It must be realized, however, that the sensitivity of the instrumentation was not sufficient to register an accurate value of the shear distortion prior to the appearance of the diagonal cracks. It is difficult to design an instrumentation that is capable of accurately measuring deformations whose value can vary in a large range as in the case of shear distortions before and after cracking.

The average measured value, GA_ν, for the uncracked specimen, SW 2, at LP 2 (Fig. 5.43) was 4.5×10^5 kips. This value should be compared with the theoretical value of 3.6×10^5 kips. After the appearance of the first flexural crack at LP 6, this value dropped to 3.2×10^5 kips. The average value for the first working load cycle from LP 17 to LP 23 was 1.3×10^5 kips. Note that diagonal cracks appeared in all three panels of the specimen under working load cycles. After the first yield cycle, the hysteretic V - γ_1 loops became pinched. The slope of these loops varied according to the load level. For instance, from the V - γ_1 curve between LP 114 and LP 118, it was observed that its slope was initially 1800 kips when the dowel action of the longitudinal reinforcement took place, later increasing to 20,000 kips around LP 116, and decreasing to 5000 kips between LP 117 and LP 118. During unloading, the average slopes of these loops varied from 60,000 kips to 72,000 kips, i.e., they had considerably smaller variation than the loading part of the loops. Note that the largest slope obtained in the V - γ_1 diagram of Specimen SW 2 (Fig. 5.43), 4.5×10^5 kips, is about 320 times the smallest slope obtained between LP 134 and LP 135 of that diagram, 1400 kips.

In the pinched range of a hysteretic loop, the slope of the V - γ_1 curves is nearly constant. Although there was still some resistance due to aggregate interlocking, most of the shear resistance in this range is due to dowel action (Sect. 5.5.2). The observed constant slope represents constant dowel action. However, a decrease in the slope of the V - γ curve could be detected in each successive loop at the same displacement ductility range. It is believed that this decrease was due to both the deterioration in the bond between the vertical reinforcement and the concrete, and the degradation in the aggregate interlocking of the concrete with each loading reversal.

5.5.2 Shear Force Transferring Mechanism and V - WD Diagrams

It is well known that under monotonically increasing loads or deformations part of the shear force in a reinforced concrete member is directly transferred through the concrete in the compression zone, while another part of it is transferred through the horizontal web reinforcement and web concrete known as the truss or arch action. A small part is also transferred through the dowel action of the vertical reinforcement [37]. After it is cyclically loaded in the inelastic range, the cracked concrete in the compression side is unable to close immediately after the loading. The shear force must then be transferred through the dowel action of the longitudinal reinforcement and the deteriorated aggregate interlocking; hence, the pinched shape in the V - γ diagrams of the wall specimens.

When the width of previously opened cracks in the compression side of the specimens gradually decreases due to an increased moment, the aggregate interlocking becomes increasingly efficient. This gradual increase in the effectiveness of the aggregate interlocking and the truss action in resisting shear can be observed by the gradual increase of the slope in the V - γ_1 diagrams. The truss action can take place only when the diagonal cracks formed in the previous loading closes.

More instrumentation was installed for Specimens SW 2 and SW 2R in order to gain a better understanding of the shear force transferring mechanism. The clip gages, WD 1 and WD 2 (Figs. 5.89 and 5.90), measured the diagonal strain at the bottom corners of the first story wall panel. When the reading of these gages was reduced from tensile strain to zero strain, the diagonal cracks perpendicular to that gage was closed and the truss action started to function. By comparing the V - γ diagram (Fig. 5.43) to the V - WD 1 and V - WD 2 diagrams (Figs. 5.89 and 5.90), it was found that an increase in the shear stiffness always occurred earlier than the formation of the truss action. For example, a gradual increase in shear stiffness of the V - γ_1 diagram began at the point between LP 126 and LP 128 where the shear force was equal to 60 kips. The V - WD 2 diagram indicated that closing of the diagonal cracks occurred at the point when the shear force reached 117 kips. Therefore, the increase in shear stiffness shown in the V - γ_1 diagram before the diagonal cracks closed was primarily due to the increase in the effectiveness of aggregate interlocking.

Specimen SW 2R was loaded monotonically. Clip gages WD 2, WD 3, and WD 4 of that specimen (Figs. 5.91 to 5.93), were installed to detect the location and the time of the first crushing of the wall panel. From these figures, it was found that at the time of crushing (LP 34), all the strains measured by these gages passed the maximum usable strain of the concrete, 0.0038.

After the wall panel crushed, the shear-resisting capacity of the specimen was restricted to that of its edge columns and the shear stiffness of the specimen was greatly reduced. Therefore, the shear distortion of the specimen increased despite the decrease in applied loads during the process of internal stress redistribution (the curve between LP 158 and LP 159 of the V - γ_1 diagram, Fig. 5.41).

Since most of the large cracks appeared only in the first story, the aggregate interlocking and truss action developed efficiently in the second or third story. Thus, small dowel action was required. The vertical reinforcement in the third story never reached yield point. Immediately after loading reversal, the compressed concrete in the third story contacted and effectively resisted the shear. (This was shown by the readings of the clip gages installed in that story.) The shear distortion measured in the third story was slightly larger than that in the second story, probably due to the local effect of the applied lateral and axial load.

5.6 M_B - θ_F DIAGRAMS

The base moment fixed-end rotation diagram of the specimens are shown in Figs. 5.37 through 5.40. The effect of the rigid body rotation of the footing was excluded in these diagrams. The fixed-end rotation, θ_F, is therefore attributable only to the slippage of the vertical reinforcement along its embedment length in the foundation of the wall.

As discussed in Sect. 4.2, the curvature, ϕ_1, was measured as the average curvature in a region extending from one to fifteen inches away from the footing. The axial deformation of the column in the one-inch region adjacent to the footing has been divided into two parts. The first part is a concentrated deformation just at the face of the footing, due to slippage of the vertical reinforcement inside the footing. The second part is the distributed deformation along the one-inch region. This distributed deformation was added to the fixed-end rotation reading although it more correctly should have been considered as part of the curvature reading along the region extending from zero, rather than one, to fifteen inches. This error had only a slight effect throughout most of the loading histories, because the distributed deformation of the one-inch region was very small. After the column crushed, however, the axial deformation within this one-inch region became significant and resulted in larger errors in the θ_F readings. Consequently, the accuracy of the θ_F values beyond LP 34 of SW 2R (Fig. 5.40) is questionable.

Generally speaking, the M_B - θ_F diagrams are similar in shape to the M - ϕ diagrams, although the former exhibited less pinching. Because the vertical reinforcement of the specimens was well anchored, the deterioration of the anchorage effectiveness of the reinforcement due to loading reversals was small.

5.7 LATERAL DISPLACEMENT COMPONENTS

The sources for the lateral displacement can be grouped into three categories of components: those resulting from (1) flexural deformation, (2) shear distortion, and (3) fixed-end rotation. The amount of these components in the total lateral displacement depends on the slenderness of the specimen. The more slender the specimen, the more significant the flexural deformation and the fixed-end rotation. Graphic information on the three components of lateral displacements at the three floor levels of the specimen is shown in Figs. 5.94 through 5.98. Precise values and percentages of these components in the total lateral displacement are listed in Tables 6 through 9.

The flexural deformation and shear distortion of Specimens SW 2 and SW 2R were measured over the entire length. If no error were committed in calibrating the instrumentation, and if the assumptions used in reducing these data are realistic (such as assuming linear strain variations along a section and uniformly distributed curvature over a measured region), then the lateral displacement measured by the linear potentiometers mounted at the mid-depth of each floor should be equal to the summation of its three components. Since the errors shown in column 6 of Tables 6 and 7 are minor for most of the load points, the experimental data appear excellent. Shear distortions in the third stories of Specimens SW 1 and SW 1R were not recorded. The error caused by these missing data is around five to ten percent for the computation of the lateral displacement at the level of the third floor. The unrecorded data did not effect computations at the level of the second and first floors.

The computation of the lateral displacement resulting from the flexural deformation was based on the assumption that the curvature was uniformly distributed over each measured region. Since most of the flexural deformation was concentrated in the first story, the error introduced by this assumption had a greater effect on computing the lateral displacement at the level of the first floor than at the third floor. According to the uniform curvature assumption, the centroid of the curvature diagram of a measuring region is assumed to be located at the center of that region. Since the distance from the center of each region in the first story to the level of the third floor is at least three times longer than the distance from the center to the level of the first floor, any error involved in locating the centroid of the curvature diagram of that region is three times greater in computing the lateral displacement at the level of the first floor than that at the third floor. This observation agrees with the test result. The largest percentage of error invariably occurred when computing the δ_{1R} values.

The component contributed from the shear distortion is dominant for the lateral displacement at the level of the first and second floors throughout the tests. For the lateral displacement at the level of the third floor, the shear distortion component is dominant under working loads. After yielding, the flexural deformation component becomes more significant. Comparing the percentage of the flexural component at the same load point but at different floor levels, it is clear that the higher the floor level, the greater the amount of displacement due to flexural deformation. Accordingly, the flexural deformation component would be considered dominant if the lateral displacement at the level of the tenth story were considered.

The contribution of the fixed-end rotation of Specimen SW 1R is so small that it cannot be clearly shown.

5.8 STRAIN IN LONGITUDINAL REINFORCEMENT

The reinforcements of Specimens SW 1 and SW 2 were mounted with the same number of microdot strain gages in similar locations. A symbol (such as CL 1) was assigned to each gage according to its location. The locations of these gages are shown in Fig. 4.10. Several gages were damaged during the tests on Specimens SW 1 and SW 2. These gages were not replaced after repair; consequently, less information on strain was obtained during tests of these specimens.

The first yield load of the specimens* can be determined from

---

* The load causing first yield is different from the yield load of the specimen. The latter is defined in Sect. 5.1(4).

their P_T - CL 1 diagram (Figs. 5.51 and 5.60). When the reinforcement in the outer steel layer of Specimen SW 2 started to yield, the load was 179 kips. This value is close to the theoretical prediction of 174 kips (Table 3). The corresponding load of SW 1 was as low as 133 kips. Although there was a large discrepency between the actual and theoretical values of the first yield of SW 1, better agreement was reached for the final yield load of the specimen.

After strain CL 1 of SW 1 exceeded the tensile yield strain of 0.0025, it never went back to compressive strain (Fig. 5.51), indicating that the flexural cracks near the bottom section of the specimen's left column never closed during the reversal loading. Strain readings CL 1 and CL 4 of Specimen SW 2 (Figs. 5.60 and 5.63) indicate closure of the flexural cracks in the bottom section of the corner. Combining the reading CL 2 with that of CL 1 and CL 3 with that of CL 4, the concrete contact length in the bottom section of Specimen SW 2 can be roughly estimated. If a linear strain variation across the column is assumed, the concrete contact length will be 7.5 inches, 5.2 inches, and 5.5 inches at LP 76, LP 100 (from CL 1 and CL 2), and LP 118 (from CL 3 and CL 4), respectively. No further information could be obtained beyond LP 118 because strain gages CL 1 and CL 2 broke.

As shown in Fig. 5.61, the slope of the P_T - CL 2 diagram of SW 2 started to increase at LP 73. This increase can be attributed to the movement of the neutral axis location toward strain gage CL 2, and to the change at LP 73 of strain CL 1 to compressive strain (Fig. 5.60). If effects of concrete shrinkage and bond deterioration are neglected, the recording of compressive strain in the steel bars will indicate that the cracked concrete in the bottom section again contacts at the extreme compression fiber and starts to resist compressive force. Therefore, the axial stiffness of the bottom section of the compression column will increase, as shown by the increase observed in the slope of the P_T - CL 1 and P_T - CL 2 diagrams. After LP 75, the slope of the P_T - CL 2 diagram became negative. This may have been due to the neutral axis passing beyond the location of strain gage CL 2 at LP 75. Similar information was obtained in the P_T - CL 3 diagram of SW 2.

The vertical reinforcement was well anchored inside the footing. The strain history recorded by gage CL 5 of Specimen SW 1 (Fig. 5.53) indicated that the strain was always below yield strain and that no significant residual strain existed. For Specimen SW 2, strain gage CL 6 recorded a maximum strain that never exceeded 0.001. The strain history recorded by gage WL 7 of Specimen SW 2 (Fig. 5.69) also indicated elastic straining throughout the test.

5.9 STRAIN IN HORIZONTAL WALL REINFORCEMENT

The only strain in the horizontal reinforcement recorded continuously by an X-Y recorder was strain WS 4 of Specimen SW 2 (Fig. 5.84). If this continuously recorded curve is correct, then the sharp changes that can be observed in the slope of this figure will imply that other similar diagrams (Figs. 5.72-5.88) which were plotted using only the discrete scanner data are in error.

The readings of these gages were small before diagonal cracks appeared. After these cracks appeared, the readings were strongly dependent on the location of the gage and the crack pattern of the specimen. Although these readings were usually below the yield strain of 0.0025 before the wall panel crushed, these gages revealed a progressive increase in residual tensile strain when the specimen was cyclically loaded into the inelastic range. This indicates that at zero lateral load, the diagonal cracks near the gages became wider as the number of inelastic cycles increased. These cracks were restrained from closing by irregularities existing at the two faces of the cracks or by loose concrete granules entrapped in the cracks.

Gages WS 1, WS 2 and WS 3 were installed in the same reinforcing bar to study the strain variation along this bar. If the bond between the reinforcement and concrete had been severely damaged, the strain readings in these gages would have been uniform. However, as the results indicate that the readings of these gages depended only on their location and crack pattern, the bond appears effective up to crushing of the concrete.

Since most of the gages were located inside the crushed band of the wall panel, no meaningful information could be obtained after crushing of the wall panel. Gage readings were completely disrupted because buckling of the reinforcement occurred immediately after crushing.

5.10 PHOTOGRAMMETRIC READINGS AND SLIPPAGE OF BASE CONSTRUCTION JOINT

The dimensions of the specimen were reduced by 24 times into a five-inch by four-inch glass plate during the photogrammetric readings. When the plate was enlarged and read by a comparator, the accuracy of the coordinates of a clearly seen target was within 0.01 inches. For obscure targets constituting about ten percent of the total targets, the error may reach 0.05 inches. This margin of error is acceptable when plotting the deformation patterns of the specimen, but it is unsatisfactory when computing the strain distribution of the specimen. Consequently, Fig. 5.101 shows only the deformation patterns.

One of the main purposes of using the photogrammetric technique is to study the slippage of the construction joints. As was discussed in Sect. 2.5, the wall specimen has three construction joints. During the tests, only the slippage of the base joint can be observed. This observation was confirmed by photogrammetric readings. A detailed discussion of these readings, together with other photogrammetric results, follows.

(1) The horizontal displacement of the targets can be detected in the bottom grid line of Figs. 5.101(b), 5.101(e) and 5.101(f). Since the targets in the bottom line were 3.5 inches away from the footing, this horizontal displacement was the result of the rigid body movement of the footing, flexural and shear deformation of the wall, as well as the slippage between the wall and the footing at the construction joint. The average horizontal displacement of these targets was 0.2 inches for SW 1 at LP 158, and 0.08 inches and 0.16 inches for SW 2 at LP 91 and LP 94, respectively. The amount of slippage can be approximately estimated by subtracting these values from the other displacement components. The slippage was equal to 0.07 inches for Specimen SW 1 at LP 158, and 0.06 inches and 0.08 inches for Specimen SW 2 at LP 91 and LP 94, respectively.

(2) A residual tensile strain can be observed at LP 90 and LP 91 of SW 2. [Figs. 5.101(d) and 5.101(e)].

(3) In addition to a flexural-type deformation, the first story tended to deform in a double curvature shape. This type of deformation

can be observed in every pattern shown in Fig. 5.101 and is particularly acute at LP 158 of SW 1 [Fig. 5.101(b)].

(4) At the peak of a load loop (LP 158 of SW1, LP 76 and LP 94 of SW 2), the neutral axis of the section at the base of the wall is very close to the edge column wall face. Thus only a small portion of the wall panel is working in compression. This is judged according to Figs. 5.101(b) and 5.101(c), where only a small portion of the wall panel was subjected to compressive strain.

(5) Only translational deformation can be observed at LP 91 of SW 2 [Fig. 5.101(e)].

5.11 FREE VIBRATION TESTS

Several free vibration tests were carried out for Specimens SW 2 and SW 2R to determine the frequency and critical damping ratio of the specimens at different loading stages. During these tests, the specimen was disconnected from the loading jacks. In this way, no axial force could be applied to the specimen. Although its effect on the dynamic response of the uncracked specimen is very small, removing the axial force from the cracked specimen may change the specimen's flexural stiffness and degree of damping. For this reason, the data reported in this section should be used only as a guideline.

To eliminate the frictional force between the slab of the specimen and the test floor, the free end of the specimen was rested on a wide-flange beam suspended from the overhead crane on a long cable. The free vibration test of the specimen was initiated by suddenly cutting a #4 rebar. Through this rebar, the specimen was pulled by a force of about ten kips. It was also possible to generate the free vibration of the specimen by manually pushing it. The acceleration history of the specimen at the top of each story was measured by accelerometers and recorded by a visicorder.

For Specimen SW 2, the free vibration tests were run before loading, after testing with three full loading reversals at a displacement ductility of one, and after incipient failure (crushing of the wall panel). The test of Specimen SW 2R was also run before loading. Except for the first free vibration test on SW 2, all the tests were run under two different amplitudes. The small vibration of the specimen was initiated by manually pushing and releasing it, or by hitting the specimen with a hammer, i.e., a type of environmental vibration test. Then two or three large amplitude vibration tests were run by pulling the specimen by means of a #4 rebar and cutting it as described above. The results of these tests are shown in Table 10. The critical damping ratio reported in this table is the result of averaging all the similar tests and averaging the data obtained from every story. Typical accelerograms of Specimen SW 2 after three yield cycles are shown in Figs. 5.99 and 5.100. The maximum acceleration of the small amplitude test (Fig. 5.99) is approximately five percent of that of the large amplitude test (Fig. 5.100). The mass was unsymmetrically distributed due to the existence of the loading yoke (see Fig. 4.2). Consequently, a torsional vibration mode was incorporated with the bending vibration mode in these accelerograms.

The load-lateral displacement diagrams of Figs. 5.5 through 5.8 indicate that the initial lateral resisting stiffness of the specimen decreased as the load level increased. This explains why the frequency of the specimen vibrated under low amplitudes is 25 percent higher than that vibrated under high amplitudes. Under low amplitudes the critical damping ratio of the specimen was no greater than 2.7 percent. The damping of a cracked reinforced concrete member was primarily due to the energy dissipated by the friction between cracks. If the member is not cracked or the amplitude of vibration is so small that little friction develops along the crack surfaces, the damping will be small. Therefore, a large difference existed in the critical damping ratio when the specimen vibrated in different amplitudes as shown in Table 10. It must be re-emphasized that had axial force been applied, the width and length of the crack would have changed, possibly affecting the dynamic response of the specimen. It must also be noted that the maximum bending moment introduced in the relatively large amplitude test was less than fourteen percent of the cracking moment of the specimen. Hence, the amplitude of the vibration in these tests is much lower than that of the structure subjected to severe seismic ground excitations. Assuming that damping will increase if the amplitude of vibration increases, the critical damping ratio of the wall specimen obtained in these tests may be conservative. Therefore, the five percent damping used in the dynamic analyses of the prototype building may be too high for the uncracked structure, although it may be conservative for the structure whose main lateral force resisting element, the framed walls, will crack under severe seismic ground motions. Similar conclusions have been reached by other investigators [38,39].*

---

*It should be noted that the damping measured and reported herein is for the structural wall alone; therefore, it cannot be used to represent the overall damping of the whole building. Damping of the entire building will depend on the damping of the frames as well as the friction developed between the structure, the walls, and the partitions.

After three yield cycles the diagonal cracks traversed all three wall panels of the specimen. The high ratio of 9.1 percent critical damping was attributed to the internal friction existing between these diagonal cracks. After crushing of the wall panel, the deformation was concentrated in a narrow band, indicating that the stiffness of the specimen depends on the flexural stiffness of its edge columns (Fig. 5.106). In this case, less internal friction can be expected; thus although the specimen was subjected to greater damage at the end of the test, its critical damping ratio dropped.

6. EVALUATION OF EXPERIMENTAL RESULTS

6.1 GENERAL REMARKS

For a better understanding of the mechanical behavior of the wall specimens, the experimental results presented in Chapter 5 are further evaluated by investigating: (1) the effect of different loading histories; (2) the failure mechanism of the specimens; (3) the energy dissipation capacities of the specimens and their components; (4) the amount of inelastic rotation, story drift index, and ductility developed by the specimens, as well as the significance of these quantities; and (5) the efficiency of the repairing technique used.

The experimental results are used in conjunction with analytical ones to assess the efficiency of the behavior of a wall-frame system designed according to the UBC provisions when this system is subjected to earthquake excitations. These combined results are also used to have a better prediction of the critical base moment-to-base shear ratio of the wall which might develop during seismic ground excitations.

6.2 EFFECTS OF DIFFERENT LOADING HISTORIES

Specimens SW 1 and SW 2 were tested under monotonic and cyclic loadings, respectively, to study the influence of loading reversals on the strength, stiffness, ductility, energy absorption and energy dissipation capacity as well as the failure mode of the framed wall specimen. Because of the unexpected malfunctioning of the testing setup (Sect. 5.2.1), Specimen SW 1 was subjected to one cycle of inelastic displacement reversal before it was loaded to first crushing of the wall panel at which stage a sharp decrease in lateral resistance was observed. Although this cycle of inelastic reversal might have affected the specimen behavior under a monotonically increased load, the test of Specimen SW 1 will herein be considered as having had a monotonically increasing load.

6.2.1 On Shear Resistance Degradation

The flexural cracks of a monotonically loaded reinforced concrete member opened only on the side subjected to tensile stress; its shear cracks only opened diagonally in one direction. This enabled the concrete in compression to offer effective resistance to shear, thereby preventing or delaying a shear type of failure. Furthermore, splitting of the concrete cover is delayed because the dowel action is not pronounced. On the other hand, flexural cracks of a member subjected to loading reversals opened on both sides, while its shear cracks opened diagonally in two symmetric directions. If the member had been cycled under full load or displacement reversal in the inelastic range, the widely opened cracks due to the inelastic deformation of the longitudinal reinforcement of the member would not have closed immediately following loading reversal. There is a range of loading when some cracks traversing the whole cross-section of the member remained open. During this period, the shear resistance of the specimen could only be offered by the dowel action of the longitudinal reinforcement and the aggregate interlocking [34]. During repeated reversal cycles, the aggregate interlocking resistance gradually deteriorates because of the grinding process that takes place at the face of the cracks. In addition, the dowel action can seriously damage the bond between the concrete and the longitudinal reinforcement and may lead to splitting of the concrete cover (Fig. 6.1). The dowel action may also cause an early, but ineffective, contact of the concrete in the compression corner (Fig. 5.118). The inefficiency is a result of the concentration of stresses in a localized area of contact in an already disrupted concrete section. All these facts may cause deterioration in the strength of the member, and accelerate a premature shear failure.

The dowel action was not pronounced in Specimen SW 1 prior to LP 158. Before this load point, the specimen was subjected to only one full loading reversal in the inelastic range. The deterioration in strength due to the effect of loading reversal was therefore small. When the specimen was loaded in the negative direction (LP 98), the inelastic deformation of the vertical reinforcement in the tension column was small. After loading reversed to the positive direction, concrete in the compression corner contacted at a low load level, building up efficient shear resistance of the specimen. Thus despite some deterioration, it is believed that the overall performance of Specimen SW 1 was not significantly affected by the loading reversal and it can be assumed that the test results on this specimen were close to that expected during a pure monotonic test.

For Specimen SW 2, the peak displacement of the loading cycles was progressively increased as shown in Fig. 5.3. The specimen was cycled three or four times at the same peak displacement. Before the wall panel crushed, a deterioration in the stiffness and strength could be observed between the first and second cycles with the same peak displacement. The maximum reduction in strength between these two cycles was five percent, a percentage obtained by comparing the lateral load at LP 35 with that at LP 44 (Fig. 5.7). The lateral load displacement hysteretic loops became stable at the third load cycle; the difference between the second and third cycles was small.

6.2.2 <u>On Crushing of Column Concrete Cover</u>

After Specimen SW 2 was cyclically loaded in the inelastic range, the vertical column reinforcement yielded in both edges throughout the height of the first story, extending partially into the second story. When the load was reversed, the contact of concrete in the extreme compression corner along the yield length of the column was delayed due to the residual tensile strain of the yielded vertical reinforcement. As a consequence, crushing of the column concrete cover was also delayed. No crushing of the concrete cover was therefore observed before the specimen's wall panel crushed. On the other hand, in the testing of Specimen SW 1, crushing of the concrete cover could be detected between LP 87 and LP 88 through reading of strain gage CC 2 and was clearly observed at LP 156 (Fig. 5.5).

6.3 FAILURE MECHANISM - CRUSHING OF WALL PANEL

6.3.1 Occurrence of First Crushing

During the tests it was observed that the failure modes of all specimens were initiated by crushing of their first story wall panels. This crushing practically eliminated one of the main sources of shear-resisting mechanism in the specimen. Buckling of the wall reinforcement in both directions could also be observed after removing the loose concrete pieces. According to these observations, the first story wall panel could fail in two possible sequences. In the first, the wall panel reinforcement buckles first and consequently damages the concrete cover of that panel. It should be recognized that in order for the reinforcement to buckle first, wide cracks must open up or the cover must split at the level of the reinforcement. In the second sequence, the wall panel concrete first crushes, thereby reducing the constraint of the wall panel reinforcement and precipitating buckling.

Evidence obtained from data on Specimen SW 1 indicates that crushing of the wall concrete occurred first and was followed by the buckling of the wall reinforcement inside the crushed zone. The evidence obtained is as follows.

First of all, the horizontal wall reinforcement could not buckle before the wall panel crushed. According to the strain reading of gages WS 1 to SW 7 (Fig. 5.72-5.78), the horizontal wall reinforcement was in tension at LP 157 and LP 158. Since none of this reinforcement had yielded before LP 158, the tensile strain could be directly interpreted as the tensile force. The reinforcement could not have buckled when it was subjected to tension.

Studying the strain history of gages WL 3 and WL 5, located near the initial crushed zone (Figs. 5.55 and 5.57), it is clear that the vertical wall reinforcement where these two gages were mounted was subjected to compression at LP 157 and LP 158. However, the maximum compressive stress in the reinforcement occurred somewhere between LP 152 and LP 153. After that point, the strain and, therefore, the compressive stress, was gradually released. According to the average strain histories recorded by clip gages W 1 to W 6 (the location of these clip gages are shown in Fig. 4.6), this gradual decrease of compressive stress in the reinforcement mounted with strain gages WL 3 and WL 5 was due to the gradual shifting of the location of the neutral axis of the bottom region of the specimen toward the extreme compression corner during the loading process. If the reinforcement did not buckle when it was subjected to maximum compressive stress, it would not have buckled later. The compressive strain read by gage WL 5 started increasing after LP 156. The increment was small, however, and should not have initiated buckling.

The crushed zone in the wall panel at LP 158 is indicated by the letters A, B and C shown in Fig. 6.2. According to the P_T -WL 3 diagram (Fig. 5.55), the net strain monitored by gage WL 3 which was located inside zone A was 0.004 in tension at that load point. This indicated that the flexural cracks in zone A might not have closed at this time.* Therefore, crushing of the concrete in zone A could not have been caused by the flexural stress. Clip gage WK 6 (Fig. 4.6) was also read in tension at LP 158; hence, the same conclusion can be drawn for zone C. Since strain gage WL 5, located very close to zone B, registered compressive strain at LP 158, only crushing of the concrete in zone B could have been influenced by the flexural stress. Crushing in zones A and C was caused by the stresses induced by the shear load.

Two diagonal clip gages were installed on Specimen SW 2, and four diagonal clip gages were installed on Specimen SW 2R (Fig. 4.7) to detect the diagonally oriented principal strain caused by the shear stress. The results are shown in Figs. 5.89 through 5.93 and have been discussed in Sect. 5.5.

6.3.2 Formation of Crushing Band

After the first story wall panel of Specimen SW 1 crushed at the lower left corner (Fig. 6.2), the specimen was unloaded and subjected to two cycles of reversals at maximum working load (Fig. 5.5). During these working load cycles, the residual tensile strain measured by all

---

* It is possible that the concrete was in contact at that time due to shear dislocation as shown in Fig. 5.118. Even if this were true, however, the compressive stress would still remain small because of the presence of the large tensile steel strain of 0.004.

the clip gages mounted along the base section of the specimen (C 1, C 11, W 1 to W 6, Fig. 4.6) indicated noticeable reduction. For instance, the average strain measured by clip gage W 3 was 0.027 in tension at LP 163, decreasing to 0.026 in tension at LP 168; a reduction of 0.001. This reduction becomes more obvious after LP 181, at which point the lower right corner of the wall panel also crushed. For example, the average strain reading of clip gage W 3 was 0.017 in tension at LP 183, decreasing to 0.0013 in tension at LP 186 (applied lateral load was zero at LP 183 and LP 186), at which time the complete crushed band across the whole cross-section of the wall panel was formed. Since the average strains measured by clip gages W 3 and W 4 at this load point were 0.013 and 0.011 in tension, respectively, spalling of the wall panel concrete around these clip gages could not have been due to the high compressive stress in the concrete. However, considering the large decrease in the residual tensile strain measured by these gages, it is possible that the vertical wall reinforcement might have been subjected to high compressive stress. Therefore, spalling of the wall concrete around the location of clip gages W 3 and W 4 might have been initiated by buckling of the vertical reinforcement in this region. According to the observations made during the test, it is also suspected that spalling of the concrete in this region was accelerated by the propagation of buckling of the horizontal wall reinforcement [Fig. 5.102(d)].

6.4 ENERGY DISSIPATION CAPACITY OF SPECIMENS

6.4.1 External Energy Dissipation Capacity

Table 5 shows the energy dissipated by each specimen at different stages of testing. For each complete loading cycle the external energy transferred to the specimen is the total work done within that cycle by all external loads, including the lateral force, tip overturning moment, net axial force, and frictional forces. Except for the frictional forces, the work done by the first three external loads can be represented by the area enclosed by the P_T - δ_{3R}, the M_T - θ_T and the net axial force versus average axial deformation diagrams, respectively. As shown in Fig. 5.5, for example, the unit of P_T is in kN (or kips) and the unit of δ_{3R} is in mm (or inches). The area enclosed by the P_T - δ_{3R} diagram thereby represents the energy in kN-mm (or kips-in.).

The net axial force was maintained at 195 kips in compression throughout the tests. The work done by the net axial force between any two load points can therefore be computed as 195 kips multiplied by the difference of the average axial deformation between these two load points. Since there was no attempt to compensate the frictional forces in the measured external forces --P_T, M_T and net axial force-- (Sect. 5.3.1), the work done by the frictional forces was also included in the P_T - δ_{3R}, the M_T - θ_T, and the net axial force versus average axial deformation diagrams. The exact amount of the work done by the frictional forces is not known. The value is believed to be negligible because the frictional forces were small during most of the testing.

In general, the work done by the net axial force was small. The value was always positive prior to the yield load. Due to the residual tensile strain generated in the vertical reinforcement after the yield load, the axial length of the specimen was stretched despite the 195 kip compressive force. In this manner, the work done by this net axial force becomes negative. The phenomenon is shown to occur in the 17th cycle of Specimen SW 1 (Table 5).

The negative work done by the net axial force means a part of the external work was stored as potential energy due to the axial deformation of the wall. The source mechanism for this increase in potential energy is not very stable since it is a consequence of plastic stretching (straining) of the main reinforcing steel, which results in an increase in the opening of cracks through practically the entire wall cross-section. The widening of these cracks leads to a decrease in the lateral stiffness of the wall which could in turn lead to out-of-plane instability of the part of the wall subjected to compression during the reversal of the loading. Furthermore, the same crack widening can be the main cause for the buckling of the wall vertical reinforcing bars when they are subjected to large inelastic compressive deformation since these could occur without closing of the cracks and would therefore leave the bars without the lateral restraint usually offered by concrete. The buckling of bars can result in a sudden shortening of the wall length and the potential energy stored through the axial deformation of the wall will be released.

It can also be seen from Table 5 that the total work done by the axial force for Specimens SW 1 and SW 2 was negative because the net residual strain existing in these edge columns at the end of the tests was in tension. On the other hand, for Specimens SW 1R and SW 2R, the total work done by these forces was positive due to the crushing of the first story edge columns of these two specimens.

6.4.2 Internal Energy Dissipation Capacity

The internal energy dissipated by the specimens must be computed by integrating the stresses multiplied by the corresponding strains over the whole volume and over the time domain:

$$\text{Internal Energy} = \oint_t dt \int_v \sigma_{ij}\dot{\varepsilon}_{ij}\, dv \tag{6.1}$$

where i,j = 1,2 in the two-dimensional case, and v is the volume of the specimen.

According to the beam theory, if the specimen is subjected only to the shear force, axial force in the 1-direction, and in-plane bending moment, the term, σ_{22}, will be equal to zero (where the 1-axis is the longitudinal axis of the flexural member). Therefore, the above equation can be simplified as:

$$\text{Internal Energy} = \oint_t dt \int_v \sigma_{11}\dot{\varepsilon}_{11}\, dv + \oint_t dt \int_v \tau\dot{\gamma}\, dv \tag{6.2}$$

where $\tau = \sigma_{12}$ and $\dot{\gamma} = 2\dot{\varepsilon}_{12}$.

If the beam theory assumption that plane sections remain plane before and after bending is employed, the strain distribution along a section can be divided into two parts as shown in Fig. 6.3, or, it can be written as:

$$\varepsilon_{11} = \varepsilon_{av} + (\varepsilon_{11} - \varepsilon_{av}) \tag{6.3}$$

Under this condition, the first term of Eq. 6.2 can be rewritten as:

$$\begin{aligned} &\oint_t dt \int_v \sigma_{11}\dot{\varepsilon}_{11}\, dv \\ &= \oint_t dt \int_v [(\sigma_{11} - \sigma_{av}) + \sigma_{av}]\,[(\dot{\varepsilon}_{11} - \dot{\varepsilon}_{av}) + \dot{\varepsilon}_{av}]\, dv \\ &= \oint_t dt \int_v \sigma_{av}\dot{\varepsilon}_{av}\, dv + \oint_t dt \int_v (\sigma_{11} - \sigma_{av})\,(\dot{\varepsilon}_{11} - \dot{\varepsilon}_{av})\, dv \\ &+ \oint_t dt \int_{x_1} \dot{\varepsilon}_{av}\, dx_1 \int_A (\sigma_{11} - \sigma_{av})\, dA + \oint_t dt \int_{x_1} \sigma_{av} dx_1 \int_A (\dot{\varepsilon}_{11} - \dot{\varepsilon}_{av})\, dA \end{aligned} \tag{6.4}$$

The last two terms of Eq. 6.4 are always equal to zero. The first term of that equation can be rewritten as:

$$\oint_t dt \int_v \sigma_{av}\dot{\varepsilon}_{av}\, dv = \oint_t dt \int_{x_1} A\, \sigma_{av}\dot{\varepsilon}_{av}\, dx_1 = \oint_t dt \int_{x_1} (-195 \text{ kips})\, \dot{\varepsilon}_{av}\, dx_1$$

$$= (-195 \text{ kips}) \times [\delta x_1(t_2) - \delta x_1(t_1)] \qquad (6.5)$$

where $\delta x_1(t_2)$ is the total axial deformation at load point 2, and $\delta x_1(t_1)$ is the corresponding deformation at load point 1. Thus the values of the first term of Eq. 6.4 are exactly equal to the external work done by the net axial force, i.e., 195 kips in compression.

The second term of Eq. 6.4 can be rewritten as:

$$\oint_t dt \int_v (\sigma_{11} - \sigma_{av})\, (\dot{\varepsilon}_{11} - \dot{\varepsilon}_{av})\, dv$$

$$= \oint_t dt \int_{x_1} dx_1 \int_{x_3} dx_3 \int_{-y_o}^{y_o} (\sigma_{11} - \sigma_{av})\, x_2\, \frac{(\dot{\varepsilon}_{11} - \dot{\varepsilon}_{av})}{x_2}\, dx_2 \qquad (6.6)$$

According to the assumption that plane sections remain plane, the term, $(\dot{\varepsilon}_{11} - \dot{\varepsilon}_{av})/x_2$, is independent of variables x_2 and x_3, and denotes the rate of curvature of section x_1, $\dot{\phi}(x_1)$. Correspondingly, Eq. 6.6 becomes:

$$\oint_t dt \int_v (\sigma_{11} - \sigma_{av})\, (\dot{\varepsilon}_{11} - \dot{\varepsilon}_{av})\, dv = \oint_t dt \int_{x_1} \dot{\phi}(x_1)\, dx_1 \int_{x_3} dx_3 \int_{-y_o}^{y_o} (\sigma_{11} - \sigma_{av}) x_2 dx_2$$

$$= \oint_t dt \int_{x_1} \dot{\phi}(x_1)\, M(x_1)\, dx_1 = \oint_t dt \sum_{i=1}^{7} (M_i)_{av} (\dot{\phi}_i)_{av} l_i \qquad (6.7)$$

where $(M_i)_{av}$, $(\dot{\phi}_i)_{av}$ and l_i are the average moment, rate of average curvature, and length of the i^{th} region, respectively. The value, $\oint_t dt (M_i)_{av}(\dot{\phi}_i)_{av}$, is therefore equal to the area enclosed by the M_i-ϕ_i diagrams. The values of Eq. 6.7 for certain cycles of the specimens are listed in column 5 of Table 5.

The last term of Eq. 6.2 can be approximated by:

$$\oint_t dt \int_v \tau\dot{\gamma}\, dv = \oint_t dt \sum_{i=1}^{3} V(\dot{\gamma}_i)_{av} l_i' \tag{6.8}$$

where V, $(\dot{\gamma}_i)_{av}$ and l_i' are shear force, rate of average shear distortion, and length of the wall panel in the i^{th} story, respectively. The term, V, is constant throughout the length of the specimen. The value of $\oint_t dt\ V(\dot{\gamma}_i)_{av}$ is equal to the area enclosed by the V - γ_i diagrams. The values of Eq. 6.8 for certain loading cycles are listed in column 7 of Table 5.

Similar to the derivation of Eq. 6.7, and its interpretation, it can be shown that the energy dissipated through the slippage of the vertical reinforcement inside the footing of the specimens can be estimated by the area enclosed by the base moment versus fixed-end rotation diagrams (Figs. 5.37 to 5.40). These values for some loading cycles are listed in column 6 of Table 5.

As discussed in the previous section, the total values of the measured external energy input shown in column 4 of Table 11 should always be greater than the total measured internally dissipated energy values shown in column 9 of the same table. This is because of the presence of frictional forces in the external energy input. The difference between the values of columns 4 and 9 of that table cannot be attributed to the energy dissipated by the frictional forces because other kinds of error are also involved. Some hysteretic loops, such as those of the M_T - θ_T, the M_B - θ_F and the M_2 - ϕ_2 diagrams, etc., were drawn based on discrete scanner readings. The curve connecting two individual points was estimated. The difference between the area enclosed by the actual curves and the estimated curves contributed to most of the error. Occasionally, the values in column 4 of Table 5 are less than the corresponding values in column 9; the difference between them is indicated by a negative error shown in column 10. In general, however, the agreement between columns 4 and 9 is excellent. The accuracy of the experimental data can be judged by the error shown in column 10 of Table 5 and in column 6 of Tables 6 to 9, and which was discussed in Sect. 5.7.

6.4.3 Components of Internal Energy Dissipation Capacity

Before the wall panel crushed, the component of energy dissipated through the flexural deformation ($M - \phi$ and $M_B - \theta_F$) was the most significant. Depending on the level of the load and the ductility of a loading cycle, the energy dissipated in this loading cycle through the flexural deformation may range from 49 (cycle numbers 1 through 7 of SW 2, Table 5) to 83 percent (cycle number 17 of SW 2, Table 5). After the wall panel crushed, the component of energy dissipated through shear distortion became more important (cycle numbers 29 and 30 of SW 1, Table 5). For Specimens SW 1 and SW 2, the energy dissipated through the flexural deformation was about 70 percent of the total energy dissipated by the specimen. This percentage dropped to 33 percent and 48 percent for Specimens SW 1R and SW 2R, respectively. From these comparisons, it can be seen that the energy dissipation capacity of Specimens SW 1 and SW 2 was controlled by flexural deformations. Therefore, classifying this type of structural wall as a "shear wall" may be misleading since it could be interpreted as denoting a shear failure where the flexural mechanism actually plays the most significant part. In this case, the designation of "shear wall" is correct only if it conveys the meaning that this is the structural component resisting most of the shear.

6.4.4 Comparison of Energy Dissipated by Different Specimens

The total energy dissipated by each specimen strongly depends on the loading history. It is believed that the energy dissipation capacity of the wall specimens could increase tremendously if the specimens were cyclically loaded in the lower ductility range which would not cause crushing of the column concrete cover or crushing of the wall panel. This belief is based on observations of the tests on reinforcing bars and concrete cylinders. Under cyclic loading, the energy dissipation capacity necessary to induce failure due to low cycle fatigue for both members is always larger than that under monotonic loading. Therefore, a comparison of the energy dissipation capacity of two specimens is meaningful only if their loading programs are similar.

The two original specimens, SW 1 and SW 2, were constructed to be identical. In comparing the energy dissipated in similar cycles of the repaired specimens, SW 1R and SW 2R, the original specimens are used as frames of reference to judge the efficiency of the repair.

Specimens SW 1 and SW 2R were both tested under monotonic loading. Only one particular cycle between them is comparable, however. The energy dissipated in the 7th cycle of SW 2R, 1148 k-in., is equivalent to the energy dissipated in the 28th and 31st cycles of SW 1, 1619 k-in. If specimen SW 1 is used as reference, the repaired specimen, SW 2R, is judged as having only 71 percent the energy dissipation capacity of the original specimen.

Specimens SW 2 and SW 1R were tested under cyclic loading with progressively increased peak loads or peak displacements. Their energy dissipation capacity prior to crushing of the first wall panel is comparable. The energy dissipated up to the 20th cycle of SW 2 was 4425 k-in.

The energy dissipated up to the 9th cycle of SW 1R was, however, 718 kips-in., which is only 16 percent of that for SW 2. In terms of the energy dissipation capacity, the repair of Specimen SW 1R was far from satisfactory.

6.5 DUCTILITY, ROTATION CAPACITY, AND STORY DRIFT OF SPECIMENS

6.5.1 Ductility and Rotation Capacity

The curvature ductility, the displacement ductility and the plastic hinge rotation capacity of the specimens are given in Table 4. The tabulated values of ϕ_y, δ_{3y}, θ_y and θ'_y are based on the experimental results. The yield curvature, ϕ_y, is defined as the value of the average curvature, ϕ_1, which was measured at the first region of the specimen at the first yield load. The yield rotation, θ_y, is defined as the total angle of rotation at the yield load of the specimen, resulting from the curvature in the first five sections, ϕ_1 - ϕ_5, excluding the fixed-end rotation. The reason why only the first five sections were selected is that the yield of the vertical reinforcement never penetrated into the sixth section during any of the tests. The definition of θ'_y is similar to that of θ_y, but the former includes the fixed-end rotation. Since the vertical reinforcement of the repaired specimens was stretched into the strain-hardening region during the previous tests, there was no clear yield point for the two repaired specimens. Therefore, the θ_y, δ_{3y}, θ_y and θ'_y values of Specimens SW 1R and SW 2R were assumed to be the same as those for Specimens SW 1 and SW 2, respectively.

The terms, μ_ϕ, $\mu_{\delta 3}$, and θ'_{pl} used in Table 4 are defined as the curvature ductility, the displacement ductility at the third floor level and the plastic hinge rotation capacity of the specimens, respectively. Their tabulated values are based on the maximum curvature, the maximum lateral displacement, and the maximum plastic hinge rotation of the specimens obtained before crushing of their first story wall panels.

To be more specific, these values were obtained before there occurred a significant drop in the lateral force resisting capacity of the specimens.

In comparing the ductility values of the specimens, two criteria were used to assess their performance. The first criterion compares their maximum displacement ductility. Under this criterion, Specimen SW 1 indicated the best performance, achieving a maximum displacement ductility value of 6.1. The other criterion compares the total values of ductility during a full loading reversal. The second method appears to be more appropriate than the first because the displacement ductility is an index for estimating the energy absorption and dissipation capacity of a specimen. Therefore, when a structure is subjected to loading or deformation reversals, the energy absorption and dissipation capacity of the structure under such a load would be more accurately estimated by the total ductility (also called cyclic ductility) during a full loading reversal than that estimated by just the maximum ductility. According to the second criterion, the performance of the two original specimens were similar because they had approximately the same cyclic ductility, 8.9 versus 8.4. The performance of the two repaired specimens, however, were relatively poor because they had about one-half the displacement ductility value of the original specimens.

By achieving a displacement ductility value of 6.1, Specimen SW 1 can be judged as behaving like a flexural member. The displacement ductility of a member strongly depends on the location where the displacement was measured, however. As shown in Fig. 5.94, the maximum displacement ductility of Specimen SW 1 achieved at the first floor level was 7.7, which is larger than that achieved at the third floor level, 6.1. The energy dissipation capacity of the specimen under one large impulse load can be more accurately estimated by its maximum plastic hinge rotation, θ'_{pl}. For example, the value of 741 k-in. obtained by multiplying the M_y (32,300 k-in.) of SW 1 with its θ'_{pl} (0.0226), is very close to the internal energy dissipated through the flexural deformation and the fixed-end rotation of SW 1 at the 28th cycle, 768 k-in. (Table 5). A comparison between the θ'_{pl} values of the wall specimen, SW 2, and other reinforced concrete flexural members and structural steel members is shown in Table 11. All the specimens listed in that table were subjected to similar, progressively increased cyclic loading. Regardless of its relatively small span-to-depth ratio, 1.84, and very high nominal unit shear stress, 11.1 $\sqrt{f'_c}$, the wall specimen still provided what is considered to be sufficient plastic hinge rotation capacity to withstand the effect of severe seismic ground excitations.

6.5.2 Story Drift Index

Another parameter frequently used in describing the general behavior of a structure is the story drift index. This is defined as the maximum relative lateral displacement between the two floor levels of the story divided by the height of that story. The story drift indices of the specimens at some load points are shown in Table 12.

To prevent nonstructural damage, the maximum allowable total drift of a building at service load levels is 0.002 H [40], where H is the height of the building. The story drifts given in Table 12 were measured during tests conducted on the wall alone; thus strictly speaking, the measured drift do not simulate the drifts in the entire building. However, because the walls are the main lateral force resisting elements of the building, the story drift of the whole building should be very close to that measured on the tests of the walls alone.

The acceptable maximum drift index that can be derived directly from dividing the total drift by the height of the building should generally not be used to represent the maximum acceptable story drift index in shear walls which can undergo considerably large inelastic deformations. In such cases, the story drift is usually not distriuted uniformly along the height of the building. However, if the story drift at each story is not allowed to exceed the total drift index multiplied by the height of each story, the resulting total drift will comply with the established allowable value. Under the working load of P_T = 90 kips, the story drift values of the original specimens, SW 1 and SW 2 were generally below this limit (LP 32 of SW 2, Table 12). For the repaired specimens, SW 1R and SW 2R, however, this limit was exceeded even under the working load (LP 32 of SW 1R and LP 28 of SW 2R). Most of the large cracks of Specimen SW 1R were repaired with epoxy; some of its small cracks were too narrow to be injected with epoxy, however. Using epoxy injection, 60 percent of the initial stiffness of the original specimen was restored for Specimen SW 1R. Most of the cracks of Specimen SW 2R were left unrepaired; consequently, the initial stiffness of that specimen was only fifteen percent of that of the original specimen. From a serviceability point of view, epoxy injection in cracks should be used whenever possible.

The average story drift index for the bottom three stories of Specimen SW 1 at the maximum load (P_T = 248 kips, LP 158) is 0.037. If the upper stories of the prototype wall have the same amount of story drift index when the prototype building is subjected to loading conditions which correspond to the maximum load of SW 1, the lateral displacement at the top of the prototype wall will be three feet and four inches (0.037 x 93 feet). This amount of displacement is classified as intolerable if the period of vibration is less than four seconds [41]. Under such a large story drift, however, it is estimated that plastic hinges will form at the bottom end of the columns in the first story of the interacting ductile frame. The amount of plastic hinge rotation could reach 0.02 when the first story undergoes a drift of 0.037 x (height of the first story). This amount of plastic hinge rotation is too large for a column subjected to considerable axial force, and could initiate collapse of the building.

As shown in Fig. 6.4, the drift of the i^{th} story of the wall, R_i, can be divided into two parts. The first part, $(R_i)_{rot}$, is due to the rotation at the top of the $(i-1)^{th}$ story. The second, $(R_i)_{tan}$, is due to the flexural and the shear deformation occurring at the i^{th} story of the wall. The latter component is a better index for judging the possible structural damage to the wall as well as the nonstructural damage at that story. Table 13 shows the components of the story drift of the specimens. As indicated in this table, the values of $(R_1)_{tan}$ are always greater than the values of $(R_2)_{tan}$ and $(R_3)_{tan}$ except at LP 28 of Specimen SW 2R. Because the crushed concrete in the lower part of the first story of Specimen SW 2R was recast, while the cracks in the upper stories remained unrepaired, it is possible that the second story wall suffered more damage and therefore resulted in more tangential drift than that in the first story at that load point. For the rest of the load points, the damage was concentrated in the first story of the specimens, particularly so after crushing of their first story wall panels.

6.6 SEISMIC RESISTANCE OF PROTOTYPE BUILDING

Well-designed framed walls coupled with ductile moment-resisting frames constitute an efficient seismic-resisting structural system. According to the linear-elastic analysis discussed in Chapter 3 and the experimental results presented in Chapter 5, the prototype building has sufficient strength and stiffness to resist moderate earthquake excitations. As shown in Fig. 3.1(2)(a), when the building is subjected to the UBC specified earthquake force* multiplied by the load factor, 1.4, the maximum base moment produced in its major lateral force resisting element, the framed walls, is still below the working moment of the wall.** The maximum story drift index of the wall specimen under working loads is 0.0016 (LP 32 of SW 2, Table 10), which is below the drift index limit of 0.002 recommended for preventing nonstructural damage. Therefore, under 1.4 E loading both structural and nonstructural damages to the building are restricted. The reasons for such excellent performance of the building under 1.4 E loading are twofold. First, the actual strength of the wall is much higher than its design strength (Table 3). Second, although during the design of the building the total lateral load, 1.4(E + torsion), was assumed to be taken by the wall system alone, in reality, the frame system also participated in resisting the lateral load.

---

* In this case, the UBC specified base shear multiplied by 1.4 (1.4 E), is equivalent to 6.7 percent of the building weight. That is, 1.4 ZKC = 0.067, where Z, K and C are the terms used in Eq. 14-1, Chap. 23 of the UBC.

** The base moment of the wall is 344,700 k-in. when the building is subjected to 1.4 E [Fig. 3.1(2)(a)]. According to the experimental data, the working moment of the wall, based on the criterion that the stress in the reinforcement is less than 24 ksi, should be 420,000 k-in. This value is equal to the corresponding value of SW 1 shown in Table 3 multiplied by the scale factor, 27.

According to the experimental results evaluated in Sects. 6.4 and 6.5, in the case of a major earthquake, the wall system of the prototype building can provide sufficient ductility and energy absorption and dissipation capacity to prevent serious damage to the building if the base moment-to-base shear ratio of the wall used in the test is the most critical one that can be developed during such an earthquake. Further investigation of this critical ratio will be carried out in Sect. 6.7 and Chapter 7.

6.7 EFFECT OF CHANGE IN STIFFNESS ON THE LOAD DISTRIBUTION OF WALLS

According to dynamic tests run after three repeated yield cycles of Specimen SW 2, the natural frequency of the specimen was reduced twofold. This does not mean that the frequency of the prototype building also decreases in the same ratio. Since the walls are much stiffer than the columns in the building, it is possible that all the columns and most of the beams will remain elastic when the walls have just yielded. According to the experimental results, the flexural stiffness of the seriously cracked wall specimen after yielding was much smaller than that of the uncracked one. The elastic response spectrum analyses carried out in Chapter 3 were based on the stiffness of the uncracked members. The distribution of the member forces of the building were studied using the smaller values of flexural stiffness obtained after yielding of the walls. Emphasis was placed on the force distribution of the walls.

The sectional flexural stiffness of the wall specimen, $(EI)_i$, can be estimated from the slope of its M_i - ϕ_i diagrams (Figs. 5.25 to 5.28). Comparing the slope of the M_i - ϕ_i diagrams before and after the three yield cycles, it can be estimated that the average sectional flexural stiffness of the first, second and third stories of the wall specimen, decreased by 2.75, 2.25 and 1.65 times, respectively. By using this reduced sectional flexural stiffness of the bottom three stories of the wall, an elastic response spectrum analysis of the prototype building was run with conditions similar to that shown in Fig. 3.1(4). As a result of this decrease in stiffness, the fundamental period of the building was increased from 0.77 seconds to 0.92 seconds, and the maximum roof displacement of the building was increased from 3.75 inches to 6.28 inches. To reach the same ultimate base moment of the specimen according to the loading condition shown in Fig. 3.1(4)(d), the shear force must increase from 243 kips to 296 kips, Figs. 3.1(4)(d) and 3.1(6)(d). Under this condition, there is a greater danger that the specimen will fail in a brittle shear mode. If the specimens had been tested under the loading condition shown in Fig. 3.1(6)(d), less ductility and a smaller energy dissipation capacity of the specimens might have been obtained. A similar conclusion was reached by using the spectrum of the derived Pacoima base rock motion of the San Fernando earthquake of 1971. Using this spectrum, the maximum shear force expected to be developed in the wall specimen is 272 kips (compared with 296 kips obtained by using the El Centro earthquake spectrum).

To obtain more accurate information on the distribution of member forces in the building after a number of its members have yielded, it was necessary to carry out a nonlinear dynamic analysis of the building. The results of this analysis will be discussed in the next chapter.

6.8 SUMMARY AND CONCLUDING REMARKS

From the evaluation of experimental results presented in this chapter, some important findings can be discerned.

(1) By subjecting the specimen to cycles of inelastic load reversal, crushing of the concrete cover of its edge columns can be delayed.

(2) Crushing of the wall panel was primarily caused by high shear stresses developed at the compression corner of the wall. As a consequence of these shear stresses, strut action developed.

(3) Under the loading condition shown in Fig. 3.1.4(d), the wall specimens could develop considerable energy dissipation capacity, ductility, and plastic hinge rotation capacity.

(4) Most of the external energy input to the wall specimen was dissipated through its inelastic deformation of flexural type. Therefore, the flexural, rather than shear, mechanism of the wall remains the more significant.

(5) The plastic hinge rotation and energy dissipation capacities of the repaired specimen (SW 1R) are substantially less than those of the original specimen. With careful repair, the plastic hinge rotation capacity and energy dissipation capacity of Specimen SW 2R reached 82 percent and 71 percent, respectively, of those of the original specimen (SW 1).

(6) Under working loads, the story drift index of the wall speciment was below 0.002.

(7) The first spalling of the edge column concrete cover of Specimen SW 1 occurred when the first story drift index reached a value of 0.019. The first story drift index at the maximum strength of this specimen was 0.037. Considerable structural, but mainly nonstructural, damage may result under such a large story drift index (0.037).

(8) In a wall-frame, most of the total seismic base shear of the building is resisted by the wall component. However, the relative

amount of this total shear resisted by the frames and the walls changes with the increase of inelastic behavior. After yielding of ductile walls, the response spectrum analysis of the prototype building with the modified wall stiffness shows that the wall actually resisted a larger part of the total shear than it did before yielding.

(9) After yielding of the wall, the flexural stiffness of the three-story subassemblage decreased considerably, the largest decrease being at the first story. The dynamic response spectrum analysis of the building considering the reduced wall stiffness observed at the bottom three stories shows that the maximum roof displacement of the building was increased from 3.75 inches to 6.28 inches. Furthermore, the base moment-to-base shear ratio of the wall becomes smaller than that of the wall with uniform stiffness throughout its height. Further investigations using nonlinear dynamic analyses are necessary to obtain more accurate values of this ratio.

7. NONLINEAR RESPONSE OF WALL-FRAME STRUCTURAL SYSTEM TO SEVERE EARTHQUAKE GROUND MOTIONS

Using the linear-elastic response spectra of some recorded earthquake ground motions, the linear-elastic response of the prototype building was analyzed in Chapter 3. In the experimental program the loading of the wall specimens was based on the most critical combination of the base moment and base shear of the wall obtained from these analyses. Results of the elastic analyses indicate that the walls and most of the beams of the prototype building are stressed into the inelastic range when subjected to ground excitations of the 1940 El Centro earthquake record and the derived Pacoima base rock motion of the 1971 San Fernando earthquake. Because of the difficulty of determining directly the inelastic response of a structure from only a linear-elastic analysis [42], it was necessary to study the nonlinear response of the building under these same earthquake ground motions.

A computer program, SERF [42], was used to carry out the nonlinear analysis of the prototype building. This program was slightly modified to incorporate the failure model of the column element. The failure criteria of the member will be discussed in detail in Sect. 7.4.

7.1 IDEALIZATION OF PROTOTYPE BUILDING

7.1.1 General Description

The prototype building (Fig. 2.1) was represented as a series of two-dimensional frames (Fig. 7.1). The strength and stiffness of the eight N-S frames without walls were summed together, and represented as the left frame in Fig. 7.1. This frame was connected to the right frame, which represented the two N-S wall frames, by means of links at every floor level.

These links had the properties of infinite rigidity in axial stiffness but nearly zero rigidity in flexural stiffness. The wall was idealized as an equivalent column in this analysis. The mass of the building was assumed to be lumped at the floor levels; their mass moments of inertia were neglected.

7.1.2 Mechanical Characteristics of Members

All the members were idealized using the two-component Clough model [43]. In this model, the member is idealized as a perfectly elastic component acting in conjunction with an elasto-plastic component. The deformations in each component are independent, except at the ends where they are identical. The stiffness of the elastic component, p(EI) (Fig. 7.2), provides the desired rate of strain-hardening. The value, p, used in this investigation, 0.025, was selected according to the M_1 - ϕ_1 diagram of Specimen SW 1 (Fig. 5.20).

The beam elements considered are inextensible, and have uniform stiffness properties along their length except at end zones of one-half column width which are rigid (Fig. 7.1). The positive and negative moment capacities at each end of the flexible portion of the beam may be assigned different values. The column elements (including walls) considered have uniform stiffness properties except at end zones of one-half beam depth which are rigid (Fig. 7.1). They also have a uniform moment capacity along their flexible length, while their moment capacity was varied with their axial force as will be referred to in Sect. 7.4.1. The axial stiffness of the column elements are also considered in the analyses. The strength of the members used in this analysis was calculated according to the real strength of the materials, i.e., f_y = 73 ksi and f'_c = 5.3 ksi (Table 2).

7.1.3 Loading

The building was analyzed under the effect of combined gravity loads and different seismic ground accelerations. Only one of the horizontal components of each of these different ground motions was considered in each analysis. Therefore, all the loads acted in the plane of the frames.

The gravity loads were treated as uniformly distributed forces over the flexible portion of the beams. Since the wall is treated as a column (282 inches wide), part of the gravity loads directly carried by the wall were represented as the concentrated forces acting on it (Fig. 7.1). The P-Δ effect was also considered in the analysis.

7.1.4 Validity of Idealizations

The validity of using the two-component model has been extensively evaluated in Ref. 42. Only the errors involved in the idealization of the building and the assumption of inextensible beams will be discussed.

Because of the presence of spandrel beams around the circumference of the prototype building (Fig. 2.1), the stiffness of the beams in the two end frames is approximately five times higher than that of the beams in the interior frames which consist of only flat slabs. The stiffness of the end frames is therefore relatively higher than that of the interior frames without walls even though the stiffness of the end frame columns is less than that of the interior frame columns. This considerable increase in stiffness points out the important role that the beams play in the lateral stiffness of a moment-resisting frame structural system. In the case that the building undergoes severe earthquake ground excitations, the plastic hinges tend to form in the beams of end frames first. Therefore, more accurate results would have been obtained by idealizing the building as three groups of frames all linked together. One group would represent the two end frames, another would represent the six interior frames, and the last would represent the two wall frames. By doing this, however, the number of elements of stiffness matrices would increase 2.4 times, thus requiring more effort to solve the equations of motion. Using a less time-consuming solution, the building is idealized as shown in Fig. 7.1. The error introduced by this idealization in the estimation of beam ductility factor and beam plastic hinge rotation might be large. However, if only the displacement history of the building or the behavior of the wall alone is considered, the errors become small. This is because the loading condition of the wall was only affected by the lateral stiffness of the whole frame system which will not change considerably either in the elastic or in the initial inelastic range where only a few plastic hinges form in the beams of the two end frames.

Another error might be introduced by the rigid diaphragm assumption. As will be discussed in Sect. 7.3, nonlinear analyses were carried out using a "ductile" and a "failure" model. The failure model allows the members to fail. Generally speaking, the error introduced by the rigid diaphragm assumption before the wall elements failed is negligible. Prior to failure, a major part of the total shear in each story of the building was transferred to the lower story directly through wall elements. After the wall elements in the bottom two stories failed in shear (Sect. 7.6), the story shear transferring mechanism changed. Since the wall elements suddenly lost their strength and stiffness in these bottom two stories, most of the total story shear that was induced in the third story (including the shear resisted by all its columns) and which was transferred dirrectly to the wall of the second story just before failure of this wall, must be transferred to the columns of the second story through the slab of the second floor after wall failure [Fig. 7.3(b)]. Furthermore, because there are three frames located on the right side of the wall frame and only one to its left side, about three-fourths of one-half of the total third story shear* must be transferred through the slab on the right side of the wall. (The story shear transferring mechanism will be discussed in more detail in Sect. 7.6.1.3.) The prototype wall has a maximum shear capacity of 2230 kips according to the test data. Therefore, about 1500 kips of shear force must be transferred through the slab to the right side of the wall. The average shear stress at the section of the slab on the right side of the wall is 670 psi ($9\sqrt{f'_c}$); this value will introduce serious shear cracks in the slab. Therefore, the rigid diaphragm assumption, which is not strictly correct even for the original structure, would introduce large errors. Had proper axial stiffness of the floor system been considered, the shear force absorbed by the wall element would be less than that indicated by the result computed according to the rigid diaphragm assumption.

7.2 STRUCTURAL ANALYSIS PROCEDURE

Only gravity loads and horizontal ground excitations were considered in this investigation. The gravity loads, corresponding to 1.0 x (D + L) of the UBC, were applied to the building prior to consideration of the ground excitations. The record of the N-S component of the 1940 El Centro

---

*After the wall elements failed in the first two stories, the total third story shear and the inertial force generated in the second floor became equal to the sum of the shear taken by all the columns in the second story. The maximum shear force that can be taken by all the columns in the second story is about 4100 kips.

earthquake and the S-16°-E component of the derived Pacoima base rock motion of the 1971 San Fernando earthquake were used as ground excitations. For the building subjected to horizontal ground excitations, the equations of motion can be expressed as:

$$[M]\,\{\ddot{r}\} + [C]\,\{\dot{r}\} + [K]\,\{r\} = -\,\ddot{r}_{gH}\,[M]\,\{b_H\} \qquad (7.1)$$

in which [M] is the diagonal mass matrix; [C] is the viscous damping matrix; [K] is the stiffness matrix; $\{\ddot{r}\}$, $\{\dot{r}\}$ and $\{r\}$ are the accelerations, velocities and displacements of the nodal points relative to the ground, respectively; $\ddot{r}_{gH}$ is the horizontal ground accelerations; and $\{b_H\}$ has zero entries except for unit terms corresponding to the lateral floor degrees-of-freedom.

The viscous damping matrix is assumed to be proportional to the mass matrix; thus:

$$[C] = \alpha[M] + \beta[K] \qquad (7.2)$$

where the scales, α and β, are determined in such a way that the damping ratio, ξ_n, for the n^{th} normal mode is given by:

$$\xi_n = \frac{\alpha T_n}{4\pi} + \frac{\beta\pi}{T_n} \qquad (7.3)$$

where T_n is the n^{th} natural period.

In this investigation, the values of α and β are determined according to $\xi_1 = \xi_4 = 5\%$, which is the same as the critical damping ratio used in the elastic spectrum analyses discussed in Chapter 3 and Sect. 6.7. The values of ξ_n corresponding to other natural periods are shown in Table 14. The T_n values shown in that table were obtained by using the TABS computer program [24].

The reasons for selecting the α and β values according to $\xi_1 = \xi_4 = 5\%$

are twofold. First, the critical damping ratios corresponding to the first five natural periods, ξ_1 to ξ_5, will be close to 5% (Table 14). Second, the critical damping ratio corresponding to the smallest natural period, ξ_{10}, will not be very large. If the α and β values were selected according to other values, for instance, $\xi_1 = \xi_2 = 5\%$, the values of ξ_4, ξ_5 and ξ_{10} would be 13%, 18% and 35%, respectively, which are considered unrealistic.

The equations of motion are formulated and solved by using a direct step-by-step method. At any short time interval, the incremental equation can be expressed as:

$$[M]\,\{d\ddot{r}\} \;+\; [C]\,\{d\dot{r}\} \;+\; [K_T]\,\{dr\} \;=\; -\,d\ddot{r}_{gH}\,[M]\,\{b_H\} \qquad (7.4)$$

in which $[K_T]$ is the tangential stiffness matrix formulated according to the yield conditions of the structural members at the end of the previous time interval. This stiffness matrix is assumed to remain constant within this time interval. The incremental relative nodal accelerations, $\{d\ddot{r}\}$, are assumed to remain constant in a time interval and equal to the average of the values at the beginning and end of this time interval. This approach is known as the "constant average acceleration method." Changes in yield state or other events that would introduce nonlinearities which occurred in a step will be introduced only at the beginning of the next step. The discrepancies detected at the end of a step between the computed element forces and their yield criteria will be approximately compensated by applying corrected nodal loads to the structure. Since no iterative scheme was used, it is desirable to use very small time increments so that the corrected nodal loads are small as will be the errors. The time increment used in this investigation is 0.01 sec., about one-hundredth of the fundamental period of the building.

7.3 RESULTS OF NONLINEAR DYNAMIC ANALYSIS - DUCTILE MODEL

As discussed in Sect. 7.1.4, when a ductile model is used herein, it is assumed that the structure or structural member under consideration has infinite shear capacity and infinite ductility. No failure of the member is thereby allowed to occur. This is not realistic for a real member, but it is necessary in order to study the amount of shear capacity and ductility required for the member to survive when the building is subjected to severe ground excitations.

7.3.1 Response to Derived Pacoima Base Rock Motion (0.4 g)

Only the strong part of the derived Pacoima base rock ground motion with maximum acceleration of 0.4 g (Fig. 7.4) is used in the analyses. The first two seconds of the ground excitations with small amplitude were omitted in the analysis. It is recognized that this initial part of the record could build up the response of the whole model and, thus, lead to a large response. However, it is believed that the increase would not have been significant in this case. The time history of floor displacement is shown in Fig. 7.4. The deformation shapes of the building are shown in Fig. 7.5; these shapes can be roughly estimated from Fig. 7.4.

7.3.1.1 Sequence of Plastic Hinge Formation

The sequence of plastic hinge formation in structural members is indicated by the progressively increasing numbers shown in Fig. 7.6(a). Using the Pacoima ground motions, first yield occurred at the left end of the sixth floor beam of the wall frame at 2.64 seconds. Two time steps later (T = 2.66 seconds), plastic hinges began to appear at the bottom of the wall.

The wall had a large width of 282 inches. When the centerline of the wall rotated under the horizontal ground motions, the vertical displacement at its edges became significant. Since one end of the beams in the wall frame is connected to the wall edge, the large vertical displacement of the wall edge imposed a large relative movement between the two ends of the beam. This relative movement combined with the effect of the gravity loads caused the plastic hinges to appear earlier in the beams of the wall frame.

After 3.08 seconds, some of the plastic hinges in the wall and beam elements shown in Fig. 7.6(a) started to unload. A few steps later (T = 3.15 seconds), all the plastic hinges shown in Fig. 7.6(a) disappeared. This indicates that practically all the members unloaded at the same time.

The maximum required plastic hinge rotation of the beams is 0.019, a value which can usually be developed for beams with large shear spans. The required plastic hinge rotation of the wall is 0.005, which is smaller than the available plastic hinge rotation of the wall, 0.014, according to the experimental data (Table 4). Since no plastic hinges appeared in any of the columns, no collapse mechanism of the building could develop, even though plastic hinges began forming at both ends of each beam. The maximum moment in the columns never exceeded 0.634 of their yield moments during the entire response.

7.3.1.2 Internal Forces of Wall

Since the wall is located along the centerline of the wall frame, the horizontal ground excitations have very little effect on its axial force. The vertical ground excitations were not considered in this study. Therefore, the axial forces of the wall elements remained approximately constant throughout the analyses.

The relationship between the base moments and the base shears of the wall at every five time steps of the first two seconds of the ground excitations are shown in Fig. 7.7. The sequence of occurrence of each individual event is indicated by the arrows connecting them. As previously discussed, the tests of the wall specimens were carried out according to the most critical M_u/V_u ratio obtained from the elastic response spectrum analyses of the prototype building. This ratio is indicated in Fig. 7.7 by the line marked with M_u/V_u = 518 inches. Although the relationship between M_u and V_u of the wall specimens is shown to move along this line, it is obvious from this figure that the M_u/V_u ratio used in the tests is not the most critical one. The most critical ratio shown in Fig. 7.7 occurs at 3.46 seconds, with an M_u/V_u ratio of 446 inches. If the wall specimens were tested under this ratio up to failure, then the base shear of the wall specimen would exceed its shear capacity before the maximum moment capacity of the wall specimen could be reached. More specifically, premature shear failure of the wall would occur before the wall could develop large ductility. Hence, this ratio was deemed critical because it indicates that brittle failure of the wall could occur when the building is subjected to very severe seismic ground excitations like the derived Pacoima base rock motion. This is so because the test results which indicated that the wall was highly ductile (displacement ductility greater than 4.2, cyclic displacement ductility greater than 8.4) were obtained under an M_B/V_B ratio considerably larger than the one that actually might be developed.

The maximum shear of the wall (which is directly printed as an output by the computer) was 2650 kips, occurring in a time of 3.46 seconds. The corresponding value of the base moment was not obtained. This was because the time of 3.46 seconds did not coincide with any of the times corresponding to the five time steps at which the member forces were output during the dynamic analysis; hence, the base moment at this time was not printed and remained unknown. Therefore, the resulting maximum wall shear (and corresponding M_B/V_B ratio) cannot be shown in Fig. 7.7.

The moment diagrams of the wall at three critical time steps are shown in Fig. 7.8. For similar base moments, M_B, shown in (a), (b) and (c) of that figure, the corresponding base shears, V_B, are 2109 kips, 1409 kips and 2078 kips, respectively.

7.3.2 Response to El Centro Earthquake Record (0.33 g)

The first second of the El Centro record was omitted in the analysis because it contained accelerations with small amplitudes. The analytical results are schematically shown in Figs. 7.9 through 7.13.

For the first response cycle (from T = 1.0 sec. to T = 2.2 sec.), the plastic hinges formed at various locations of the beams first, Fig. 7.11(a). These hinges were unloaded after a value for T of 1.99 seconds. For the second response cycle (T = 2.2 sec. to T = 3.2 sec.), however, the hinges formed at the bottom of the wall first. Comparing Figs. 7.11(a) and 7.11(b) with Fig. 7.6(a), it was found that the sequence of plastic hinge formation is strongly dependent upon the type of ground excitations acting on the structural system.

The maximum plastic hinge rotation of the beam and wall elements is 0.0086 and 0.0018, respectively. The maximum moment of the columns is less than 0.49 of their yield moment.

The relationship between the base moments and base shears of the wall occurring simultaneously at consecutive time steps are shown in Fig. 7.12. The sequence of occurrence of each pair of values is indicated numerically. It is also clear from this figure that the M_u/V_u

ratio used in the tests of the wall specimens was not the most critical one that can be expected. The most critical M_u/V_u ratio shown in that figure, 399 inches, occurred at 2.71 sec. (indicated by the sequence number 18). The maximum shear force of 2234 kips was also developed at the same time (2.71 sec.). It can be seen from Fig. 7.7 that the maximum base shear, V_B, did not occur simultaneously with the maximum base moment, M_B. This is contrary to the situation during the tests wherein the maximum V_B always occurred simultaneously with the maximum M_B. However, Fig. 7.7 also shows that the value of M_B (10.1×10^5 k-in., at 2.83 sec.) corresponding to the maximum V_B was larger than the yield moment of the wall (8.1×10^5 k-in.). The maximum shear was reached when the wall was strained in the flexural strain-hardening range, and the shear increased to values larger than that which would have resulted from the M_B/V_B ratio used in the tests. Therefore, the combination of maximum V_B with a large M_B can produce a critical loading condition.

The moment diagrams of the wall are shown in Fig. 7.13. The corresponding base shears for diagrams (a), (b) and (c) of this figure are 2234 kips, 1741 kips and 2022 kips, respectively.

7.3.3 Concluding Remarks

By using the ductile model and other idealizations previously discussed, the overall performance of the prototype building under the derived Pacoima base rock (0.4 g) and El Centro earthquake ground motions normalized to a peak acceleration of 0.33 g can be described as follows.

(1) The sequence of plastic hinge formation is very sensitive to the interaction between the dynamic characteristics of the ground excitations and those of the structure.

(2) There is no danger of structural members (including walls) failing in flexure. The required plastic hinge rotations of the members

will not exceed their rotation capacities if proper detailing is used.

(3) As long as the wall remains ductile, the columns will remain elastic. Therefore, there is no danger of a collapse mechanism developing for the building.

(4) The required shear capacity of the wall when the building is subjected to the Pacoima (0.4 g) and El Centro ground motions (0.33 g), 2650 kips and 2234 kips, respectively, exceeds the shear capacity of the wall estimated from the experimental data, 2230 kips. Therefore, the wall could fail in shear. For this reason, analyses using a ductile model cannot adequately describe the response of the building if the wall elements failed in shear in the lower few stories.

7.4 MEMBER FAILURE CRITERIA

Depending on the geometry, amount and detailing of reinforcement, and loading condition, a reinforced concrete member could fail in shear, in flexure, under high axial force, or due to a combination of two or all of these internal forces. Possible types of failures of the prototype building members will be discussed herein.

7.4.1 Framed Wall

The type of wall failure which might occur depends mainly on the loading condition of the wall. As shown in Fig. 7.7, if the wall is loaded in such a way that its M_u/V_u ratio is less than 300 inches, its shear capacity will be exceeded before yielding, and it might undergo a brittle shear failure. Otherwise, the failure will be of a flexure-shear type.

A parameter extensively used to evaluate the inelastic behavior of a member is the maximum plastic hinge rotation capacity. This parameter also depends on the loading conditions (shear span, amount of axial force, etc.) and the loading history of the member. For example, having the same loading conditions, monotonically loaded Specimen SW 1 had a larger plastic hinge rotation capacity (0.023) than that of cyclically loaded Specimen SW 2 (0.014). As discussed in Sect. 7.3.1.2, the M_u/V_u ratio of the wall is not fixed when the building is subjected to seismic ground excitations. With the limited experimental data available, it is difficult to define the shear capacity and plastic hinge rotation capacity of the wall according to its loading condition (relationship among internal forces) and loading history. For simplicity, the maximum shear capacity of the prototype wall will be taken as the corresponding value obtained from the tests, i.e., 248 kips x 9 = 2230 kips, and the plastic hinge rotation capacity of the wall will be restricted to 0.014. Whenever the shear or plastic hinge rotation of the wall element exceeds these limits, this wall element is considered as failed in the computer program. Treatment of the failed elements in the computer program will be discussed in Sect. 7.5.

7.4.2 Columns

The axial force due to gravity loads for the columns in the upper few stories is small. The external columns in these stories may be loaded into tension under certain circumstances. Therefore, there is a possibility of these columns failing in shear or in flexure-shear.

The columns located in the bottom story are subjected to very high axial compressive stresses. According to the analytical results of Sect. 7.3, the axial compressive stress of these columns ranges from 365 psi to 1450 psi, or their axial force ranges from 0.2 P_b to 0.78 P_b, when the building is subjected to the ground excitations as described in that section. The lateral reinforcement of these columns were designed to fulfill the confinement requirement [Eq.(2605), Chap. 26 of the UBC] and provides such a high shear capacity that no problem of shear failure ever arises. Under such high axial force (0.78 P_b), however, the available ductility or plastic hinge rotation capacity of the column will be small. Unfortunately, no reliable data on the plastic hinge rotation capacity of these columns are available. To roughly estimate how large it will be, the experimental results of Kustu [44] and Hisada [45] are evaluated.

7.4.2.1 Experimental Results of Kustu

The column section used in Kustu's investigation was 12 inches by 12 inches, and was reinforced with ten longitudinal #4 rebars. The column was 36 inches long and was subjected to moment with the same magnitude and direction at both ends as well as axial force. For column model 7, the plastic hinge rotation capacity estimated from its M - ϕ diagram is approximately 0.01 radians. The maximum nominal unit shear stress of this column was 7.1 $\sqrt{f'_c}$, and the axial force was 144 kips (0.6 P_b, corresponding to an axial stress of 1000 psi).

7.4.2.2 Experimental Results of Hisada

The column section of Specimen A-P_w 0.9 is shown in Fig. 7.14. The length of the column was 60 inches (1500 mm) and was subjected to a loading condition similar to that described by Kustu. The column was subjected to very high axial stresses [1700 psi (1/3 f'_c)] and high nominal unit shear stress (7.8 $\sqrt{f'_c}$) yet maintained ductile behavior. The maximum plastic hinge rotation estimated according to Fig. 7.14 is approximately 0.01. It should be noted, however, that this column specimen had been subjected to 30 full loading reversals around R = ± 0.01 and six full loading reversals around an R = ± 0.02. If it had been loaded monotonically, or subjected to fewer loading reversals in the low ductility range, its plastic hinge rotation capacity might have been larger.

7.4.3 Beams

For beams designed according to Eq.(26-3), Chap. 26 of the UBC, there is usually no danger of shear failure. Since the length-to-total depth ratio of the beams in the prototype building is relatively large, they should be able to develop large plastic hinge rotation capacity. (The length-to-total depth ratio of the spandrel beams is 9.1, and that for the beams consisting of flat slabs is 27.) According to the analytical results of Sect. 7.3, therefore, no danger of beam failure is expected.

7.5 MODIFICATION OF PROPERTIES OF FAILED MEMBER

The SERF computer program [42] was modified to accommodate member failures. According to the analytical results discussed in Sect. 7.3, the wall element will fail first. The primary purposes of the investigation herein are to study the overall behavior of the building after wall failure and to determine the required plastic hinge rotation capacities of the beams and the columns for avoiding complete collapse of the building. In the analyses, the ductile model was adopted for beams and columns, and the failure model was adopted for the wall.

A progressive failure model [42] was selected for the wall for the following reason: If the wall strength is removed immediately after its failure, the unbalanced nodal force will become too large an impulsive load for the remainder of the building because of the large moment and shear capacity of the wall element that has to be removed. In order to obtain accurate results using SERF, it is necessary to keep the incremental inertial force small in each time step. A sudden removal of all the strength of the wall element after it failed will violate this principle. As indicated in the $P_T - \delta_{3R}$ diagrams of the wall specimens (Figs. 5.5 to 5.8), wall strength dropped gradually even after failing in shear. It was also observed in the tests that the wall specimens maintained their axial force carrying capacity up to the stage where the spirals of their edge columns broke. For these reasons, the wall properties after failure were modified as follows.

(1) After a wall element failed, its axial stiffness and axial force carrying capacity remained unchanged (Fig. 7.16).

(2) If the wall element fails in flexure, i.e., the plastic hinge rotation of the wall element exceeds its capacity, its yield moment will be reduced according to Figs. 7.15(a) and 7.16, starting from the same time step that failure is detected; its flexural stiffness will be reduced according to Fig. 7.15(b) starting from the next time step. As shown in Fig. 7.15, eight steps after failure, the strength and stiffness of the wall element is reduced to 30 and 0.5 percent of its original values, respectively. With the same reduction rate, the strength and stiffness of the wall element are nearly all removed after 20 steps.

(3) The amount of yield moment to be reduced at the same time step when shear failure in the wall element is detected will be discussed in the next paragraph. In subsequent steps, the yield moment of the wall will be reduced according to Fig. 7.15(a). Similarly, approximately 20 steps after failure, the strength of the wall element is neglected altogether.

Immediately after the shear failure of the wall element is detected, the yield moment of the wall will be reduced in such a way that, after this moment correction, the new shear force in that wall element will not be higher than its shear capacity. To determine if the shear wall fails in shear, the shear force of the wall, V, is computed according to the following equation:

$$V = \frac{M_I + M_J}{H} \tag{7.5}$$

in which M_I and M_J are the existing moment at nodal points I and J of that wall, respectively, at the instant of the time under study, and where H is the story height. If this computed shear force is higher than the shear capacity of the wall, then failure in shear occurs, and the yield moment of that wall element must be reduced as described in the flow chart shown in Fig. 7.17. The values of M_I and M_J will be reduced automatically according to the yield state. Hence, after this correction, the V value will be below the shear capacity of the wall. Symbols M_y and V_{max} in the flow chart denote the yield moment and shear capacity of the wall, respectively.

7.6 RESULTS OF NONLINEAR DYNAMIC ANALYSES - FAILURE MODEL

The ground excitation selected for the first analysis is the derived Pacoima base rock motion, with a maximum ground acceleration of 0.4 g. From this analysis, it was found that no collapse mechanism of the building could be formed with this particular excitation. To study the collapse mechanism of the building, a similar analysis was carried out using the same type of ground excitation, but with its maximum acceleration normalized to 0.5 g. That is, at each time interval, the acceleration intensity of the derived Pacoima base rock motion was multiplied by a factor of 0.5/0.4.

7.6.1 Response to 0.4 g Derived Pacoima Base Rock Motion

7.6.1.1 General Response and Sequence of Wall Failure and Plastic Hinge Formation

The comparison between the roof and first floor displacements obtained by using the ductile and failure models is shown in Fig. 7.18. As expected, before the wall element failed in shear, the response of the building to the derived Pacoima base rock motion is identical for these two models (Figs. 7.4 and 7.18). At 2.80 sec., after plastic hinges formed at both ends of the wall element in the first story and several locations of the beams, the wall element in the second story failed in shear. Two steps later at a value of T = 2.82 sec., the wall element in the first story also failed in shear.

The sequence of plastic hinge formation and member failure from 2.64 sec. to 2.86 sec. is shown in Fig. 7.6(b). At 2.90 sec., before the plastic hinges appeared at the bottom of the columns, some plastic hinges in the beams started to unload. At 2.94 sec., when plastic hinges formed at the bottom of Column Lines 2 and 3, nearly all the plastic hinges in the beams above the third story disappeared. Finally, a sidesway collapse mechanism was nearly formed in the bottom two stories of the building at 3.15 sec. [Fig. 7.6(c)]. When the formation of the plastic hinges of the building is similar to that shown in Fig. 7.6(c), the building behaves like a structure with soft, first two stories.

7.6.1.2 Moment Diagram of Wall and Column

The moment diagrams of the wall and of a typical column, before and after wall elements failed in the first two stories, are shown in Fig. 7.19. After the wall failed in the first two stories, the shear force of the wall (indicated as the slope of the wall moment diagram) was concentrated at the third story. Before the wall elements failed, the moment in column 1 was very small. After failure, the elements of column 1 in the first two stories deformed like a long column, as indicated by the second moment diagram of this column in Fig. 7.19. The moment diagrams of other columns (not shown) are similar in shape to that of column 1.

7.6.1.3 Story Shear and Transferring Mechanism

At 2.77 sec., the total second story shear was 2750 kips. Only 16 percent of this shear force (780 kips) was resisted by the columns. Twenty time steps after the wall failed in that story (T = 3.01 sec.), the total second story shear became 3110 kips, all resisted by the columns. At the same time, the total third story shear was 2140 kips. However, 180 percent of this shear force was taken by the two walls (3968 kips), and -80 percent (1828 kips) was taken by the columns. The free-body diagram of the distribution of the second and third story shear is shown in Fig. 7.20. This free-body diagram was drawn according to the assumption that all ductile frames take the same amount of shear force. From Fig. 7.20, it can be seen that about 1450 kips of shear force was transferred to the third story wall through the second floor slab connected to the right side of the wall. The average shear stress in that wall-slab connection was 650 psi ($9\sqrt{f'_c}$). The slab could be severely cracked under such a high shear stress.

7.6.1.4 Required Plastic Hinge Rotation of Beams and Columns

After the wall elements failed, building displacement at the levels of the first two stories rapidly increased. This can be clearly observed in Fig. 7.5 where the lateral deformation shapes of the building are indicated by short dashed lines. The maximum drift of the first story obtained in the analysis using a ductile model was 0.006. Using a failure model, this value increased to 0.028. The required plastic hinge rotations of the beams and columns using the failure model were 0.033 and 0.019, respectively, compared with those values obtained using the ductile model, 0.019 and 0.0, respectively. It is clear from these values that wall elements should be kept ductile in order to control structural and nonstructural damage to the building.

7.6.1.5 Column Axial Force and Possibility of Column Failure

The maximum axial compressive force in the interior and exterior columns was 749 kips (0.68 P_b^{*}) and 578 kips (0.78 P_b^{**}), respectively. The corresponding axial stress was 1300 psi and 1445 psi, respectively. One important factor which is not considered by either the UBC or this nonlinear dynamic analysis is the vertical ground acceleration. As discussed in Sect. 3.6, vertical ground accelerations have little effect on the ductility of the wall since the wall is subjected to a relatively small axial force. Nonetheless, vertical ground accelerations become critical for columns if the peaks of the axial force developed by the vertical acceleration coincide with the maximum axial force response due to horizontal ground accelerations. The total axial compressive force in the exterior column could have reached 1.0 P_b had the vertical ground acceleration been considered. Under such a high axial compressive force, the column may not be able to provide the required rotation capacity, 0.019 (Sect. 7.6.1.4), to prevent the building from collapse.

---

* The P_b value of interior columns (24 in. x 24 in., reinforced with twelve No. 10 bars) is equal to 1105 kips. This value is computed according to the actual strength of materials used in the models, i.e., f_y = 73 ksi, and f'_c = 5.3 ksi. If the code specified strength of materials is used, i.e., f_y = 60 ksi, and f'_c = 4 ksi, then P_b will equal 875 kips (without ϕ factor). The designed axial force of interior columns, 1230 kips, is equal to 1.4 P_b, being the P_b computed according to code.

** The P_b value of exterior columns (20 in. x 20 in., reinforced with twelve no. 10 bars) computed according to the actual strength of materials and to the code is 740 kips and 580 kips, respectively.

7.6.2 Response to 0.5 g Derived Pacoima Base Rock Motion

The results from this ground motion are similar to those discussed in Sect. 7.6.1, except under this intensified ground motion, wall elements failed earlier (at T = 2.76 sec.) and the collapse mechanism of the building formed at 2.98 seconds. However, since all members had a strain-hardening stiffness of 2.5 percent, even after the collapse mechanism formed and with the influence of the P-Δ effect, the building will not collapse if its beams and columns remain ductile. The time-history of the floor displacements is shown in Fig. 7.21, and the sequence of plastic hinge formation between 2.73 sec. to 3.01 sec. is shown in Fig. 7.22(a).

At 3.01 sec. there are already two more plastic hinges than required to develop a collapse mechanism. These two extra plastic hinges were located at the second story of columns 2 and 3 (indicated by sequence number 39). After 3.04 sec., the plastic hinges shown in Fig. 7.22(a) began to unload. At 3.25 sec. the plastic hinges with different sense appeared at the bottom of columns 2 and 3. The location of the plastic hinges at 3.75 sec. is shown in Fig. 7.22(b).

Comparing Figs. 7.6(c) with 7.22(a), two different collapse mechanisms are shown to form in the building under a similar type of ground motion with different intensities. The lateral deformation shapes of the building corresponding to these two collapse mechanisms are shown in Fig. 7.5.

The maximum column plastic hinge rotation of 0.025 occurred at the bottom of column line 2, at 3.84 seconds. The maximum plastic hinge rotation of the flat slab beam, 0.042, occurred at the eighth floor beam of the wall frame when reaching 3.34 sec., and that of the spandrel beam, 0.026, occurred at the third floor beam of the ductile frame at 3.34 seconds. It is doubtful whether such a large rotation, 0.025, can ever be developed in a column with high axial compressive force. If the plastic hinge rotation of the columns were restricted to 0.01 as estimated in Sect. 7.4.2, then the building would have collapsed at 3.44 sec., at which time the plastic hinge rotation at the bottom of column lines 2, 3 and 4 exceeded the limit value of 0.01. The roof displacement of the building at this time was equal to 17.5 in. Compared with the maximum plastic hinge rotations, 0.026 and 0.035, developed in reinforced concrete cantilever specimens B 33 and B 35I, respectively (Table 11 and Ref. 12), the amount of plastic hinge rotation, 0.042 and 0.026, should be tolerable for flat slab and spandrel beams, respectively, belonging to the prototype building.

7.7 DYNAMIC RESPONSE OF PROTOTYPE BUILDING WITH STIFFER AND STRONGER WALLS

In the original design of the prototype building, two N-S framed walls were selected (Chapter 2). Due to the interaction with the ductile frames of the building, these two walls could fail in shear when the whole building responds to severe seismic excitations. It is usually desirable to increase the number of the walls and, consequently, to increase the degree of indeterminacy of the main lateral force resisting system of the building. In general, the larger the degree of external (support) indeterminacy of a structural system, or the larger the degree of indeterminacy of the less redundant story, rather than that of the overall structure, the larger the probability that it can survive an earthquake. Furthermore, application of the AIJ Code [26,27] has shown that the total shear force for which the walls of the prototype building should be designed is 460 percent of the unfactored value specified by the UBC (536 kips, Sect. 2.2) It is for this same reason that if design is carried out according to the AIJ Code, a minimum number of four walls is required [27]. For these reasons, it was decided to investigate the response of four, rather than two, walls in the prototype building. Two cases were studied. In the first case, four walls were designed according to UBC requirements. Hence, the total strength of these four alternatively designed walls is approximately equal to the total strength of the two prototype walls.* In the second case, the seismic response of the building consisting of four walls, each identical to the prototype wall, was studied. In this manner, the strength and stiffness of the main lateral force resisting system of this building is twice as large as the corresponding values of the originally designed building.

7.7.1 Prototype Building with Alternative Design

Based on the same code provisions, it is possible to make several different designs of the main lateral force resisting system of a building. These different designs do not necessarily ensure that the building will have the same safety against a major earthquake. It is therefore desirable to study the possibility of improving the overall behavior of the prototype building with an alternative UBC design. The floor plan of this building is shown in Fig. 7.23, and indicates the four N-S framed walls.

7.7.1.1 Design of Four Framed Walls

These alternatively designed walls also consist of wall panels and spirally reinforced edge columns. The design procedures are similar

---

* The prototype wall is referred to as the wall used in the original design.

to those discussed in Sect. 2.2. The total design base shear for the entire building is 950 kips, the total design torsional moment is 8550 k-in., and the design dead and live loads per wall are 782 kips and 98 kips, respectively.

(a) Design of Outside Walls

(i) compression column

$$\frac{P_u}{\phi} = \frac{1.4\ (782 + 98 + 900)}{0.75} = 3323 \text{ kips} \tag{7.6}$$

where 900 kips is due to overturning moment.

Using a 28 in. x 28 in. column with twelve #9 rebars:

$$P_u = 0.85 \times 4 \times (28 \times 28 - 12) + 60 \times 12$$

$$= 3345 \text{ kips} > 3323 \text{ kips} \tag{7.7}$$

(ii) column spirals

$$P_s = 0.45\left(\frac{A_g}{A_c} - 1\right)\frac{f'_c}{f_y} = 0.45\left(\frac{784}{491} - 1\right) \times \frac{4}{60} = 0.0179 \tag{7.8}$$

If #5 rebars are used at 2-3/4-in. intervals:

$$P_s = \frac{4A''_s}{D_s{}^2} = \frac{4 \times 0.31}{25 \times 2.75} = 0.0180 > 0.0179 \tag{7.9}$$

(iii) tension columns

$$\frac{P_u}{\phi} = \frac{1.4 \times 900 - 0.9 \times 782}{0.9} = 618 \text{ kips} \tag{7.10}$$

Using twelve #9 rebars:

$$P_u = 12 \times 60 = 720 \text{ kips} > 618 \text{ kips} \tag{7.11}$$

(iv) wall panel

$$\frac{V_u}{\phi} = \frac{2.8 \times (950/4 + 51.6)}{0.85} = 952 \text{ kips} \tag{7.12}$$

Selecting an eight-in. thick wall panel:

$$\nu_u = \frac{V_u}{\phi bd} = \frac{952000}{8 \times (0.8 \times 280)} = 531 \text{ psi} = 8.4\sqrt{f'_c} < 10\sqrt{f'_c} \tag{7.13}$$

and

$$\nu_c = 2\sqrt{f'_c} = 127 \text{ psi}$$

If #6 rebars are used in a single layer for horizontal reinforcement,

$$S = \frac{A_\nu f_y}{(\nu_u - \nu_c)b} = \frac{0.44 \times 60000}{(531 - 127) \times 8} = 8.2 \text{ in.} \qquad (7.12)$$

use S = 8 in.

The vertical panel reinforcement was selected to be the same as the horizontal reinforcement.

(b) Design of Inside Walls

Following the same design procedure, the size of the edge columns of the inside walls was selected to be 28 in. x 28 in., reinforced with nine #9 rebars to fulfill the design tensile and compressive force, 475 kips and 2150 kips, respectively. The same amount of spiral was selected: #5 rebars at 2-3/4-in. intervals. The design shear force, V_u/ϕ, for these walls is 855 kips. The thickness of the wall panels was selected to be eight in.; these panels were reinforced in both directions with a single layer of #6 rebars at twelve-in. intervals.

These computations indicate that the gravity loads governed the design of the edge columns. Even though very small reinforcement ratios were selected for these columns (0.015 and 0.011), the longitudinal reinforcement of the tension columns was slightly overdesigned. Although the two systems of walls were designed to carry the same lateral loads, the sum of the actual flexural strength and of the flexural stiffness capacities of these four walls are 122 and 150 percent of the corresponding capacities of the two prototype walls of the original design. The sum of the shear capacity of these four walls, however, is the same as that of the two prototype walls.

7.7.1.2 Response to 0.4 g Derived Pacoima Base Rock Motion

The analytical model for the building with the alternative design is similar to that of the original building. The model for the alternative design is similar to that shown in Fig. 7.1 except that the left and right frames represent the six N-S ductile frames and the four N-S wall frames of the building shown in Fig. 7.23, respectively. The total stiffness of the frame system of the building with alternative design is slightly less than that of the original design. This is because four of the columns, which in the original design formed part of the frame system, now become part of the walls.

The time-history of the floor displacement of the building with alternative design is shown in Fig. 7.24. To permit comparison, the time-history of the floor displacements of the building with different designs are shown in Fig. 7.25. The sequence of plastic hinge formation and failure of the walls is shown in Fig. 7.26. This figure indicates that the plastic hinges were first formed at the bottom of the wall and at the left end of the six beams located in the sixth bay at 2.63 seconds. A few steps later, the second story wall element failed in shear.

Due to the restraint provided by the frame system, the wall tended to be loaded with a smaller shear span than that of the cantilever walls acting alone. Consequently, the walls could have failed in brittle shear. In theory, if the total stiffness of the walls is increased, the frame system should put less restraint on them. However, although the total stiffness of the four walls of the building with alternative design was 50 percent larger than the corresponding value of the two prototype walls, the former failed earlier (Fig. 7.25). One reason for the earlier failure of the stiffer walls follows.

After the plastic hinge formed at the base of the wall, the stiffness of the wall system was greatly reduced. Because only a few of the beams yielded when the wall yielded, the frame system offered relatively more restraint to the wall. The larger amount of initial flexural stiffness in the four alternatively designed walls had little effect on the restraint provided by the frame system after the wall yielded. Thus, the advantage provided by having large initial stiffness of the four alternatively designed walls was lost as soon as the walls yielded. Since the sum of the flexural strength of the four walls is 22 percent higher than that of the two prototype walls, and the dynamic response of these two systems shows that the minimum values of the shear span were very similar, the total shear developed in the four walls can be higher. Although the shear capacities of these two systems of walls are the same, the four walls which developed higher shear failed earlier.

After 2.80 sec., some of the plastic beam hinges shown in Fig. 7.26(a) started to unload. At 2.87 sec., when the plastic hinges formed at the bottom of columns 2 and 3, all the plastic beam hinges above the second floor disappeared. Finally, a near-collapse mechanism similar to that shown in Fig. 7.6(c) was formed at 3.10 sec. [Fig. 7.26(b)].

Under the same seismic excitations, less plastic hinges formed in the beams of the building with stiffer walls [compare Figs. 7.26(a) with 7.8(b)]. However, the maximum plastic hinge rotation of the beams and columns of the building with alternative design were 0.067 and 0.052, respectively; these values are considerably larger than the corresponding ones of the original building, 0.033 and 0.019, respectively.

Judging by these large rotation requirements, both the columns and beams of the alternatively designed building could fail.

7.7.2 Building with Four Prototype Walls

The fundamental period of the building with four prototype walls was 0.76 sec., which is smaller than that (0.87 sec.) of the prototype building. (The latter consisted of only two prototype walls.) However, the mode shapes of these two buildings were similar.

The analytical results of the dynamic response of the building with four prototype walls to the 0.4 g derived Pacoima base rock motion are schematically shown in Figs. 7.25, 7.27 and 7.28. Since the wall system of this building had twice the moment and shear capacities of those of the wall system of the prototype building (the latter was designed according to UBC provisions), no member failure was found during the whole response history. Although the designed earthquake force of this building is twice as large as that specified by the UBC, yielding still occurred at the bottom of the walls and at both ends of the beams as shown in Fig. 7.27. This indicates that the earthquake force specified by the UBC for the prototype building (fundamental period = 0.87 sec.) is considerably lower than that which can be developed in the building under severe earthquake ground motions.

A comparison of the analytical results from this building with those from the prototype building using the ductile model (Sect. 7.3.1) is shown in Table 15. This table indicates that the improvement in overall performance of the building with four prototype walls is not very significant under a ground motion like the derived Pacoima base rock motion. The maximum displacements and required plastic hinge rotation capacities of the walls and beams were reduced by only 30 percent.

Under this type of ground motion, it is therefore economical to keep the walls of the original prototype building, making them very ductile. More specifically, it is desired to increase the shear capacity of the walls to avoid the brittle shear failure.

7.8 CONCLUDING REMARKS

From the information obtained from analyses using different models (ductile and failure), some observations can be made regarding the performance of the prototype building under seismic excitations.

(1) The behavior of the building under severe seismic ground excitations is satisfactory if its wall elements remain ductile.

(2) The required shear capacity of the wall (assumed to be an infinitely ductile flexural member), 2651 kips, is 1.5 times higher than the ultimate design shear capacity required by the UBC provision, 1765 kips (Sect. 2.2.2). This value is also 1.2 times higher than the actual shear capacity of the wall estimated from the experimental results, 2230 kips. Therefore, more stringent code provisions are needed to guarantee ductile behavior of walls.

(3) By using the failure model, the maximum first story drifts of the building under response to the derived Pacoima base rock motion with maximum ground accelerations of 0.4 g and 0.5 g are 0.028 and 0.030, respectively. Judging from these values, it is believed that even if the building did not collapse after the wall elements failed, the structural and nonstructural damages as well as the residual deformations in the first two stories of the building after the earthquake excitations would be so large that repair would be difficult and costly.

(4) The danger of total collapse of the building when subjected to ground excitations like the derived Pacoima base rock motion with a

maximum ground acceleration normalized to 0.5 g is great.

(5) Depending on the characteristics of ground motions, different collapse mechanisms can develop in the prototype building after its walls fail.

(6) Comparison of nonlinear dynamic analyses results with those obtained from elastic spectrum analyses show that, although the latter yield better results than analyses of the building with UBC specified lateral forces, the use of elastic spectrum alone does not permit accurate prediction of the critical M_B/V_B ratio of the wall. However, in this particular case, by reducing 2.75, 2.25, and 1.65 times the flexural stiffness of the wall in the first three stories according to the test results (Sect. 6.5), the elastic response spectrum analyses provided better results.

(7) Due to the interaction between the walls and the frames of a building with a dual seismic resisting system, the movement of the walls in the upper stories are usually restrained by the frames. Increasing the elastic stiffness of the walls has little effect on the restraint provided by the frames, especially after the walls yield.

(8) Increasing the shear capacity of the walls is a very efficient method of improving the overall performance of the prototype building under severe seismic excitations (such as the derived Pacoima base rock motion).

(9) If the shear capacity of a wall controls failure, it is worthless to increase its flexural capacity without increasing the shear capacity. When a wall suddenly fails in shear, the large amount of energy originally absorbed is suddenly released and acts as an impulsive load (impact) on the remainder of the building. The larger the energy originally absorbed, the worse the effect of this impact on the building.

This is the reason why the performance of the alternatively designed building was worse than that of the prototype building when subjected to the derived Pacoima base rock motion.

(10) After the wall fails in the bottom two stories, the second floor slab will be subjected to high shear stress which can lead to serious cracking in the slab.

(11) Regarding the validity of the above discussions, it should be kept in mind that while interpreting the results obtained from the time-history dynamic analyses, these results were compared with the results obtained in experiments which were carried out under pseudo-static conditions. Thus, strictly speaking, this comparison is not valid, for, while the M_B/V_B ratio at the stage near failure was kept constant during the experiments, such a value varies continuously during the actual dynamic response of the building.

8. PARAMETRIC STUDIES OF FRAMED WALL SPECIMEN

The behavior of framed walls under severe seismic conditions is very complex, especially when they form part of a wall-frame system. Depending on the relative values of the different internal forces (axial force, moment and shear), the behavior of framed walls may be of a ductile or brittle type. Although the overall performance of the wall specimens was excellent during testing, nonlinear dynamic analyses of the prototype building (Chapter 7) indicate that framed walls may be subjected to a more critical loading condition during a major earthquake than the one to which they were subjected during the tests. Under such a critical loading condition, wall specimens may not develop displacement ductility factors as large as those developed during the tests.

Most of the shear wall experiments carried out in the past [17-22] did not consider the effect of slabs. However, the test results of this investigation suggest that slabs can offer considerable restraint to prevent wide openings of the diagonal cracks passing through them, i.e., they act as very effective horizontal ties.

Without carrying out another series of experiments, the finite element analysis technique was selected to study the effect of shear span and slabs on the behavior of the wall specimen under seismic loads. It was also attempted to predict theoretically the obtained experimental results.

8.1 FINITE ELEMENT ANALYSES

The computer program, NONSAP [46], has been developed to handle static and dynamic, linear and nonlinear finite element analysis. The NONSAP computer program has six two-dimensional models. For this study, one of these two-dimensional models (Curve-Description Model) was modified to simulate the properties of concrete. The original program was also slightly modified to analyze more efficiently the problems of using this modified model.

The original curve description model assumes that the material can take no tension and that once a crack opens perpendicular to the principal tensile direction, the crack direction will be fixed for the rest of the solution steps. For a cracked element, axial stiffness across the crack and shear stiffness can be individually reduced by a different user selected factor. If a large factor is selected to reduce both shear and axial stiffnesses (e.g., 10^4), the cracked two-dimensional element will become a one-dimensional element which can resist only the stress along the crack direction. The modified model maintains most of the character of the original curve description model, except that it assumes the material has a certain amount of tensile strength supplied by the user. Once the principal tensile strength of an element exceeds its tensile strength, this element will be assumed to have cracked. The entire principal tensile stress of this cracked element will be released by applying equivalent nodal forces.

Equilibrium iteration was not programmed for this model. The accuracy of the analysis, however, can be achieved by assigning small load increments for each solution step or by assigning an arbitrary number of equilibrium iterations at any solution step predetermined by the user. This type of equilibrium iteration was introduced by assigning two solution steps with the same external loads. In this manner, any unbalanced forces generated in the first step will be corrected in the second step. This modified cracking model cannot be adopted to perform dynamic analysis.

8.2 COMPARISON BETWEEN TEST RESULTS AND FINITE ELEMENT ANALYSES

The finite element grids of the analytical model are shown in Fig. 8.1. The reinforcement is idealized with the one-dimensional truss elements connecting the nodes; the reinforced area is also marked in this figure. As observed during the tests, the cracks did not penetrate through the whole width of the slabs. Therefore, only part of the slab was considered to provide effective restraint to prevent wide openings of the diagonal cracks passing through them. The width of the slabs used in the analyses, 60 in., was arbitrarily selected to be three-quarters of the 80-in. wide slabs of the test specimens. Except for the width of the slabs, the dimensions of the wall panels and the edge columns, as well as the amount of reinforcement for the standard specimen of the analytical model (Fig. 8.1), are identical to those of the test specimens. However, to reduce computer time, the analytical model was designed with only two stories. Since failure was initiated in the first story, it is believed that this two-story analytical model can provide useful information regarding the behavior of the critical region of the specimen tested.

The analytical model was loaded with uniform horizontal forces at the nodes along the upper boundary of the specimen. The axial forces were applied on the same nodes and were distributed according to the variation of the axial stiffness across the top section of the specimen. The top overturning moment was applied by using equivalent vertical forces which were distributed according to the variation of the axial stiffness of a cracked section.

The stress-strain curves of the concrete and the steel used in the analyses are shown in Fig. 8.2. The concrete curve is observed to have very large ductility, which is characteristic of the confined concrete. Since 64 percent of the column concrete was composed of the confined concrete, the stress-strain curve shown in Fig. 8.2(a) represents the average behavior of the column concrete. No failure criteria were programmed for the unconfined wall panel concrete. The user must determine the crushing of the unconfined concrete according to the stress output of the program. If the stress of an unconfined concrete element reached 4.5 ksi, which corresponds to a strain of 0.0031 [Fig. 8.2(a)], this concrete element was considered to have crushed.

The comparison between the overall load-displacement curves obtained from the tests and the finite element analysis is shown in Fig. 8.3(a). The experimental curve is taken from the P_T - δ_{2P} diagram of Specimen SW 1 (Fig. 5.9) except that the total measured displacement, δ_{2R}, has been reduced by subtracting the displacement component at the second floor level resulting from the measured fixed-end rotation. This subtraction was made because in the analytical model it was assumed that no rotation can take place at the fixed base. The experimental curve of Specimen SW 3 (taken from Ref. 47) has better agreement with the analytical curve. This is because Specimen SW 3 was subjected to a lesser number of working load cycles before it was monotonically loaded to failure. From Fig. 8.3(a) it can be seen that the analytical curve is stiffer than the experimental curves.

The crack direction of the elements in the first story is shown in Fig. 8.4(a). Since only the results from some selected solution steps were printed out, the cracking load of a particular element could not be detected. The load shown in each cracked element of this figure corresponds to the load attained at the end of a printing step; the element was cracked either before or in this step. The crack direction agrees very well with the experimental results; see Fig. 5.102 and 6.2. Information on the crack width and spacing between the cracks cannot be obtained from the finite element analysis.

The contour lines of the principal compressive stress in the first story is shown in Fig. 8.5(a). This figure was plotted according to the average stress in the elements. Because the principal directions of the elements in the edge columns are quite different from those of the elements in the wall panel, there is a discontinuity of principal compressive stress existing in the column face. Figure 8.5(a) indicates that the principal compressive stress is concentrated at the lower left corner of the wall panel, where crushing of the test specimen was first initiated [Fig. 5.102(d)]. In this figure the maximum compressive stress of the wall panel is shown to have reached 4.5 ksi at the lateral shear of 250 kips. Therefore, the wall panel is considered to be crushed at this lateral shear

The stress of the reinforcement in the first story of the analytical model is shown in Fig. 8.6(a). For the vertical reinforcement, the compressive stress is marked on its left side and the tensile stress on its right side. For the horizontal reinforcement, the compressive stress is marked below it and the tensile stress is marked above it. The stress in the vertical reinforcement agrees well with the experimental results, but the stress in the horizontal reinforcement does not. Before LP 90, the strains monitored by gages WS 1 - WS 6 of Specimen SW 1, (Fig. 5.72 to 5.77) never reached yield strain of 0.0025.

Therefore, the stress in the corresponding locations of the horizontal reinforcement of Specimen SW 1 can be converted directly from their strain reading. According to the experimental results, the stresses corresponding to gages WS 1, WS 2 and WS 3 at LP 90 are 30 ksi, 17 ksi and 50 ksi, respectively. The corresponding stresses for the analytical results are 2 ksi, 16 ksi, and 10 ksi, respectively. The large discrepancies existing between them may be attributed to the following reasons: (1) the test specimen had been subjected to several loading reversals before it was monotonically loaded to LP 90; (2) the deterioration of the bond between the concrete and the reinforcement was not taken into consideration for the analytical model; (3) the analytical results represent the average stress of the reinforcement over a length of 12.33 in., rather than the stress over the length of the gage, 1.5 in.; and (4) the experimental results could have been affected by localized cracks.

8.3 PARAMETRIC STUDIES OF WALL SPECIMEN

8.3.1 Standard Specimen Loaded with Short Shear Span

For a medium-rise wall, ductility and shear strength may be significantly affected by the variation of shear span. The shear span of the wall can be approximately represented by its base moment-to-shear ratio, M_B/V_B. The tests of the wall specimens were carried out according to an M_B/V_B of 173 in., which is equivalent to 4.5 stories high. According to the analytical results discussed in Chapter 7, however, the most probable critical loading condition of the wall is that corresponding to the approximately three-story high shear span of 119 in. for the model specimen. The load-displacement curve of the wall specimen loaded with this shear span is shown as Curve B in Fig. 8.3(b).

The displacement ductility of this curve is much lower than that of Curve A which is loaded with the shear span of 173 in. However, the shear strength of the specimen loaded under the most critical loading condition is increased to 310 kips, about 22 percent higher than that of the specimen loaded with the same loading condition as the test specimen. The wall panel of this specimen was considered to be crushed at the lateral shear of 310 kips because its maximum stress reached 4.5 ksi [Fig. 8.5(b)]. The analytical results for the specimen loaded with the short shear span are shown in Figs. 8.4(b), 8.5(b), and 8.6(b). Comparison between Figs. 8.4(a) and 8.4(b) indicates the insensitivity of the crack direction to the loading condition. At the wall panel crushing load, the stress in both the vertical and horizontal reinforcement of the specimen was lower when the specimen was loaded with the short shear span.

The maximum base moment of the specimen loaded with an M_B/V_B of 119 in. is 36,900 k-in., a value considerably lower than that of the specimen loaded with an M_B/V_B of 173 in., 44,000 k-in. It can therefore be concluded that the failure mode of the former is primarily controlled by shear since it failed before its moment capacity was reached. This is also the reason why the principal compressive stress in the left edge column of Fig. 8.5(b) is smaller than that shown in Fig. 8.5(a). However, the area of the wall panel subjected to high stress in Fig. 8.5(b) is larger than that in Fig. 8.5(a), due to the higher shear force.

8.3.2 Wall Specimen without Slabs

The best method of assessing the effectiveness of the slabs, as part of the wall, in resisting shear is to compare the behavior of the specimen without the slabs to that of the standard specimen with slabs.

Curves A and C, shown in Fig. 8.3(b), correspond to the specimens, with and without slabs, loaded with an M_B/V_B of 173 in. (which corresponds to an M_T = 92 V). Before the shear force reached 115 kips, the analytical load-displacement curves for these two specimens were almost identical. Above this load, a large number of wall panel elements cracked diagonally, and the slope of Curve C became smaller than that of Curve A. At the wall panel crushing load, both the strength and ductility of the specimen without slabs were slightly lower than those of the other specimen.

By comparing Figs. 8.4(a) and 8.4(c), it can be concluded that the crack directions were not significantly affected by the removal of the slabs. However, the principal compressive stress in the first story wall panel of the specimen without slabs [Fig. 8.5(c)] seems more concentrated on the left side. As expected, the stress in the horizontal reinforcement of the specimen without slabs is much higher than that of the specimen with slabs [Fig. 8.6(a) and 8.6(c)]. The maximum value of the former is 60 ksi, which is still below the yield stress, 73 ksi. It must be emphasized, however, that since the finite element analysis tends to underestimate the stress in the horizontal reinforcement, it is possible, in an actual case, for some horizontal reinforcement of the specimen without slabs to reach the tensile yield stress before the shear force reaches the wall panel crushing load of 245 ksi obtained from the analysis. If this occurs, the specimen will fail earlier than predicted by the finite element analysis, and the effect of slabs in resisting shear will become more important.

8.3.3 Specimen with Minimum Amount of Horizontal Reinforcement

According to the analytical results of the previous section, it can be speculated that the slabs serve a function similar to the horizontal reinforcement in resisting shear. To demonstrate this point, another analytical study was made. For this study, the amount of horizontal reinforcement of the specimen was reduced to 0.0025 (the original value being 0.00815), the minimum amount allowed by Section 2614(d) of the UBC. The specimen tested was designed so that 80 percent of its shear strength was contributed by its horizontal reinforcement. Reducing the amount of horizontal reinforcement of the specimen from 0.00815 to 0.0025 will reduce its shear capacity, V_u, from 158 kips to 65 kips.* Comparing the results of the finite element analyses of these two specimens, only a very small reduction in shear strength can be detected [Compare Curve A with Curve D, Fig. 8.3(b)]. Therefore, depending on the amount of horizontal reinforcement used, large errors may result if the effect of the slabs is neglected. In other words, if the failure mode is due to yielding of the horizontal reinforcement, the presence of slabs will increase the shear capacity of the specimen tremendously, possibly up to 242 percent (158/65) of the strength of the specimen without slabs. On the other hand, if the failure mode is due to crushing of the wall panel before the horizontal reinforcement yields, then the presence of slabs will not significantly increase the shear capacity of the specimen (Sect. 8.3.2).

For the specimen with a minimum amount of horizontal reinforcement, the principal compressive stress in its first story wall panel seems more concentrated at the lower left corner. This can be observed by comparing Figs. 8.5(a) with 8.5(d). The specimen's crack direction underwent little change [Fig. 8.4(d)], and its horizontal reinforcement

---

*The values of V_u reported here were computed according to the UBC. The computational procedures were similar to those discussed in Sect. 9.4.2.

had higher stress [Fig. 8.6(d)]. It must again be stated that the finite element analysis used tends to underestimate the stress in the horizontal reinforcement. The specimen with minimum horizontal reinforcement could fail earlier than expected. It must also be recognized that the wall panels of the specimen used in this investigation have a height-to-width ratio of less than one. If a specimen consists of a wall panel with a height-to-width ratio greater than one, a 45-degree oriented crack, initiated from the critical lower left corner region of the wall panel could traverse the whole cross-section of the wall panel without running into the slabs. In this case, the slabs may not be similar to the distributed horizontal reinforcement in resisting shear.

8.4 CONCLUDING REMARKS

(1) The shear strength and ductility of the wall specimen are extremely sensitive to loading conditions, particularly to the shear-to-overturning moment ratio.

(2) The crack directions in the first story of the wall specimen are not affected by the amount of horizontal reinforcement or the presence of slabs, but can be slightly affected by the loading condition. Under different loading conditions, the crack directions in the upper right corner of the first story wall panel are different [Figs. 8.4(a) and 8.4(b)].

(3) Since the crack directions in the critical region of the first story wall panel have an orientation of approximately 45 degrees (Fig. 8.4), the function of a slab when acting together with a wall panel having a height-to-width ratio less than one somewhat resembles that of the horizontal reinforcement.

The conclusions made above are based on the results of the finite element analysis. This analytical method, however, fails to take some important factors into consideration. These include, among others, the bond between the concrete and the reinforcement, the effect of crack width and crack spacing, and the effect of loading reversals. A widely opened crack could lead to local yielding of the reinforcement traversing through it while the average strain of the reinforcement remains below the yield strain. The aggregate interlocking force can be more efficiently developed if the cracks are closely spaced because they will be narrower. Although the results of the finite element analysis show that the shear strength of the specimen will not be significantly affected by reducing the amount of its horizontal reinforcement, it is believed that the existence of horizontal reinforcement will lead to a better distribution of cracks, i.e., a large number of narrow cracks at closer spacing, hence improving the overall performance of the specimen. This kind of information can only be obtained from experimental studies and requires further investigations.

9. CONCLUSIONS AND RECOMMENDATIONS

9.1 CONCLUSIONS

From evaluation of the experimental and analytical results just reported and their implications in the dynamic analysis and design of wall-frame structural systems, a series of conclusions have been drawn. Some concluding remarks have already been presented at the ends of Chapters 6, 7, and 8. The main conclusions are presented herein and grouped in four categories. First, conclusions regarding the behavior of the tested wall specimens will be presented. These will be followed by an assessment of present techniques of repairing walls. Then implications of the results obtained on the overall behavior of the prototype building under seismic excitations and on the possibility of improving the seismic response of this building with different designs will be discussed. Finally, conclusions will be offered for the parametric studies of the wall specimen. It should be recognized that the conclusions made are based on only the few experimental and analytical results presented and should therefore be considered as preliminary findings.

9.1.1 Behavior of Tested Wall Specimens

The specimens were tested under the most critical M_u/V_u ratio, 173 inches (2.3 d or 1.84 l_w), that was obtained from the linear-elastic response spectrum analyses of the prototype building. The loading condition of the specimens at their estimated ultimate state has been shown in Fig. 3.1(4)(d). Results of tests under this type of loading condition permit formulation of the following conclusions regarding the overall behavior of the specimens.

(1) The approximate monotonically loaded Specimen SW 1 was able to resist a combined force of M, 43220 k-in., and V_u, 248 kips

[$M_u = 1.32\ M_y$ and $V_u = 11.3\sqrt{f'_c}\ b_w(0.8\ l_w)$]. The maximum resistance of Specimen SW 2 subjected to cycles of loading reversals was reduced to 98.4 percent of SW 1.

(2) Despite the high nominal unit shear stress ($11.3\sqrt{f'_c}$), Specimen SW 1 was able to develop a high displacement ductility (6.1), high cyclic ductility (8.9), large energy dissipation capacity (3507 k-in.), and large plastic hinge rotation capacity (0.0226 rads.). All these values were strongly affected by the loading program of the specimen. For example, the displacement ductility and plastic hinge rotation capacity of cyclically loaded (inducing full reversals of displacements) Specimen SW 2 were reduced to 4.2 (cyclic ductility of 8.4) and 0.014 rads., respectively, while the energy dissipation capacity of the specimen was increased to 7174 k-in.

(3) The incipient failure of all specimens was due to crushing of the concrete at their first story wall panel. This crushing was mainly introduced by the shear stresses. If the specimens had been loaded with a smaller M_u/V_u ratio (less than 173 inches), the ultimate moment capacity and the large ductility of the specimens might not have been reached. On the other hand, if the wall had been designed for a larger shear capacity (i.e., with a thicker wall panel), it might have been able to develop a somewhat larger moment than the ultimate moment capacity obtained in this study, and perhaps a greater amount of ductility. Therefore, a balanced design for the moment and shear capacity of the wall according to the most probable critical M_u/V_u ratio that could be developed in the wall during its seismic response is necessary. This M_u/V_u ratio can be obtained from the dynamic analysis of the building as discussed in Chapters 3 and 7, and the required shear capacity of the wall can be determined by this ratio and the

calculated maximum moment capacity of the wall.

(4) The high curvature ductility and rotation capacity of Specimens SW 1 and SW 2 (Table 4) can be attributed to the spirally confined concrete core of the edge columns of the specimens. When cyclically loaded under high axial strains (ranging from -0.015 to 0.04 for SW 1, and from -0.007 to 0.035 for SW 2), the column concrete cover spalled off, and the spirals prevented buckling of the longitudinal reinforcement of the column. This provided sufficient confinement for the concrete core so that the compression capacity of the column could be maintained. The closely spaced spirals also increased the dowel resistance of the longitudinal reinforcement which consequently increased the shear capacity of the specimens.

(5) Gradual crushing of the edge column concrete cover had little effect on the overall behavior of the specimens.

(6) Although loading reversals precipitated panel failure, they had little effect on the strength and type of incipient failure of the specimen.

(7) The final failure of the edge column in compression of Specimens SW 1R and SW 2R was due to the combined effect of high shear and axial compressive stresses.

(8) Buckling of the wall reinforcement of Specimens SW 1 and SW 2 did not occur before the initiation of crushing of the wall panel.

(9) Spalling of the concrete at the center of the bottom region of the first story wall panel was due to buckling of the vertical wall reinforcement around that region. The propagation of buckling of the horizontal wall reinforcement might have also accelerated the spalling process.

(10) No significant distress of the anchorage of the vertical reinforcement of the specimens at the foundation occurred. Thus, more liberal designs (such as using smaller embedment lengths for the vertical reinforcement) could be used for the specimens. Because of different bond characteristics of the prototype bar, this conclusion cannot be extended to the prototype wall without further study.

(11) The flexural deformation was the main source of internal energy dissipation of the specimens.

(12) After the loading stage where closely spaced diagonal cracks developed in the wall panels, the sectional flexural and shear stiffness (the slope of $M_i - \phi_i$ and $V_i - \gamma_i$ diagrams) decreased considerably throughout the height of the specimen. At this loading stage, the wall specimen had a very high critical damping ratio of 9.1 percent.

(13) Both the flexural and shear strengths of specimens predicted according to UBC equations were lower than the actual strengths of the specimens, even without applying the strength reduction factor. This disagreement is primarily due to the difference between the specified UBC strength of materials and their actual strength.

9.1.2 Repairing Technique of Wall Specimens

(1) The maximum resistance of the original specimen could not be fully restored after repairing. The maximum resistance of repaired Specimens SW 1R and SW 2R was reduced to 88.5 and 93 percent, respectively, of that of SW 1 (Table 3).

(2) The ductility, rotation capacity, and energy dissipation capacity of the repaired specimens were also substantially less than those of the original specimens with a similar loading history (Tables 4 and 11).

(3) After the specimen was severely cracked, 60 percent of its initial stiffness was recovered by injecting epoxy into the large cracks.

(4) The incipient failure of Specimen SW 1R was initiated by spalling of the wall panel concrete cover. However, spalling of the concrete cover was caused by pushing of the already buckled vertical wall panel reinforcement. As demonstrated by Specimen SW 2R, this type of failure could be prevented or delayed by carefully straightening the buckled reinforcement, putting additional reinforcement in the crushed zone, and tying the two layers of wall reinforcement with hooks, during repair.

(5) The newly cast concrete cover of the edge columns tended to spall earlier. This was due to the discontinuity between the original and newly cast concrete (Fig. 5.109) as well as the poor bond between them.

9.1.3 Overall Behavior of Prototype Building

According to linear-elastic spectrum analyses and nonlinear dynamic analyses of the prototype building, as well as experimental results of the wall specimens, the following conclusions regarding the overall behavior of the prototype building were made.

(1) The wall-frame system designed according to UBC provisions had sufficient strength and stiffness to resist moderate earthquake ground motions.

(2) Under the most severe earthquake ground motions that have been derived from recorded ground motions up to date (the Pacoima base rock motion of 0.4 g), the performance of the wall-frame system should be satisfactory if the premature shear failure of the walls can be prevented. In this case, the plastic hinges would form in the beams and walls but not in the columns, and both structural and nonstructural damage to the building would be limited. However, nonlinear dynamic

analyses of the prototype building indicated that values of M_B/V_B smaller than that used in the tests can occur; thus, the bottom two stories of the wall could fail in shear. In this case, the plastic hinges would form in the columns, and the required rotation capacity of these plastic hinges might exceed their limit. Hence, the safety of the building against collapse would be jeopardized.

(3) Brittle wall failure could also cause the floor slab above the story where such failure occurred to be subjected to high shear stress as discussed in Sects. 7.1.4 and 7.6.1.3. Under such high shear stress, the slab could be severely cracked.

(4) By using elastic response spectrum analyses to estimate the critical value of M_B/V_B, better results (more conservative values) can be obtained if the elastic flexural stiffness of the wall in the first three stories is reduced.

(5) Increasing the shear capacity and ductility of the wall is a very efficient method of improving the overall performance of the prototype building under seismic excitations such as the derived Pacoima base rock motion.

(6) A brittle wall with large flexural strength is undesirable.

9.1.4 Parametric Studies of Wall Specimen

(1) The finite element technique can predict the strength, crack pattern and failure mode of the wall specimen with reasonable accuracy, but not the displacement ductility of the specimen.

(2) A decrease in the M_B/V_B ratio will lead to an increase in the shear that the wall specimen can resist under this ratio, but to a reduction in its ductility capacity.

(3) The slab acting together with the wall functions in a manner similar to the horizontal reinforcement if the story height-to-width

ratio of the wall is less than one.

9.2 RECOMMENDATIONS FOR IMPROVING CODE PROVISIONS AND SUGGESTIONS FOR FOR FUTURE STUDIES

Recommendations for revising and improving UBC provisions in the seismic design of wall-frame structural systems as well as suggestions for future studies are presented below.

9.2.1 Wall Strength

(1) Application of UBC provisions for the design of walls leads to a design without sufficient shear strength to prevent the premature shear failure of the wall. Therefore, to guarantee ductile behavior of the wall when the building was subjected to the derived Pacoima base rock motion having a peak acceleration of 0.4 g, it was necessary to increase the shear capacity of the wall by 20 percent. This increase was achieved by increasing the thicknesss of the wall panel from 12 inches to 15 inches and proportionally increasing the horizontal wall reinforcement.

(2) Although the UBC requirement of a large load factor, 2.8, for designing the walls against shear is desirable from the point of view of preventing brittle shear failure of the wall, it proved to be inadequate in this investigation because of the completely different distribution pattern of story shear force along the height of the building. A recommendation for improving the design against shear failure by accounting for the effects of a force distribution pattern different from that presently suggested by the UBC will be discussed in the next item.

(3) Although the distribution of total base shear along the height of the building as recommended by the UBC is conservative for computing the moment capacity of the wall in a wall-frame system, it is not so for computing its shear capacity. The shear span of the wall

is overestimated by using such a distribution of base shear. Although the correct distribution of the lateral force on the wall depends upon the relative stiffness of the walls and frames, a rectangular distribution pattern for the base shear appears to be more realistic than the triangular pattern suggested by the UBC. This rectangular pattern yields a more realistic shear span for the wall. Therefore, in designing the walls of a wall-frame system, it is recommended to change the distribution pattern of the base shear from a triangular to a rectangular type and, at the same time, to increase the base shear so as to produce the same amount of base moment as that which is calculated according to UBC provisions. In this way, the wall will be designed for the same moment capacity as that suggested by the UBC but will have a larger shear capacity in order to reduce the probability of brittle shear failure.

(4) It is necessary to carry out linear and, if possible, nonlinear dynamic analysis of the whole wall-frame system to check the maximum shear that could probably be developed in the wall.

(5) It is recommended to overdesign slightly the shear capacity of the wall to reduce the probability of its shear failure due to the uncertainty of future earthquakes and the possible errors involved in the dynamic analysis.

(6) Further experiments should be conducted to investigate the participation of slabs in resisting shear forces. In carrying out such studies, it should be considered that slab participation can be affected by the amount of horizontal web reinforcement and the height-to-width ratio of the wall panel.

9.2.2 Comments on Table No. 23-I of UBC, Item (3) for K = 0.8

The concept of dual bracing systems for buildings is to provide a secondary means of defense against lateral forces in the event that the wall system of a building fails. As discussed in Chapter 7, however, serious problems may result if wall failure occurs. Therefore, in addition to item (3) of Table No. 23-I of the UBC, which specifies the minimum lateral stiffness and strength of a frame system, two more items should be considered.

(1) To ensure sufficient plastic hinge rotation capacity of the columns, it is necessary to restrict the maximum axial force of columns in terms of their balanced axial force, P_b. It is suggested that the designed axial force of a column shall not exceed P_b (without ϕ) which is computed according to the code specified strength of materials. To fulfill this requirement, the size of interior columns in the bottom three stories of the prototype building must change from 24 in. x 24 in. to 28 in. x 28 in., reinforced with eight #10 bars. The size of exterior columns in the bottom stories must change from 20 in. x 20 in. to 22 in. x 22 in., reinforced with twelve #9 bars.

(2) The shear transferring capacity of the slab must be considered if the wall is externally located. Shear can be transferred to an external wall through only one side of the slab connected to it. To be conservative, this wall-slab connection should be able to transfer the amount of shear equal to the shear capacity of the wall.

9.2.3 Damping

At present, a large uncertainty exists in the selection of the proper value for the equivalent linear viscous damping that is used in dynamic analysis. Further integrated experimental and analytical research is needed in this area. Reliable experiments should be conducted to determine the variations of the critical damping ratio of structural elements and of whole buildings when they are vibrated with different amplitudes. Although there are some data for the values of damping under small amplitude vibration, there is practically no data available for large amplitude vibrations.

9.2.4 Construction Joints - Splices

Because the specimens were one-third-scale models, no splices were required for the vertical reinforcement. In the case of real buildings splices are necessary and are usually located in the critical regions of the wall. Surveys of earthquake damage [7,9,10] show that the wall regions that were splices are usually the weakest link and that damage can be concentrated in these regions. Therefore, it is planned to incorporate splices in the critical regions of the wall as a new parameter in some of the specimens to be tested in the future.

9.2.5 Foundations

The specimens tested had been cast with a rigid foundation prestressed to the rigid blocks of the testing facility, thus resulting in a system with a nearly perfect rigid base. In real buildings the walls are built in relatively more flexible foundations. Not only can these foundations suffer some rotations as a whole (since they are not prestressed against rigid rock or soil), but also their flexibility may affect the failure mechanism or failure pattern. Rather than occurring a certain distance from the base (where a construction joint is usually located) as in the tests, failure could occur just at the construction joint. The effect of using more realistic foundations should therefore be studied.

REFERENCES

1. ACI Committee 442, "Response of Buildings to Lateral Forces," ACI Journal, Proceedings, Vol. 68, February 1971, pp. 81-106.

2. Blume, J. A., Newmark, N. M., and Corning, L. H., Design of Multistory Reinforced Concrete Buildings for Earthquake Motions, Portland Cement Association, Skokie, Illinois, 1961, 318 pp.

3. Fintel, M., "Resistance to Earthquakes - Philosophy, Ductility and Details," ACI Publication SP-36, 1973, pp. 75-91

4. Derecho, A. T., "Frames and Frame-Shear Wall Systems," ACI Publication SP-36, 1973, pp. 13-37.

5. Khan, F. R. and Iyengar, H. S., "Optimization Approach for Concrete High-rise Buildings," ACI Publication SP-36, 1973, pp. 61-74.

6. Paulay, T. A., "Some Aspects of Shear Wall Design," Bulletin of the New Zealand Society for Earthquake Engineering, Vol. 5, No. 3, September 1972, pp. 89-105.

7. Fergus, J. W., The Prince William Sound, Alaska, Earthquake of 1964 and Aftershocks, U. S. Department of Commerce, Environmental Science Services Administration, Vol. 2, Part A, 1967, 392 pp.

8. Earthquakes, American Iron and Steel Association, Washington, D. C., 1975, 319 pp.

9. Jennings, P. C. (ed.), "Engineering Features of the San Fernando Earthquake: February 9, 1971," Report EERL 71-02, Earthquake Engineering Research Laboratory, California Institute of Technology, June 1971, 512 pp.

10. Clarkson, W. P., "A Review of the Repair of Two Concrete Buildings Damaged by the San Fernando Earthquake," ACI Journal, Proceedings, Vol. 70, No. 25, March 1973, pp. 237-241.

11. Berg, G. V. and Degenkolb, H. J., "Engineering Lessons from Managua Earthquake," Conference Proceedings on the Managua, Nicaragua Earthquake of Dec. 23, 1972, Engineering Research Institute, Vol. 2, San Francisco, November 29 and 30, 1973.

12. Bertero, V. V., Popov, E. P., and Wang, T. Y., "Hysteretic Behavior of Reinforced Concrete Flexural Members with Special Web Reinforcement," Report No. EERC 74-9, Earthquake Engineering Research Center, University of California, Berkeley, August 1974.

13. Vallenas, J., "Hysteretic Behavior of Repaired R/C Flexural Members with Special Web Reinforcement," (in-house report).

14. Shiga, T., Shibata, A., and Takahashi, T., "Earthquake Damage and Wall Modulus of Reinforced Concrete Building," Report No. 12, Totoku Branch, Architecture Institute of Japan, December 1968, pp. 29-32 (in Japanese).

15. Bertero, V. V. and Collins, R. G., "Investigation of the Failures of the Olive View Stairtowers during the San Fernando Earthquake and their Implications in Seismic Design," Report No. EERC 73-26, Earthquake Engineering Research Center, University of California, Berkeley, 1973.

16. Wiegel, R. L. (ed.), Earthquake Engineering, Prentice-Hall, Inc., 1970, 518 pp.

17. Cardenas, A. and Magura, D., "Strength of High-rise Shear Walls-Rectangular Cross Section," ACI Publication SP-36, 1973, pp. 119-150.

18. Barda, F., "Shear Strength of Low-rise Walls with Boundary Elements," Ph.D. Dissertation, Department of Civil Engineering, Lehigh University, 1972, 265 pp.

19. Benjamin, J. and Williams, H., "The Behavior of One-story Reinforced Concrete Shear Walls," Journal of the Structural Division, ASCE, Vol. 83, No. ST 3, May 1957, pp. 1254.1-1254.49.

20. Galletly, G. D., "Behavior of Reinforced Concrete Shear Walls under Static Load," Department of Civil and Sanitary Engineering, Massachusetts Institute of Technology, Cambridge, August 1952.

21. Antebi, J., Utku, S., and Hansen, R. J., "The Response of Shear Walls to Dynamic Loads," Department of Civil and Sanitary Engineering, Massachusetts Institute of Technology, Cambridge, August 1960.

22. Cervenka, V. and Gerstle, K. H., "Inelastic Analysis of Reinforced Concrete Panels: Experimental Verification and Application," IABSE Publication 32-II, 1972, pp. 25-38.

23. Uniform Building Code, International Conference of Building Officials, Pasadena, 1973 edition.

24. Wilson, E. L. and Dovey, H. H., "Three Dimensional Analysis of Building Systems - TABS," Report No. EERC 72-8, Earthquake Engineering Research Center, University of California, Berkeley, December 1972.

25. "Building Code Requirements for Reinforced Concrete," ACI Standard 318-71, Detroit, Michigan.

26. Building Code and Commentary for Reinforced Concrete Structures, Architectural Institute of Japan, 1971 (in Japanese).

27. Hatakeyama, H., "Comparative Study of Design of Shear Walls in High-rise Buildings," CE 299 Report, Department of Civil Engineering, SESM, University of California, Berkeley, 1973.

28. Seismology Committee, Recommended Lateral Force Requirements and Commentary, Structural Engineers' Association of California, San Francisco, 1973.

29. Gardens, A. E., et al., "Design Provisions for Shear Walls," ACI Journal, Proceedings, Vol. 70, March 1973, pp. 221-230.

30. ASCE-ACI Task Committee 426, "The Shear Strength of Reinforced Concrete Members," Journal of the Structural Division, ASCE, Vol. 99, No. ST6, June 1973, pp. 1091-1187.

31. Gamble, W. L., "Some Observations of the Strengths of Large Reinforcing Bars," ACI Journal, Proceedings, Vol. 70, No. 6, Jan. 1973, pp. 31-35.

32. Clough, R. W. and Penzien, J., Dynamics of Structures, McGraw-Hill, New York, 1975, 634 pp.

33. Lotz, B. and Clyde, D., "Variation of Friction Coefficient using Different Lubrications and Types of Loading," in-house report.

34. Ma, S. M., Bertero, V. V., and Popov, E. P., "Experimental and Analytical Studies of Hysteretic Behavior of Reinforced Rectangular and T-Beams," Report No. EERC 76-2, Earthquake Engineering Research Center, University of California, Berkeley, 1976.

35. Richart, F. E., Brandtxaeg, A., and Brown, R. L., "The Failure of Plain and Spirally Reinforced Concrete in Compression," University of Illinois Engineering Experiment Station Bulletin No. 190, Urbana, Illinois, April 1929.

36. Bresler, B. and Bertero, V. V., "Influence of High Strain Rate and Cyclic Loading on Behavior of Unconfined and Confined Concrete in Compression," Preprint for Second Canadian Conference on Earthquake Engineering, McMaster University, Hamilton, Ontario, July 1975.

37. Bresler, B. and MacGregor, J., "Review of Concrete Beams Failing in Shear," Journal of the Structural Division, ASCE, Vol. 93, No. ST1, February 1967, pp. 343-372.

38. Newmark, N. M. and Hall, W., "Seismic Design Criteria for Nuclear Reactor Facilities," Proceedings of the Fourth World Conference on Earthquake Engineering, Vol. II, Section B4, 1969, pp. 37-50.

39. Blume, J. A., Sharpe, R. L., and Cost, G., Earthquake Engineering for Nuclear Reactor Facilities, John A. Blume and Associates, JAB-101, 1971, 147 pp.

40. ACI Committee 435, "Allowable Deflections," ACI Journal, Proceedings, Vol. 65, No. 6, June 1968, pp. 433-444.

41. Chang, F. K., "Human Response to Motions in Tall Buildings," Journal of the Structural Division, ASCE, Vol. 99, No. ST6, June 1973, pp. 1259-1272.

42. Mahin, S. A., and Bertero, V. V., "An Evaluation of Some Methods for Predicting Seismic Behavior of Reinforced Concrete Buildings," Report No. EERC 75-5, Earthquake Engineering Research Center, University of California, Berkeley, February 1975.

43. Clough, R. W., Benuska, K. L., and Wilson, E. L., "Inelastic Earthquake Response of Tall Buildings," Proceedings of the Third World Conference on Earthquake Engineering, Vol. II, Wellington, New Zealand, 1965, pp. 68-84.

44. Kustu, O. and Bouwkamp, J., "Behavior of Reinforced Concrete Deep Beam-Column Subassemblages under Cyclic Loads," Report No. EERC 73-8, Earthquake Engineering Research Center, University of California, Berkeley, May 1975.

45. Hisada, T., Ohmori, N., and Bessho, S., "Earthquake Design Considerations in Reinforced Concrete Columns," KICT Report No. 1, Kajima Institute of Construction Technology, January 1972, 20 pp.

46. Bathe, K. J., Wilson, E. L., and Iding, R. H., "NONSAP - A Structural Analysis Program For Static and Dynamic Response of Nonlinear Systems," SESM Report No. 74-3, Department of Civil Engineering, University of California, Berkeley, February, 1974.

47. Vallenas, J., "Analytical and Experimental Investigation of the Hysteretic Behavior of R/C Shear Wall Structural System," Ph.D. Dissertation, Department of Civil Engineering, University of California, Berkeley, in preparation.

TABLE 1 A_w/A_t RATIO OF BUILDINGS

BUILDING	Mt. McKinley and 1200L Apt.	J.C. Penney Building	Indian Hills Medical Center	Four Seasons Apt.	Prototype Building
$\frac{A_w}{A_t}$	2.8 %	0.8 %	0.5 %	0.6 %	0.6 %

TABLE 2 CHARACTERISTICS OF MATERIALS

Parameters		Specified for Design	At time of Testing Specimen SW 1	Specimen SW 2
Concrete Strength (fc') kN/cm^2 (psi)	footing	2.76 (4000) @28 days	2.49 (3600)	2.56 (3710)
	1st Fl.		3.66 (5300)	3.71 (5380)
	2nd Fl.		3.44 (4990)	3.62 (5250)
	3rd Fl.		3.26 (4720)	3.35 (4860)
Splitting tensile stress (1st Fl. kN/cm^2 (psi)			0.334 (484)	0.349 (506)
Flexural tensile stress (1st Fl. kN/cm^2 (psi)			0.441 (639)	0.449 (650)
Wall Steel (#2 Bars) kN/cm^2 (psi)	f_y	41.4 (60,000)	50.7 (73,400)	
	f_{max}		73.0(105,800)	
Col. Long. Steel (#6 Bars) kN/cm^2 (psi)	f_y	41.4 (60,000)	50.2 (72,700)	
	f_{max}		73.1(106,000)	
Col. Spiral Steel (0.207" ϕ) kN/cm^2 (psi)	f_y	41.4 (60,000)	57.1 (82,800)	
	f_{max}		69.7(101,000)	

TABLE 3 COMPUTED AND MEASURED STRENGTH OF SPECIMENS

Load Level	Computed Strength		Measured Strength							
	M_B	V	SW 1		SW 2		SW 1R		SW 2R	
	KN-M (k-in)	KN (kips)	M_B KN-M(k-in)	V KN(kip)	M_B KN-M(k-in)	V KN(kip)	M_B KN-M(k-in)	V KN(kip)	M_B KN-M(k-in)	V kN(kip)
Flexural Crack Load	1040 (9200)	237 (53.3)	978 (8650)	223 (50)	977 (8645)	223 (50)	-	-	-	-
Diagonal Crack Load	1483 (13120)	338 (76.0)	1526 (13500)	347 (78)	1294 (11450)	294 (66)	-	-	-	-
Working Load ($f_s \leq 24$ ksi)	1695 (15000)	387 (87.0)	1756 (15540)	401 (90)	1770 (15660)	405 (91)	-	-	-	-
Working Load ($f_c \leq 0.45\ f'_c$)	2362 (20900)	539 (121.0)	2497 (22100)	570 (128)	2836 (25100)	641 (144)	-	-	-	-
Yielding Load ($f_y = 72.4$ ksi)	3594 (31800)	821 (184.0)	3706 (32800)	846 (190)	3948 (34940)	899 (202)	-	-	-	-
Ultimate Load ($\varepsilon_{cu} = 0.0038$)	4746 (42000)	1082 (243.0)	4588 (40600)	1046 (235)	-	-	-	-	3927 (34750)	890 (200)
Computed Strength by UBC	2882 (25500)	703 (158.0)	-	-	-	-	-	-	-	-
Measured Positive Maximum Load	-	-	4884 (43220)	1104 (248)	4790 (42390)	1086 (244)	3731 (33020)	847 (190.3)	4560 (40350)	1031 (231.7)
Measured Negative Maximum Load	-	-	-4079 (-36100)	-926 (-208)	-4805 (-42520)	-1090 (-245)	-4321 (-38240)	-981 (-220.4)	-1912 (-16920)	-433 (-97.4)

TABLE 4 DUCTILITY AND ROTATION CAPACITY

Specimen	ϕ_y $(\times 10^{-4}\frac{1}{in})$	μ_ϕ	δ_{3y} (in)	$\mu_{\delta 3}$	Rotation Capacity (Rad.)			
					Excluding FER		Including FER	
					θ_y*	θ^{+}_{pl}	θ'_y**	θ'_{pi}
SW 1	0.44	11.5 - 3.0	0.7	6.1 -2.8	0.0034	0.0207 -0.0056	0.0036	0.0226 -0.0063
SW 1R	0.44***	3.5 - 3.3	0.7	1.9 -2.0	0.0034	0.0045 -0.0043	0.0036	0.0045 -0.0045
SW 2	0.312	10.5 -10.2	0.7	4.2 -4.2	0.0033	0.0125 -0.0120	0.0039	0.0142 -0.0132
SW 2R	0.312	12.5	0.7	4.7	0.0033	0.0166	0.0039	0.0186

* $\theta_y = \sum_{i=1}^{5} \phi_i(\Delta\ell_i)$ at yielding

\+ $\theta_{pl} = \theta_{max} - \theta_y$ is defined as the plastic hinge rotation capacity of the specimen

** $\theta'_y = \sum_{i=1}^{5} \phi_i(\Delta\ell_i) + \theta_F$ at yielding

*** The values ϕ_y, δ_y, θ_y and θ'_y of Specimens SW 1R and SW 2R are taken as the same as those values of Specimens SW 1 and SW 2, respectively.

TABLE 5 ENERGY DISSIPATION CAPACITY

Displ. Ductility Range $<\mu_{\delta_3}<$	Cycle No.	Ext. Energy Input (KIPS-IN) 1 $P_T-\delta_{3R}$	2 $M_T-\theta_T$	3 Axial	4 $\Sigma 1,2,3$	Internal Energy Diss. (KIPS-IN) 5 $M-\phi$	6 $M_B-\theta_F$	7 $V-\gamma$	8 Axial	9 $\Sigma 5,6,7,8$	10 Error $\frac{4-9}{4}$ (%)
SPECIMEN SW 1											
$\mu_{\delta_3}<1$	1-16	51	13	9	73				9		
-2,4	17	884	286	-39	1131	735	88	247	-39	1031	9
-1,1	18-27	171	25	19	215				19		
0,6	28	820	266	-74	1012	679	89	309	-74	1003	1
1,4	29-30	140	13	2	155	32.5	13	91.5	2	139	10
-2,3	31	434	154	19	607	393	28	159	19	599	1
-1,2	32-34	270	36	8	314				8		
SUM		2770	793	-56	3507				-56		
SPECIMEN SW 1R											
$\mu_{\delta_3}<1$	1-7	59	12	11	82				11		
-2,2	8	248	90	-17	321	223	8	113	-17	326	-1
	9	258	42	15	315	104	14	175	15	308	2
	10	137	14	3	154			103	3		
	11	122	10	1	133			91	1		
	12	102	8	2	112			82	2		
-6,6	13	866	68	7	941			775	7		
SUM		1792	244	22	2058				22		
SPECIMEN SW 2R											
$\mu_{\delta_3}<1$	1-6	113	15	18	146	34	7	84	18	142	3
-1,6	7	918	226	4	1148	574	135	406	4	1119	2
SUM		1031	241	22	1294	608	142	590	22	1261	

TABLE 5 (Continued)

SPECIMEN SW 2											
Displ. Ductility Range $<\mu_{\delta_3}<$	Cycle No.	Ext. Energy Input				Internal Energy Diss.					10 Error
		1	2	3	4	5	6	7	8	9	$\frac{4-9}{4}$
		$P_T-\delta_{3R}$	$M_T-\theta_T$	Axial	$\Sigma 1,2,3$	$M-\phi$	$M_B-\theta_F$	$V-\gamma$	Axial	$\Sigma 5,6,7,8$	
		(KIPS-IN)				(KIPS-IN)					(%)
$\mu_{\delta_3}<1$	1-7	26	8	6	40	13	3.5	15.5	6	38	5
-1,1	8	106	26	-3	129	38.5	16.5	75	-3	127	2
	9	68	15.5	1	84.5	26.5	9	44.5	1	81	4
	10	60	14	0	74				0		
$\mu_{\delta_3}<1$	11-12	46	6.5	1	53.5				1		
-1,1	13	60	13.5	-1	72.5				-1		
-2,2	14	359	137	-38	458	297	76	126	-38	461	-1
	15	314	120	-2	432	263	63	114	-2	438	-1
	16	284	110	-2	392				-2		
-3,3	17	634	256	-46	844	593	107	188	-46	842	0
	18	600	250	4	854	586	99	172	4	864	-1
	19	565	238	-1	802				-1		
-4,4	20	943	372	-34	1281	893	136	279	-34	1274	1
	21	869	276	25	1170				25		
	22	457	?	22	479				22		
SUM		5404	1837.5	-68	7173.5				-68		

TABLE 6 DISPLACEMENT COMPONENTS - SW 1

	Load Point	1 Fixed-End Rotation (in)	$\frac{1}{5}$ (%)	2 $\delta_{FLEX.}$ (in)	$\frac{2}{5}$ (%)	3 δ_{SHEAR} (in)	$\frac{3}{5}$ (%)	4 $\Sigma 1,2,3$ (in)	5 Rel. Lat. Displ. (in)	6 Error $\frac{5-4}{5}$ (%)	7 μ_δ $\frac{\delta_{iR}}{\delta_{iy}}$
Displacement at Tip of 3rd Floor	76	0.012	4	0.163	54	0.089	30	0.264	0.300	12	0.43
	79	0.028	4	0.342	45	0.264	35	0.634	0.760	17	1.1
	86	0.073	5	0.756	50	0.479	31	1.308	1.540	15	2.2
	88	0.138	6	1.177	51	0.660	29	1.975	2.300	14	3.3
	90	0.160	6	1.425	53	0.766	28	2.351	2.700	13	3.9
	152	0.064	5	0.593	48	0.520	42	1.177	1.246	5	1.8
	154	0.147	6	1.444	60	0.829	34	2.420	2.425	0	3.5
	156	0.193	6	2.076	61	1.118	33	3.387	3.406	1	4.9
	158	0.249	6	2.473	58	1.488	35	4.210	4.248	1	6.1
Displacement at Tip of 2nd Floor	76	0.008	4	0.079	43	0.089	49	0.176	0.183	4	0.41
	79	0.018	4	0.162	33	0.264	54	0.444	0.487	9	1.1
	86	0.050	5	0.423	43	0.479	48	0.952	0.990	4	2.2
	88	0.094	6	0.673	46	0.660	45	1.427	1.470	3	3.3
	90	0.109	6	0.820	48	0.766	45	1.695	1.704	1	3.4
	152	0.044	5	0.286	31	0.520	57	0.850	0.919	7	2.0
	154	0.102	6	0.730	43	0.829	48	1.661	1.713	6	3.9
	156	0.132	6	1.130	47	1.118	47	2.380	2.383	0	5.3
	158	0.172	6	1.306	44	1.488	50	2.966	2.991	1	6.7
Displacement at Tip of 1st Floor	76	0.005	6	0.027	33	0.060	73	0.092	0.082	-13	0.36
	79	0.010	4	0.054	22	0.164	68	0.228	0.242	5	1.1
	86	0.029	5	0.172	32	0.351	65	0.552	0.537	- 3	2.4
	88	0.053	6	0.261	33	0.515	64	0.829	0.803	- 3	3.6
	90	0.062	6	0.317	34	0.616	66	0.995	0.936	- 6	4.2
	152	0.025	5	0.099	20	0.393	79	0.517	0.497	- 4	2.2
	154	0.057	6	0.272	28	0.655	68	0.984	0.962	- 2	4.3
	156	0.075	6	0.405	30	0.900	68	1.380	1.330	- 4	5.9
	158	0.097	5	0.497	29	1.237	71	1.831	1.739	- 5	7.7

TABLE 7 DISPLACEMENT COMPONENTS - SW 1R

	Load Point	1 Fixed-End Rotation (in)	$\frac{1}{5}$ (%)	2 $\delta_{FLEX.}$ (in)	$\frac{2}{5}$ (%)	3 δ_{SHEAR} (in)	$\frac{3}{5}$ (%)	4 $\Sigma 1,2,3$ (in)	5 Rel. Lat. Displ. (in)	6 Error $\frac{5-4}{5}$ (%)	7 μ_δ $\frac{\delta_{iR}}{\delta_{iy}}$
Disp. at Tip of 3rd Floor	32	0.002	1	0.193	44	0.130	30	0.325	0.440	26	0.63
	33	0.005	1	0.401	48	0.264	31	0.670	0.842	20	1.2
	34	0.007	1	0.704	53	0.408	31	1.119	1.330	16	1.9
	69	0.005	0	0.351	25	0.942	65	1.298	1.418	8	2.0
	70	0.002	0	0.502	25	1.378	68	1.882	2.030	7	2.9
	71	-0.009	0	0.696	25	1.923	69	2.610	2.790	6	4.0
	72	-0.048	-1	0.911	25	2.648	72	3.511	3.660	4	5.2
Disp. at Tip of 2nd Floor	32	0.001	1	0.102	40	0.130	50	0.232	0.258	9	0.57
	33	0.003	1	0.221	43	0.246	47	0.488	0.520	6	1.2
	34	0.005	1	0.399	47	0.408	48	0.812	0.850	4	1.9
	69	0.004	0	0.220	19	0.942	80	1.166	1.180	1	2.6
	70	0.001	0	0.295	18	1.378	82	1.674	1.680	0	3.7
	71	-0.006	0	0.413	17	1.923	81	2.330	2.370	2	5.3
	72	-0.034	-1	0.546	17	2.648	84	3.161	3.160	0	7.0
Disp. at Tip of 1st Floor	32	0.001	1	0.034	31	0.057	51	0.092	0.111	17	0.49
	33	0.002	1	0.076	31	0.153	62	0.231	0.246	6	1.1
	34	0.003	1	0.146	33	0.270	61	0.419	0.442	5	2.0
	69	0.002	0	0.079	8	0.860	87	0.941	0.970	3	4.3
	70	0.001	0	0.111	8	1.278	92	1.390	1.390	0	6.2
	71	-0.004	0	0.157	8	1.806	91	1.959	1.980	1	8.8
	72	-0.018	-1	0.208	8	2.518	94	2.708	2.690	-1	11.9

TABLE 8 DISPLACEMENT COMPONENTS - SW 2

	Load Point	1 Fixed-End Rotation (in)	$\frac{1}{5}$ (%)	2 $\delta_{FLEX.}$ (in)	$\frac{2}{5}$ (%)	3 δ_{SHEAR} (in)	$\frac{3}{5}$ (%)	4 $\Sigma 1,2,3$ (in)	5 Rel. Lat. Displ. (in)	6 Error $\frac{5-4}{5}$ (%)	7 $\frac{\delta_{iR}}{\delta_{iy}}$
Displacement at Tip of 3rd Floor	32	0.023	1	0.086	52	0.058	35	0.169	0.165	-2	0.24
	33	0.045	11	0.170	42	0.194	48	0.409	0.403	-1	0.58
	35	0.075	11	0.268	38	0.363	52	0.706	0.702	-1	1.0
	40	-0.095	13	-0.294	41	-0.318	44	-0.707	-0.720	-2	-1.0
	70	0.161	11	0.658	46	0.622	43	1.443	1.434	-1	2.0
	76	-0.170	12	-0.707	48	-0.633	43	-1.510	-1.478	2	-2.1
	94	0.234	11	1.056	48	0.875	40	2.165	2.210	2	3.2
	100	-0.219	10	-1.086	49	-0.932	42	-2.237	-2.220	1	-3.2
	118	0.270	9	1.411	48	-1.254	63	2.935	2.931	0	4.2
	124	-0.218	7	-1.385	47	-1.347	46	-2.950	-2.936	1	-4.2
Displacement at Tip of 2nd Floor	32	0.016	15	0.044	41	0.044	41	0.104	0.108	4	0.23
	33	0.032	12	0.084	32	0.140	53	0.256	0.262	2	0.56
	35	0.052	11	0.136	29	0.264	56	0.452	0.471	4	1.0
	40	-0.066	15	-0.156	35	-0.258	57	-0.480	-0.452	6	-0.96
	70	0.112	12	0.378	39	0.472	49	0.962	0.957	-1	2.0
	76	-0.119	12	-0.409	41	-0.483	48	-1.011	-1.004	2	-2.1
	94	0.163	11	0.609	41	0.715	48	1.487	1.490	0	3.2
	100	-0.152	10	-0.635	41	-0.760	49	-1.547	-1.540	0	-3.3
	118	0.188	9	0.820	40	1.075	52	2.083	2.060	-1	4.4
	124	-0.152	7	-0.821	39	-1.048	50	-2.021	-2.088	-3	-4.4
Displacement at Tip of 1st Floor	32	0.009	17	0.014	26	0.031	59	0.054	0.053	-2	0.23
	33	0.018	13	0.026	19	0.089	66	0.133	0.135	2	0.58
	35	0.030	13	0.041	18	0.163	70	0.234	0.233	0	1.0
	40	-0.038	17	-0.054	25	-0.156	73	-0.248	-0.214	16	-0.9
	70	0.064	12	0.142	27	0.348	65	0.554	0.532	-4	2.3
	76	-0.067	13	-0.153	29	-0.350	67	-0.570	-0.524	9	-2.2
	94	0.092	11	0.217	25	0.572	65	0.881	0.873	-1	3.7
	100	-0.086	10	-0.231	27	-0.606	71	-0.923	-0.852	8	-3.6
	118	0.106	9	0.294	24	0.852	69	1.252	1.239	-1	5.3
	124	-0.086	7	-0.306	24	-0.975	77	-1.367	-1.266	8	-5.4

TABLE 9 DISPLACEMENT COMPONENTS - SW 2R

	Load Point	1 Fixed-End Rotation (in)	$\frac{1}{5}$ (%)	2 $\delta_{FLEX.}$ (in)	$\frac{2}{5}$ (%)	3 δ_{SHEAR} (in)	$\frac{3}{5}$ (%)	4 $\Sigma 1,2,3$ (in)	5 Rel. Lat. Displ. (in)	6 Error $\frac{5-4}{5}$ (%)	7 μ_δ $\frac{\delta_{iR}}{\delta_{iy}}$
Displacement at Tip of 3rd Floor	2	0.003	1	0.106	24	0.334	76	0.443	0.437	-1	0.62
	28	0.005	1	0.219	32	0.456	67	0.680	0.685	1	1.0
	29	0.025	2	0.368	38	0.585	60	0.978	0.98	0	1.4
	30	0.073	5	0.534	40	0.703	52	1.310	1.354	3	1.9
	31	0.075	4	0.794	47	0.799	47	1.668	1.699	2	2.4
	32	0.095	4	1.244	56	0.931	42	2.270	2.239	-1	3.2
	33	0.137	5	1.552	56	1.101	39	2.790	2.790	0	4.0
	34	0.234	7	1.759	53	1.349	40	3.340	3.333	0	4.8
	35	0.292	7	1.684	43	1.998	51	3.974	3.920	-1	5.6
	36	0.459	10	1.765	39	2.265	51	4.489	4.471	0	6.4
Displacement at Tip of 2nd Floor	2	0.002	1	0.053	18	0.231	79	0.286	0.293	2	0.62
	28	0.004	1	0.115	24	0.324	66	0.443	0.488	9	1.0
	29	0.017	2	0.198	29	0.425	61	0.640	0.694	7	1.5
	30	0.051	6	0.290	32	0.520	57	0.861	0.913	6	1.9
	31	0.052	4	0.451	38	0.609	52	1.112	1.179	6	2.5
	32	0.066	4	0.668	44	0.731	48	1.465	1.510	3	3.2
	33	0.095	5	0.929	48	0.889	46	1.913	1.943	2	4.1
	34	0.163	7	1.056	44	1.138	48	2.357	2.390	1	5.1
Displacement at Tip of 1st Floor	2	0.001	1	0.014	9	0.132	85	0.147	0.155	5	0.66
	28	0.002	1	0.035	15	0.200	87	0.237	0.231	-3	1.0
	29	0.010	3	0.063	18	0.276	79	0.349	0.350	0	1.5
	30	0.029	6	0.091	19	0.350	74	0.470	0.471	0	2.0
	31	0.030	5	0.156	25	0.430	68	0.616	0.628	2	2.7
	32	0.038	5	0.244	30	0.539	66	0.821	0.812	-1	3.5
	33	0.054	5	0.353	32	0.688	62	1.095	1.107	1	4.7
	34	0.093	6	0.429	30	0.945	65	1.467	1.450	-1	6.2

TABLE 10 FREE VIBRATION TEST RESULTS

Specimen	Stage of Loading	Small Ampli. Test*: Frequency (cps) Hz	Small Ampli. Test*: Damping Ratio (%)	Large Ampli. Test*: Frequency (cps) Hz	Large Ampli. Test*: Damping Ratio (%)
SW 2	Before Loading			39.5	2.7
	After 3 Yielding Cycles($\mu_{\delta 3}$=-1,1)	23	2.5	18.5	9.1
	After Failure	10	2.7	8.5	5.6
SW 2R	Before Loading	20	2.5	16.3	6.0

*Free vibration of the specimen was initiated by hitting with hand.

**Free vibration of the specimen was initiated by pulling it with 10 kips of lateral force and suddenly releasing it.

TABLE 11 COMPARISON OF PLASTIC HINGE ROTATION CAPACITY

Type of Specimen	Shear Wall	R/C Beam		W 24x76 Beam		
Specimen No.	SW 3	B 33	B 35I	5	6	7
Span/Total Depth	1.84	2.69		3.50		
θ'_{pl}	0.014	0.026	0.035	0.054	0.021	0.057
Nominal Shear Stress	$11.1\sqrt{f'_c}$	$5.8\sqrt{f'_c}$	$6\sqrt{f'_c}$	$0.14\sigma_y$	$0.13\sigma_y$	$0.16\sigma_y$

TABLE 12 STORY DRIFT INDEX

Specimen	Load Point	Relative Tip Displ. (in.)			Story Drift Index		
		δ_{1R}	δ_{2R}	δ_{3R}	R1	R2	R3
SW 1	76	0.082	0.183	0.300	0.0017	0.0028	0.0033
	77	0.141	0.290	0.450	0.0030	0.0041	0.0044
	79	0.242	0.488	0.778	0.0051	0.0068	0.0081
	86	0.537	0.990	1.565	0.0114	0.0126	0.0160
	88	0.303	1.470	2.330	0.0171	0.0186	0.0239
	90	0.936	1.704	2.734	0.0199	0.0213	0.0286
	154	0.962	1.713	2.425	0.0205	0.0209	0.0198
	156	1.330	2.383	3.406	0.0283	0.0293	0.0284
	157	1.537	2.729	3.896	0.0327	0.0331	0.0324
	158*	1.739	2.911	4.248	0.0370	0.0326	0.0371
SW 1R	32	0.111	0.258	0.440	0.0024	0.0041	0.0051
	33	0.246	0.520	0.842	0.0052	0.0076	0.0089
	34*	0.442	0.850	1.330	0.0094	0.0113	0.0133
	69	0.970	1.180	1.418	0.0206	0.0058	0.0066
	70	1.390	1.680	2.030	0.0296	0.0081	0.0097
	72	2.690	3.160	3.660	0.0572	0.0131	0.0139
SW 2R	28	0.231	0.488	0.685	0.0049	0.0071	0.0055
	29	0.350	0.694	0.980	0.0075	0.0096	0.0080
	30	0.471	0.913	1.354	0.0100	0.0123	0.0123
	31	0.628	1.179	1.699	0.0134	0.0153	0.0144
	32	0.812	1.510	2.239	0.0173	0.0194	0.0203
	33	1.107	1.913	2.790	0.0236	0.0224	0.0244
	34*	1.450	2.357	3.333	0.0309	0.0252	0.0271
	35	2.190	3.057	3.920	0.0466	0.0241	0.0240
SW 2	32	0.053	0.108	0.165	0.0011	0.0015	0.0016
	33	0.135	0.262	0.403	0.0029	0.0035	0.0039
	34	0.217	0.436	0.653	0.0046	0.0061	0.0060
	35	0.244	0.471	0.702	0.0052	0.0063	0.0064
	40	-0.204	-0.442	-0.720	-0.0043	-0.0066	-0.0077
	69	0.301	0.562	0.883	0.0064	0.0073	0.0089
	70	0.532	0.957	1.434	0.0113	0.0118	0.0133
	76	-0.524	-1.004	-1.478	-0.0112	-0.0133	-0.0132
	94	0.873	1.490	2.210	0.0186	0.0171	0.0200
	100	-0.852	-1.540	-2.220	-0.0181	-0.0191	-0.0189
	118	1.239	2.060	2.931	0.0264	0.0228	0.0242
	124	-1.266	-2.088	-2.936	-0.0269	-0.0228	-0.0236
	129	1.326	2.129	2.957	0.0282	0.0223	0.0230
	133*	-1.452	-2.000	-2.566	-0.0309	-0.0152	-0.0157
	135	2.317	2.634	2.972	0.0493	0.0088	0.0094
	137	-1.365	-1.692	-2.010	-0.0290	-0.0091	-0.0088

*Crushing of wall concrete.

TABLE 13. COMPONENTS OF STORY DRIFT INDEX

Specimen	Load Point	Story Drift Index	Story Drift Index	Components of R2		Story Drift Index	Components of R3	
		$R1=(R1)_{tan}$		$(R2)_{Rot.}$	$(R2)_{tan}$	R3	$(R3)_{Rot.}$	$(R3)_{tan}$
SW 1	76	0.0017	0.0028	0.0013	0.0015	0.0033	0.0019	0.0014
	79	0.0051	0.0068	0.0026	0.0040	0.0081	0.0039	0.0042
	88	0.0171	0.0186	0.0118	0.0068	0.0239	0.0136	0.0103
	90	0.0199	0.0213	0.0141	0.0072	0.0286	0.0163	0.0123
	156	0.0283	0.0293	0.0185	0.0108	0.0284	0.0223	0.0061
	158*	0.0370	0.0326	0.0223	0.0103	0.0371	0.0265	0.0106
SW 1R	32	0.0024	0.0041	0.0017	0.0024	0.0051	0.0024	0.0027
	34*	0.0094	0.0113	0.0063	0.0050	0.0133	0.0081	0.0052
	70	0.0296	0.0081	0.0048	0.0033	0.0097	0.0056	0.0041
	72	0.0572	0.0131	0.0084	0.0047	0.0139	0.0095	0.0044
SW 2R	28	0.0049	0.0071	0.0019	0.0052	0.0055	0.0027	0.0028
	30	0.0100	0.0123	0.0053	0.0070	0.0123	0.0069	0.0054
	32	0.0173	0.0194	0.0115	0.0079	0.0203	0.0136	0.0059
	34*	0.0309	0.0252	0.0188	0.0064	0.0271	0.0213	0.0058
	35	0.0466	0.0241	0.0188	0.0053	0.0240	0.0207	0.0033
SW 2	32	0.0011	0.0015	0.0009	0.0006	0.0016	0.0012	0.0004
	35	0.0046	0.0063	0.0027	0.0036	0.0064	0.0039	0.0025
	40	-0.0043	-0.0066	-0.0031	-0.0035	-0.0077	-0.0044	-0.0033
	94	0.0186	0.0171	0.0120	0.0051	0.0200	0.0141	0.0059
	100	-0.0181	-0.0191	-0.0122	-0.0069	-0.0189	-0.0143	-0.0046
	129	0.0282	0.0223	0.0146	0.0077	0.0230	0.0171	0.0059
	133*	-0.0309	-0.0152	-0.0099	-0.0053	-0.0157	-0.0110	-0.0047

* Crushing of first story wall panel

TABLE 14 SELECTED CRITICAL DAMPING RATIOS

n	1	2	3	4	5	6	7	8	9	10
T_n (sec.)	0.87	0.220	0.100	0.07	0.050	0.040	0.033	0.029	0.027	0.025
ξ_n*	0.05	0.026	0.038	0.05	0.067	0.083	0.100	0.110	0.120	0.130

$*\xi_n = \alpha \frac{T_n}{4\pi} + \beta \frac{\pi}{T_n}$, where $\alpha = 0.669$ and $\beta = 0.00103$.

TABLE 15 COMPARISON BETWEEN OVERALL PERFORMANCE OF BUILDINGS UNDER 0.4g PACOIMA BASE ROCK MOTION

		Prototype Building (Ductile Model)	Building with Four Prototype Walls
Max. Roof Displacement		11.8 in.	8.2 in.
Max. First Story Drift Index		0.006	0.0042
Max. Plastic Hinge Rotation	Wall	0.005	0.0034
	Beam	0.019	0.0130
Max. Shear Developed in a Single Wall		2650 kips	1900 kips
Most Critical M_B/V_B Ratio of Wall		446 in.	505 in.

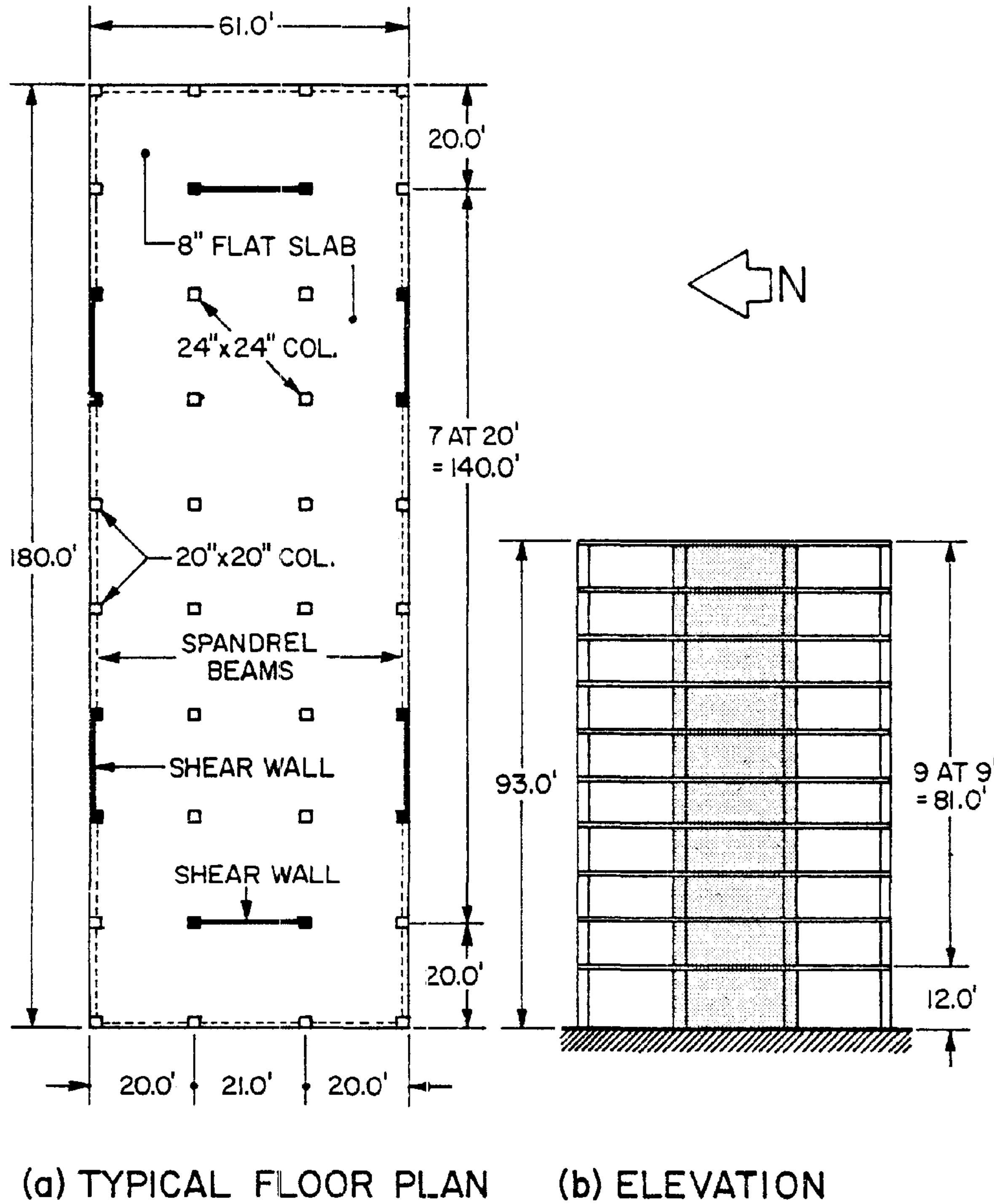

FIG. 2.1 PROTOTYPE BUILDING

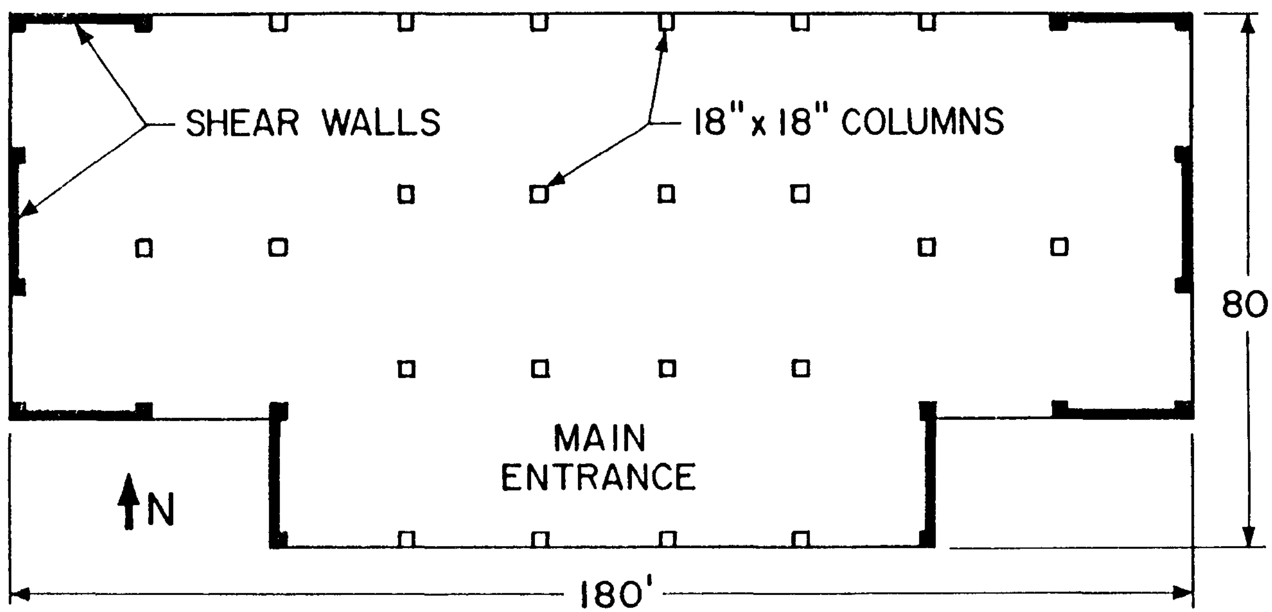

FIG. 2.2 FLOOR PLAN OF INDIAN HILLS MEDICAL CENTER
(FROM REF. 9)

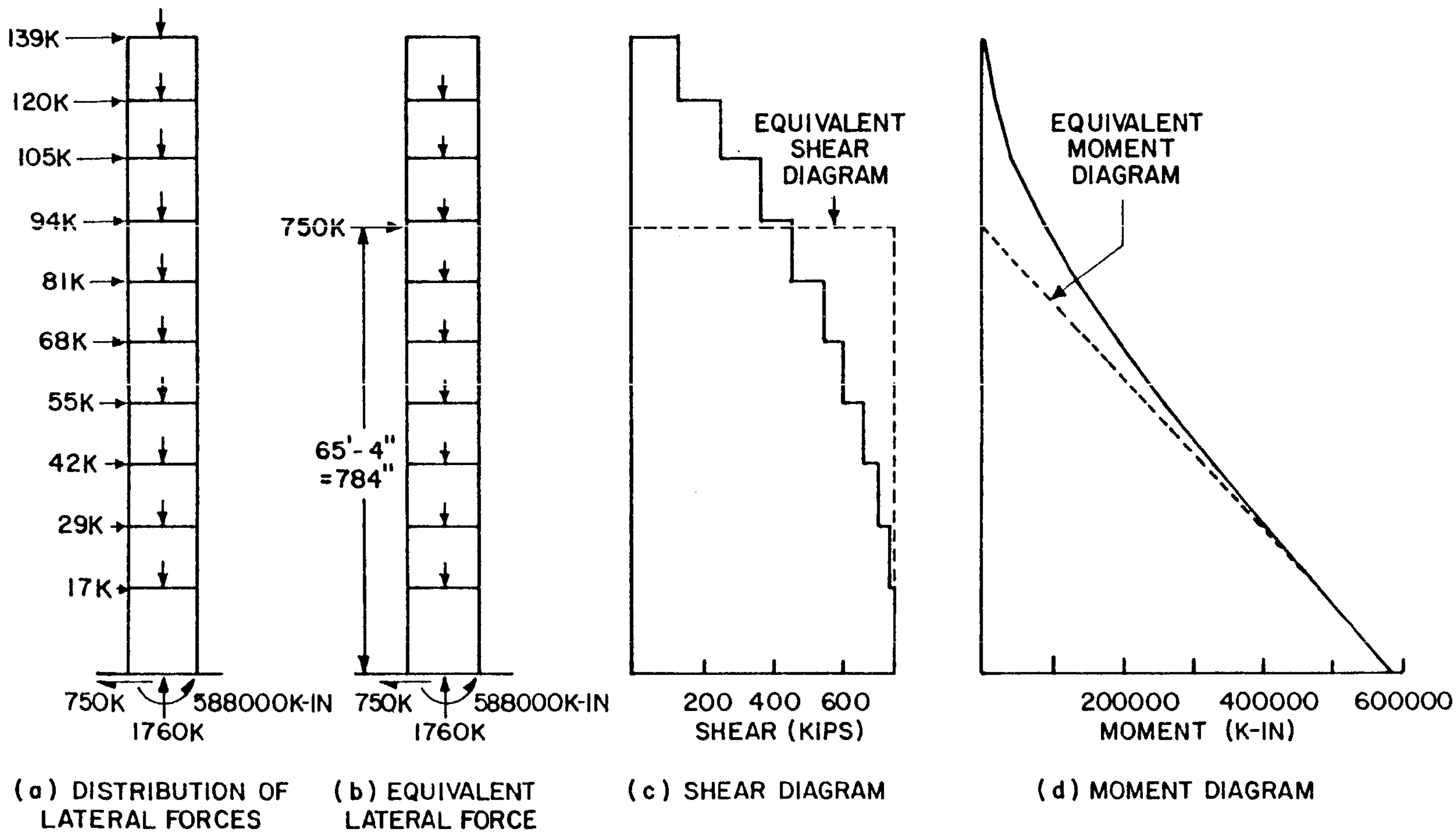

FIG. 2.3 SHEAR AND MOMENT DIAGRAMS OF A SINGLE N-S WALL WHEN SUBJECTED TO 1/2 (1.4E) + 1.4 (TORSION) CODE FORCES.

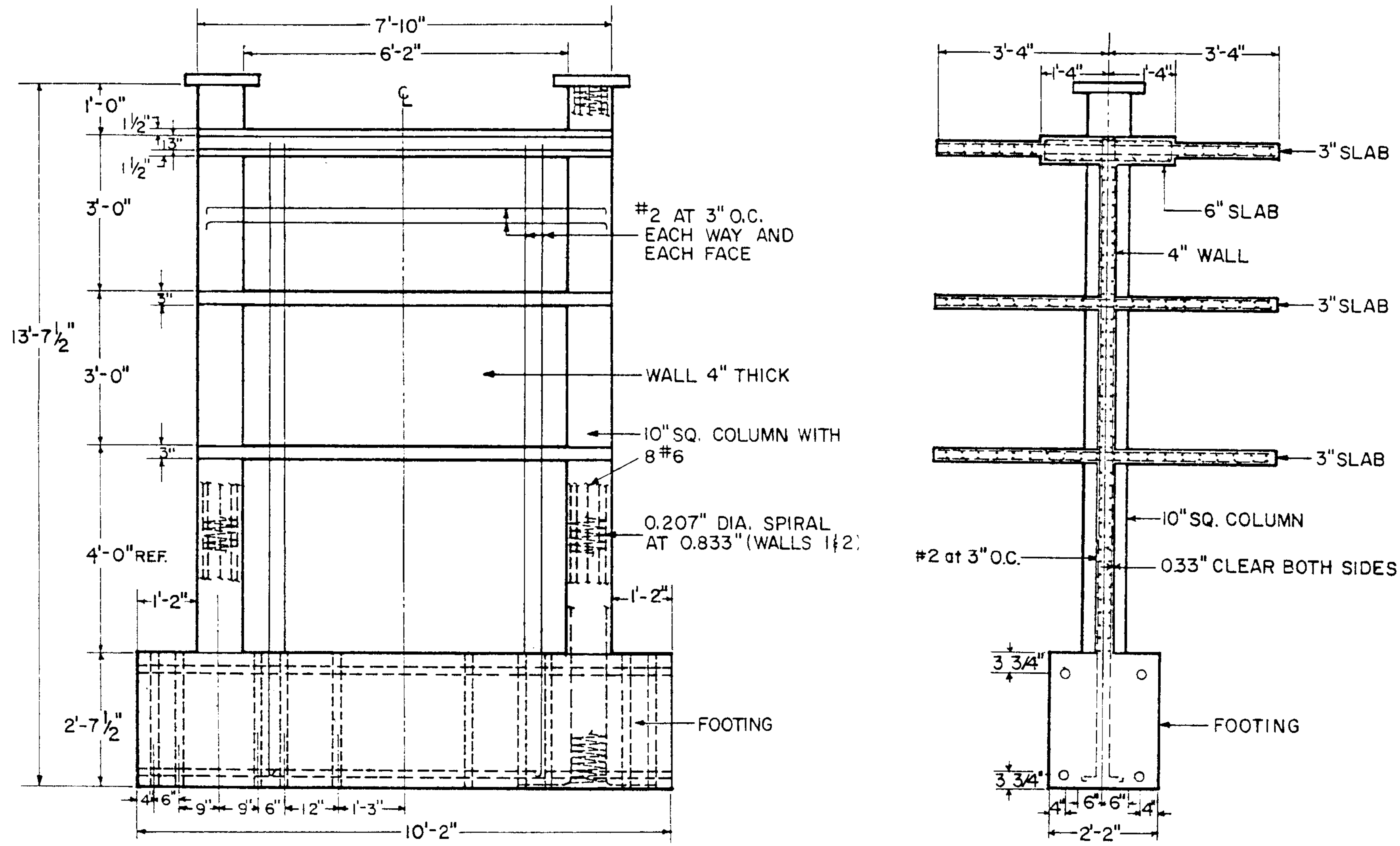

(a) ELEVATION (b) SECTION

FIG. 2.4 DIMENSIONS AND DETAILS OF WALL SPECIMENS

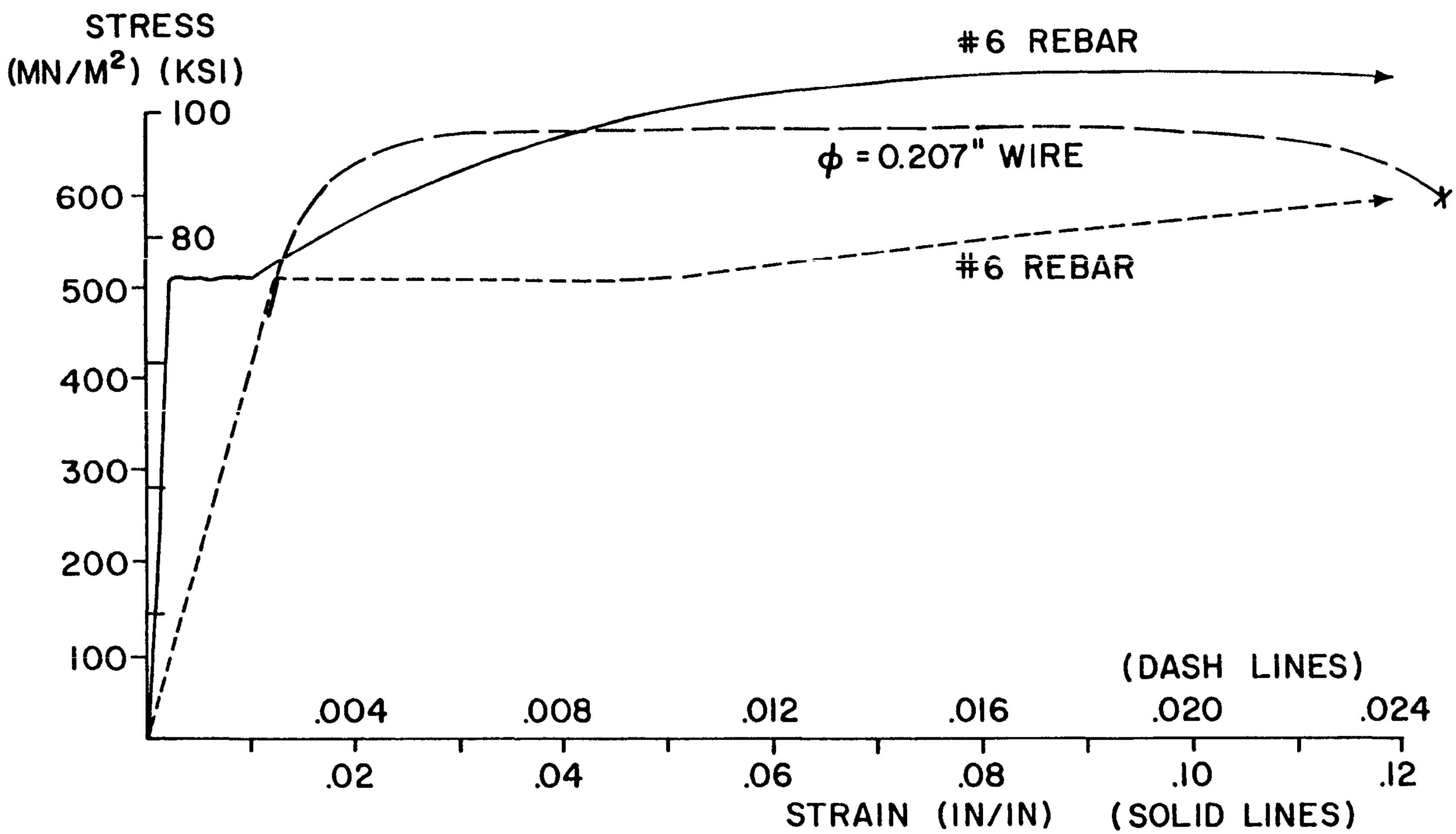

FIG. 2.5 STRESS-STRAIN DIAGRAMS OF REINFORCEMENT

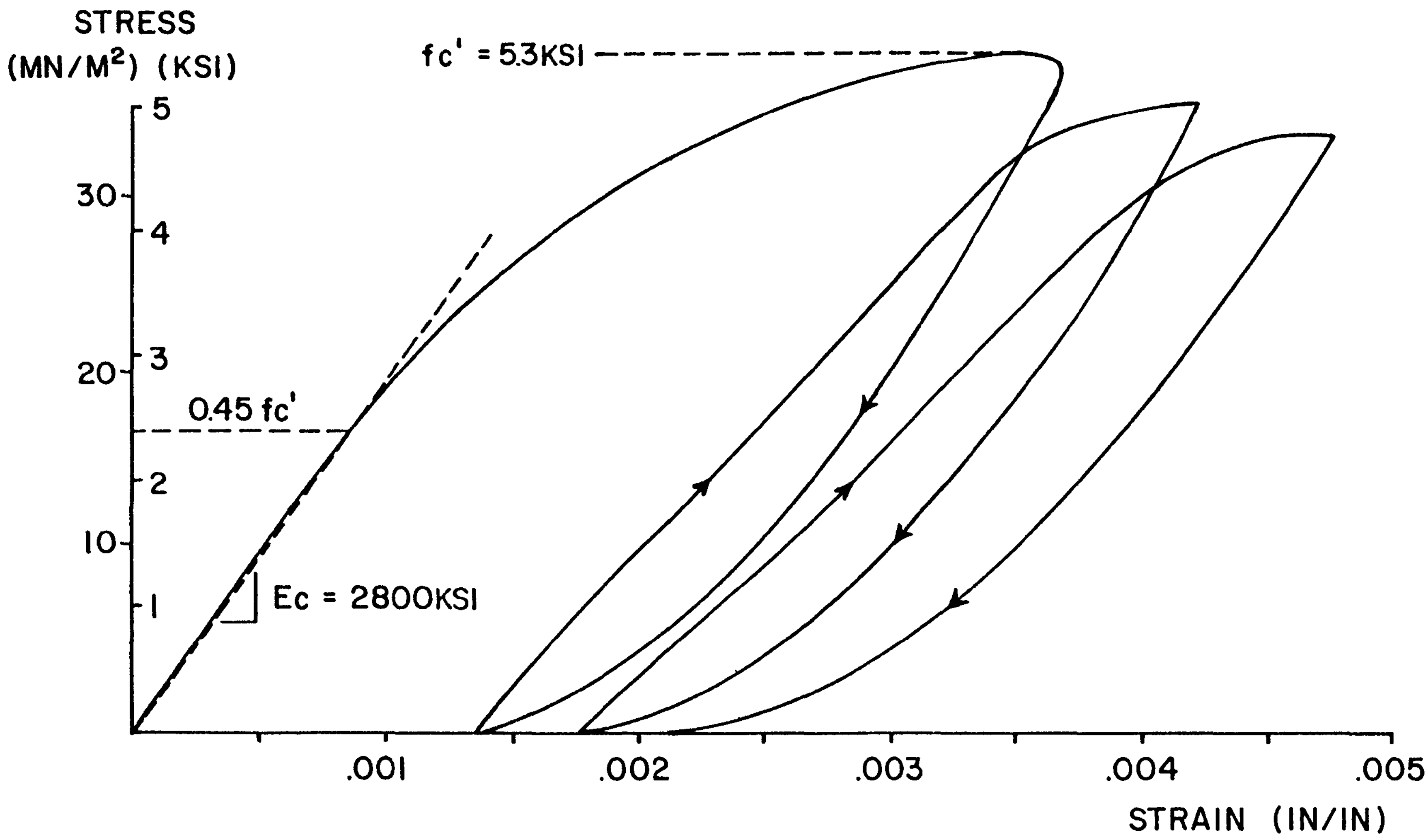

FIG. 2.6 STRESS-STRAIN DIAGRAM OF CONCRETE

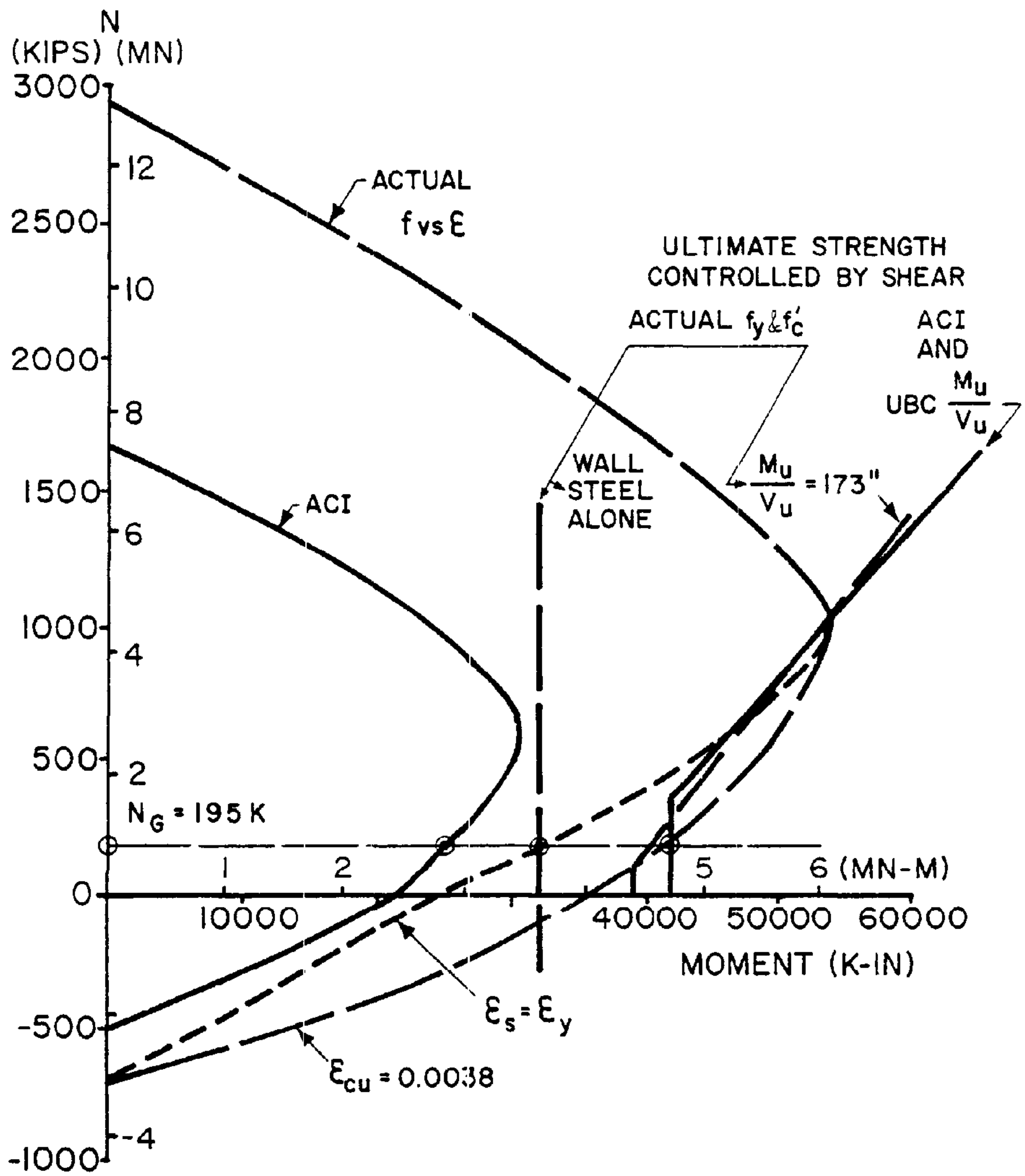

FIG. 2.7 MOMENT-AXIAL FORCE DIAGRAM OF WALL SPECIMEN

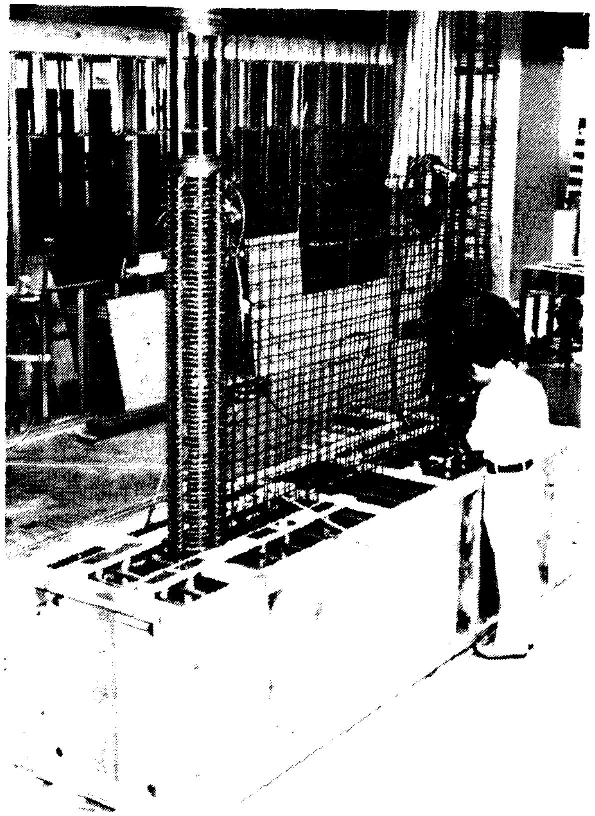

FIG. 2.8 FRAMEWORK READY FOR CASTING FOUNDATION

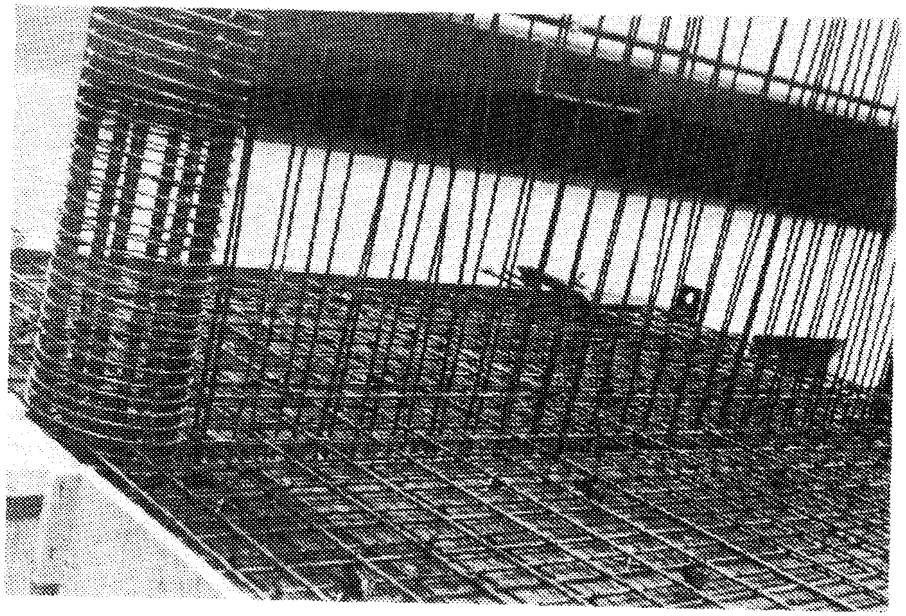

FIG. 2.9 SLAB REINFORCEMENT

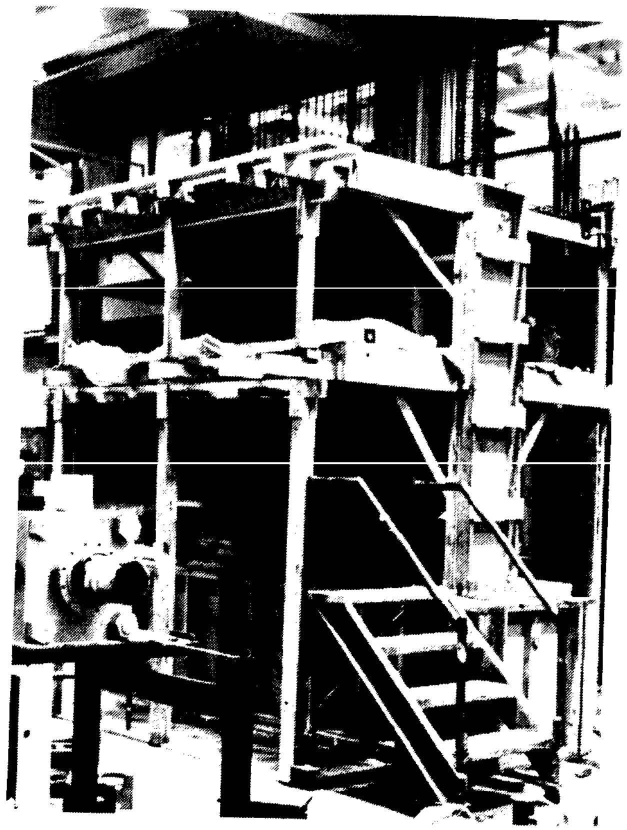

FIG. 2.10 FORMWORK READY FOR CASTING $2^{\underline{nd}}$ STORY

FIG. 2.11 PICK-UP FRAME ATTACHED TO SPECIMEN

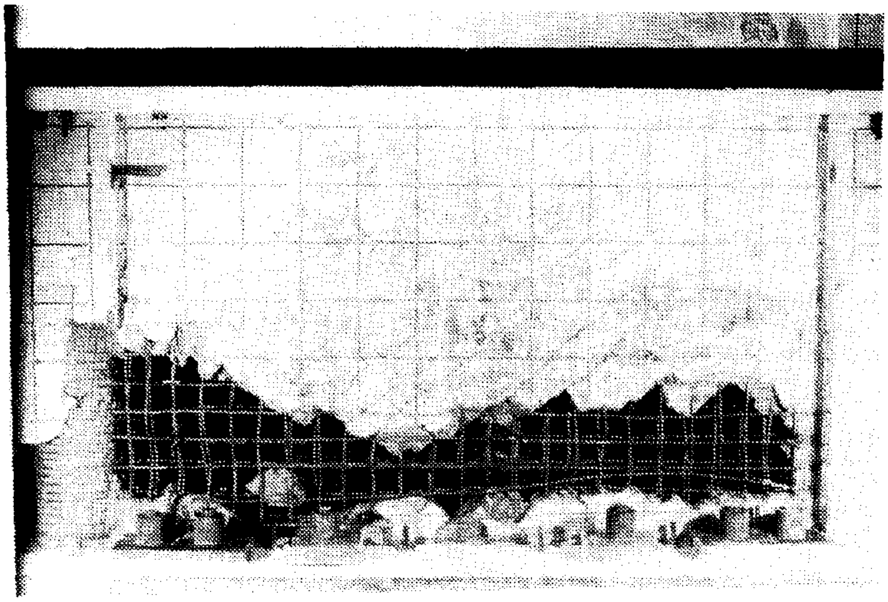

FIG. 2.12 CRUSHED CONCRETE OF SHEAR WALL 1 REMOVED FOR REPAIR

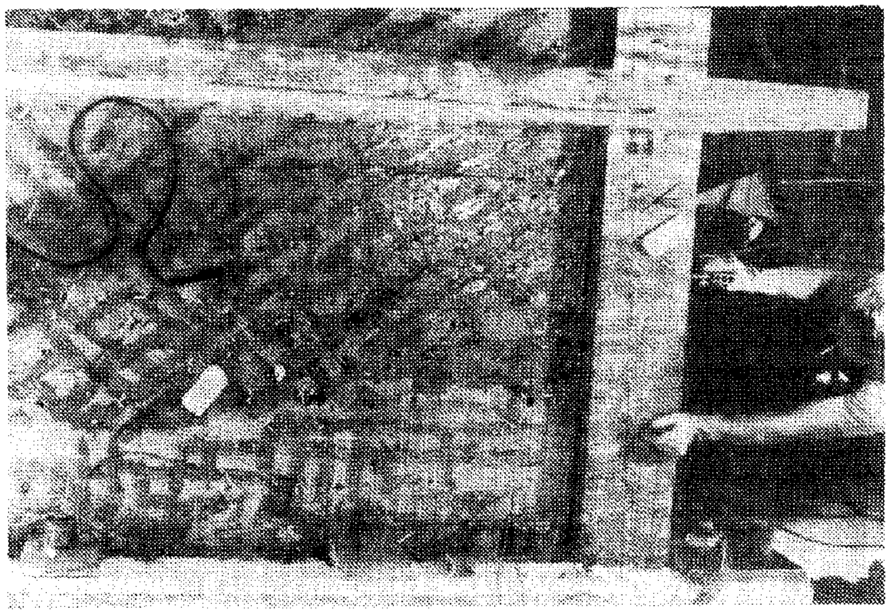

FIG. 2.13 EPOXY REPAIR OF SHEAR WALL 1

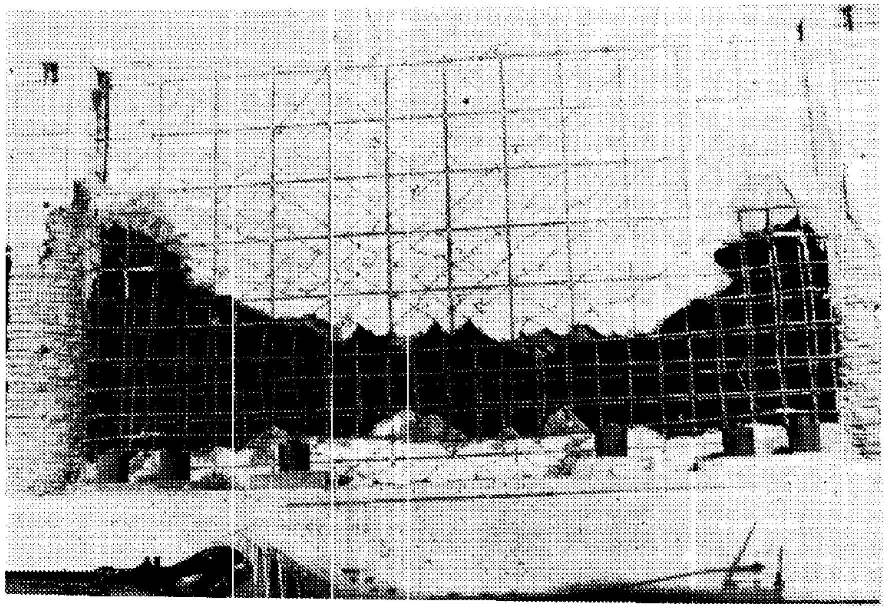

FIG. 2.14 CRUSHED CONCRETE OF SHEAR WALL 2 REMOVED FOR REPAIR

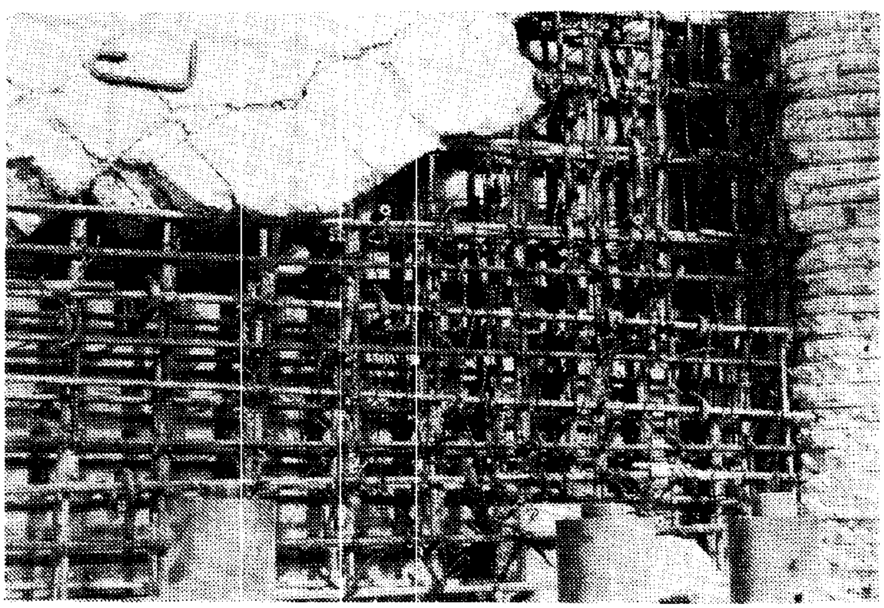

FIG. 2.15 WALL REINFORCEMENT OF SHEAR WALL 2R BEFORE CASTING

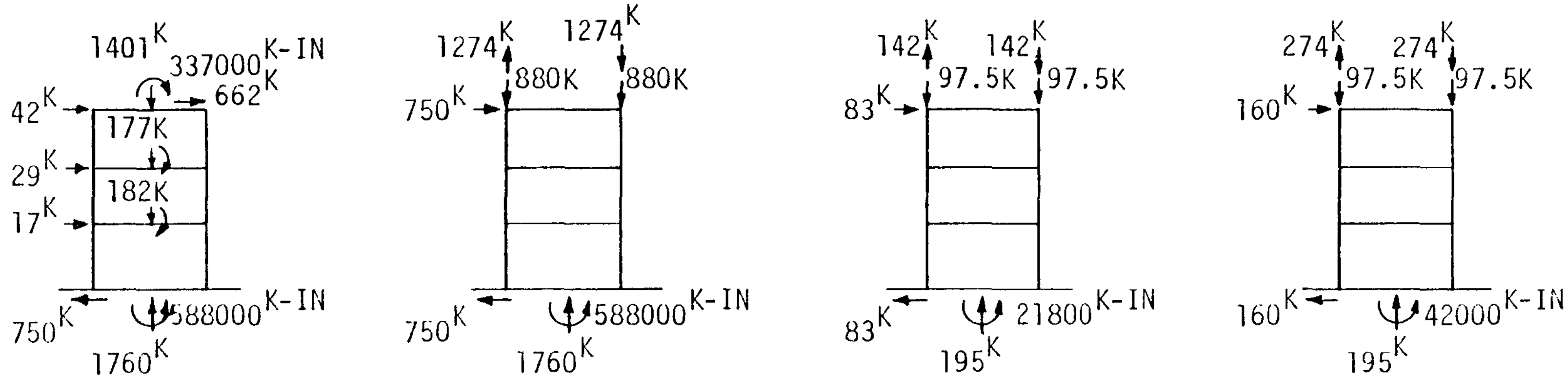

(a) ACTUAL LOADING CONDITION OF PROTOTYPE

(b) SIMPLIFIED LOADING CONDITION OF PROTOTYPE

(c) SIMPLIFIED LOADING CONDITION OF MODEL

(d) ULTIMATE LOADING CONDITION OF MODEL

(1) TWO WALLS RESIST TOTAL EARTHQUAKE LOAD AND TORSION SPECIFIED BY UBC

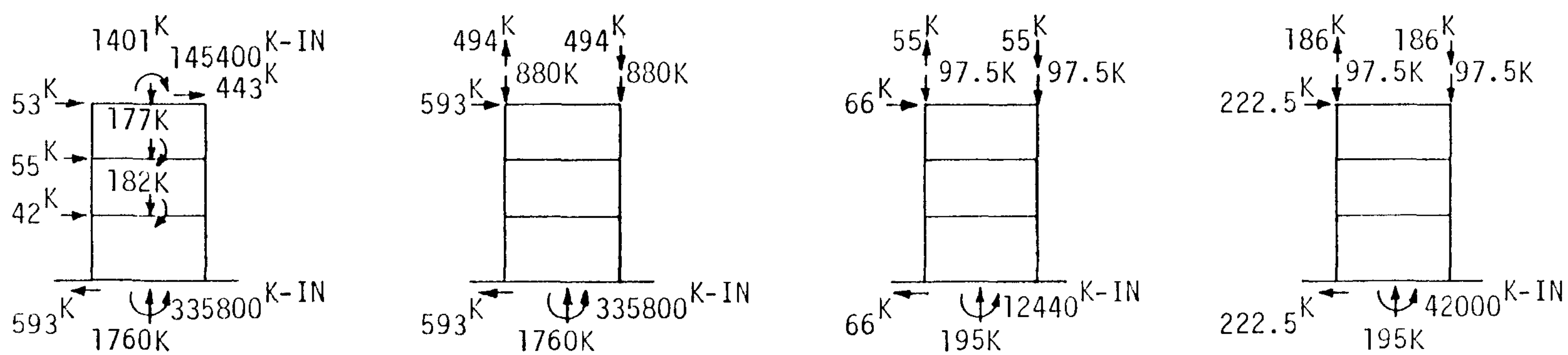

(a)

(b)

(c)

(d)

(2) WALLS AND FRAMES ACTING TOGETHER TO RESIST TOTAL EARTHQUAKE LOAD SPECIFIED BY UBC

FIG. 3.1 LOADING CONDITIONS OF PROTOTYPE AND MODEL

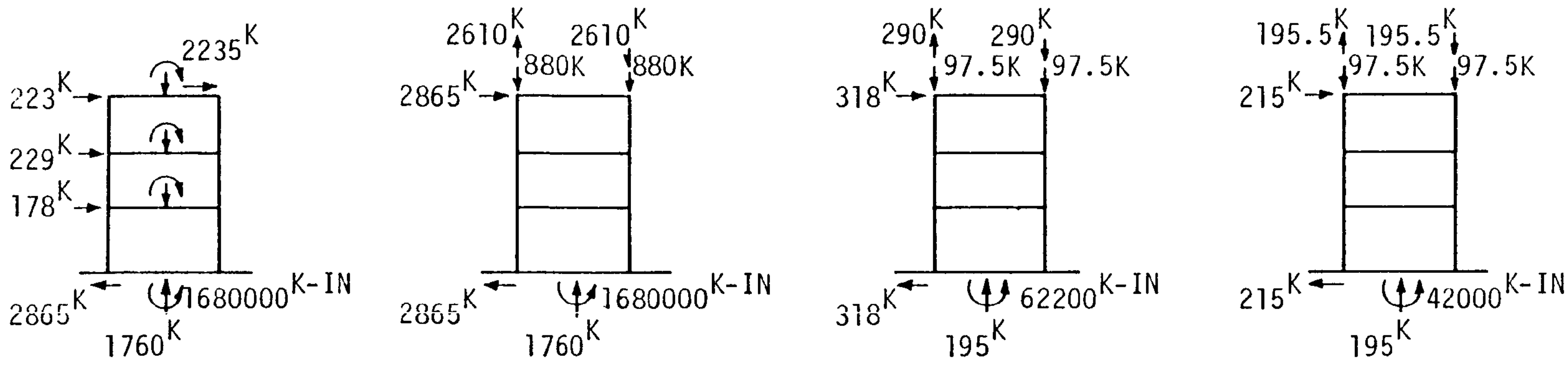

(a) ACTUAL LOADING CONDITION OF PROTOTYPE

(b) SIMPLIFIED LOADING CONDITION OF PROTOTYPE

(c) SIMPLIFIED LOADING CONDITION OF MODEL

(d) ULTIMATE LOADING CONDITION OF MODEL

(3) EL CENTRO EQ RESPONSE SPECTRUM ANALYSIS OF ENTIRE BUILDING, FIRST MODE ONLY, 5% DAMPING

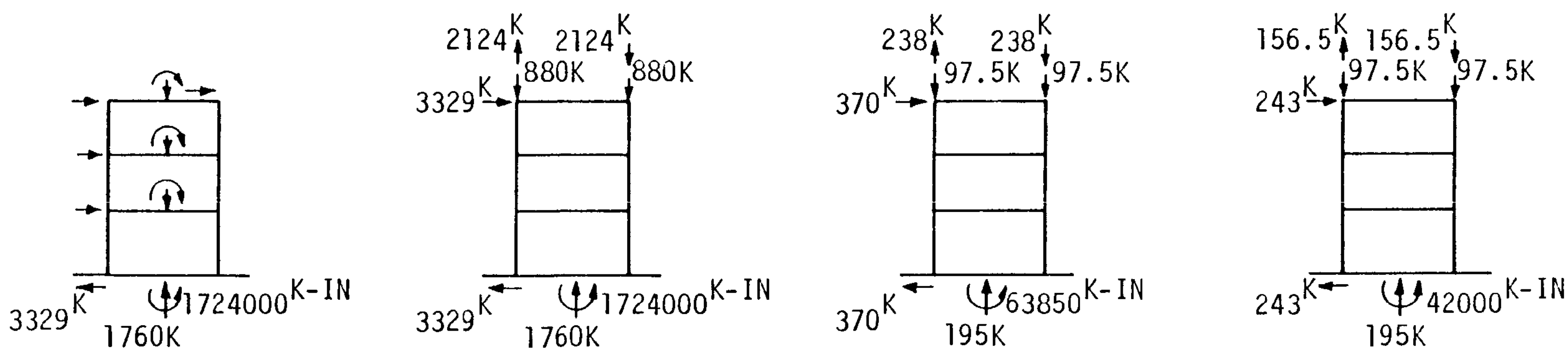

(a) ROOT MEAN SQUARE COMBINATION OF LOADS

(b)

(c)

(d)

(4) EL CENTRO EQ RESPONSE SPECTRUM ANALYSIS OF ENTIRE BUILDING, FIRST THREE MODES, 5% DAMPING

FIG. 3.1 (CONT'D)

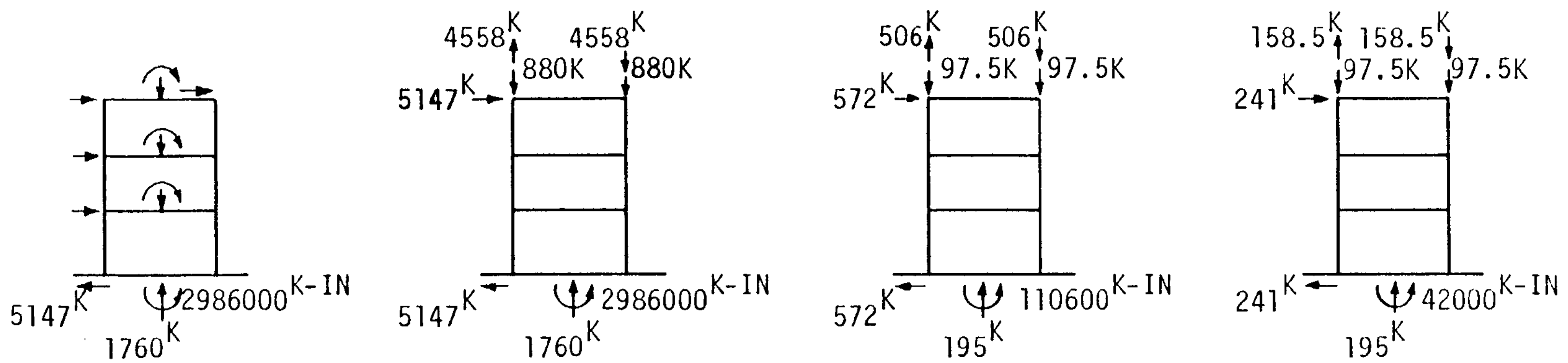

(a) ROOT MEAN SQUARE COMBINATION OF LOADS

(b) SIMPLIFIED LOADING CONDITION OF PROTOTYPE

(c) SIMPLIFIED LOADING CONDITION OF MODEL

(d) ULTIMATE LOADING CONDITION OF MODEL

(5) SAN FERNANDO EQ RESPONSE SPECTRUM ANALYSIS OF ENTIRE BUILDING, FIRST THREE MODES, 5% DAMPING

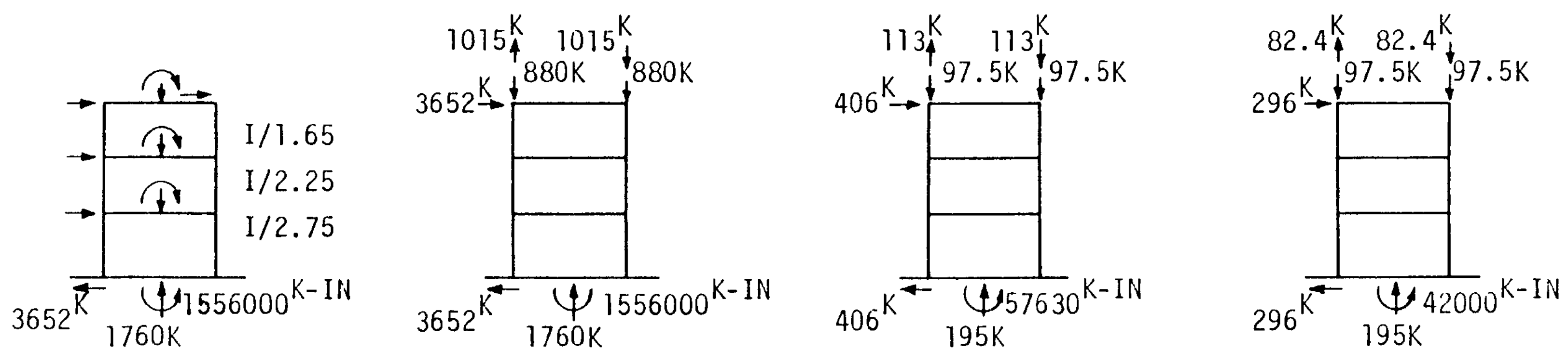

(a)

(b)

(c)

(d)

(6) SIMILAR TO (4), BUT SECTIONAL FLEXURAL STIFFNESS OF FIRST THREE STORIES OF WALLS WERE REDUCED

FIG. 3.1 (CONT'D)

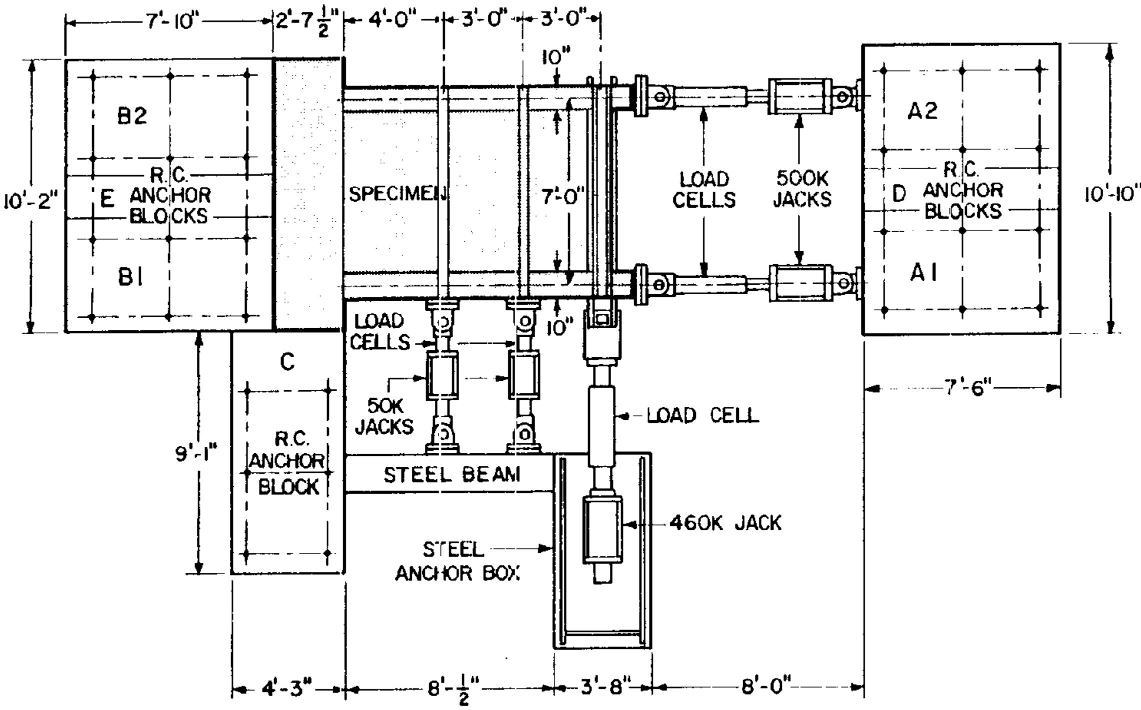

(a) PLAN

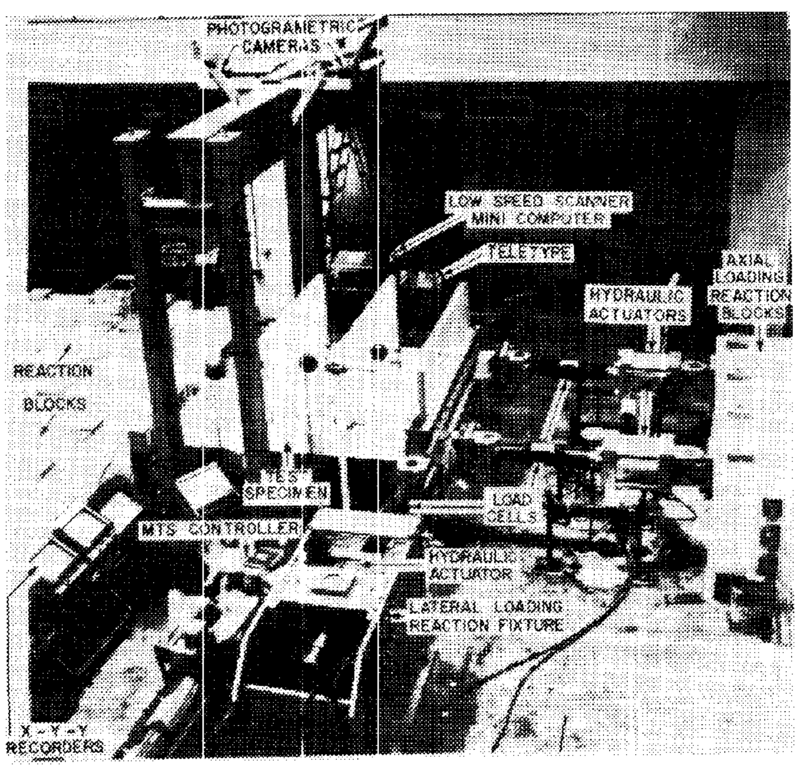

(b) GENERAL VIEW

FIG. 4.1 PLAN AND GENERAL VIEW OF TESTING FACILITY

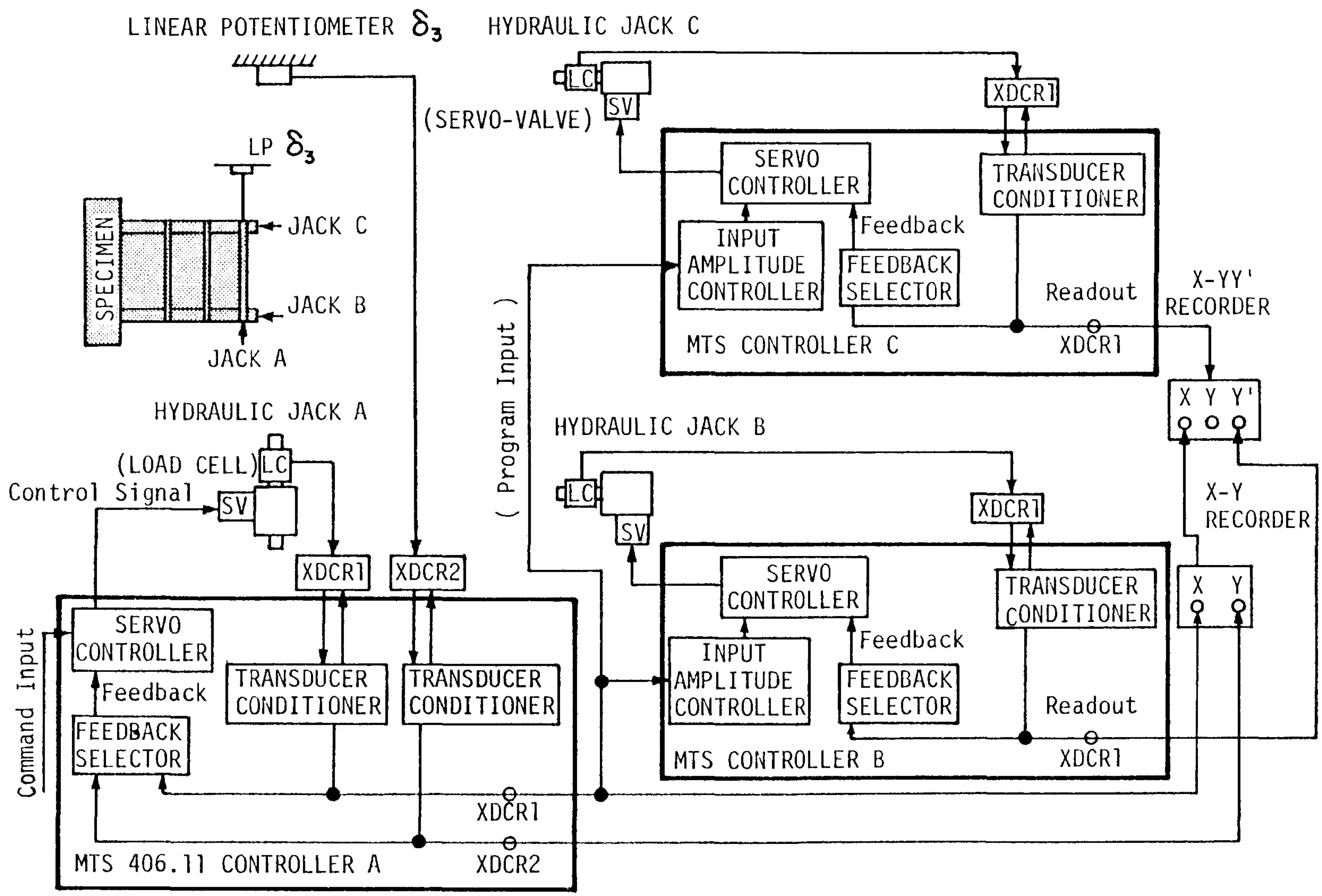

FIG. 4.2 SERVO-HYDRAULIC TESTING SYSTEM

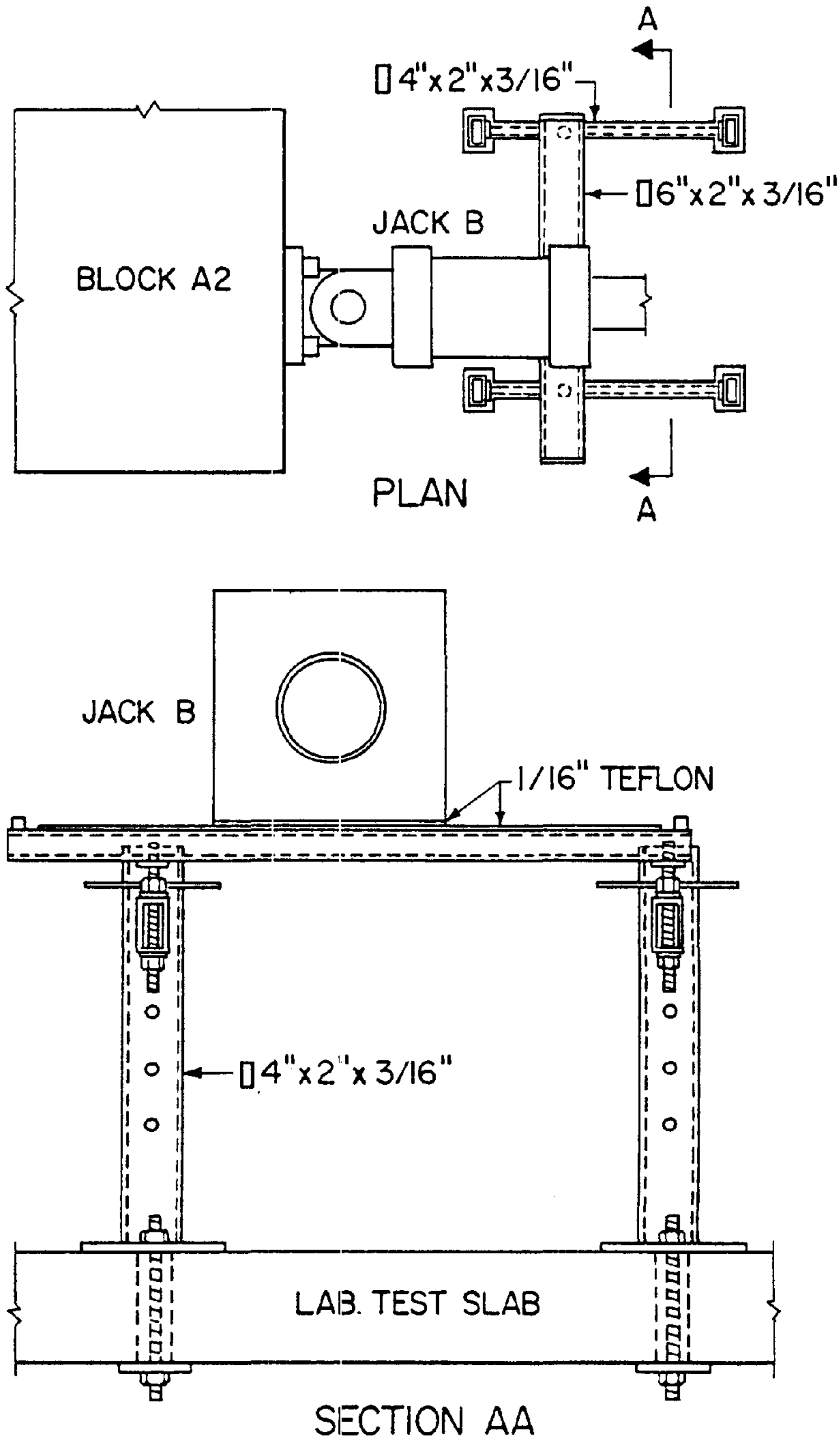

FIG. 4.3 HYDRAULIC JACK SUPPORTING DEVICE

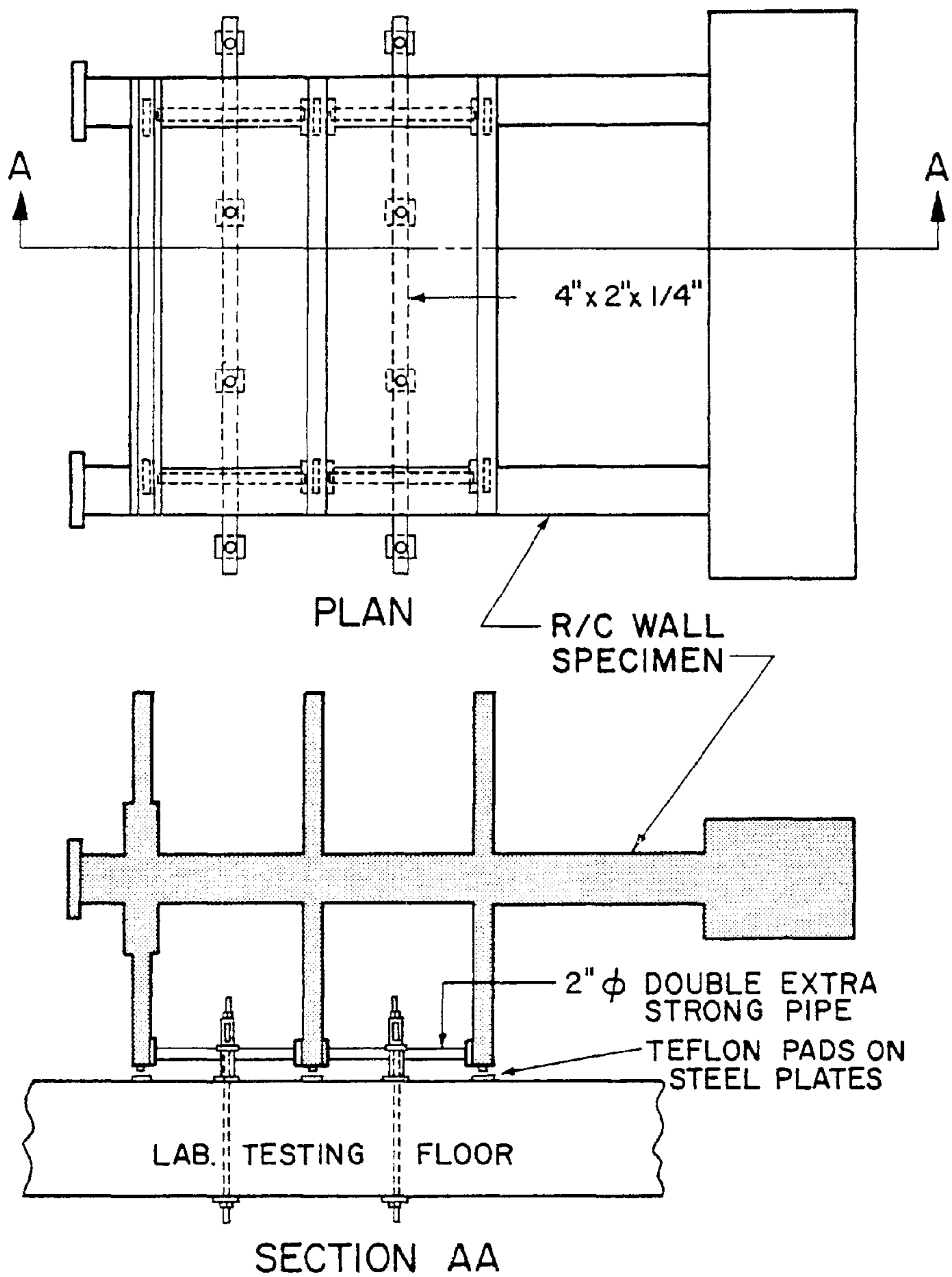

FIG. 4.4 DEFORMATION GUIDANCE DEVICE

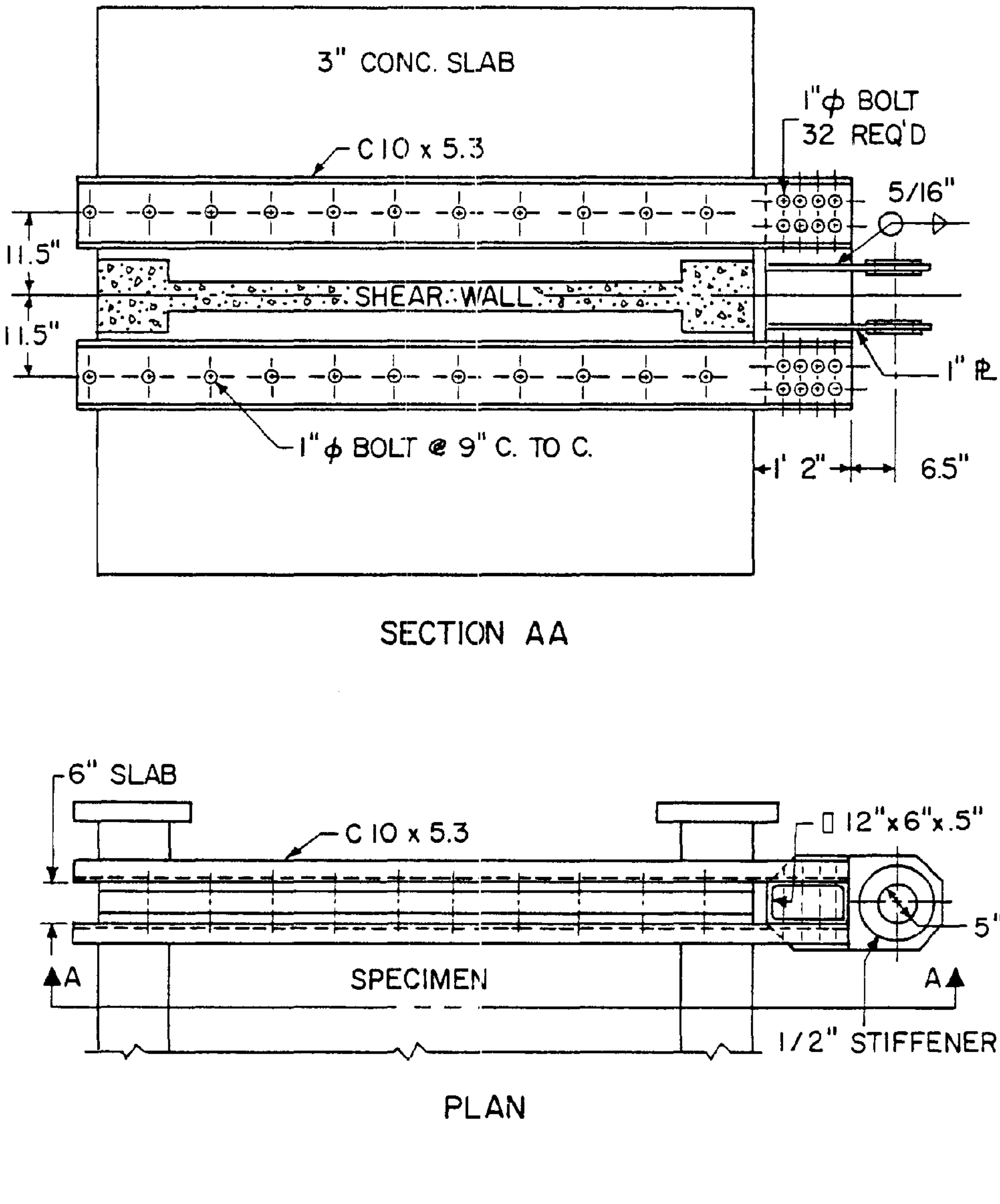

FIG. 4.5 DETAILS OF THE SHEAR FORCE TRANSFERRING DEVICE

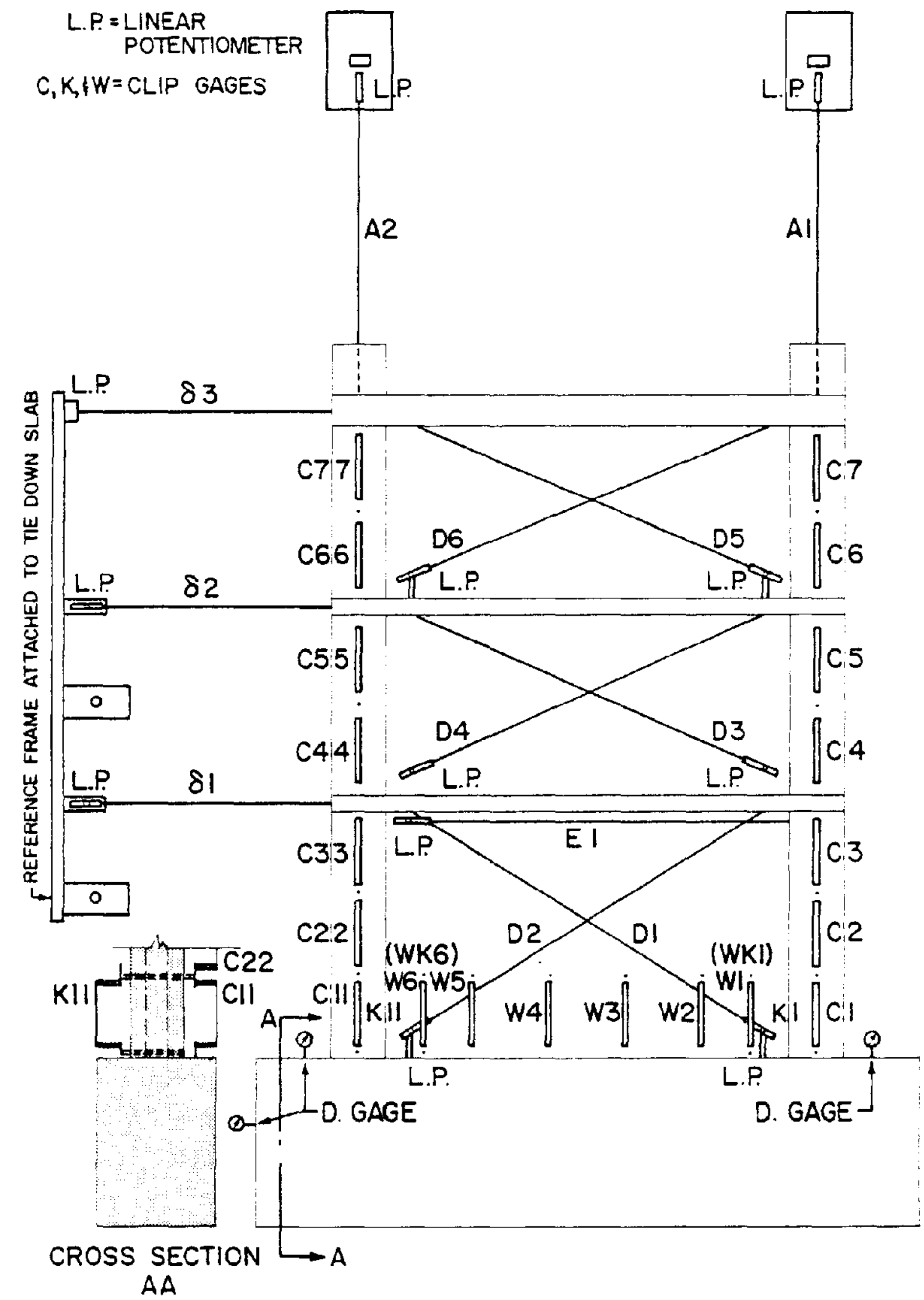

FIG. 4.6 EXTERNAL INSTRUMENTATION OF WALL SPECIMEN

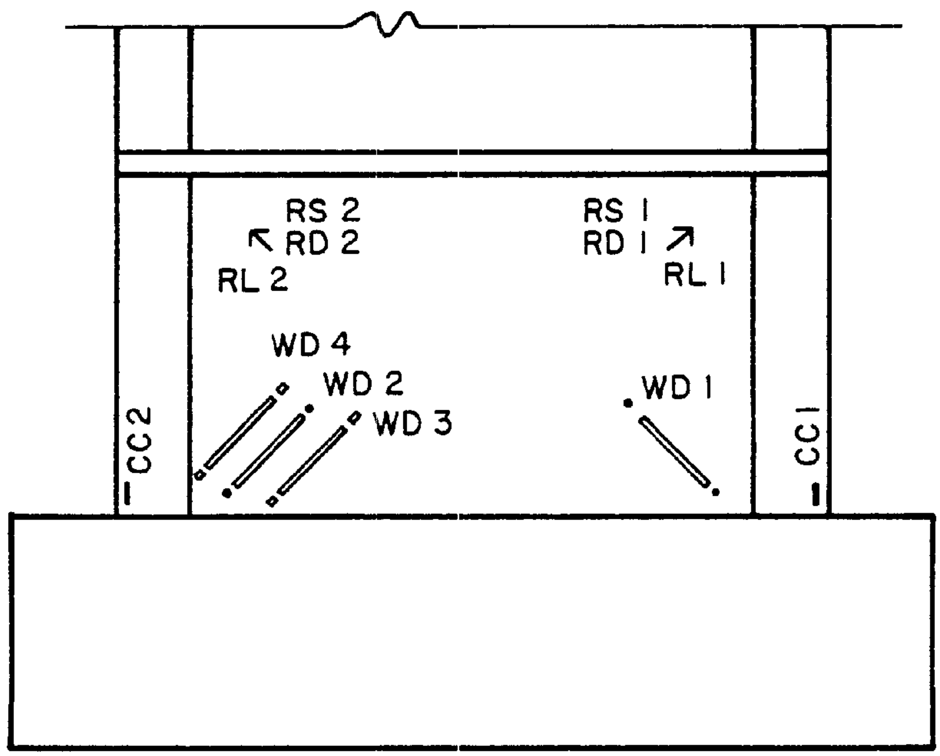

FIG. 4.7 LOCATION OF DIAGONAL CLIP GAGES
AND CONCRETE STRAIN GAGES

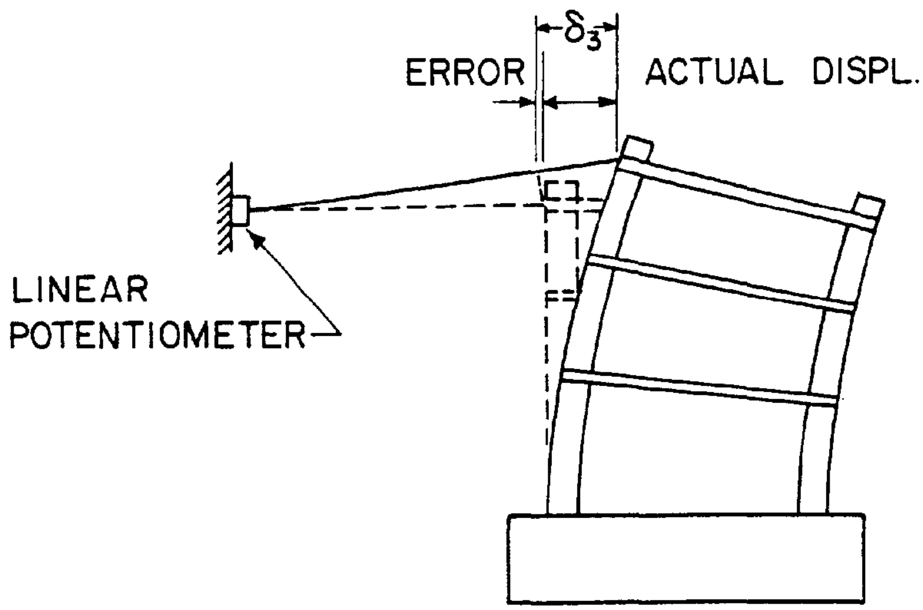

FIG. 4.8 ERROR IN LATERAL DISPLACEMENT MEASUREMENT

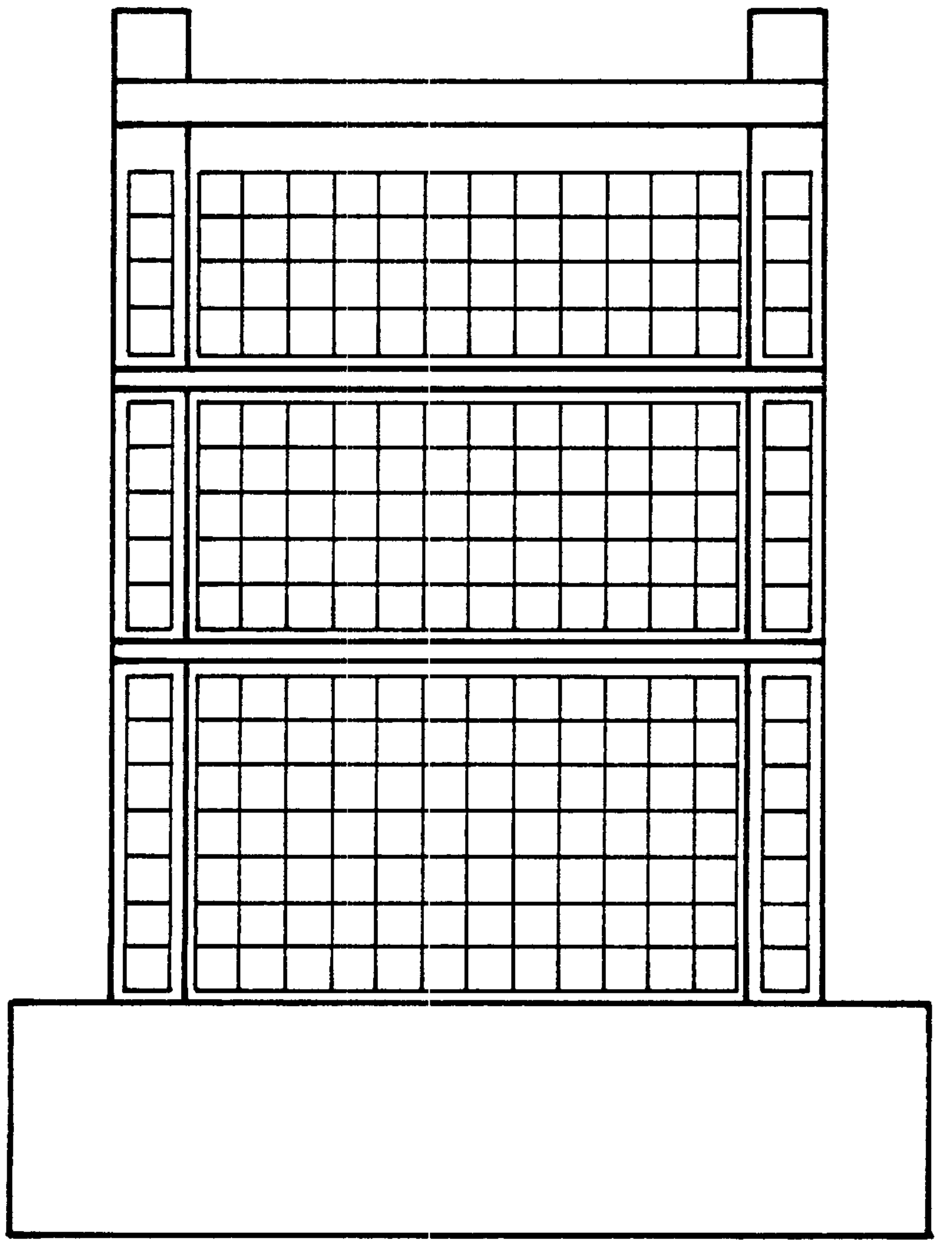

FIG. 4.9 GRID FOR PHOTOGRAMMETRIC MEASUREMENT

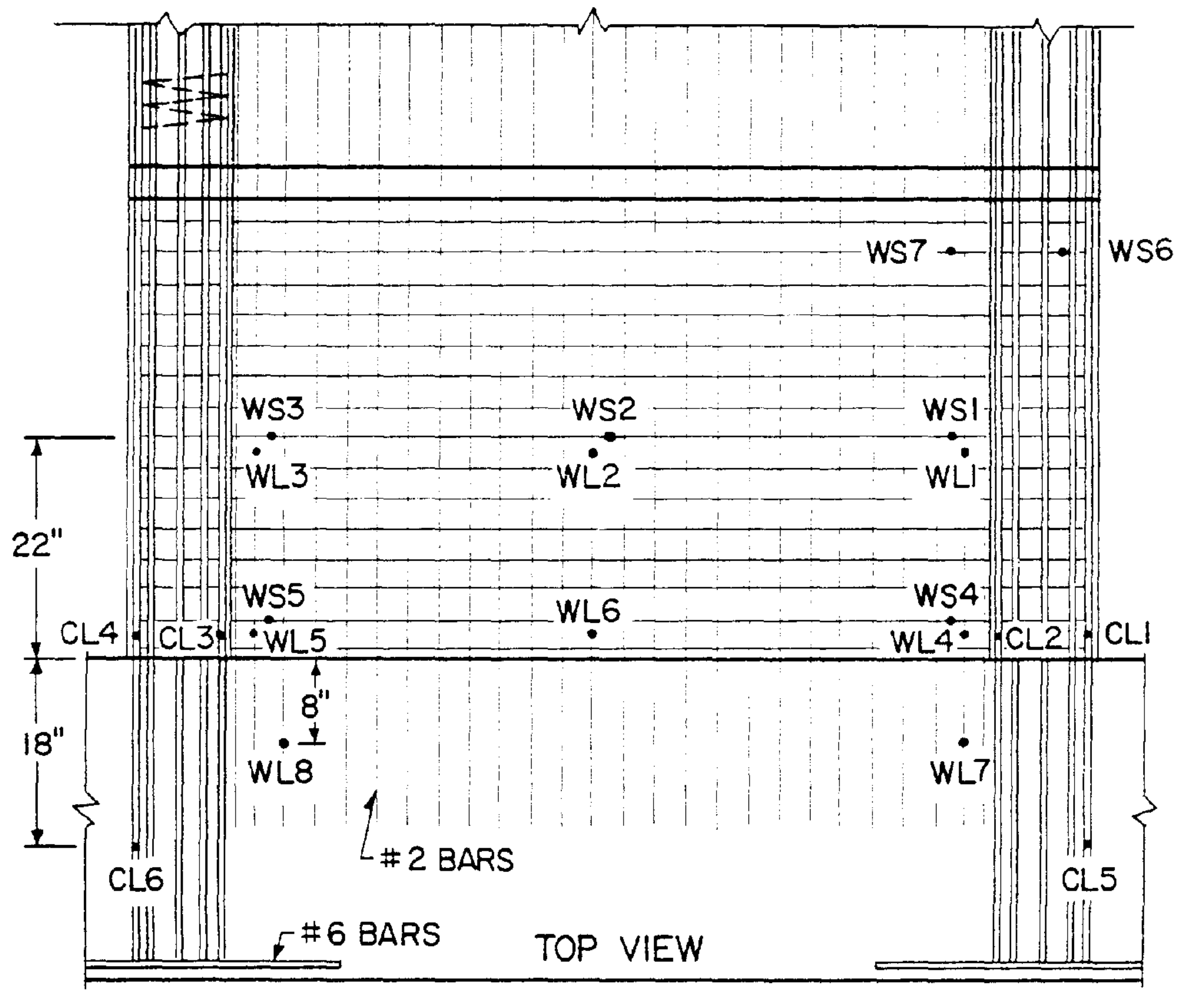

FIG. 4.10 LOCATION OF STRAIN GAGES

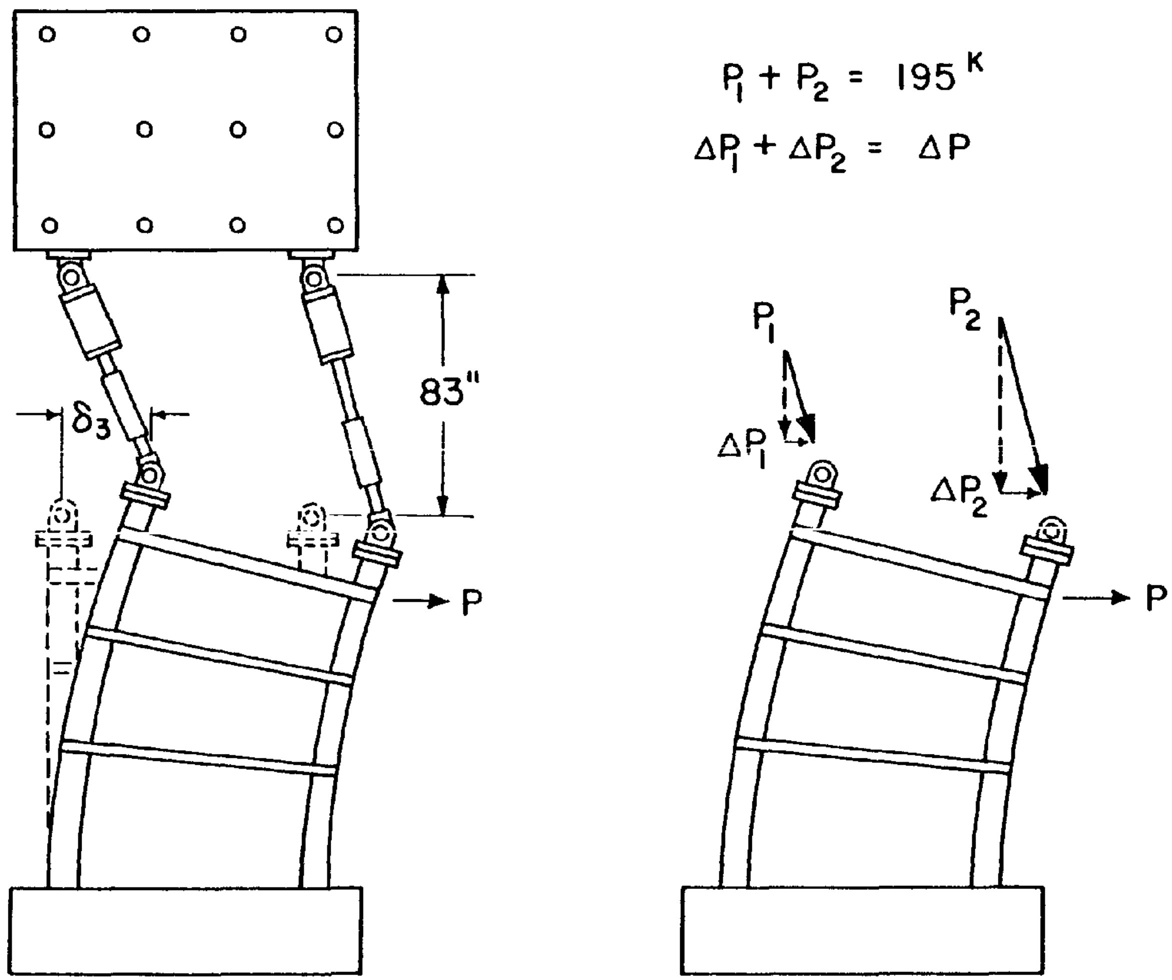

FIG. 4.11 HORIZONTAL COMPONENT OF NET AXIAL FORCE

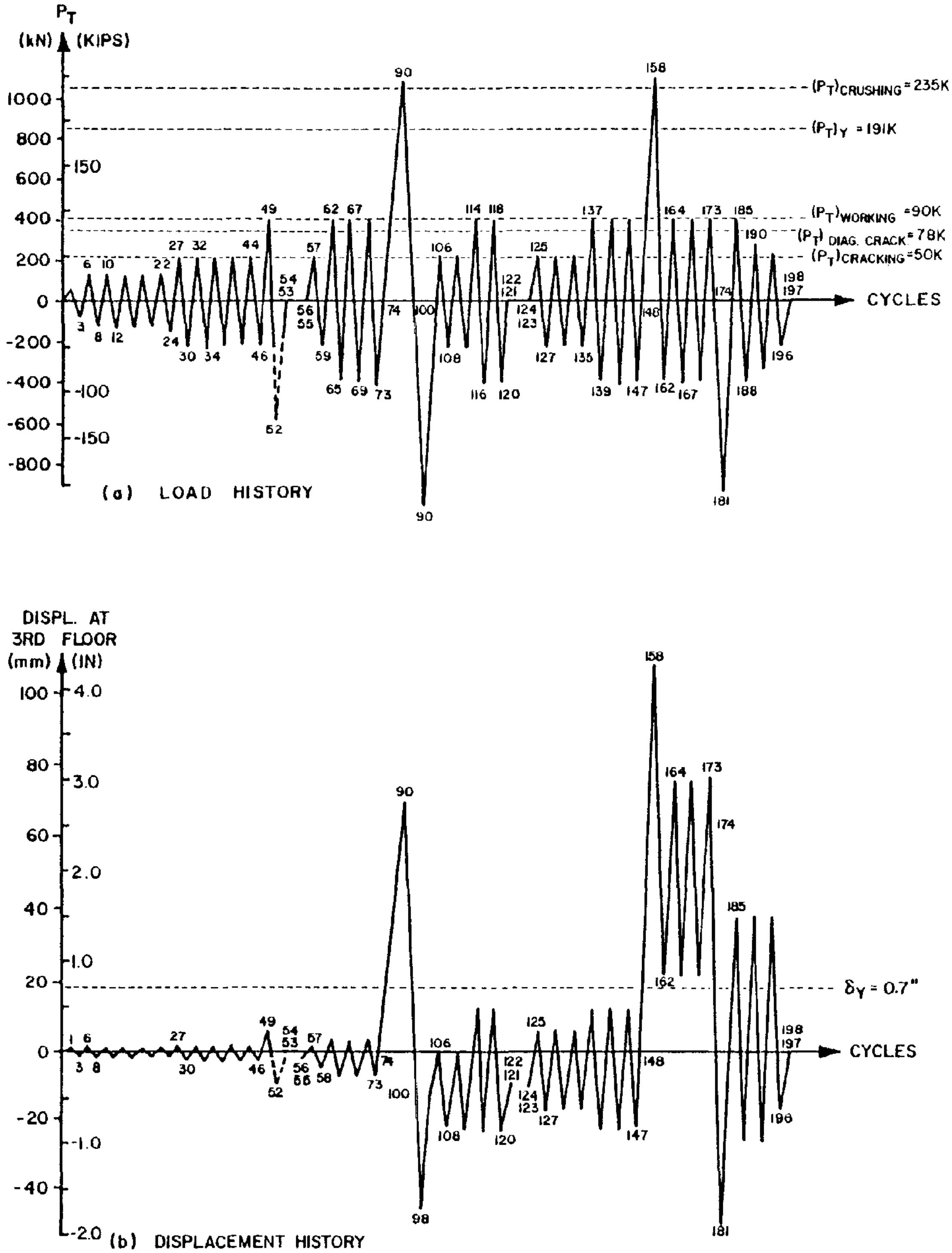

FIG. 5.1 LOADING PROGRAM-SHEAR WALL 1

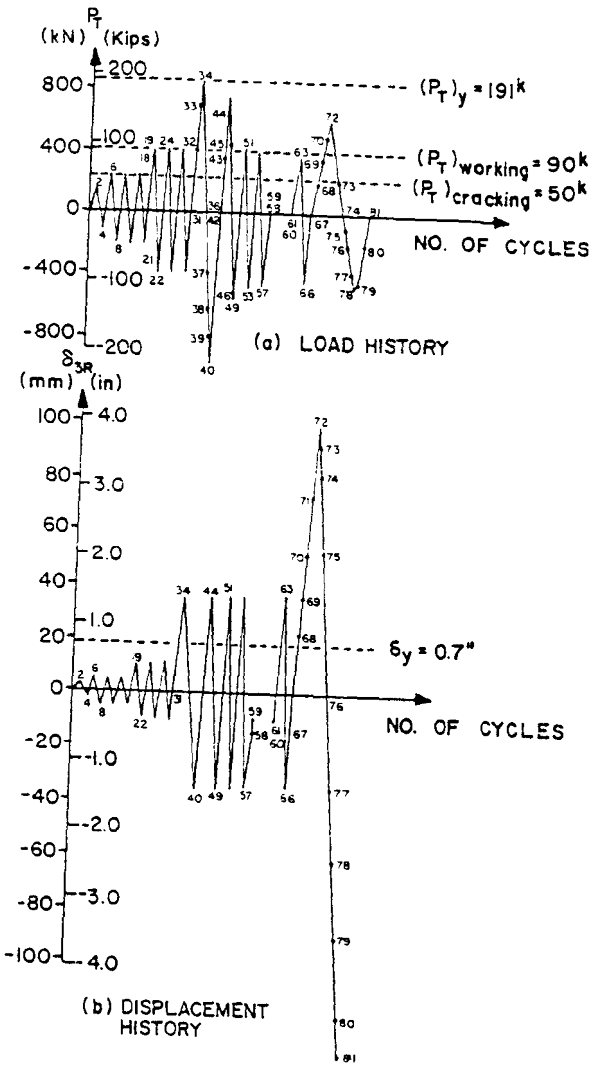

FIG. 5.2 LOADING PROGRAM-SHEAR WALL 1R

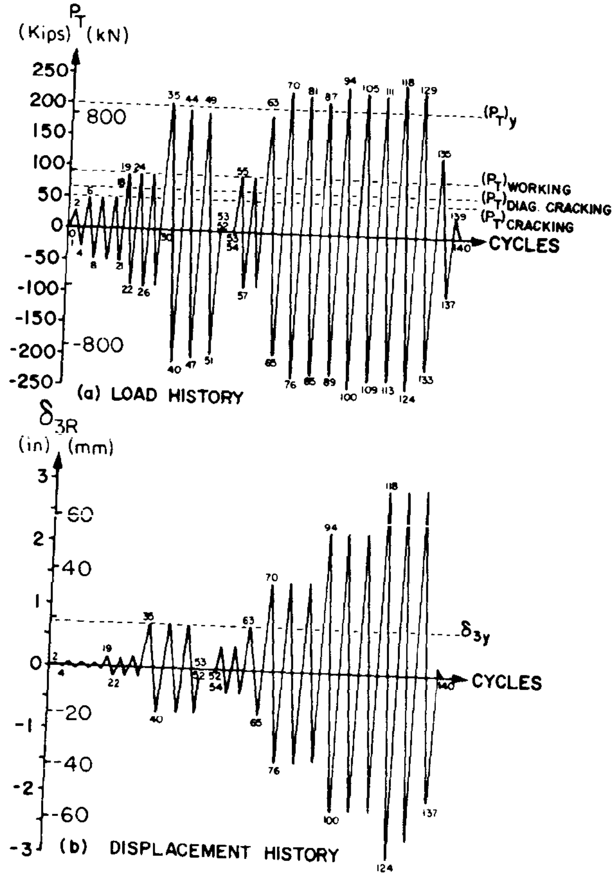

FIG. 5.3 LOADING PROGRAM-SHEAR WALL 2

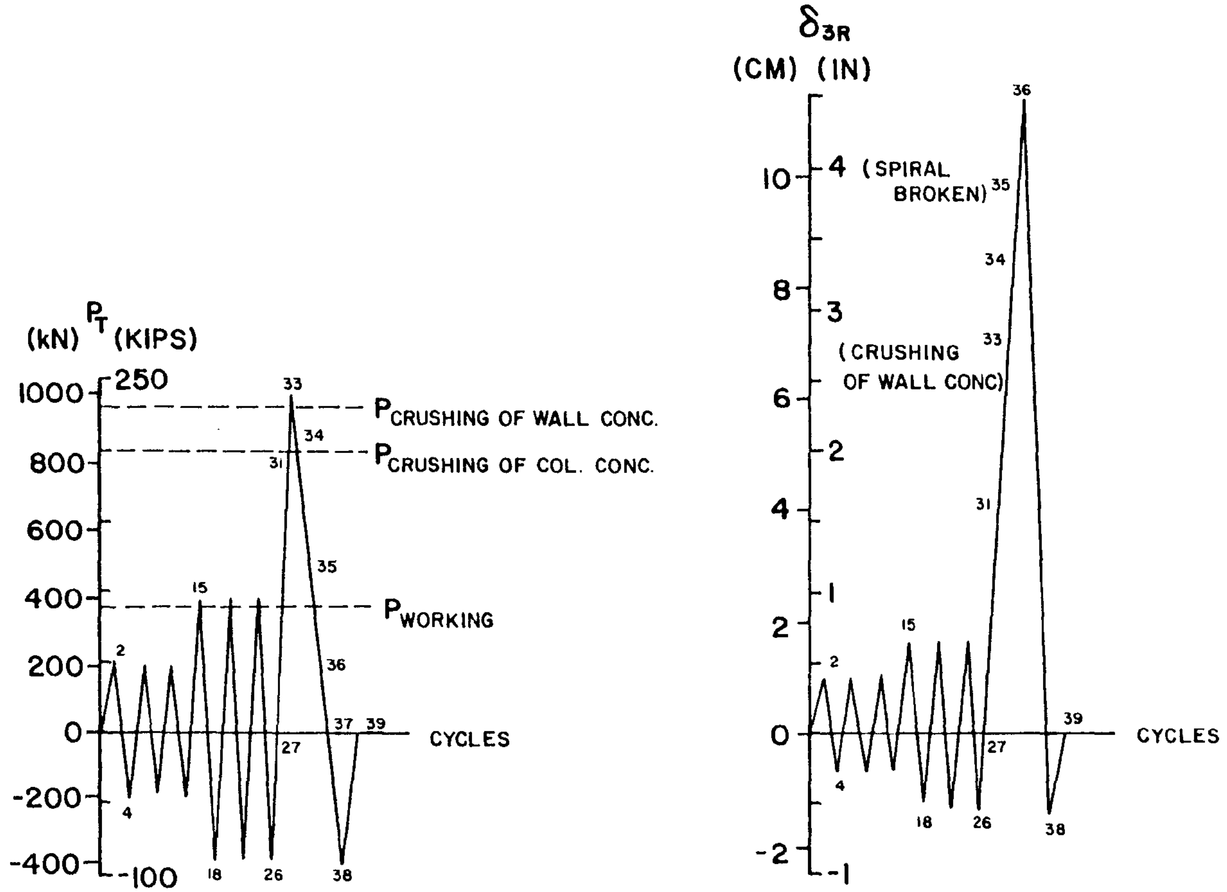

(a) LOAD HISTORY

(b) DISPLACEMENT HISTORY

FIG. 5.4 LOADING PROGRAM-SHEAR WALL 2R

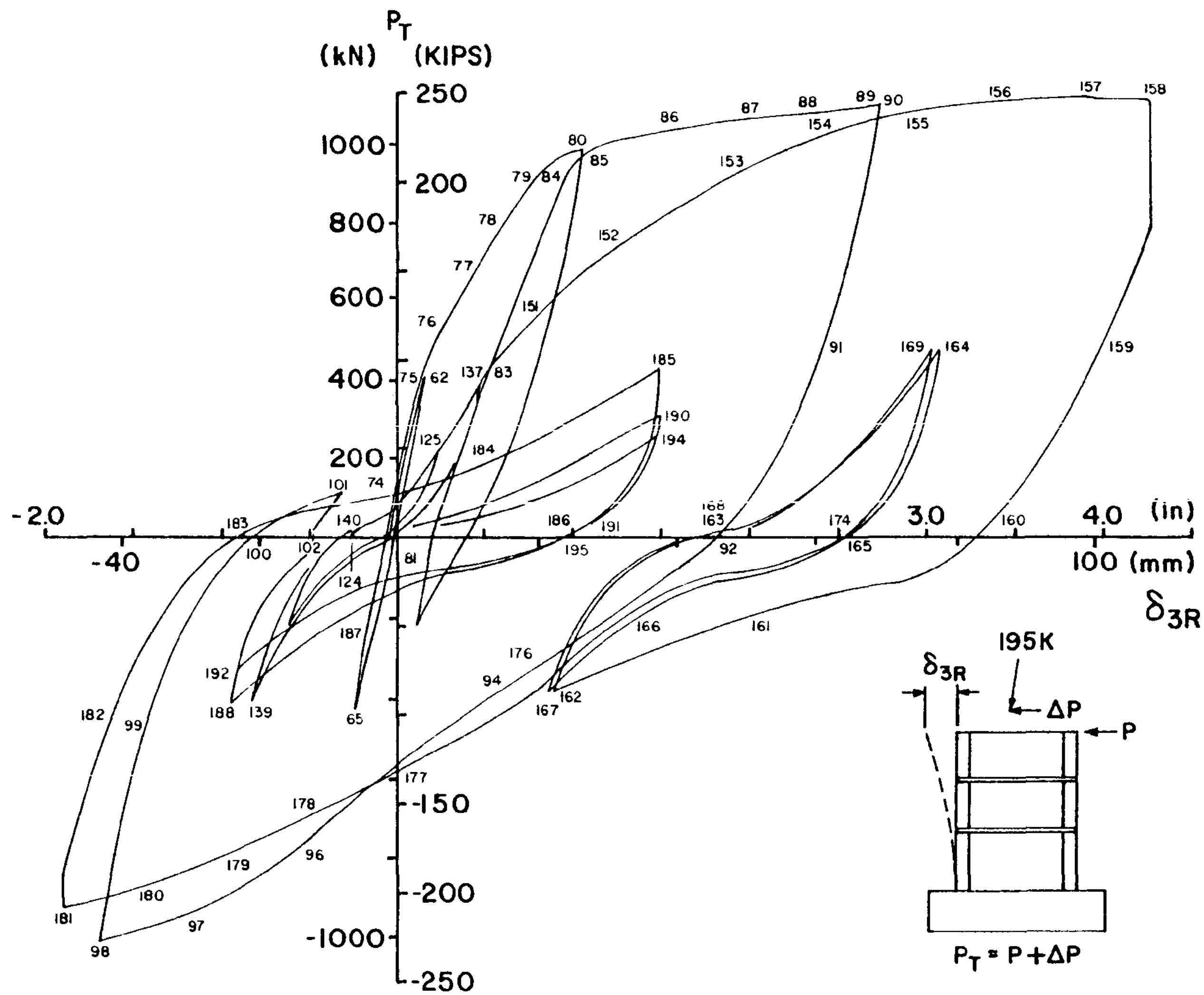

FIG. 5.5 P_T-δ_{3R} DIAGRAM-SHEAR WALL 1

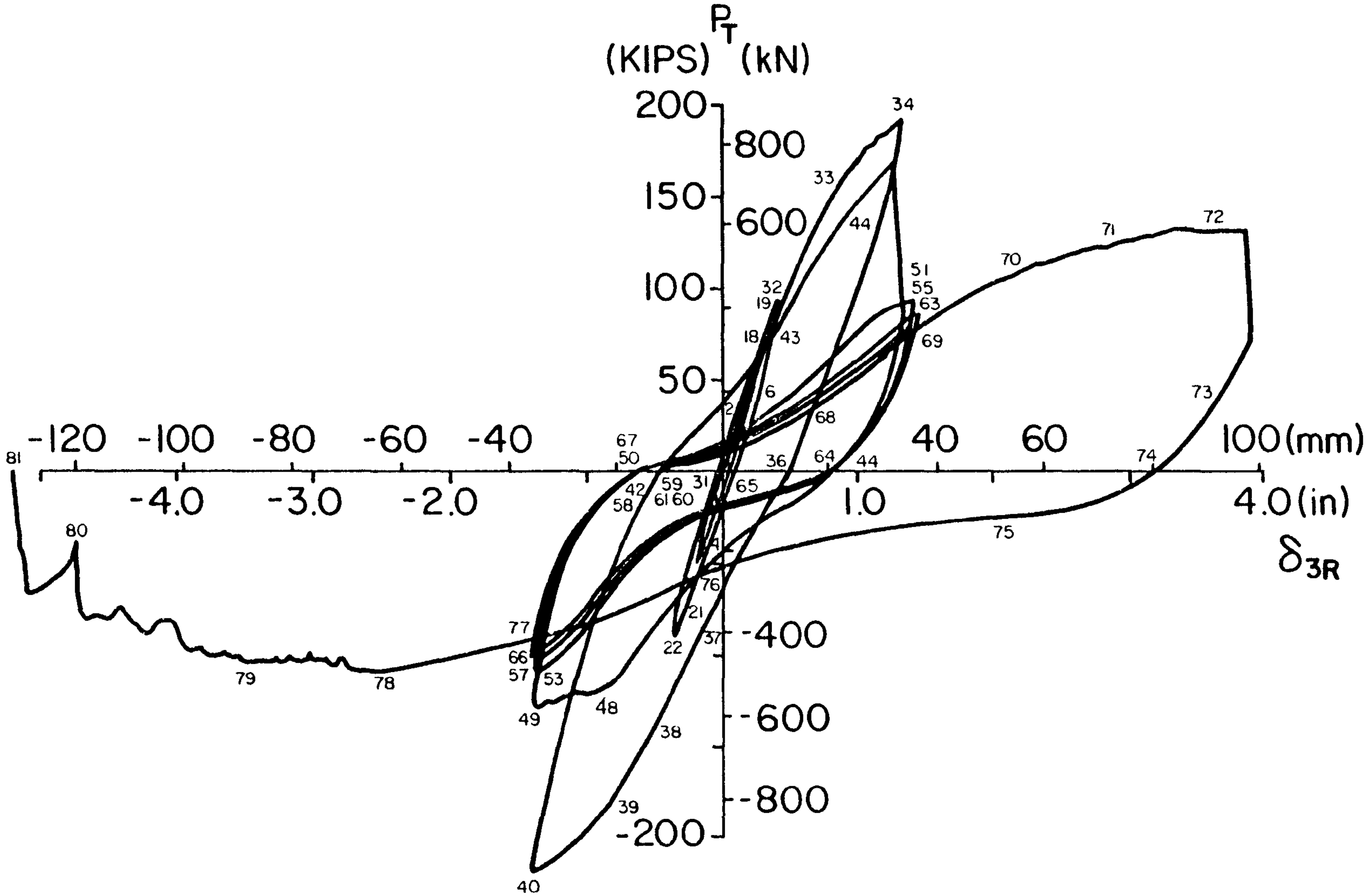

FIG. 5.6 P_T-δ_{3R} DIAGRAM-SHEAR WALL 1R

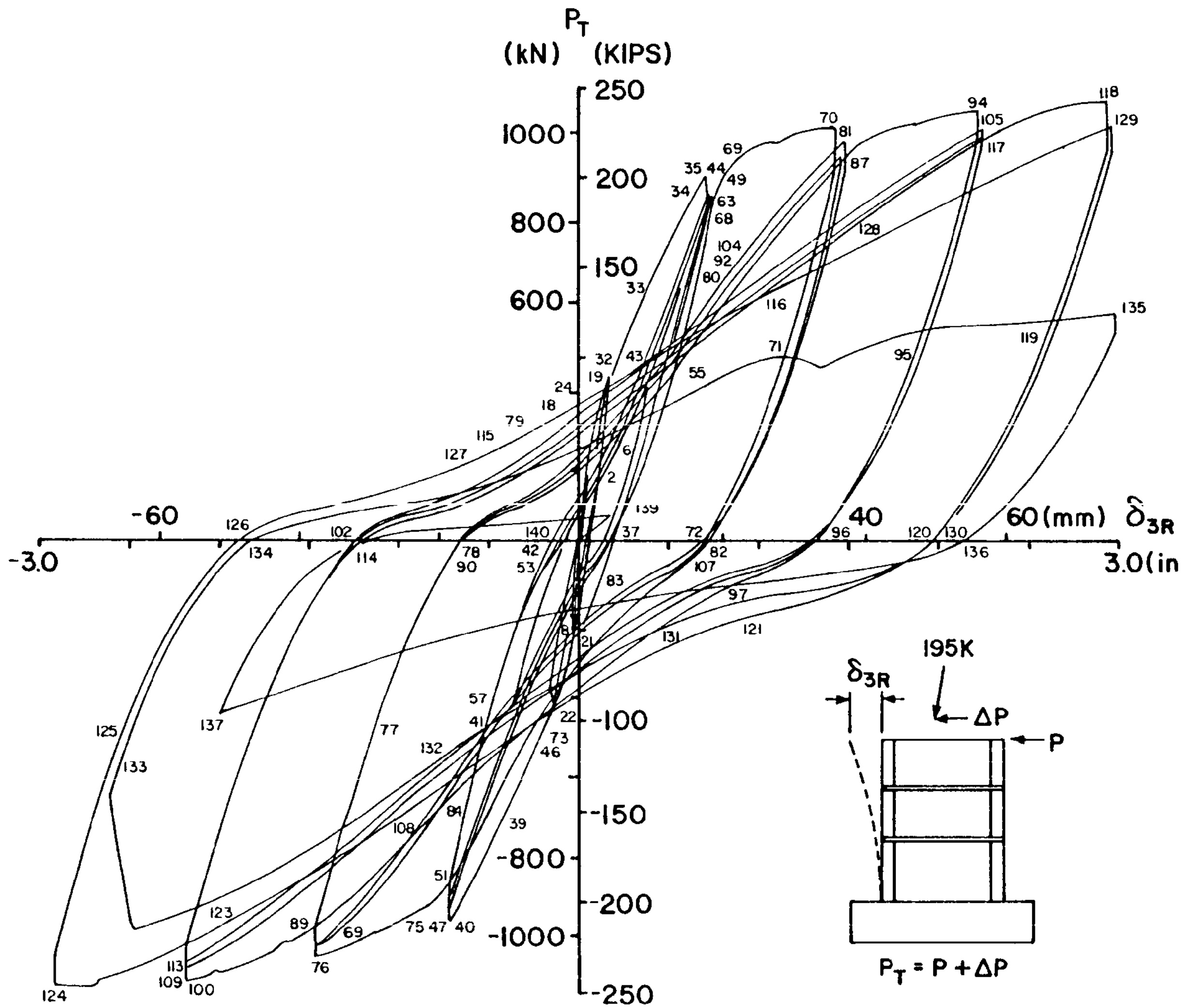

FIG. 5.7 P_T-δ_{3R} DIAGRAM-SHEAR WALL 2

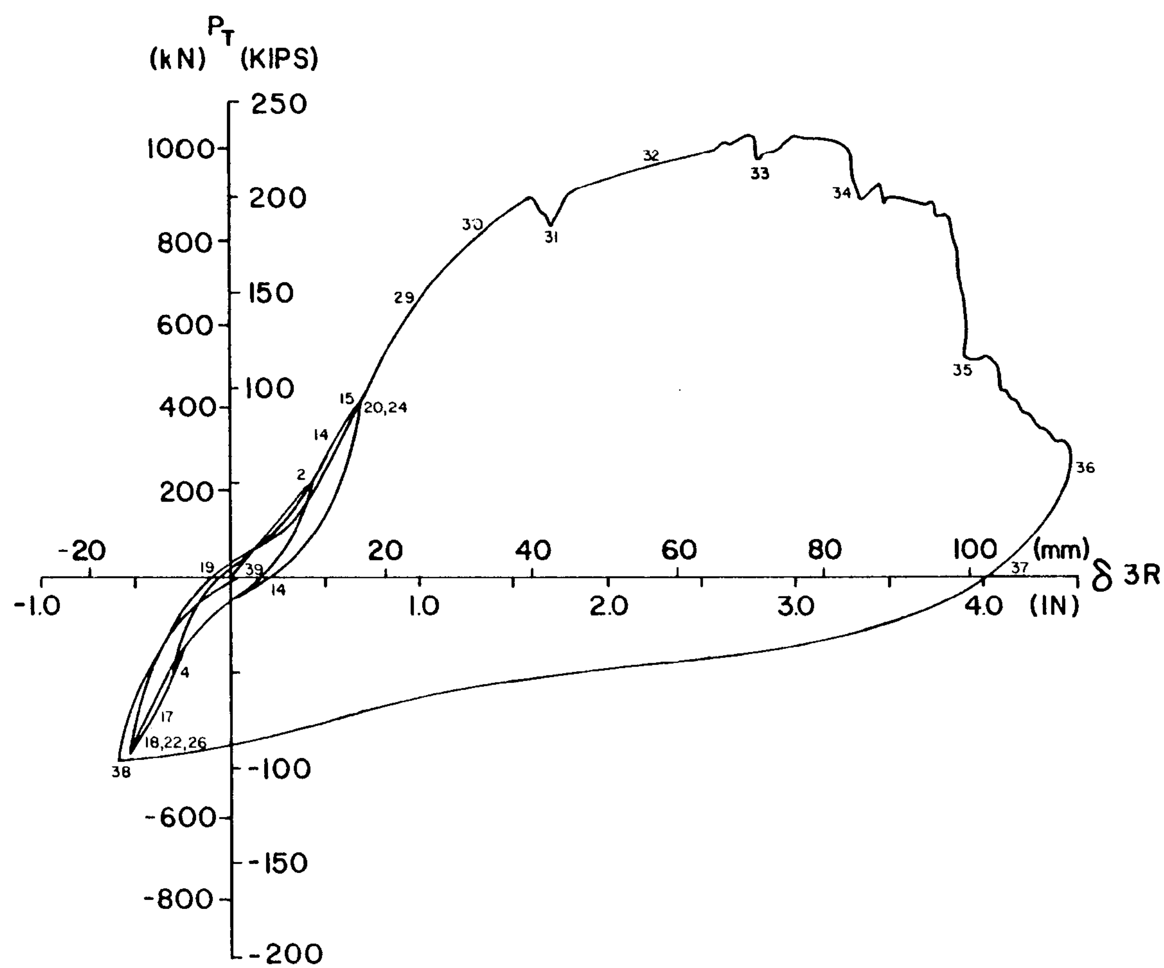

FIG. 5.8 P_T-δ_{3R} DIAGRAM-SHEAR WALL 2R

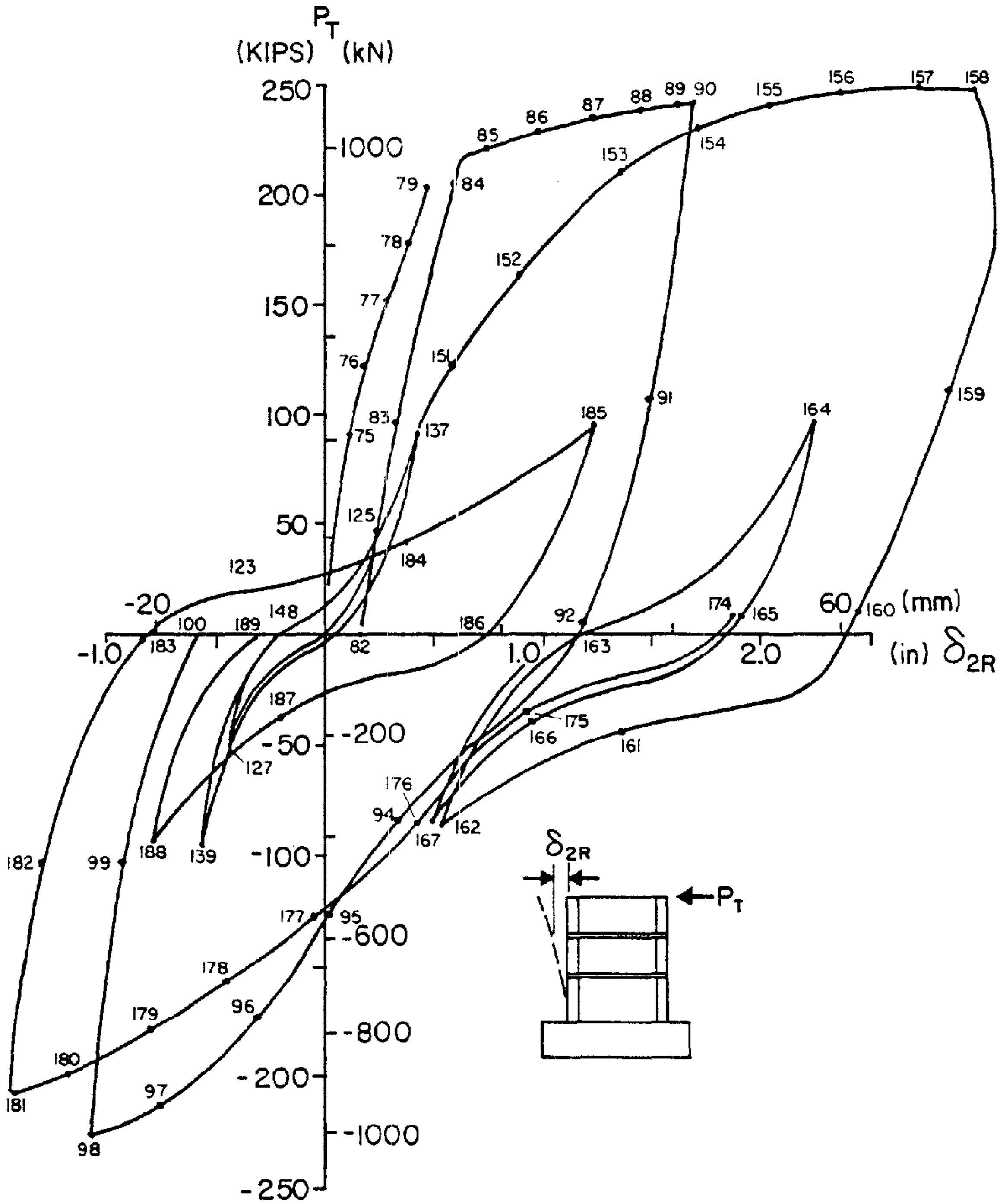

FIG. 5.9 TOTAL LATERAL LOAD VS. SECOND FLOOR RELATIVE DISPLACEMENT DIAGRAM - SHEAR WALL 1

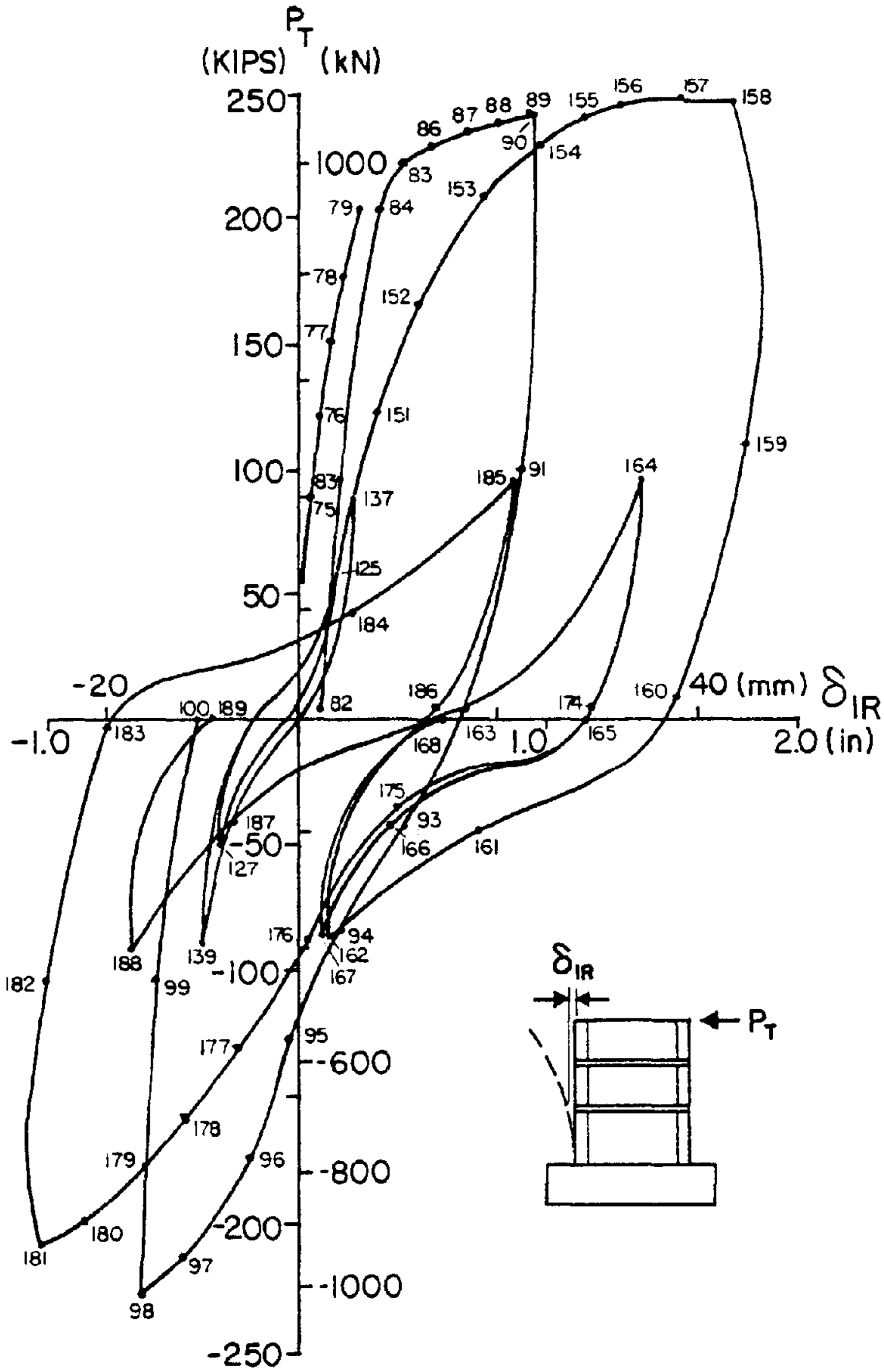

FIG. 5.10   TOTAL LATERAL LOAD VS. FIRST FLOOR RELATIVE DISPLACEMENT DIAGRAM - SHEAR WALL 1

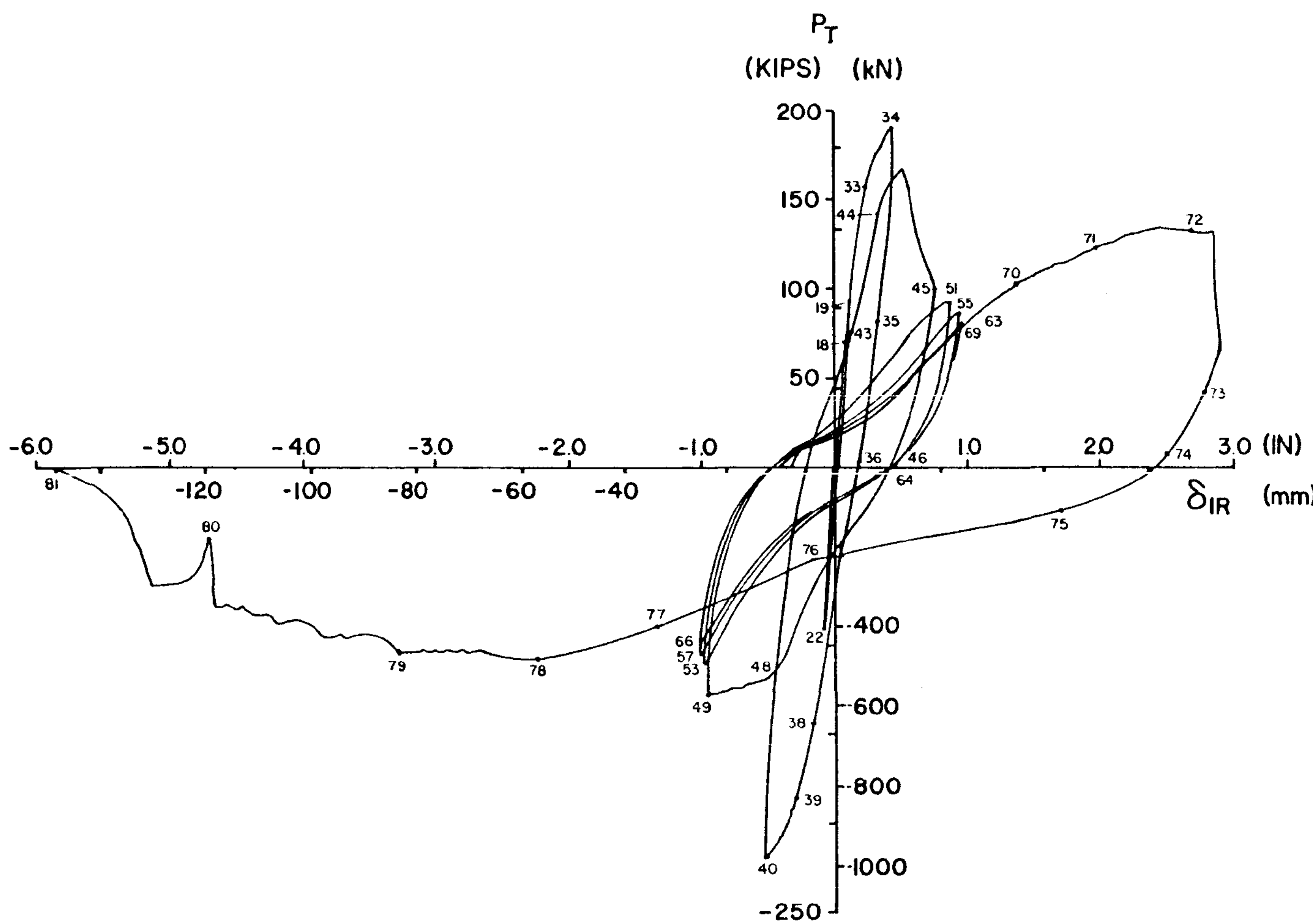

FIG. 5.11 P_T-δ_{1R} DIAGRAM - SHEAR WALL 1R

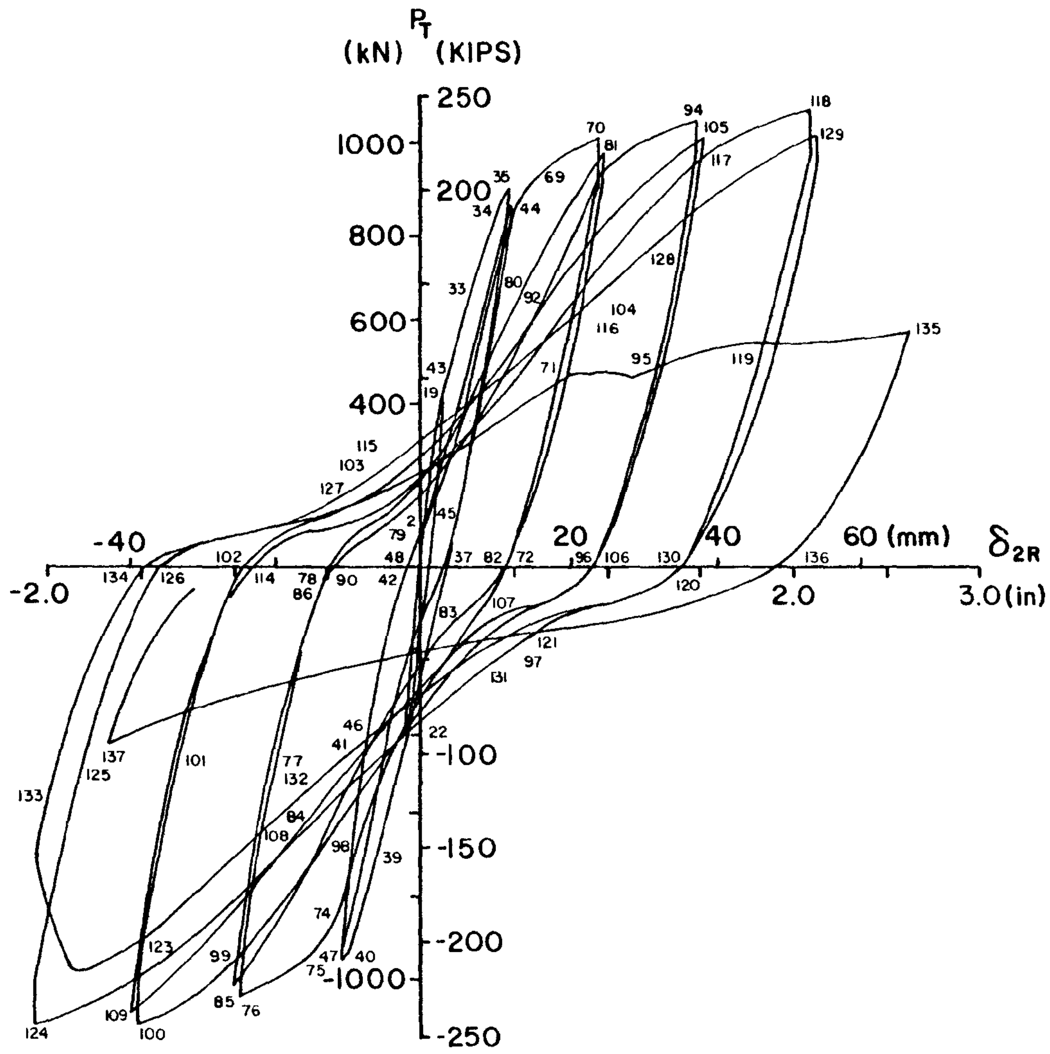

FIG. 5.12 P_T-δ_{2R} DIAGRAM-SHEAR WALL 2

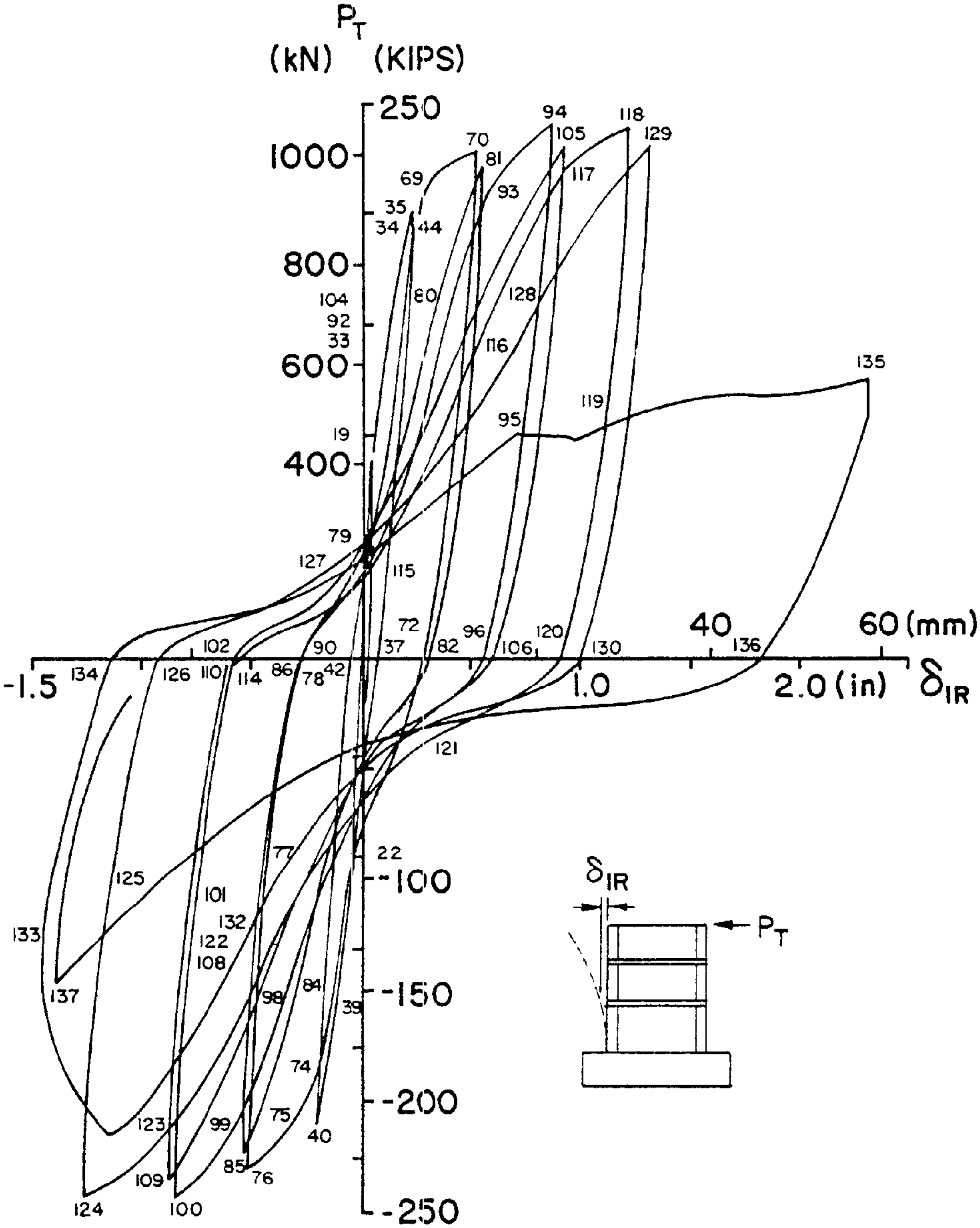

FIG. 5.13 P_T-δ_{IR} DIAGRAM-SHEAR WALL 2

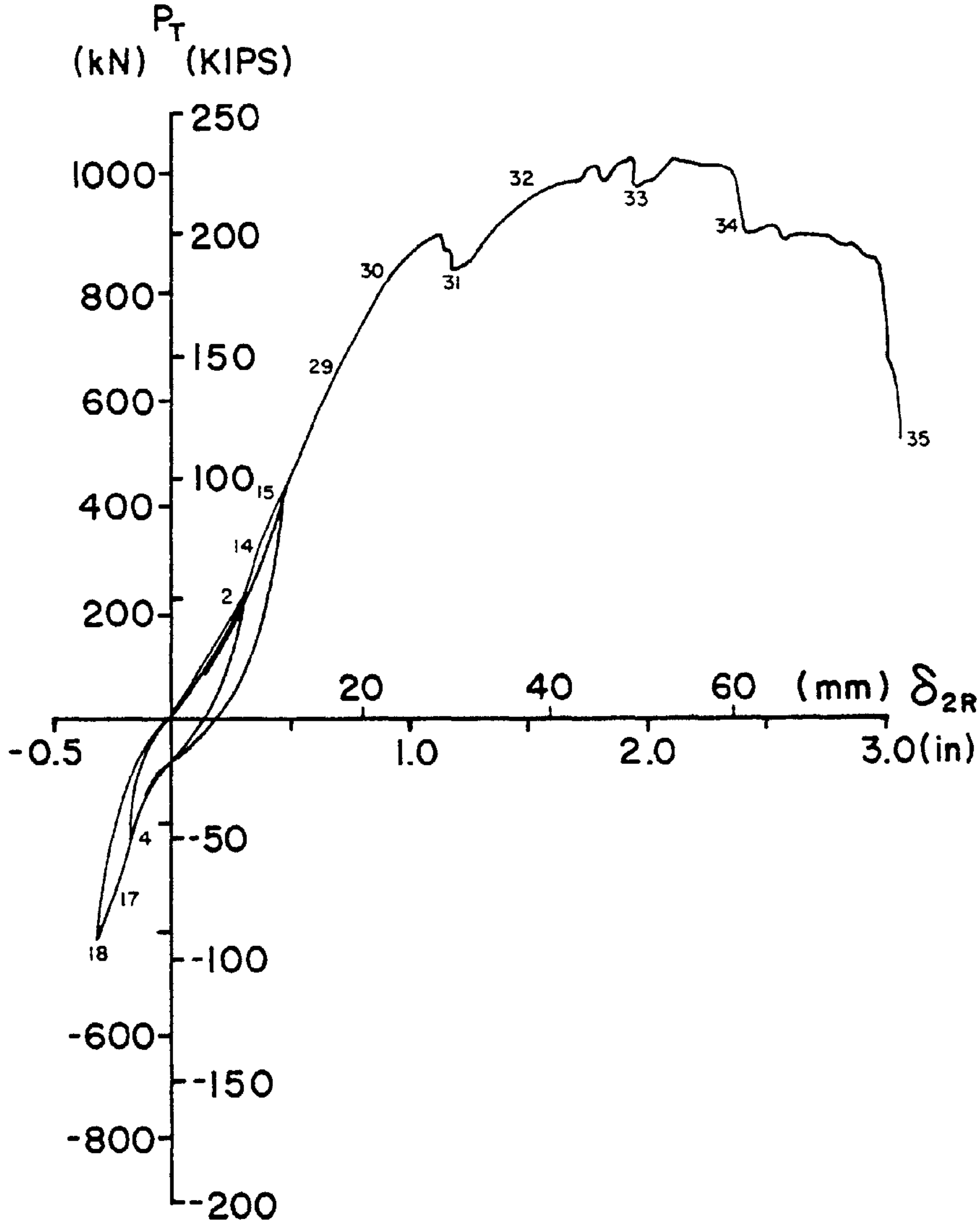

FIG. 5.14 P_T-δ_{2R} DIAGRAM-SHEAR WALL 2R

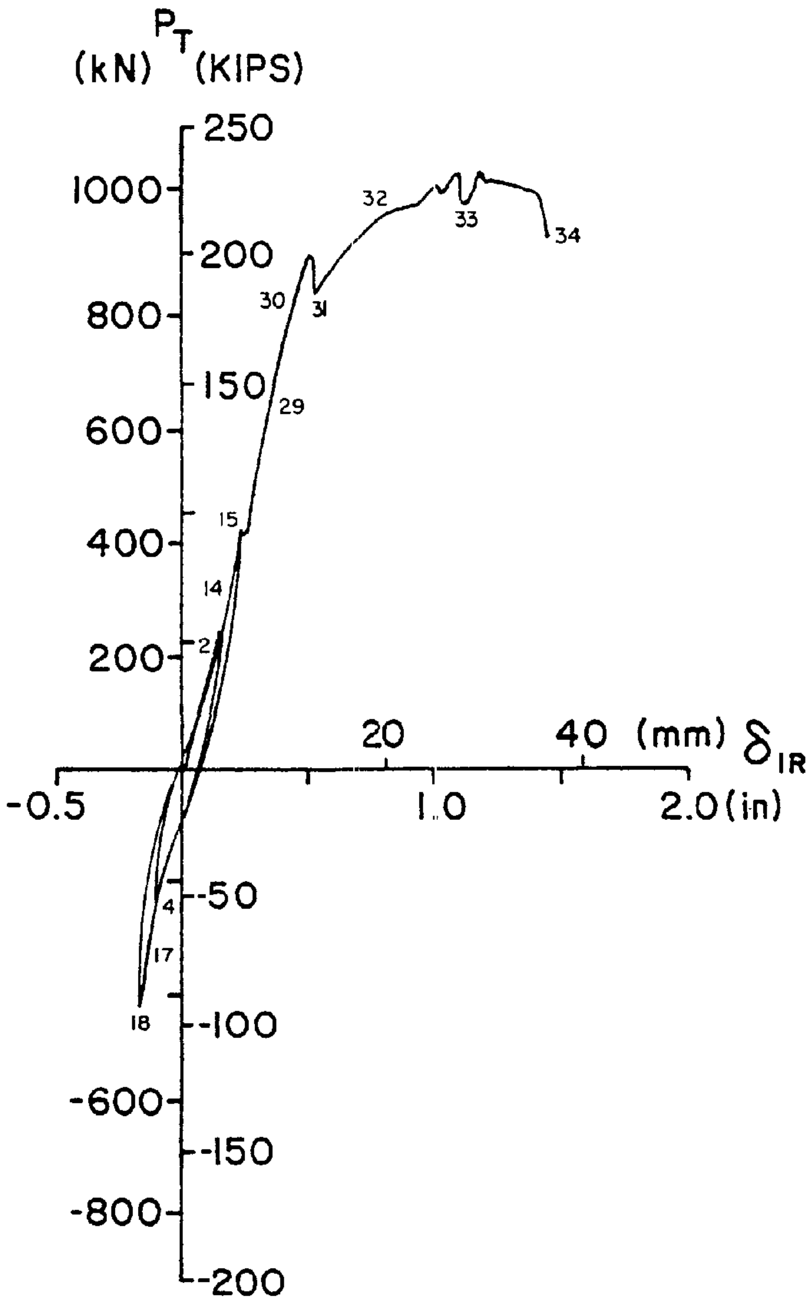

FIG. 5.15 P_T-δ_{IR} DIAGRAM-SHEAR WALL 2R

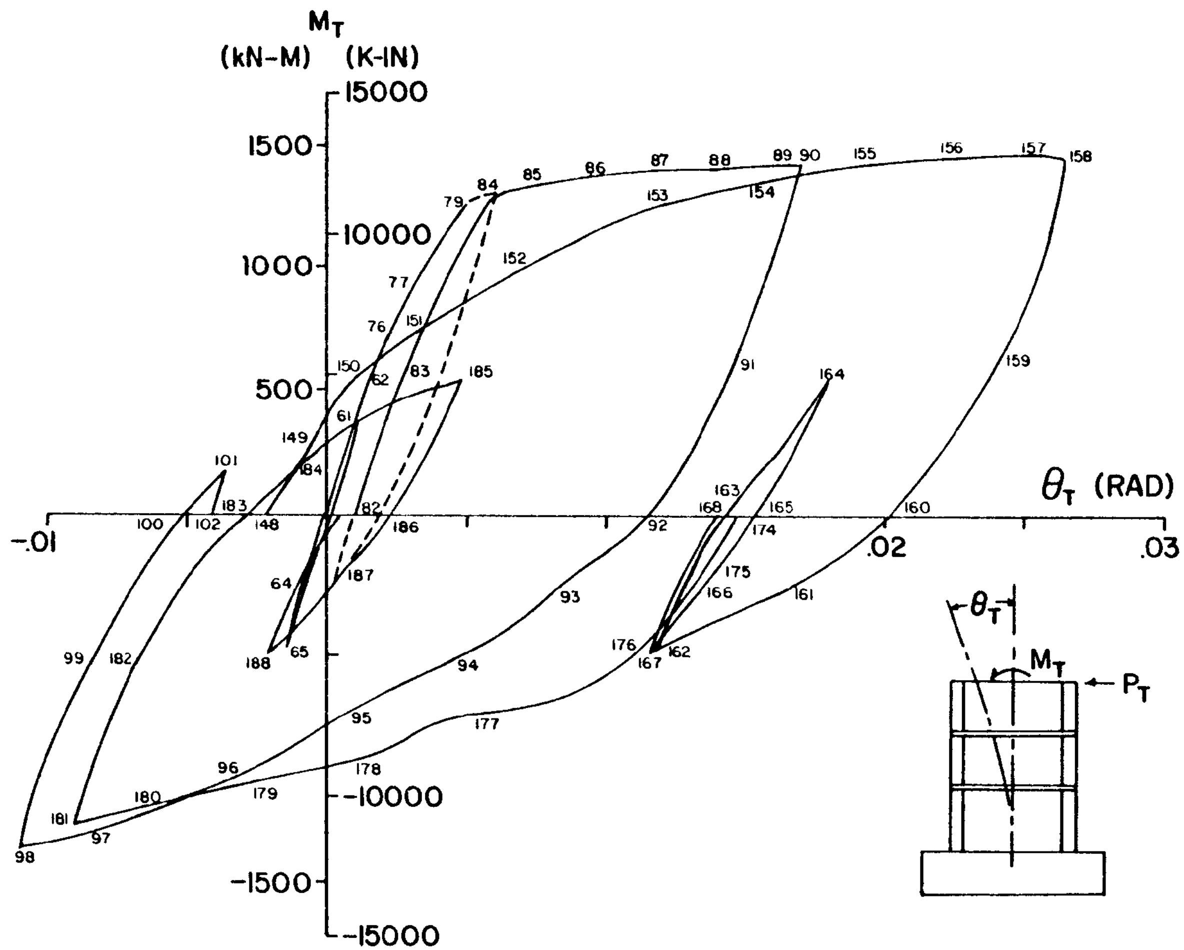

FIG. 5.16 M_T-θ_T DIAGRAM-SHEAR WALL 1

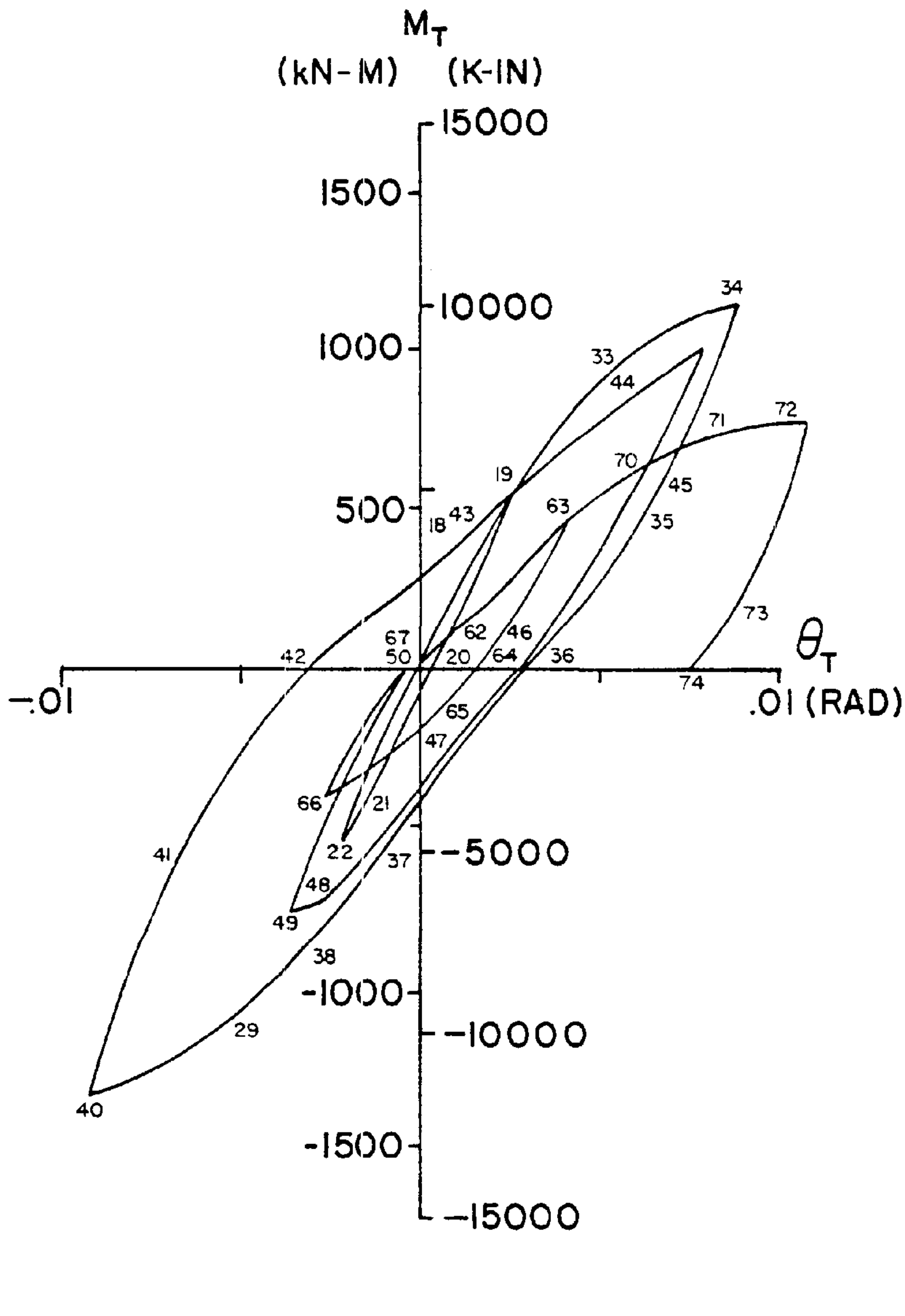

FIG. 5.17 M_T-θ_T DIAGRAM - SHEAR WALL 1R

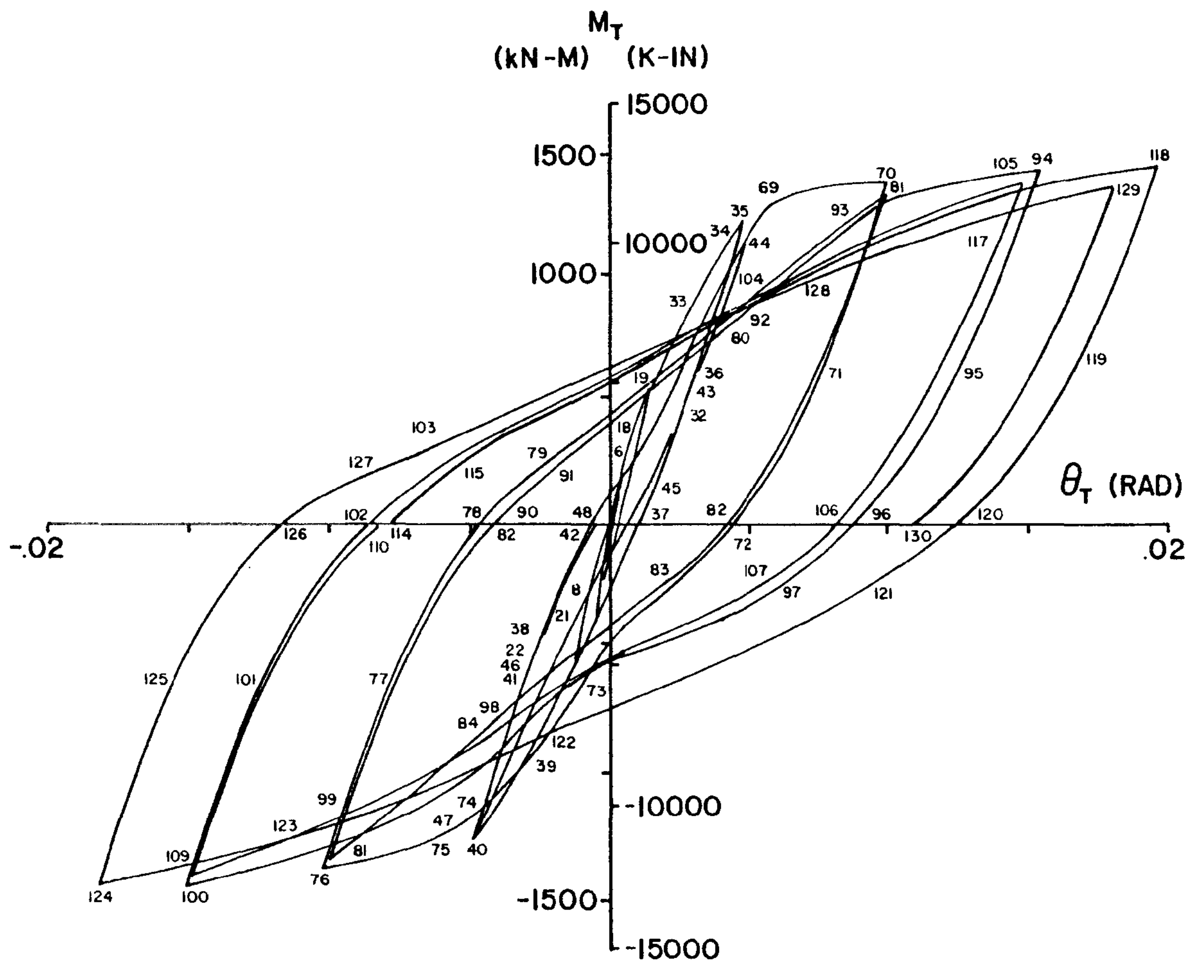

FIG. 5.18 M_T-θ_T DIAGRAM-SHEAR WALL 2

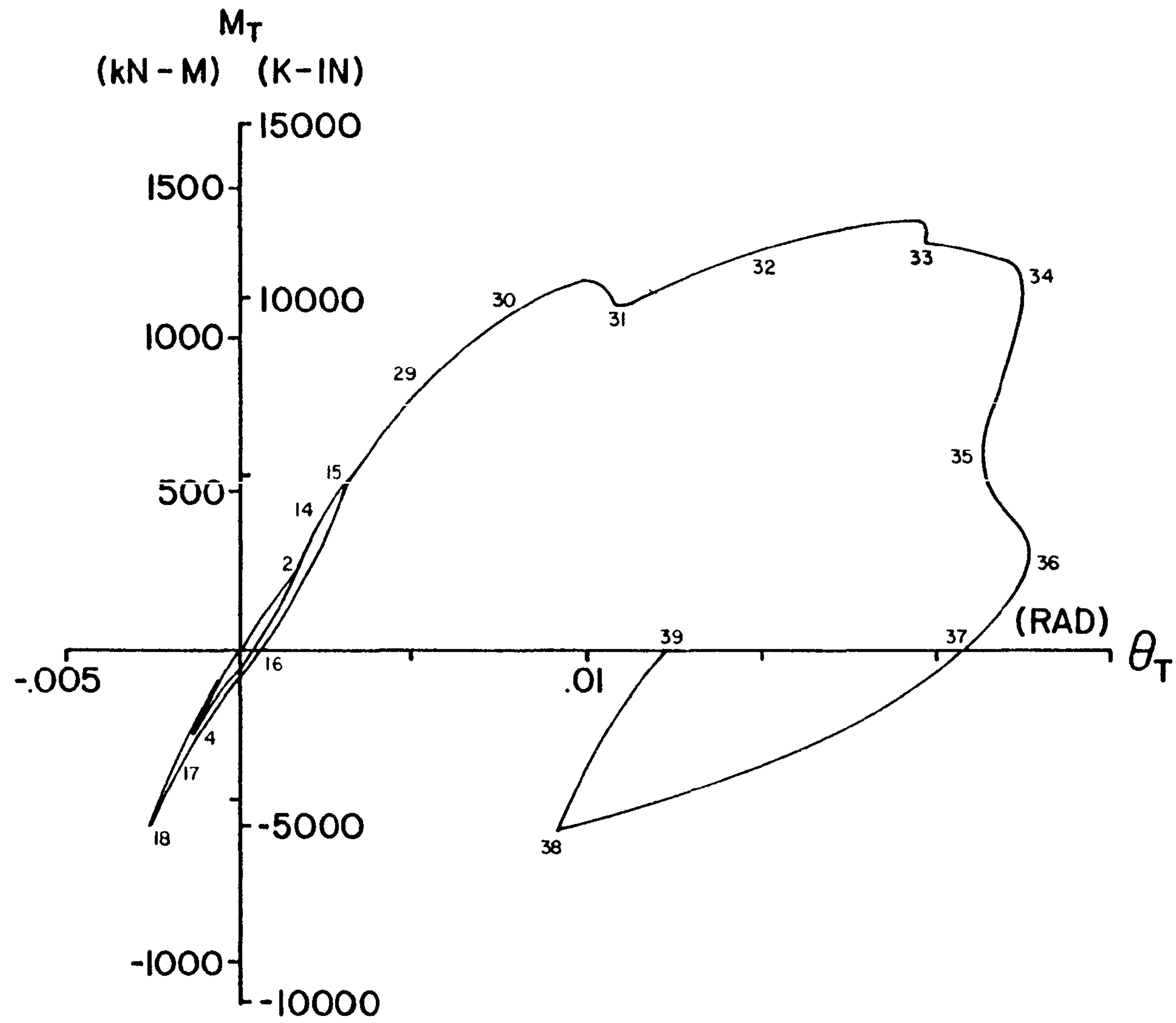

FIG. 5.19 M_T-θ_T DIAGRAM-SHEAR WALL 2R

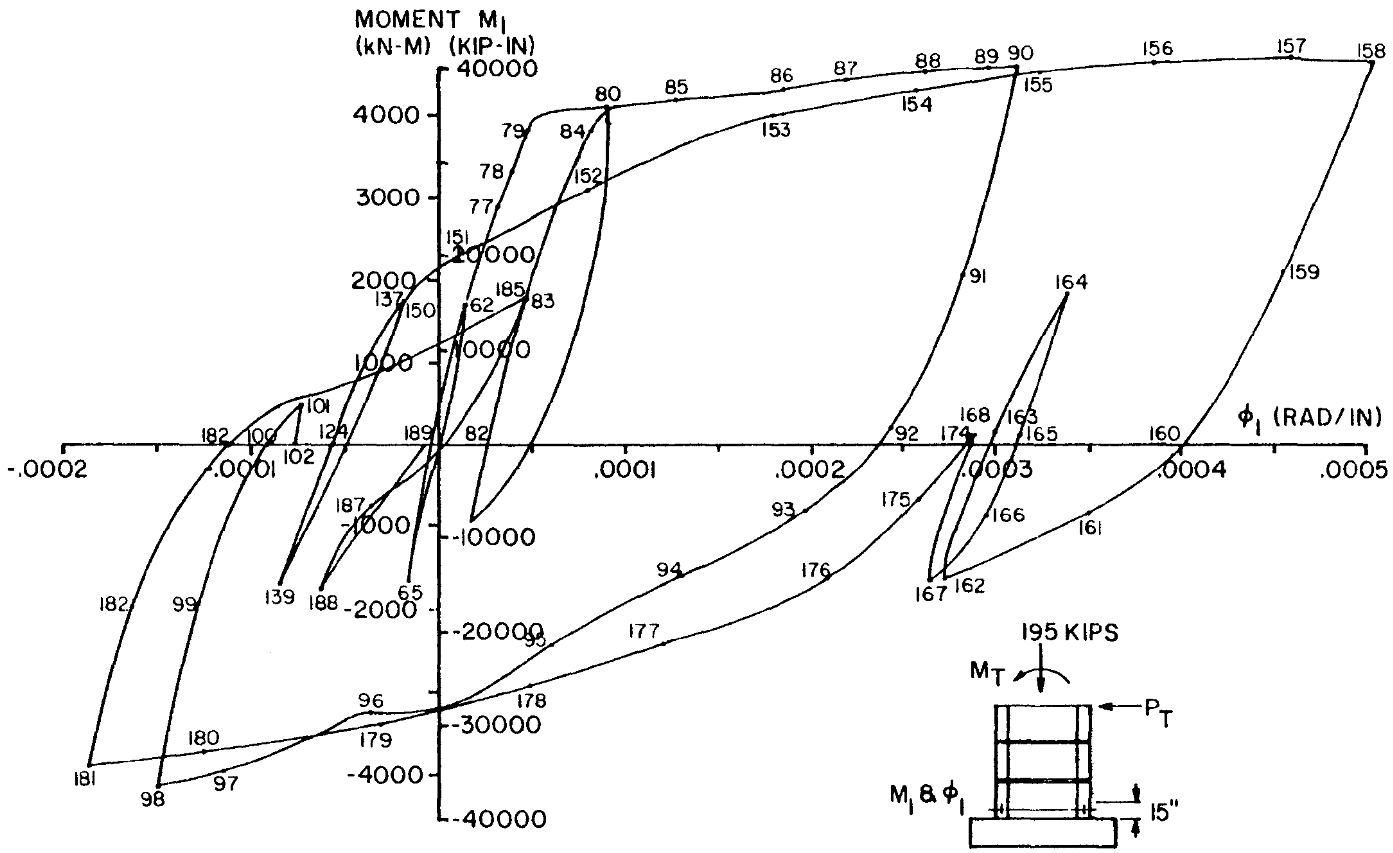

FIG. 5.20 M_1-ϕ_1 DIAGRAM-SHEAR WALL 1

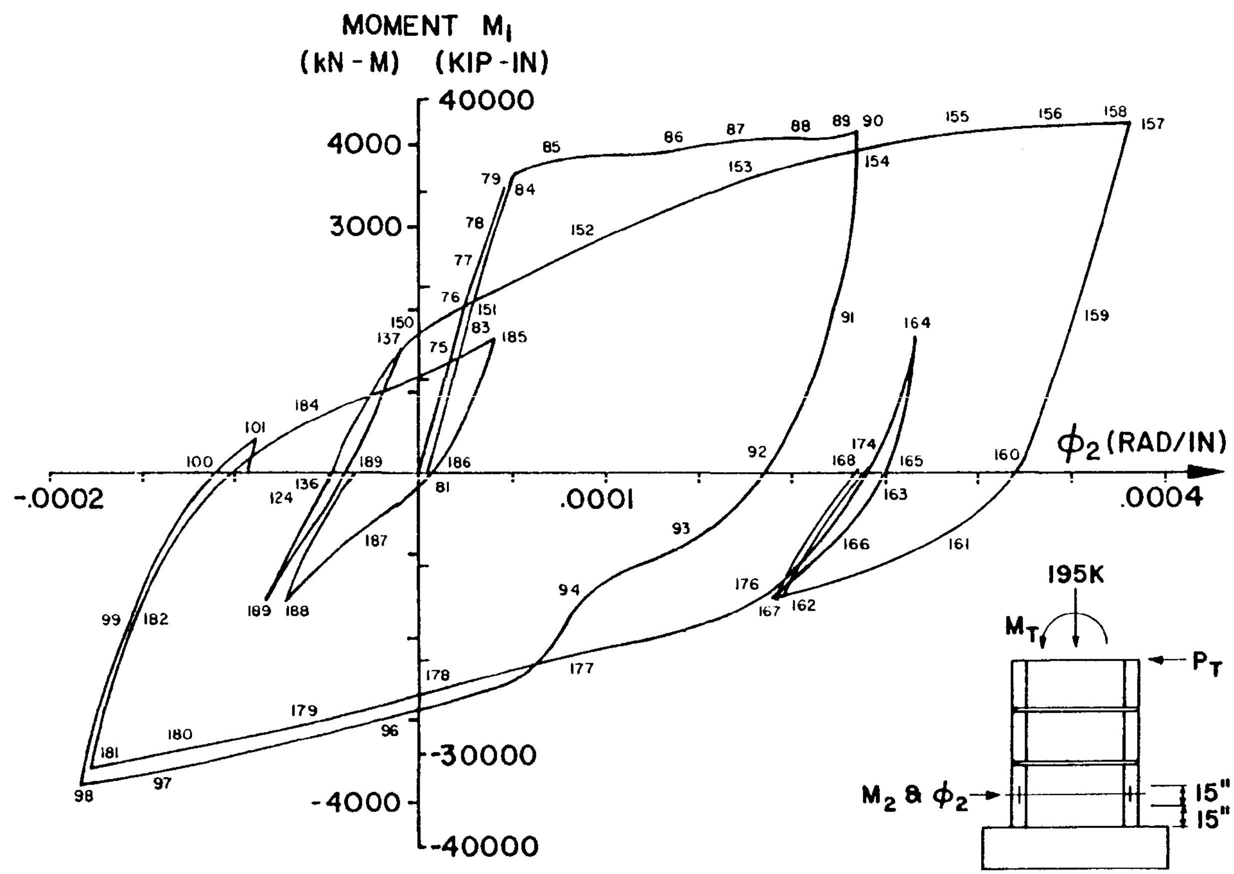

FIG. 5.21 M_2-ϕ_2 DIAGRAM-SHEAR WALL 1

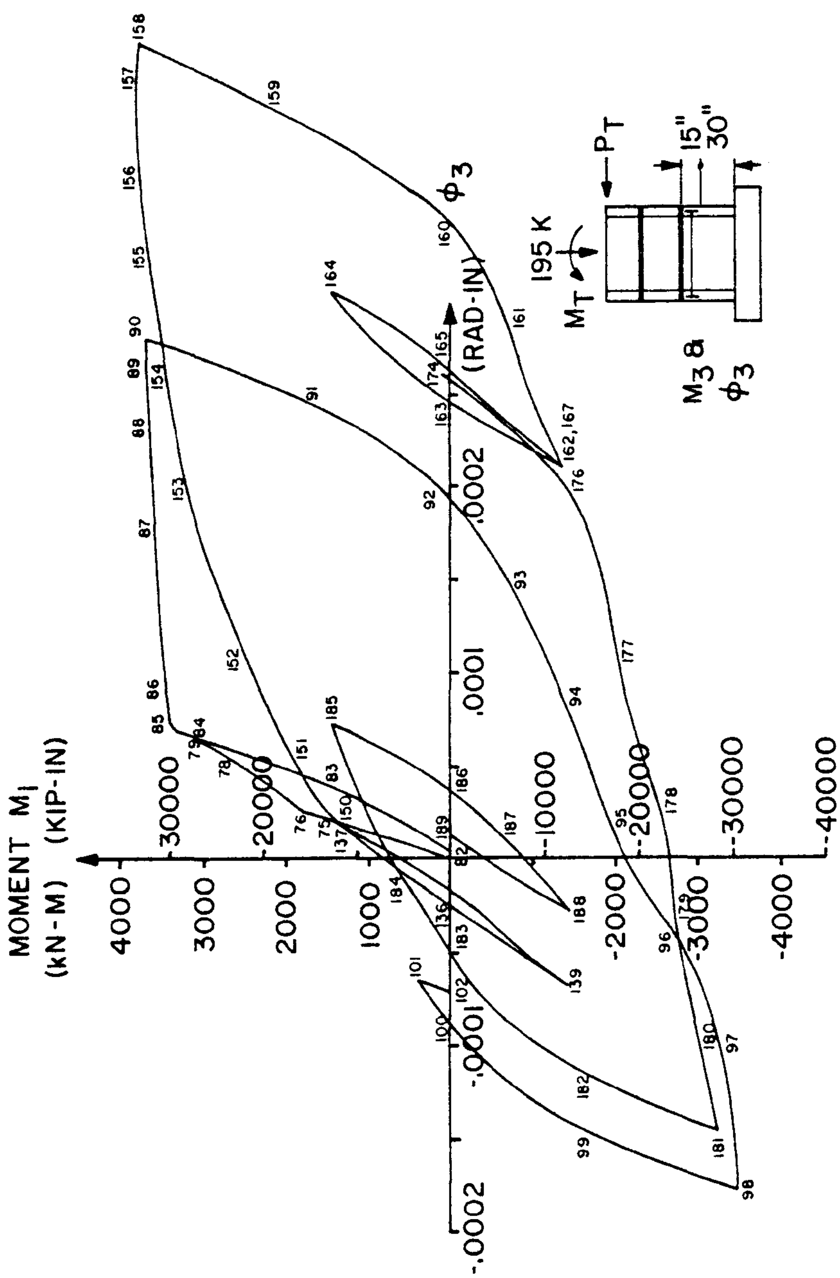

FIG. 5.22 M_3-ϕ_3 DIAGRAM-SHEAR WALL 1

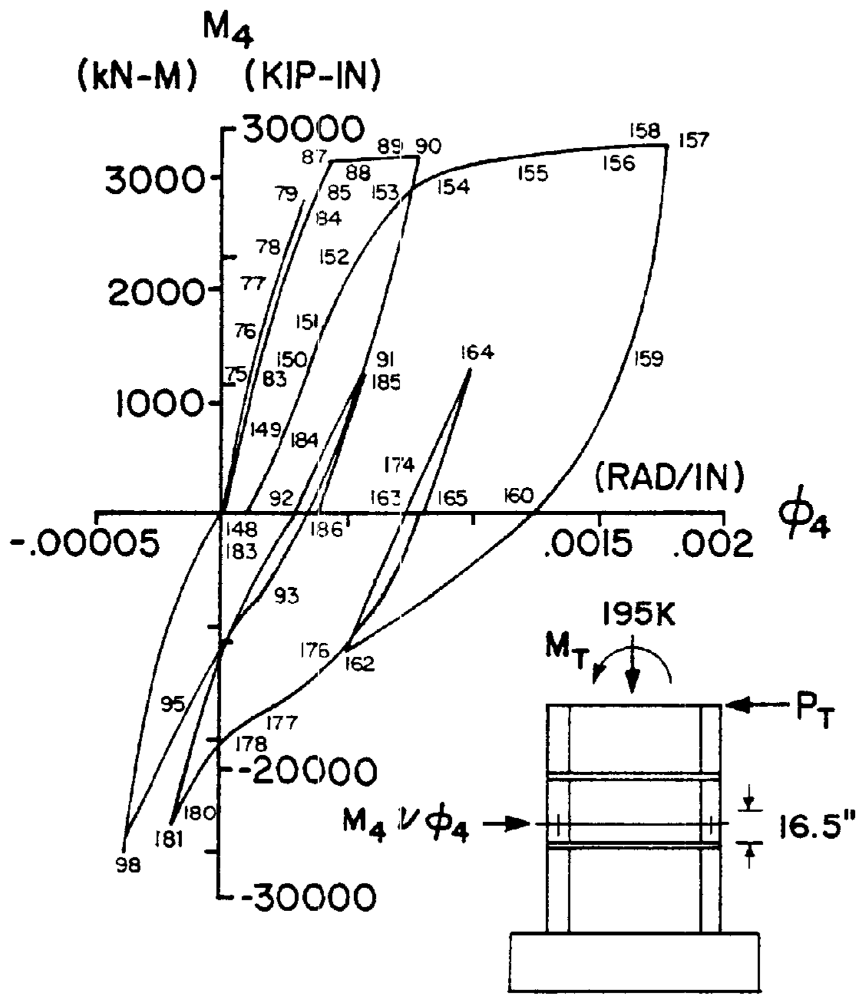

FIG. 5.23 M_4-Φ_4 DIAGRAM - SHEAR WALL 1

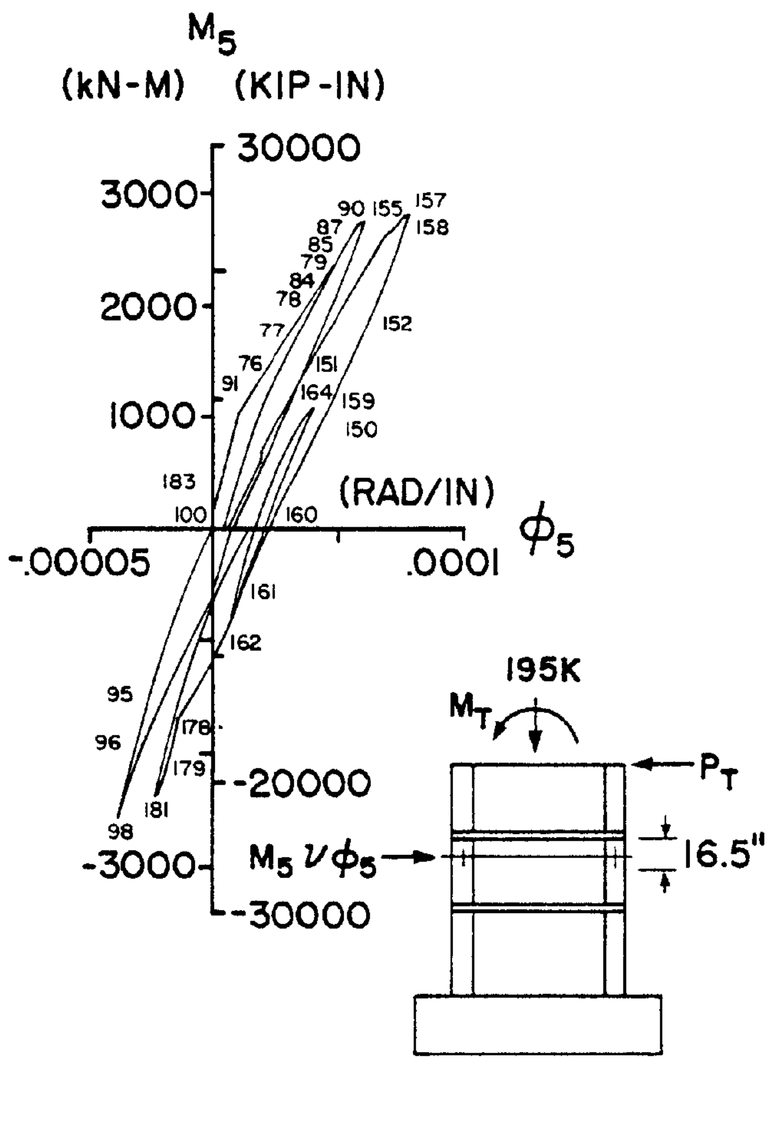

FIG. 5.24 M_5-ϕ_5 DIAGRAM - SHEAR WALL 1

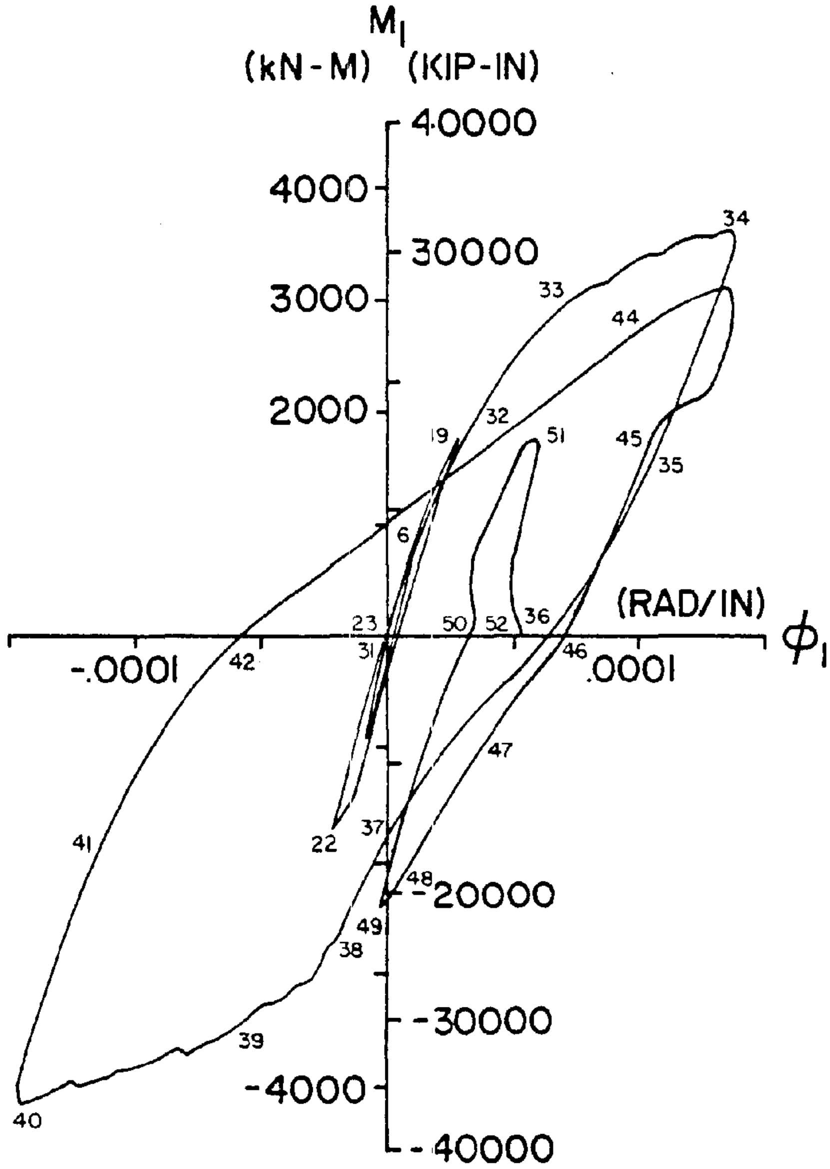

FIG. 5.25 M_1-ϕ_1 DIAGRAM - SHEAR WALL 1R

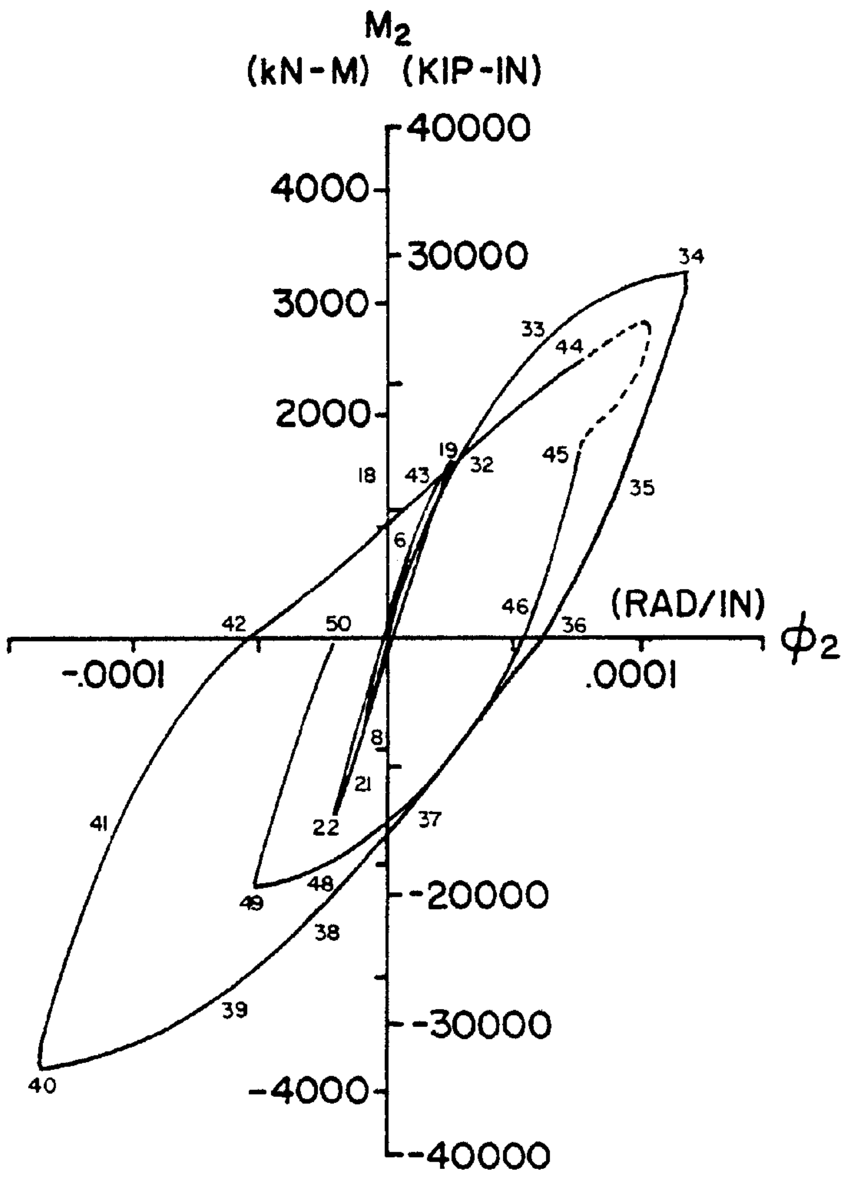

FIG. 5.26 M_2-ϕ_2 DIAGRAM - SHEAR WALL 1R

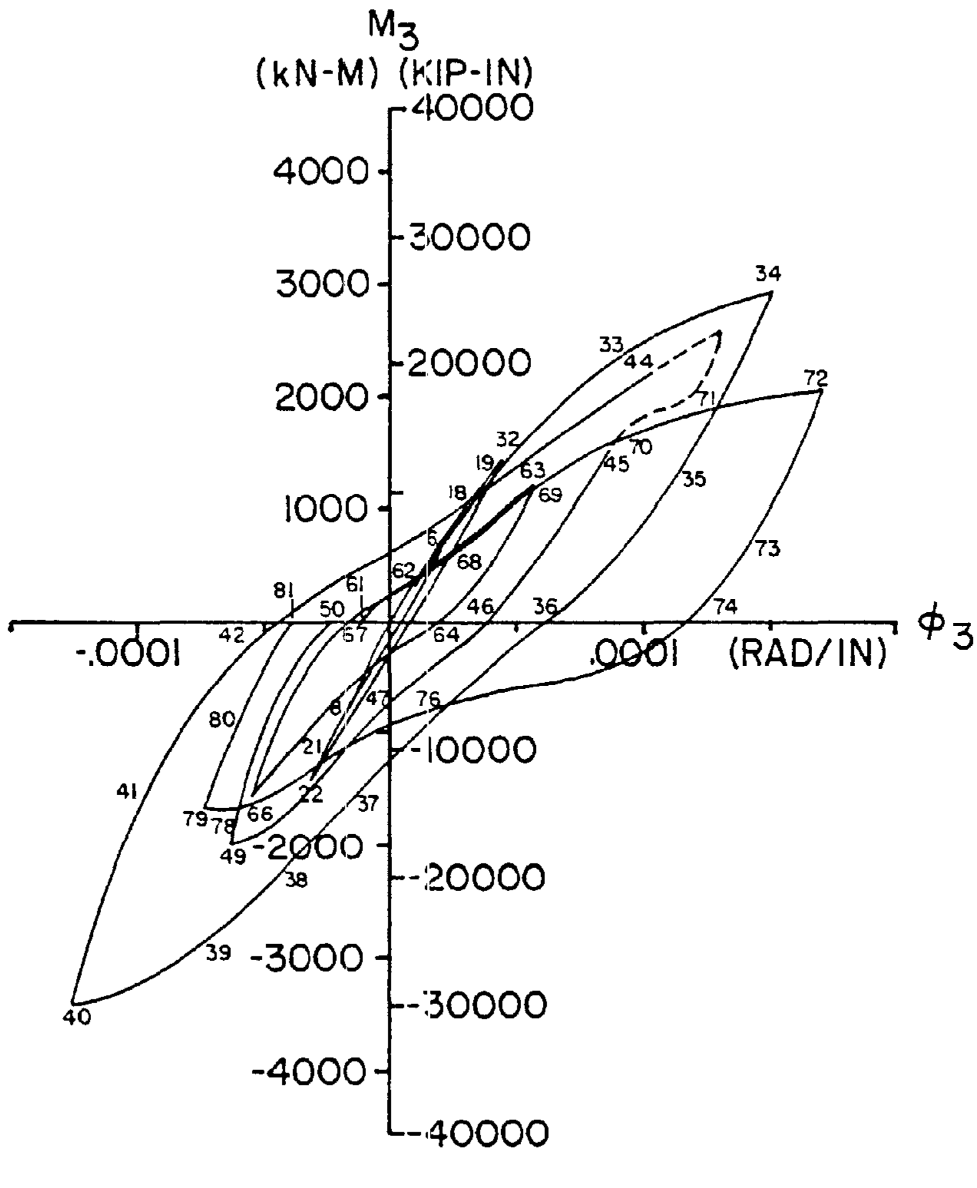

FIG. 5.27 M_3-ϕ_3 DIAGRAM-SHEAR WALL 1R

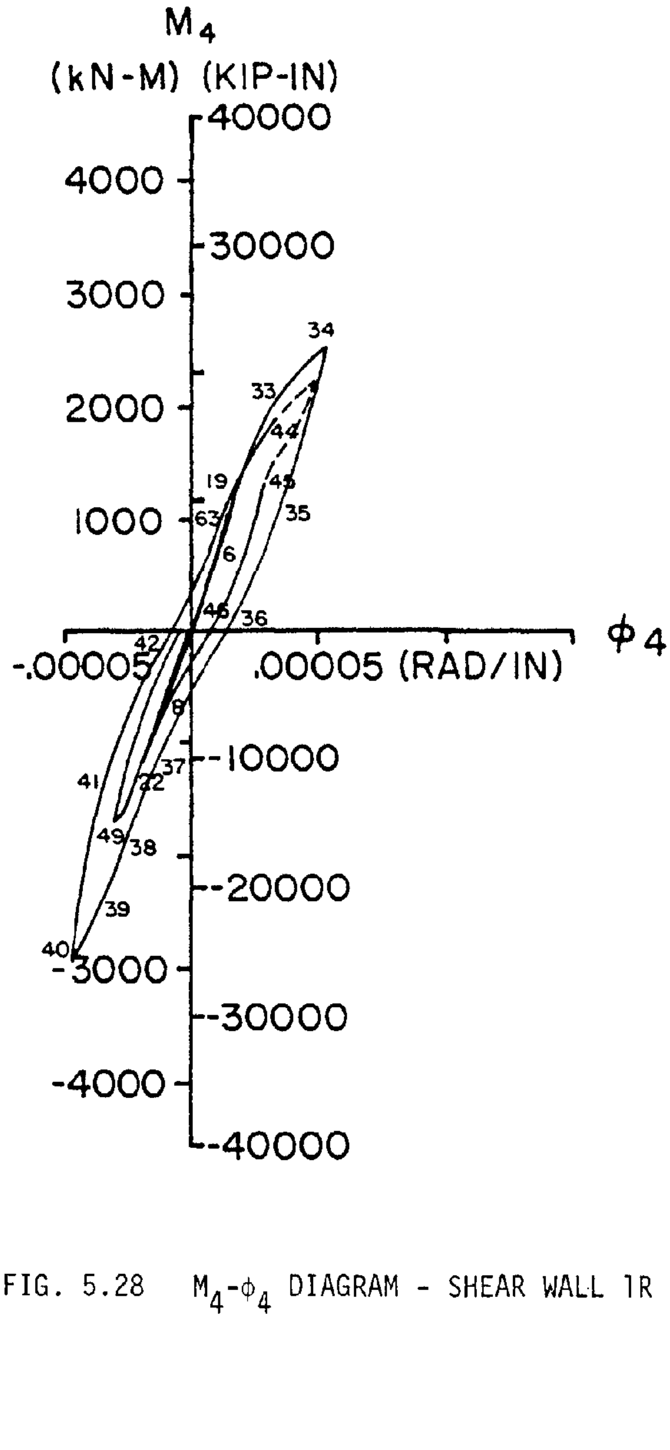

FIG. 5.28 M_4-ϕ_4 DIAGRAM - SHEAR WALL 1R

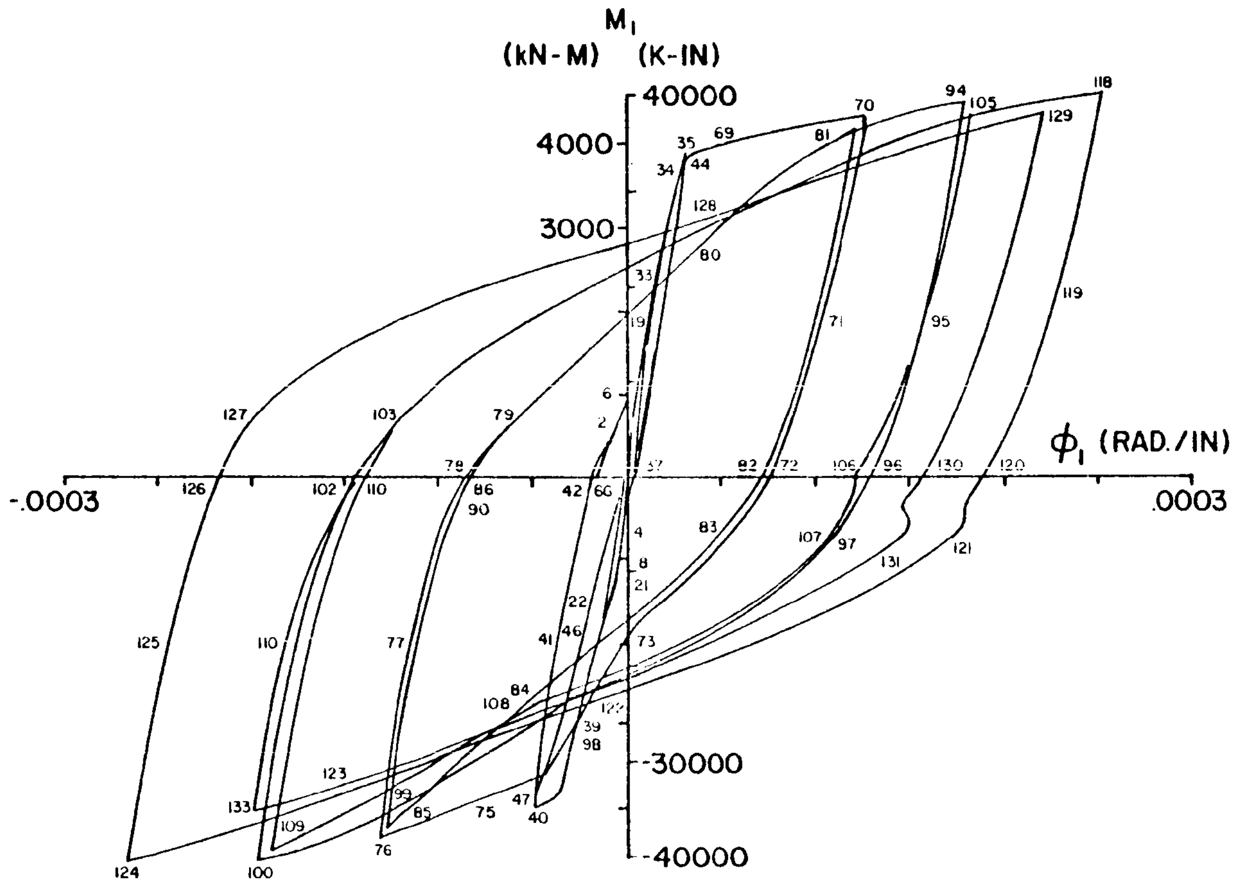

FIG. 5.29 M_1-ϕ_1 DIAGRAM-SHEAR WALL 2

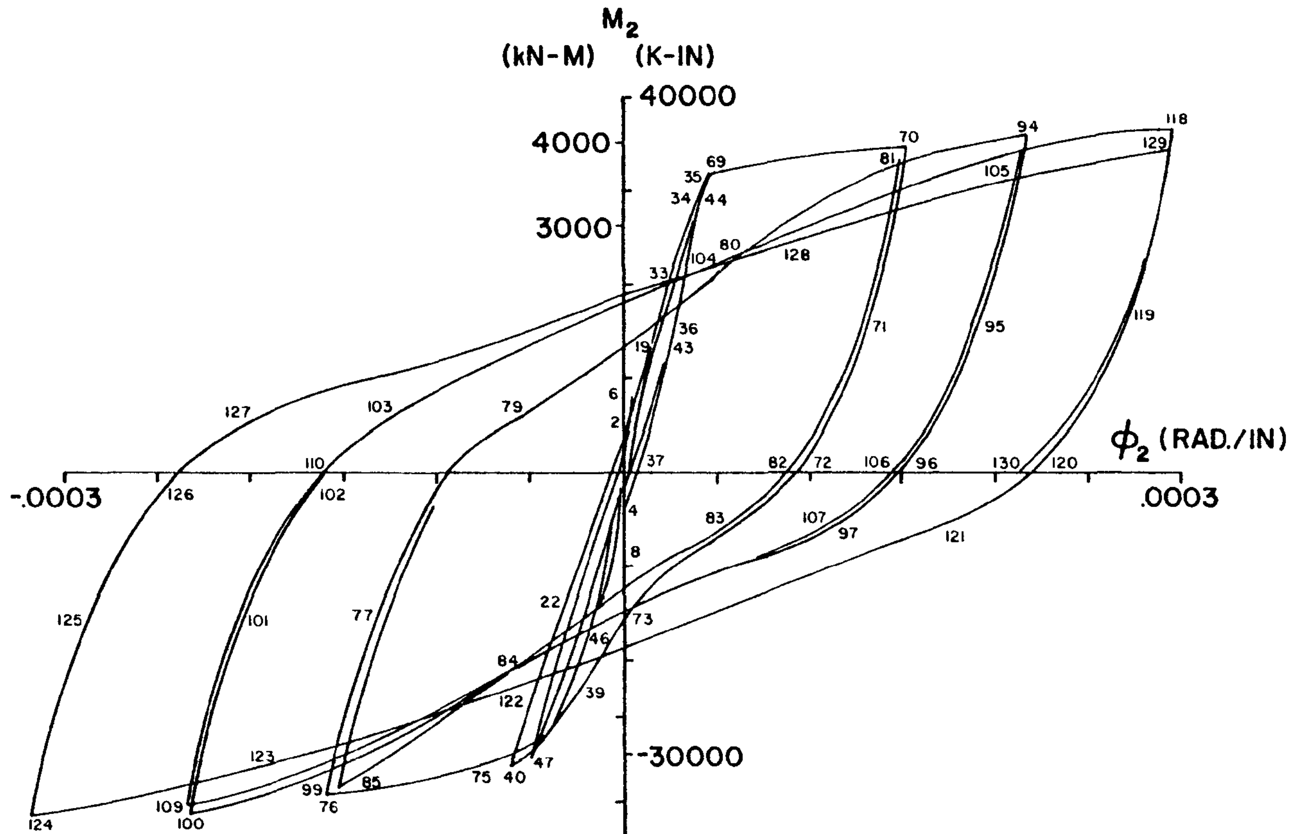

FIG. 5.30 M_2-ϕ_2 DIAGRAM-SHEAR WALL 2

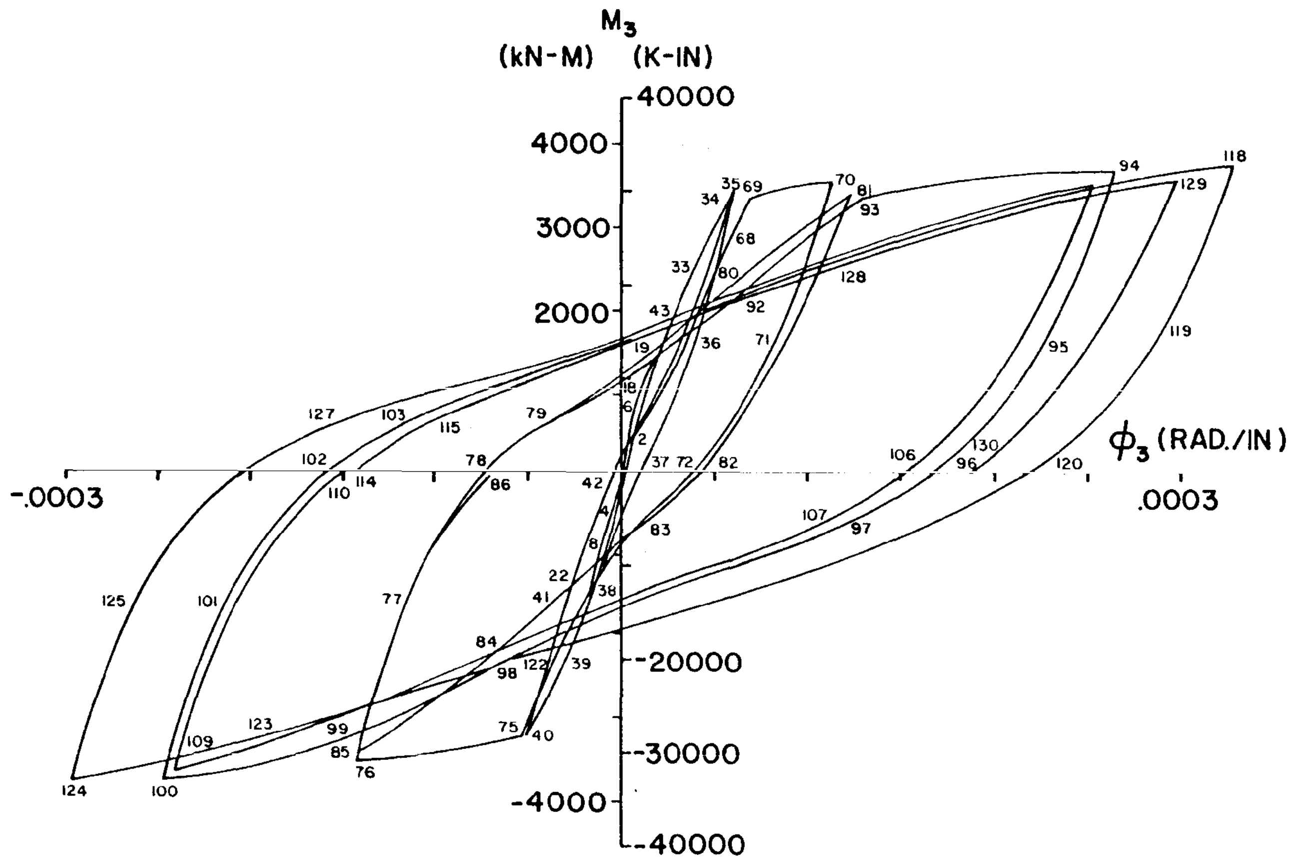

FIG. 5.31 M_3-ϕ_3 DIAGRAM-SHEAR WALL 2

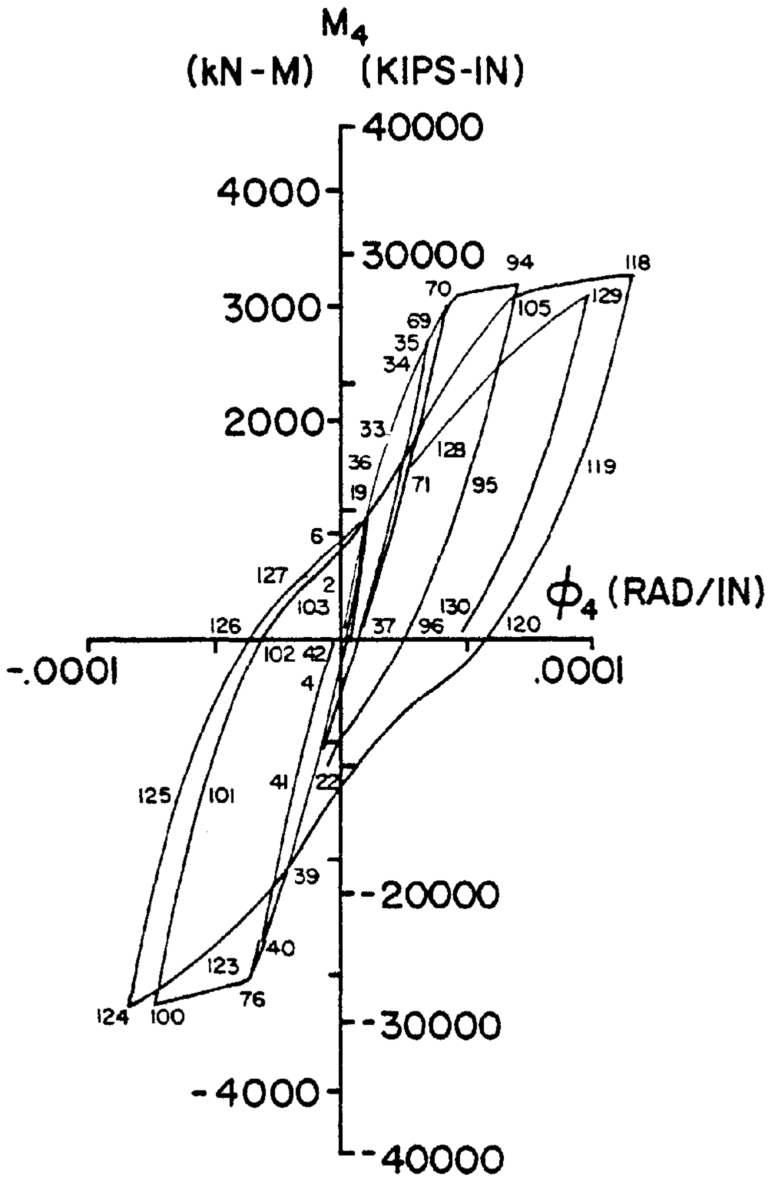

FIG. 5.32 M_4-ϕ_4 DIAGRAM - SHEAR WALL 2

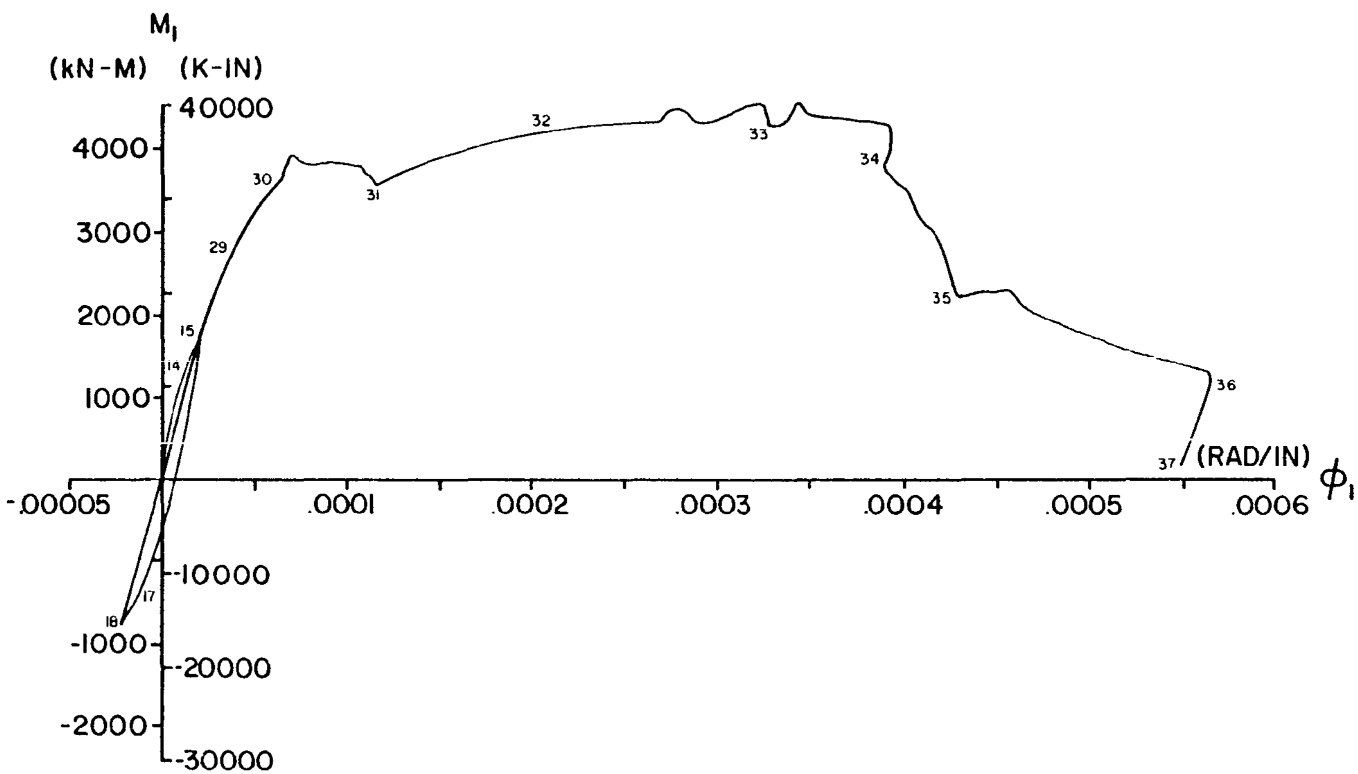

FIG. 5.33 M_1-ϕ_1 DIAGRAM - SHEAR WALL 2R

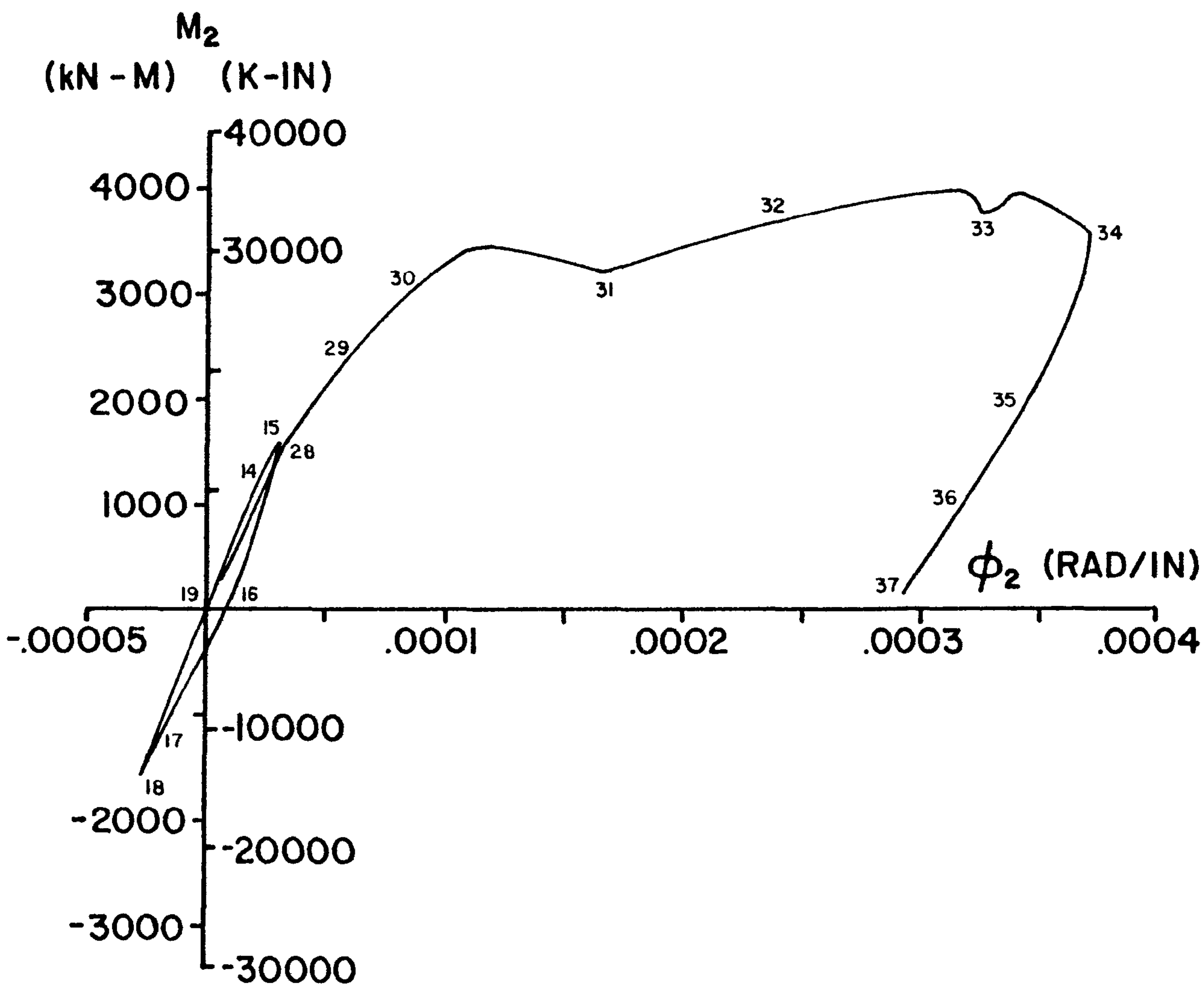

FIG. 5.34 M_2-ϕ_2 DIAGRAM - SHEAR WALL 2R

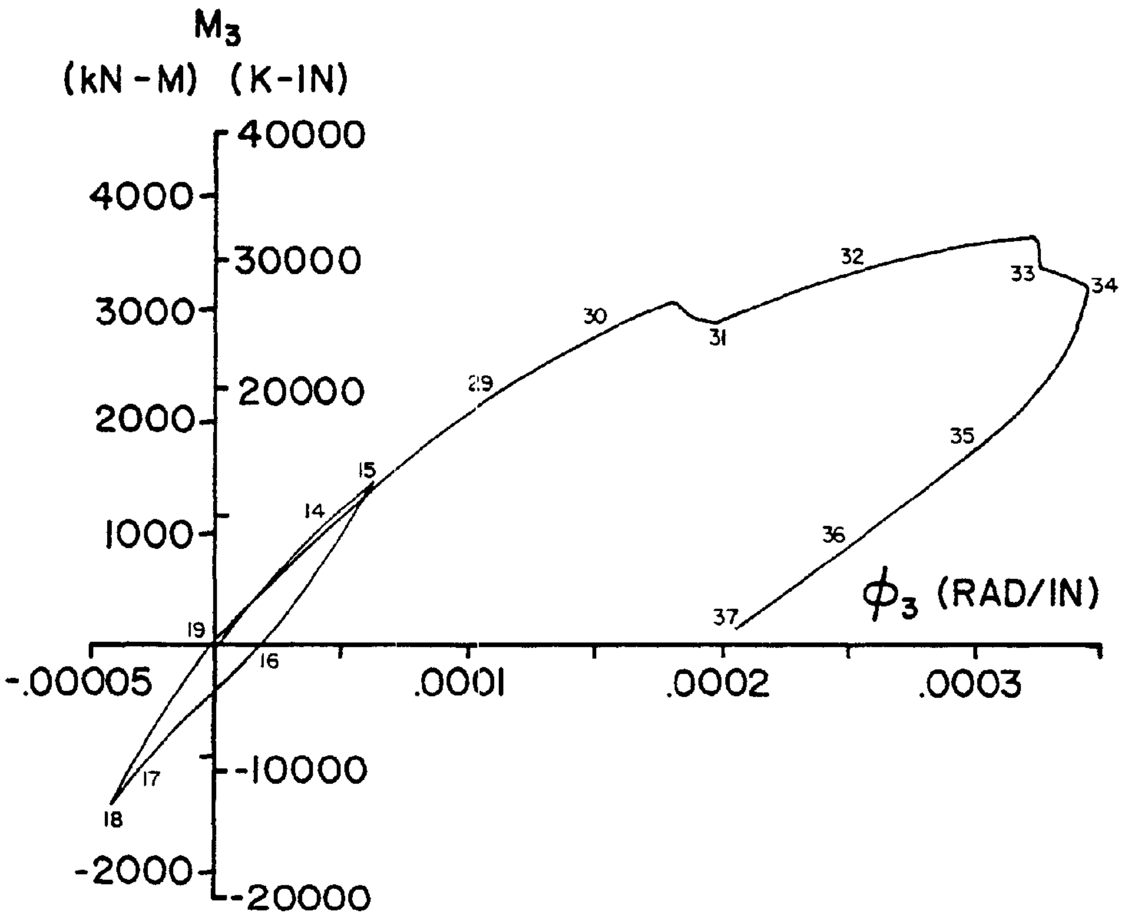

FIG. 5.35 M_3-ϕ_3 DIAGRAM - SHEAR WALL 2R

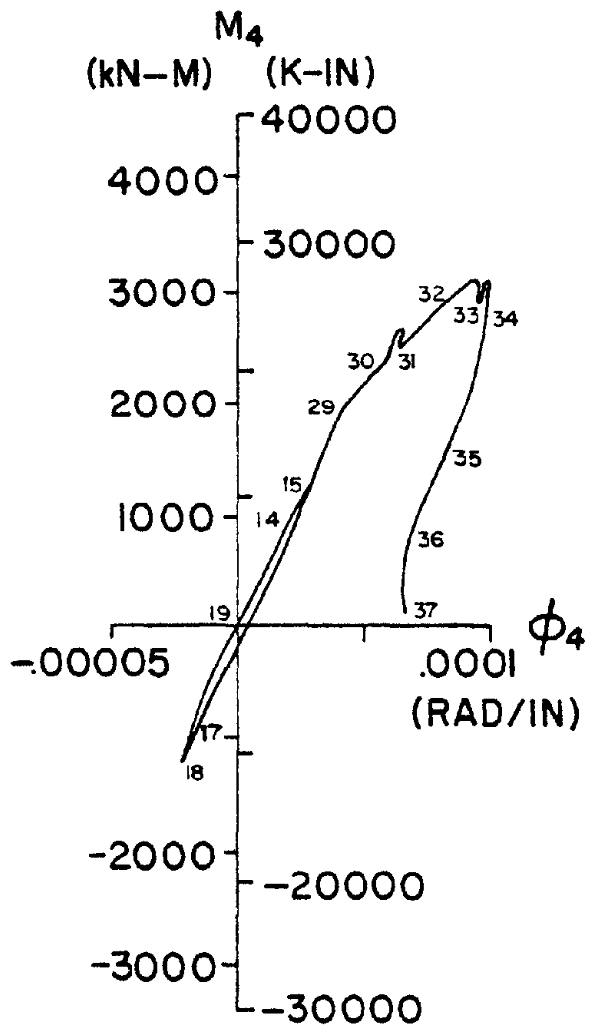

FIG. 5.36 M_4-ϕ_4 DIAGRAM - SHEAR WALL 2R

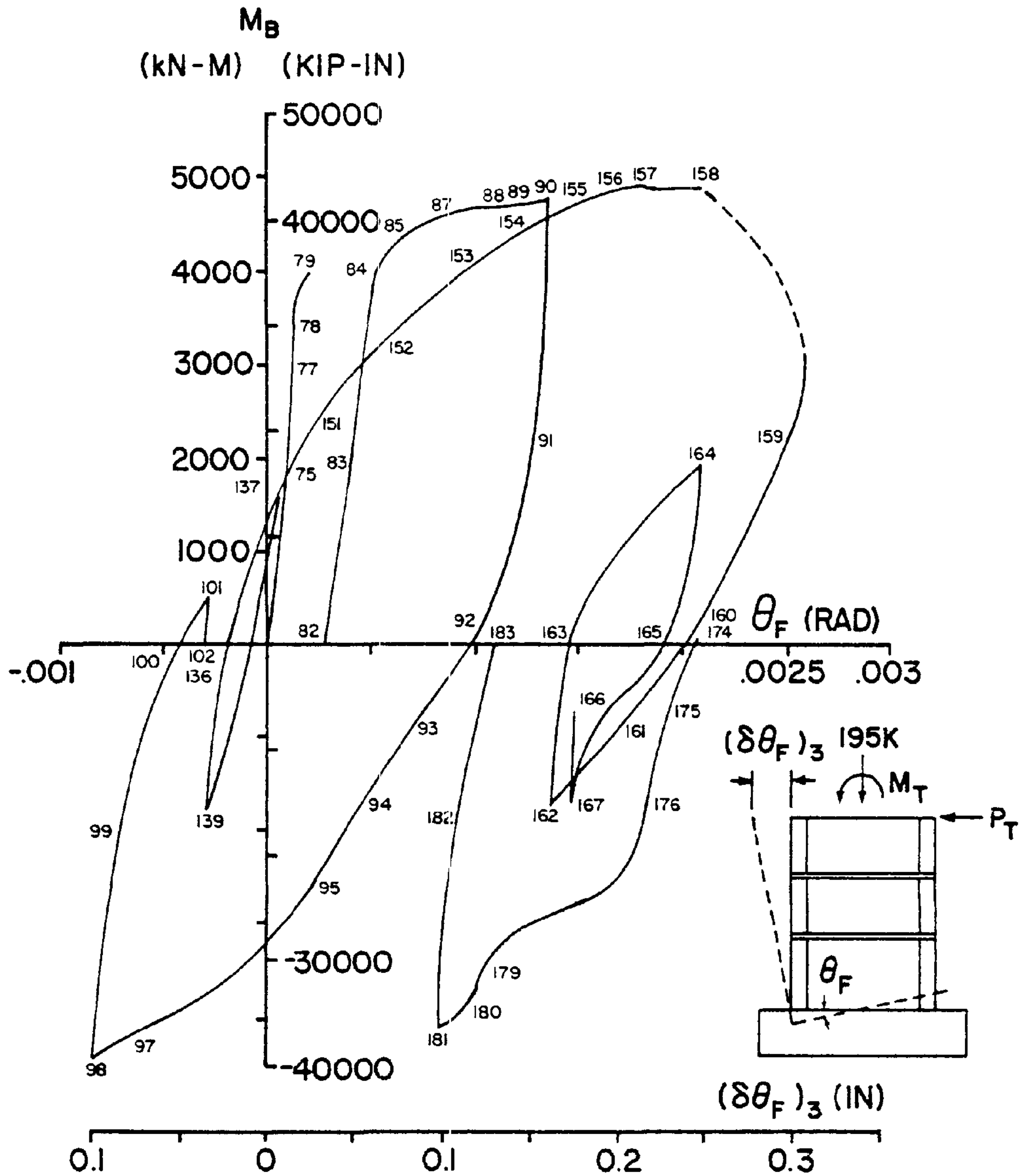

FIG. 5.37 M_B-θ_F DIAGRAM - SHEAR WALL 1

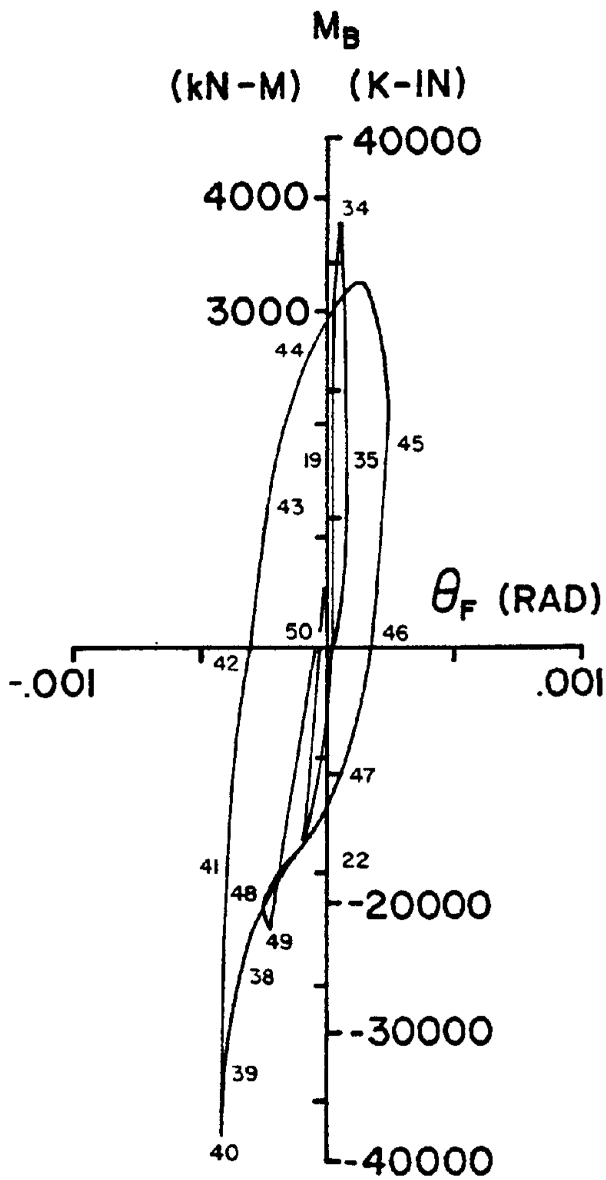

FIG. 5.38 M_B-θ_F DIAGRAM - SHEAR WALL 1R

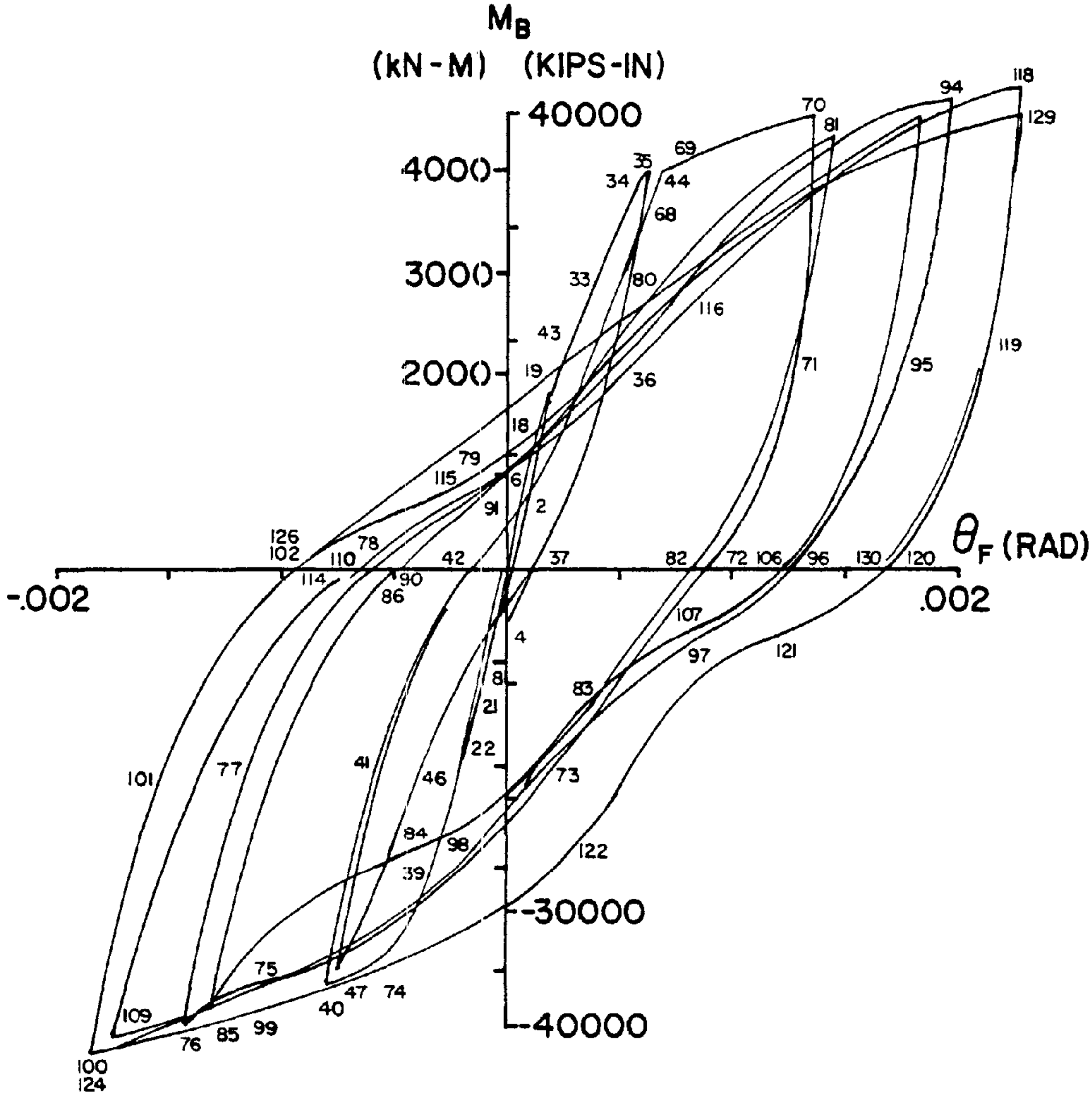

FIG. 5.39 M_B-θ_F DIAGRAM - SHEAR WALL 2

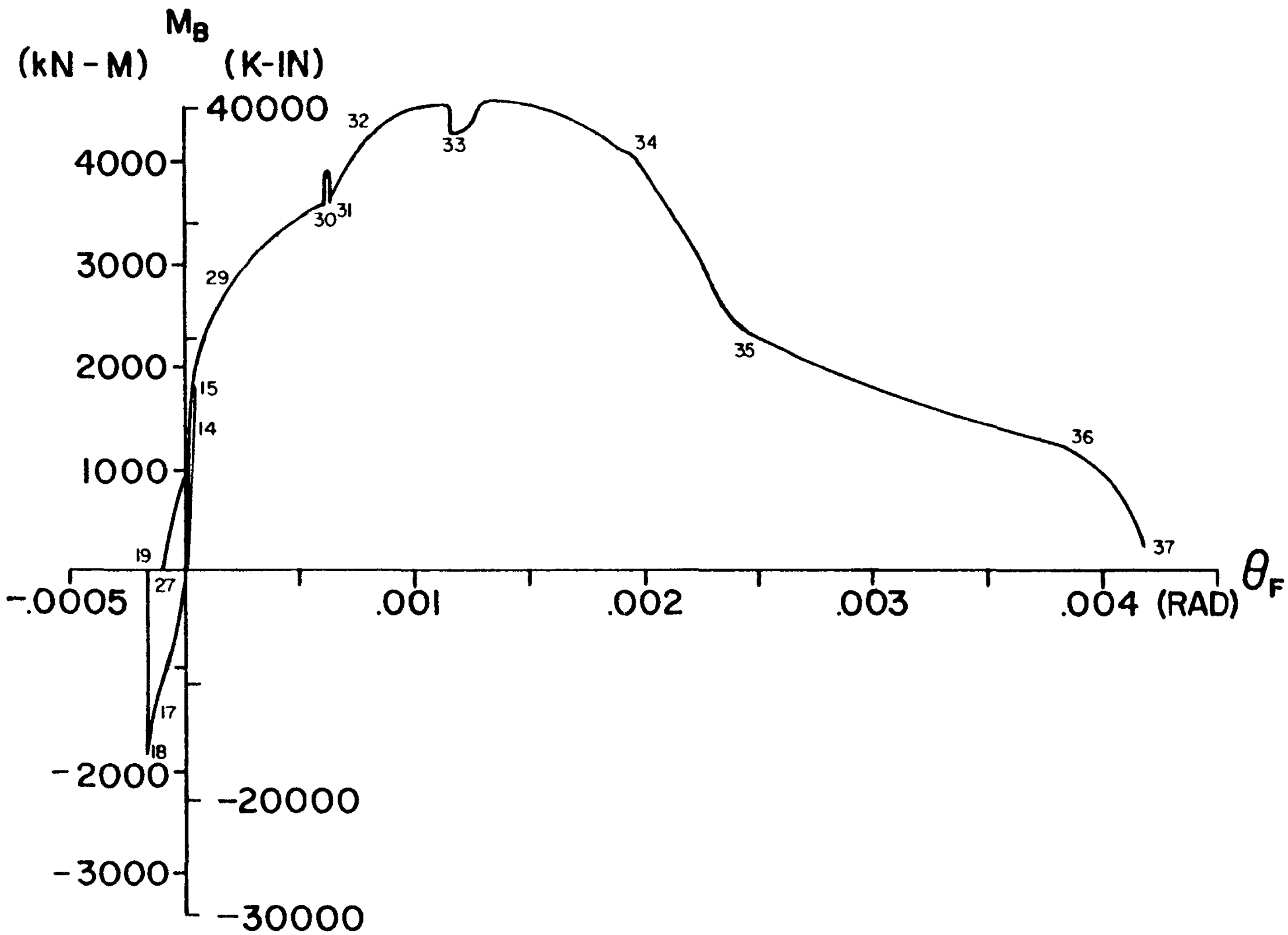

FIG. 5.40 M_B-θ_F DIAGRAM - SHEAR WALL 2R

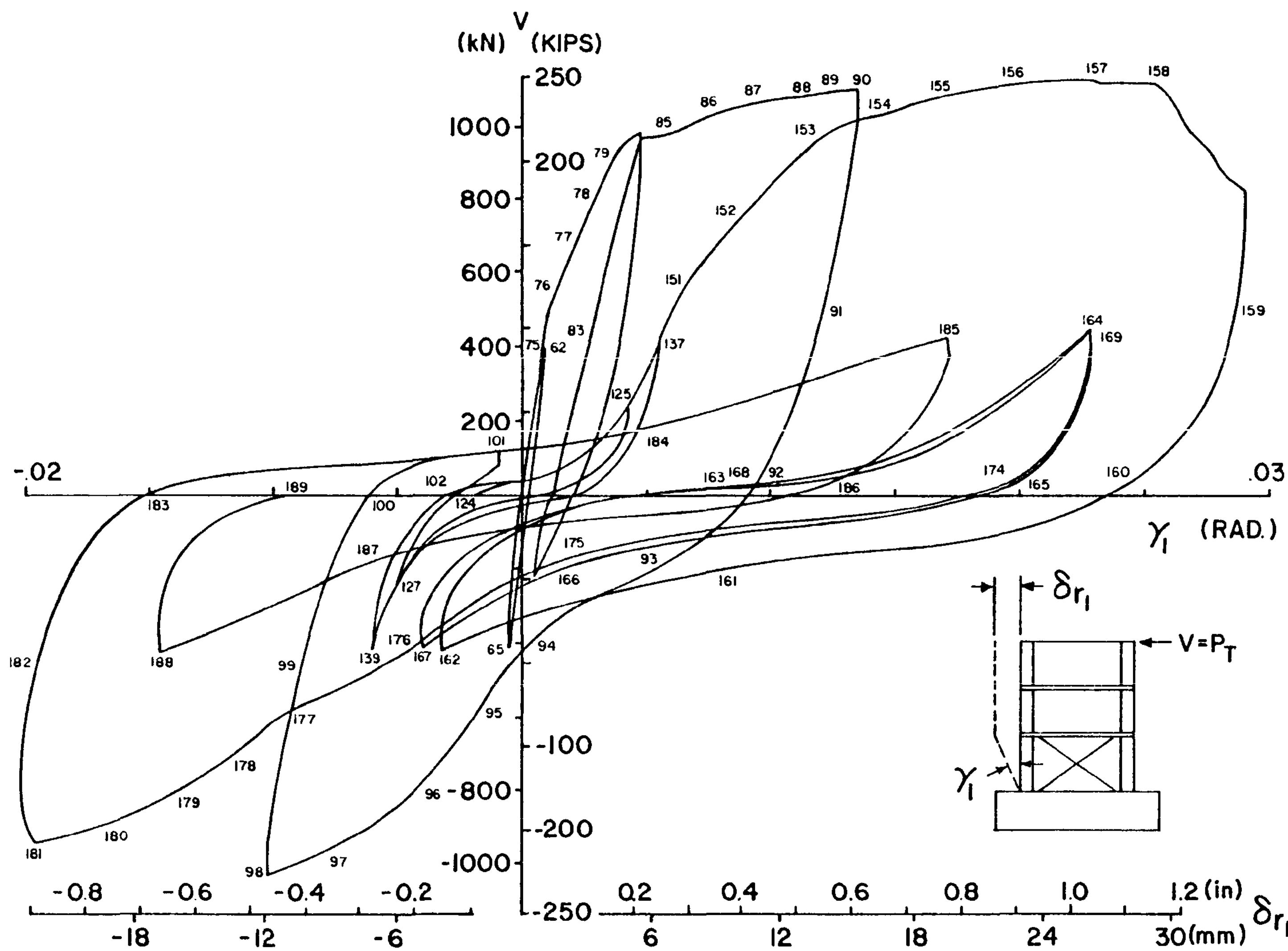

FIG. 5.41 V-γ_1 DIAGRAM - SHEAR WALL 1

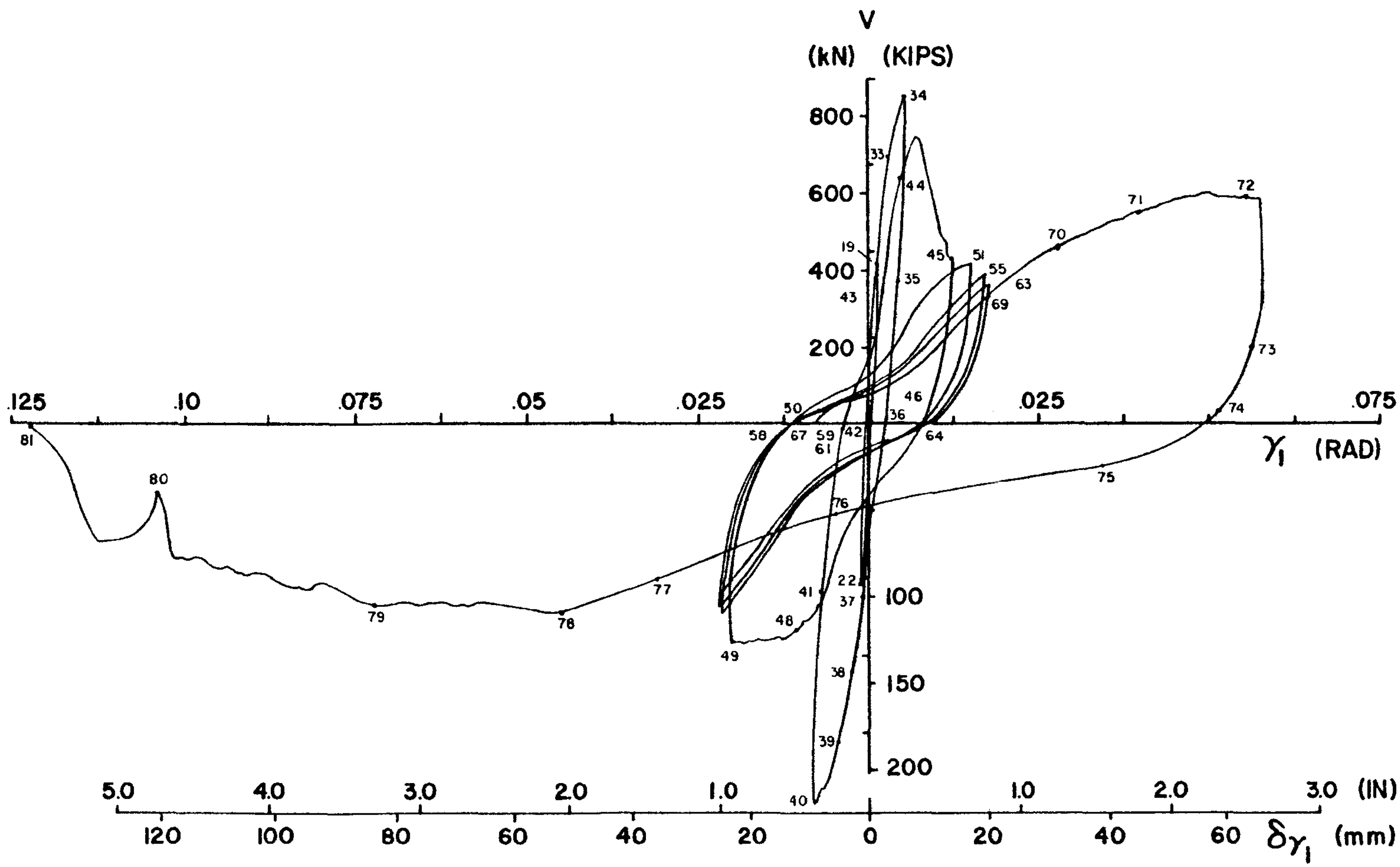

FIG. 5.42 V-γ_1 DIAGRAM - SHEAR WALL 1R

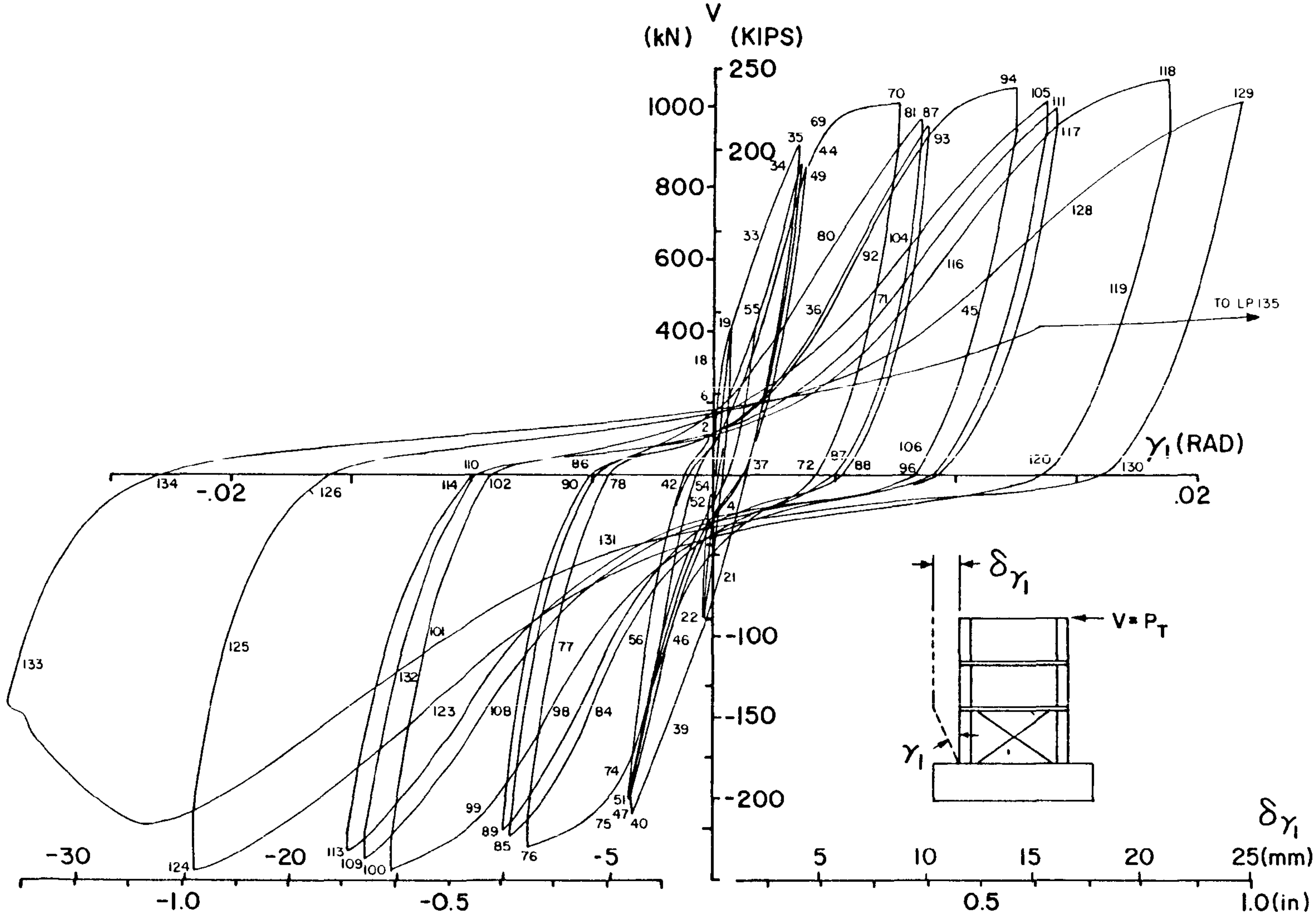

FIG. 5.43 V-γ_1 DIAGRAM - SHEAR WALL 2

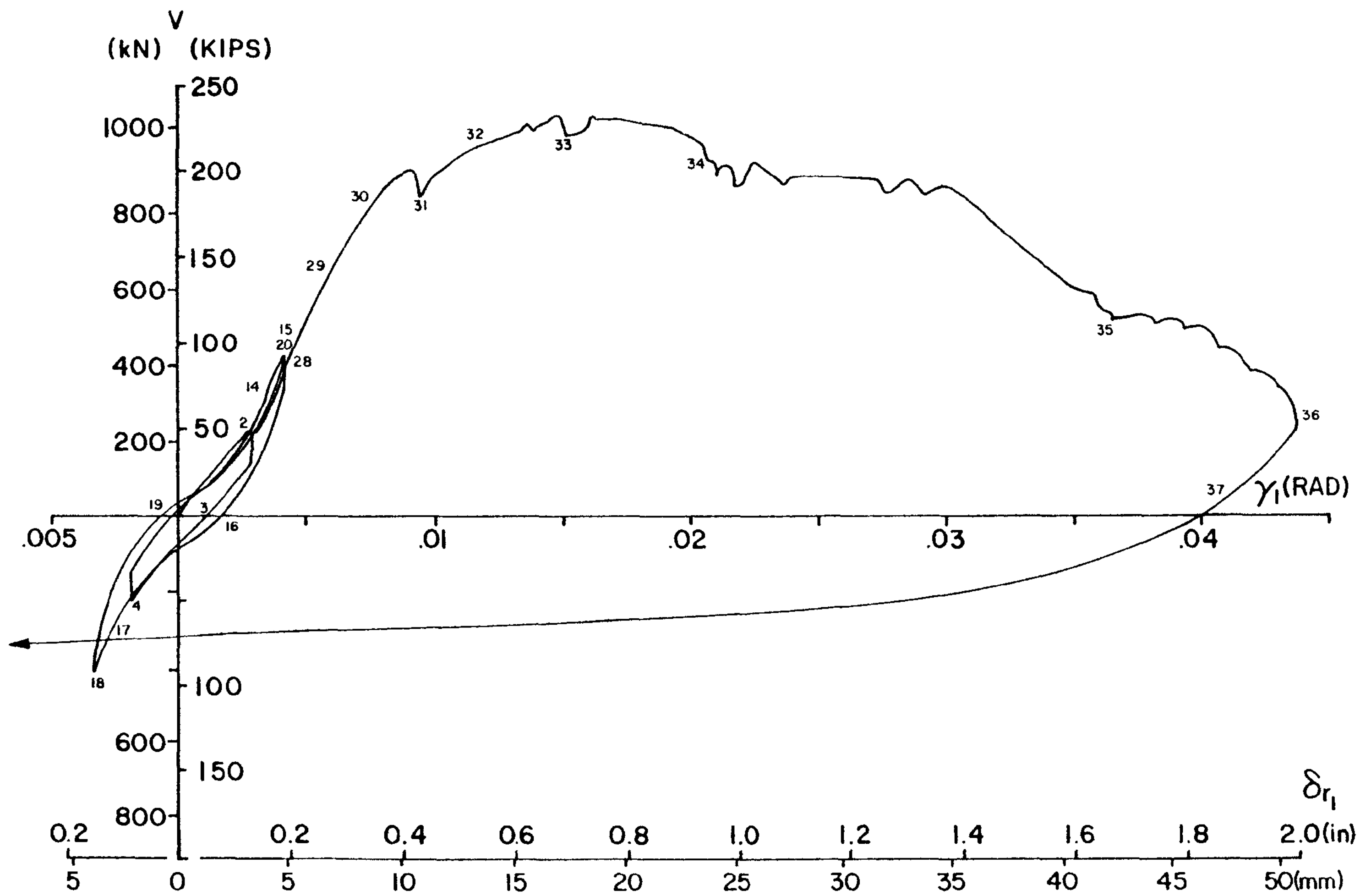

FIG. 5.44 V-γ_1 DIAGRAM - SHEAR WALL 2R

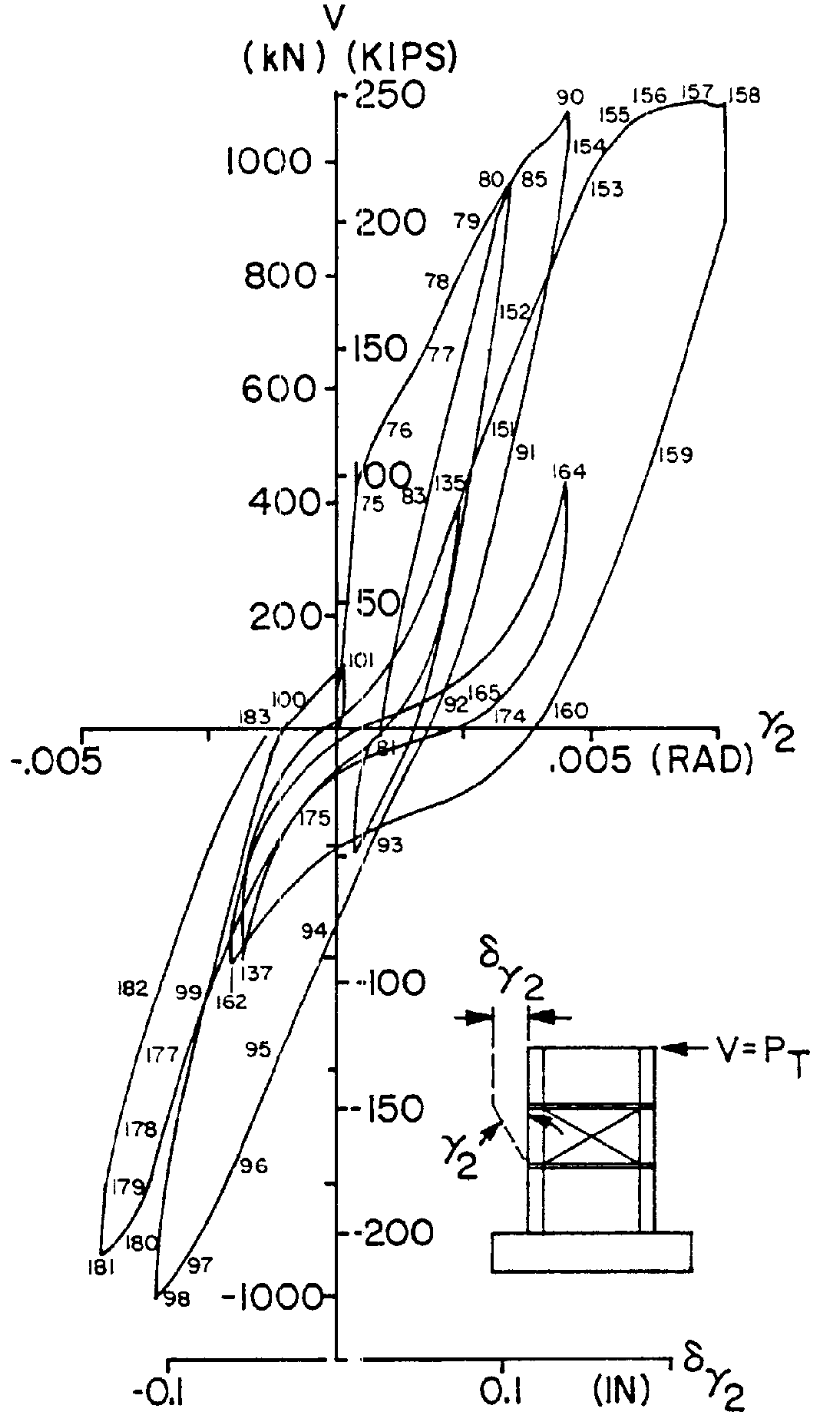

FIG. 5.45 V-γ_2 DIAGRAM - SHEAR WALL 1

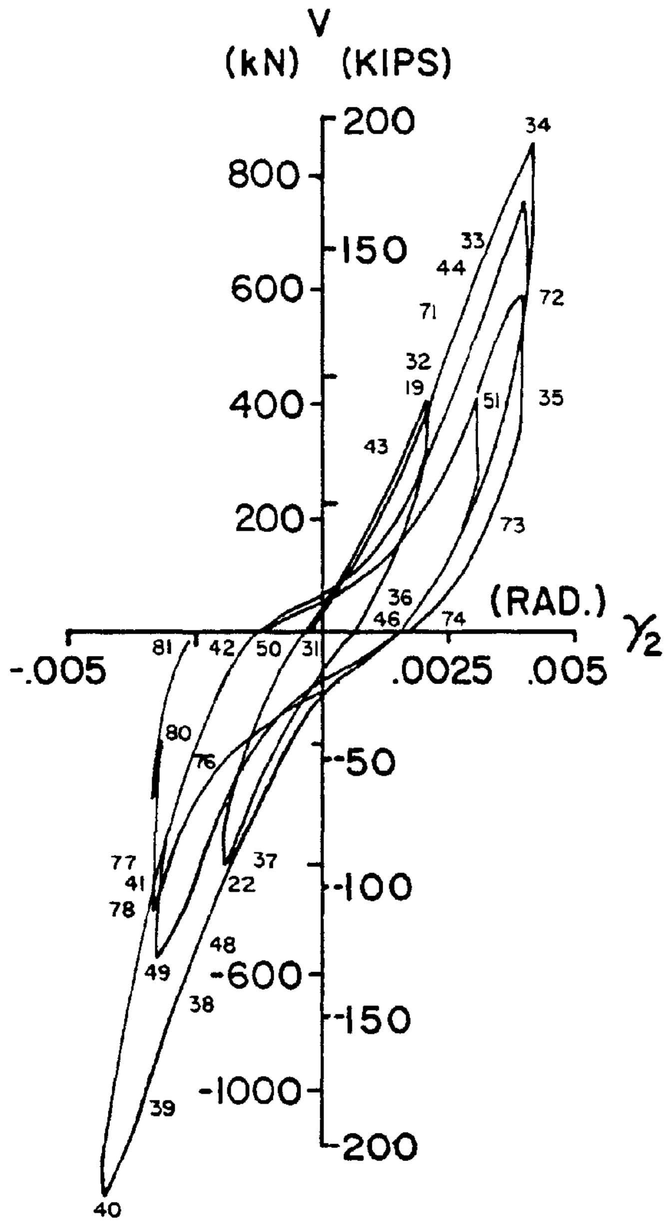

FIG. 5.46 V-γ_2 DIAGRAM - SHEAR WALL 1R

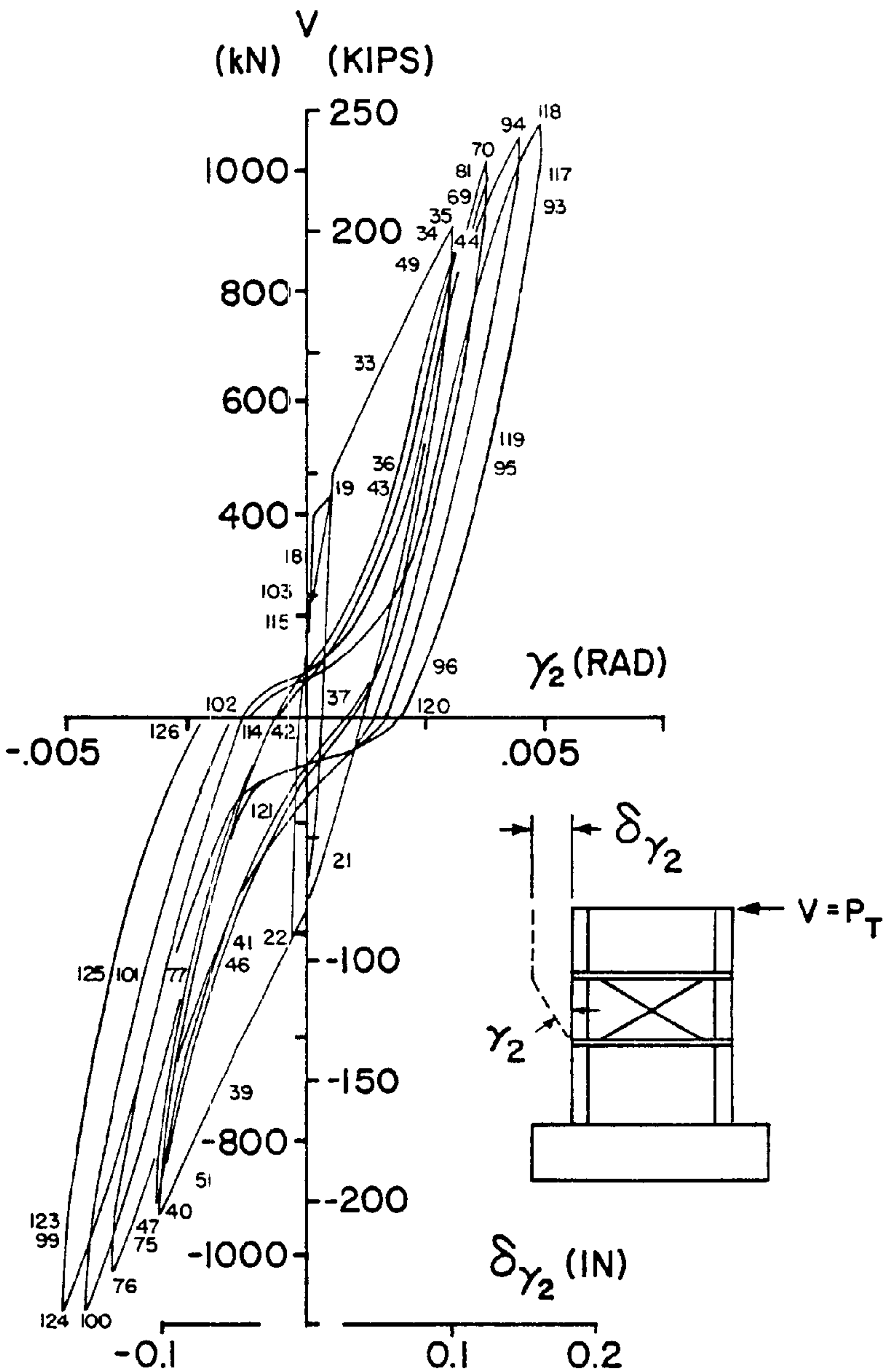

FIG. 5.47 V-γ_2 DIAGRAM - SHEAR WALL 2

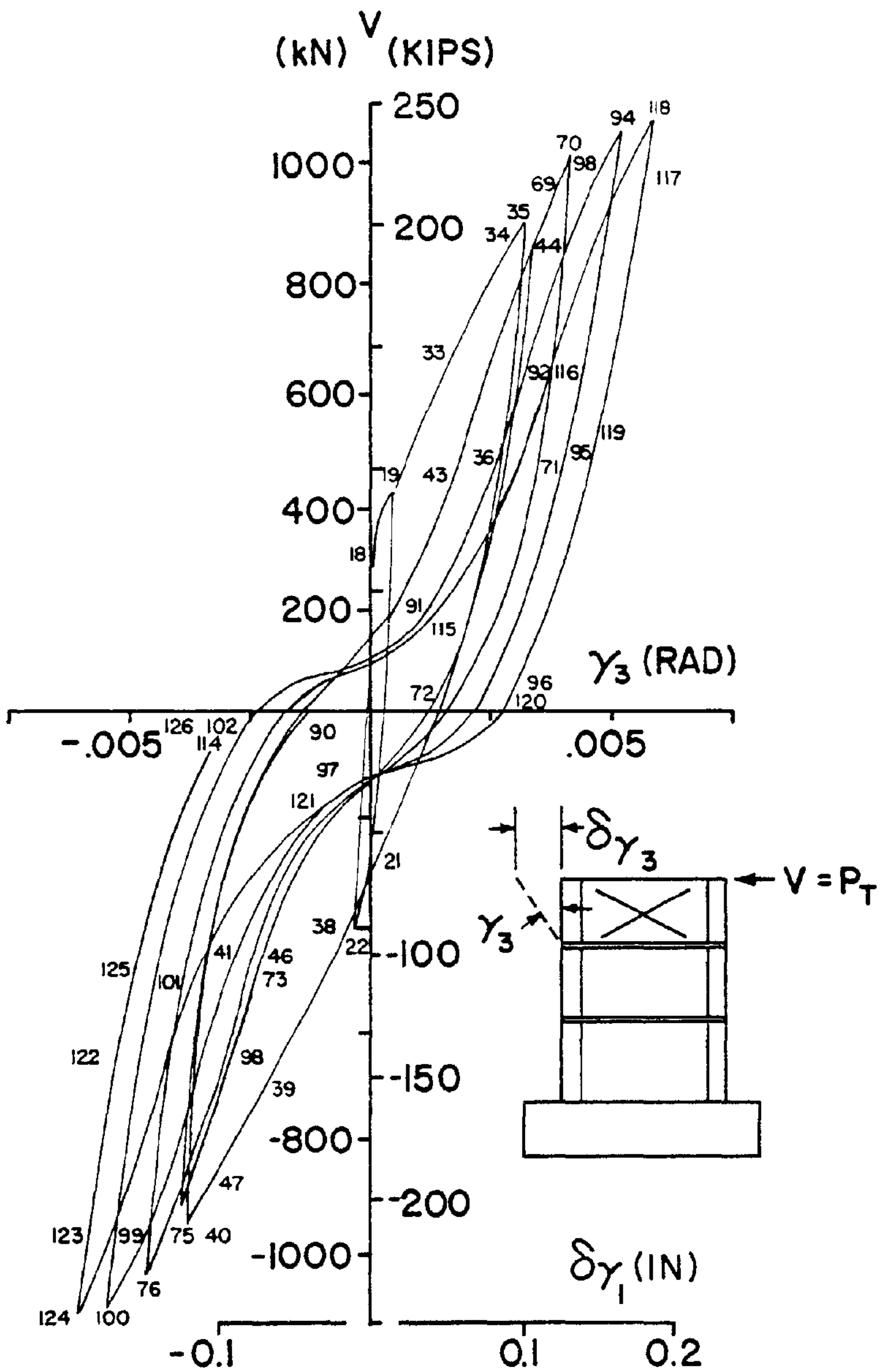

FIG. 5.48 V-γ_3 DIAGRAM - SHEAR WALL 2

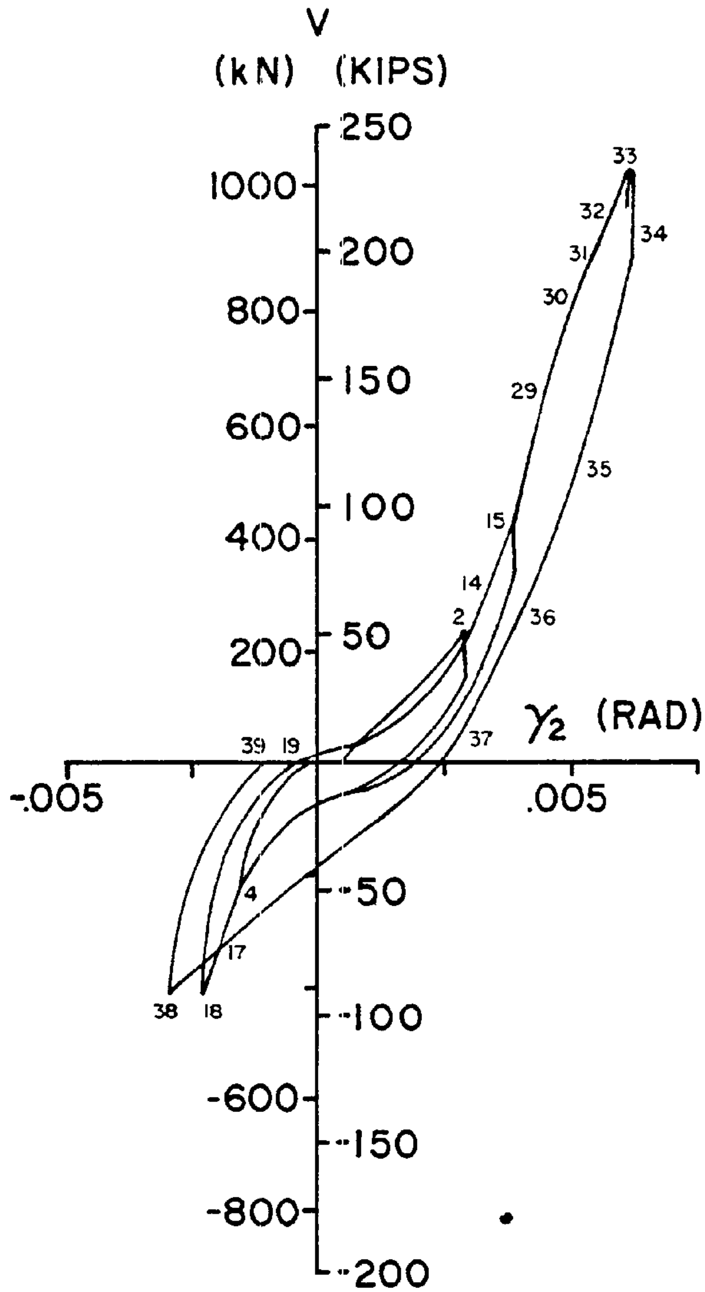

FIG. 5.49 V-γ_2 DIAGRAM - SHEAR WALL 2R

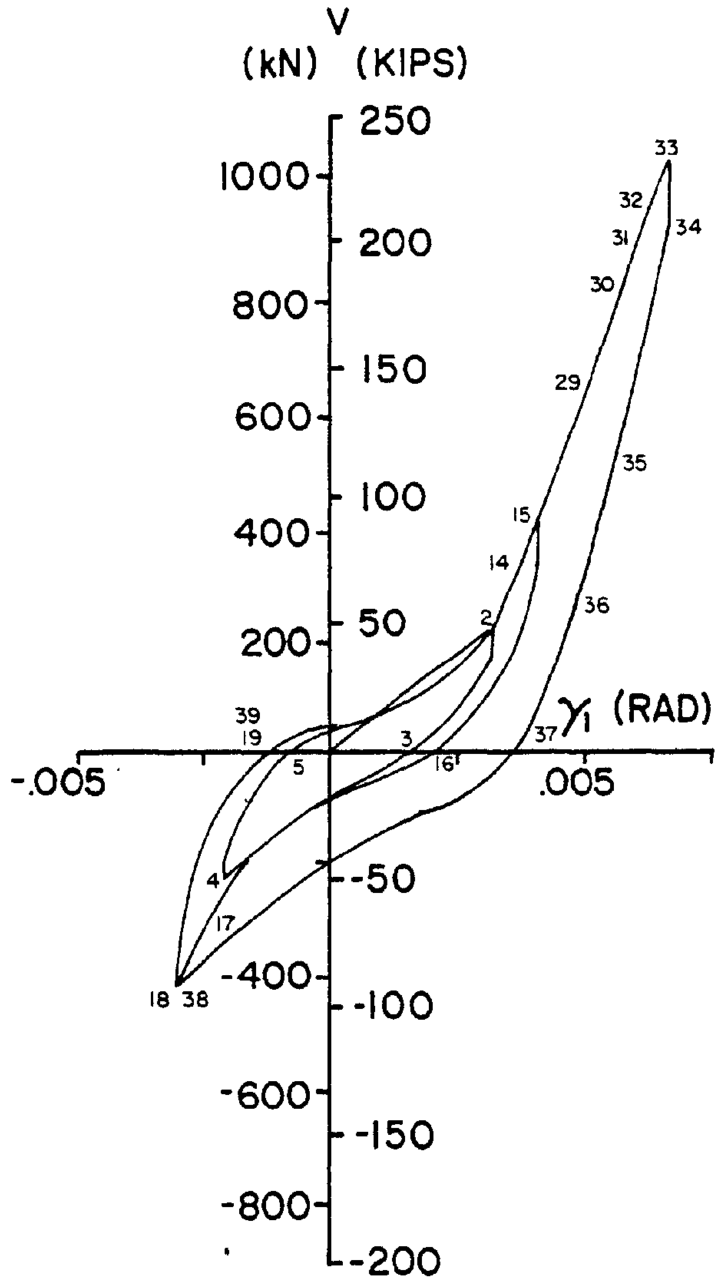

FIG. 5.50 V-γ_3 DIAGRAM - SHEAR WALL 2R

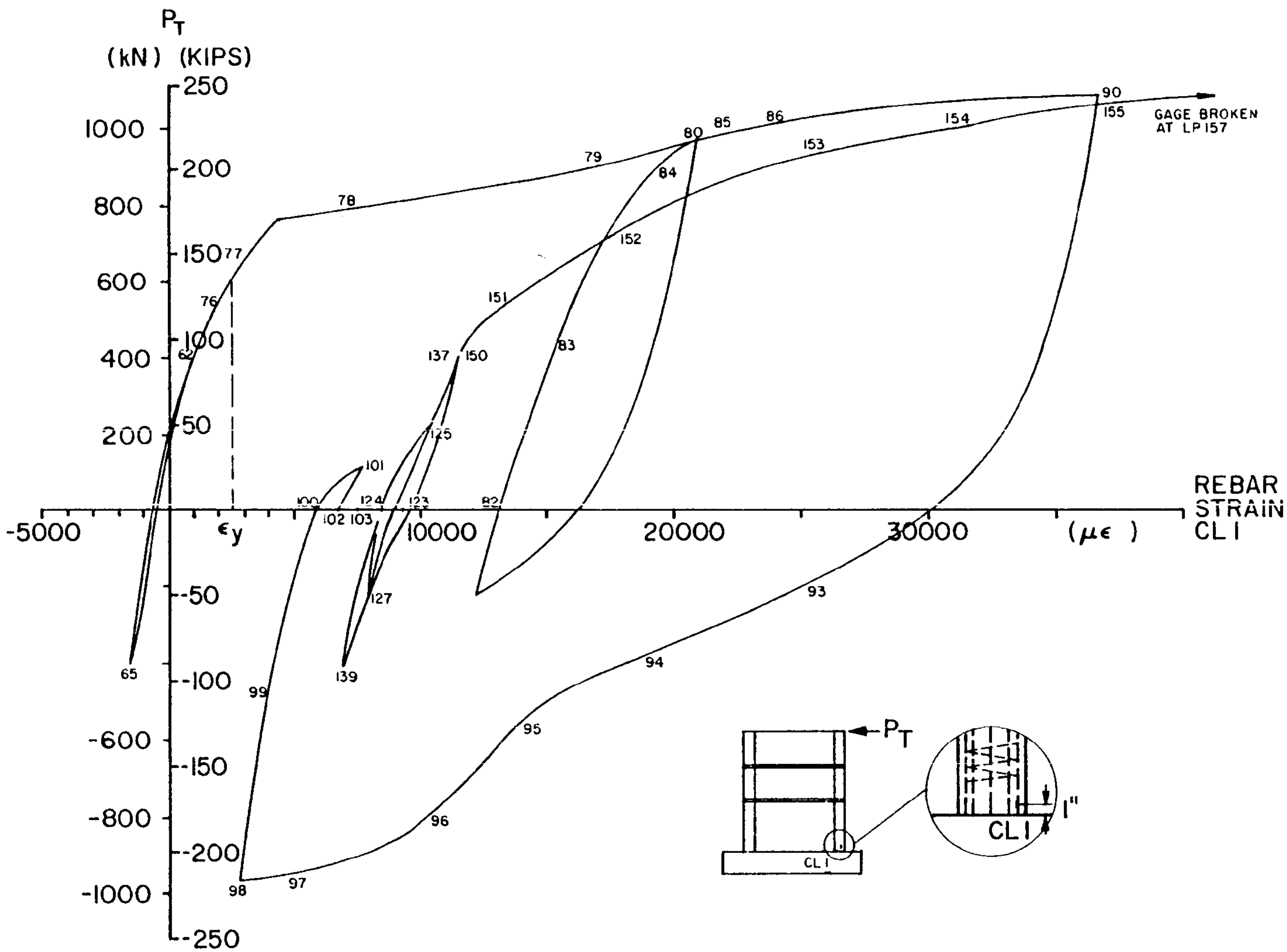

FIG. 5.51 P_T-CL 1 DIAGRAM - SHEAR WALL 1

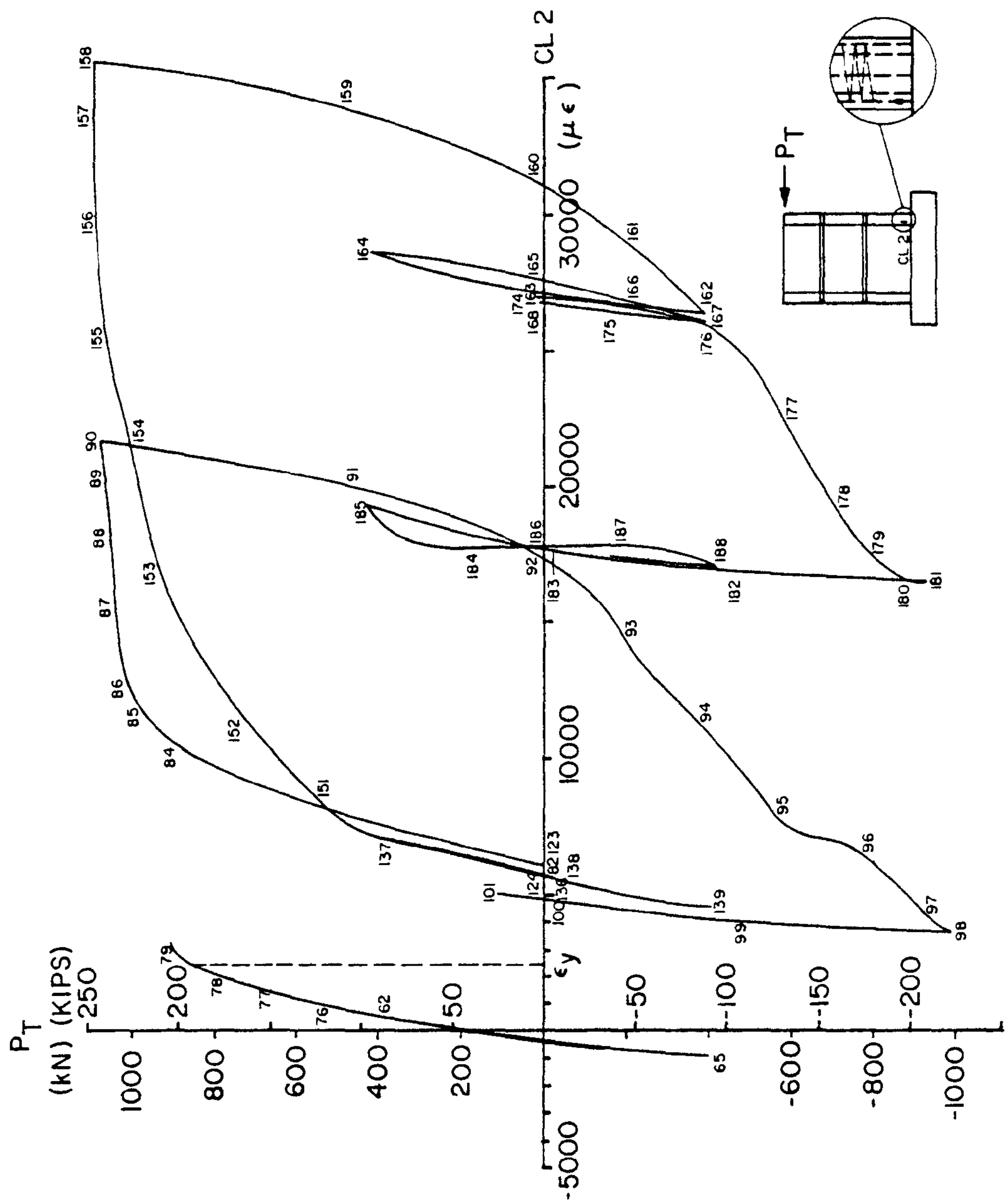

FIG. 5.52 P_T-CL 2 DIAGRAM - SHEAR WALL 1

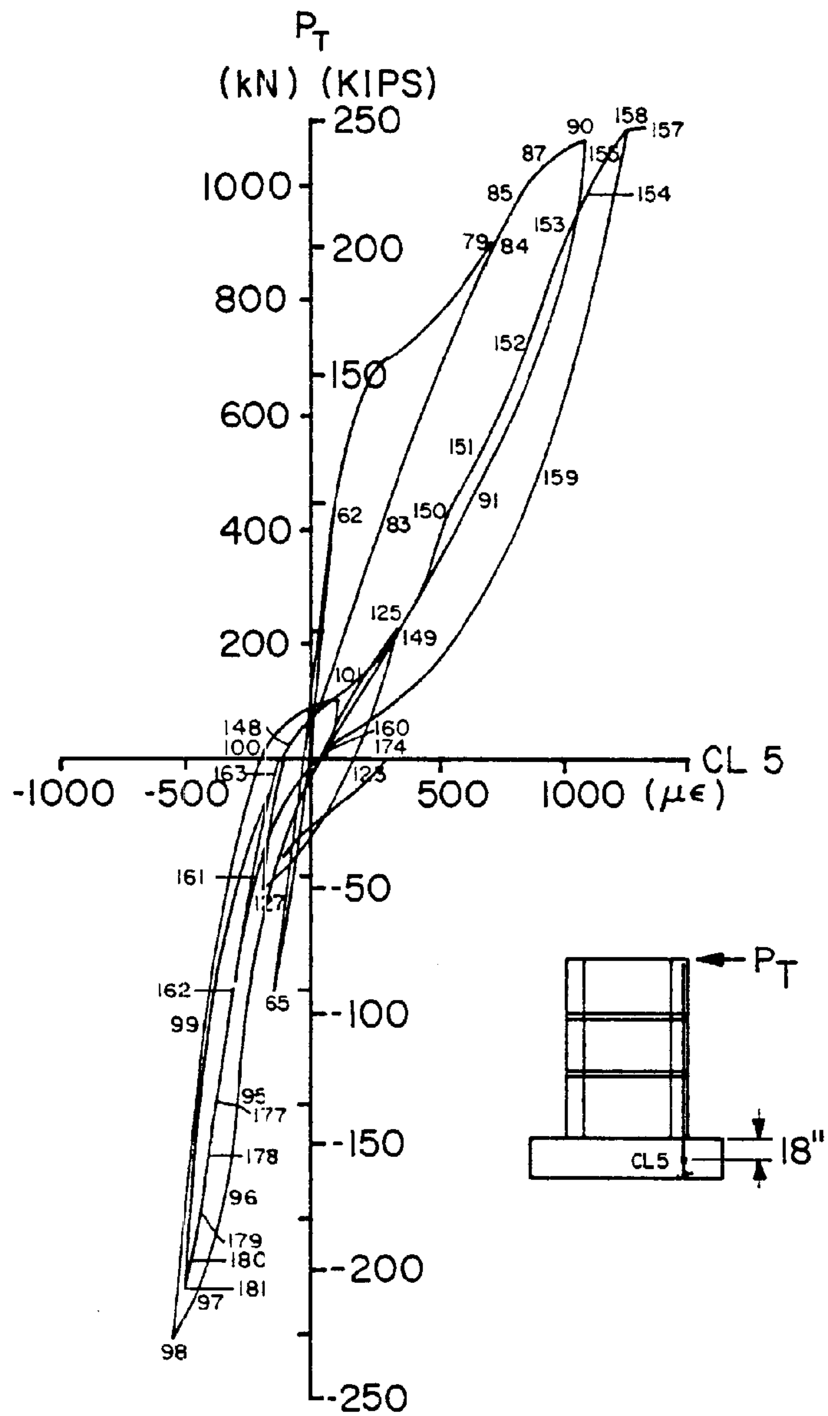

FIG. 5.53 P_T-CL 5 DIAGRAM - SHEAR WALL 1

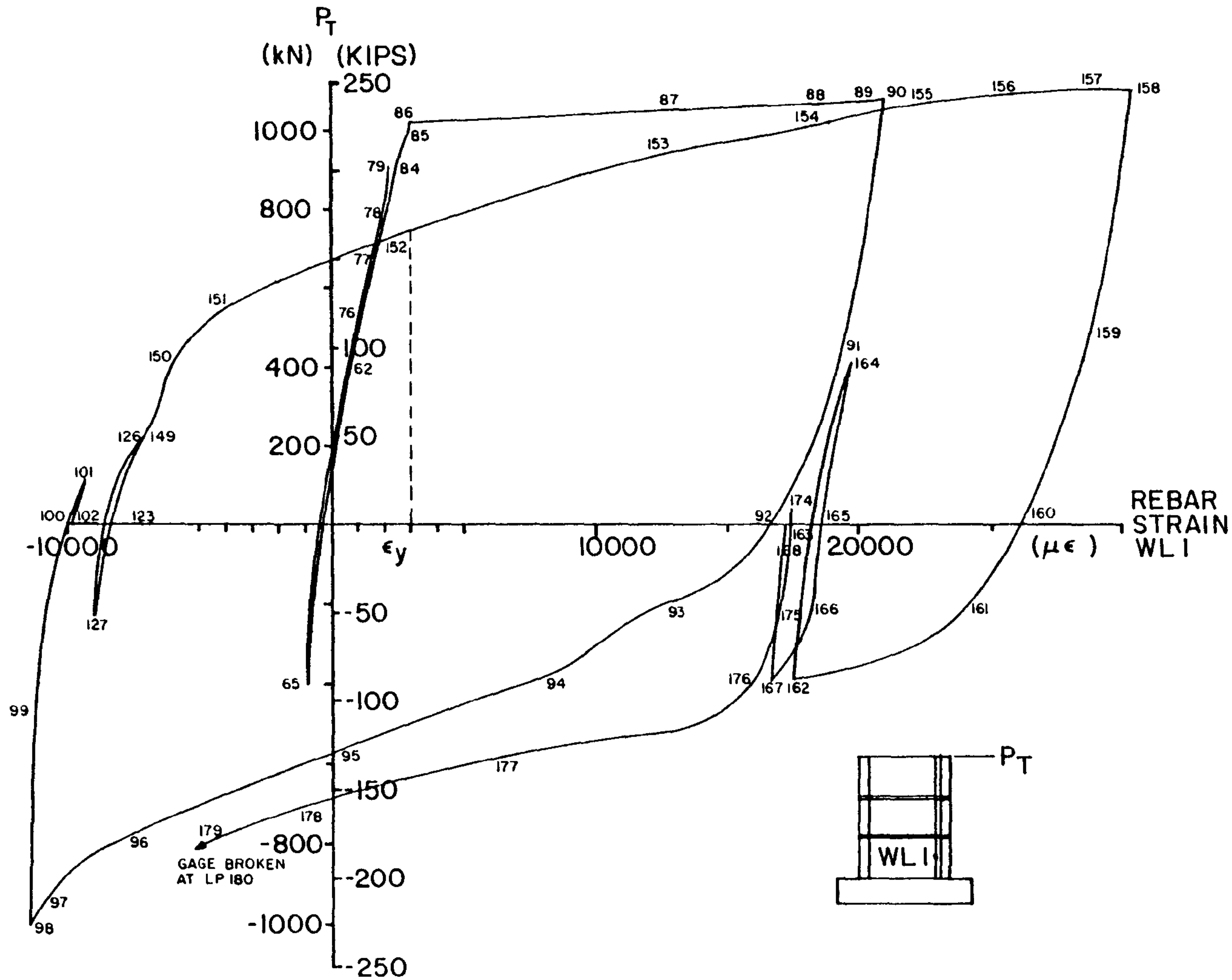

FIG. 5.54 P_T-WL 1 DIAGRAM - SHEAR WALL 1

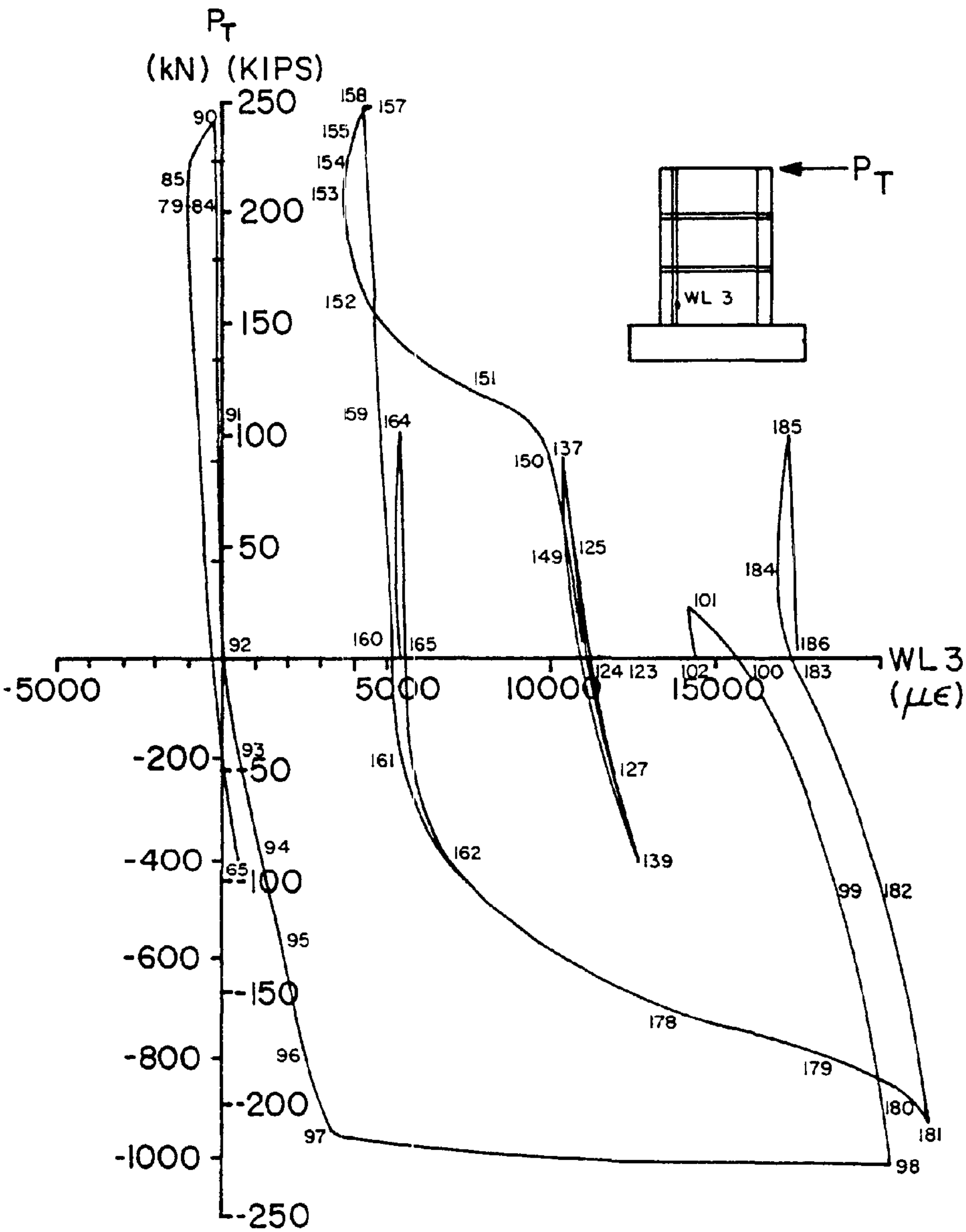

FIG. 5.55 P_T-WL 3 DIAGRAM - SHEAR WALL 1

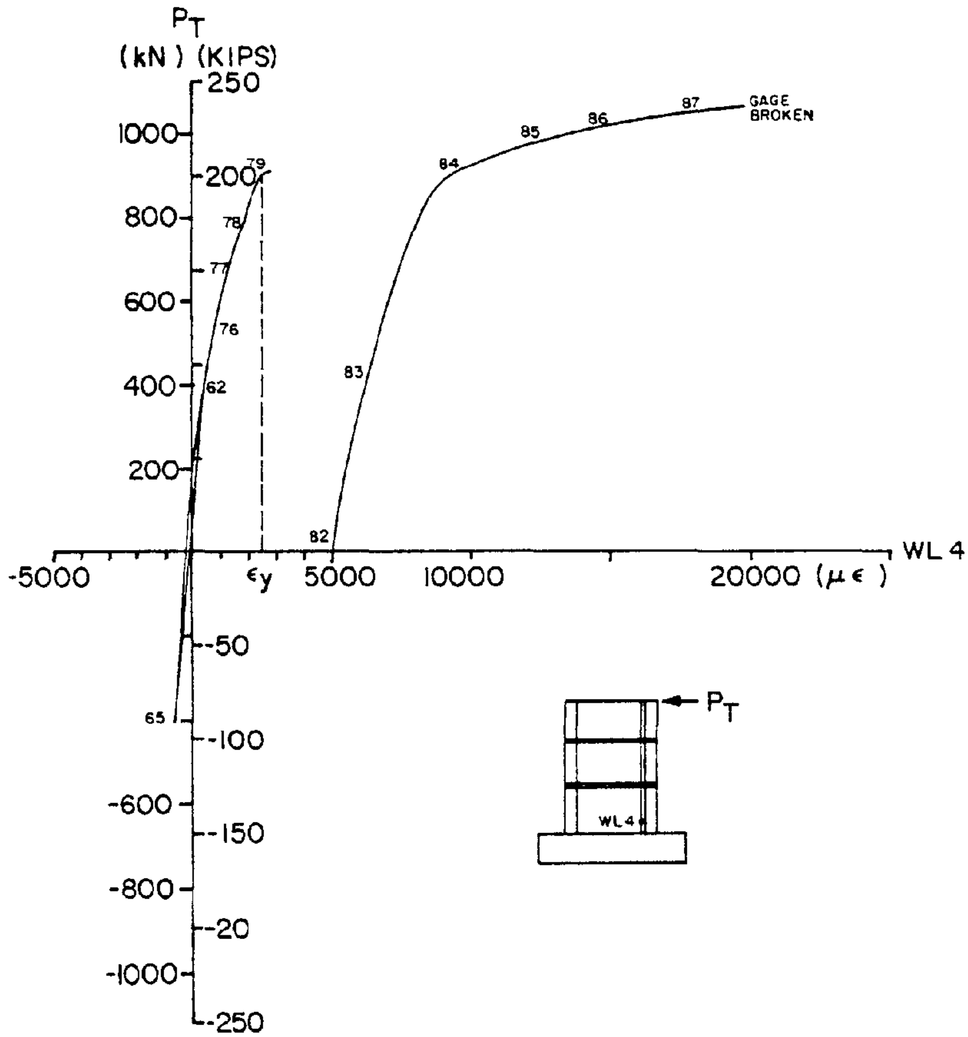

FIG. 5.56 P_T-WL 4 DIAGRAM - SHEAR WALL 1

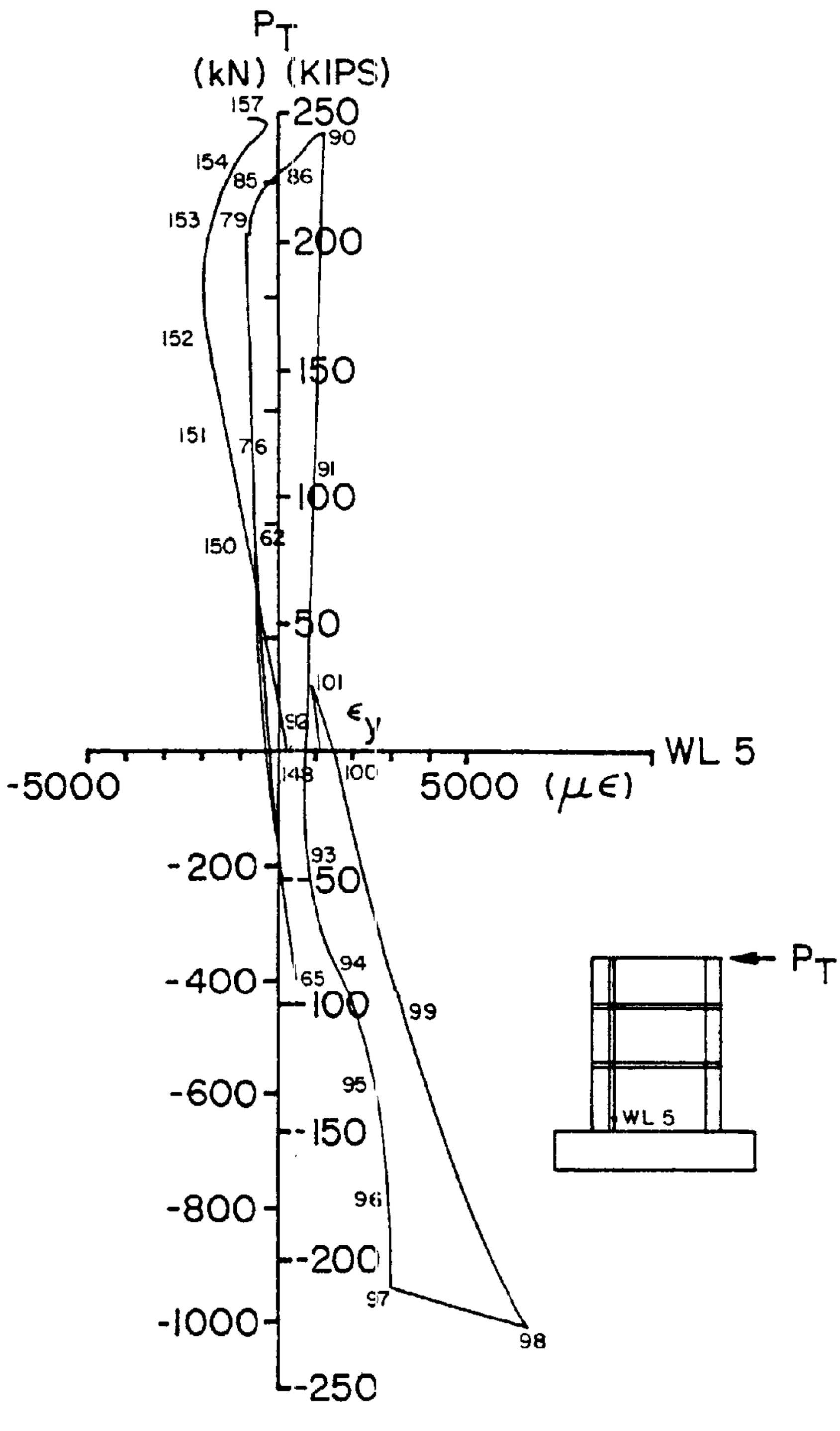

FIG. 5.57 P_T-WL 5 DIAGRAM - SHEAR WALL 1

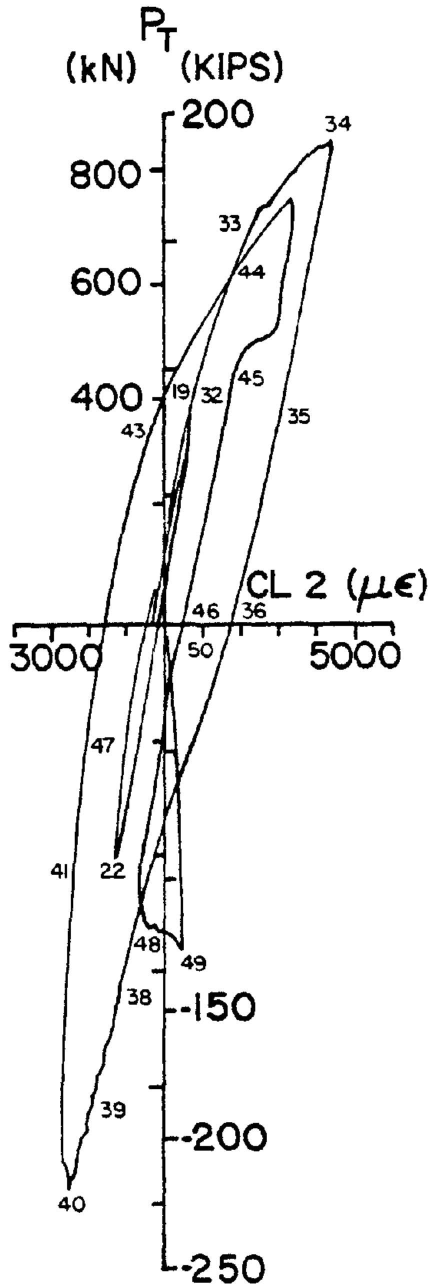

FIG. 5.58 P_T-CL 2 DIAGRAM - SHEAR WALL 1R

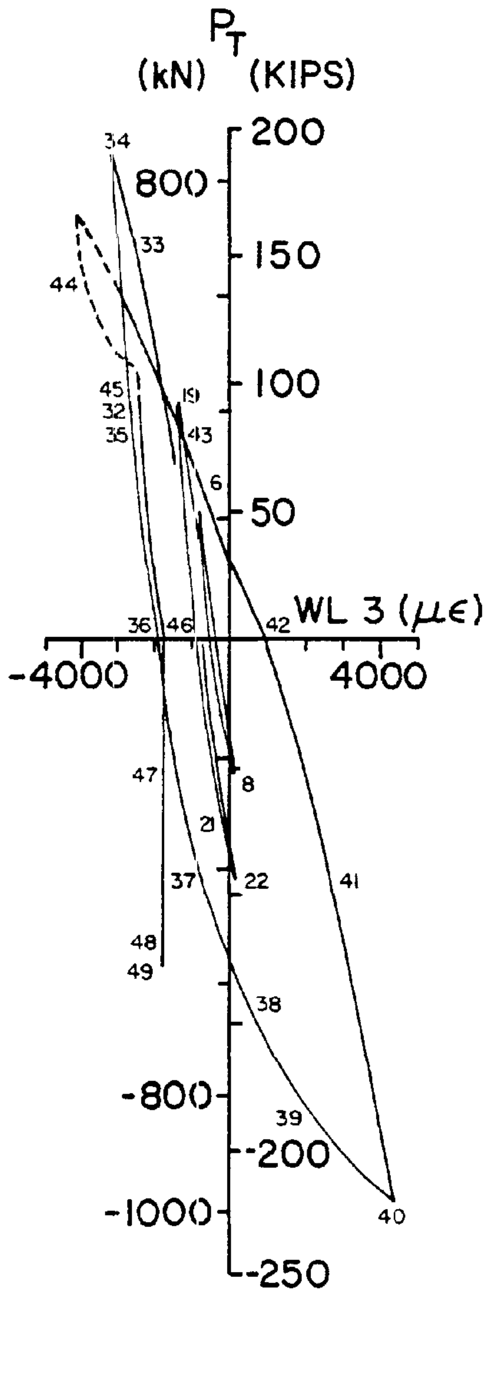

FIG. 5.59 P_T-WL 3 DIAGRAM - SHEAR WALL 1R

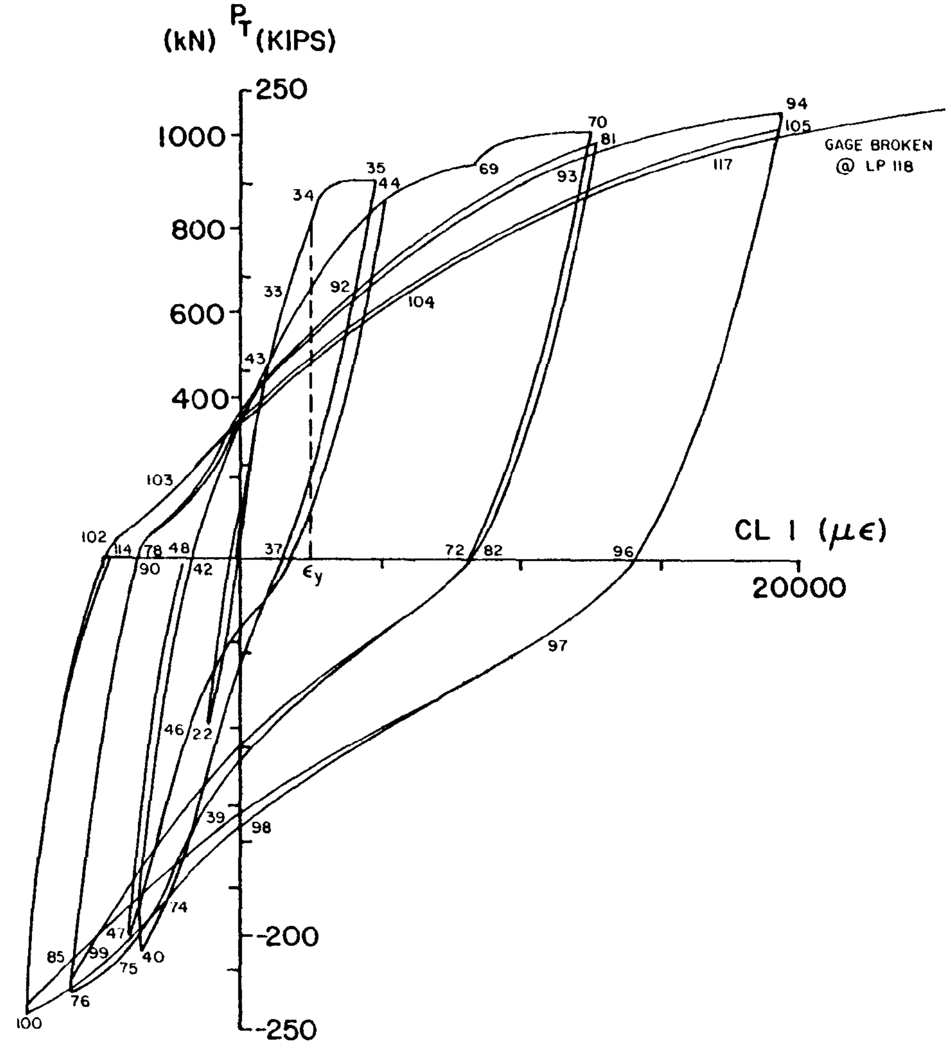

FIG. 5.60 P_T-CL 1 DIAGRAM - SHEAR WALL 2

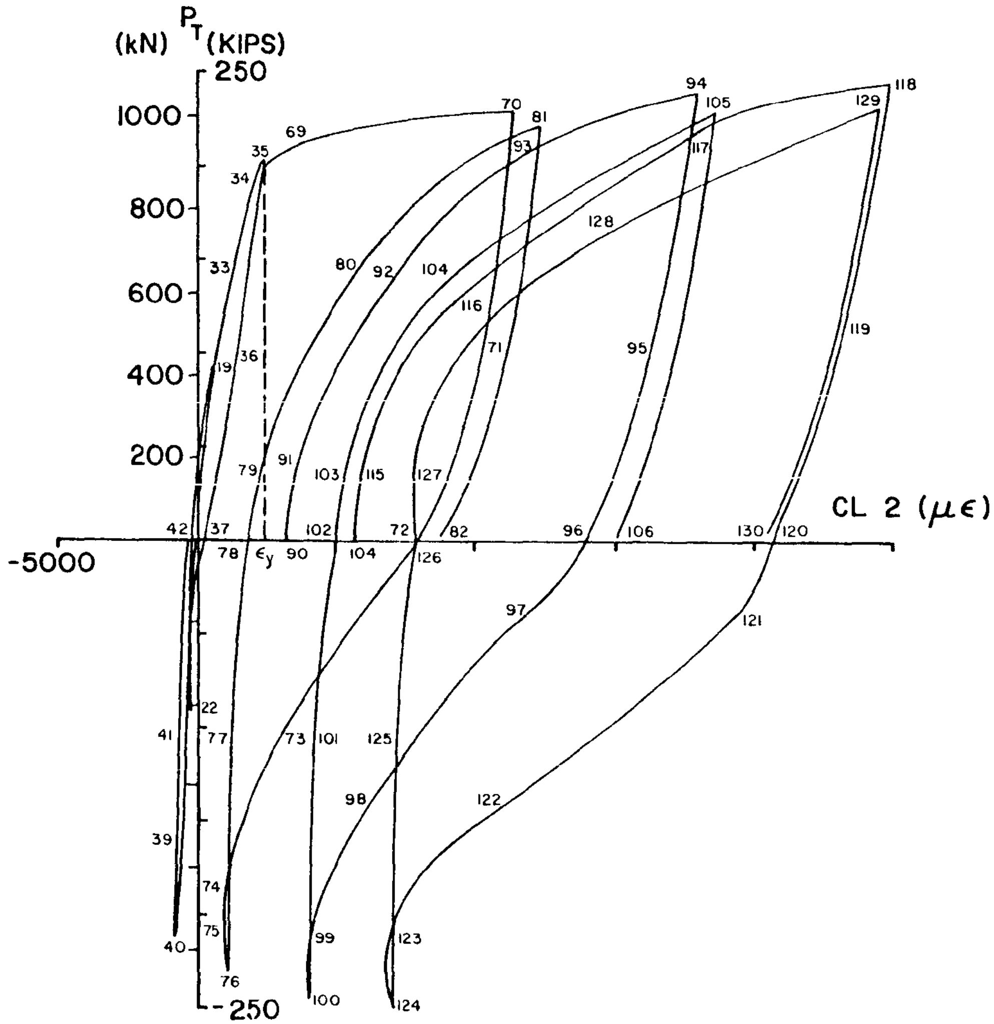

FIG. 5.61 P_T-CL 2 DIAGRAM - SHEAR WALL 2

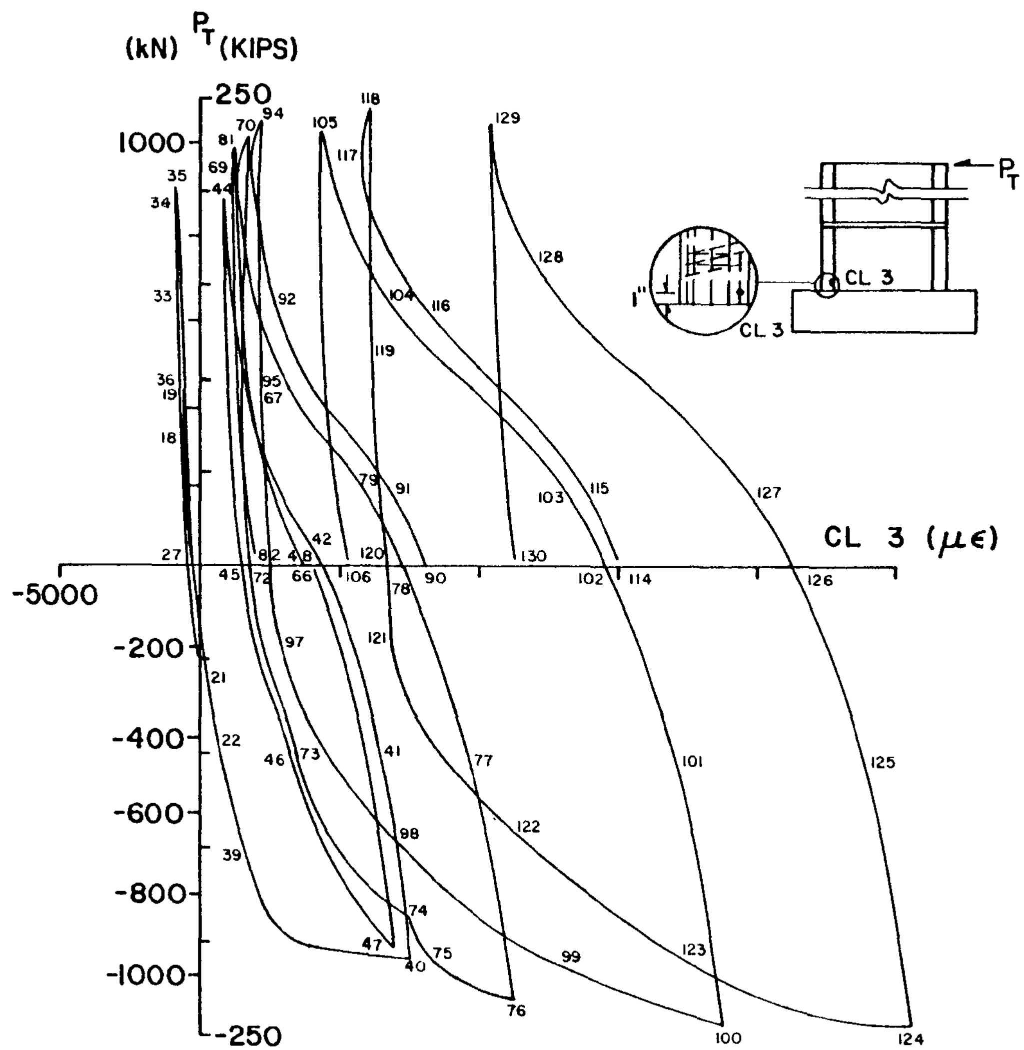

FIG. 5.62 P_T-CL 3 DIAGRAM - SHEAR WALL 2

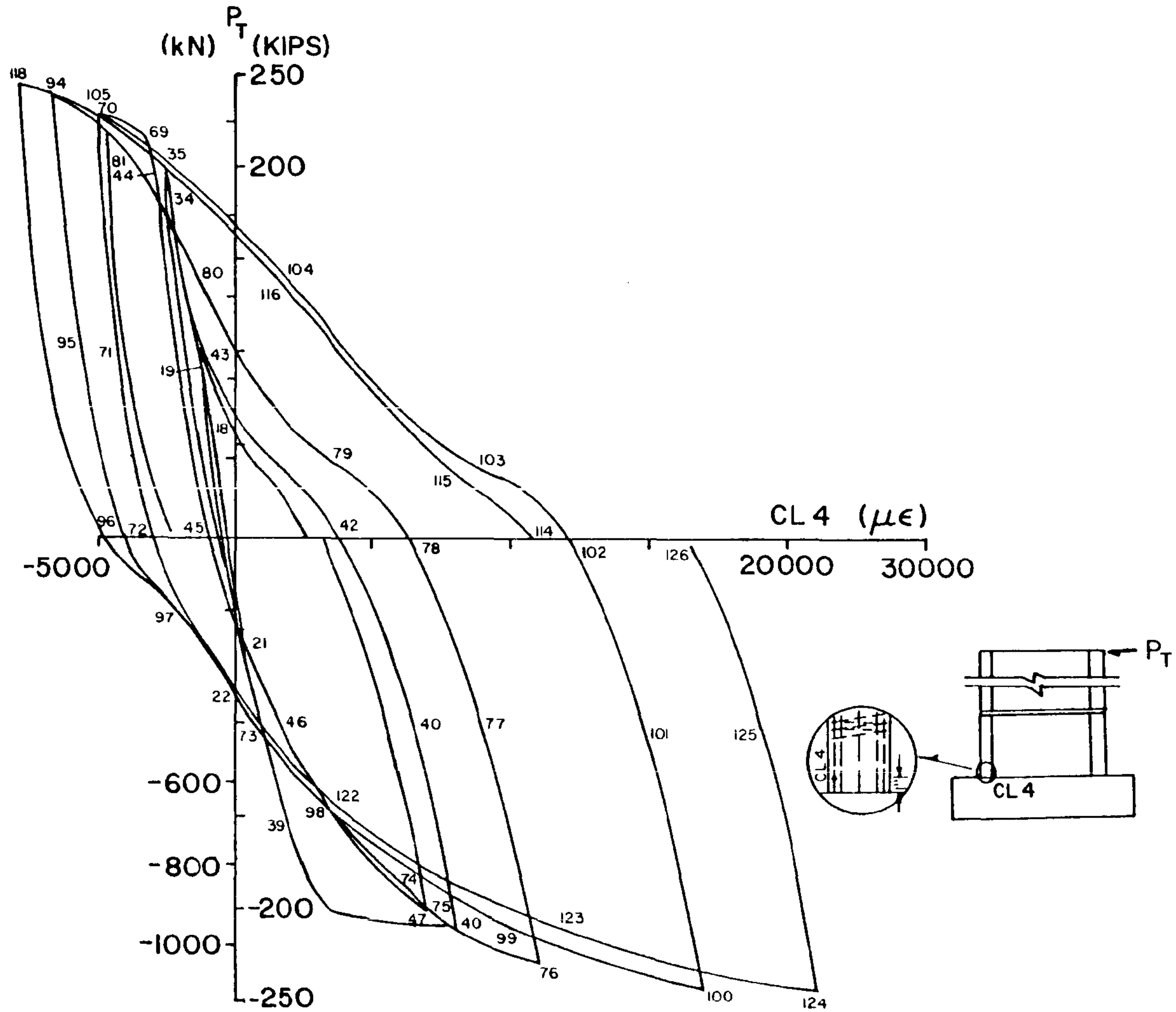

FIG. 5.63 P-CL 4 DIAGRAM - SHEAR WALL 2

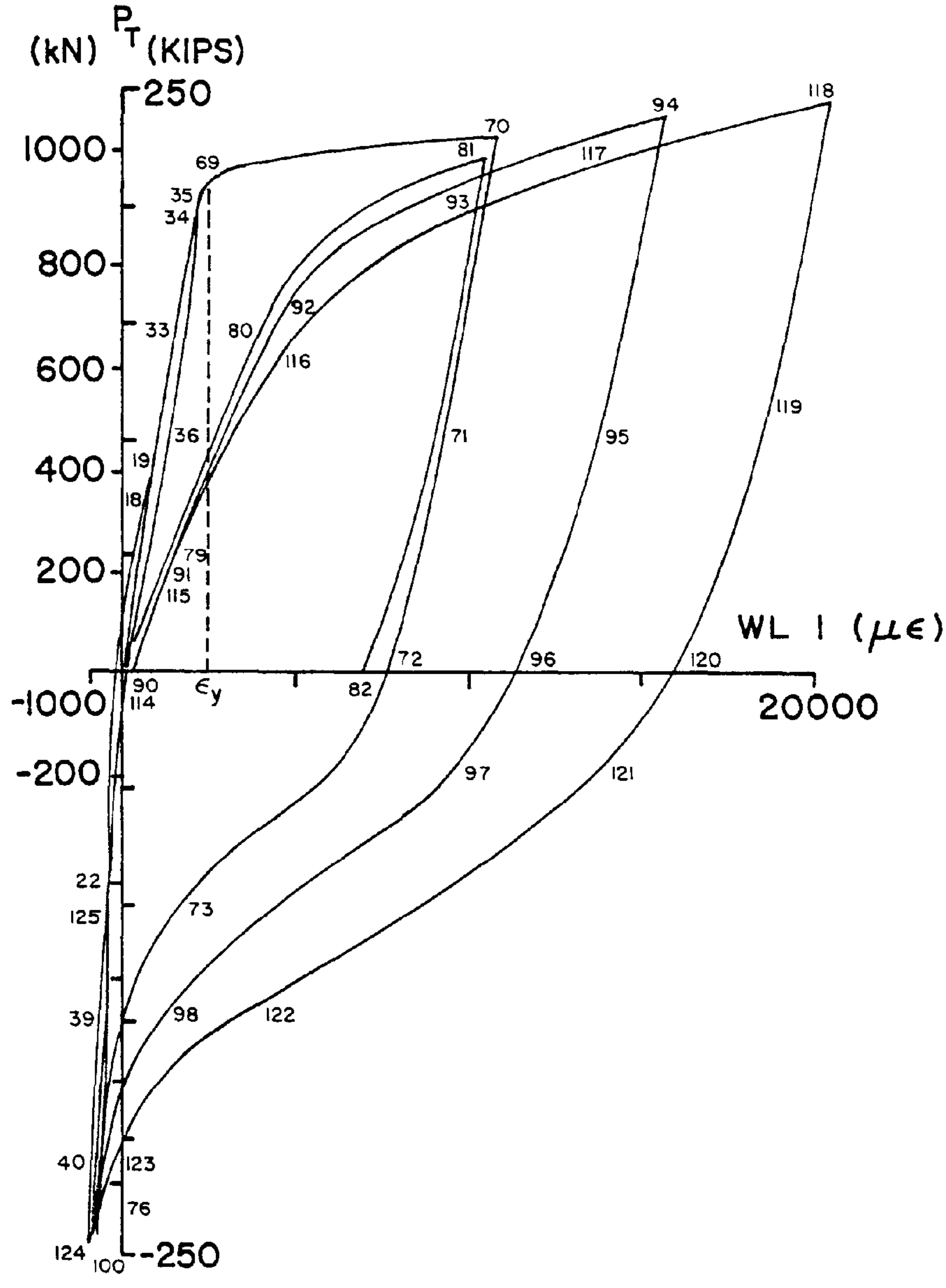

FIG. 5.64 P_T-WL 1 DIAGRAM - SHEAR WALL 2

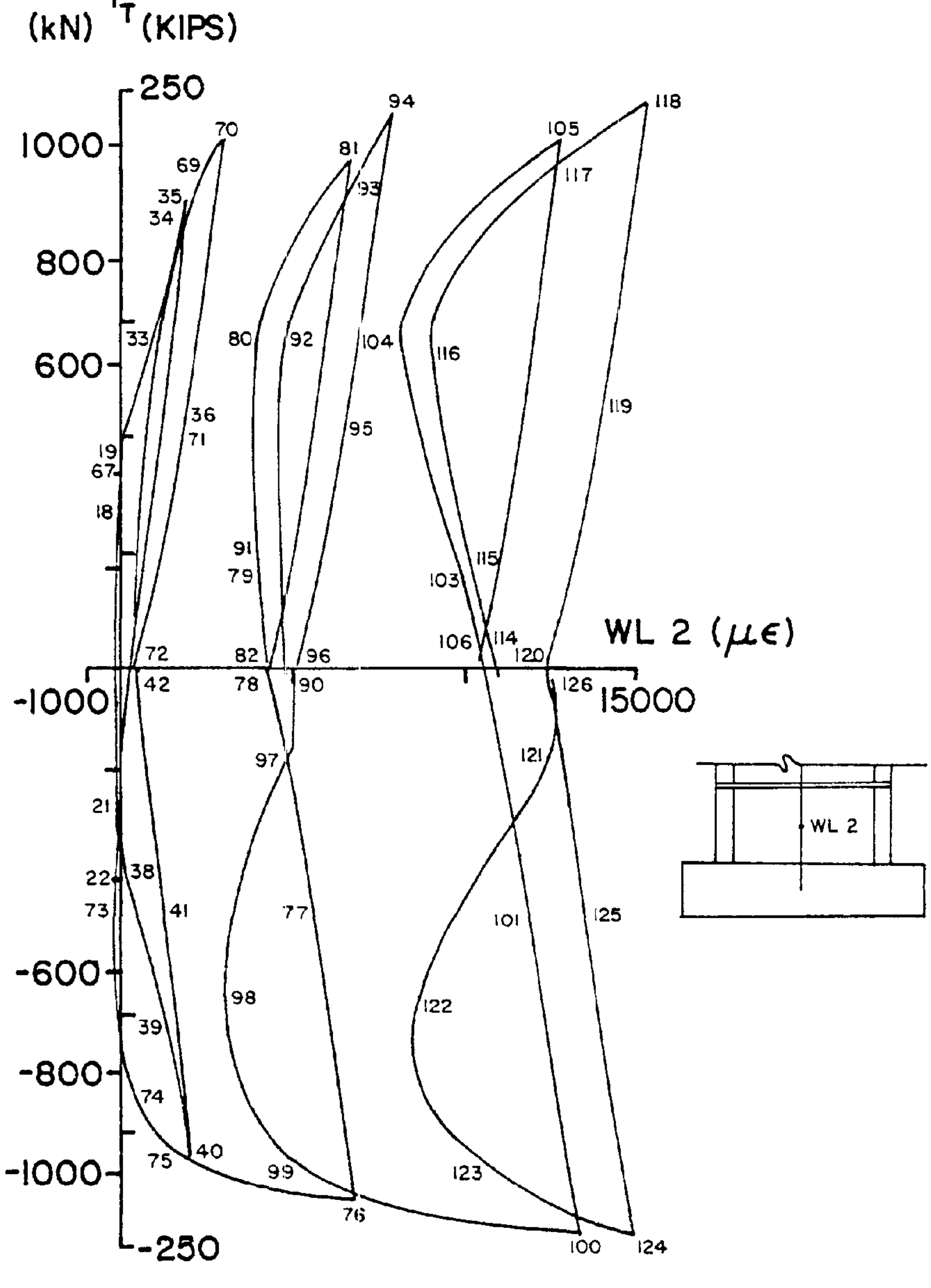

FIG. 5.65 P_T-WL 2 DIAGRAM - SHEAR WALL 2

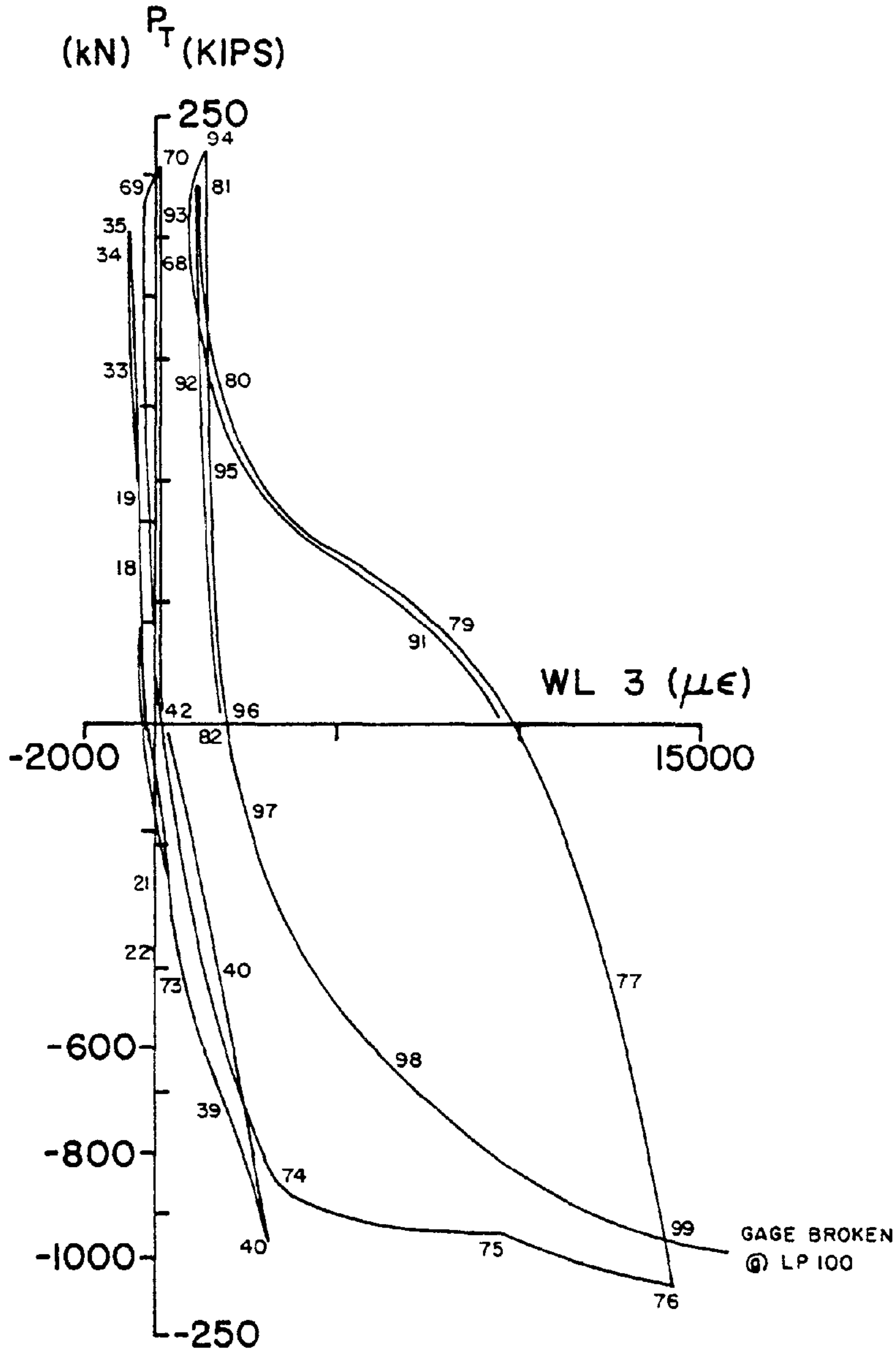

FIG. 5.66 P_T-WL 3 DIAGRAM - SHEAR WALL 2

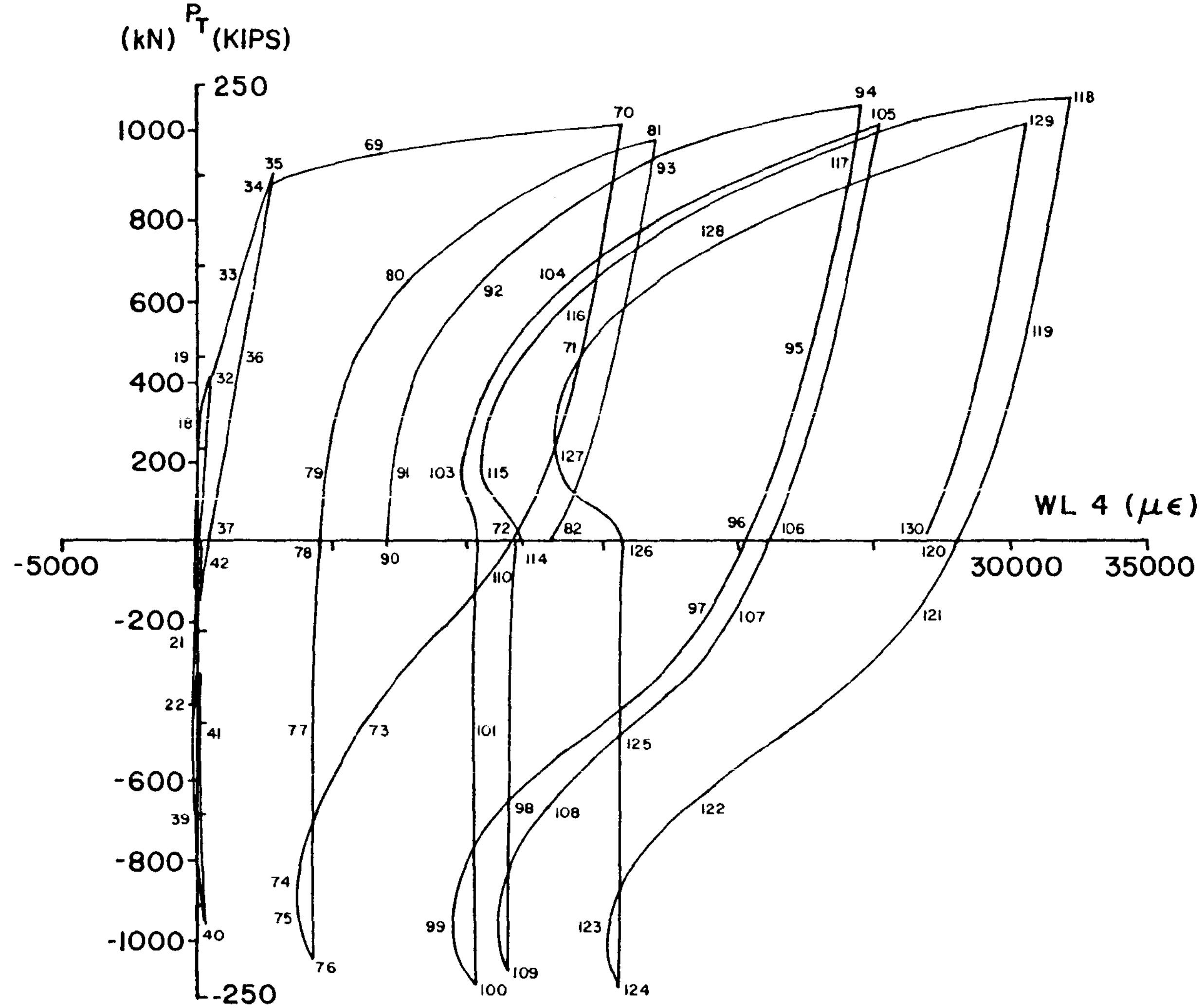

FIG. 5.67 P_T-WL 4 DIAGRAM - SHEAR WALL 2

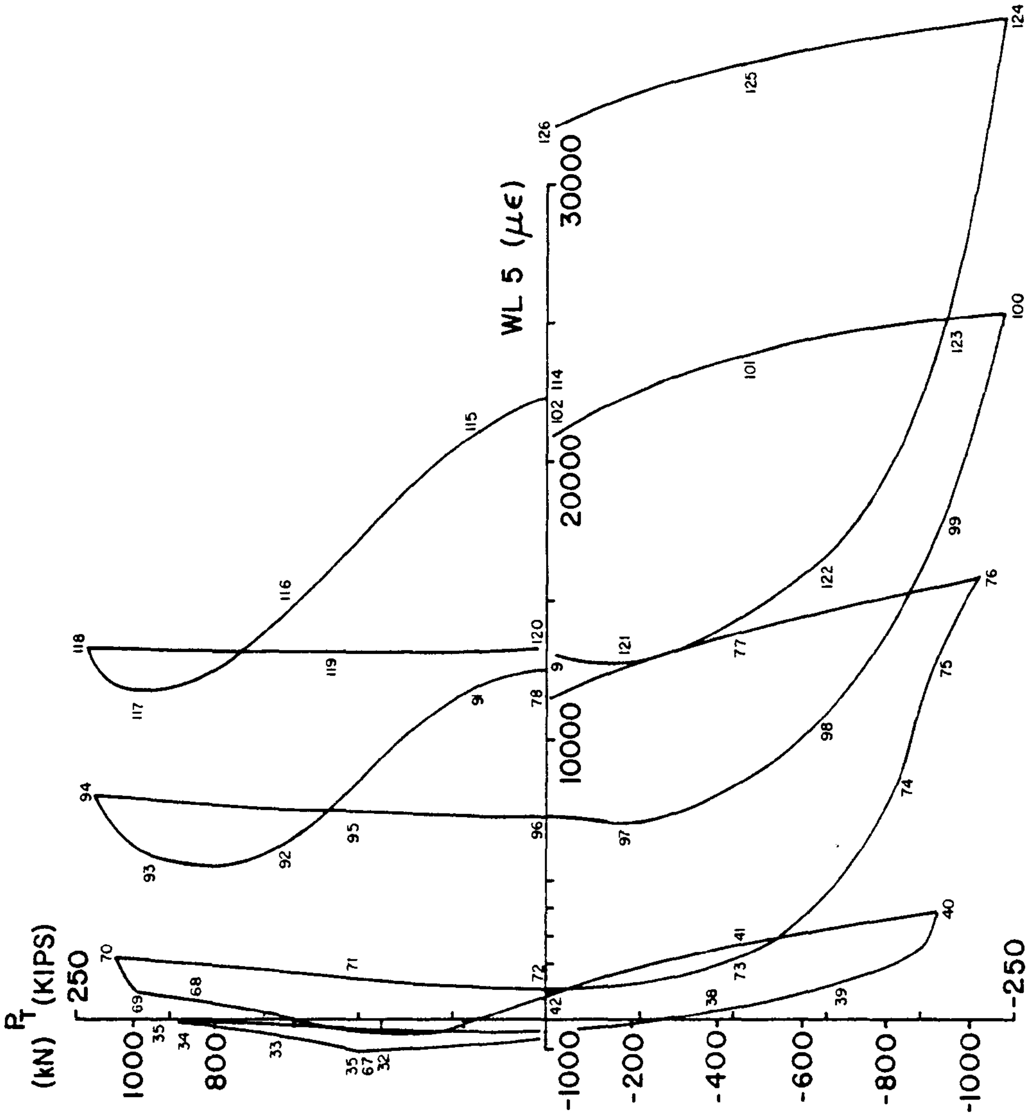

FIG. 5.68 P_T-WL 5 DIAGRAM - SHEAR WALL 2

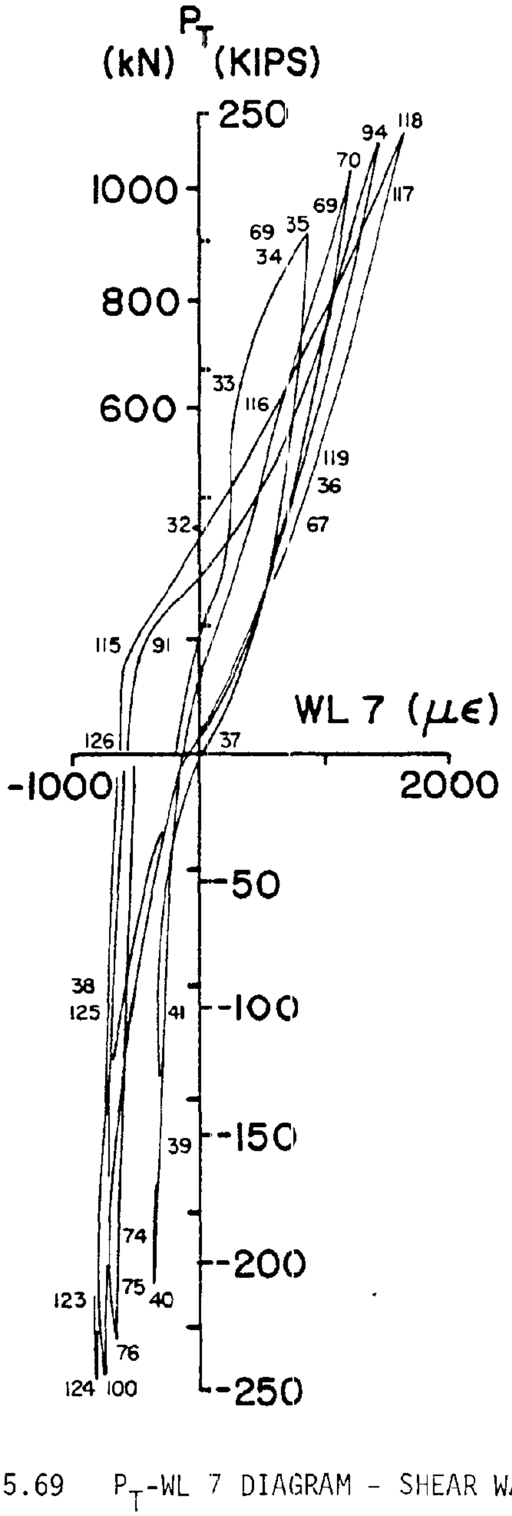

FIG. 5.69 P_T-WL 7 DIAGRAM - SHEAR WALL 2

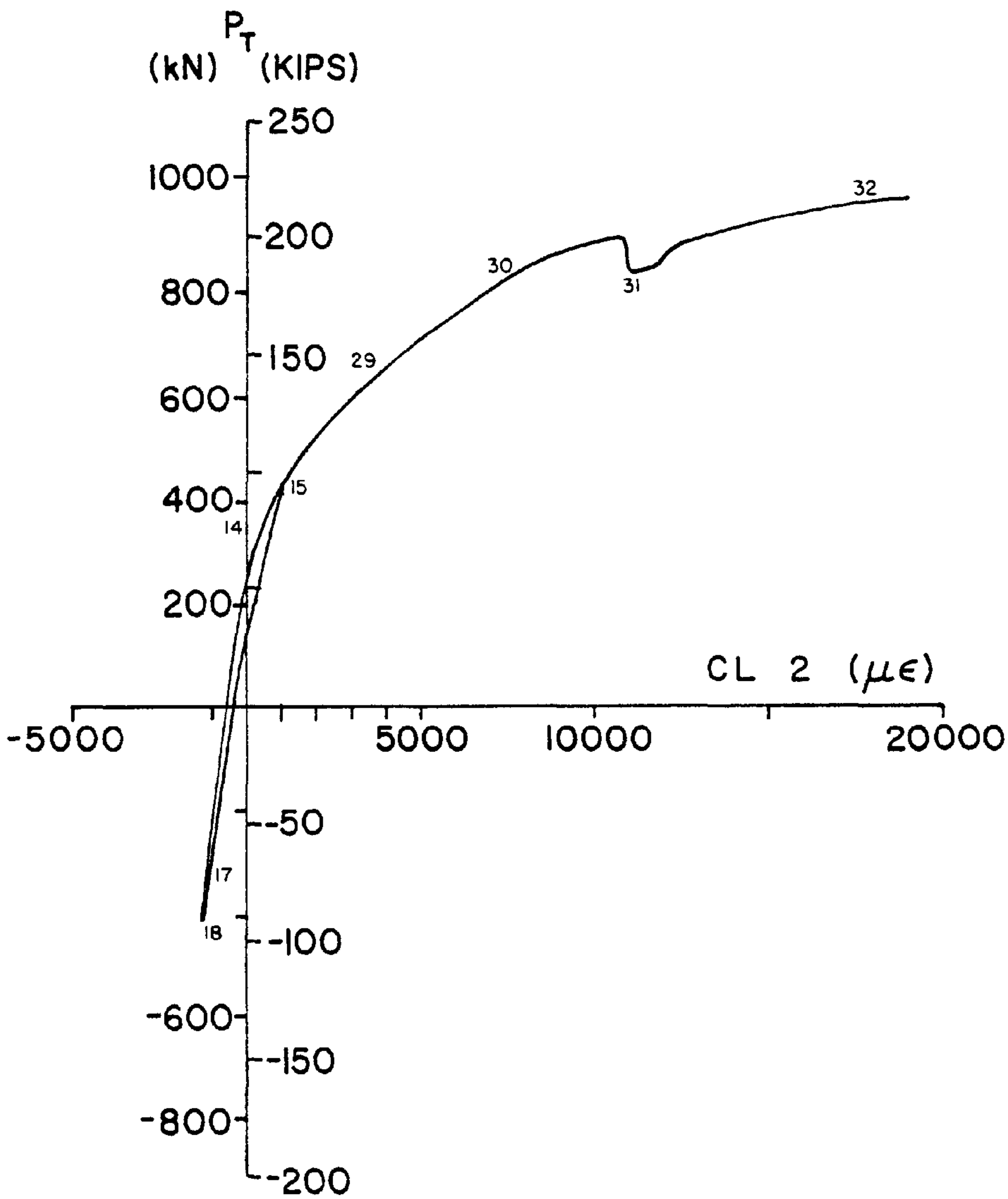

FIG. 5.70 P_T-CL 2 DIAGRAM - SHEAR WALL 2R

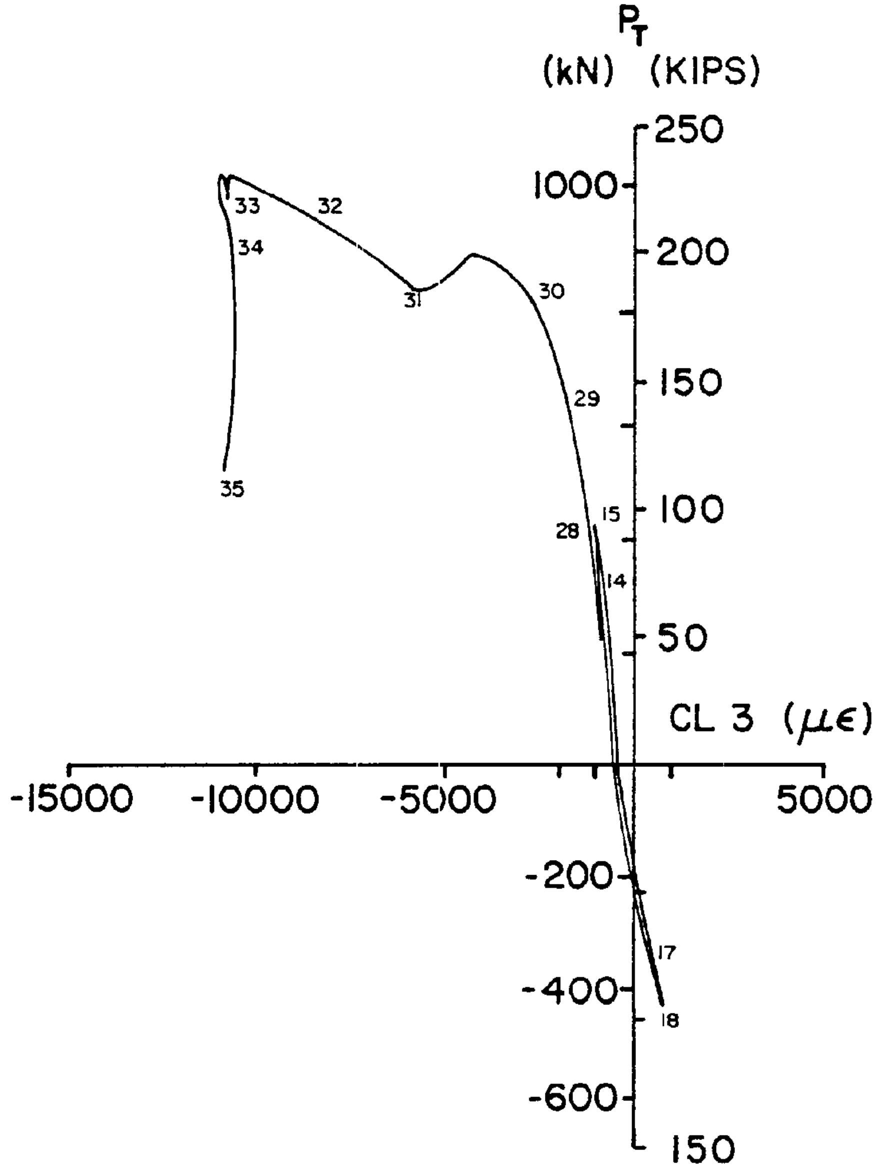

FIG. 5.71 P_T-CL 3 DIAGRAM - SHEAR WALL 2R

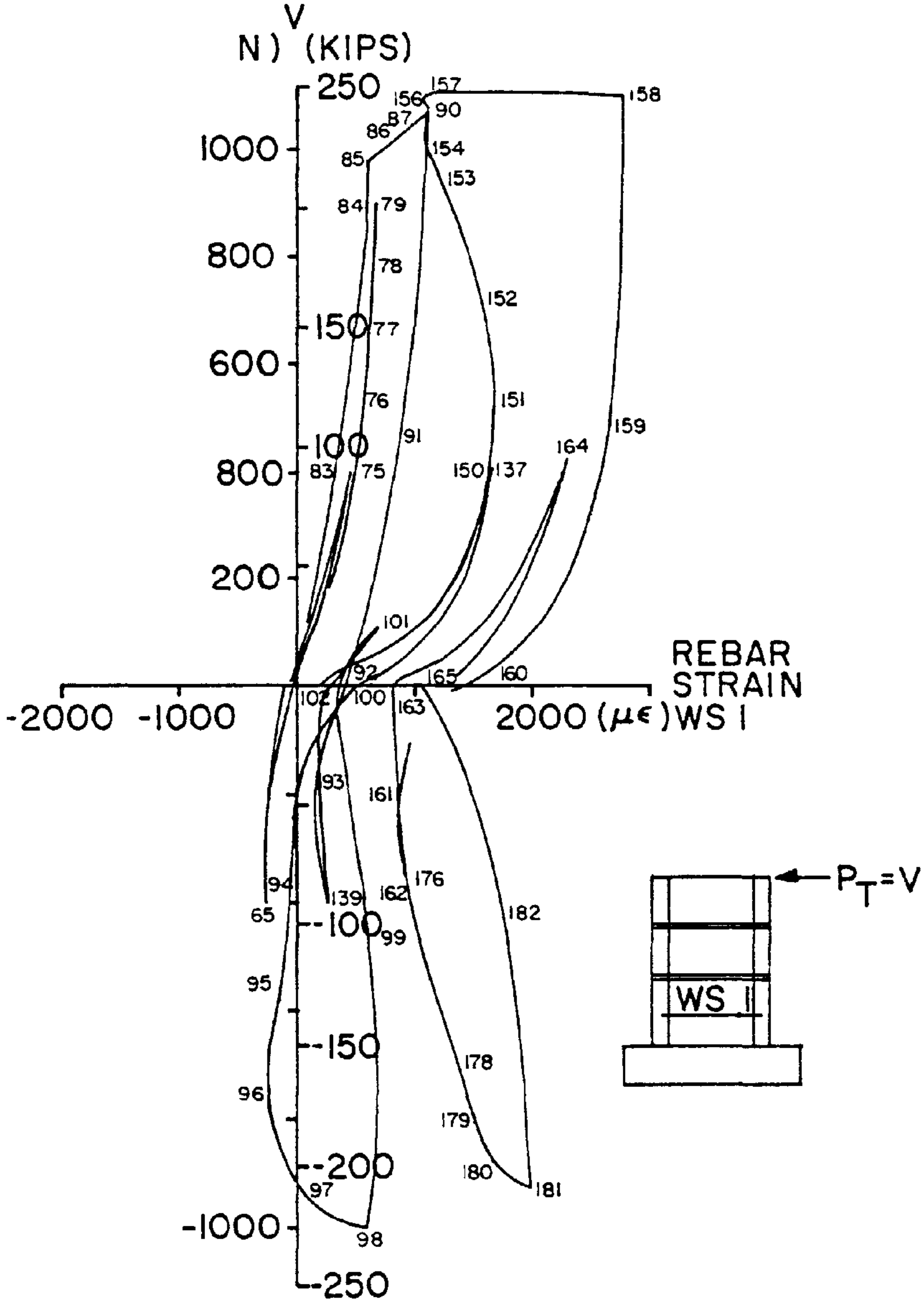

FIG. 5.72 V-WS 1 DIAGRAM - SHEAR WALL 1

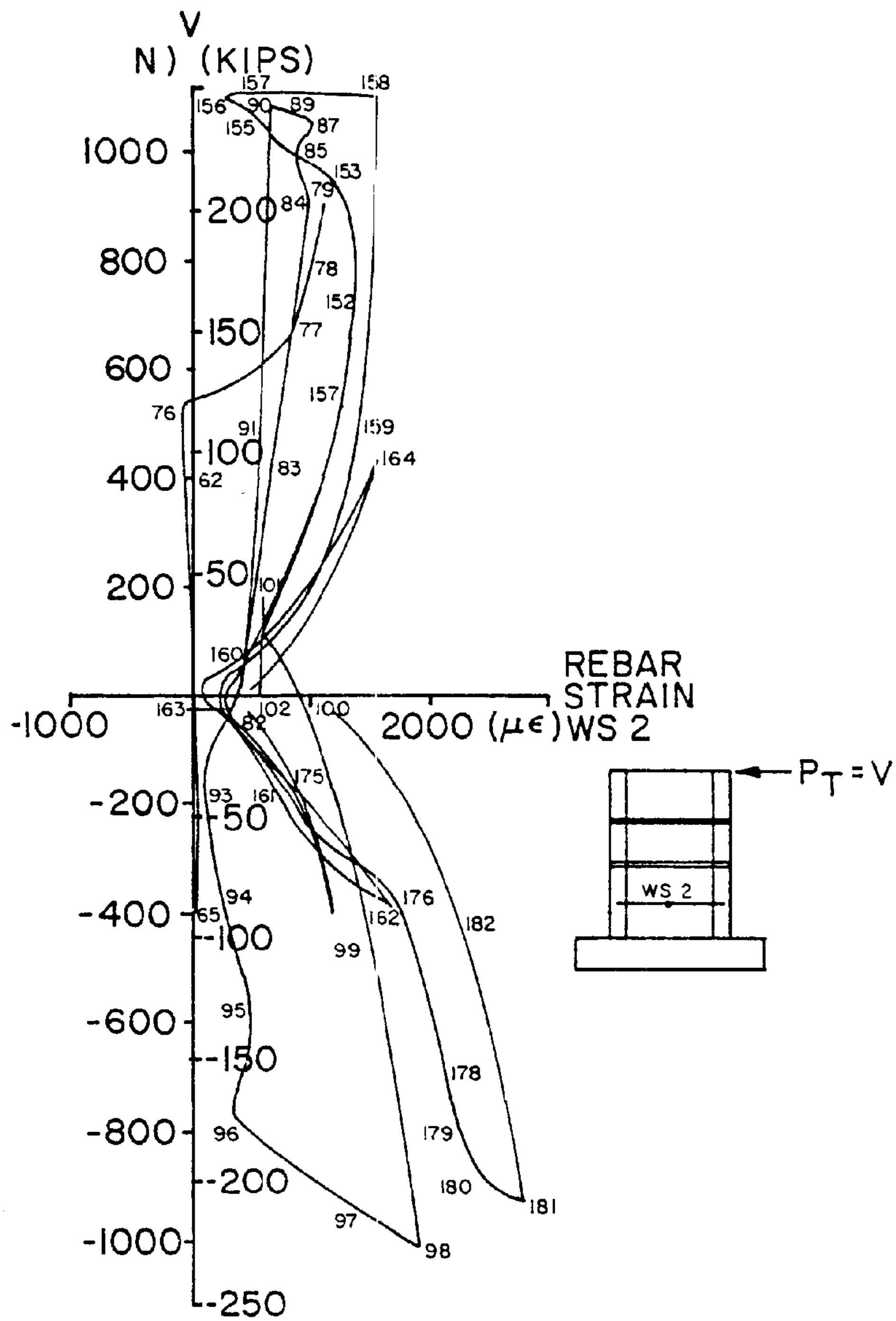

FIG. 5.73 V-WS 2 DIAGRAM - SHEAR WALL 1

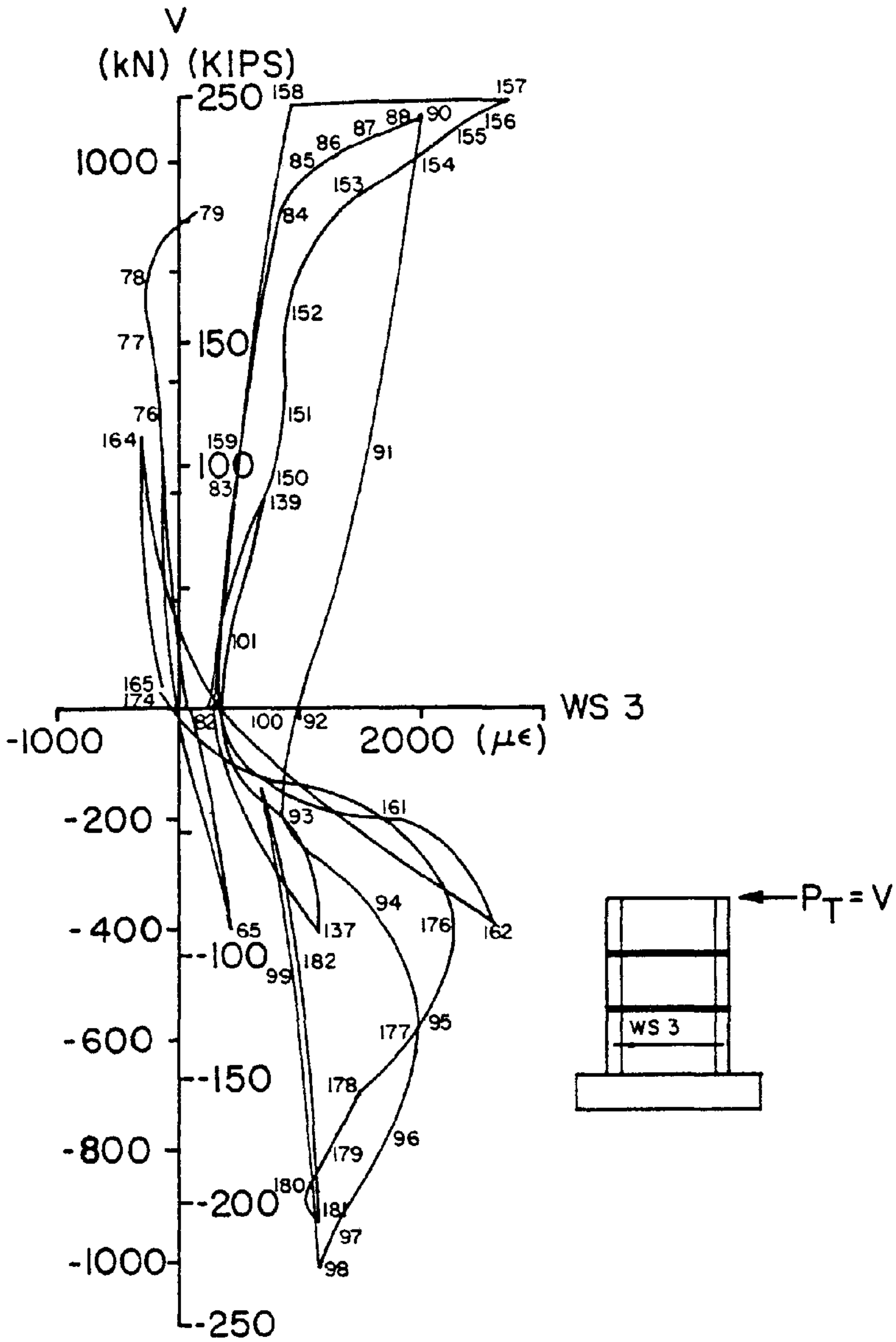

FIG. 5.74 V-WS 3 DIAGRAM - SHEAR WALL 1

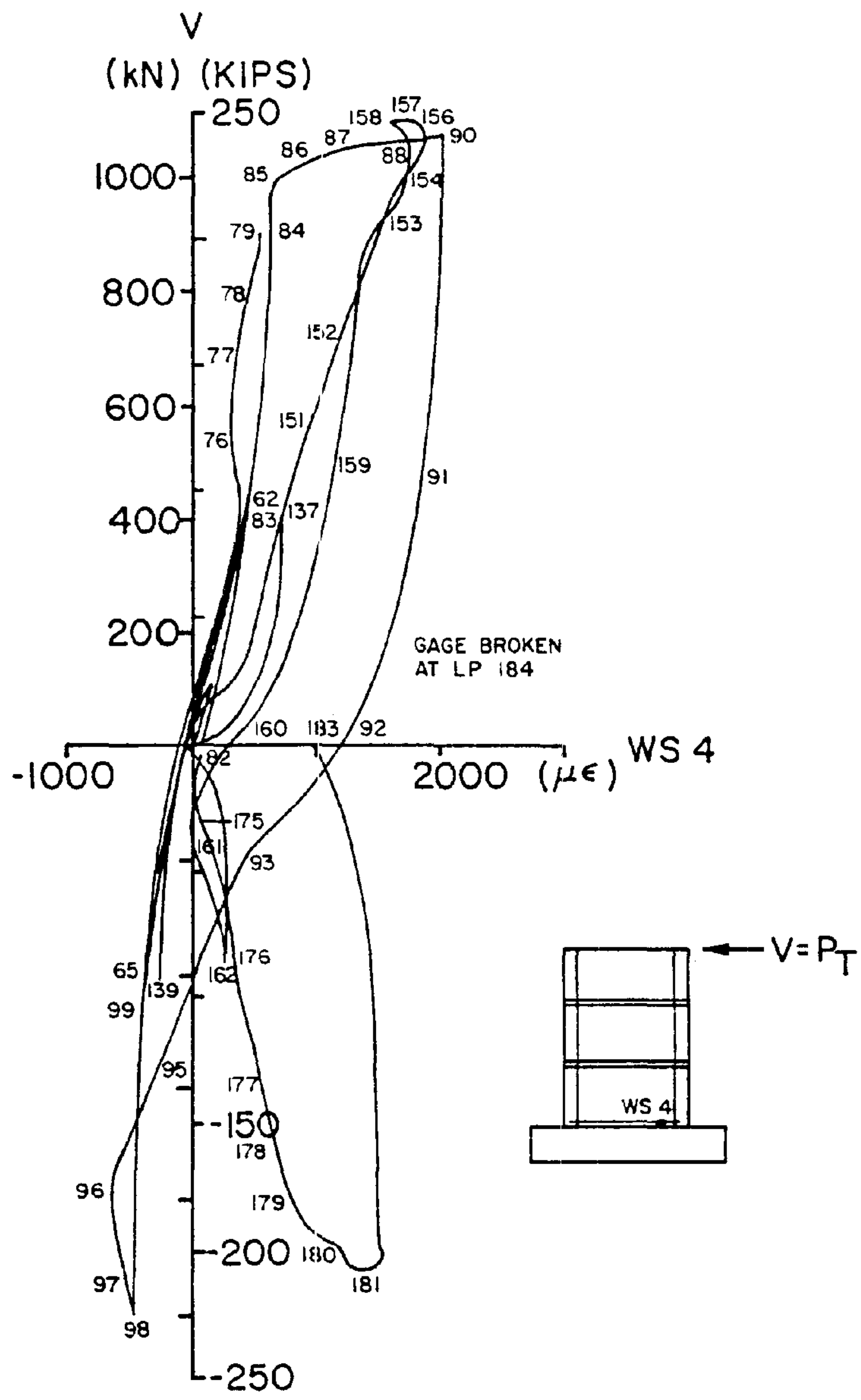

FIG. 5.75 V-WS 4 DIAGRAM - SHEAR WALL 1

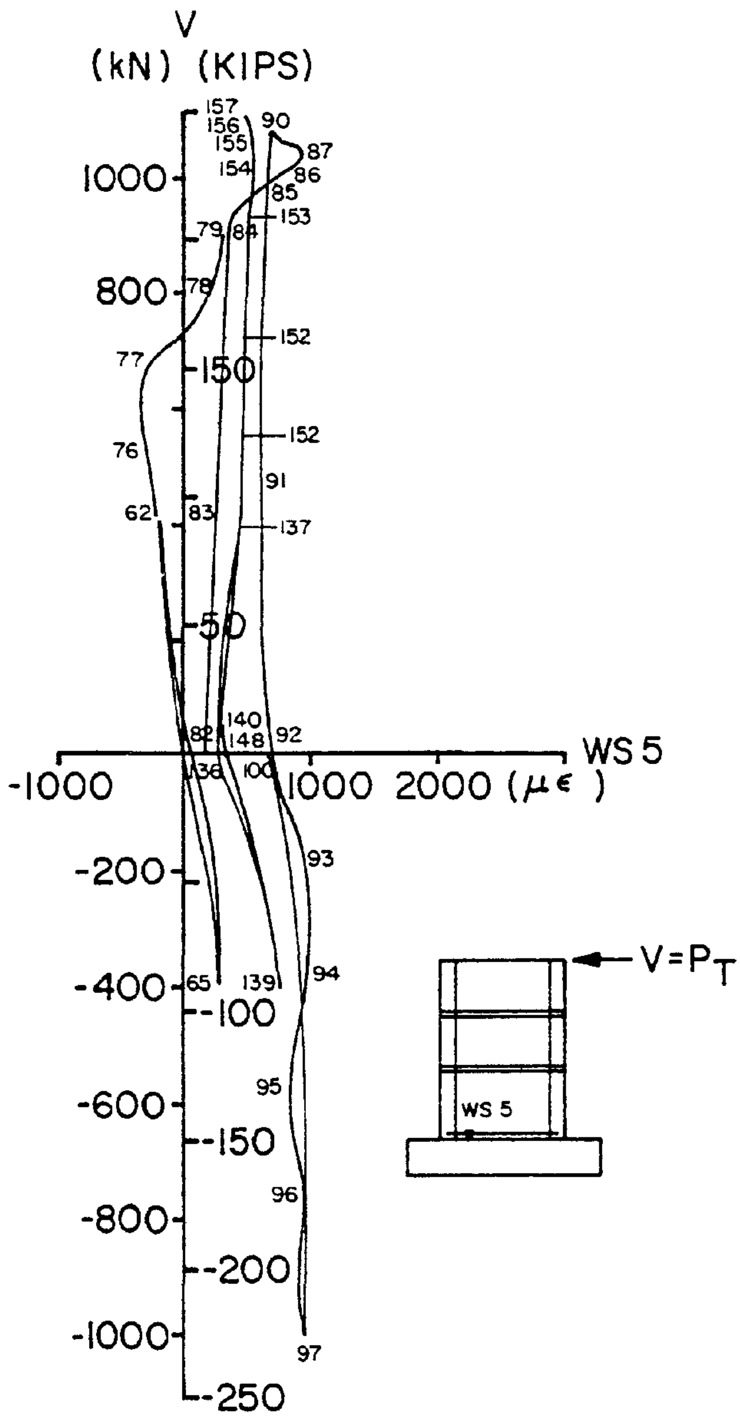

FIG. 5.76 V-WS 5 DIAGRAM - SHEAR WALL 1

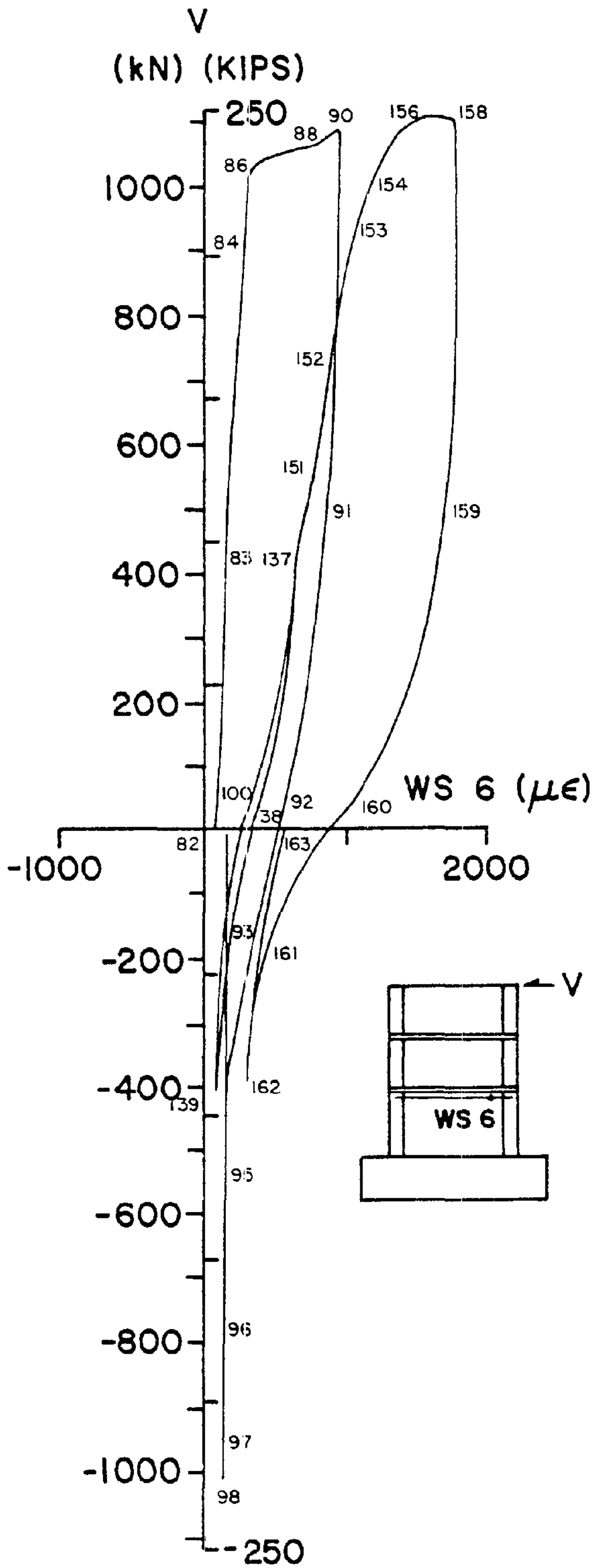

FIG. 5.77 V-WS 6 DIAGRAM - SHEAR WALL 1

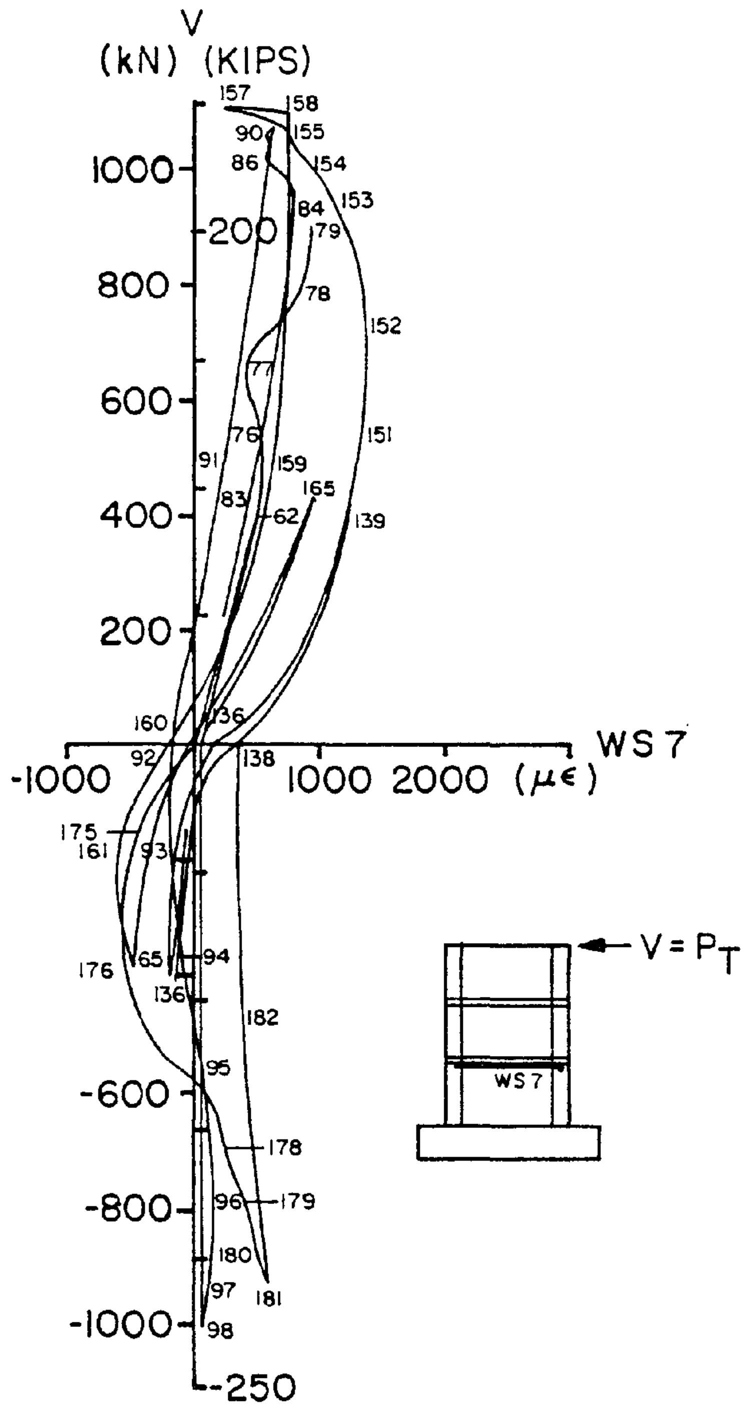

FIG. 5.78 V-WS 7 DIAGRAM - SHEAR WALL 1

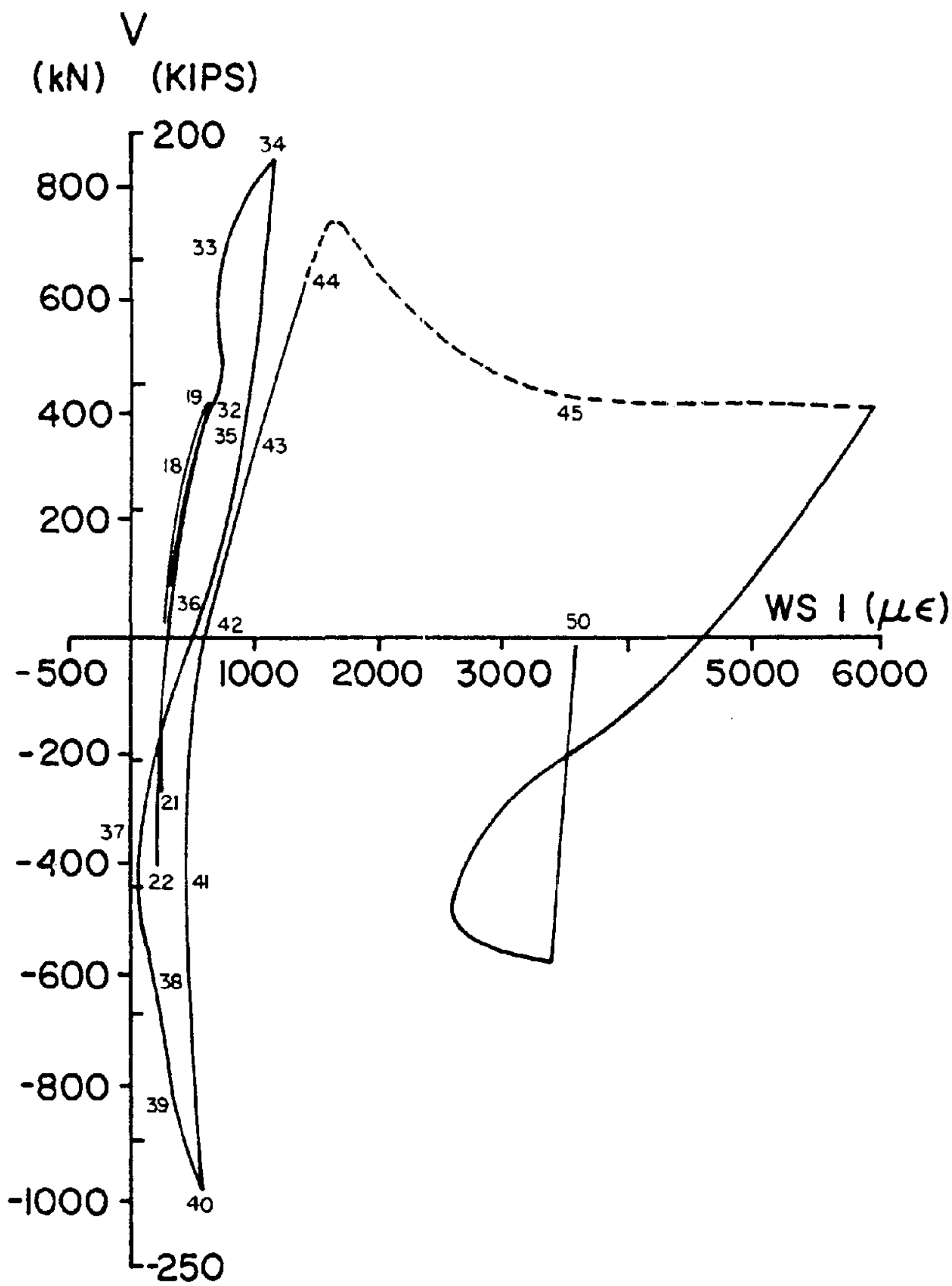

FIG. 5.79 V-WS 1 DIAGRAM - SHEAR WALL 1R

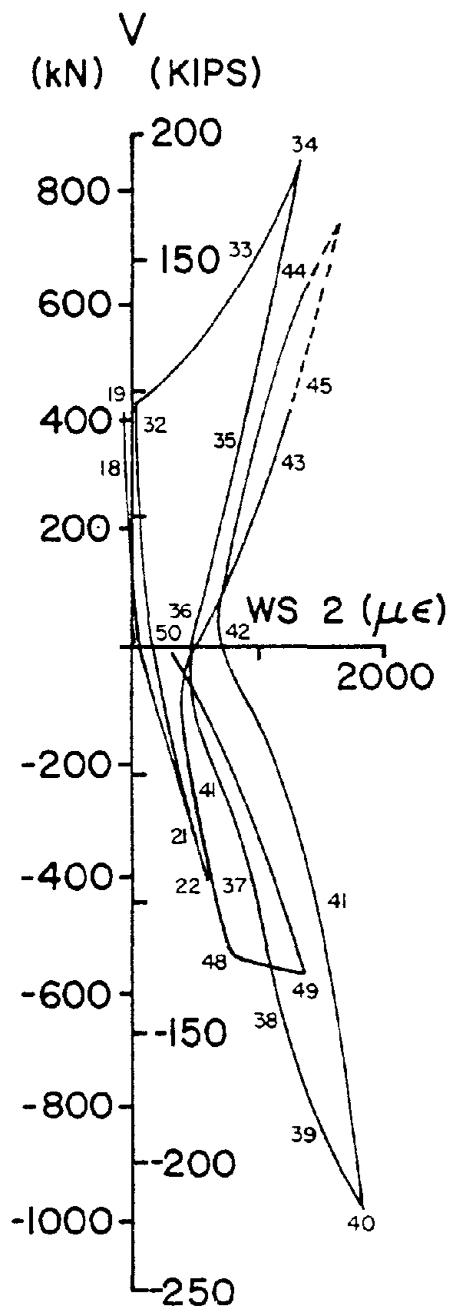

FIG. 5.80 V-WS 2 DIAGRAM - SHEAR WALL 1R

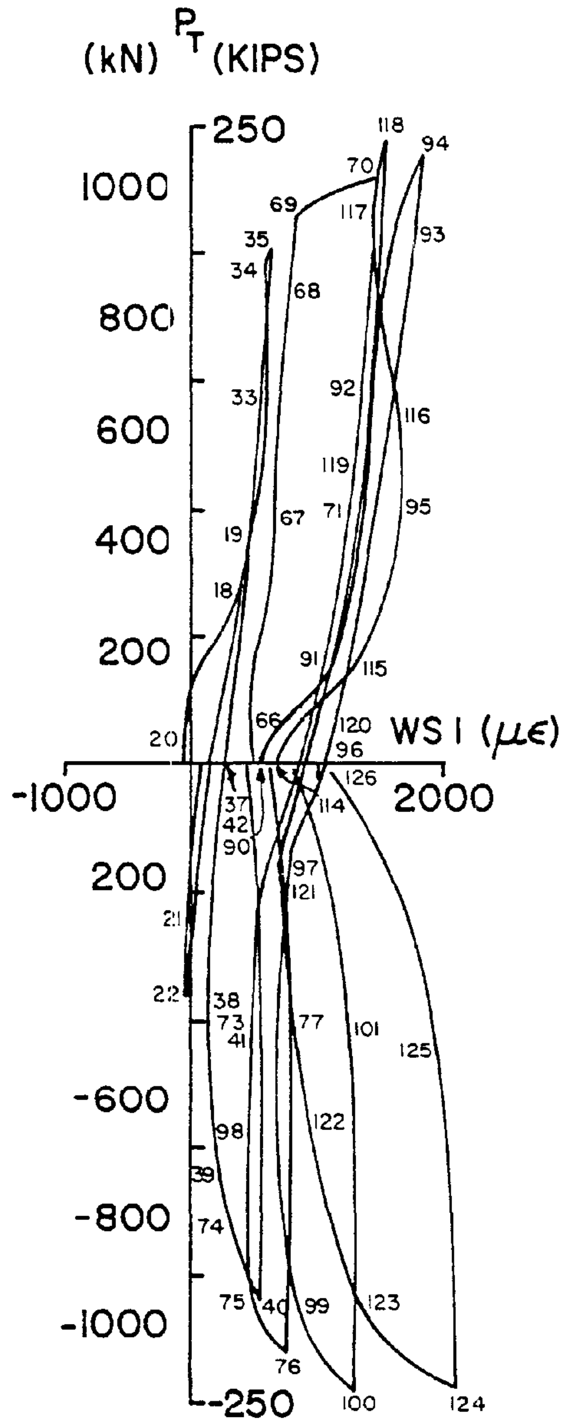

FIG. 5.81 V-WS 1 DIAGRAM - SHEAR WALL 2

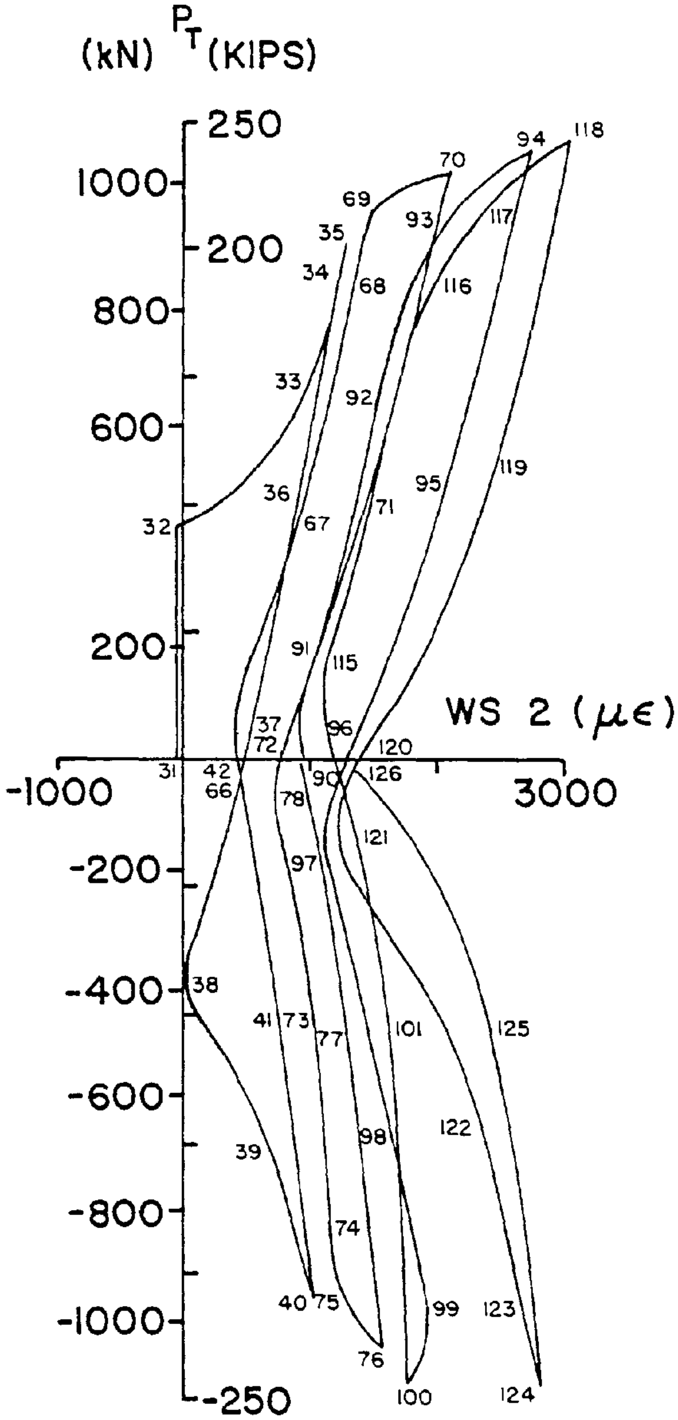

FIG. 5.82 V-WS 2 DIAGRAM - SHEAR WALL 2

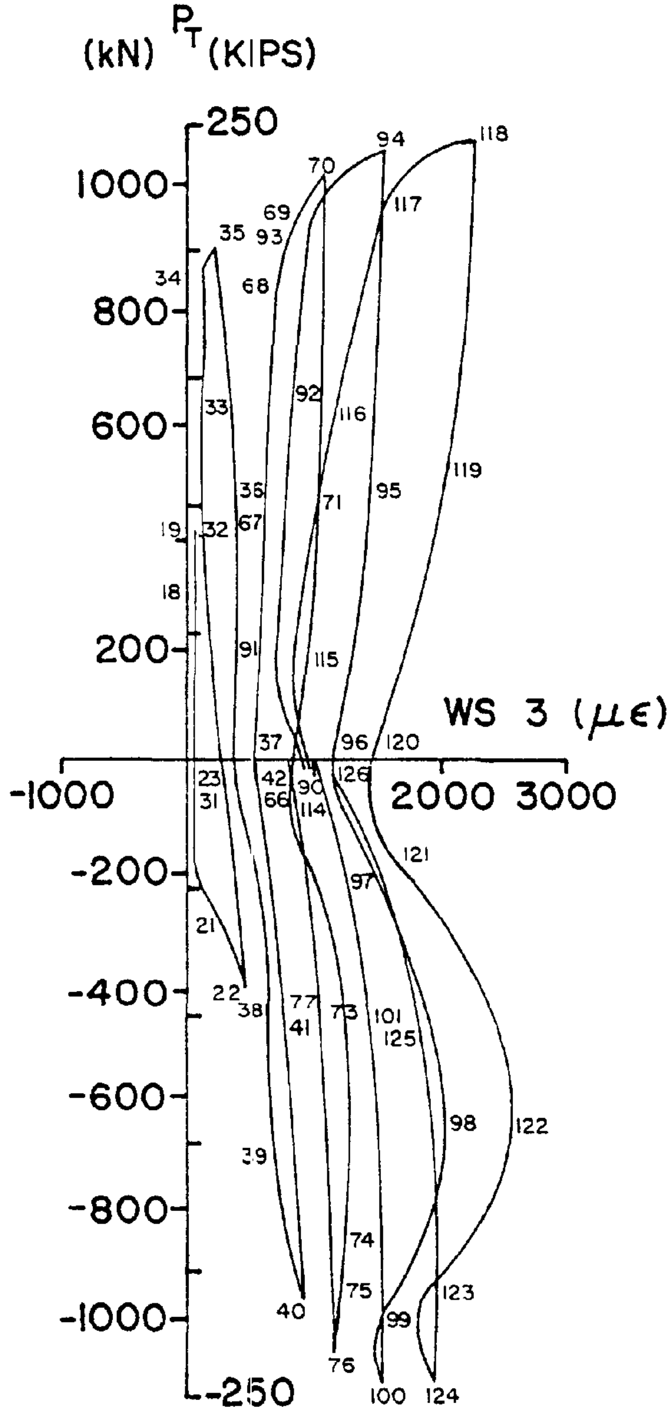

FIG. 5.83 V-WS 3 DIAGRAM - SHEAR WALL 2

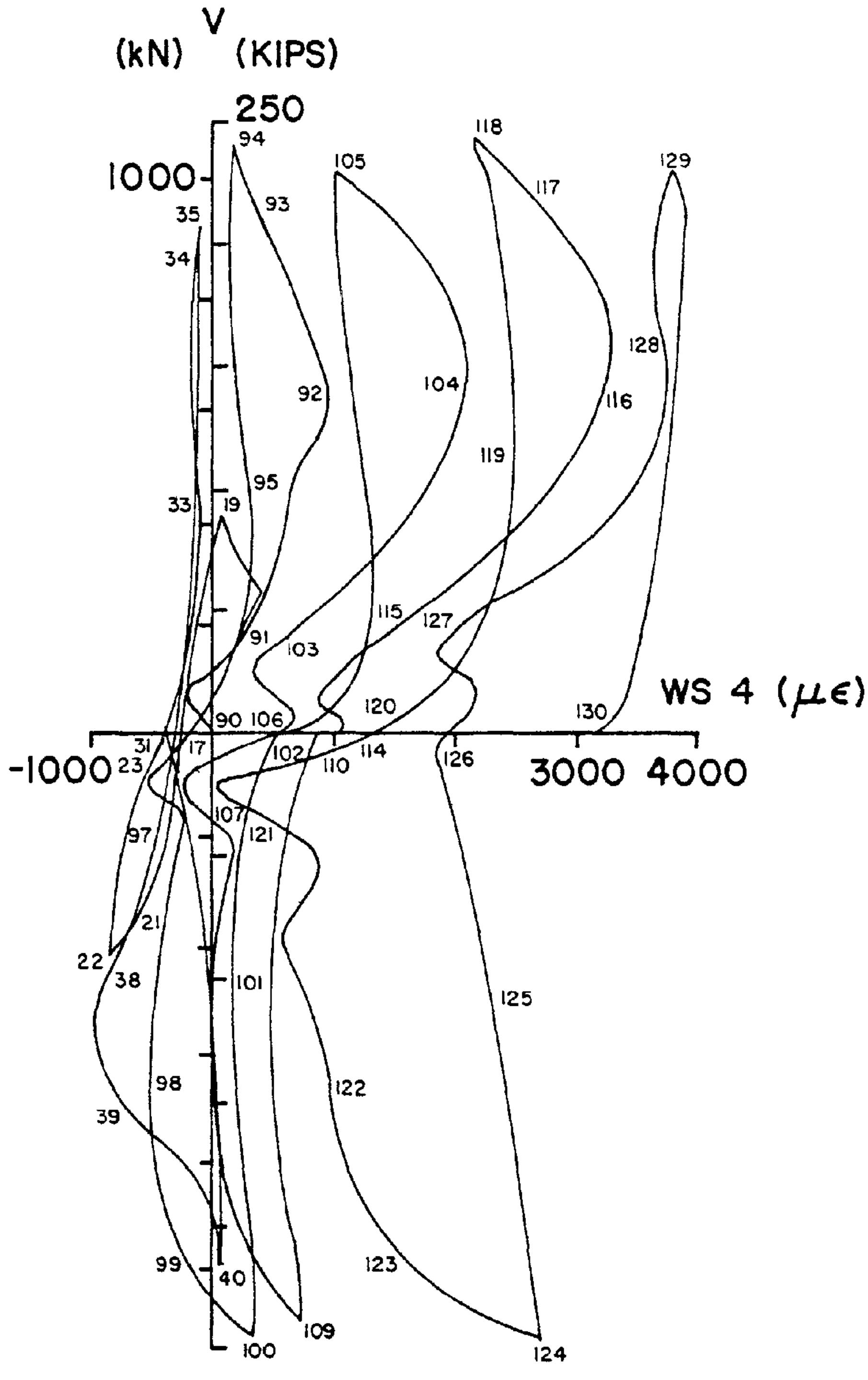

FIG. 5.84 V-WS 4 DIAGRAM - SHEAR WALL 2

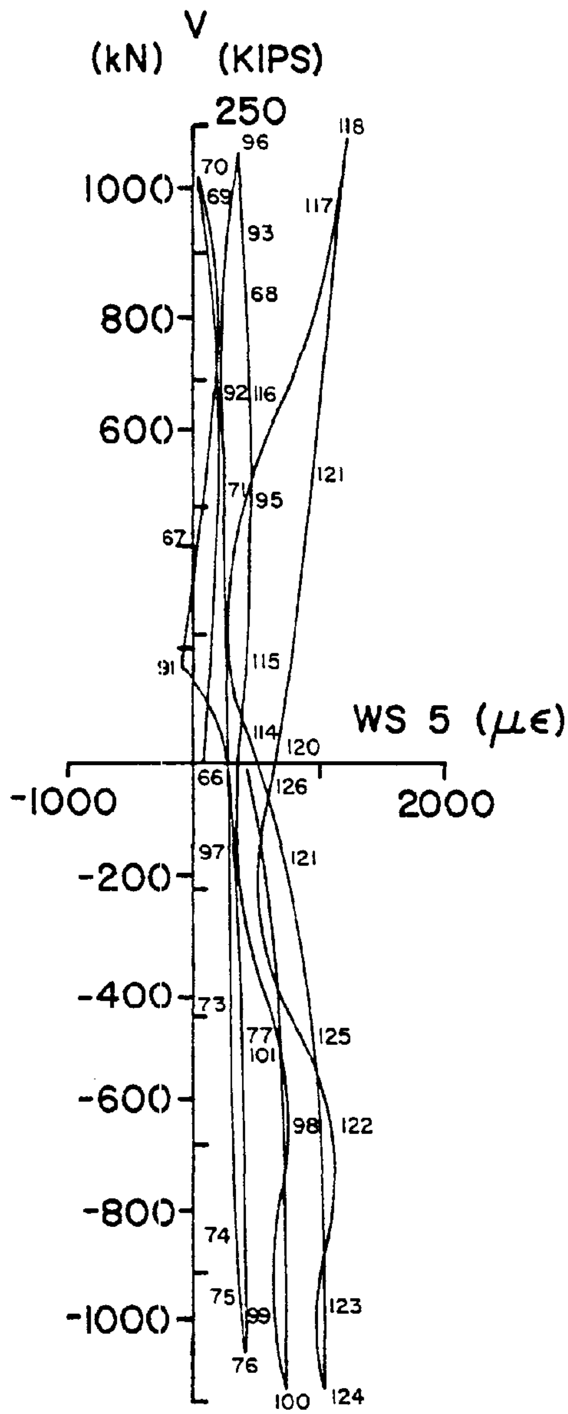

FIG. 5.85 V-WS 5 DIAGRAM - SHEAR WALL 2

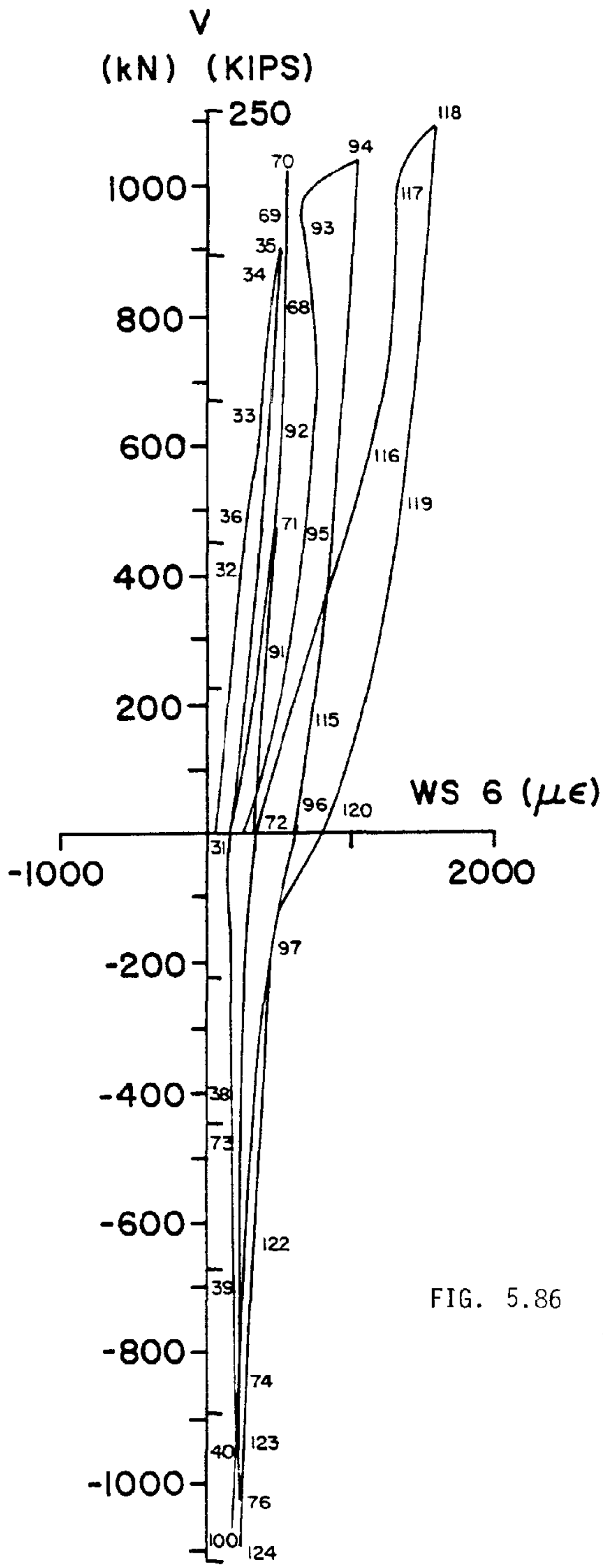

FIG. 5.86 V-WS 6 DIAGRAM - SHEAR WALL 2

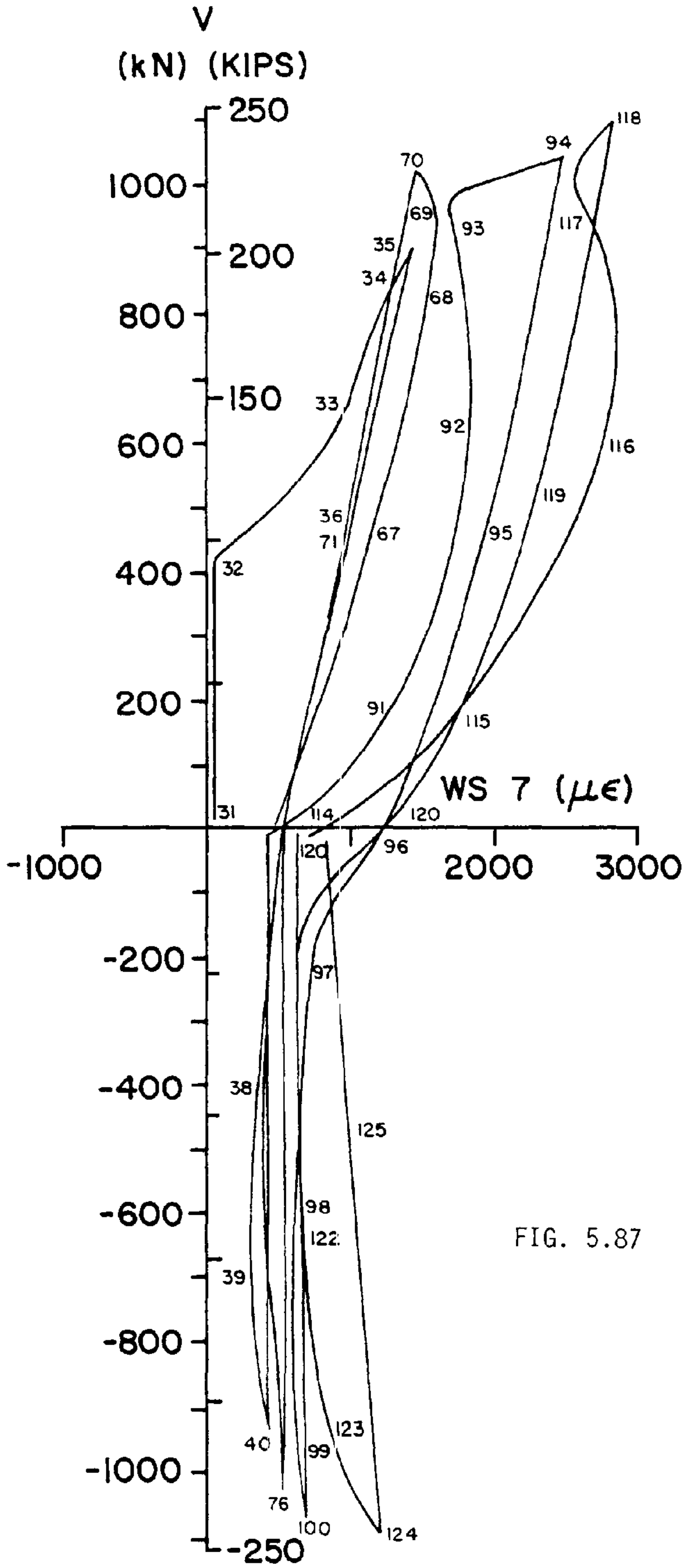

FIG. 5.87 V-WS 7 DIAGRAM - SHEAR WALL 2

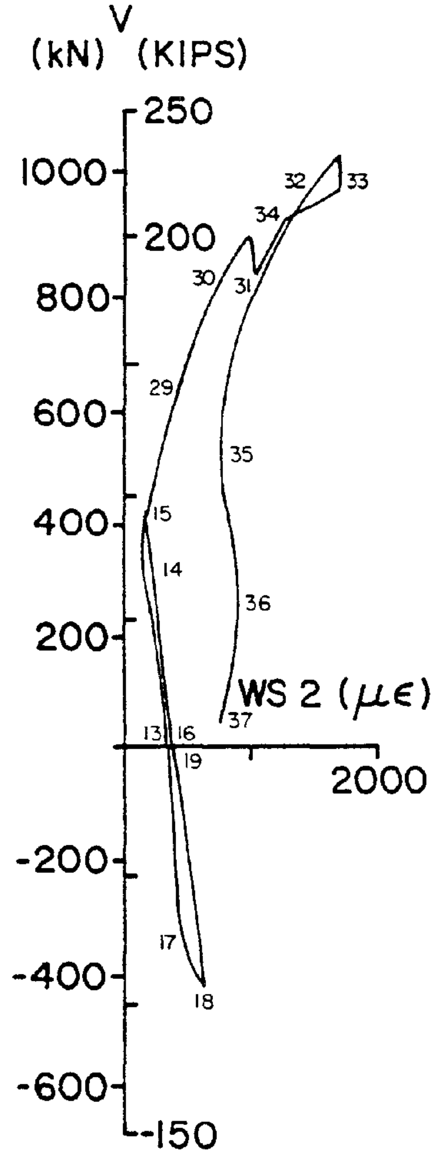

FIG. 5.88 V-WS 2 DIAGRAM - SHEAR WALL 2R

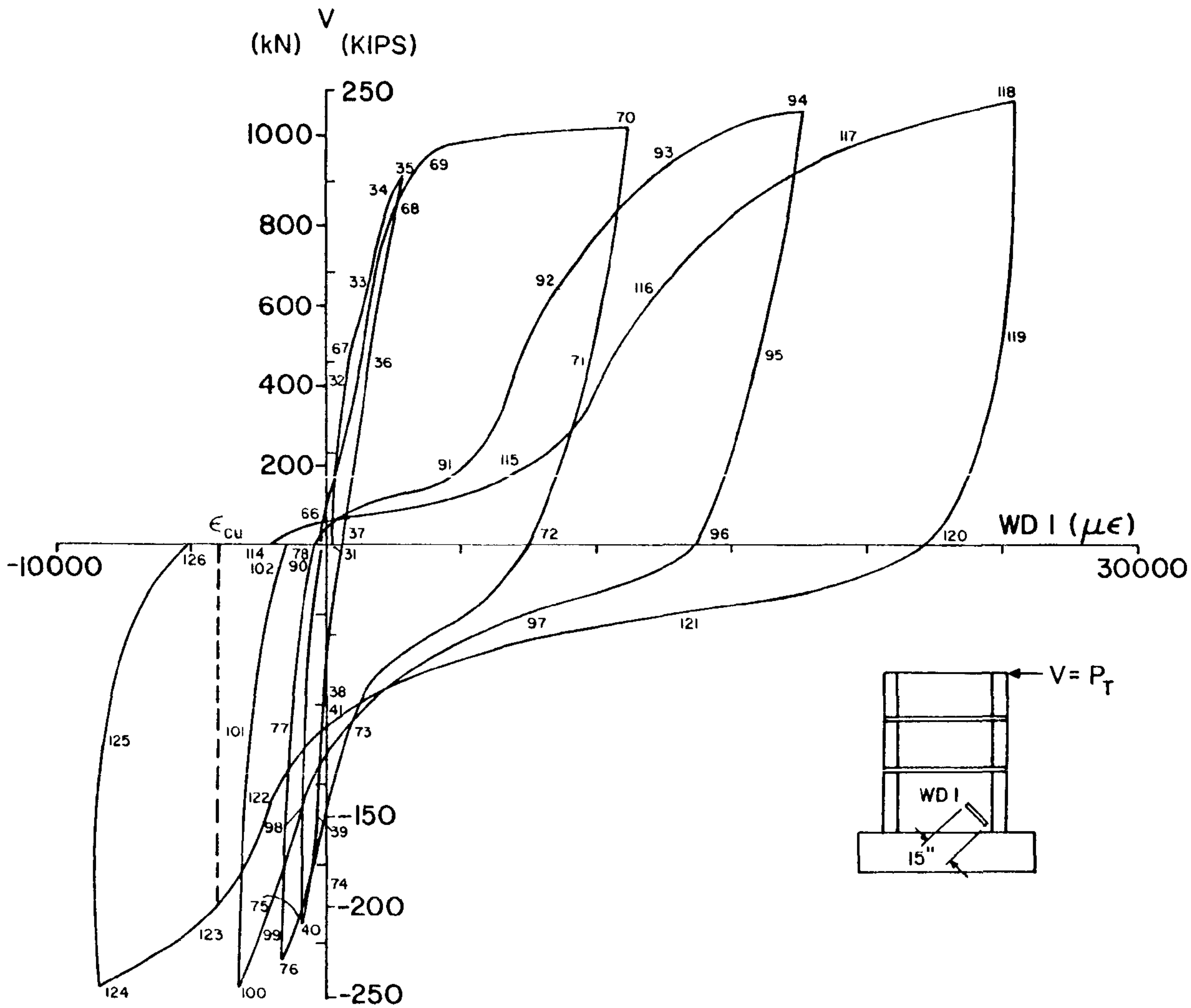

FIG. 5.89 V-WD 1 DIAGRAM - SHEAR WALL 2

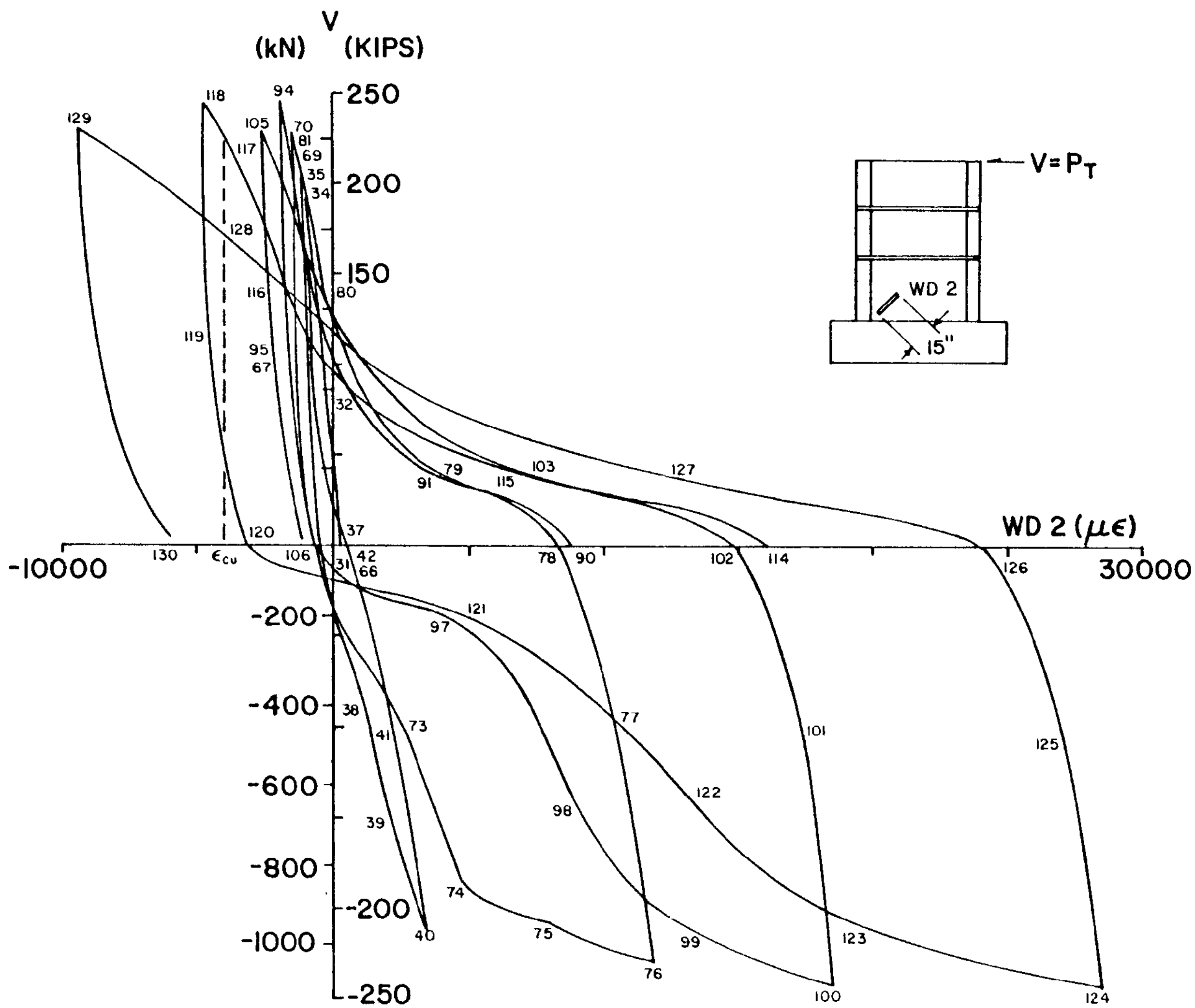

FIG. 5.90 V-WD 2 DIAGRAM - SHEAR WALL 2

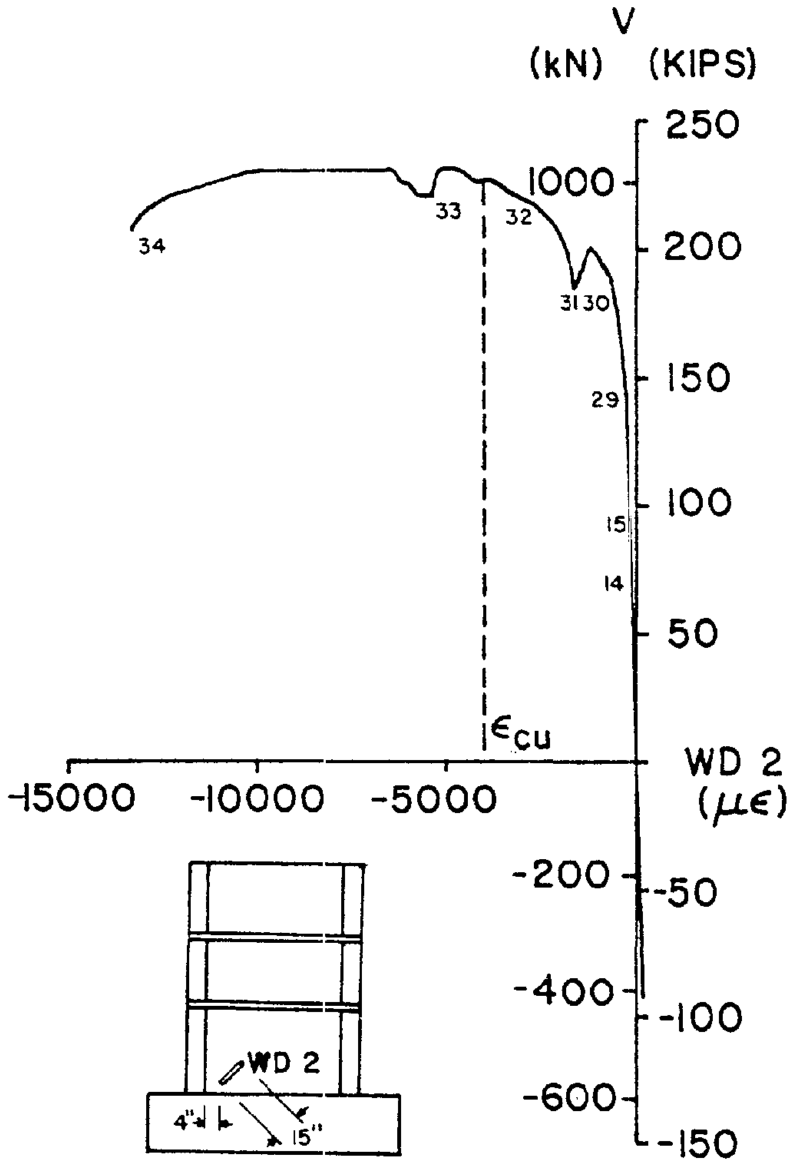

FIG. 5.91 V-WD 2 DIAGRAM - SHEAR WALL 2R

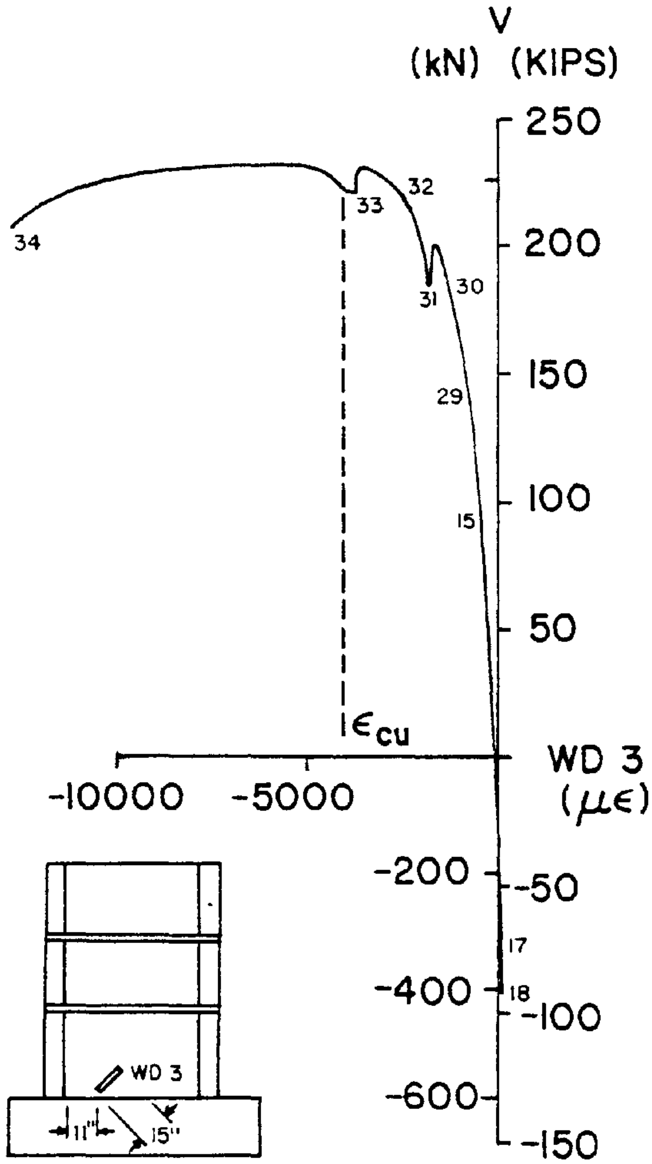

FIG. 5.92 V-WD 3 DIAGRAM - SHEAR WALL 2R

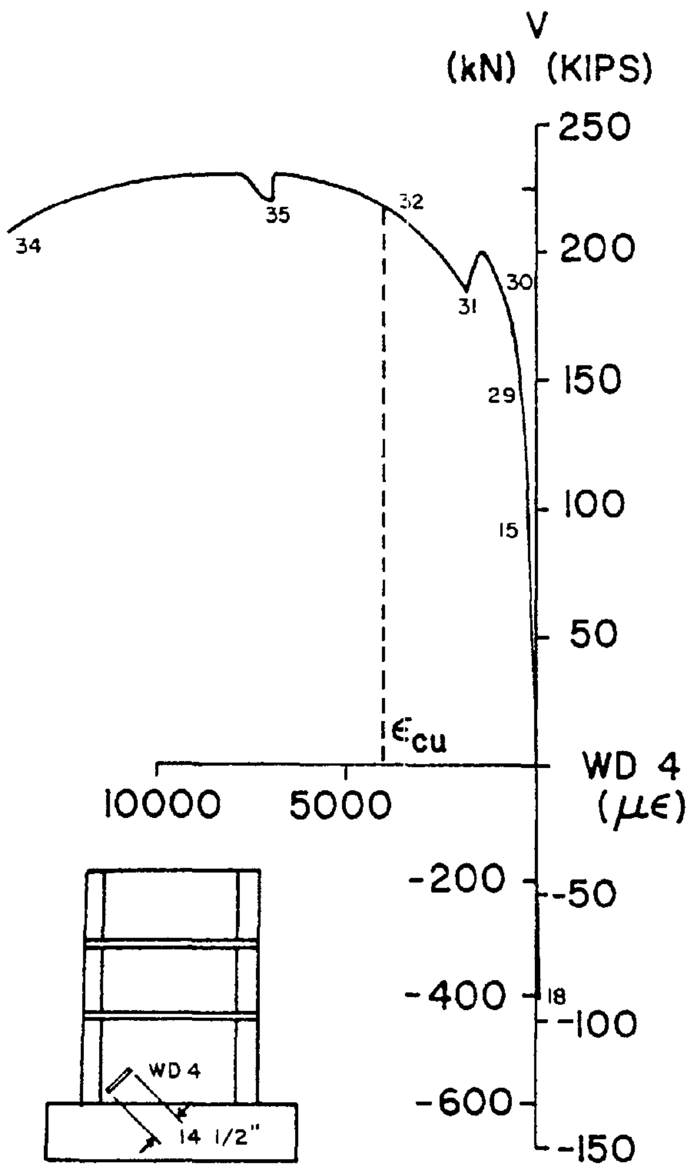

FIG. 5.93 V-WD 4 DIAGRAM - SHEAR WALL 2R

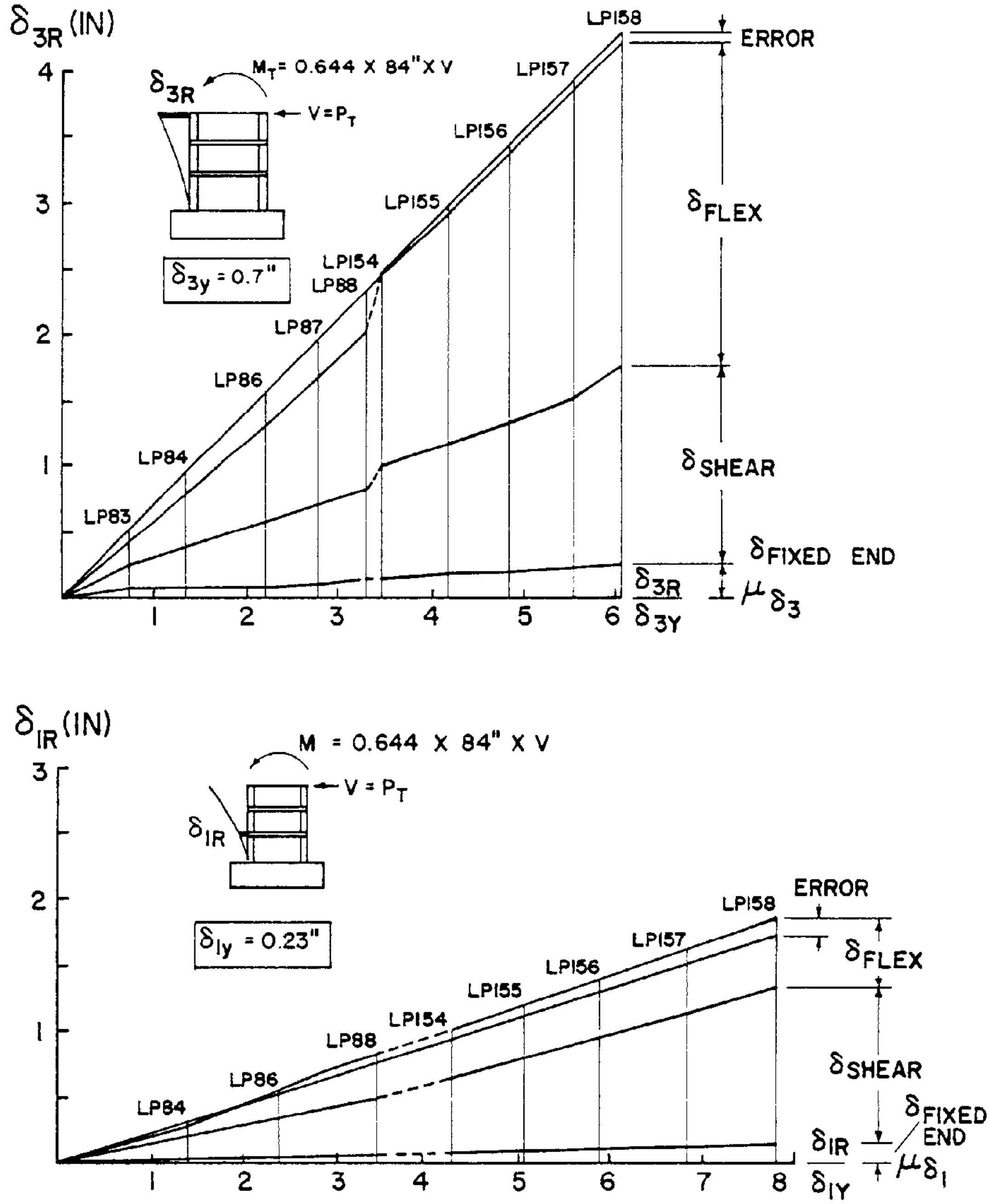

FIG. 5.94 VARIATION OF DISPLACEMENT COMPONENTS WITH DUCTILITY - SHEAR WALL 1

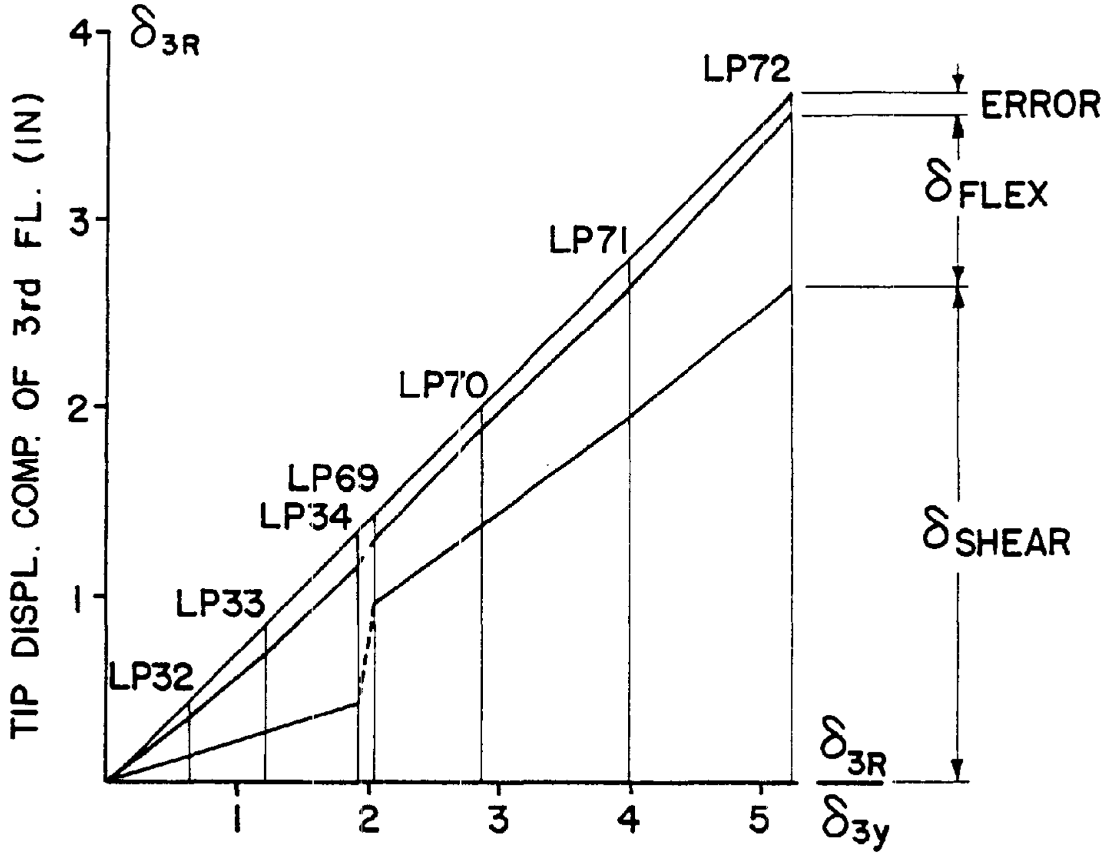

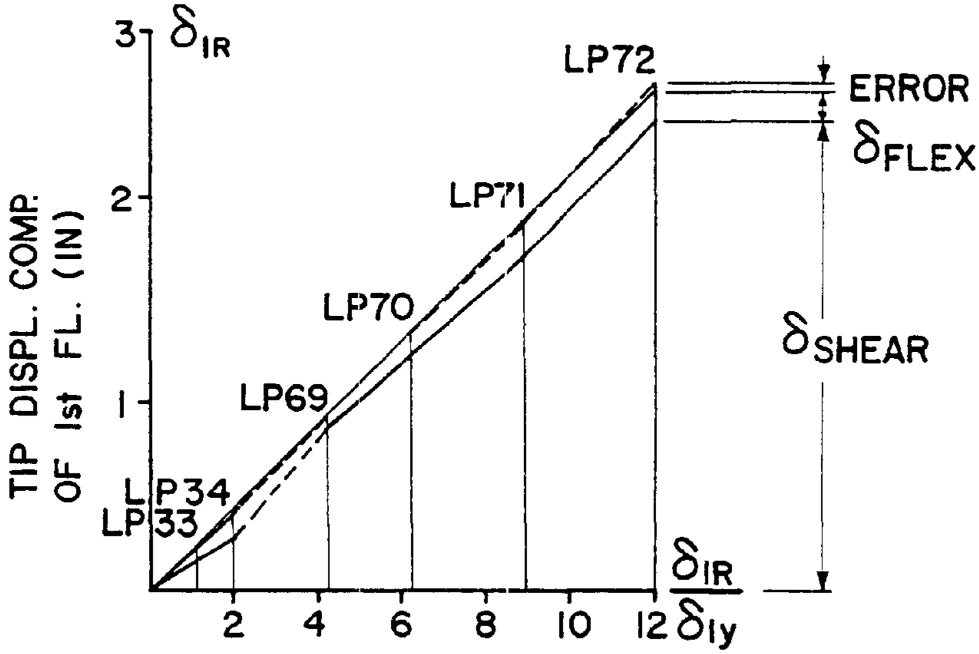

FIG. 5.95 VARIATION OF DISPLACEMENT COMPONENTS WITH DUCTILITY - SHEAR WALL 1R

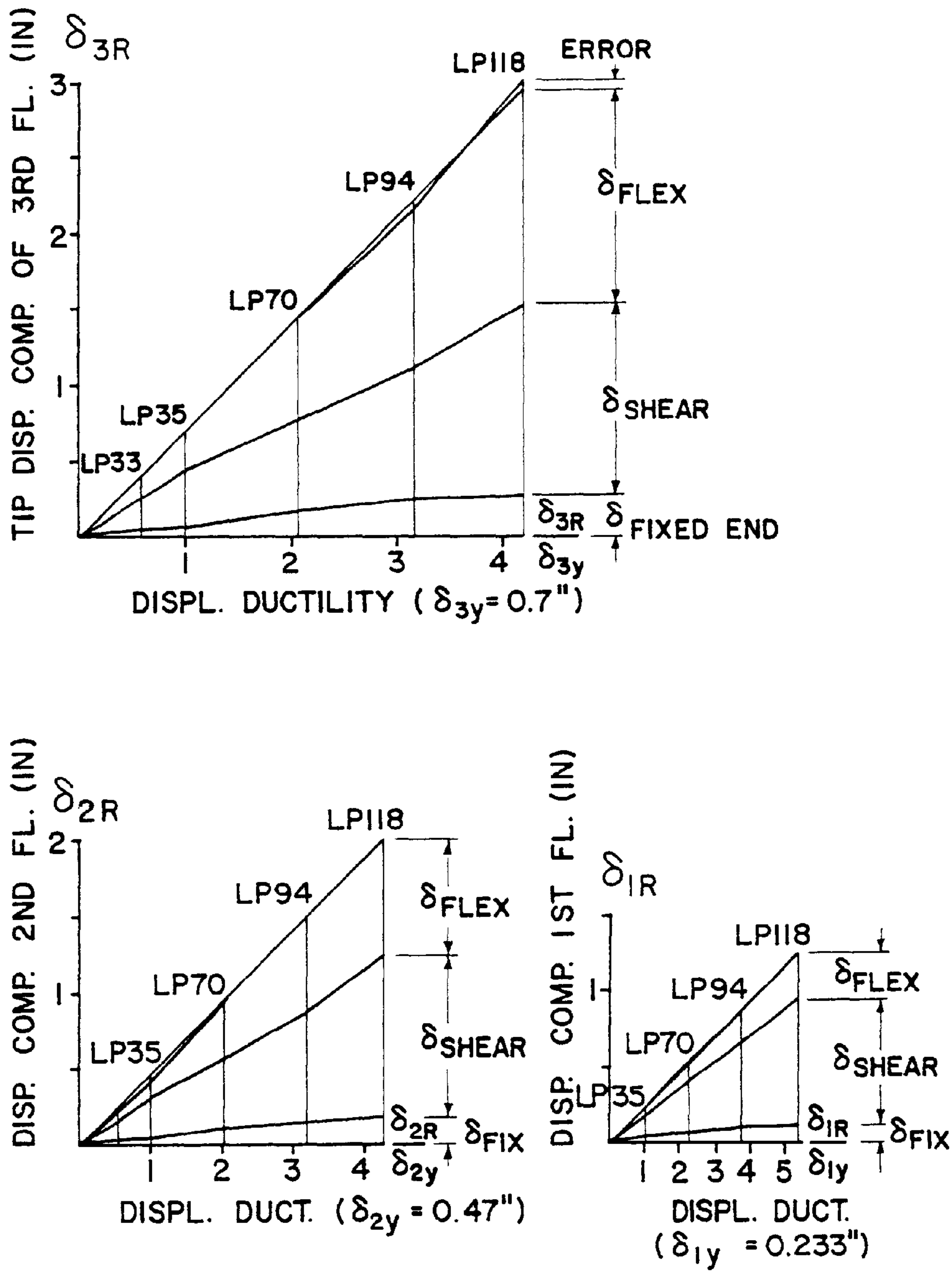

FIG. 5.96 VARIATION OF DISPLACEMENT COMPONENTS WITH DUCTILITY - SHEAR WALL 2

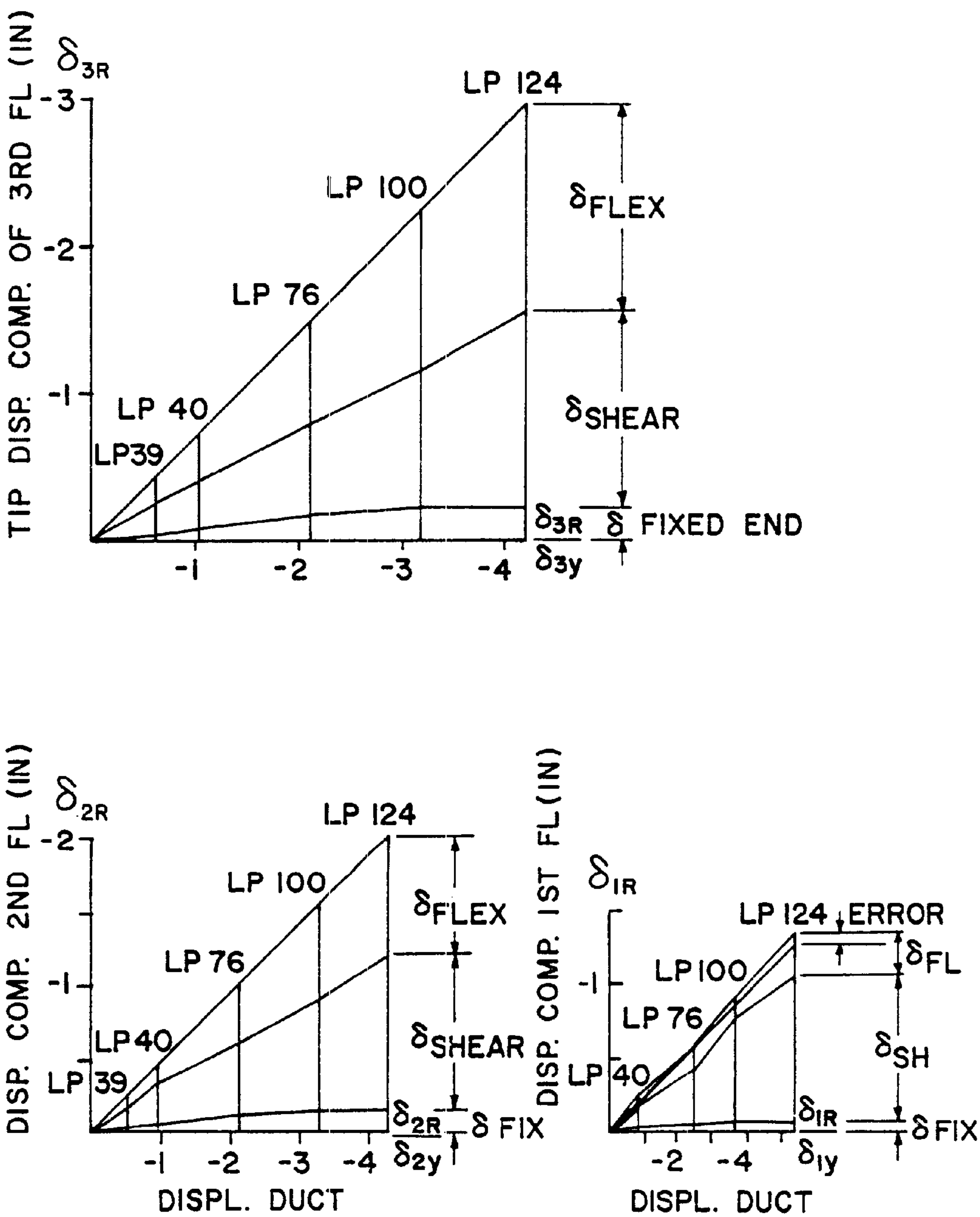

FIG. 5.97 VARIATION OF DISPLACEMENT COMPONENTS WITH DUC¯ILITY - SHEAR WALL 2

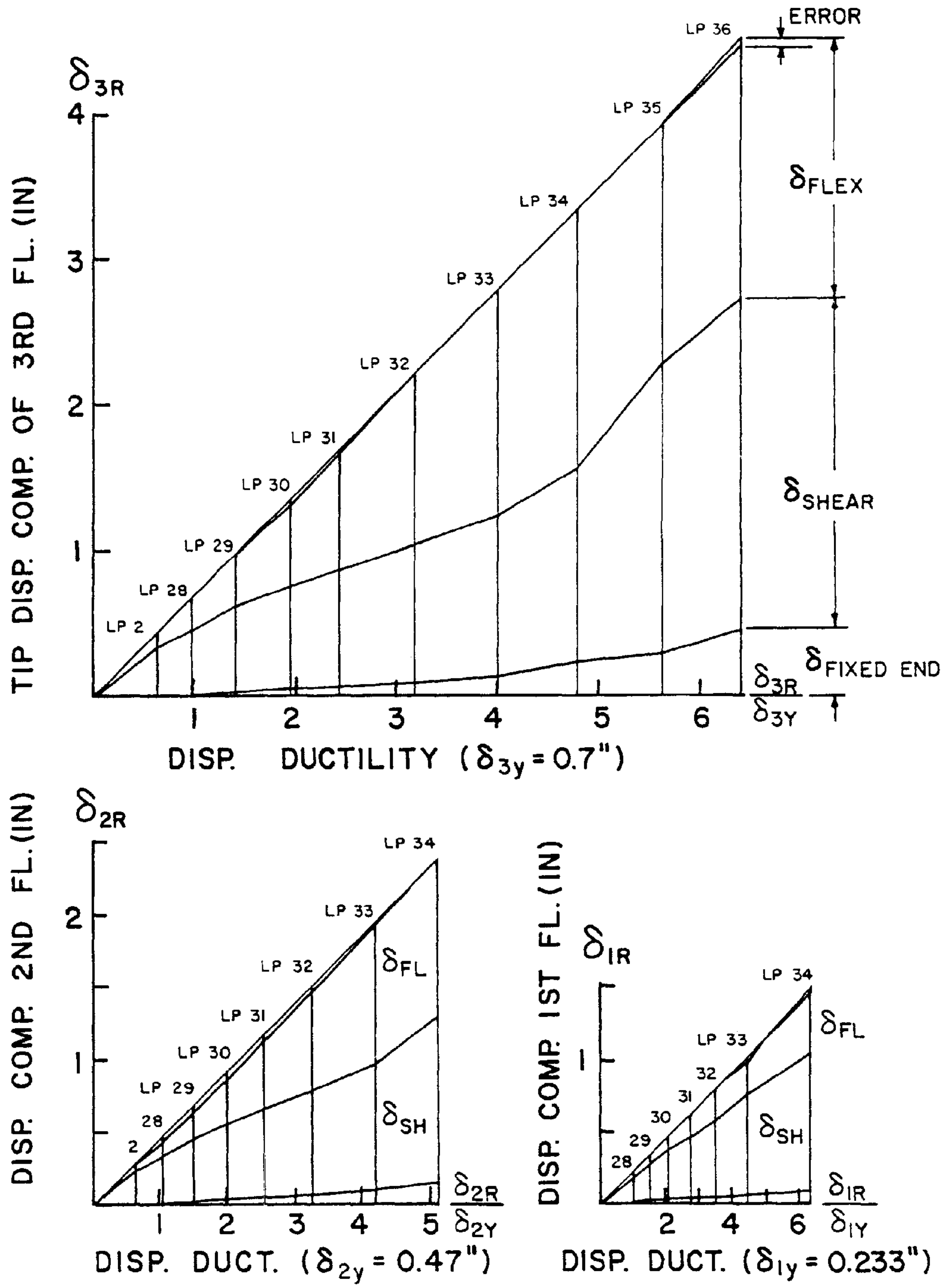

FIG. 5.98 VARIATION OF DISPLACEMENT COMPONENTS WITH DUCTILITY - SHEAR WALL 2R

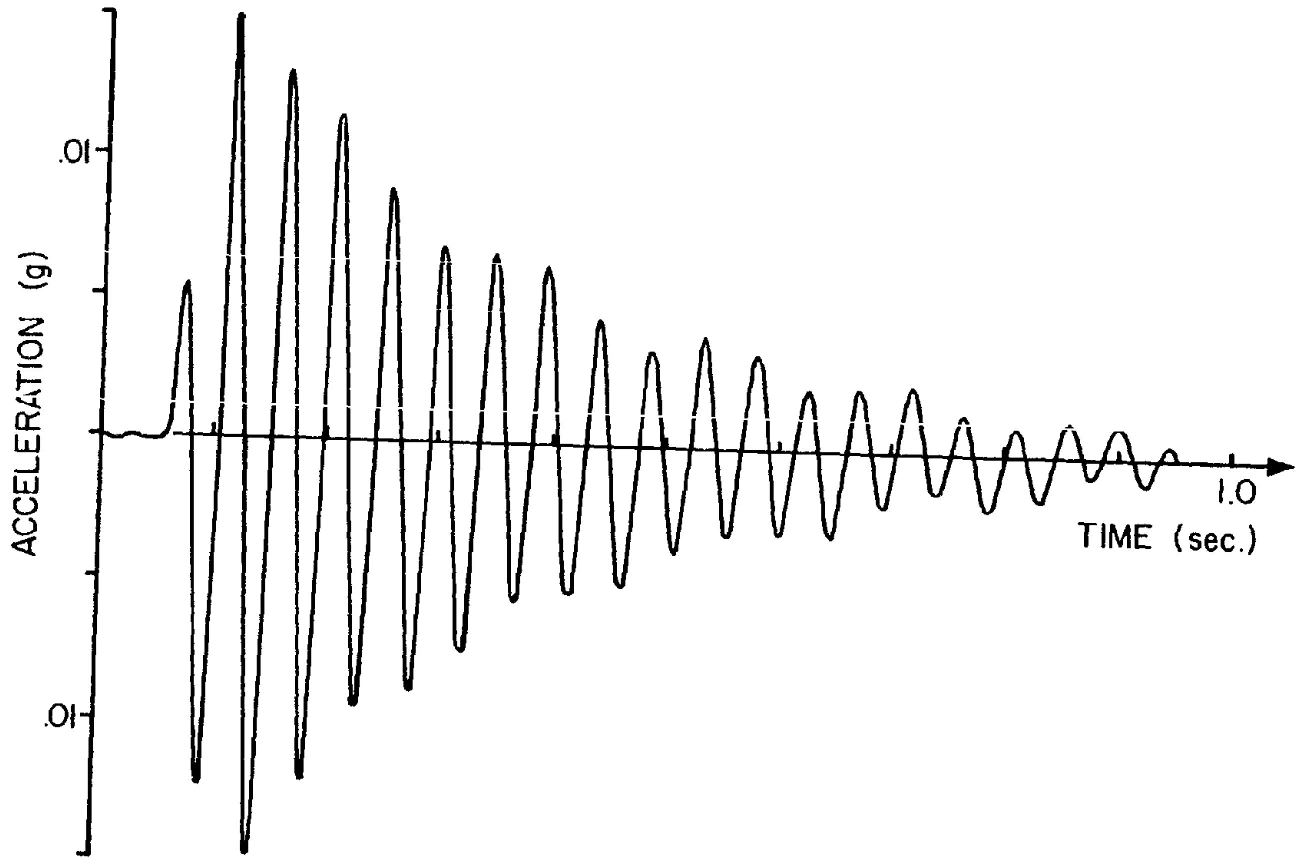

FIG. 5.99 SMALL AMPLITUDE FREE VIBRATION TEST - SHEAR WALL 2 (AFTER YIELDING)

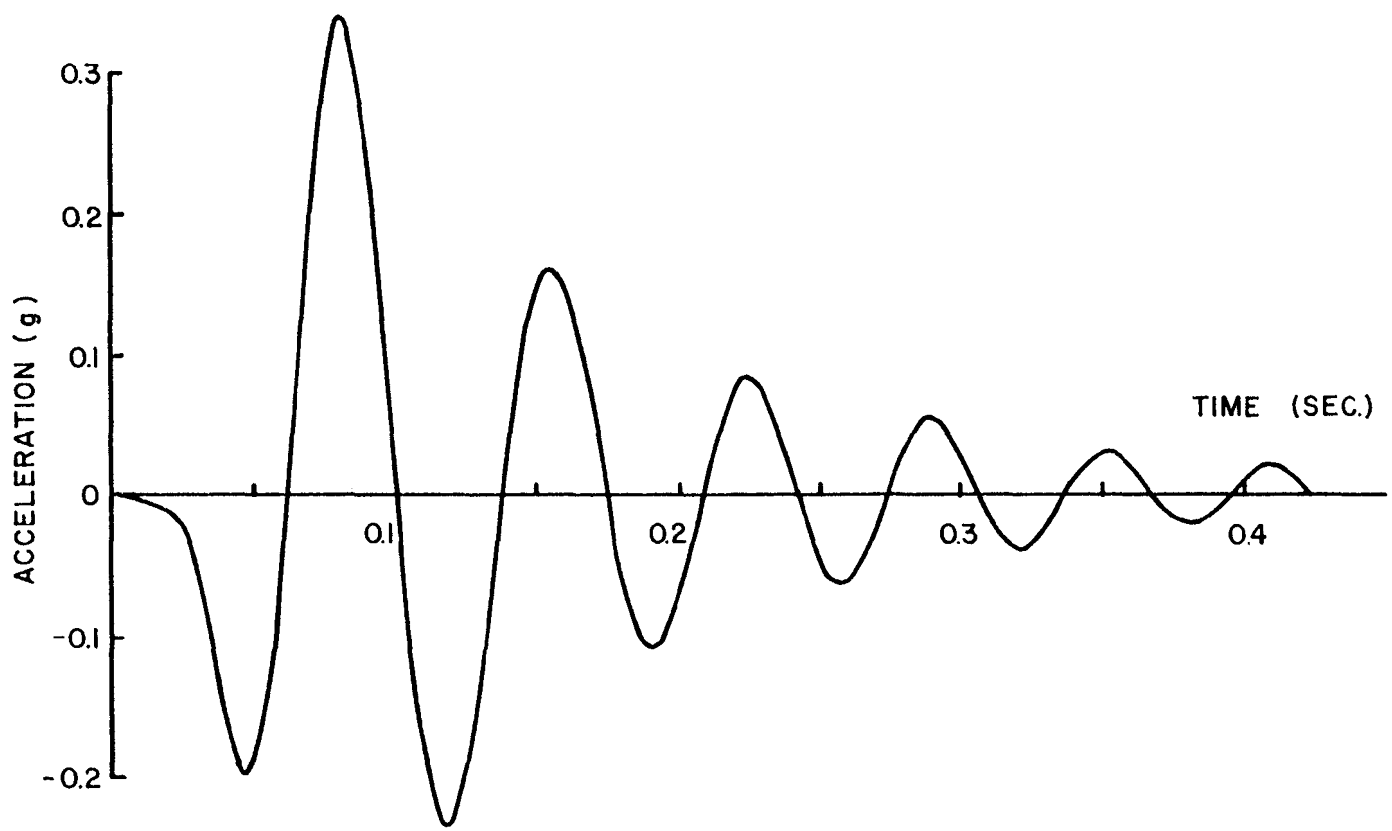

FIG. 5.100 LARGE AMPLITUDE FREE VIBRATION TEST - SHEAR WALL 2 (AFTER YIELDING)

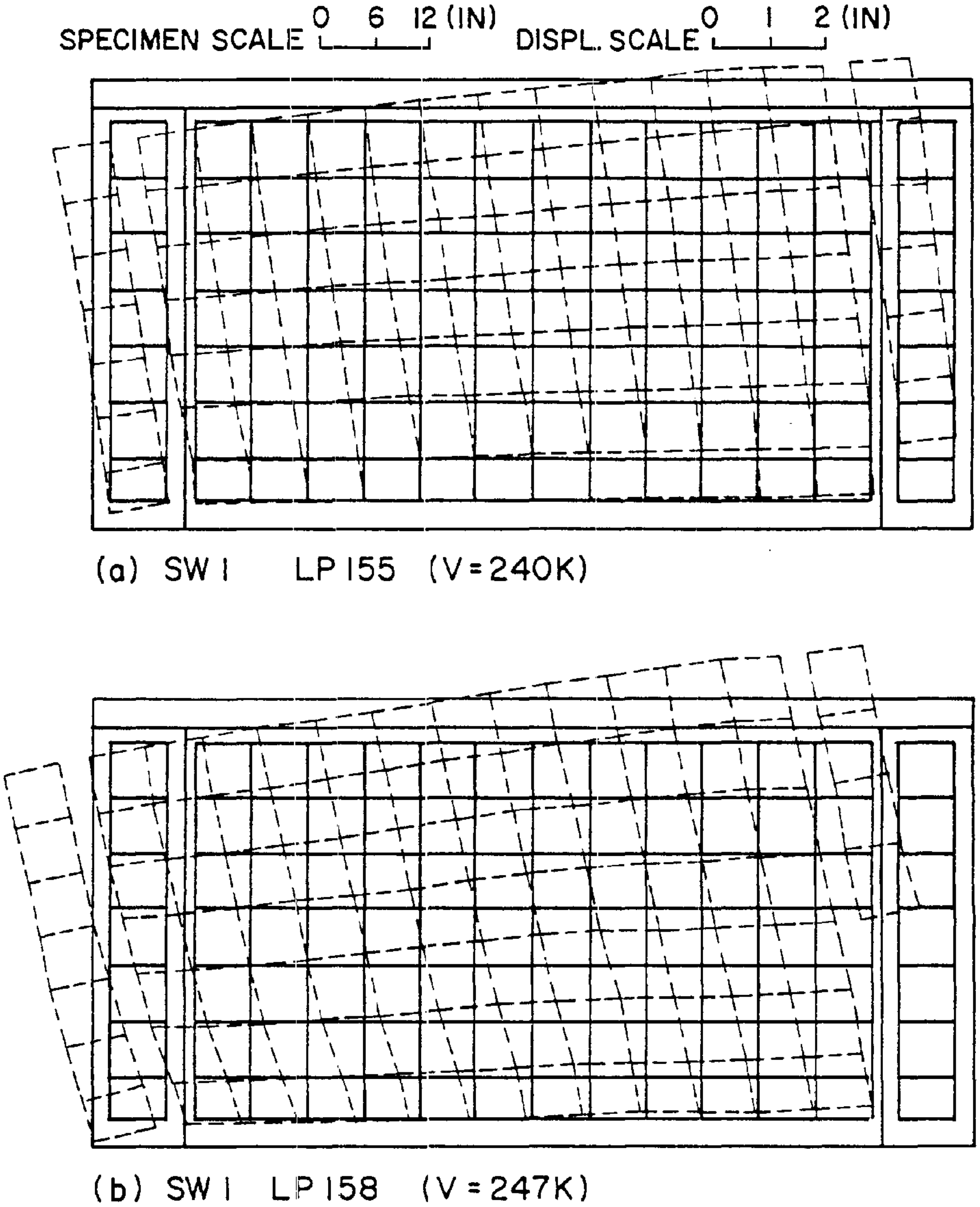

FIG. 5.101 DEFORMATION PATTERN OF FIRST STORY SPECIMEN - FROM PHOTOGRAMMETRIC READINGS

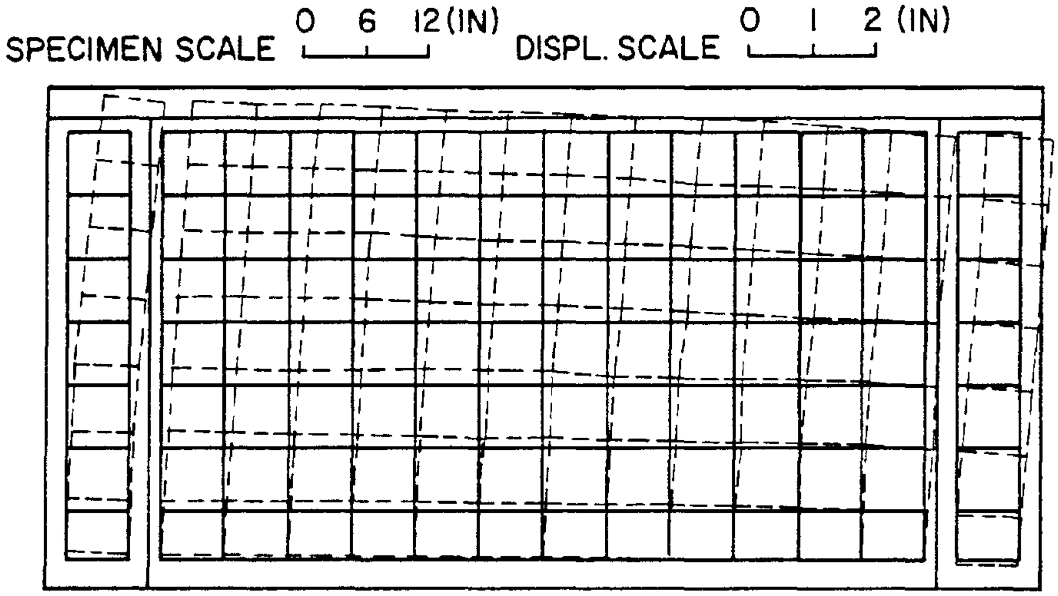

(c) SW 2 LP 76 (V = -230K)

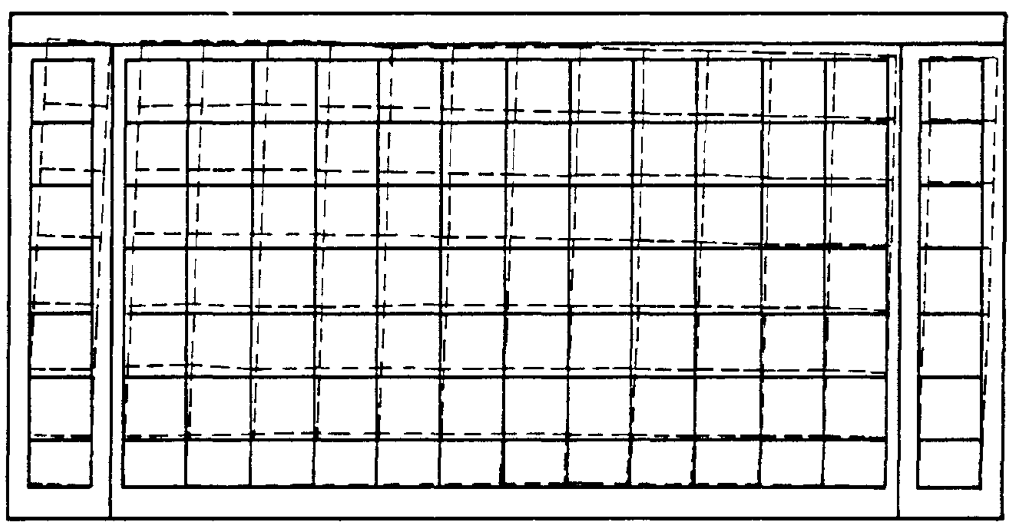

(d) SW 2 LP 90 (V = -2K)

FIG. 5.101 (CONT'D)

SPECIMEN SCALE 0 6 12 (IN) DISPL. SCALE 0 1 2 (IN)

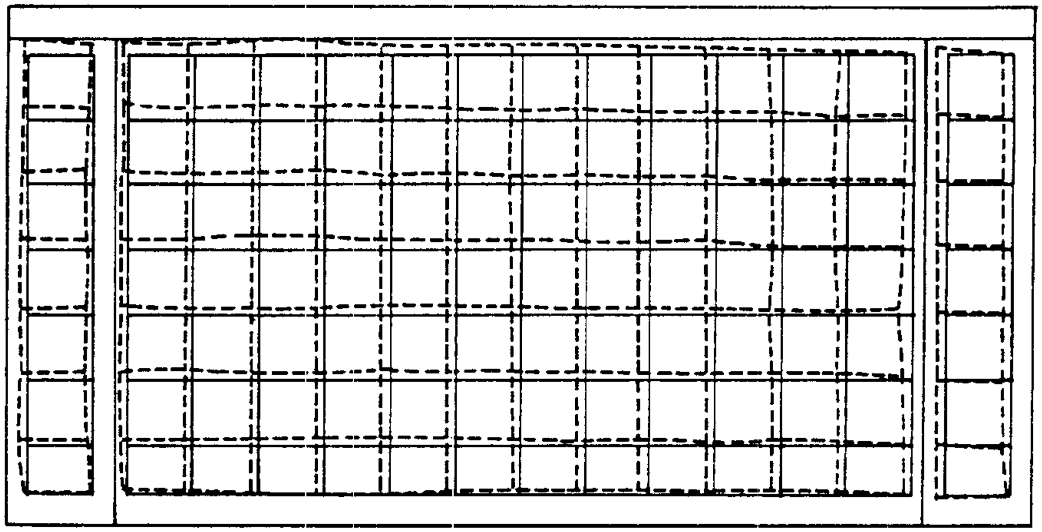

(e) SW 2 LP 91 (V = 40 K)

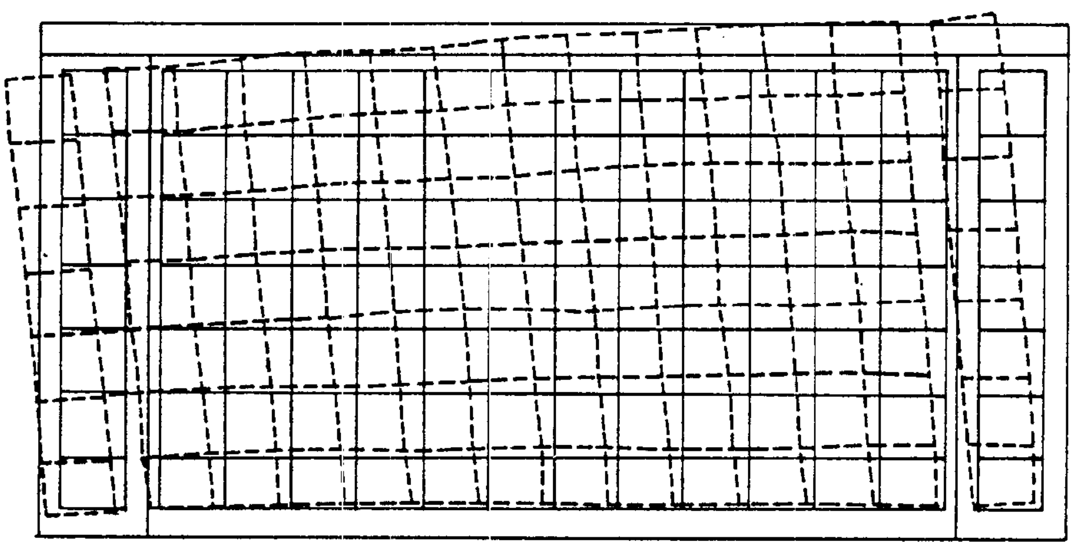

(f) SW 2 LP 94 (V = 239 K)

FIG. 5.101 (CONT'D)

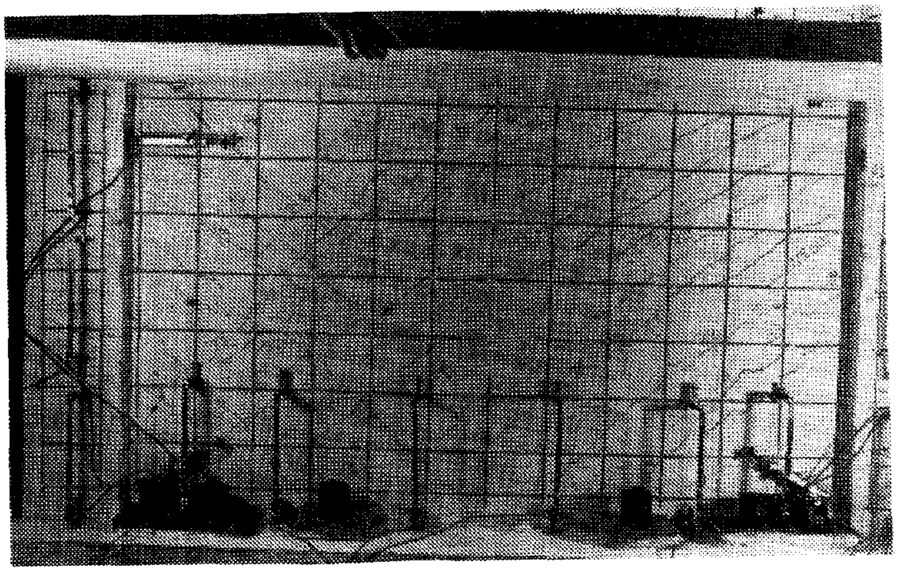

(a) AT FIRST YIELDING δ_{3R}=0.76 IN., LP 79

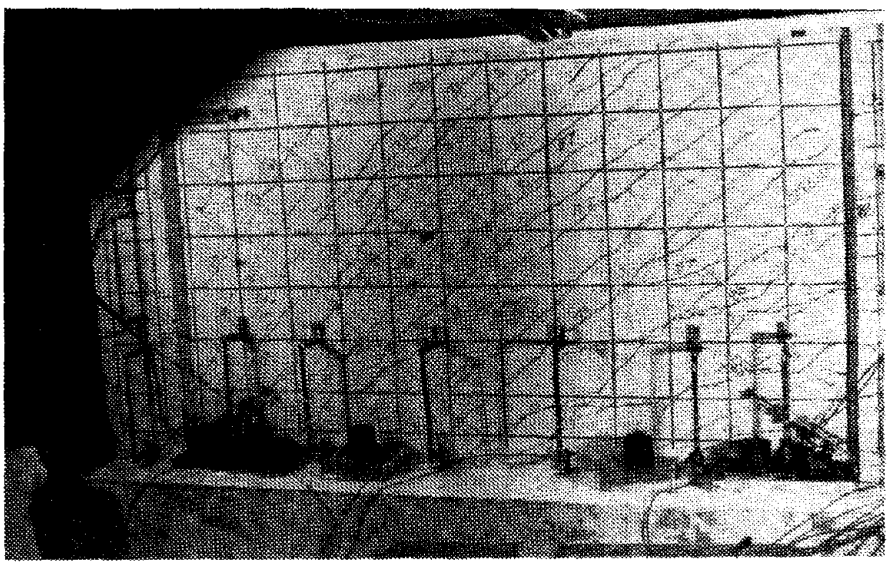

(b) AT δ_{3R}=2.3 IN. ($\mu \doteq 3$) LP 88, P_T=225 K

FIG. 5.102 FIRST STORY OF WALL 1 - ILLUSTRATION OF DAMAGE INDUCED AT DIFFERENT STAGES OF TESTING

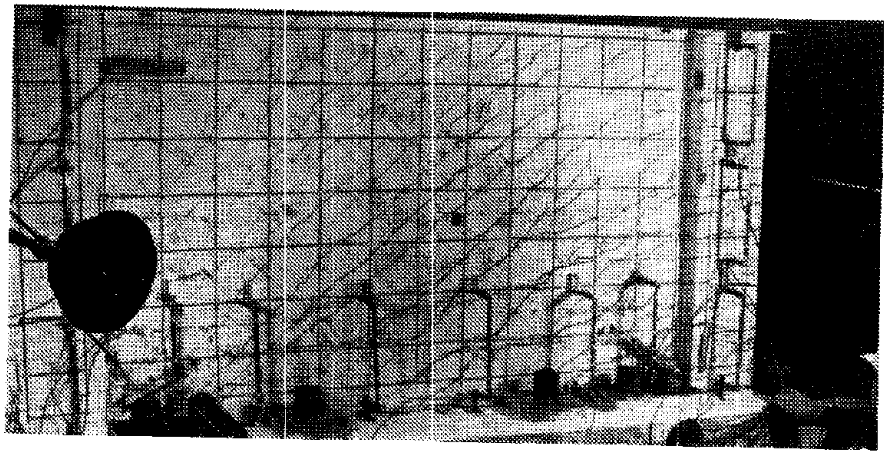

(c) AT δ_{3R}=4.25 IN. ($\mu \doteq 6.1$) LP 158, P_T=248 K

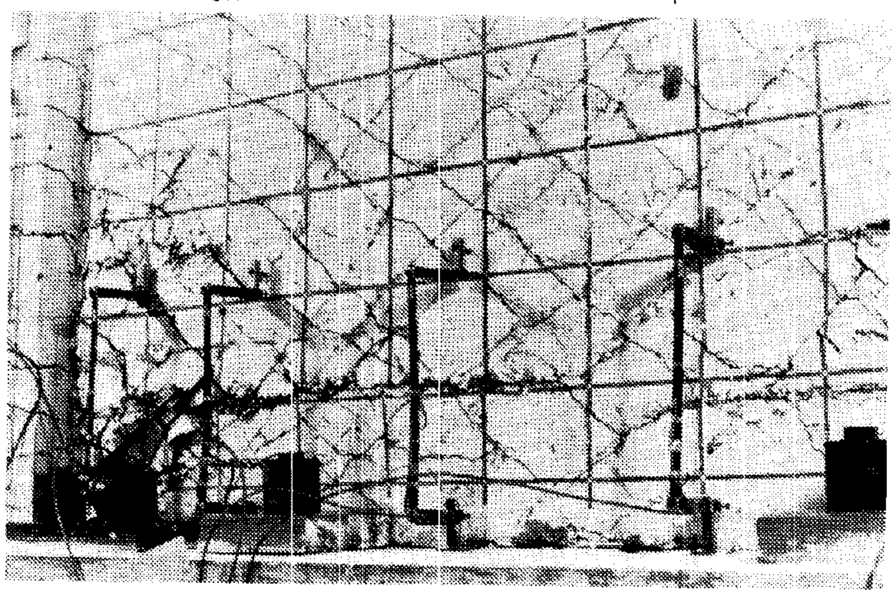

(d) CRUSHING OF CONCRETE AT LP 158

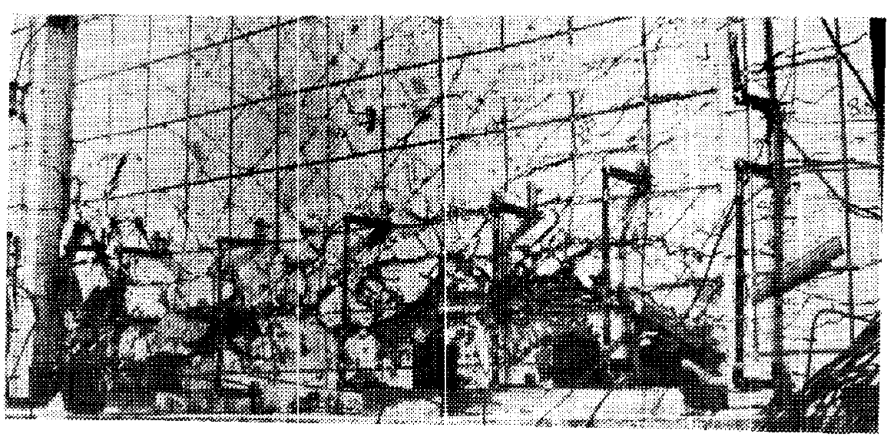

(e) AFTER δ_{3R}= -1.9 IN., LP 197

FIG. 5.102 (CONT'D)

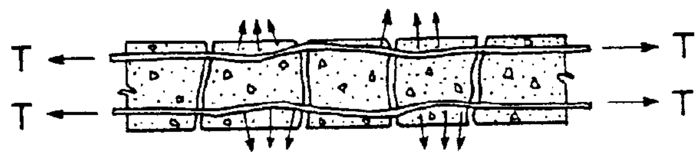

FIG. 5.103 FORCE GENERATED IN BENT PORTION OF WALL REINFORCEMENT

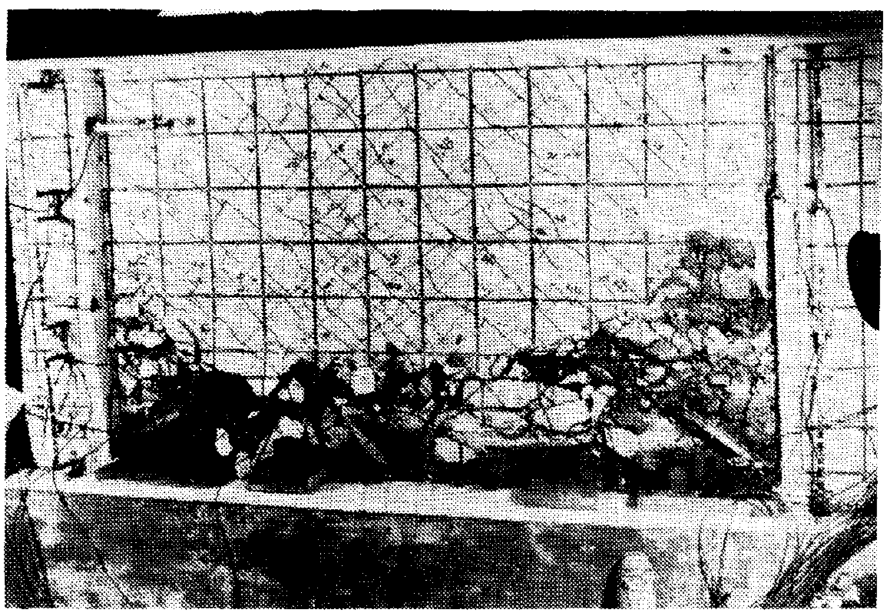

FIG. 5.104 CRUSHED ZONE OF SHEAR WALL 1R

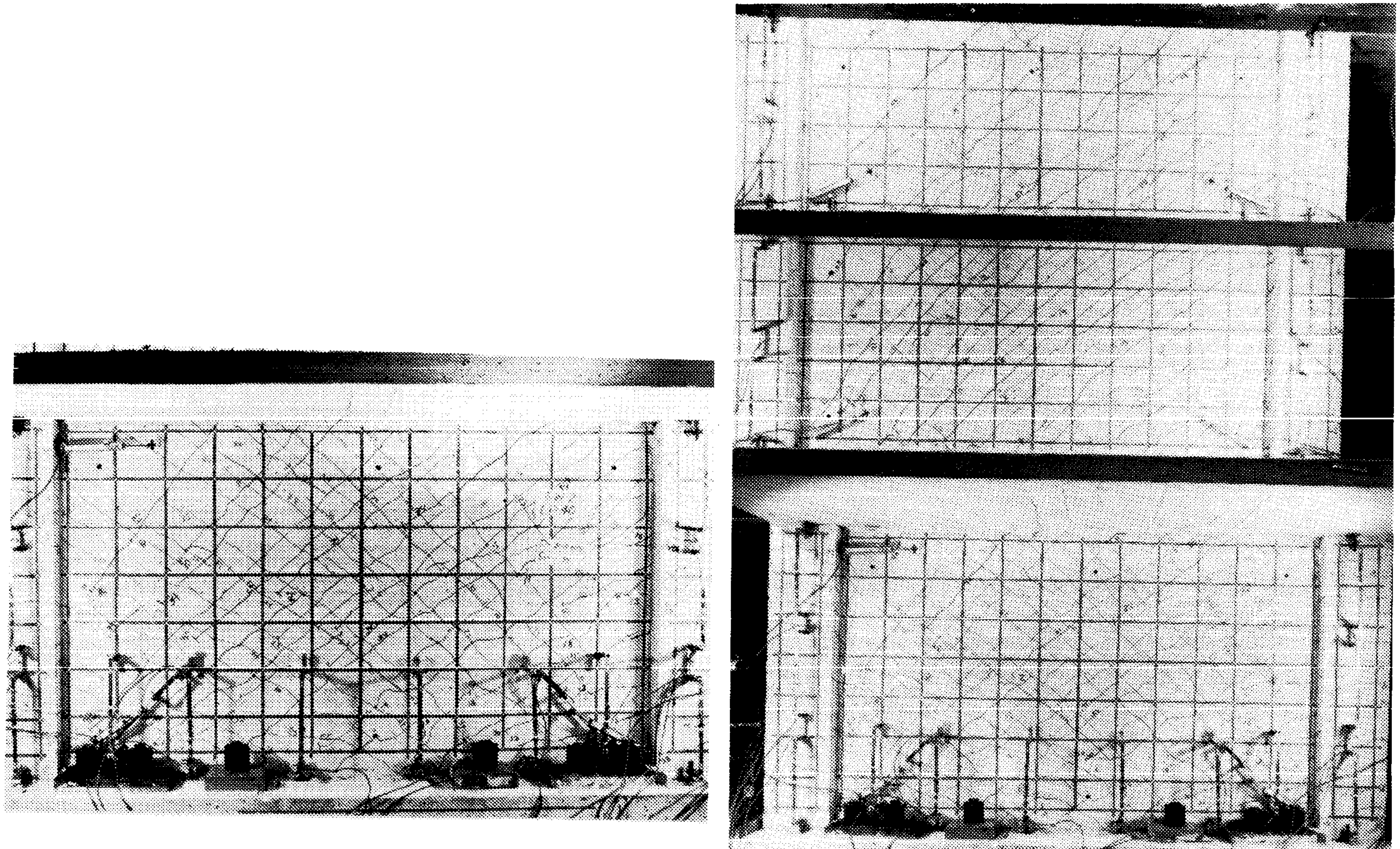

(a) FIRST STORY CRACK PATTERN AFTER CYCLE WITH $\delta_{3R} \doteq \pm 0.45$ IN.

(b) CRACK PATTERN THROUGH WHOLE SPECIMEN AFTER CYCLE WITH $\delta_{3R} \doteq \pm 1.45$ IN. ($\mu \doteq \pm 2$)

FIG. 5.105 FIRST STORY OF WALL 2 - ILLUSTRATION OF DAMAGE INDUCED AT DIFFERENT STAGES OF TESTING

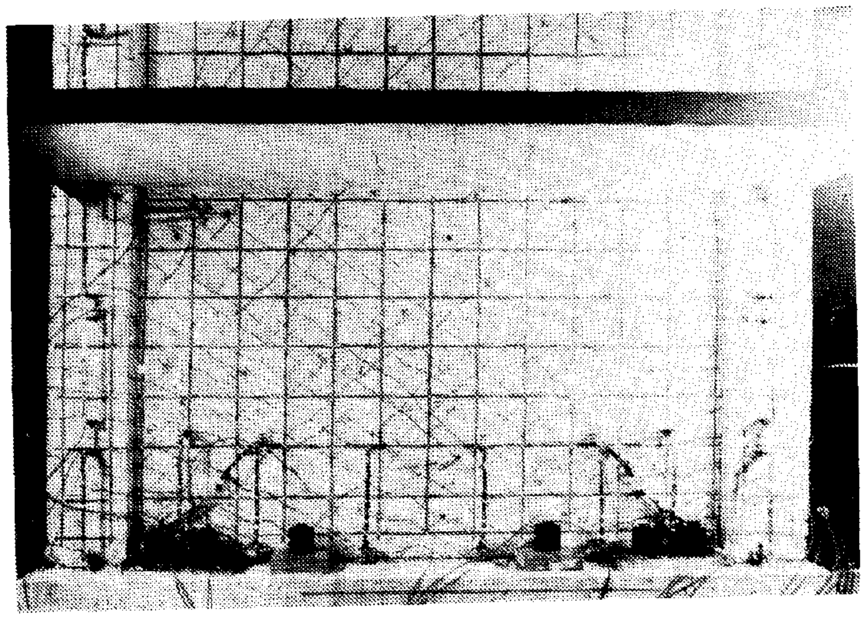

(c) FIRST STORY AFTER CYCLE WITH $\delta_{3R} \doteq \pm 2.94$ IN. ($\mu \doteq \pm 4$)

FIG. 5.105 (CONT'D)

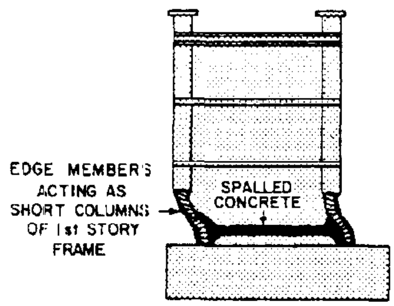

FIG. 5.106 MECHANISM OF FAILURE OF WALL SPECIMEN

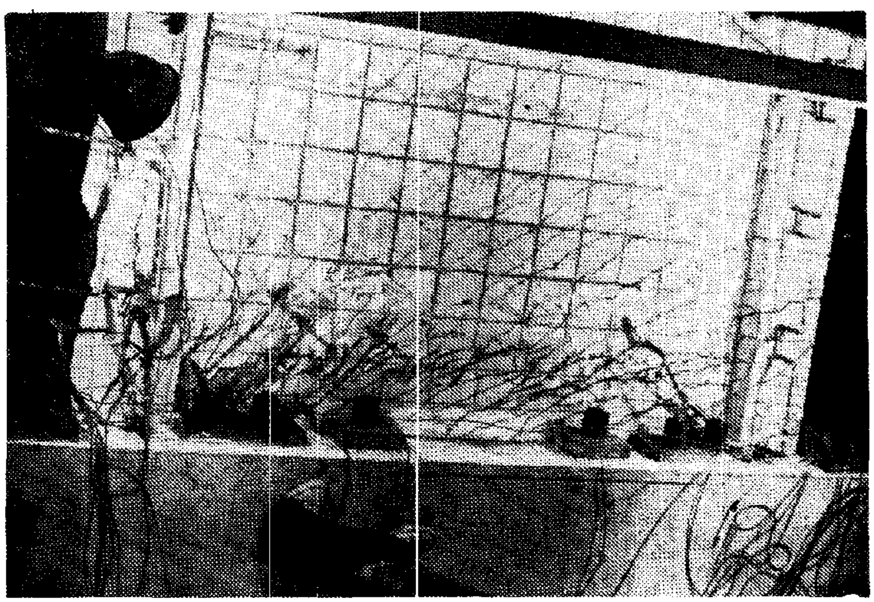

FIG. 5.107 CRUSHED ZONE OF SHEAR WALL 2R

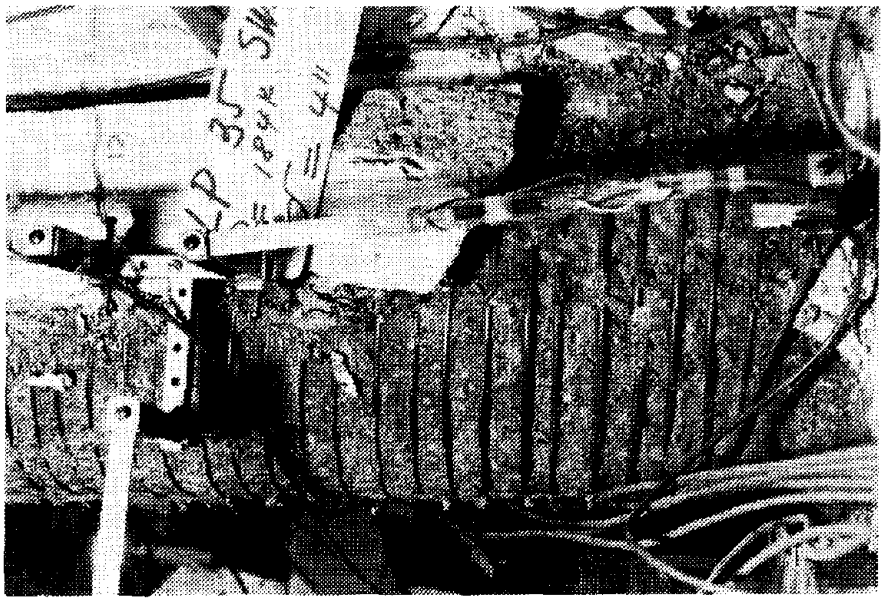

FIG. 5.108 BROKEN COLUMN SPIRALS
OF SHEAR WALL 2R

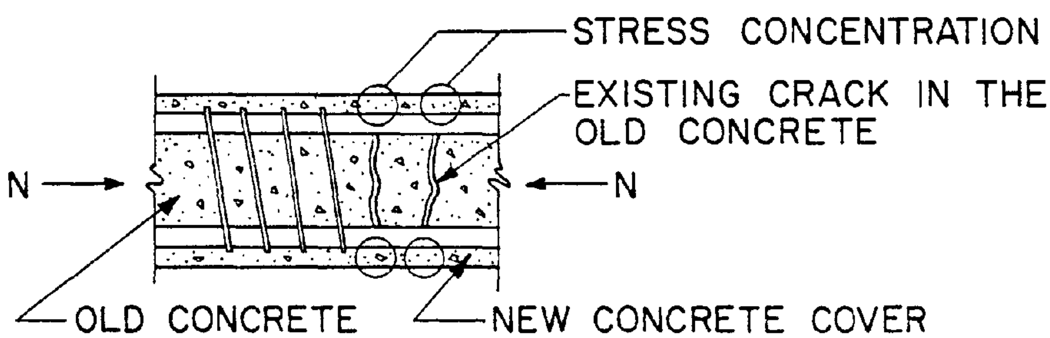

FIG. 5.109 STRESS CONCENTRATION IN REPAIRED EDGE COLUMN

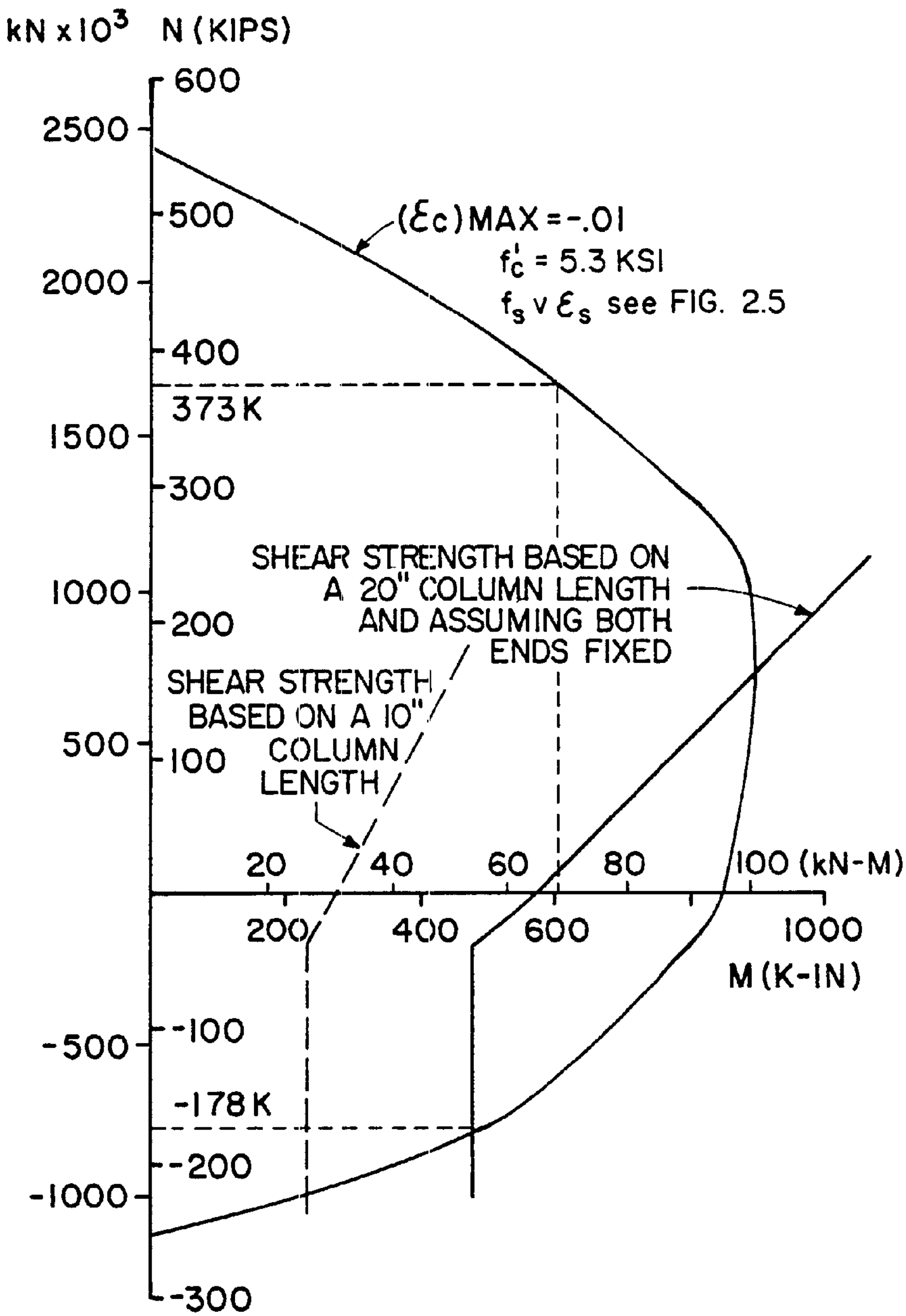

FIG. 5.110 N-M INTERACTION DIAGRAM OF CONFINED COLUMN CORE

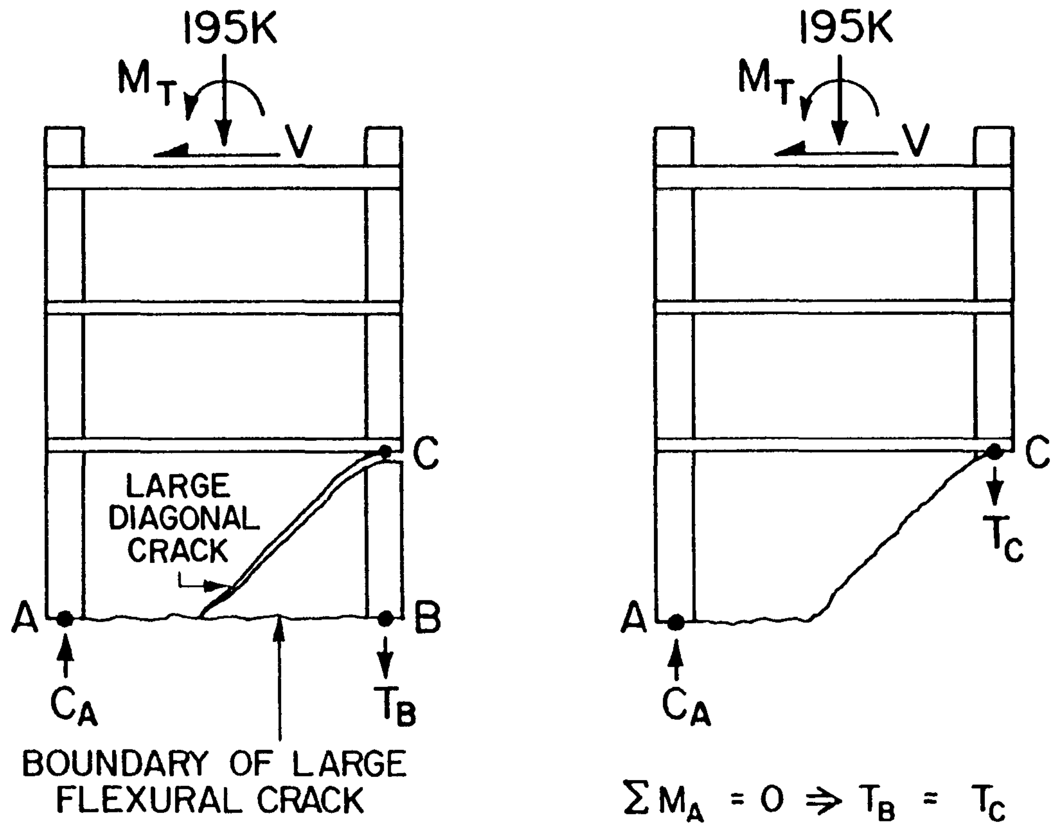

FIG. 5.111 INFLUENCE OF DIAGONAL CRACK

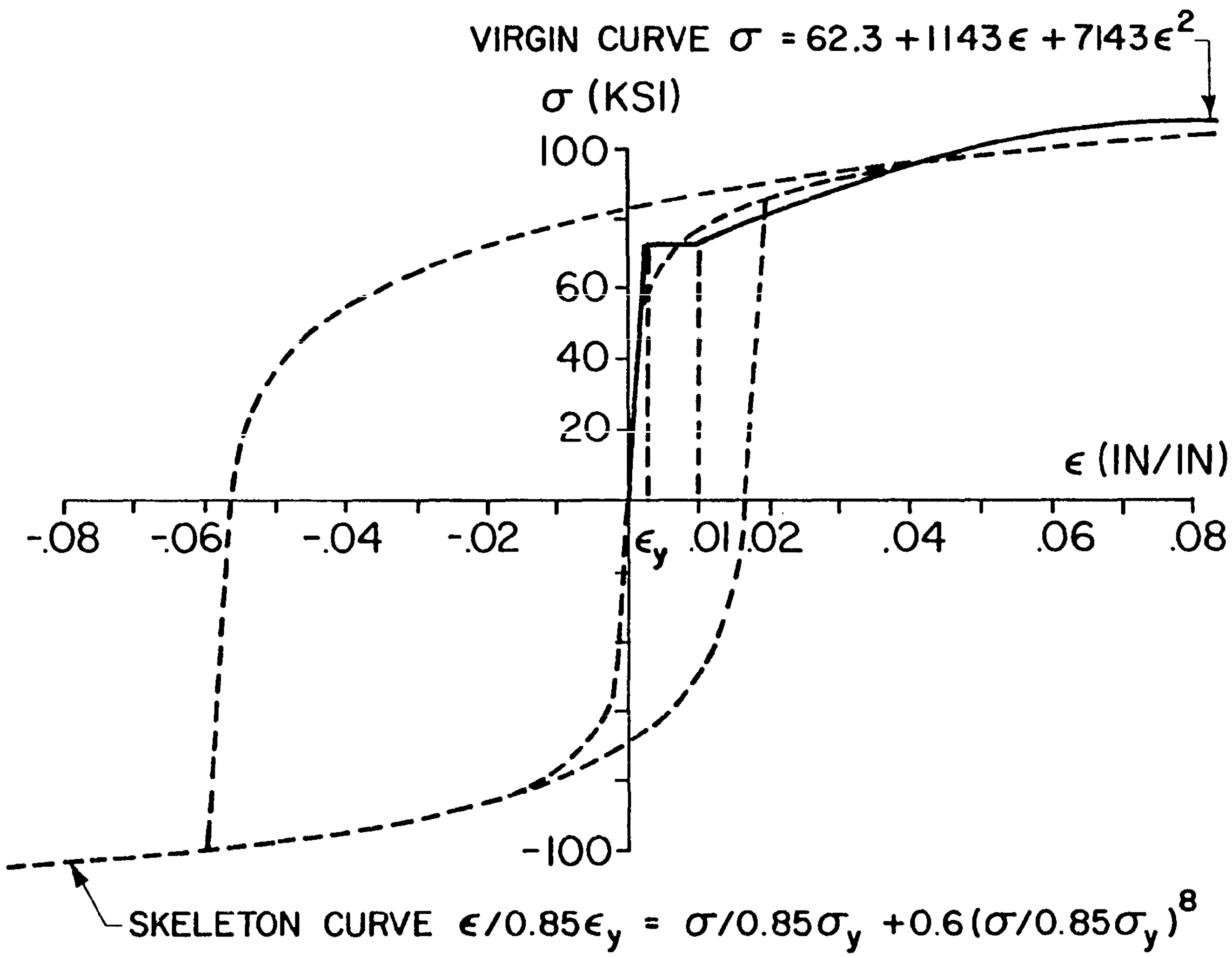

FIG. 5.112 CYCLIC STRESS-STRAIN DIAGRAM OF STEEL

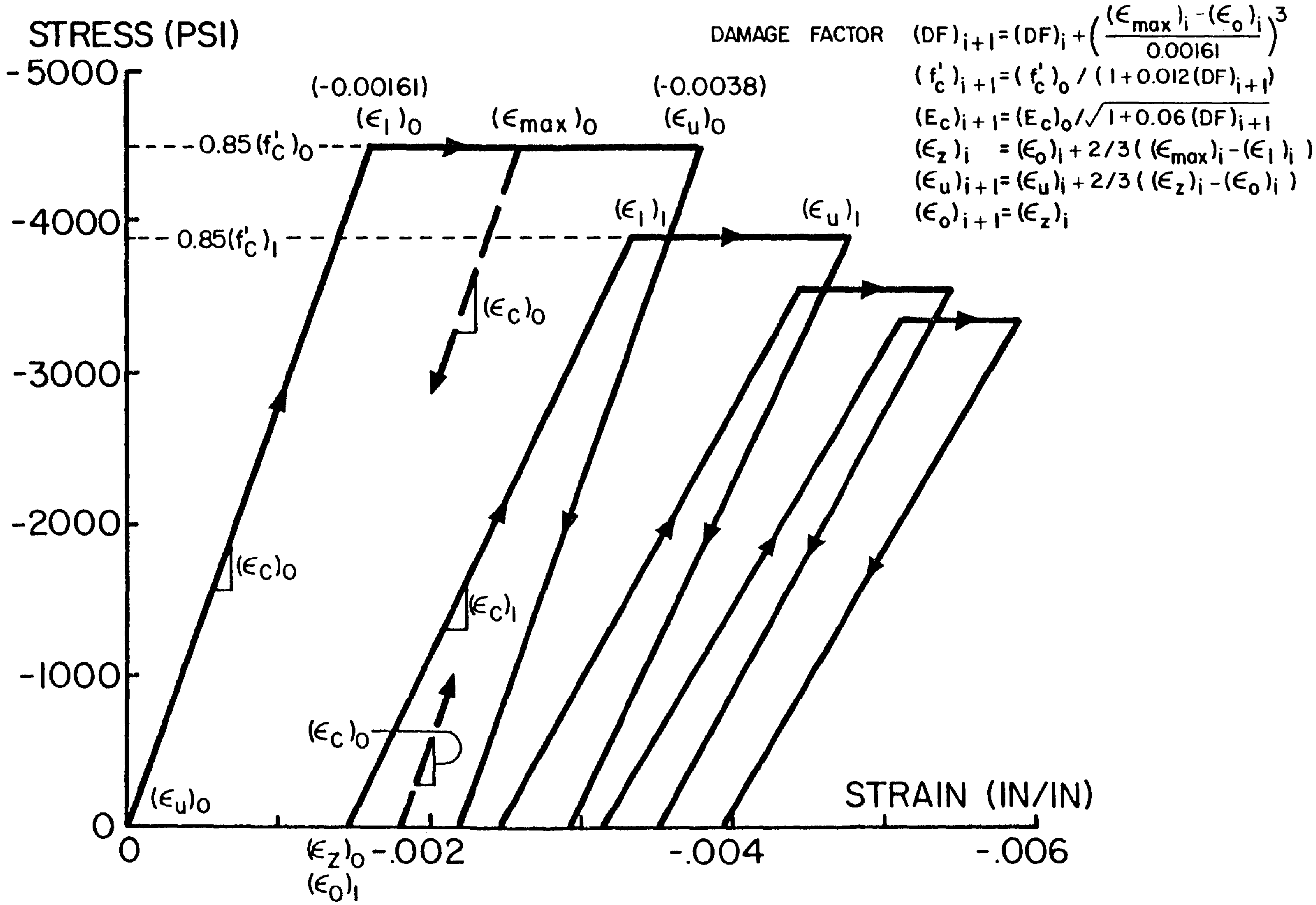

FIG. 5.113 IDEALIZED CYCLIC STRESS-STRAIN DIAGRAM OF UNCONFINED CONCRETE

DAMAGE FACTOR

$$(DF)_{i+1} = (DF)_i + \left(\frac{(\epsilon_{max})_i + (\epsilon_o)_i}{0.003}\right)^2$$

$$(f'_c)_{i+1} = (f'_c)_o \,/\, (1 + 0.012\,(DF)_{i+1})$$

$$(E_c)_{i+1} = (E_c)_o / \sqrt{1 + 0.15\,(DF)_{i+1}}$$

$$(\epsilon_t)_{i+1} = (\epsilon_t)_{i+1}{}^{*}(1 + 0.012\,(DF)_{i+1})$$

$$(\epsilon_R)_i = 1/3\,((\epsilon_{max})_i - (\epsilon_1)_i) \le 0.0012$$

$$(\epsilon_z)_i = (\epsilon_{max})_i - (f_{max})_i / (E_c)_i - (\epsilon_R)_i$$

$$(\epsilon_o)_{i+1} = (\epsilon_z)_i$$

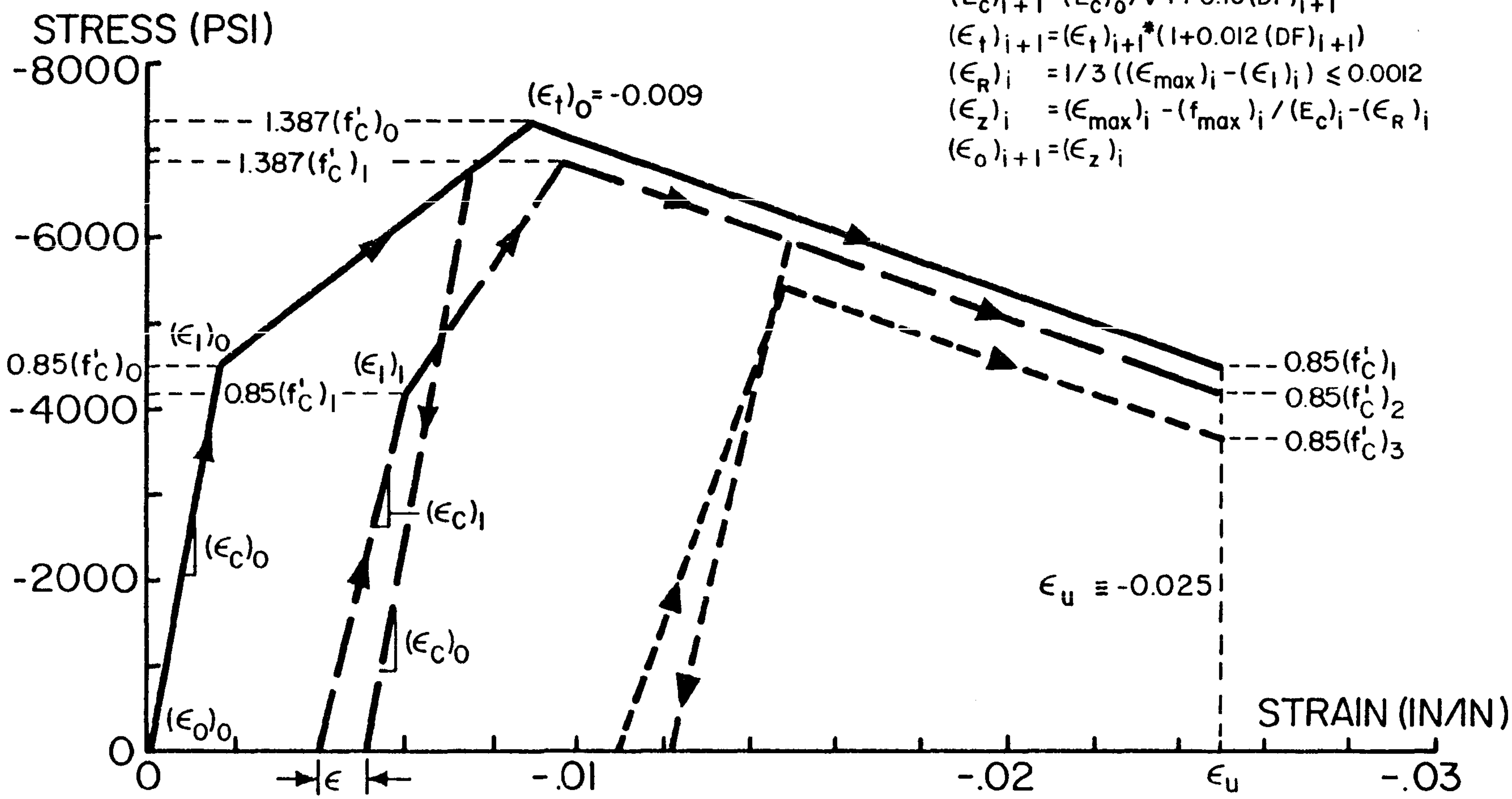

FIG. 5.114 IDEALIZED CYCLIC STRESS-STRAIN DIAGRAM OF CONFINED CONCRETE

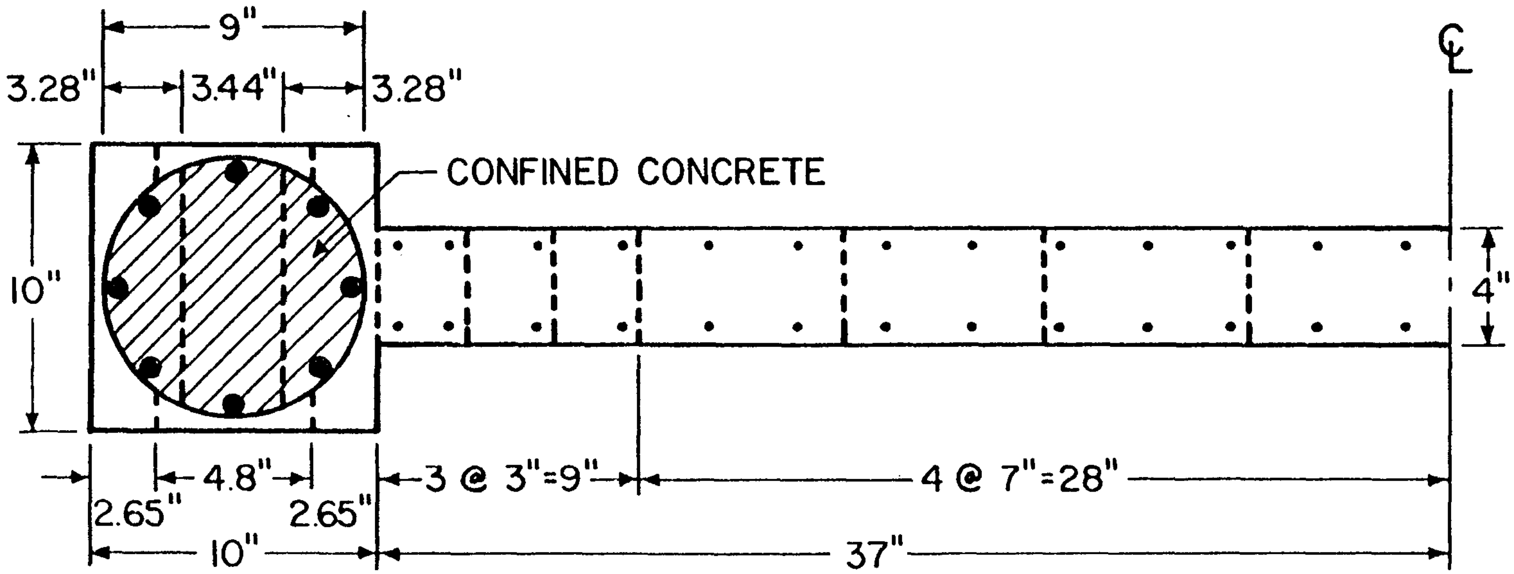

FIG. 5.115 FINITE SEGMENTS OF WALL CROSS SECTION CONSIDERED FOR ANALYTICAL PREDICTION OF M-ϕ RELATIONSHIP

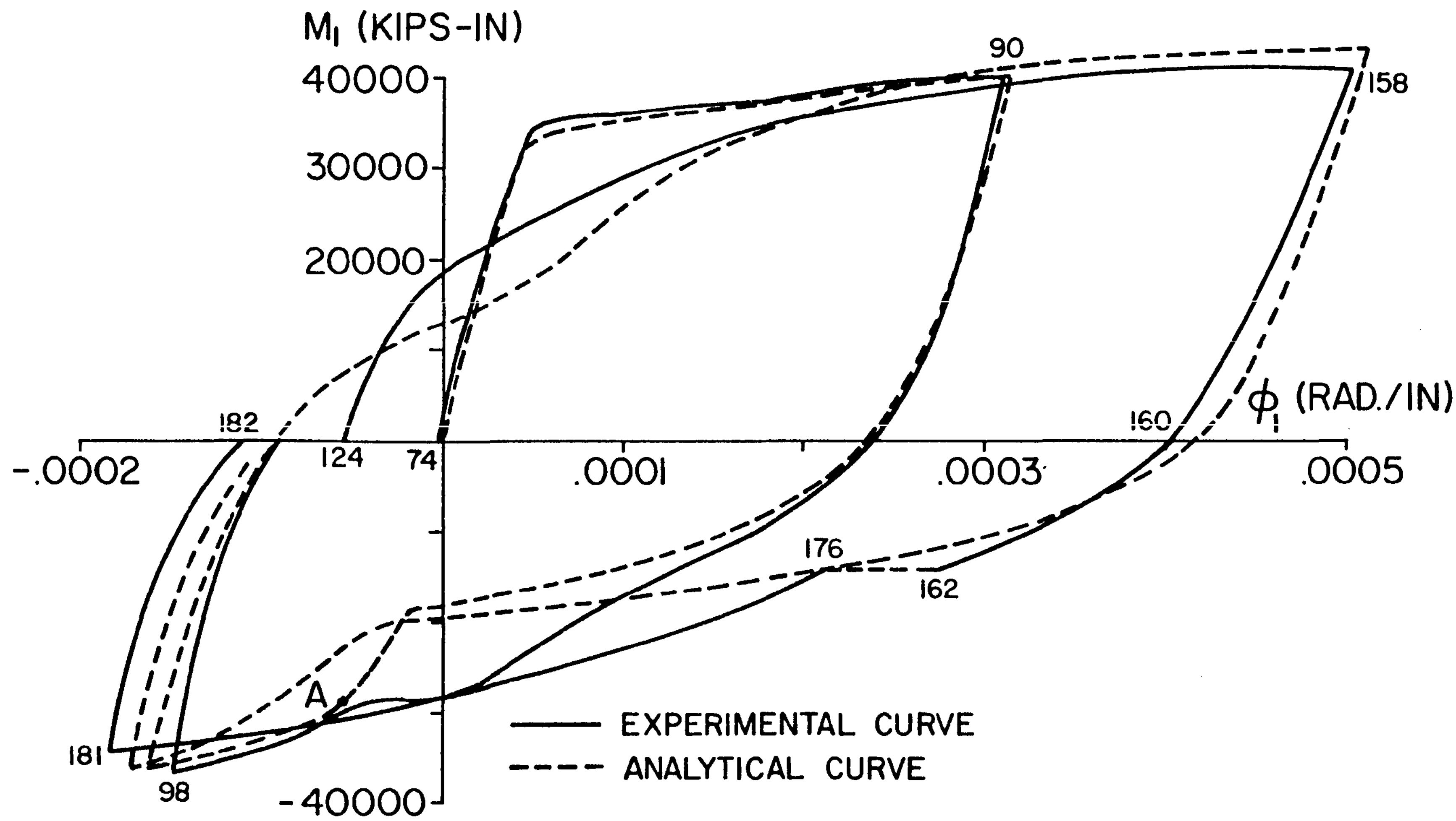

FIG. 5.116 COMPARISON OF ANALYTICAL AND EXPERIMENTAL M-ϕ DIAGRAMS - SHEAR WALL 1

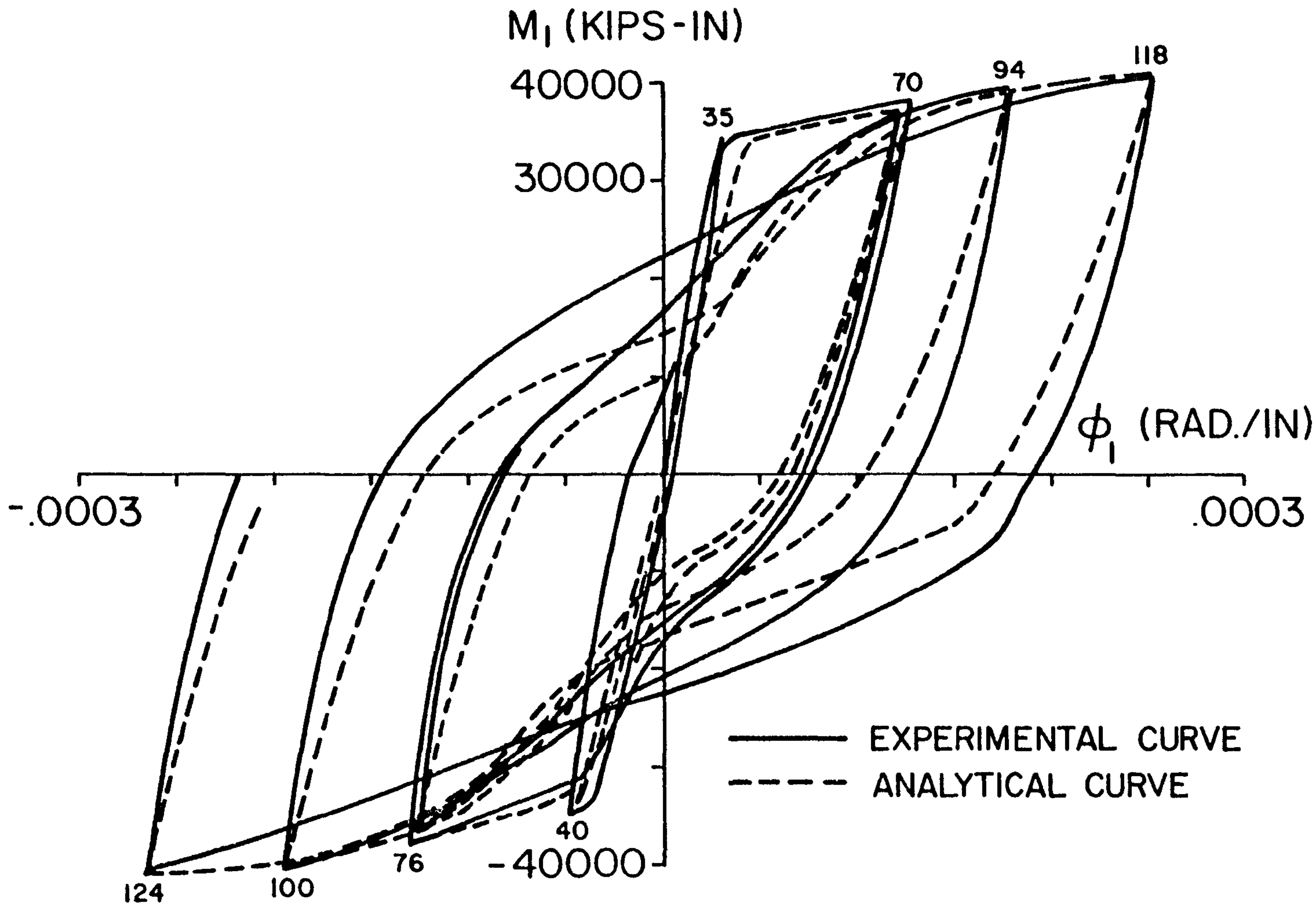

FIG. 5.117 COMPARISON OF ANALYTICAL AND EXPERIMENTAL M-ϕ DIAGRAMS - SHEAR WALL 2

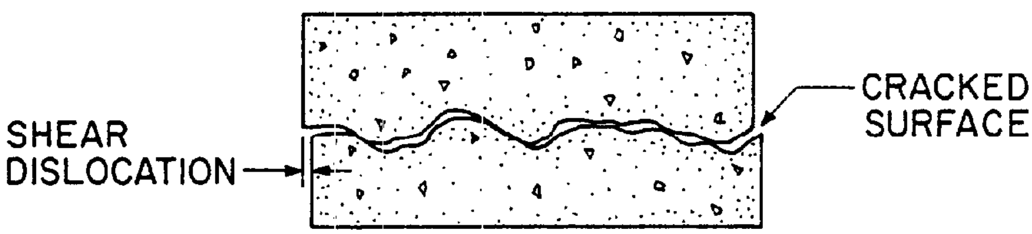

FIG. 5.118 EARLY CONCRETE CONTACT DUE
TO SHEAR DISLOCATION

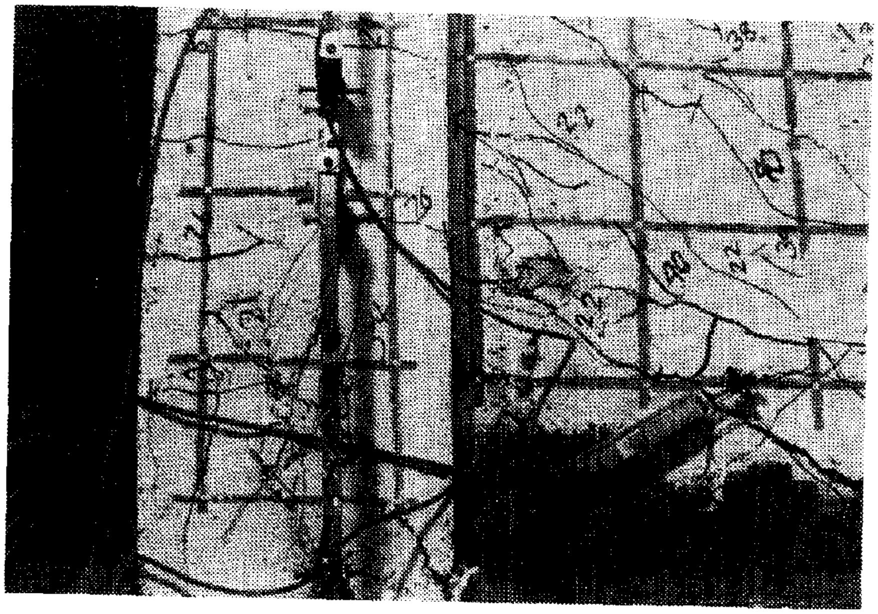

FIG. 6.1 CRUSHING OF WALL PANEL AND SPLITTING OF COLUMN CONCRETE COVER AT LP 45 OF SHEAR WALL 1R

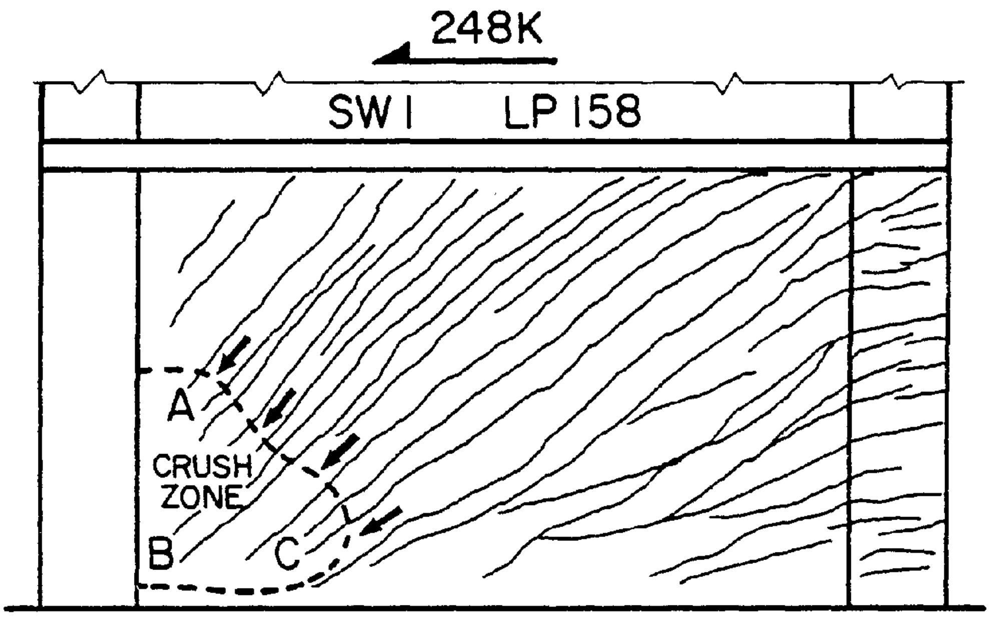

FIG. 6.2 CRACK PATTERN AND CRUSHING ZONE OF SHEAR WALL 1

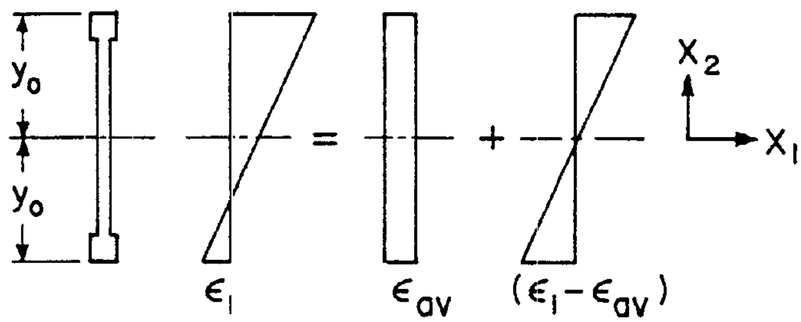

FIG. 6.3 LINEAR VARIATION OF STRAIN

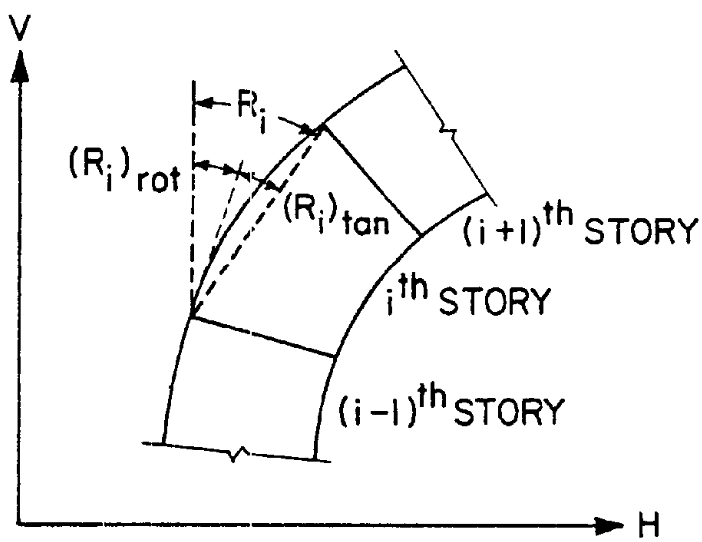

FIG. 6.4 COMPONENTS OF STORY DRIFT

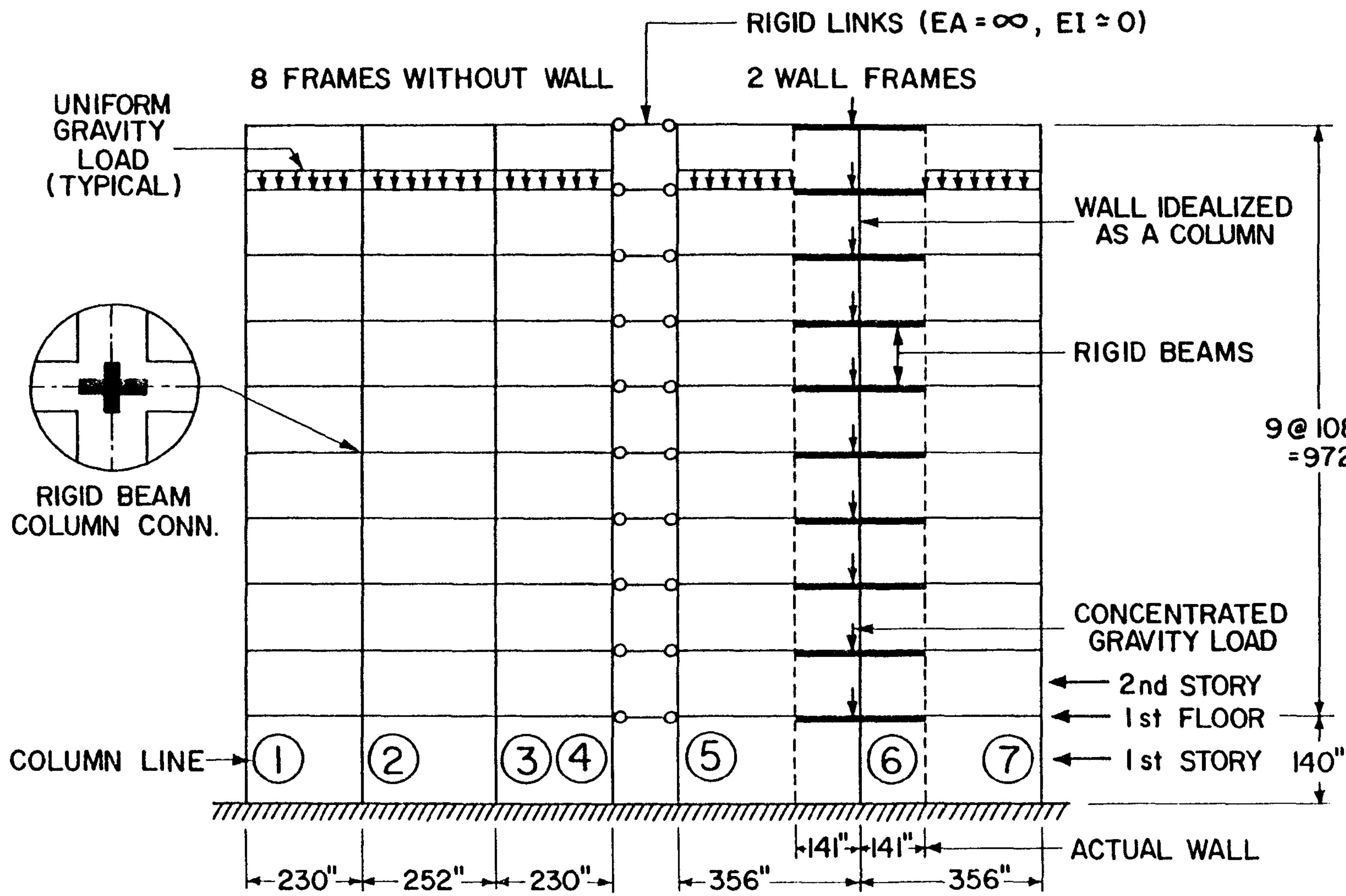

FIG. 7.1 IDEALIZATION OF PROTOTYPE BUILDING

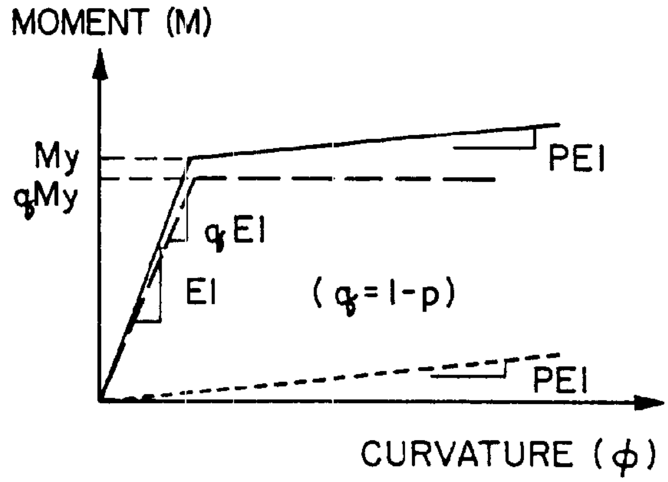

FIG. 7.2 BILINEAR M-φ RELATIONSHIP FOR TWO-COMPONENT FLEXURAL MEMBER

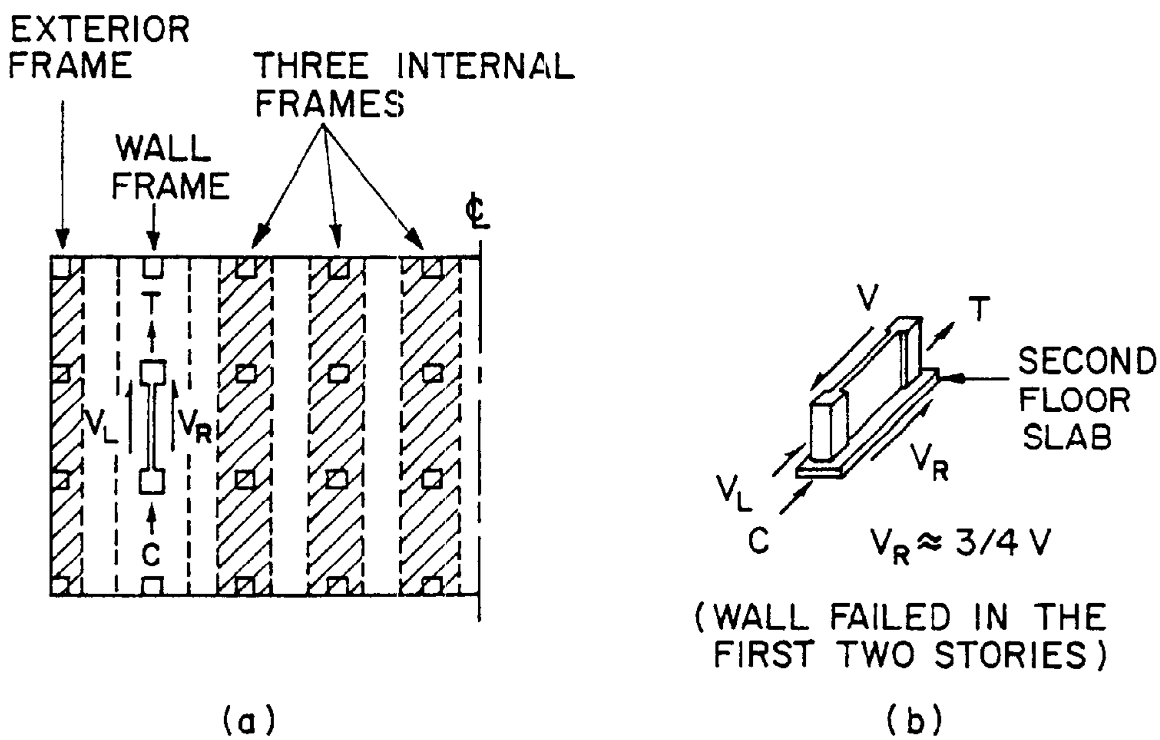

FIG. 7.3 TRANSFERRING OF THIRD STORY SHEAR

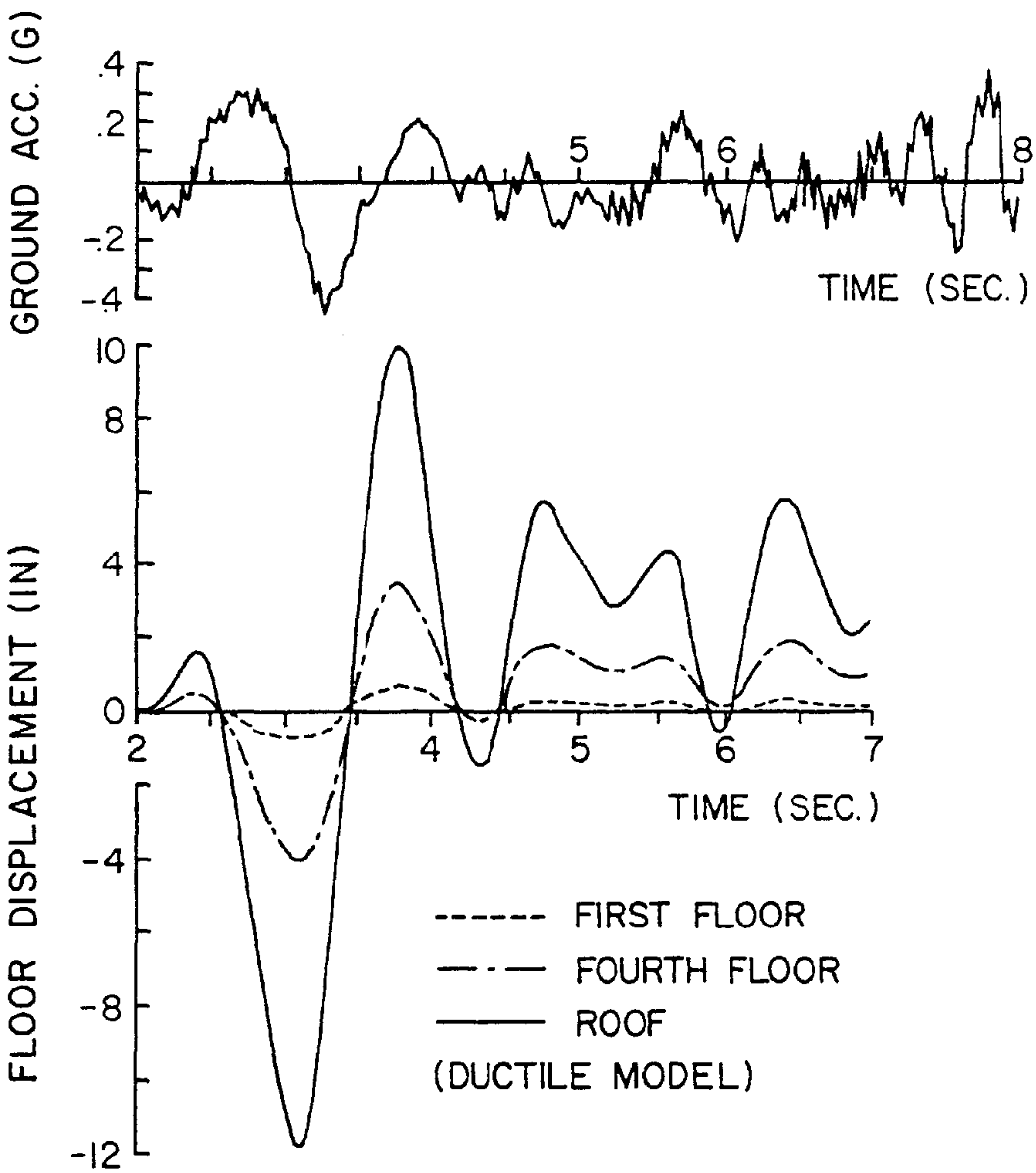

FIG. 7.4 TIME HISTORY OF FLOOR DISPLACEMENTS UNDER DERIVED PACOIMA BASE ROCK MOTION (0.4 g)

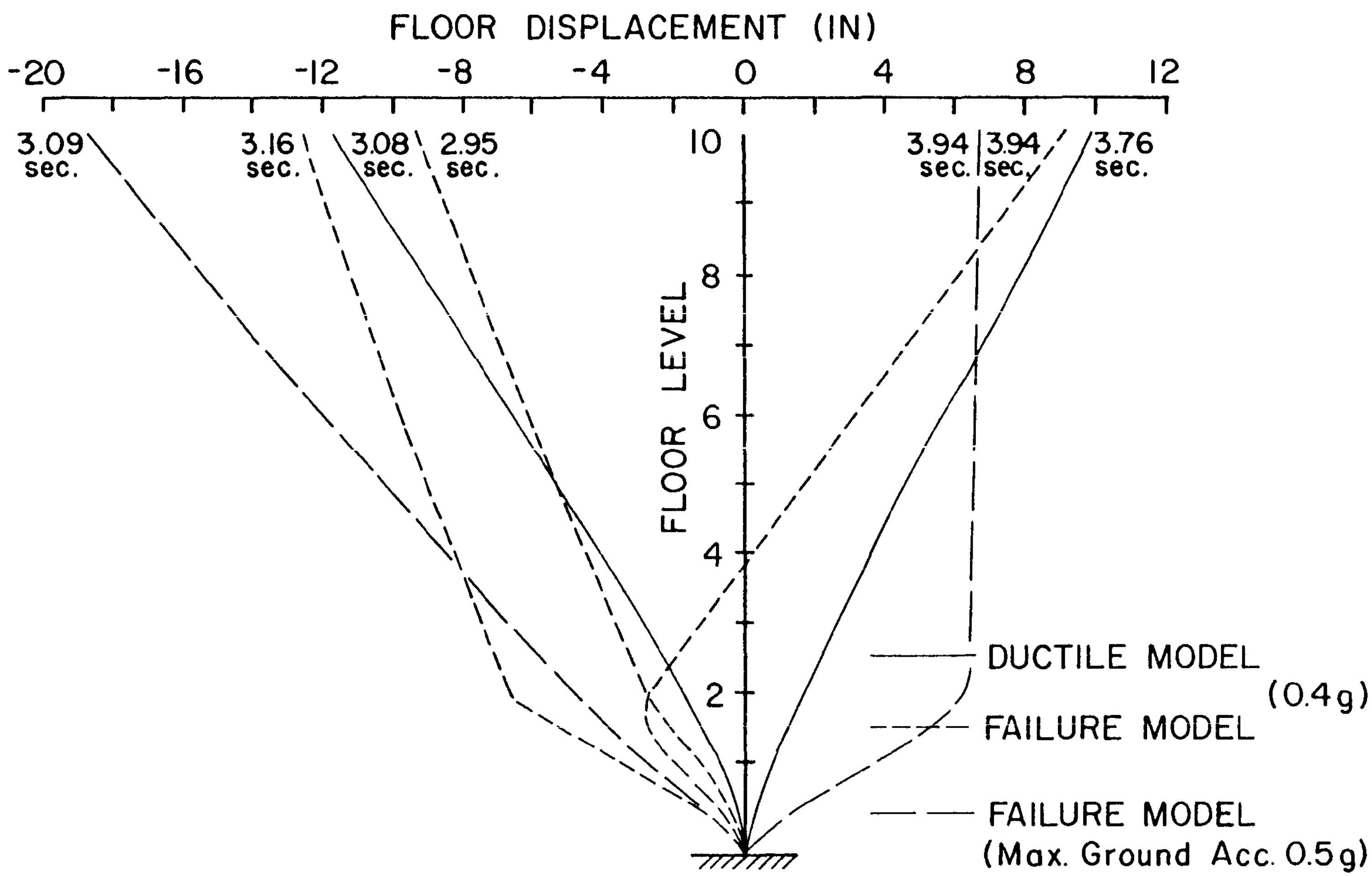

FIG. 7.5 LATERAL DEFORMATION SHAPES OF PROTOTYPE BUILDING UNDER DERIVED PACOIMA BASE ROCK MOTION (0.4 g)

SEQ.	TIME (SEC.)
1	2.64
7	2.70
12	2.75
17	2.80
22	2.85
27	2.90
32	2.95

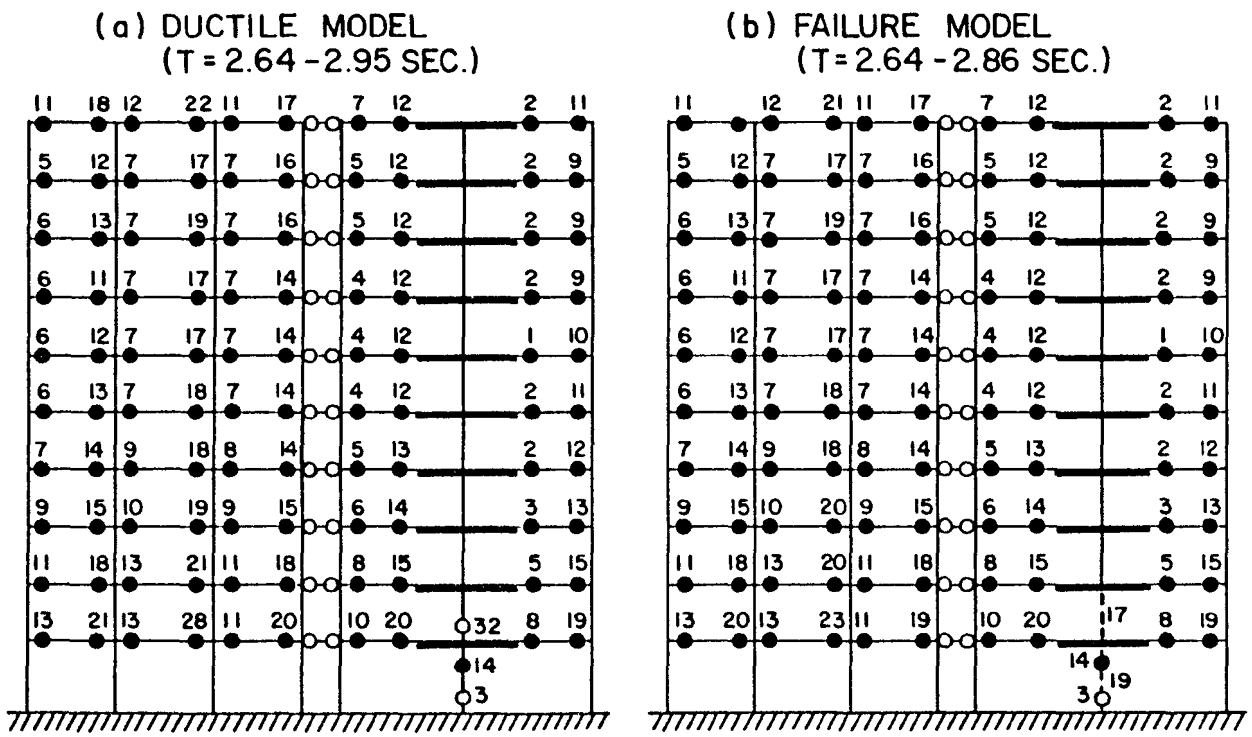

FIG. 7.6 SEQUENCE AND LOCATION OF PLASTIC HINGES UNDER DERIVED PACOIMA BASE ROCK MOTION (0.4 g)

(c) FAILURE MODEL
(T = 3.16 SEC.)

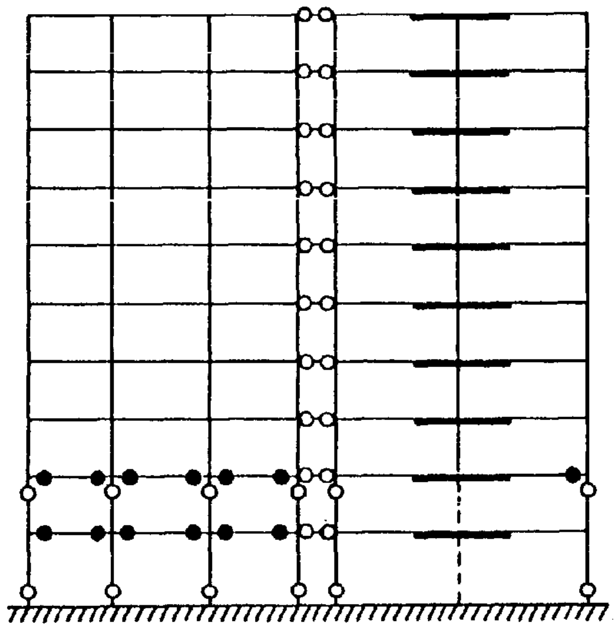

FIG. 7.6 (CONT'D)

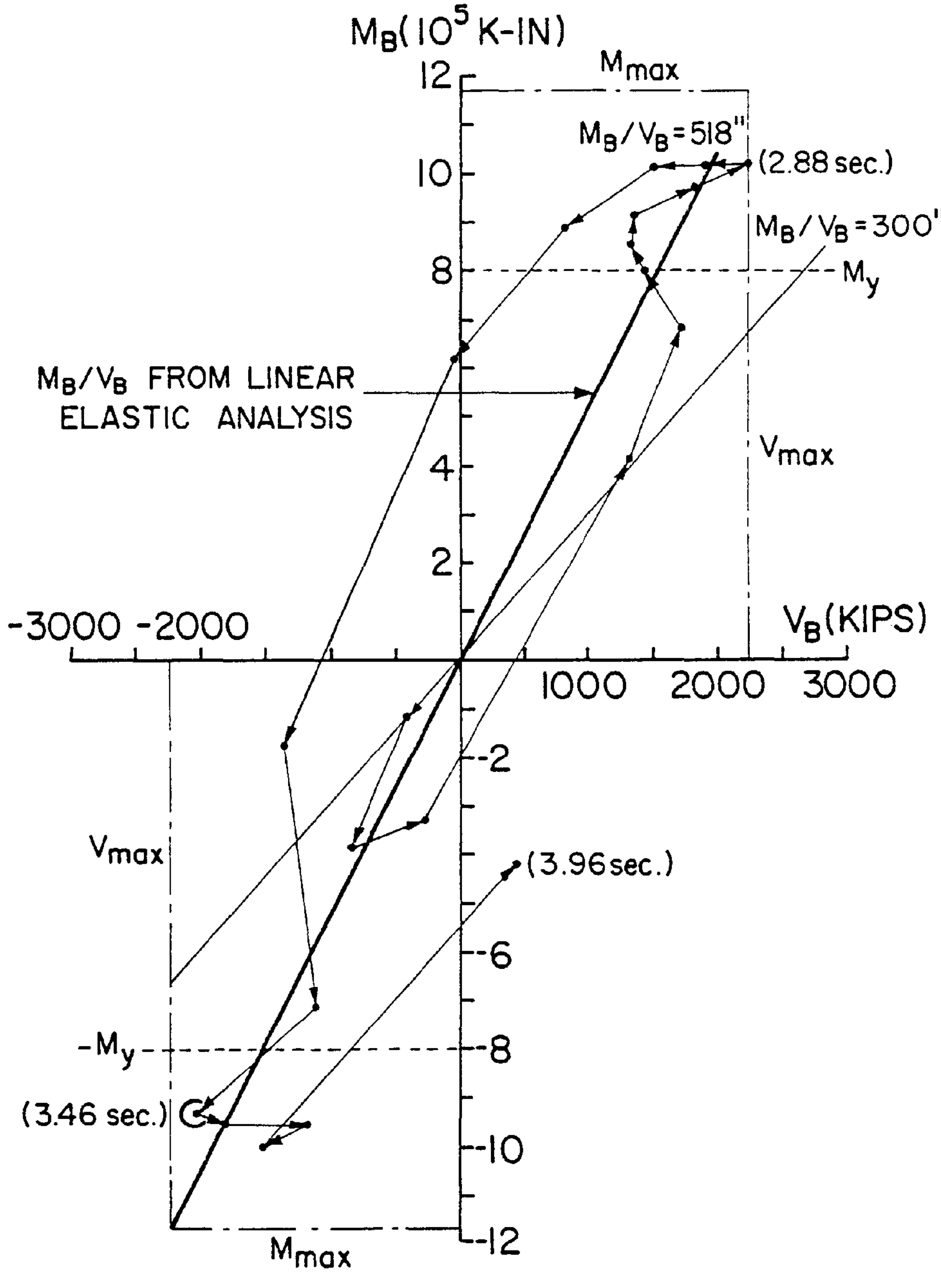

FIG. 7.7 RELATIONSHIP BETWEEN M_B AND V_B UNDER DERIVED PACOIMA BASE ROCK MOTION (0.4 g)

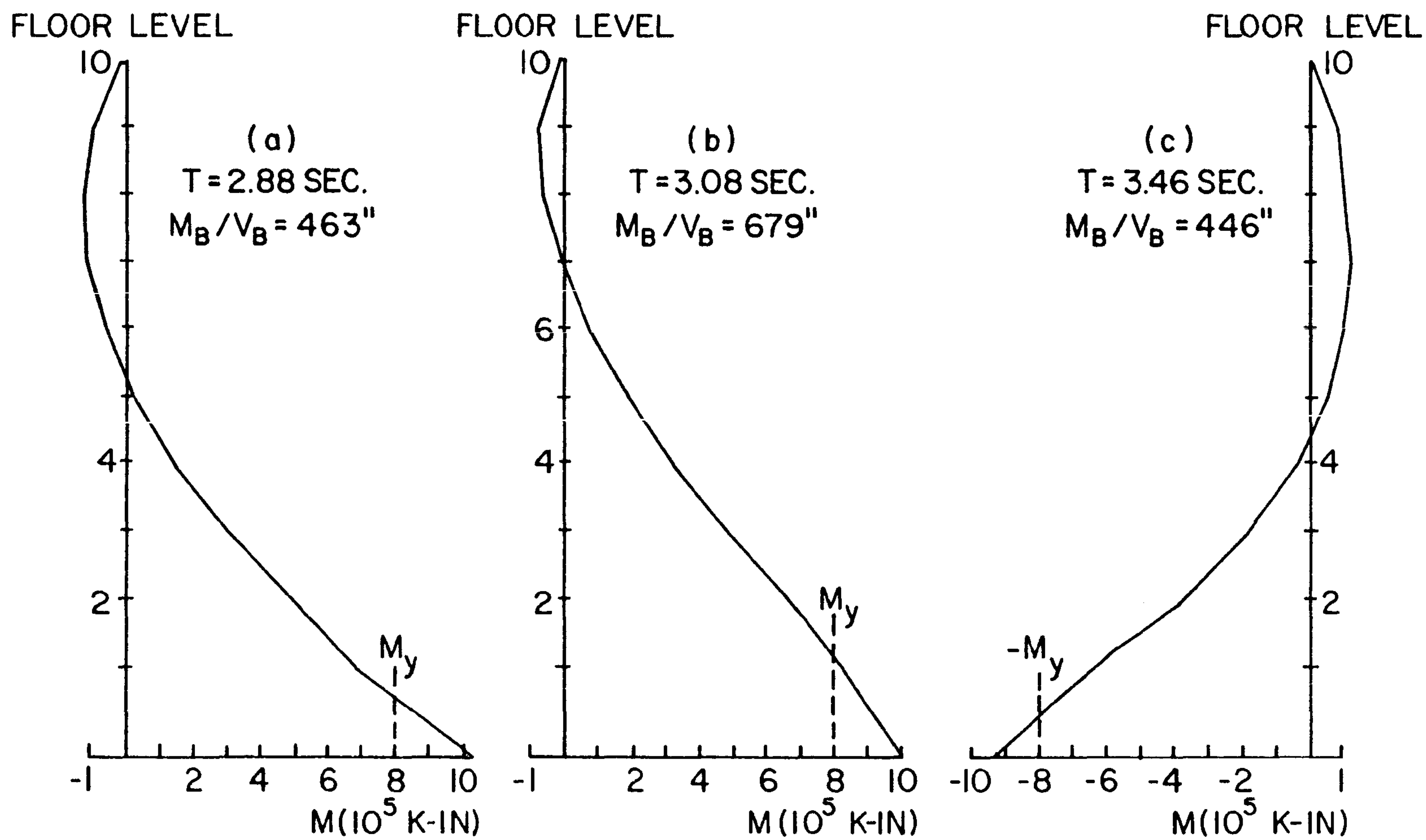

FIG. 7.8 VARIATION OF MOMENT DIAGRAM OF WALL UNDER DERIVED PACOIMA BASE ROCK MOTION (0.4 g) - DUCTILE MODEL

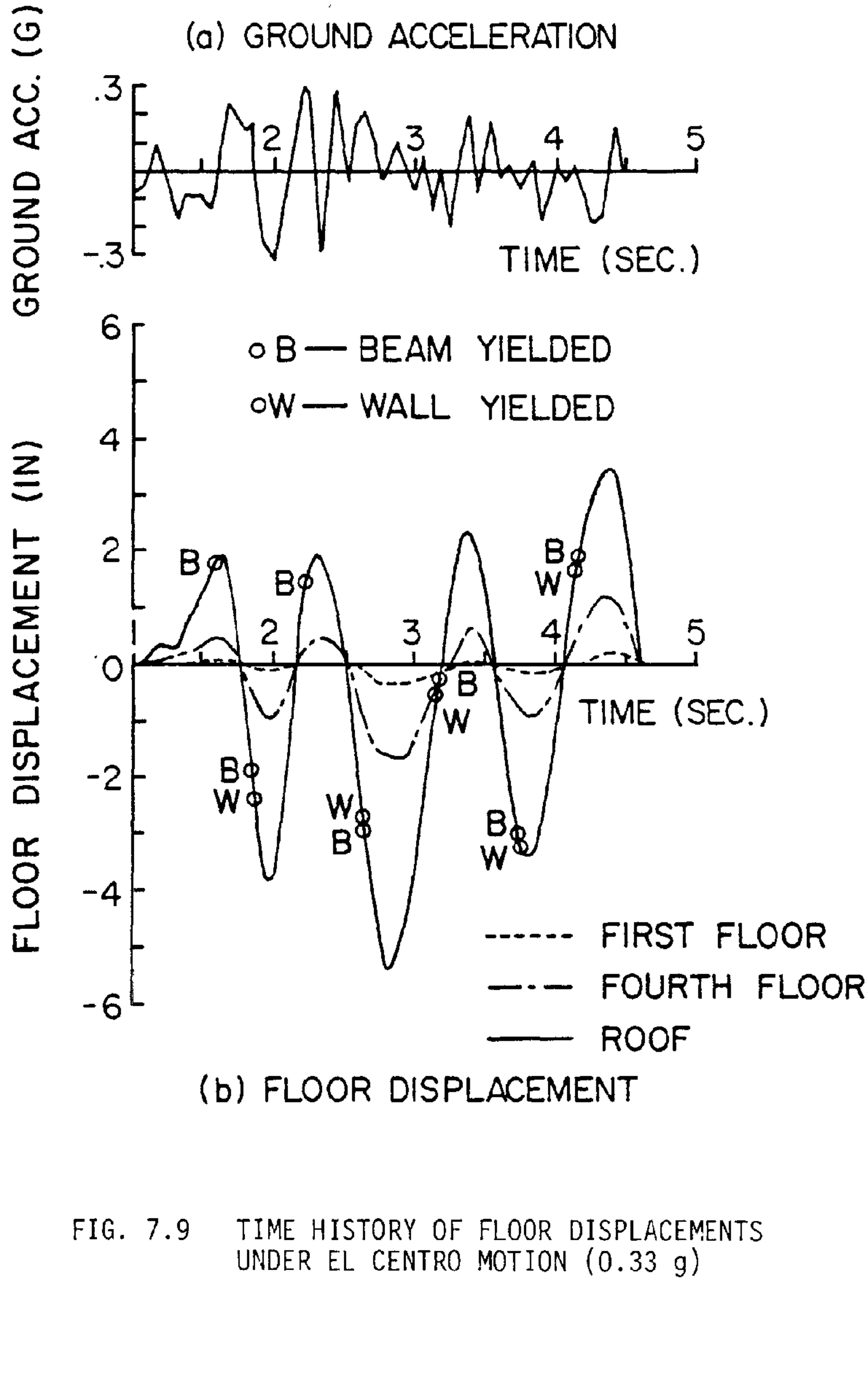

FIG. 7.9 TIME HISTORY OF FLOOR DISPLACEMENTS UNDER EL CENTRO MOTION (0.33 g)

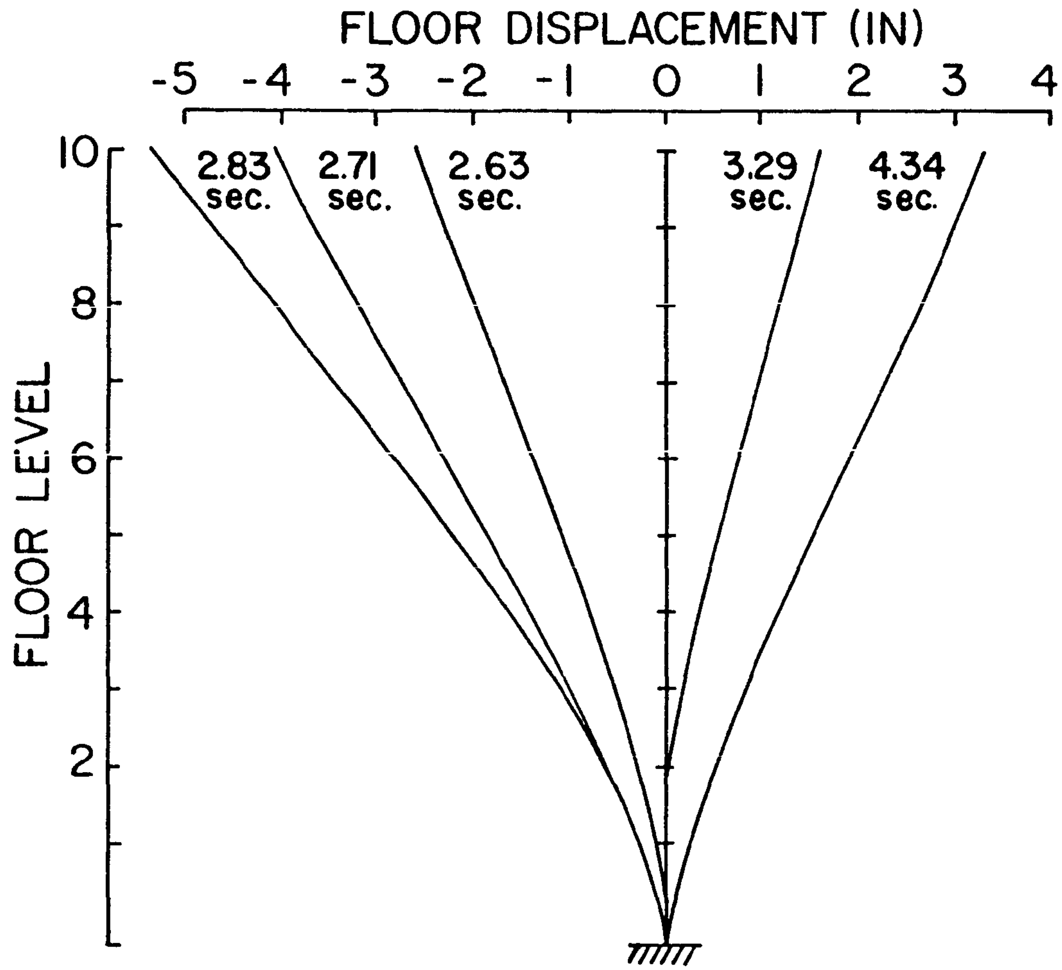

FIG. 7.10 DEFORMATION SHAPES FOR DUCTILE MODEL UNDER N-S COMPONENT OF EL CENTRO MOTION (0.33 g)

SEQ.	TIME (SEC.)
1	1.85
6	1.90
11	1.95
80	2.64
86	2.70
91	2.75

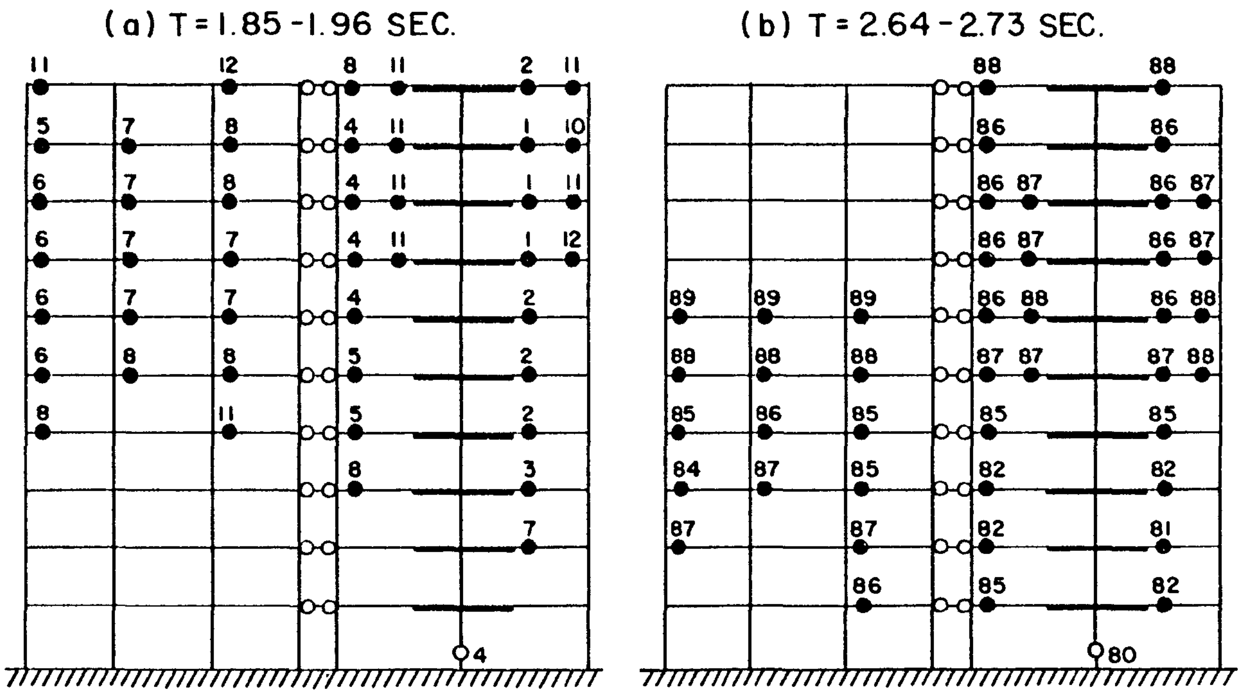

FIG. 7.11 SEQUENCE AND LOCATION OF PLASTIC HINGES UNDER EL CENTRO MOTION (0.33 g)

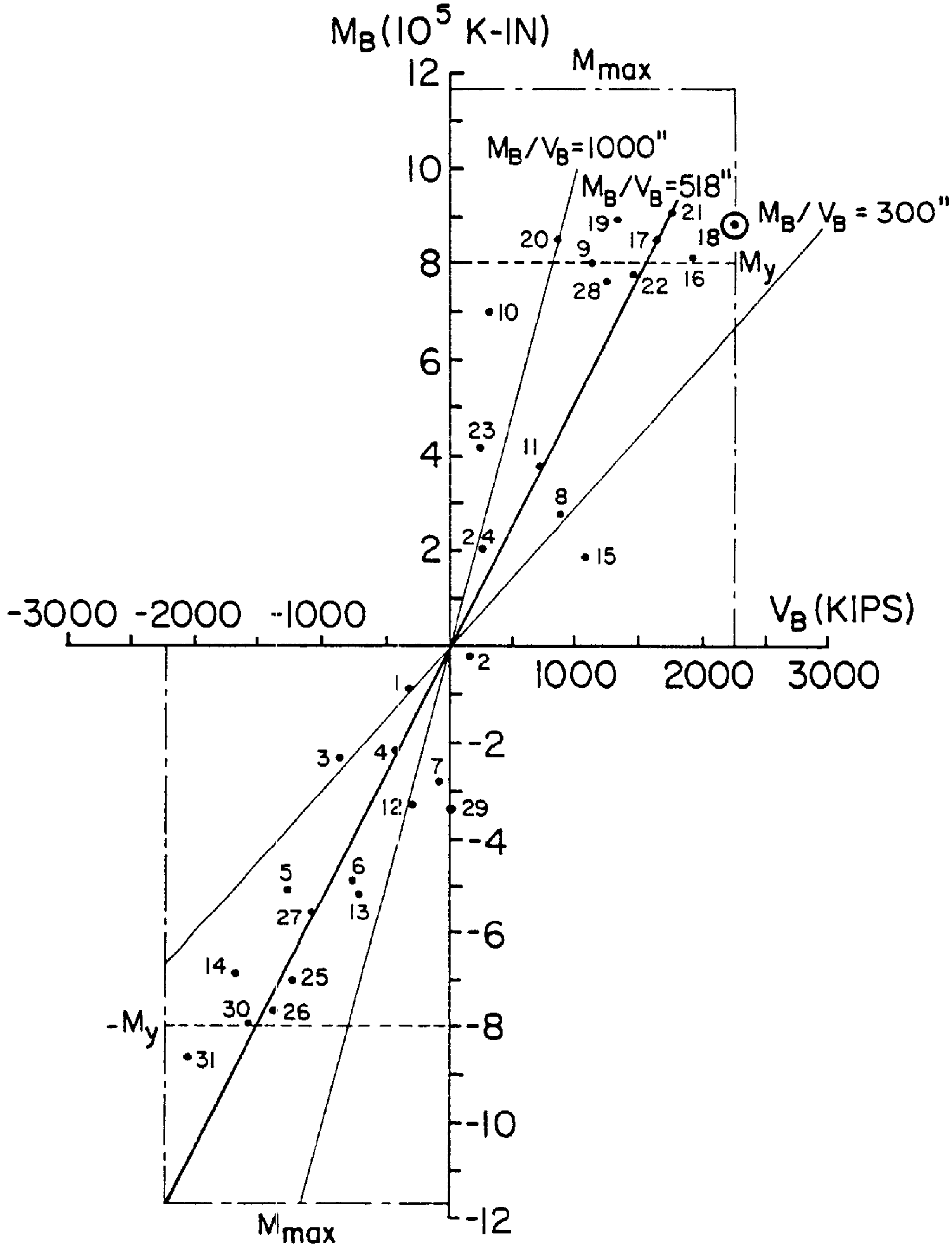

FIG. 7.12 RELATIONSHIP BETWEEN M_B AND V_B UNDER EL CENTRO MOTION (0.33 g)

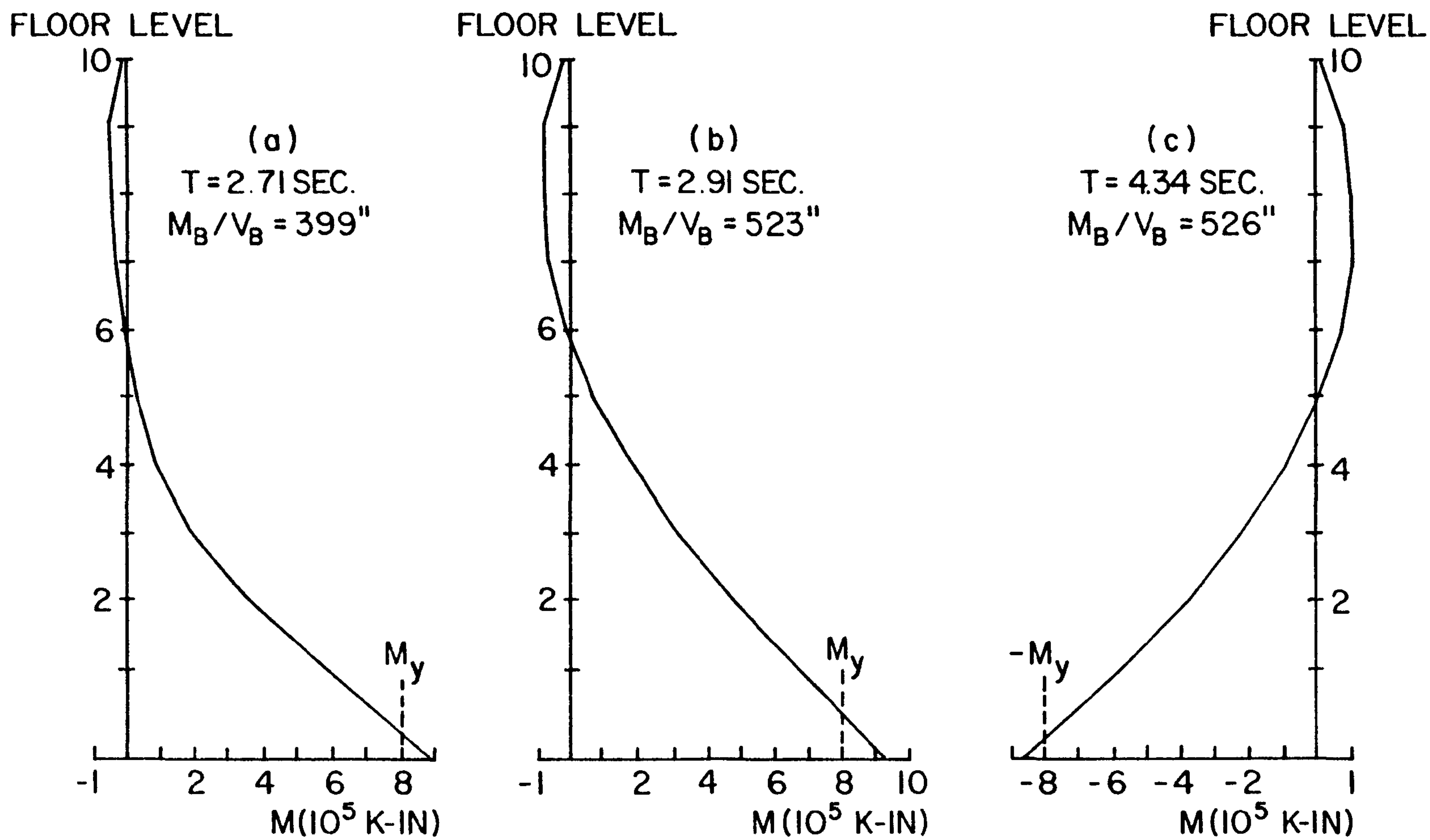

FIG. 7.13 VARIATION OF MOMENT DIAGRAM OF WALL UNDER EL CENTRO MOTION (0.33 g)

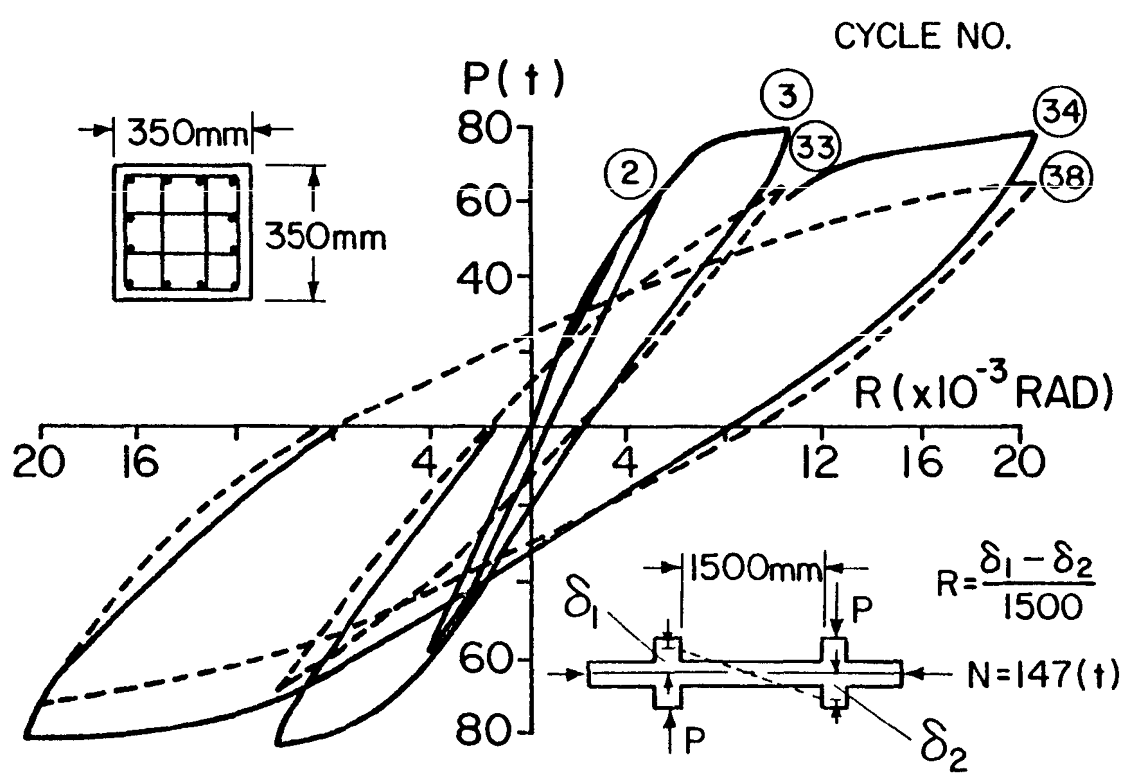

FIG. 7.14 LOAD-DEFLECTION CURVE OF A-P_W0.9 SPECIMEN

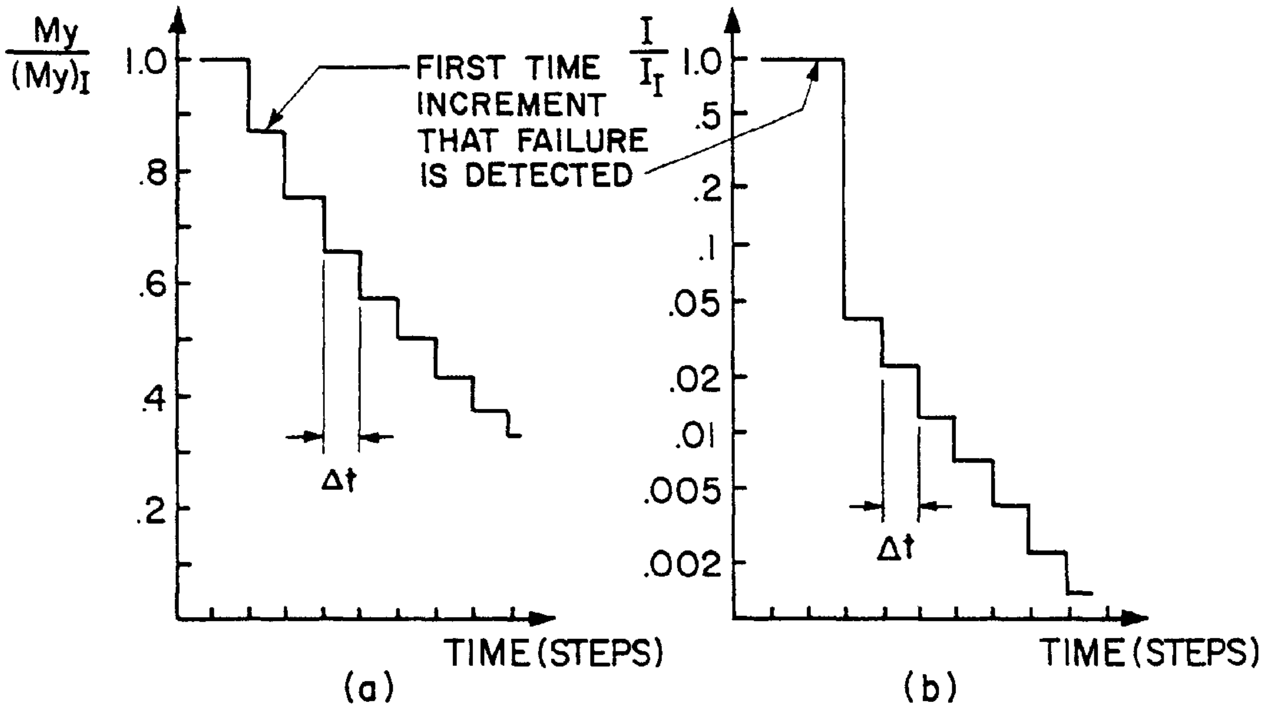

FIG. 7.15 PROGRESSIVE FAILURE MODEL

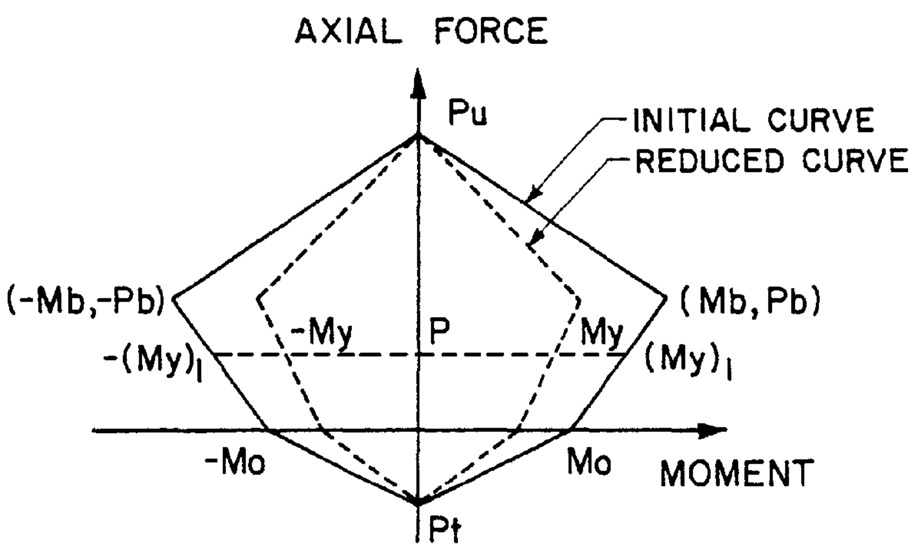

FIG. 7.16 INITIAL AND REDUCED COLUMN YIELD INTERACTION CURVE

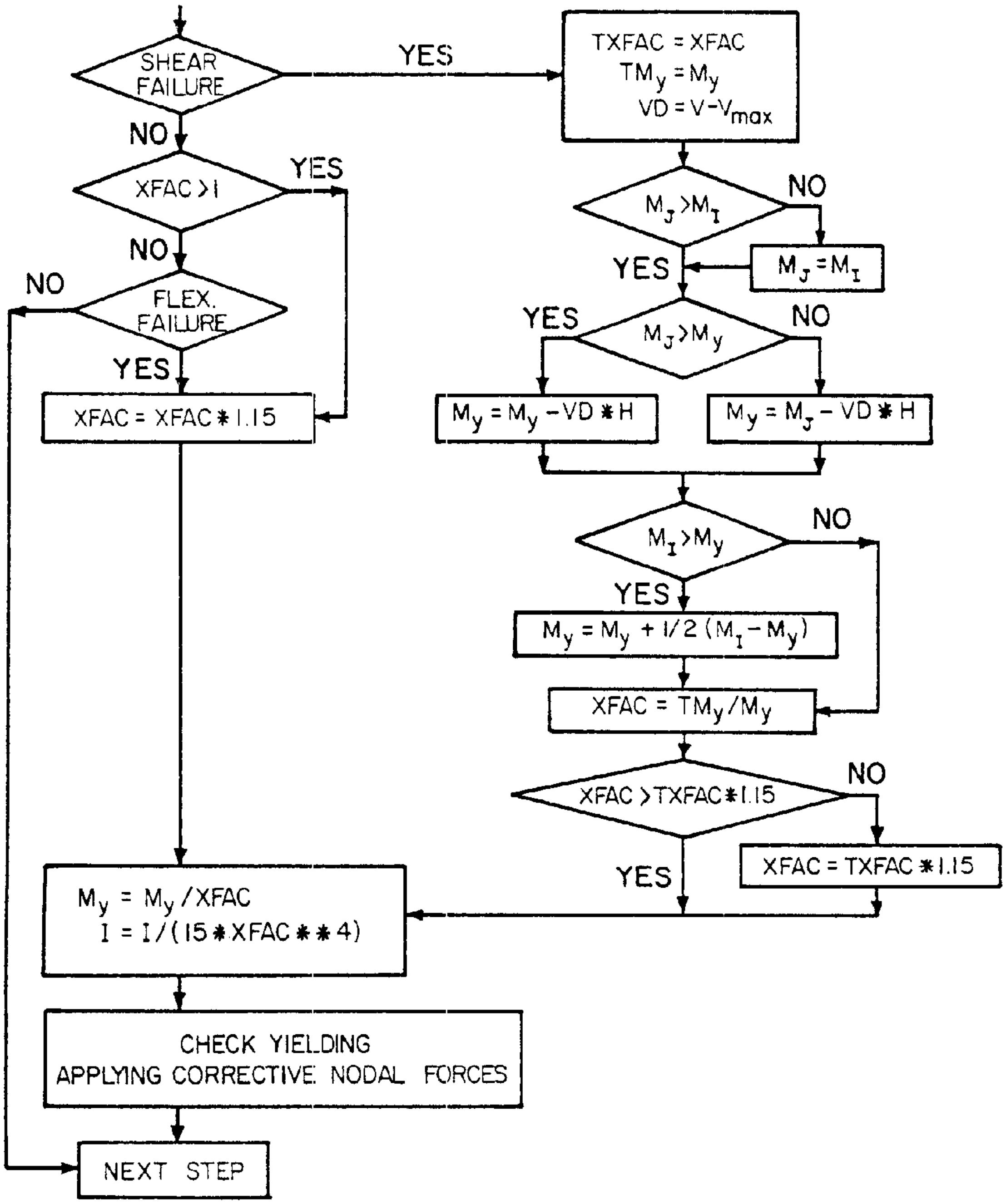

FIG. 7.17 MEMBER FAILURE PROCESS

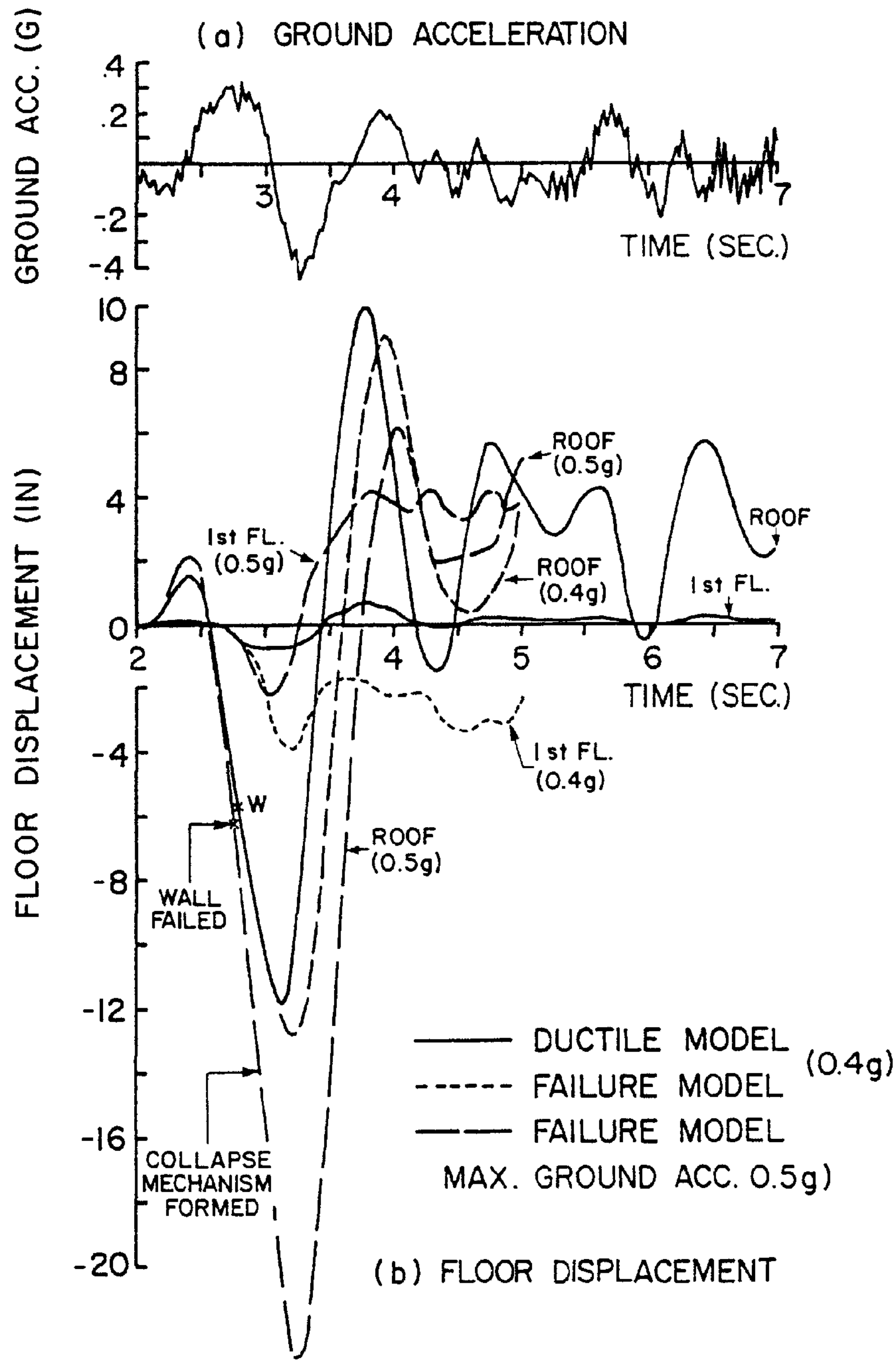

FIG. 7.18 TIME HISTORY OF FLOOR DISPLACEMENTS UNDER DERIVED PACOIMA BASE ROCK MOTION (0.4 g)

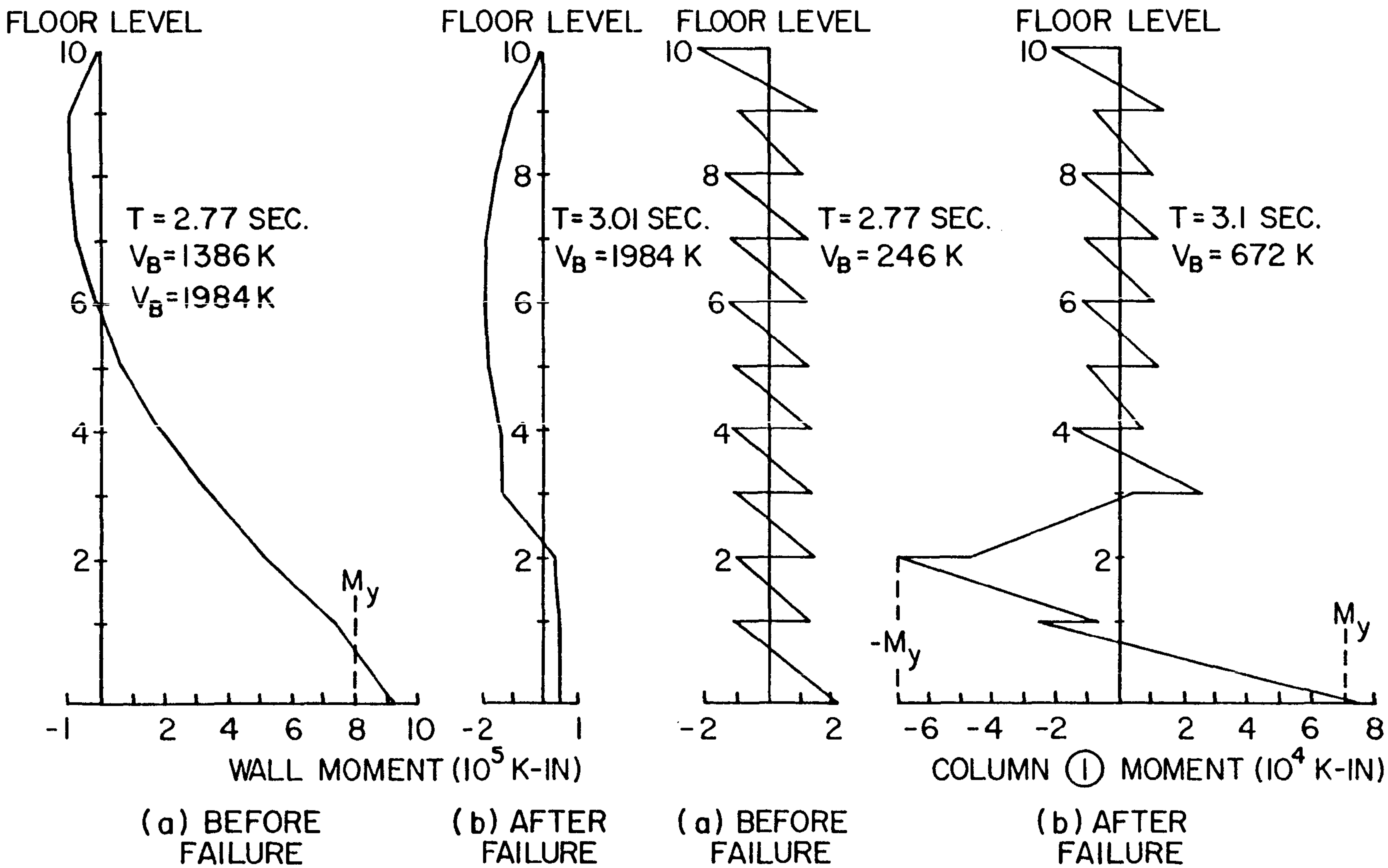

FIG. 7.19 VARIATION OF MOMENT DIAGRAMS OF WALL AND COLUMN UNDER DERIVED PACOIMA BASE ROCK MOTION (0.4 g) - FAILURE MODEL

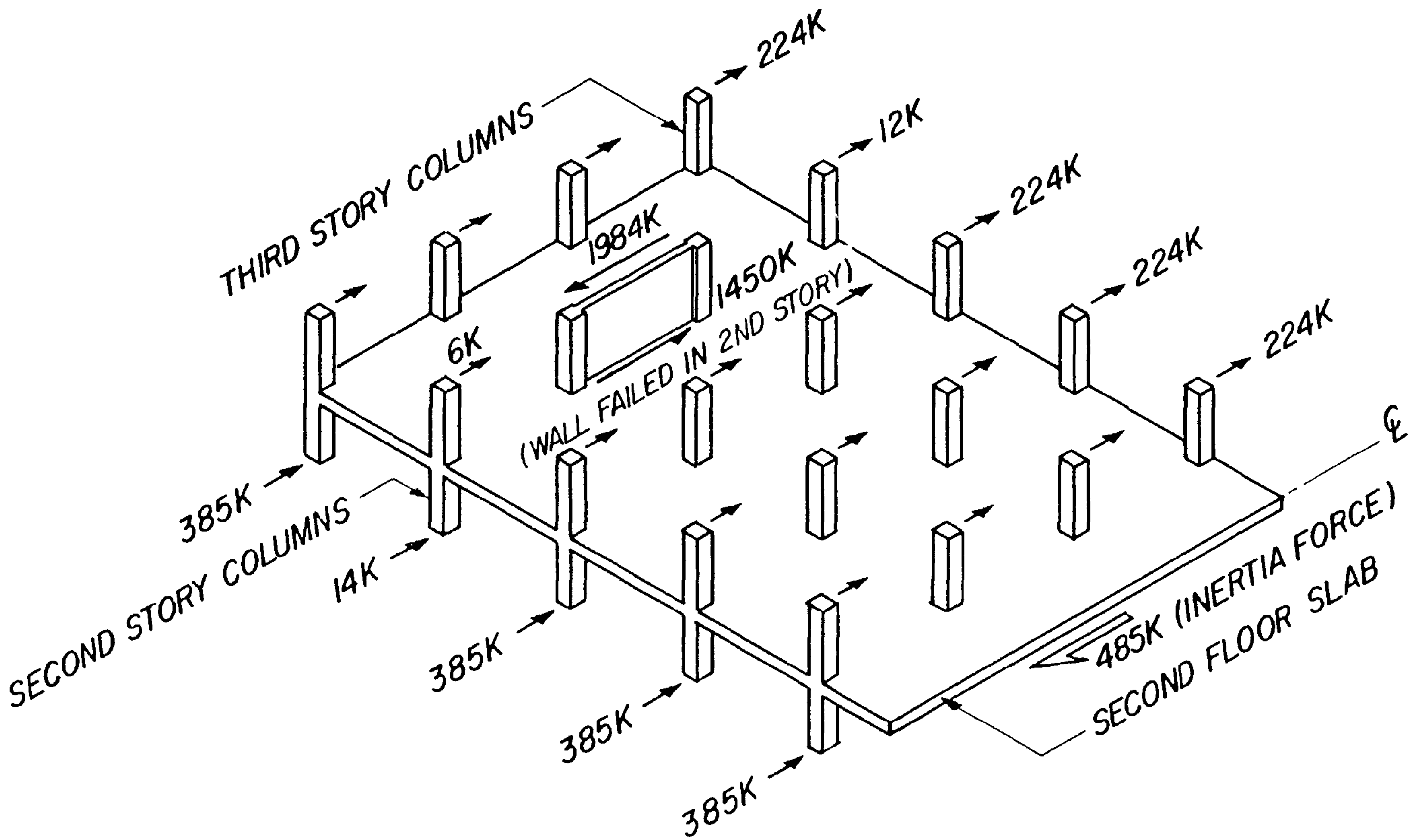

FIG. 7.20 STORY SHEAR TRANSFERRING MECHANISM AT T = 3.01 SEC. UNDER DERIVED PACOIMA BASE ROCK MOTION (0.4 g) - FAILURE MODEL

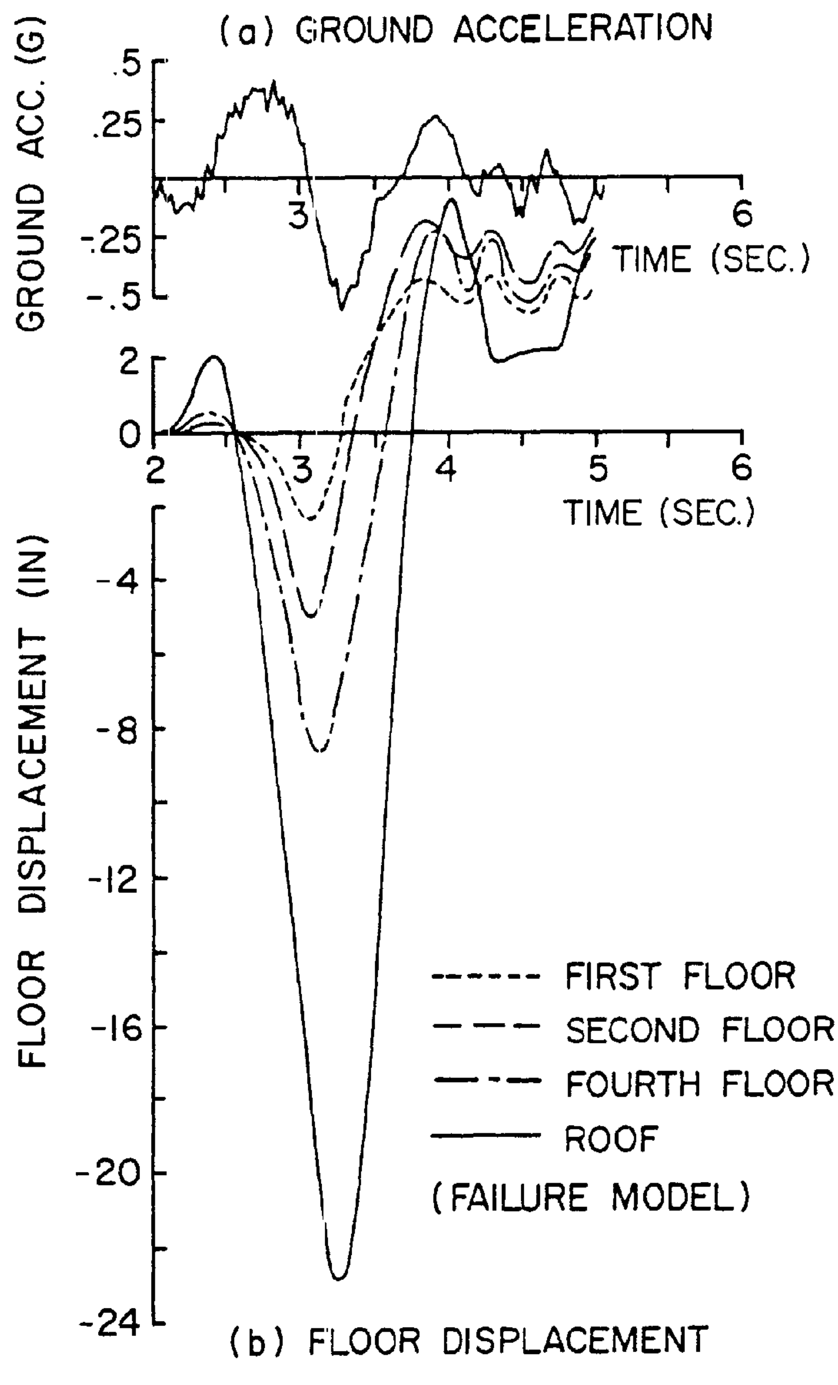

FIG. 7.21 TIME HISTORY OF FLOOR DISPLACEMENTS UNDER DERIVED PACOIMA BASE ROCK MOTION (0.5 g)

SEQ.	TIME (SEC.)
1	2.63
8	2.70
13	2.75
18	2.80
23	2.85
28	2.90
33	2.95
38	3.00

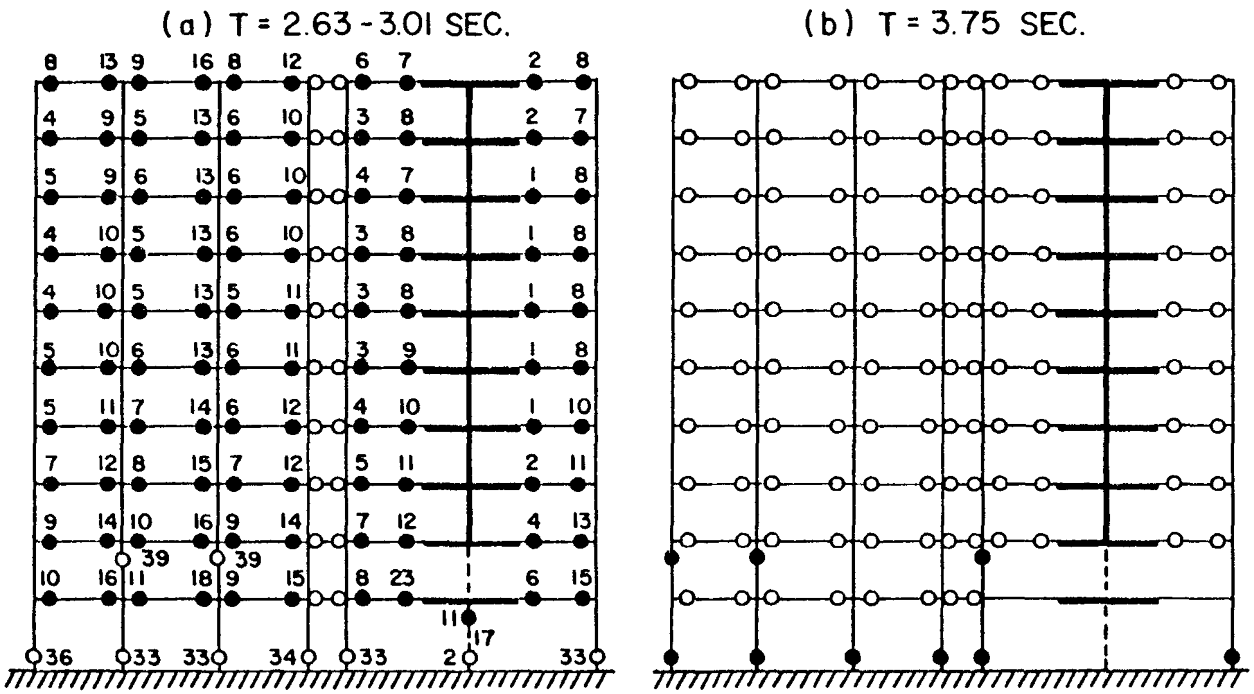

FIG. 7.22 SEQUENCE AND LOCATION OF PLASTIC HINGES UNDER DERIVED PACOIMA BASE ROCK MOTION (0.5 g) - FAILURE MODEL

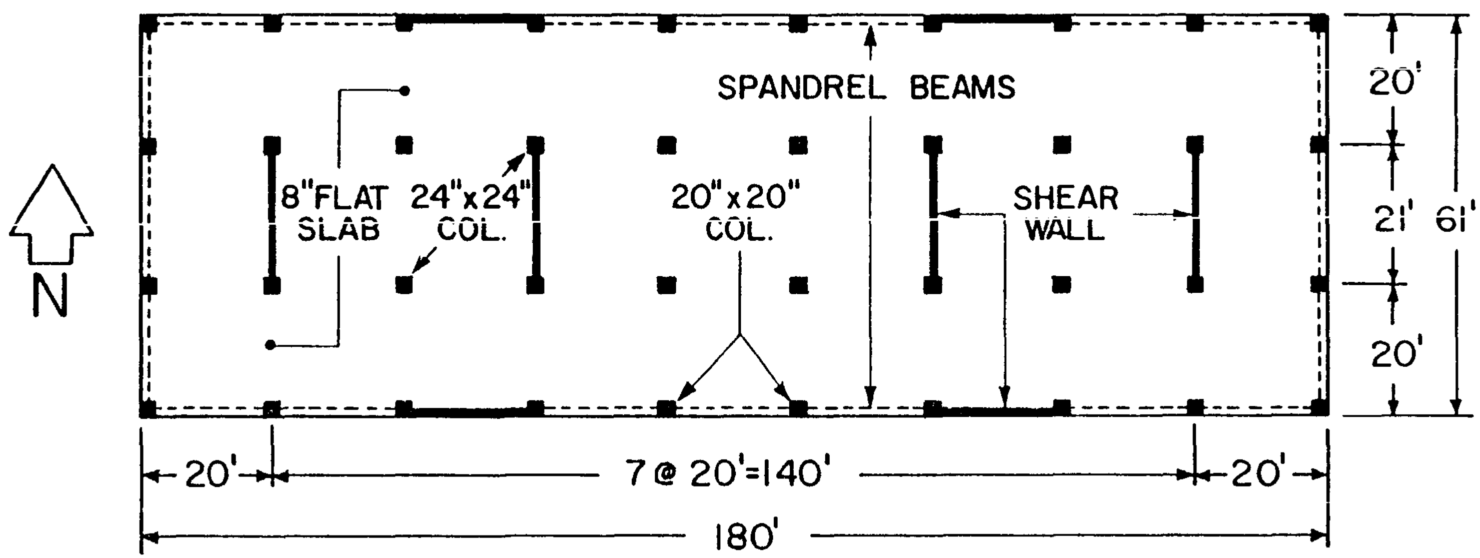

FIG. 7.23 FLOOR PLAN OF BUILDING WITH ALTERNATIVE DESIGN

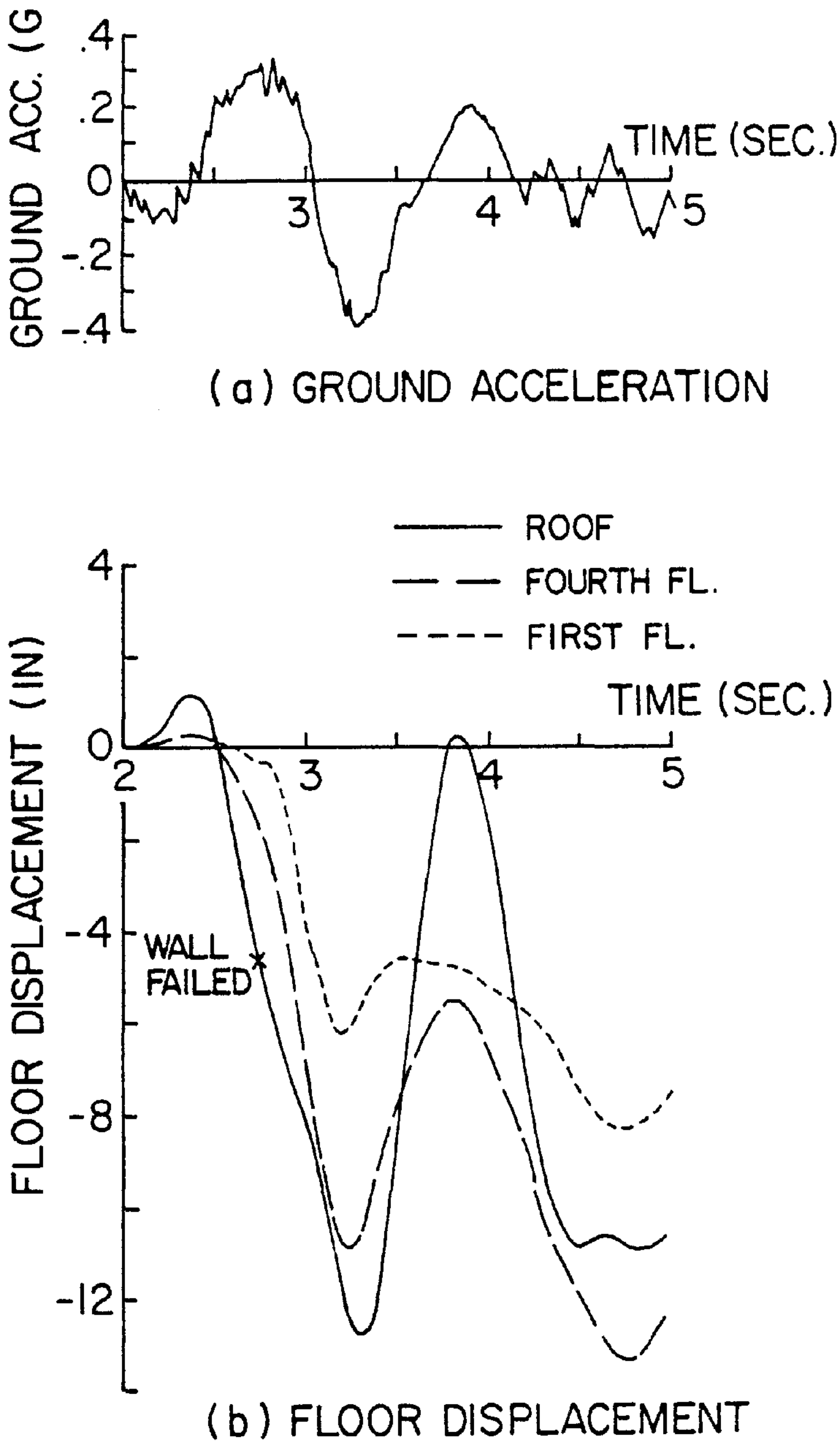

FIG. 7.24 TIME HISTORY OF FLOOR DISPLACEMENTS FOR ALTERNATIVELY DESIGNED BUILDING UNDER DERIVED PACOIMA BASE ROCK MOTION (0.4 g)

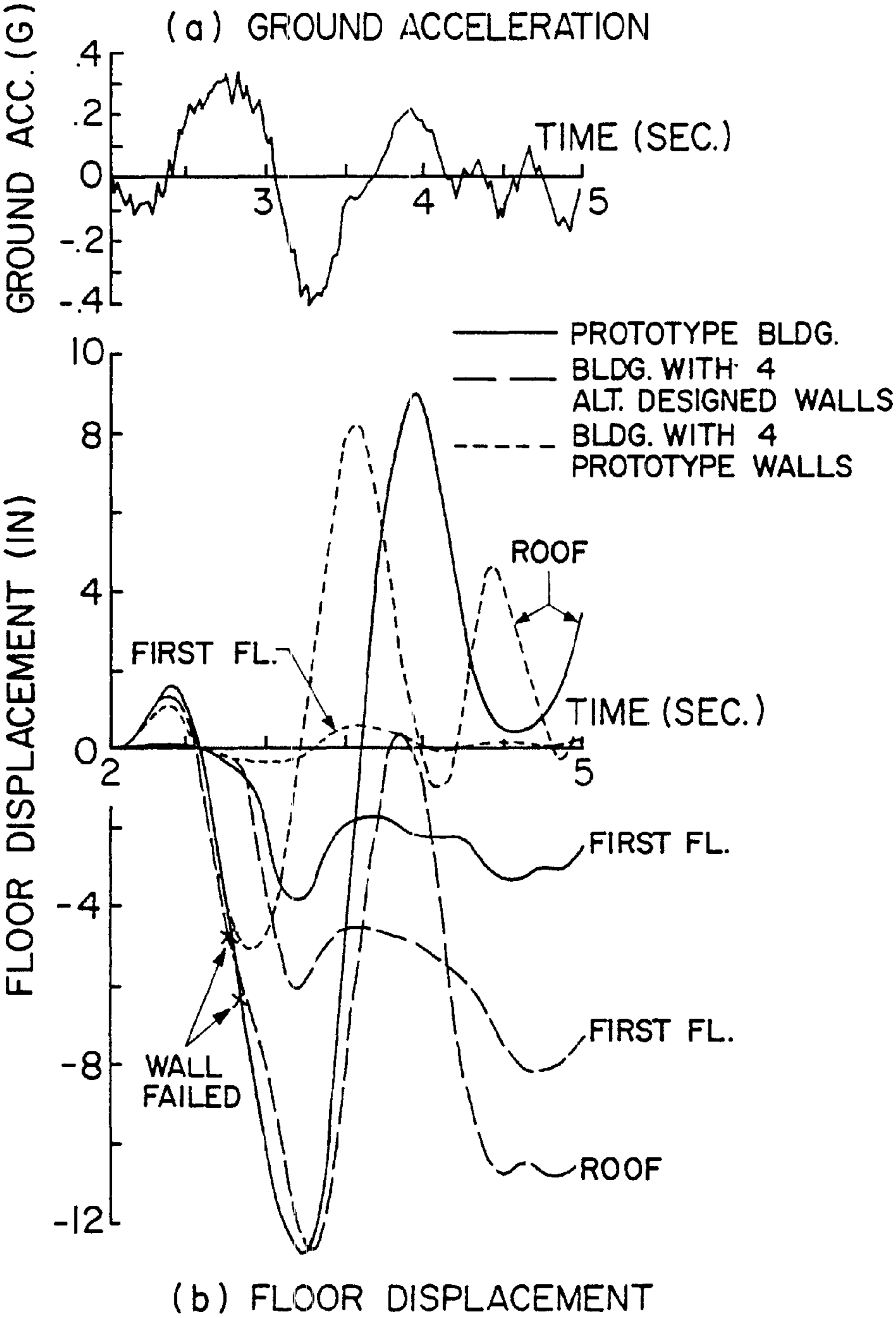

FIG. 7.25 TIME HISTORY OF FLOOR DISPLACEMENTS FOR THREE DIFFERENT BUILDINGS UNDER DERIVED PACOIMA BASE ROCK MOTION (0.4 g)

SEQ.	TIME (SEC.)
1	2.63
8	2.70
13	2.75
18	2.80

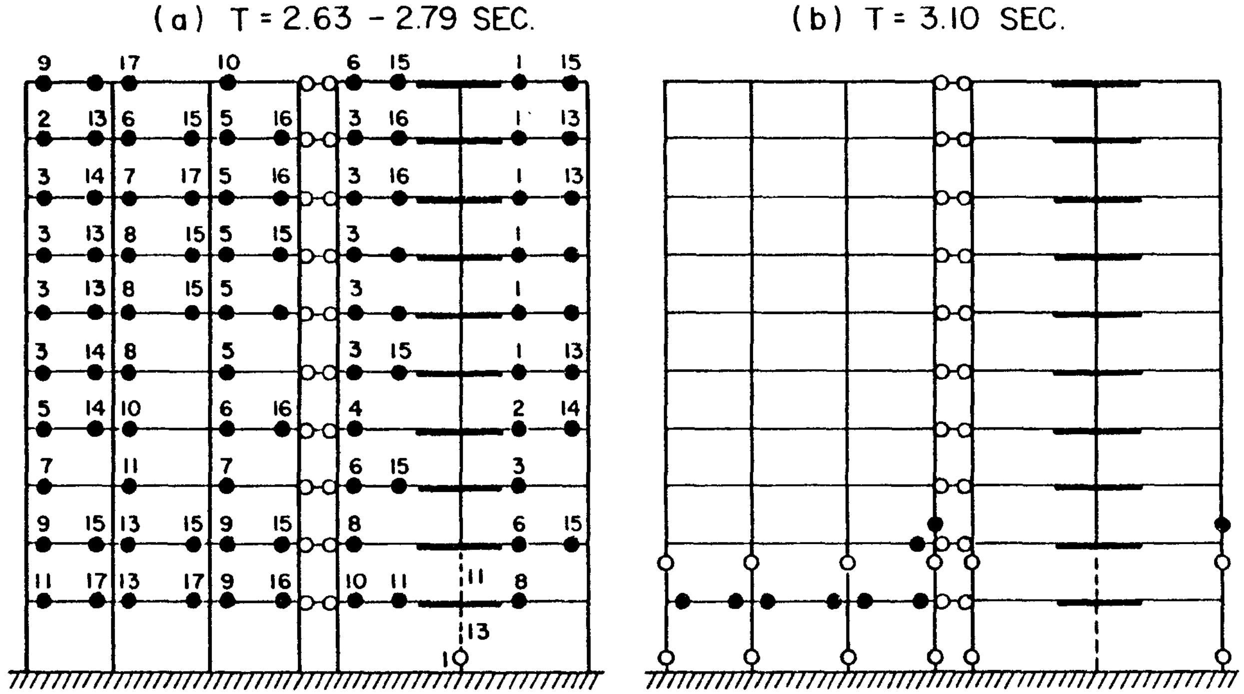

FIG. 7.26 SEQUENCE OF PLASTIC HINGE FORMATION AND WALL FAILURE FOR ALTERNATIVELY DESIGNED BUILDING UNDER DERIVED PACOIMA BASE ROCK MOTION (0.4 g)

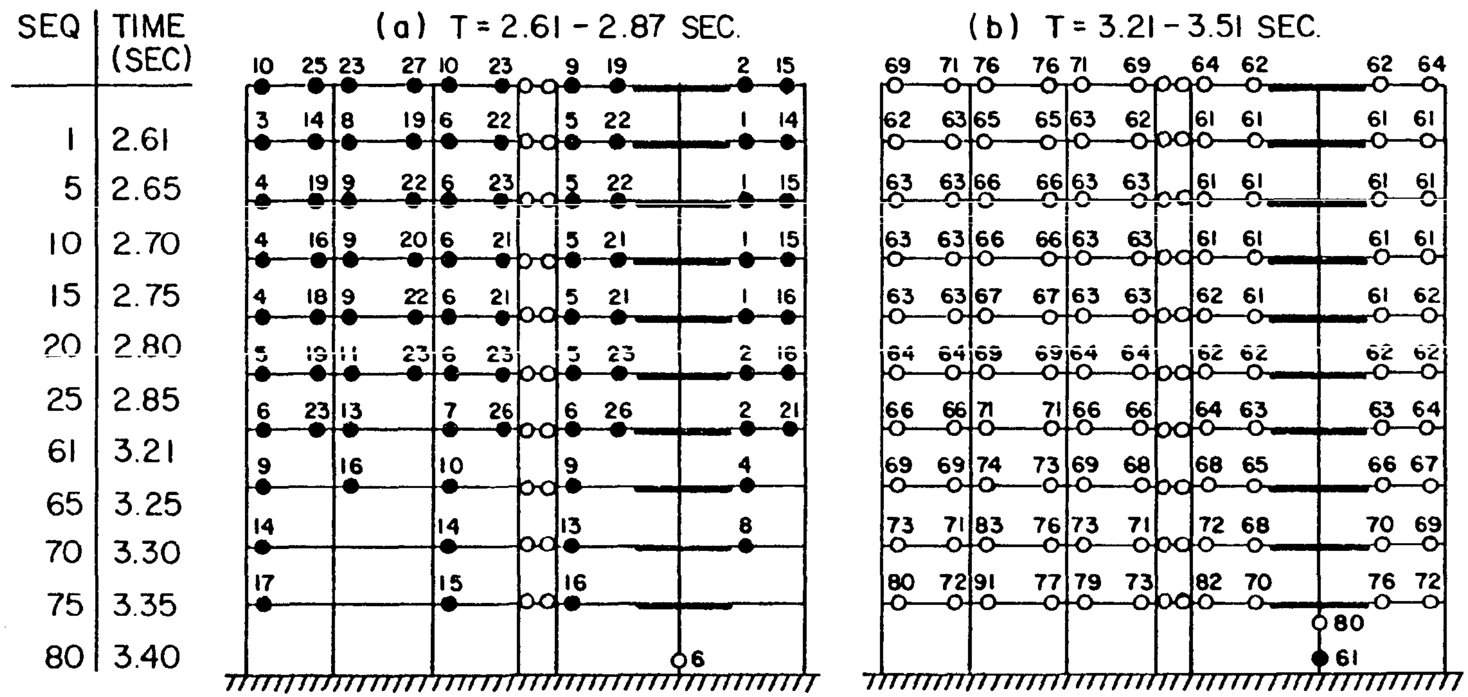

FIG. 7.27 SEQUENCE OF PLASTIC HINGE FORMATION FOR BUILDING WITH FOUR PROTOTYPE WALLS UNDER DERIVED PACOIMA BASE ROCK MOTION (0.4 g)

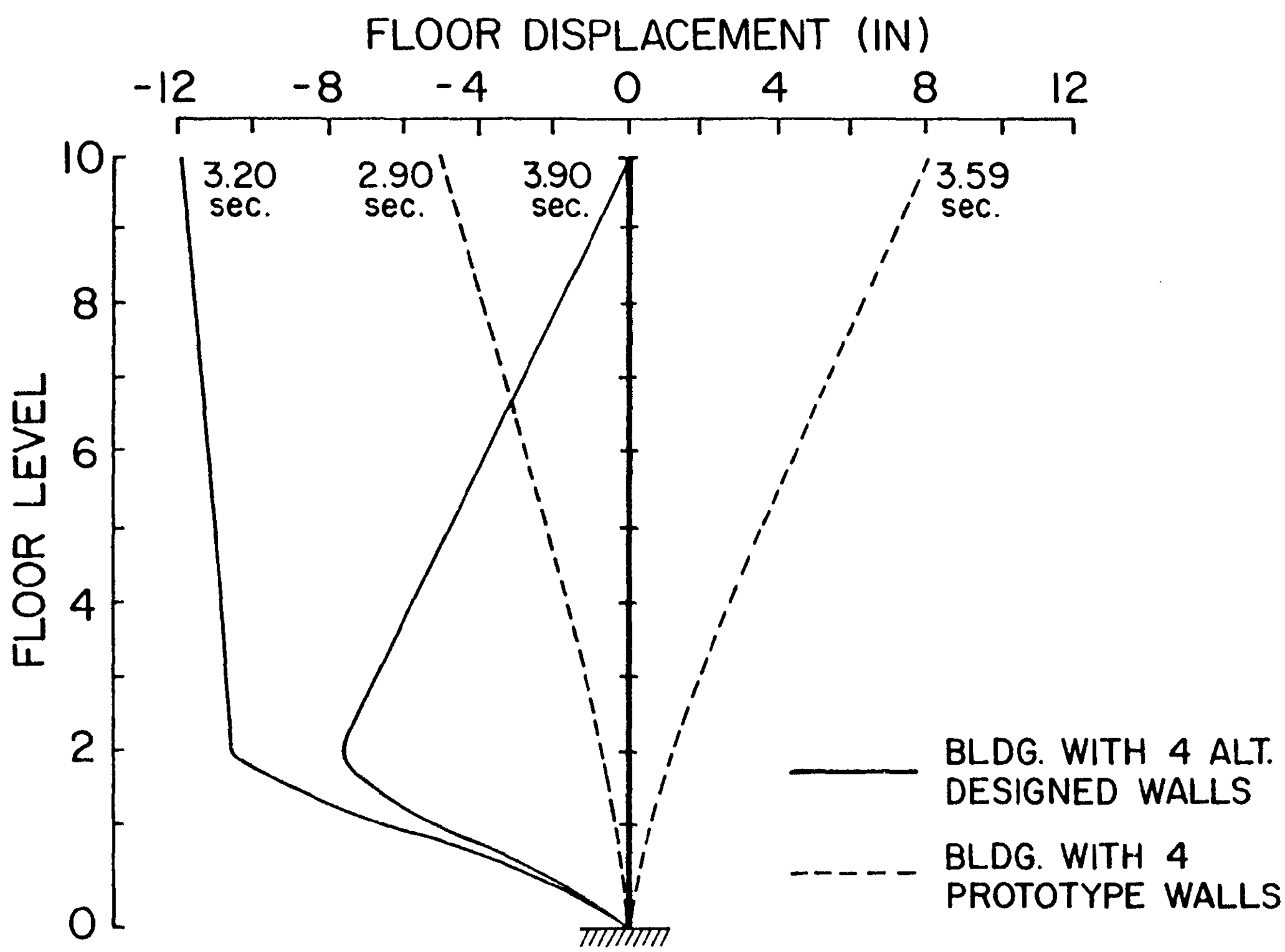

FIG. 7.28 LATERAL DEFORMATION SHAPES UNDER DERIVED PACOIMA BASE ROCK MOTION (0.4 g)

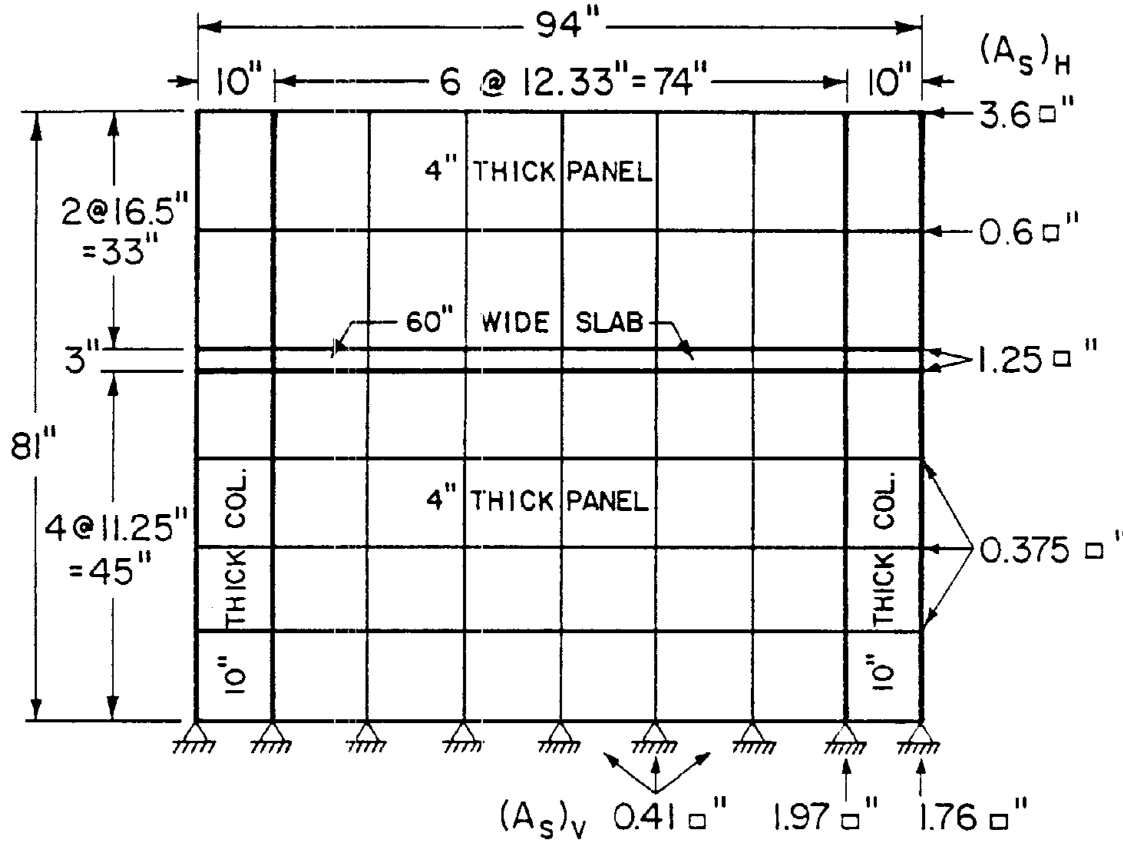

FIG. 8.1 DIMENSIONS AND REINFORCEMENT OF STANDARD FINITE ELEMENT MODEL

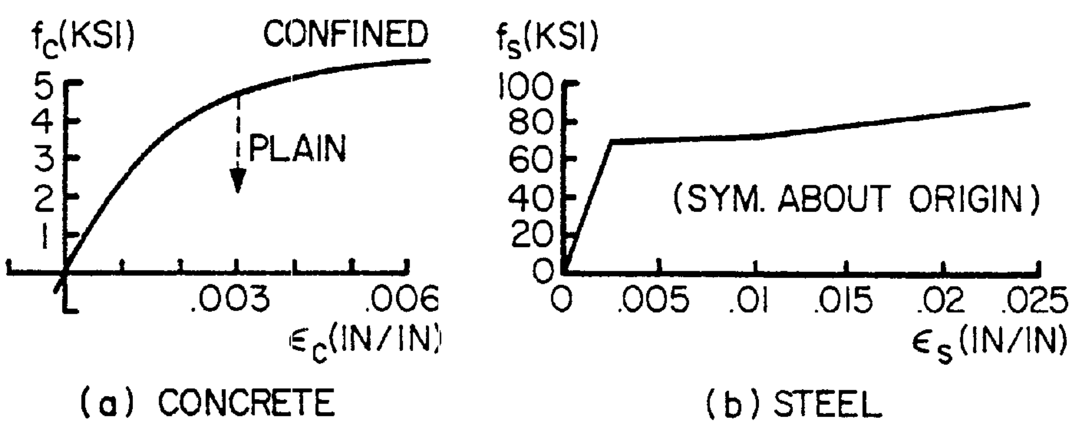

FIG. 8.2 STRESS-STRAIN CURVE FOR CONCRETE AND STEEL

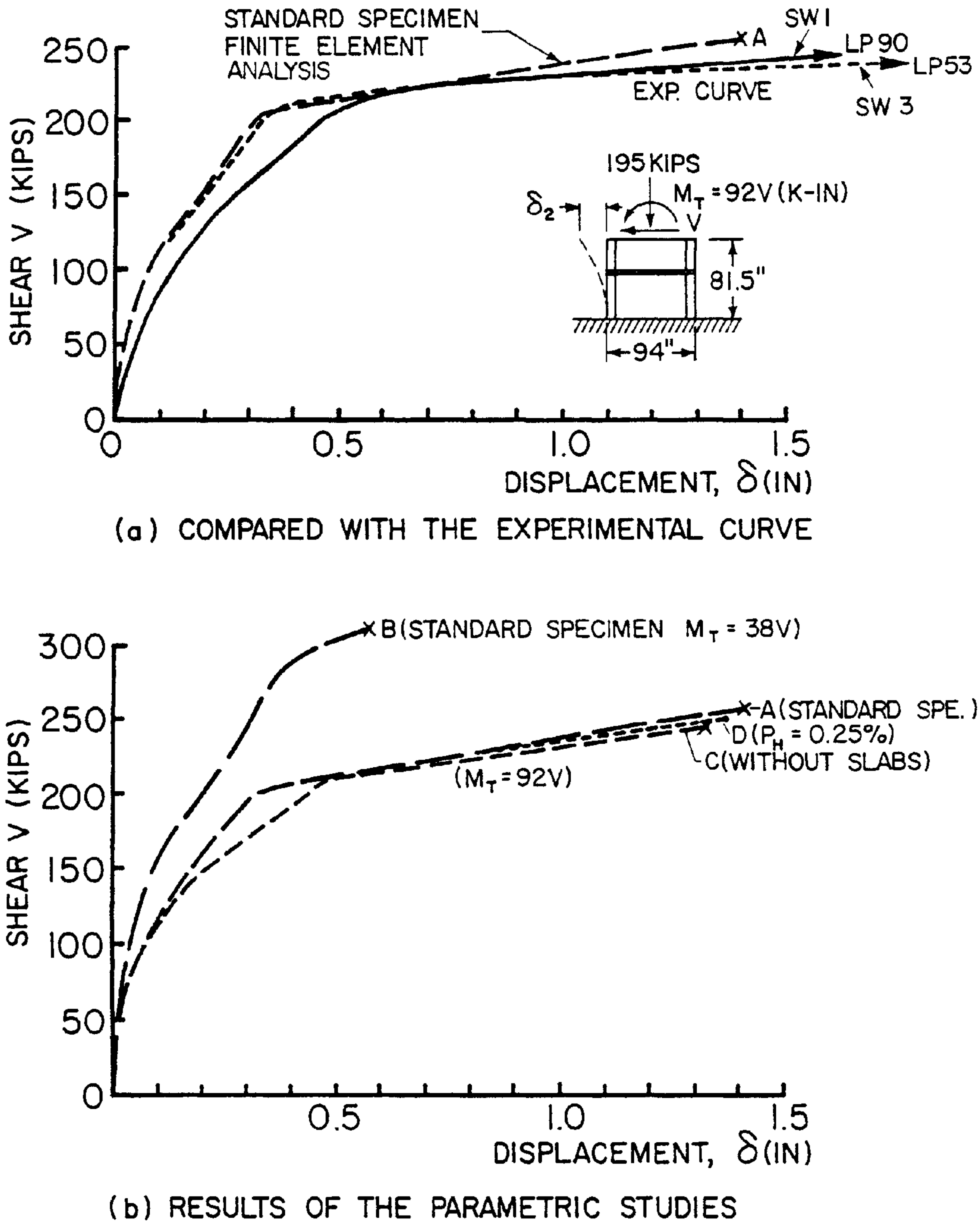

FIG. 8.3 LOAD-DISPLACEMENT CURVES OBTAINED FROM FINITE ELEMENT ANALYSES

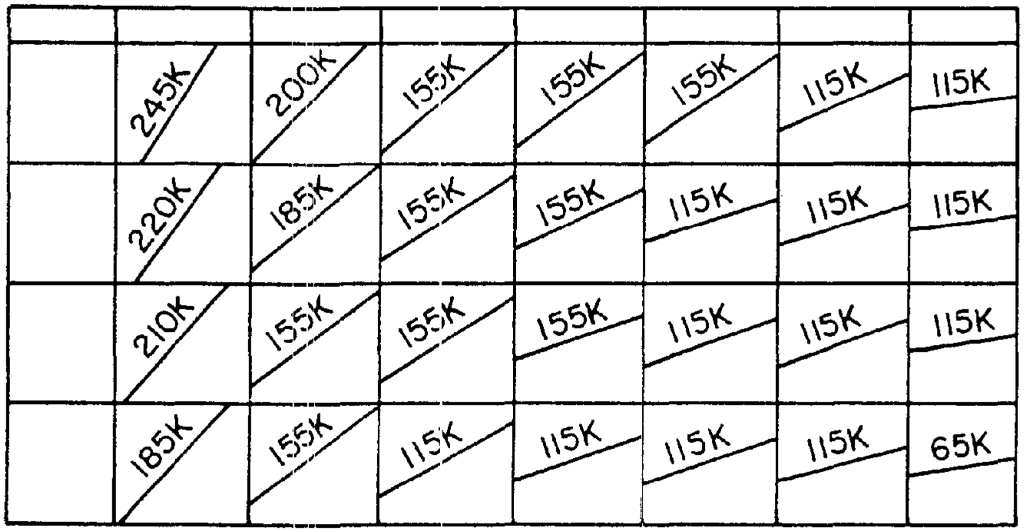

(a) STANDARD SPECIMEN, $M_B/V = 173''$

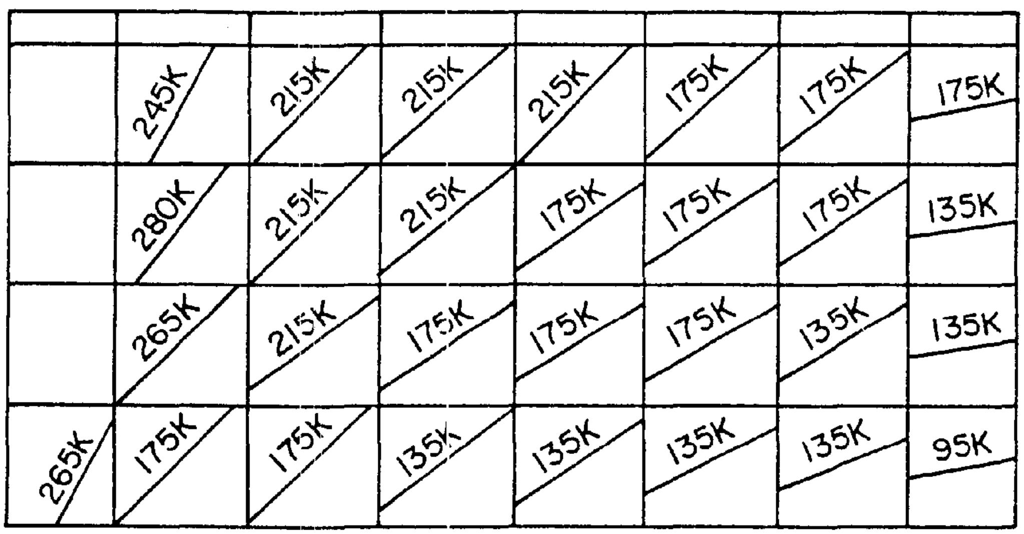

(b) STANDARD SPECIMEN, $M_B/V = 119''$

FIG. 8.4 CRACK DIRECTIONS FROM FINITE ELEMENT ANALYSES

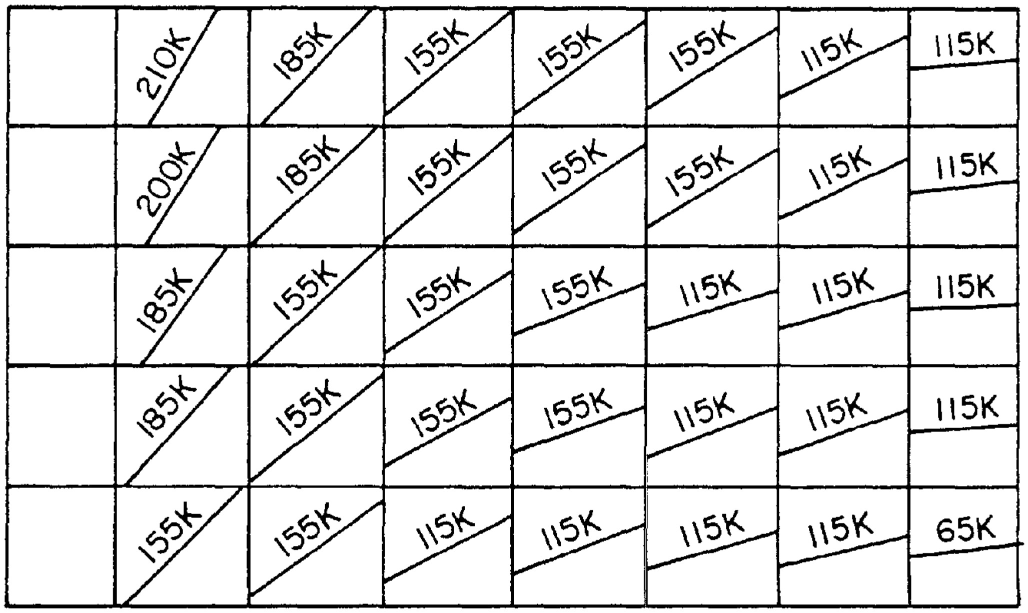

(c) WITHOUT SLABS, $M_B/V = 173''$

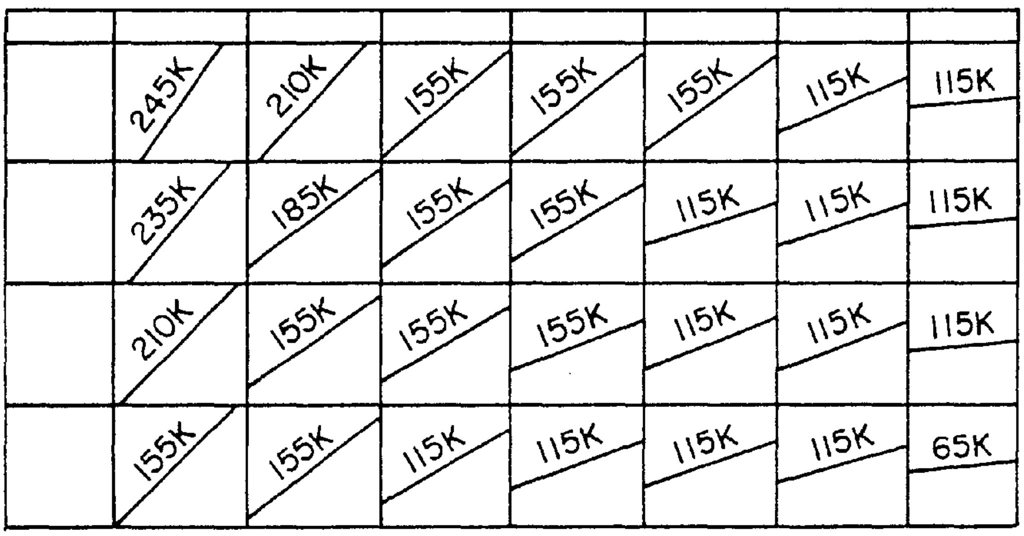

(d) $P_H = 0.0025$, $M_B/V = 173''$

FIG. 8.4 (CONT'D)

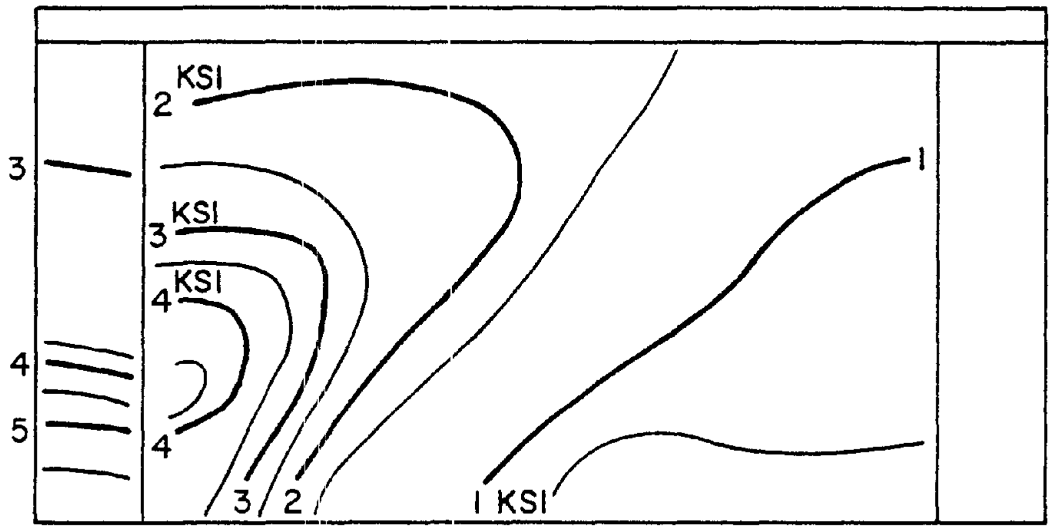

(a) STANDARD SPECIMEN, $M_B/V = 173''$, @ V = 255 KIPS

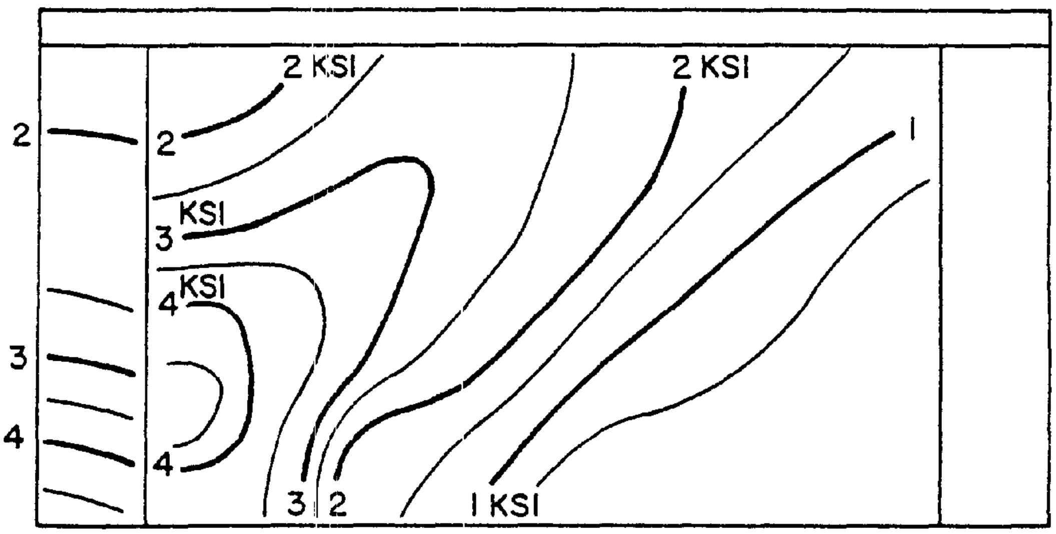

(b) STANDARD SPECIMEN, $M_B/V = 119''$, @ V = 310 KIPS

FIG. 8.5 CONTOUR LINES OF PRINCIPAL COMPRESSIVE STRESS

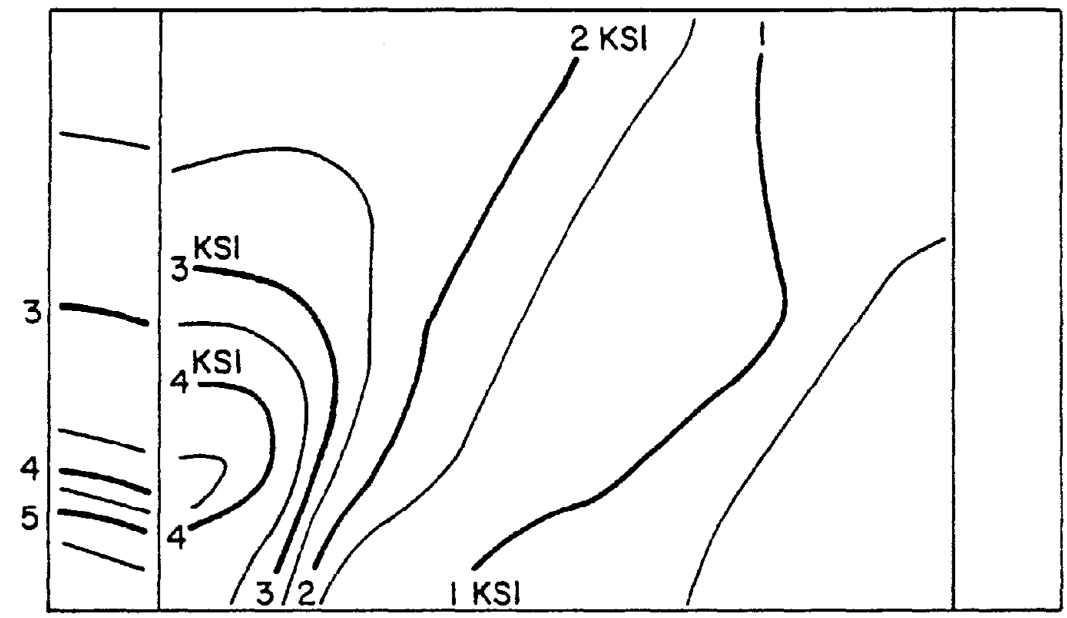

(c) WITHOUT SLABS, $M_B/V = 173''$, @ V = 245 KIPS

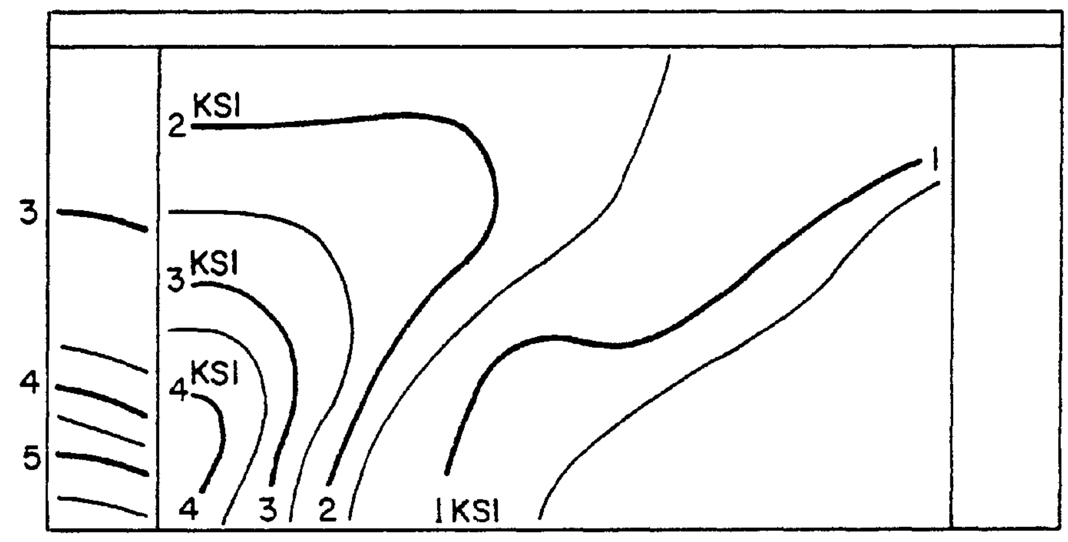

(d) WITH MIN. PANEL REINFORCEMENT (0.25%)
$M_B/V = 173''$ @ V = 245 KIPS

FIG. 8.5 (CONT'D)

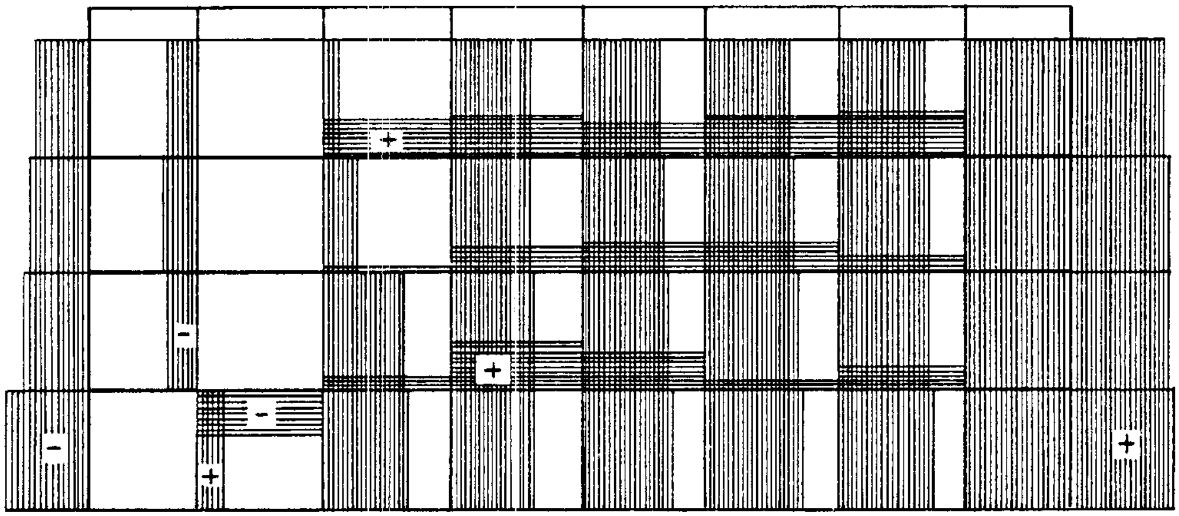

(a) STANDARD SPECIMEN, $M_B/V = 173''$, @ V = 255 KIPS

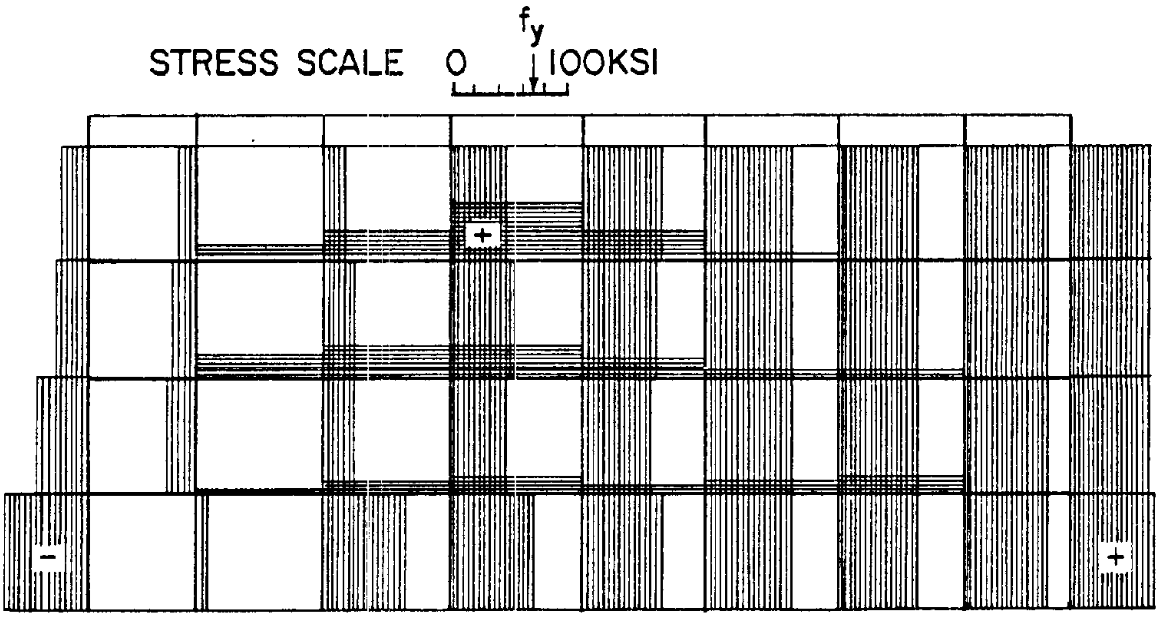

(b) STANDARD SPECIMEN, $M_B/V = 119''$, @ V = 310 KIPS

FIG. 8.6 REINFORCEMENT STRESS FROM FINITE ELEMENT ANALYSES

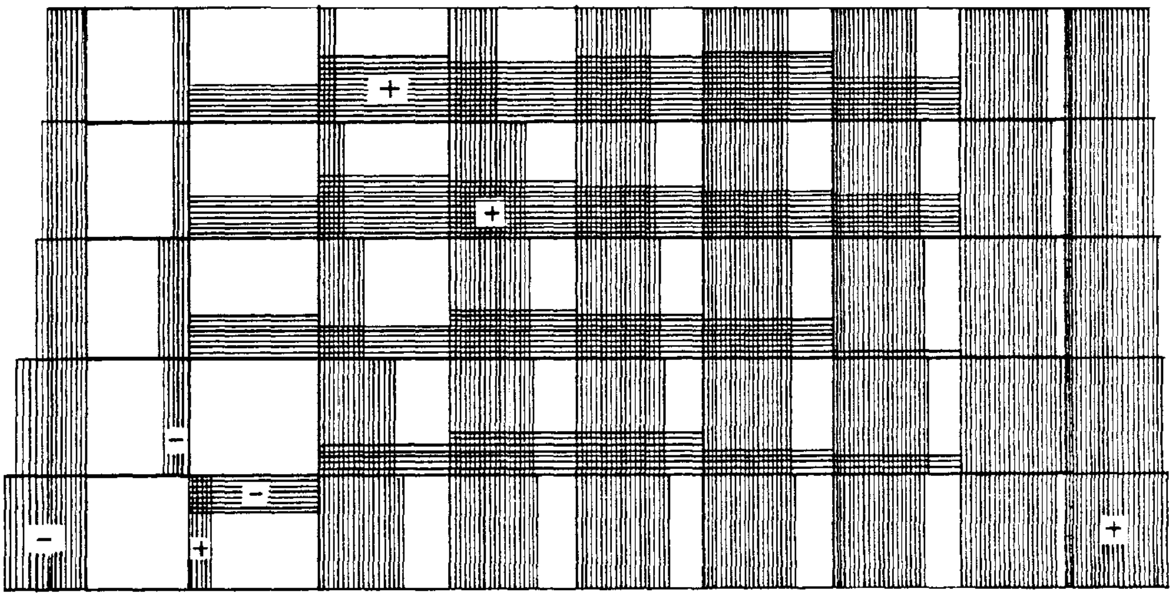

(c) WITHOUT SLABS, $M_B/V = 173''$, @ $V = 245$ KIPS

STRESS SCALE 0 f_y 100KSI

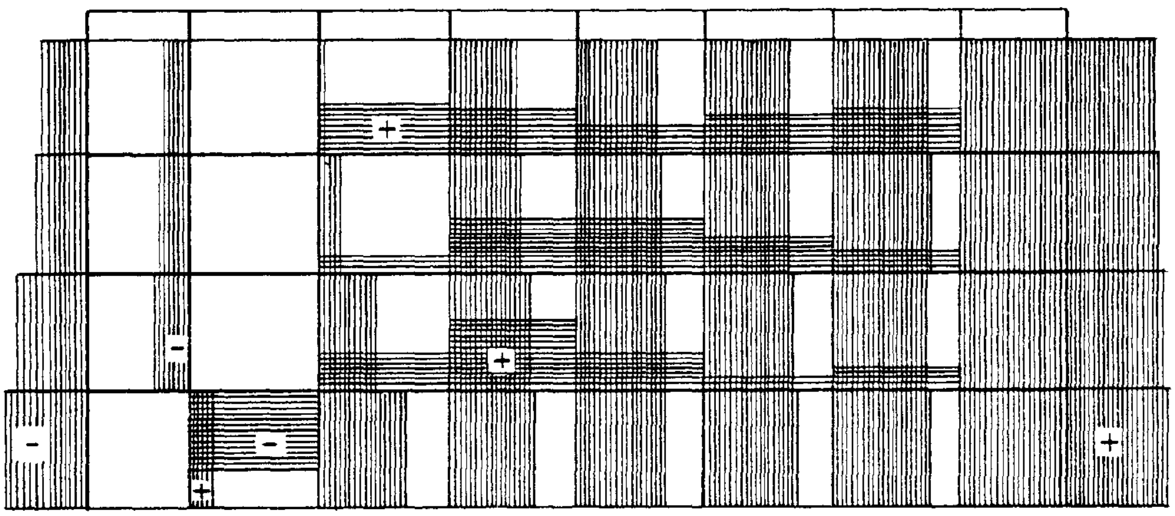

(d) WITH SLAB $P_H = 0.0025$, $M_B/V = 173''$, @ $V = 245$ KIPS

FIG. 8.6 (CONT'D)

APPENDIX A - ESTIMATED WEIGHT OF PROTOTYPE BUILDING

Floor area of building = 11340 ft^2

ROOF WEIGHT

SLAB	(0.150 k/cu.ft) (8/12) (11340)	= 1134 k
MECH. & RFG.	(0.020 ksf) (11340)	= 227 k
PARTITION	(0.010 ksf) (11340)	= 114 k
COLUMNS	(0.3 k/ft) (4.6') (36)	= 50 k
SHEAR WALLS	(0.150) (30 ft^2 x2+25 ft^2 x4) (4.1')	= 98 k
EXT. WALLS	(0.2 k/ft) (482')	= 96 k
SPANDREL	(0.3 k/ft) (482')	= 145 k
	TOTAL ROOF WEIGHT	= 1864 k

TYPICAL FLOOR WEIGHT (2nd Floor to 9th Floor)

SLAB	(0.150 k/cu.ft) (8/12) (11340)	= 1134 k
MECH. & FLG.	(0.010 ksf) (11340)	= 114 k
PARTITION	(0.020 ksf) (11340)	= 227 k
COLUMNS	(0.3 k/ft) (8.33) (36)	= 90 k
SHEAR WALLS	(0.150) (30 ft^2 x2+25 ft^2 x4) (8.33)	= 200 k
EXT. WALLS	(0.2 k/ft) (482')	= 96 k
SPANDREL	(0.3 k/ft) (482')	= 145 k
	TOTAL TYP. FLOOR WEIGHT	= 2006 k

FIRST FLOOR WEIGHT

SLAB	(0.150 k/cu.ft) (8/12) (11340)	= 1134 k
MECH. & FLG.	(0.010 ksf) (11340)	= 114 k
PARTITION	(0.020 ksf) (11340)	= 227 k
COLUMNS	(0.3 k/ft) (10.33) (36)	= 112 k
SHEAR WALLS	(0.150) (30x2+25x4) (10.33)	= 248 k
EXT. WALLS	(0.2 k/ft) 482)	= 96 k
SPANDREL	(0.3 k/ft) (482)	= 145 k
	TOTAL FIRST FLOOR WEIGHT	= 2076 k

TOTAL BUILDING WEIGHT = 1864+(8)(2006)+2076 = 19988 k

EARTHQUAKE ENGINEERING RESEARCH CENTER REPORTS

EERC 67-1 "Feasibility Study Large-Scale Earthquake Simulator Facility," by J. Penzien, J. G. Bouwkamp, R. W. Clough and D. Rea - 1967 (PB 187 905)

EERC 68-1 Unassigned

EERC 68-2 "Inelastic Behavior of Beam-to-Column Subassemblages Under Repeated Loading," by V. V. Bertero - 1968 (PB 184 888)

EERC 68-3 "A Graphical Method for Solving the Wave Reflection-Refraction Problem," by H. D. McNiven and Y. Mengi 1968 (PB 187 943)

EERC 68-4 "Dynamic Properties of McKinley School Buildings," by D. Rea, J. G. Bouwkamp and R. W. Clough - 1968 (PB 187 902)

EERC 68-5 "Characteristics of Rock Motions During Earthquakes," by H. B. Seed, I. M. Idriss and F. W. Kiefer - 1968 (PB 188 338)

EERC 69-1 "Earthquake Engineering Research at Berkeley," - 1969 (PB 187 906)

EERC 69-2 "Nonlinear Seismic Response of Earth Structures," by M. Dibaj and J. Penzien - 1969 (PB 187 904)

EERC 69-3 "Probabilistic Study of the Behavior of Structures During Earthquakes," by P. Ruiz and J. Penzien - 1969 (PB 187 886)

EERC 69-4 "Numerical Solution of Boundary Value Problems in Structural Mechanics by Reduction to an Initial Value Formulation," by N. Distefano and J. Schujman - 1969 (PB 187 942)

EERC 69-5 "Dynamic Programming and the Solution of the Biharmonic Equation," by N. Distefano - 1969 (PB 187 941)

Note: Numbers in parenthesis are Accession Numbers assigned by the National Technical Information Service. Copies of these reports may be ordered from the National Technical Information Service, 5285 Port Royal Road, Springfield, Virginia, 22161. Accession Numbers should be quoted on orders for the reports (PB --- ---) and remittance must accompany each order. (Foreign orders, add $2.50 extra for mailing charges.) Those reports without this information listed are not yet available from NTIS. Upon request, EERC will mail inquirers this information when it becomes available to us.

EERC 69-6 "Stochastic Analysis of Offshore Tower Structures," by A. K. Malhotra and J. Penzien - 1969 (PB 187 903)

EERC 69-7 "Rock Motion Accelerograms for High Magnitude Earthquakes," by H. B. Seed and I. M. Idriss - 1969 (PB 187 940)

EERC 69-8 "Structural Dynamics Testing Facilities at the University of California, Berkeley," by R. M. Stephen, J. G. Bouwkamp, R. W. Clough and J. Penzien - 1969 (PB 189 111)

EERC 69-9 "Seismic Response of Soil Deposits Underlain by Sloping Rock Boundaries," by H. Dezfulian and H. B. Seed - 1969 (PB 189 114)

EERC 69-10 "Dynamic Stress Analysis of Axisymmetric Structures under Arbitrary Loading," by S. Ghosh and E. L. Wilson - 1969 (PB 189 026)

EERC 69-11 "Seismic Behavior of Multistory Frames Designed by Different Philosophies," by J. C. Anderson and V. V. Bertero - 1969 (PB 190 662)

EERC 69-12 "Stiffness Degradation of Reinforcing Concrete Structures Subjected to Reversed Actions," by V. V. Bertero, B. Bresler and H. Ming Liao - 1969 (PB 202 942)

EERC 69-13 "Response of Non-Uniform Soil Deposits to Travel Seismic Waves," by H. Dezfulian and H. B. Seed - 1969 (PB 191 023)

EERC 69-14 "Damping Capacity of a Model Steel Structure," by D. Rea, R. W. Clough and J. G. Bouwkamp - 1969 (PB 190 663)

EERC 69-15 "Influence of Local Soil Conditions on Building Damage Potential during Earthquakes," by H. B. Seed and I. M. Idriss - 1969 (PB 191 036)

EERC 69-16 "The Behavior of Sands under Seismic Loading Conditions," by M. L. Silver and H. B. Seed - 1969 (AD 714 982)

EERC 70-1 "Earthquake Response of Concrete Gravity Dams," by A. K. Chopra - 1970 (AD 709 640)

EERC 70-2 "Relationships between Soil Conditions and Building Damage in the Caracas Earthquake of July 29, 1967," by H. B. Seed, I. M. Idriss and H. Dezfulian - 1970 (PB 195 762)

EERC 70-3 "Cyclic Loading of Full Size Steel Connections," by E. P. Popov and R. M. Stephen - 1970 (PB 213 545)

EERC 70-4 "Seismic Analysis of the Charaima Building, Caraballeda, Venezuela," by Subcommittee of the SEAONC Research Committee: V. V. Bertero, P. F. Fratessa, S. A. Mahin, J. H. Sexton, A. C. Scordelis, E. L. Wilson, L. A. Wyllie, H. B. Seed and J. Penzien, Chairman - 1970 (PB 201 455)

EERC 70-5 "A Computer Program for Earthquake Analysis of Dams," by A. K. Chopra and P. Chakrabarti - 1970 (AD 723 994)

EERC 70-6 "The Propagation of Love Waves across Non-Horizontally Layered Structures," by J. Lysmer and L. A. Drake - 1970 (PB 197 896)

EERC 70-7 "Influence of Base Rock Characteristics on Ground Response," by J. Lysmer, H. B. Seed and P. B. Schnabel - 1970 (PB 197 897)

EERC 70-8 "Applicability of Laboratory Test Procedures for Measuring Soil Liquefaction Characteristics under Cyclic Loading," by H. B. Seed and W. H. Peacock - 1970 (PB 198 016)

EERC 70-9 "A Simplified Procedure for Evaluating Soil Liquefaction Potential," by H. B. Seed and I. M. Idriss - 1970 (PB 198 009)

EERC 70-10 "Soil Moduli and Damping Factors for Dynamic Response Analysis," by H. B. Seed and I. M. Idriss - 1970 (PB 197 869)

EERC 71-1 "Koyna Earthquake and the Performance of Koyna Dam," by A. K. Chopra and P. Chakrabarti - 1971 (AD 731 496)

EERC 71-2 "Preliminary In-Situ Measurements of Anelastic Absorption in Soils Using a Prototype Earthquake Simulator," by R. D. Borcherdt and P. W. Rodgers - 1971 (PB 201 454)

EERC 71-3 "Static and Dynamic Analysis of Inelastic Frame Structures," by F. L. Porter and G. H. Powell - 1971 (PB 210 135)

EERC 71-4 "Research Needs in Limit Design of Reinforced Concrete Structures," by V. V. Bertero - 1971 (PB 202 943)

EERC 71-5 "Dynamic Behavior of a High-Rise Diagonally Braced Steel Building," by D. Rea, A. A. Shah and J. G. Bouwkamp - 1971 (PB 203 584)

EERC 71-6 "Dynamic Stress Analysis of Porous Elastic Solids Saturated with Compressible Fluids," by J. Ghaboussi and E. L. Wilson - 1971 (PB 211 396)

EERC 71-7 "Inelastic Behavior of Steel Beam-to-Column Subassemblages," by H. Krawinkler, V. V. Bertero and E. P. Popov - 1971 (PB 211 335)

EERC 71-8 "Modification of Seismograph Records for Effects of Local Soil Conditions," by P. Schnabel, H. B. Seed and J. Lysmer - 1971 (PB 214 450)

EERC 72-1 "Static and Earthquake Analysis of Three Dimensional Frame and Shear Wall Buildings," by E. L. Wilson and H. H. Dovey - 1972 (PB 212 904)

EERC 72-2 "Accelerations in Rock for Earthquakes in the Western United States," by P. B. Schnabel and H. B. Seed - 1972 (PB 213 100)

EERC 72-3 "Elastic-Plastic Earthquake Response of Soil-Building Systems," by T. Minami - 1972 (PB 214 868)

EERC 72-4 "Stochastic Inelastic Response of Offshore Towers to Strong Motion Earthquakes," by M. K. Kaul - 1972 (PB 215 713)

EERC 72-5 "Cyclic Behavior of Three Reinforced Concrete Flexural Members with High Shear," by E. P. Popov, V. V. Bertero and H. Krawinkler - 1972 (PB 214 555)

EERC 72-6 "Earthquake Response of Gravity Dams Including Reservoir Interaction Effects," by P. Chakrabarti and A. K. Chopra - 1972 (AD 762 330)

EERC 72-7 "Dynamic Properties on Pine Flat Dam," by D. Rea, C. Y. Liaw and A. K. Chopra - 1972 (AD 763 928)

EERC 72-8 "Three Dimensional Analysis of Building Systems," by E. L. Wilson and H. H. Dovey - 1972 (PB 222 438)

EERC 72-9 "Rate of Loading Effects on Uncracked and Repaired Reinforced Concrete Members," by S. Mahin, V. V. Bertero, D. Rea and M. Atalay - 1972 (PB 224 520)

EERC 72-10 "Computer Program for Static and Dynamic Analysis of Linear Structural Systems," by E. L. Wilson, K.-J. Bathe, J. E. Peterson and H. H. Dovey - 1972 (PB 220 437)

EERC 72-11 "Literature Survey - Seismic Effects on Highway Bridges," by T. Iwasaki, J. Penzien and R. W. Clough - 1972 (PB 215 613)

EERC 72-12 "SHAKE-A Computer Program for Earthquake Response Analysis of Horizontally Layered Sites," by P. B. Schnabel and J. Lysmer - 1972 (PB 220 207)

EERC 73-1 "Optimal Seismic Design of Multistory Frames," by V. V. Bertero and H. Kamil - 1973

EERC 73-2 "Analysis of the Slides in the San Fernando Dams during the Earthquake of February 9, 1971," by H. B. Seed, K. L. Lee, I. M. Idriss and F. Makdisi - 1973 (PB 223 402)

EERC 73-3 "Computer Aided Ultimate Load Design of Unbraced Multistory Steel Frames," by M. B. El-Hafez and G. H. Powell - 1973

EERC 73-4 "Experimental Investigation into the Seismic Behavior of Critical Regions of Reinforced Concrete Components as Influenced by Moment and Shear," by M. Celebi and J. Penzien - 1973 (PB 215 884)

EERC 73-5 "Hysteretic Behavior of Epoxy-Repaired Reinforced Concrete Beams," by M. Celebi and J. Penzien - 1973

EERC 73-6 "General Purpose Computer Program for Inelastic Dynamic Response of Plane Structures," by A. Kanaan and G. H. Powell - 1973 (PB 221 260)

EERC 73-7 "A Computer Program for Earthquake Analysis of Gravity Dams Including Reservoir Interaction," by P. Chakrabarti and A. K. Chopra - 1973 (AD 766 271)

EERC 73-8 "Behavior of Reinforced Concrete Deep Beam-Column Subassemblages under Cyclic Loads," by O. Kustu and J. G. Bouwkamp - 1973

EERC 73-9 "Earthquake Analysis of Structure-Foundation Systems," by A. K. Vaish and A. K. Chopra - 1973 (AD 766 272)

EERC 73-10 "Deconvolution of Seismic Response for Linear Systems," by R. B. Reimer - 1973 (PB 227 179)

EERC 73-11 "SAP IV: A Structural Analysis Program for Static and Dynamic Response of Linear Systems," by K.-J. Bathe, E. L. Wilson and F. E. Peterson - 1973 (PB 221 967)

EERC 73-12 "Analytical Investigations of the Seismic Response of Long, Multiple Span Highway Bridges," by W. S. Tseng and J. Penzien - 1973 (PB 227 816)

EERC 73-13 "Earthquake Analysis of Multi-Story Buildings Including Foundation Interaction," by A. K. Chopra and J. A. Gutierrez - 1973 (PB 222 970)

EERC 73-14 "ADAP: A Computer Program for Static and Dynamic Analysis of Arch Dams," by R. W. Clough, J. M. Raphael and S. Majtahedi - 1973 (PB 223 763)

EERC 73-15 "Cyclic Plastic Analysis of Structural Steel Joints," by R. B. Pinkney and R. W. Clough - 1973 (PB 226 843)

EERC 73-16 "QUAD-4: A Computer Program for Evaluating the Seismic Response of Soil Structures by Variable Damping Finite Element Procedures," by I. M. Idriss, J. Lysmer, R. Hwang and H. B. Seed - 1973 (PB 229 424)

EERC 73-17 "Dynamic Behavior of a Multi-Story Pyramid Shaped Building," by R. M. Stephen and J. G. Bouwkamp - 1973

EERC 73-18 "Effect of Different Types of Reinforcing on Seismic Behavior of Short Concrete Columns," by V. V. Bertero, J. Hollings, O. Kustu, R. M. Stephen and J. G. Bouwkamp - 1973

EERC 73-19 "Olive View Medical Center Material Studies, Phase I," by B. Bresler and V. V. Bertero - 1973 (PB 235 986)

EERC 73-20 "Linear and Nonlinear Seismic Analysis Computer Programs for Long Multiple-Span Highway Bridges," by W. S. Tseng and J. Penzien - 1973

EERC 73-21 "Constitutive Models for Cyclic Plastic Deformation of Engineering Materials," by J. M. Kelly and P. P. Gillis - 1973 (PB 226 024)

EERC 73-22 "DRAIN - 2D User's Guide," by G. H. Powell - 1973 (PB 227 016)

EERC 73-23 "Earthquake Engineering at Berkeley - 1973" - 1973 (PB 226 033)

EERC 73-24 Unassigned

EERC 73-25 "Earthquake Response of Axisymmetric Tower Structures Surrounded by Water," by C. Y. Liaw and A. K. Chopra - 1973 (AD 773 052)

EERC 73-26 "Investigation of the Failures of the Olive View Stairtowers during the San Fernando Earthquake and Their Implications in Seismic Design," by V. V. Bertero and R. G. Collins - 1973 (PB 235 106)

EERC 73-27 "Further Studies on Seismic Behavior of Steel Beam-Column Subassemblages," by V. V. Bertero, H. Krawinkler and E. P. Popov - 1973 (PB 234 172)

EERC 74-1 "Seismic Risk Analysis," by C. S. Oliveira - 1974 (PB 235 920)

EERC 74-2 "Settlement and Liquefaction of Sands under Multi-Directional Shaking," by R. Pyke, C. K. Chan and H. B. Seed - 1974

EERC 74-3 "Optimum Design of Earthquake Resistant Shear Buildings," by D. Ray, K. S. Pister and A. K. Chopra - 1974 (PB 231 172)

EERC 74-4 "LUSH - A Computer Program for Complex Response Analysis of Soil-Structure Systems," by J. Lysmer, T. Udaka, H. B. Seed and R. Hwang - 1974 (PB 236 796)

EERC 74-5 "Sensitivity Analysis for Hysteretic Dynamic Systems: Applications to Earthquake Engineering," by D. Ray - 1974 (PB 233 213)

EERC 74-6 "Soil-Structure Interaction Analyses for Evaluating Seismic Response," by H. B. Seed, J. Lysmer and R. Hwang - 1974 (PB 236 519)

EERC 74-7 Unassigned

EERC 74-8 "Shaking Table Tests of a Steel Frame - A Progress Report," by R. W. Clough and D. Tang - 1974

EERC 74-9 "Hysteretic Behavior of Reinforced Concrete Flexural Members with Special Web Reinforcement," by V. V. Bertero, E. P. Popov and T. Y. Wang - 1974 (PB 236 797)

EERC 74-10 "Applications of Reliability-Based, Global Cost Optimization to Design of Earthquake Resistant Structures," by E. Vitiello and K. S. Pister - 1974 (PB 237 231)

EERC 74-11 "Liquefaction of Gravelly Soils under Cyclic Loading Conditions," by R. T. Wong, H. B. Seed and C. K. Chan - 1974

EERC 74-12 "Site-Dependent Spectra for Earthquake-Resistant Design," by H. B. Seed, C. Ugas and J. Lysmer - 1974

EERC 74-13 "Earthquake Simulator Study of a Reinforced Concrete Frame," by P. Hidalgo and R. W. Clough - 1974 (PB 241 944)

EERC 74-14 "Nonlinear Earthquake Response of Concrete Gravity Dams," by N. Pal - 1974 (AD/A006583)

EERC 74-15 "Modeling and Identification in Nonlinear Structural Dynamics, I - One Degree of Freedom Models," by N. Distefano and A. Rath - 1974 (PB 241 548)

EERC 75-1 "Determination of Seismic Design Criteria for the Dumbarton Bridge Replacement Structure, Vol. I: Description, Theory and Analytical Modeling of Bridge and Parameters," by F. Baron and S.-H. Pang - 1975

EERC 75-2 "Determination of Seismic Design Criteria for the Dumbarton Bridge Replacement Structure, Vol. 2: Numerical Studies and Establishment of Seismic Design Criteria," by F. Baron and S.-H. Pang - 1975

EERC 75-3 "Seismic Risk Analysis for a Site and a Metropolitan Area," by C. S. Oliveira - 1975

EERC 75-4 "Analytical Investigations of Seismic Response of Short, Single or Multiple-Span Highway Bridges," by Ma-chi Chen and J. Penzien - 1975 (PB 241 454)

EERC 75-5 "An Evaluation of Some Methods for Predicting Seismic Behavior of Reinforced Concrete Buildings," by Stephen A. Mahin and V. V. Bertero - 1975

EERC 75-6 "Earthquake Simulator Study of a Steel Frame Structure, Vol. I: Experimental Results," by R. W. Clough and David T. Tang - 1975 (PB 243 981)

EERC 75-7 "Dynamic Properties of San Bernardino Intake Tower," by Dixon Rea, C.-Y. Liaw, and Anil K. Chopra - 1975 (AD/A008406)

EERC 75-8 "Seismic Studies of the Articulation for the Dumbarton Bridge Replacement Structure, Vol. I: Description, Theory and Analytical Modeling of Bridge Components," by F. Baron and R. E. Hamati - 1975

EERC 75-9 "Seismic Studies of the Articulation for the Dumbarton Bridge Replacement Structure, Vol. 2: Numerical Studies of Steel and Concrete Girder Alternates," by F. Baron and R. E. Hamati - 1975

EERC 75-10 "Static and Dynamic Analysis of Nonlinear Structures," by Digambar P. Mondkar and Graham H. Powell - 1975 (PB 242 434)

EERC 75-11 "Hysteretic Behavior of Steel Columns," by E. P. Popov, V. V. Bertero and S. Chandramouli - 1975

EERC 75-12 "Earthquake Engineering Research Center Library Printed Catalog" - 1975 (PB 243 711)

EERC 75-13 "Three Dimensional Analysis of Building Systems," Extended Version, by E. L. Wilson, J. P. Hollings and H. H. Dovey - 1975 (PB 243 989)

EERC 75-14 "Determination of Soil Liquefaction Characteristics by Large-Scale Laboratory Tests," by Pedro De Alba, Clarence K. Chan and H. Bolton Seed - 1975

EERC 75-15 "A Literature Survey - Compressive, Tensile, Bond and Shear Strength of Masonry," by Ronald L. Mayes and Ray W. Clough - 1975

EERC 75-16 "Hysteretic Behavior of Ductile Moment Resisting Reinforced Concrete Frame Components," by V. V. Bertero and E. P. Popov - 1975

EERC 75-17 "Relationships Between Maximum Acceleration, Maximum Velocity, Distance from Source, Local Site Conditions for Moderately Strong Earthquakes," by H. Bolton Seed, Ramesh Murarka, John Lysmer and I. M. Idriss - 1975

EERC 75-18 "The Effects of Method of Sample Preparation on the Cyclic Stress-Strain Behavior of Sands," by J. Paul Mulilis, Clarence K. Chan and H. Bolton Seed - 1975

EERC 75-19 "The Seismic Behavior of Critical Regions of Reinforced Concrete Components as Influenced by Moment, Shear and Axial Force," by B. Atalay and J. Penzien - 1975

EERC 75-20 "Dynamic Properties of an Eleven Story Masonry Building," by R. M. Stephen, J. P. Hollings, J. G. Bouwkamp and D. Jurukovski - 1975

EERC 75-21 "State-of-the-Art in Seismic Shear Strength of Masonry - An Evaluation and Review," by Ronald L. Mayes and Ray W. Clough - 1975

EERC 75-22 "Frequency Dependencies Stiffness Matrices for Viscoelastic Half-Plane Foundations," by Anil K. Chopra, P. Chakrabarti and Gautam Dasgupta - 1975

EERC 75-23 "Hysteretic Behavior of Reinforced Concrete Framed Walls," by T. Y. Wong, V. V. Bertero and E. P. Popov - 1975